Cornell NanoScale Facility (CNF)

2024-2025

RESEARCH ACCOMPLISHMENTS

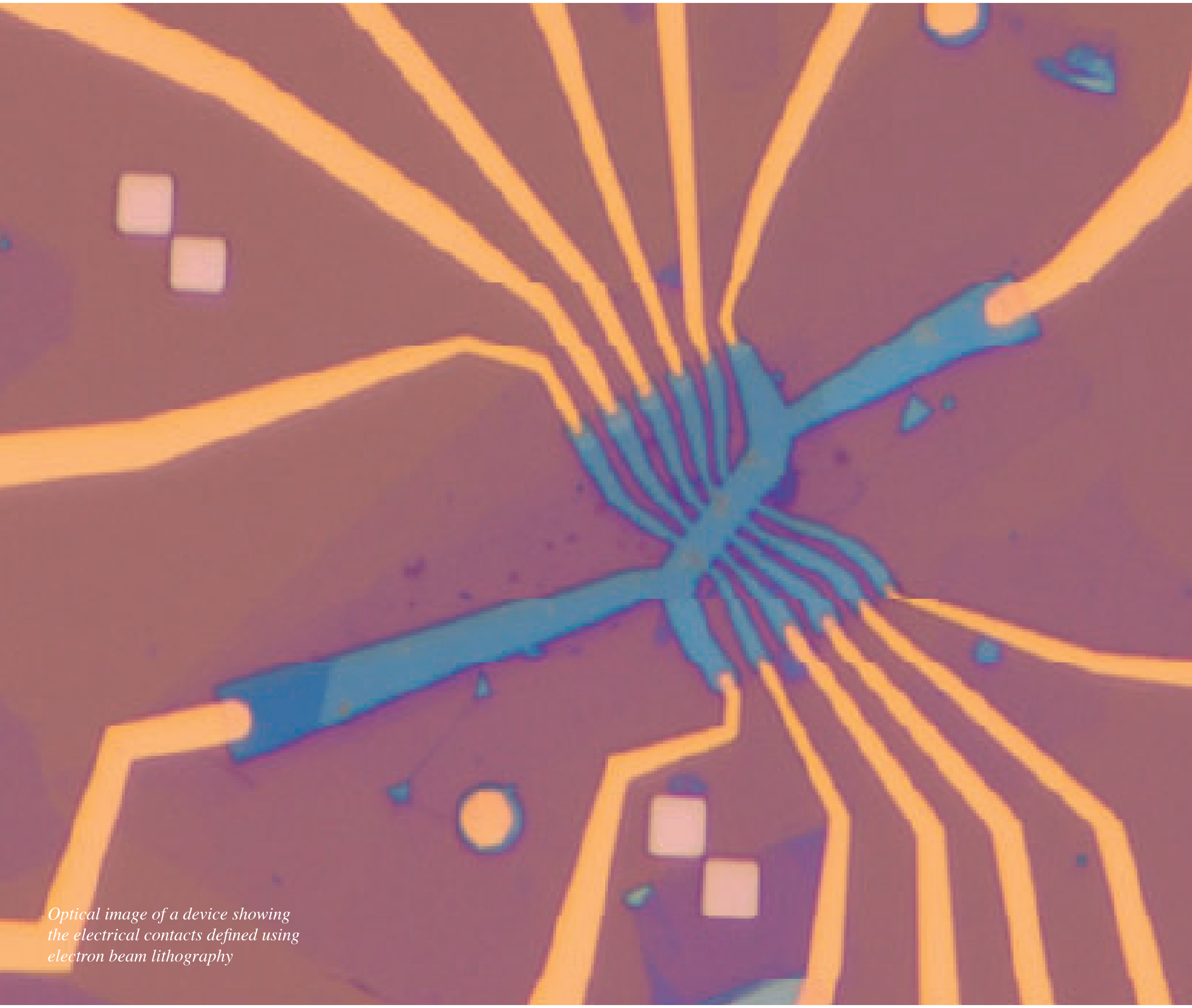

Optical image of a device showing the electrical contacts defined using electron beam lithography

CNF

Cornell NanoScale
Science and Technology Facility

250 Duffield Hall • 343 Campus Road • Ithaca NY 14853-2700
Phone: 607.255.2329 • Fax: 607.255.8601
Email: information@cnf.cornell.edu • Website: www.cnf.cornell.edu

Cornell NanoScale Facility 2024-2025 Research Accomplishments

CNF Lester B. Knight Director:
Jeeyoung Judy Cha

CNF Director of Operations:
Ronald Olson

Cornell NanoScale Facility (CNF) is a member of the
National Nanotechnology Coordinated Infrastructure *(www.nnci.net)*
and is supported by the National Science Foundation under Grant No. NNCI-2025233,
the New York State Office of Science, Technology and Academic Research,
Cornell University, Industry, and our Users.

The 2024-2025 CNF Research Accomplishments are also available on the web in full color:
http://cnf.cornell.edu/publications/research_accomplishments

National Nanotechnology Coordinated Infrastructure

Cornell University

NEW YORK STATE OF OPPORTUNITY. Empire State Development

NSF

2024-2025 CNF Research Accomplishments

TABLE of CONTENTS

BIOLOGICAL APPLICATIONS, 2-34

CHEMISTRY, 36-38

ELECTRONICS, 40-64

MATERIALS, 66-96

MECHANICAL DEVICES, 98-102

OPTICS & OPTO-ELECTRONICS, 104-118

PHYSICS & NANO-STRUCTURE PHYSICS, 120-180

PROCESS & CHARACTERIZATION, 182-202

PHOTOGRAPHY CREDITS

This year's front cover image is from the report "Fabrication of 2D Graphene Devices for Low Temperature Transport Measurement"; CNF Project 3125-23, Principal Investigator: Kenji Yasuda; Users: Benjamin Byrd, Lujin Min, and Zhen Yang; Affiliation: Department of Physics, Cornell University — and was used with their permission. The full report starts on page 168.

This year's back cover image is from the report "Fabrication of Fluxonium-Like Qubits"; CNF Project 3125-23, Principal Investigator: Ivan Pechenezhskiy; Users: Benjamin Byrd, and Kesavan Manivannan; Affiliation: Department of Physics, Syracuse University — and was used with their permission. The full report starts on page 156.

COMMENTS, FEEDBACK, AND SUGGESTIONS ARE ALWAYS WELCOME.

FEEL FREE TO USE OUR ONLINE USER COMMENT FORM AT HTTPS://WWW.CNFUSERS.CORNELL.EDU/USER_FEEDBACK

2024-2025 CNF Research Accomplishments

DIRECTORS' INTRODUCTION

The Cornell NanoScale Science and Technology Facility (CNF) takes pride in presenting the research achievements of our users and research groups who utilize the extensive array of resources provided by the CNF. We appreciate all the contributors who provided input to this publication. The Research Accomplishments showcases excellence in research while underscoring the diverse array of cutting-edge advancements spanning various fields of science and technology. Together with the spotlight on 104 featured research reports, CNF-related patents, presentations, and publications (totaling over 400 in 2024) have been included.

NNCI

For the last 10 years CNF has been a member of the National Nanotechnology Coordinated Infrastructure (NNCI), supported by the National Science Foundation (NSF). Cornell was one of 16 collaborative sites within this national user consortium, dedicated to providing start-to- finish fabrication and characterization capabilities to a diverse range of users from both academia and industry. As of August 31, 2025, funding from this NSF program ended. We have been granted a no-cost extension from September 1, 2025 to August 31, 2026 to facilitate the orderly wind-down of our programs. Earlier this year the CNF submitted "The Year 10 Annual Report" and a final report will be submitted after September 2026. We gratefully acknowledge the steadfast support from the NSF over the years, and are looking ahead to the future and the next nanotechnology infrastructure program. In the meantime, we will continue to support the research activities of both Cornell and non-Cornell users.

NORDTECH

In 2023, CNF received $8.2 million to expand fabrication capabilities through NORDTECH, one of eight Microelectronics (ME) Commons hubs selected by the Department of Defense (DOD) and supported by the CHIPS and Science Act. This funding is part of a $2 billion initiative to enhance U.S. microelectronics development. CNF is a founding partner of the NORDTECH hub alongside IBM, University at Albany, NY CREATES, and RPI. This initial investment was used to expand our capabilities in Quantum Science and Technology, Heterointegration, and 200mm wafer processing. These upgrades represent CNF's largest capital expansion since its inception, with numerous new tools and capabilities acquired, installed, or qualified over the past year (see Table 1). The ME Commons seeks to bolster U.S. microelectronics development and manufacturing in support of DOD mission priorities, particularly by promoting the "Lab to Fab" transition.

NEW TOOLS AND CAPABILITIES

New, more advanced capabilities are constantly being added at CNF to improve the user experience and enable new frontiers of research. Acquisitions of new tools of interest are based on consultation with the CNF user community, our User Committee, the Executive Committee, External Advisory Board, and Cornell faculty. The following equipment has been acquired over the past year and either is installed or being installed. Please visit our website https://www.cnf.cornell.edu/equipment for more information.

EDUCATION AND OUTREACH

CNF has a comprehensive education and workforce development effort that spans K through 12, post-secondary, professional, and public audiences. CNF views traditional education and outreach programs as critical pipeline for developing a skilled high-tech workforce. There has been an increased focus on workforce development brought about by programs such as the CHIPS & Science Act and the DOD ME Commons programs. This past year CNF reached over 9,000 individuals through 139 events, offering hands on learning and engagement opportunities to build awareness and interest in nanotechnology. CNF programs include: Nanooze, a kid-friendly science magazine distributed to over 100,000 readers annually; our biannual "Technology and Characterization at the Nanoscale" (TCN), a three-day course that covers core nanotechnologies taught by CNF staff; our New Visions Engineering Accelerated Training for Labor Advancement in Semiconductors (ATLAS) program in collaboration with Tompkins Seneca Tioga (TST) Boards of Cooperative Educational

Recent Capital Equipment Acquisitions			
200 mm capable - Zeiss GeminiSEM 560 *Funded by ME Commons*	**Plasma-Therm Plasma Dicing System** *Funded by ME Commons*	**Osiris- Temporary Bonding and Debonding** *Funded by ME Commons*	**Logitech Orbis 200 mm CMP Upgrade Kit** *Funded by ME Commons*
AJA UHV Sputter Deposition- Quantum applications *Funded by ME Commons*	**YES Polyimide Cure Oven** *Funded by ME Commons*	**Nano- Master SWC-4000** Brush Cleaner *Funded by ME Commons*	**Heidelberg MLA150-** Maskless lithography *Funded by ME Commons*
Angstrom UHV E-beam Evap - superconducting materials and JJs *Funded by ME Commons*	**KLA SPTS E2 XeF2 Etcher** *Funded by ME Commons*	**REYNOLDSTECH Custom Electroplating** *Funded by ME Commons*	**Oxford ASP ALD –** superconducting materials and nitride materials *Funded by ME Commons*
SEKI Microwave Plasma CVD – quantum grade diamond *Funded by ME Commons*	**Oxford PlasmaPro 100 Cobra 300** – oxide and diamond etching *Funded by ME Commons*	**Disco Wafer Back Grinding and DI H20 Recycling Unit** *Funded by ME Commons*	**Keyence Digital Microscope** *Funded by ME Commons*
AJA Q Deposition system - for superconducting materials and devices	**KLA Filmetrics R50-200** – Resistivity	**Oxford Cobra ALE**- for quantum device etching	**TPT Semi-Automatic Thermosonic Wire Bonder**

Table 1: Tools/capabilities that have been acquired or installed/qualified over the past year at the CNF.

Services (BOCES), which provides high school students access to the CNF cleanroom; Micron “Chip Camps” that provide middle school students with cleanroom and nanotechnology experiences; and a High Purity Welding program that introduces vocational students to high tech career paths, in partnership with BOCES. The CNF also supported internships and research experience for undergraduates (REUs). CNF staff members played key mentoring roles, ensuring the interns and REUs gained valuable skills and experience to support their career development. CNF also continued its annual outreach events, including Tompkins County Expanding Your Horizons, 4-H Career Explorations, New York State Fair, alumni reunion tours, STEM EXPO (Junior First Lego League 2.0), Kangaroo Math, and various science classroom visits.

CNF has been working with Tompkins-Cortland Community College (TC3) to establish a Micro-Nanotechnology (MNT) concentration within their existing A.A.S. degree program. This past year CNF staff have assisted with the procurement of vacuum and metrology equipment that will enable additional micro-credentials within the existing A.A.S degree programs at TC3. In addition, CNF and TC3 also collaborate in the NSF funded Microfabrication and Nanotechnology Certificate Program (MNCP) for veterans in partnership with Penn State University, providing veterans with pathways into the semiconductor industry.

Our most compelling education and workforce development activity is our digital learning and virtual reality (VR) educational initiative. We are working with e-Cornell to create digital classroom content focused on the core principles of semiconductor processing. And over the last two years the CNF has been working with the staff at the Cornell Center for Teaching Innovation, to develop a series of short (~20 minutes) VR cleanroom training experiences which bring learners directly into the CNF using high resolution, immersive 360-degree video with embedded interactive content and quizzes. This effort, led by CNF Workforce Development Program Manager Tom Pennell, will ultimately produce 20 – 30 modules that create a unique, immersive learning experience accessible from anywhere, expanding Cornell’s educational reach far beyond the walls of the CNF cleanroom facility. To date, CNF has had over 1,600 users of our VR educational content with over 1,000 hours of combined time spent in VR. The VR modules were also used as supplementary materials in Cornell engineering courses, such as MSE5410/ECE4360 “Nanofabrication and Characterization of Electronics.”

STAFF AWARDS

Congratulations to CNF staff members **Stacy Clementson** and **Jeremy Clark** who were honored with a national award from the NNCI. Annually, the NNCI acknowledges the efforts of NNCI staff who provide exceptional service and support to network users in the categories of Technical Staff, Education and Outreach, and User Support. This past year Stacy was recognized by the NNCI in the **User Support** category and Jeremy Clark was honored with the Technical Staff award. Both received plaques, acknowledgement at the NNCI Annual Conference in Louisville and are recognized on the NNCI website and in the NNCI yearly report to the NSF. We are proud of their efforts and contributions.

The exceptional staff at the CNF have been consistently recognized with NNCI Outstanding Staff Member Awards. Past award recipients include Chris Alpha – Technical Staff (2018), Tom Pennell – Education and Outreach (2020), Phil infante – Technical staff (2021) and Mike Skvarla – User Support (2021), Melanie -Clair Mallison – Education and Outreach (2022) and Aaron Windsor (2022) – User Support, and Karis Musa – User Support (2023).

Congratulations to Tom Pennell who was awarded an Hornory EPICC award in the category of “Purpose” by the College of Engineering for his impact on workforce development activities. In 2024 Tom was also honored with the Distinguished Alumni Award from TC3. This award recognizes TC3 graduates who have made a meaningful impact through their careers and service to the community.

STAFF UPDATES

Departures

Melanie-Claire Mallison retired in September 2024 after 28 years at CNF. Melanie was responsible for the CNF REU program, the CNF Research Accomplishments, newsletters, corporate sponsors, visitors, web site, and other forms of external communications.

Alan Bleier retired in January 2025 after 24 years at CNF. Alan supported CNF users for both scanning electron microscopy and electron beam lithography.

In June 2025 Roberto Panepucci left CNF to become Managing Director of the Microelectronics Research Center at the University of Texas at Austin.

In August 2025 Paul Pelletier who specialized in the installation of the NORDETCH equipment left CNF to start Northeast Orbital Welding, a startup business based in the Albany area.

Welcomes

In January 2025, Emma Carlo, a recent graduate from SUNY Oneonta with a degree in Communications, joined CNF as Student Program and Events Coordinator. In her role, she oversees the REU program, manages and updates CNF publications, website, and social media, and coordinates CNF events.

Philip Schneider joined CNF in February 2025. Phillip holds a B.S. degree in Nanoscale Engineering from SUNY Poly and an M.S. degree in Materials Science from SUNY Binghamton. He most recently served as a Metrology Engineer at Wolfspeed in Marcy, NY. Philip supports both CNF’s metrology and Reactive Ion Etching technology.

Shilling Du, Ph.D joined CNF in April 2025 with a Ph.D. from Washington University in St. Louis. She has expertise in quantum devices and will largely support the new NORDTECH quantum deposition tools.

With your support, we look forward to the next nanotechnology infrastructure and continuing CNF’s role as one of the nation’s leading academic nanofabrication facilities, providing world class facilities and technical expertise to our user community. We appreciate all the contributors who provided input to this publication, which can also be found online at https://www.cnf.cornell.edu/publications/research_accomplishments We welcome your comments, questions and suggestions. Use the link below to share your feedback with us: https://cornellcnf.link/feedback

Judy Cha, Lester B. Knight Director

Allison Godwin, Associate Director

Ron Olson, Director of Operations

Lynn Rathbun, Laboratory Manager

2024-2025 CNF Research Accomplishments

A SELECTION OF 2024 CNF-RESEARCH-RELATED PATENTS, PRESENTATIONS, AND PUBLICATIONS

"(Real2Sim)-1:3D Branch Point Cloud Completion for Robotic Pruning in Apple Orchards"; Tian Qiu, Alan Zoubi, Nikolai Spine, Lailang Cheng, Yu Jiang, 2024 IEEE/RSJ International Conference on Intelligent Robots and Systems (IROS), 23-30 (2024).

">200 GHz fMAX MBE Grown AlScN/GaN High Electron Mobility Transistors"; K. Nomoto, T.S. Nguyen, C.P. Savant, D. Jena, And H.G. Xing, 15th Topical Workshop on Heterostructure Microelectronics (TWHM) 2024, Aug. 26-29, 2024, Sendai, Japan (2024).

"1D Topological Systems for Next-Generation Electronics"; Judy Cha, Rice Workshop on Quantum Materials Synthesis (4/2024, Houston, TX) (2024).

"1D Topological Systems for Next-Generation Electronics"; Judy Cha, XIth Symposium in Quantum Materials Synthesis (1/2024, Physikzentrum Bad Honnef, Germany) (2024).

"2D Micropatterned Membrane for Studying Mechanotransduction in Striated Muscle"; Eitan Jentis, Poster Presentation (2024).

"2D Nanopatterned Membrane for Studying Mechanotransduction in Striated Muscle"; Eitan Jentis, Julie Heffler Ph. D., Jan Lammerding Ph. D., Biomedical Engineering Society (2024).

"2D Nanopatterned Membrane for Studying Mechanotransduction in Striated Muscle"; Eitan Jentis, Julie Heffler Ph. D., Jan Lammerding Ph. D., CNF Annual Meeting Poster Session 17 September 2024 (2024).

"3 W/Mm Output Power, High Breakdown in Volume-Scalable MOCVD- Grown AlN-Buffer HEMTs on 4-Inch Sic"; Reet Chaudhuri, Austin Hickman, Shankar Miller-Murthy, International Workshop on Nitride Semiconductors November 8, 2024 (2024).

"A 3D In Vitro Model of Secondary Lymphatic Valve Morphogenesis Reveals WNT as a Therapeutic Target for Inflammation-Induced Lymphatic Valve Dysfunction"; Renhao Lu, Rafael S. Czepielewski, And Esak Lee, Lymphatics Gordon Research Conference 2024, Ventura, CA (2024).

"A D-Band Frequency-Doubling Solid-State Traveling-Wave Amplifier"; L. Li, T. Li, J. C. M. Hwang, And P. Fay, In Gov. Microcircuits Appl. Critical Technol. Conf. (Gomactech), Charleston, SC, USA, March 2024, Pp. 1-6 (2024).

"A D-Band Frequency-Doubling Traveling-Wave Amplifier Through Monolithic Integration of a SiC SIW and GaN HEMTs"; L. Li, P. Fay, And J. C. M. Hwang, IEEE Journal of Microwaves, Volume 4, No. 1, Pp. 158-166, Jan. 2024, Doi: 101109/JMW.2023.3340117 (2024).

"A D-Band Traveling-Wave Amplifier by Embedding GaN HEMTs as Current Probes in a SiC SIW"; L. Li, T. Li, P. Fay, and J. C. M. Hwang, In 2024 IEEE MTT-S Int. Microw. Symp. (IMS) Dig., Washington, DC, USA, June 2024, Pp. 686-689, Doi: 10.1109/IMSS40175.2024.10600279 (2024).

"A Design Methodology for a Dual-Mode Coplanar Waveguide Junction Circulator"; K. Srinivasan, A. El-Ghazaly, International Microwave and Antenna Symposium (IMAS), Marrakesh, Morocco (2024).

"A Fully Programmable On-Chip Planar Waveguide for Machine Learning"; Stein, M. M., Onodera, T., Ash, B. A., Sohoni, M. M., Bosch, M., Yanagimoto, R., … & Mcmahon, P. L., In CLEO: Science and Innovations (Pp. SF2M-1). Optica Publishing Group (2024).

"A Fully Programmable Two-Dimensional Photonic Chip for Machine Learning"; Onodera, T., Stein, M. M., Ash, B. A., Sohoni, M. M., Bosch, M. J., Yanagimoto, R., … & Mcmahon, P. L., Nanoscience + Engineering 2024: In Photonic Computing: From Materials and Devices to Systems and Applications (P. PC1311303) SPIE. (2024).

"A High Throughput Array Microhabitat Platform Reveals How Light and Nitrogen Colimit the Growth of Algal Cells"; Fangchen Liu, Larissa Gaul, Andrea Giometto & Mingming Wu, Scientific Reports 14, Article Number: 9860 (2024).

"A Human Initial Lymphatic Chip Reveals Distinct Mechanisms of Primary Lymphatic Valve Dysfunction in Acute and Chronic Inflammation"; Kraus S., Lee E., Biomedical Engineering Society (BMES) Annual Meeting, Baltimore, MD (2024).

"A Human Initial Lymphatic Chip Reveals Distinct Mechanisms of Primary Lymphatic Valve Dysfunction in Acute and Chronic Inflammation"; Kraus S., Lee E., Gordon Research Conference (GRC Lymphatics, Ventura, CA, 2024) (2024).

"A Miniaturized High-Density Soft Brain Probe for Stable, Long-Term Hippocampus Recordings"; Jaehyo Park (Presenter), Zifang Zhao, Lindsay Karaba, Azahara Olivia, Antonio Fernandez-Ruiz, 2024 NNN Symposium (2024).

"A Mm-Wave Blocker-Tolerant Harmonic-Resilient N-Path Mizer-First Receiver with 6.2 dB NF and 5 D=dBm)) B-B1dB"; Shimin Huang, Jamie C. Ye, Shahaboddin Ghajari, Alyosha C. Molnar, 2024 IEEE Custom Integrated Circuits Conference (CICC), Denver, CO, USA, 2024, Pp. 1-2 (2024).

"A Multiplexed Microfluidic Continuous-Flow Electroporation System for Efficient Cell Transfection"; Jacob A. Vanderburgh, Grant T. Corso, Stephen L. Levy, & Harold G. Craighead, Springer Nature Link: Volume 26, Article Number 10, 2024 (2024).

"A Pseudo-Surfactant Chemical Permeation Enhancer to Treat Otitis Media Via Sustained Transtympanic Delivery of Antibiotics"; Sophie S. Liu, Joanna M. White, Zhongmou Chao, Ruye Li, Shuxian Wen, Ally Garza, Wenjing Tang, Xiaojing Ma, Pengyu Chen, Susan Daniel, Frank S. Bates, Jingjie Yeo, Michelle A. Calabrese, Rong Yang, Advanced Healthcare Materials, Volume 13, Issue 22, September 1, 2024. 2400457 (2024).

"A Quantized Anomalous Hall Effect Above 4.2 K in Stacked Topological Insulator/Magnet Bilayers"; Rakshit Jain, Matthew Roddy, Vishakha Gupta, Benjamin Huang, Hasan M. Sayeed, Husain F. Alnaser, Amit Vashist, Kenji Watanabe, Takashi Taniguchi, Vikram V. Deshpande, Taylor D. Sparks, Daniel C. Ralph, Mesoscale and Nanoscale Physics arXiv: 2412.05380 6 December 2024 (2024).

"A Randomized Trial of Aerobic Exercise in Colorectal Cancer: Rationale, Design, Recruitment, and Exercise Adherence Results"; Stephanie LE Compton, Shengping Yang, Lauren S Maniscalco, Reem A Muhsen, Pratibha Shrestha, Xiaocheng Wu, Kaylee T Woodard, Elizabeth RM Zunica, Eunhan Cho, Rachel L Wall, John Brown, Anjana Jayaraman, Brian J Kirby, L Anne Gilmore, Frank L Greenway, Guillaume Spielmann, Justin C Brown, Contemporary Clinical Trials Volume 146, Pp. 107702 2024/11/1 (2024).

"A Sound Approach for Ova Denudation"; Amir Mokhtare Ph. D., Amirhossein Favakeh M.S., Philip Xie B.Sc., Zev Rosenwaks M.D., Alireza Abbaspourrad Ph.D., Gianpiero Palermo M.D. Ph.D., Science Direct: F&S Science (2024).

"A<5dBNF, >17dbm OP1dB F-Band GaN-On-SiC HEMT LNA with a Monolithic Substrate-Integrated Waveguide Filer"; F. Thome, D. Schwantuschke, P. Brueckner, X. Wang, J. C. M. Hwang, and R. Quay, In 2024 IEEE MTT-S Int. Microw. Symp. (IMS) Dig., Washington, DC, USA, June 2024, Pp. 314-317, Doi: 10.1109/IMS40175.2024.10600353 (2024).

"Absence of 3a0 Charge Density Wave Order in the Infinite-Layer Nickelate NdNiO2"; C. T. Parzyck, N. K. Gupta, Y. Wu, V. Anil, L. Bhatt, M. Bouliane, R. Gong, B. Z. Gregory, A. Luo, R. Sutarto, F. He, Y.-D. Chuang, T. Zhou, G. Herranz, L. F. Kourkoutis, A. Singer, D. G. Schlom, D. G. Hawthorn & K. M. Shen, Nature Materials 23, 486-491 (2024).

"Absorption and Scattering Limits of Silicon Nitride Integrated Photonics in the Visible Spectrum"; Mateus Corato-Zanarella, Xingchen Ji, Aseema Mohanty, And Michal Lipson, Optica Publishing Group: Optics Express; Volume 32, Issue 4, Pp. 5718-5728 (2024).

"Active Topography with Mucin Coating for Biofilm Control"; Zehui Han, Yikang Xu, Dacheng Ren, BMES 2024, Oct. 2024, Baltimore MD (2024).

"Addition to "All-Glass 100 Mm Diameter Visible Metalens for Imaging the Cosmos"; Joon-Suh Park, Soon Wei Daniel Lim, Arman Amirzhan, Hyukmo Kang, Karlene Karrfalt, Daewook Kim, Joel Leger, Augustine Urbas, Marcus Ossiander, Zhaoyi Li, Federico Capasso, ACS Nano, Volume 18, Issue 25, 16324 (June 2024) (2024).

"Additive Manufacturing and Characterization of Porous Glass Electrospray Emitters"; Suhail Chamieh, Carl Geiger, Giancarlo D'Orazio, & Sadaf Sobhani, Research Gate; In 38th International Electric Propulsion Conference (IEPC) (2024).

"Advancements in GaN-Based HEMTs: Exploring High-K Barrier Materials AlScN, AlBN, And AlYN for Enhanced Performance"; Kazuki Nomoto, T.S. Nguyen, C.P. Savant, Debdeep Jena, and Huili Grace Xing, ASPIRE Symposium, Tokai Open Innovation Complex (TOIC) Nagoya University, Sep. 13, 2024 (2024).

"Advancing Glucose Sensing Through Auto-Fluorescent Polymer Brushes: From Surface Design to Nano-Arrays"; Gozde Aktas Eken, Yuming Huang, Oswald Prucker, Jürgen Rühe, Christopher Ober, Small. 2024 May; 20 (22): E2309040. Doi: 10.1002/Smll.202309040. (2024).

"AIGaN Channel POLJFET with an Ultrawide Bandgap DPD Pn Junction Gate"; Madhav Ramesh, Shivali Agrawal, Huili (Grace) Xing, Debdeep Jena, PowerPoint Presentation, 2024 DRC (2024).

"All-Dielectric Hybrid VIS-NIR Dual-Function Metaoptic"; Pei Xiong, Daniel K Nikolov, Fei Cheng, Jannick P Rolland and a N Vamivakas, Journal of Optics, Volume 26, Number 7 DOI: 10.1088/2040-8986/Ad4721 (2024).

"All-Glass 100 Mm Diameter Visible Metalens for Imaging the Cosmos"; Joon-Suh Park, Soon Wei Daniel Lim, Arman Amirzhan, Hyukmo Kang, Karlene Karrfalt, Daewood Kim, Joel Leger, Augustine Urbas, Marcus Ossiander, Zhaoyi Li, And Federico Capasso, ACS Nano Volume 18, Issue 4, 17 January 2024 (2024).

"All-Mist-CVD NiO/Ga2O3 Diodes"; Bennett Cromer, IWGO 2024, Berlin Germany (2024).

"All-Optical Frequency Division On-Chip Using a Single Laser"; Yun Zhao, Jae K. Jang, Garrett J. Beals, Karl J. Mcnulty, Xingchen Ji, Yoshitomo Okawachi, Michal Lipson & Alexander L. Gaeta, Nature 627, Pp. 546-522 (11 March 2024) (2024).

"Amidst Whispers of Ice and Fire: Kinetics and Mechanisms of Retention and Transformation of Glyphosate at Organo-Mineral Interfaces"; Azimzadeh Ismali Kandi, Behrooz, Cornell University Proquest Dissertations & Theses, 2024.31484490 (2024).

"An Introduction to Engineered Living Materials"; Hernandez, C.J., Multifunctional Materials and Structures Gordon Research Conference Ventura, CA, USA. (2024).

"An Optical Sensor Path for the Measurement of Water Activity"; Wu, I. -F., Stroock, A. D., Jain, P., Huber, A. E. & Sen, S., US Provisional Patent Application. 63/573,961 (2024).

"Anisotropic Spin Stripe Domains in Bilayer La3Ni2O7"; N. K Gupta, R. Gong, Y. Wu, M. Kang, C. T. Parzyck, B. Z. Gregory, N. Costa, R. Sutarto, S. Sarker, A. Singer, D. G. Schlom, K. M. Shen, D. G. Hawthorn, Cond-Mat-arXiv:2409.03210 (2024).

"Arbitrarily Programmable Wave Propagation on a Photonic Chip"; Stein, M. M., Onodera, T., Ash, B. A., Sohoni, M. M., Bosch, M., Yanagimoto, R., … & Mcmahon, P. L., In Machine Learning in Photonics (Vol. 13017, Pp. 96-99) (2024).

"Artificial Cilium and Arrays Thereof"; I. Cohen, W. Wang, O. Liu, US Patent Appl. 18/783,271. (2024).

"Atomic Fluorescence Collection into Planar Photonic Devices"; Orion Smedley, Vighnesh Natarajan, Oscar Jaramillo, Hamim Mahmud Rivy, Karan K. Mehta, arXiv:2408.07068 13 August 2024 (2024).

"Beyond Proof of Concept NanoSQUID's"; Striff, Alex, Lecture at Stanford University, December 16, 2024 (This Work Is Supported by the Air Force Office of Scientific Research's (AFOSR) Multidisciplinary University Research Initiative (MURI) Through Award No. FA9550-21-1-0429 (2024).

"Bioinspired Active Topographies with Mucin Coating of Micron-Sized Pillars"; Zehui Han, Yikang Xu, Dacheng Ren, ICBZM2024, July 2024, Cornell University, Ithaca NY (2024).

"Bio-Inspired Flow-Sensing Capacitive MEMS Microphone"; Johar Pourghader, Weili Cui, Junpeng Lai, Mahdi Farahikia, Changhong Ke, Morteza Karimi, Ronald N Miles, Techrxiv. IEEE Sensors Journal, January 22, 2024. DOI: 10.36227/Techrxiv.170595888.89023812/V1 (2024).

"Bone Matrix Mineral Content Regulates Early-Stage Metastasis by Altering Mesenchymal Stem Cell Fat"; N. Sempertegui, Y. Yan, M. Whitman, S. Choi, L. Estroff, and C. Fischbach, (Poster Presentation) Signal Transduction by Engineered Extracellular Matrices Gordon Research Conference, Manchester NH, July 21-26, 2024 (2024).

"Bone Mineral Density Loss Permits Breast Cancer Metastasis and Growth Via Microenvironmental Alterations"; Matthew Whitman, PhD Thesis (2024).

"Bridging Simulation and Experiment: Tuning Dimensional Order in Feco Magnetic Nanostructures"; Y. Chen, H. Zhang, A. El-Ghazaly, Intermag Conference, Rio De Janeiro, Brazil (2024).

"Cavity Controlled Upconversion in CdSe Nanoplatelet Polaritons"; Mitesh Amineric R. Koesslerovishek Morshedfarwa Awannicole M. B. Coganrobert Collisontrevor M. Tumielwilliam Girtenchristopher Leitera. Nickolas Vamivakaspengfei Huo, Todd D. Krauss, ACS Nano Volume 18, Issue 32, July 30, 2024 (2024).

"CCAT: Characterizing the Fabry-Perot Interferometer Mirrors and Mount for the Epoch of Reionization Spectrometer"; Bugao Zou, J. Richard Bond, Victoria Butler, Rodrigo Freundt, Zachary B. Huber, Michael D. Niemack, Thomas Nikola, Gordon J. Stacey, Eve M. Vavagiakis Millimeter, Submillimeter, and Far-Infrared Detectors and Instrumentation for Astronomy XII. Vol. 13102. SPIE (2024).

"Characterization and Testing of Additively Manufactured Porous Ceramic Electrospray Emitters"; Luke S. D'Cruz, Carl J. Geiger, Suhail Chamieh, Benjamin Inbar, Sadaf Sobhani, & Elaine Petro, In AIAA SCITECH 2024 Forum (2024).

"Characterization of Joined Alumina Components Manufactured Via Digital Light Processing"; Brooklyn Jenkins, CNF REU Program Report (2024).

"Characterization of Thermalization Timescales in Superconducting Qubits Using Quasiparticle Poisoning Rates"; K.Dodge, Contributed Talk: American Physical Society March Meeting, Minneapolis, MN, March 2024 (2024).

"Chasing Schottky–Mott: Metal-First Non-Alloyed Contacts to β-Ga2O3 for Interface Quality and Minimal Surface Modification; Kathleen T. Smith"; Cameron A. Gorsak; Joshua T. Buontempo; Bennett J. Cromer; Takumi Ikenoue; Hemant Gulupalli; Michael O. Thompson; Debdeep Jena; Hari P. Nair; Huili Grace Xing, Journal of Applied Physics Volume 136, Issue 21, 7 December 2024 (2024).

"Chemical Control of Semiconductor Surface: XPS And STM"; Qingyuan Zhu, Ph.D. Theses, Cornell University (2024).

"Chemical-Vapor-Deposition (CVD) Growth of Porous Two-Dimensional Polymer for Dielectric Applications in Microelectronics"; Qiyi Fang, Yu Zhong, Jun Lou, MRS Fall 2024 (2024).

"Chromatin Buffers Torsional Stress During Transcription"; Jin Qian, Lucyna Lubkowska, Shuming Zhang, Chuang Tan, Yifeng Hong, Robert M Fulbright, James T Inman, Taryn M Kay, Joshua Jeong, Deanna Gotte, James M Berger, Mikhail Kashlev, Michelle D Wang, Biorxiv 2024 Oct. 18 Doi: 10.1101/2024.10.15.618270 (2024).

"CMOS on AlN Platform"; Kazuki Nomoto, T.S. Nguyen, C.P. Savant, Debdeep Jena, And Huili Grace Xing, University of Tokyo, Tokyo, Japan 4 September 2024 (2024).

"Co-Designed Silicon Photonics Chip I/O for Energy-Efficient Petascale Connectivity"; Yuyang Wang, Songli Wang, Robert Parsons, Swarnava Sanyal, Vignesh Gopal, Asher Novick, IEEE Transactions on Components, Packaging and Manufacturing Technology, Pp. 1-1. (2024).

"Coherent Acoustic Control of Defect Orbital States in the Strong-Driving Limit"; B.A. Mccullian, V. Sharma, H.Y. Chen, J.C. Crossman, E.J. Mueller, & G.D. Fuchs, PRX Quantum 5, 030336-19 August 2024 (2024).

"Collagen Mineralization Decreases NK Cell-Mediated Cytotoxicity of Breast Cancer Cells Via Increased Glycocalyx Thickness"; Sangwoo Park, Siyoung Choi, Adrian A. Shimpi, Lara A. Estroff, Claudia Fischbach, Matthew J. Paszek, Advanced Materials, Volume 36, Issue 43, Special Issue: Engineering Active Materials for Biomedical Applications, October 24, 2024, 2311505 (2024).

"Compact Narrow-Linewidth Integrated Laser"; Brian Stern, Xingchen JI, Michal Lipson, US11870216B2, 1 January 2024 (2024).

"Comparing Micro- and Nanoscale NbO2 Devices for Memristive Applications"; Matthew C Sullivan, 2024 APS March Meeting (2024).

"Comparison of Torque Generated by In-Plane and Out-Of-Plane Anisotropic Magnetorheological Elastomers"; H. Htet, L. Cestarollo, A. El-Ghazaly, Intermag Conference, Rio De Janeiro, Brazil (2024).

"Complex Permittivities of Ultra-Low-Loss 4H-SiC from 55 GHz to 330 GHz"; Y. Yanagimoto, S. Yanagimoto, T. Li, And J. C. M. Hwang, In 2024 103rd ARFTG Microw. Meas. Symp. (ARFTG), Washington, DC, USA, June 2024, Pp. 1-4, Doi:10.1109/ARFTG61196.2024.10660704 (2024).

"Compositions, Methods, and Devices for Integrated Photonics"; O. Jaramillo, K.K. Mehta, Provisional Application No. 63/643, 779 May (2024).

"Continuous Tuning from Bright to Dark States in Coupled Photonic Resonators"; Graydon J. K. Flatt, Karl J. Mcnulty, Oliver L. Wang, And Michal Lipson, In CLEO 2024 (2024), Paper Stu4q.1. CLEO: Science And Innovations, Optica Publishing Group, P. Stu4q.1. (2024).

"Controllable Suppression of the Unconventional Superconductivity in Bulk and Thin-Film Sr2RuO4 via High-Energy Electron Irradiation"; Jacob P. Ruf, Hilary M. L. Noad, Romain Grasset, Ludi Miao, Elina Zhakina, Philippa H. Mcguinness, Hari P. Nair, Nathaniel J. Schreiber, Naoki Kikugawa, Dmitry Sokolov, Marcin Konczykowski, Darrell G. Schlom, Kyle M. Shen, And Andrew P. Mackenzie, Physical Review Research 6, 033178- 16 August 2024 (2024).

"Controlling Anisotropy in Magnetic Thin-Films for Integrated Device Operations"; A. El-Ghazaly, Emerging Leader Award Session, 35th Annual Symposium of the Pacific Northwest Chapter (PNWAVS) Of AVS, Richland, Washinton, August 7, 2024 (2024).

"Controlling Anti-Penetration Performance by Post-Grafting of Fluorinated Alkyl Chains onto Polystyrene-Block-Poly (Vinyl Methyl Siloxane)"; Zhenglin Zhang, Krishnaroop Chaudhuri, Florian Kaefer, Anthony P. Malanoski, Kirt A. Page, Louisa M. Smieska, Jonathan T. Pham, & Christopher K. Ober, ACS Applied Materials & Interfaces Volume 16, Issue 15, April 8, 2024, 19594-19604 (2024).

"Coordinated Behavior of Autonomous Microscopic Machines Through Local Electronic Pulse Coupling"; Milad Taghavi, Wei Wang, Kyubum Shim, Jinsong Zhang, Itai Cohen, & Alyssa Apsel, Science Robotics Volume 9, Issue 96, DOI:10.1126/Scirobotics.Adn8067 (2024).

"Correlated Phonon-Mediated Quasiparticle Poisoning of Superconducting Qubit"; Britton Plourde, Invited Talk: Conference on Noise and Decoherence in Qubits, Aspen Winter Conference, Aspen, CO, February 2024 (2024).

"Coupling Between Charge Density Waves and Stacking Order in Layered Quantum Materials Probed by In-Situ Cryo STEM"; Judy Cha, Microscopy and Microanalysis Conference (M&M 2024) (7/2024, Cleveland, OH) (2024).

“Deciphering Bacterial Cell Envelope Mechanics and Mechanosensing: A Mechanical Engineering Approach”; Junsung Lee, Cornell University ProQuest Dissertations & Theses (2024).

“Decoding Physical Principles of Cell Migration Under Controlled Environment Using Microfluidics”; Young Joon Suh; Alan T. Li; Mrinal Pandey; Cassidy S. Nordmann; Yu Ling Huang; Mingming Wu, Biophysics Reviews Volume 5, Issue 3 September 2024 (2024).

“Deep Inverse Design of an Infrared Metasurface Diffuser”; Natalie Rozman, Rixi Peng, Willie J. Padilla, Advanced Optical Materials Volume 12, Issue 33, 25 November 2024 2401462 (2024).

“Deep-UV Distributed Feedback Laser Diode Design with Ultrawide Bandgap Semiconductor Aigan”; Hsin Wei (Sheena) Huang, Shivali Agrawal, Huili (Grace) Xing, and Debdeep Jena, PowerPoint Presentation, 2024 ICPS, Ottawa, Canada (2024).

“Defect Discovery and Identification”; Gregory Fuchs, Cussion Leader, Defects in Semiconductors GRC, Newry, ME (2024).

“Design, Fabrication and Characterization of Multi-Qubit Devices for Quasiparticle Injection Studies”; Presenter: Ben Byrd -Authors: Ben Byrd, Kesavan Manivannan, Nada Elmeligy, Ivan V. Pechenezhskiy, 2024 APS March Meeting; Minneapolis & Virtual S48.00007 (2024).

“Designing Magnetic Manipulation at the Nanoscale”; A. El-Ghazaly, ECE Graduate Seminar, Carnegie Mellon University, September 27, 2024 (2024).

“Designing Magnetic Manipulation at the Nanoscale”; A. El-Ghazaly, IEEE Electron Device Society Seminar, Cornell University, September 13, 2024 (2024).

“Designing Magnetic Manipulation at the Nanoscale”; A. El-Ghazaly, IEEE Magnetics Society Boston Chapter Distinguished Speaker Event, Northeastern University, August 19, 2024 (2024).

“Determining the Young’s Modulus of the Bacterial Cell Envelope”; Junsung Lee, Karan Jha, Christine E. Harper, Wenyao Zhang, Malissa Ransukh, Nikolaos Bouklas, Tobias Dorr, Peng Chen, And Christopher J. Hernandez, ACS Biomaterials Science & Engineering Volume 10, Issue 5, April 9, 2024 (2024).

“Development of a 3D Microfluidic Platform for Dynamic Compression of Tumor Spheroids”; Young Joon Suh, Mrinal Pandey, Tao Luo, Jeffrey E Segall & Mingming Wu, Cornell BEE Annual Research Symposium (Poster Presentation), Ithaca, NY, Feb 16, 2024 (2024).

“Development of a Microphysiological System to Model Human Cancer Metastasis from the Colon to the Liver”; Paula G. Miller, Emina Huang, Robert Fisher, Michael L. Shuler, Biotechnology Bioengineering 2024:1-14 Volume 122, Issue 3, Pp. 481-494 (2024).

“Differential Displacement of Immunofluorescent Markers in Sarcomeric Titin During History Dependent Properties”; Skehon A, Tiessen C, Leonard T, Herzog W, 68th Meeting of the Biophysical Society, Philadelphia PA, Feb 10-14, 2024 -Podium Presentation (2024).

“Differential Displacement of Sarcomeric Titin Elastic Segments During Isometric Contractions and Residual Force Enhancement”; Sekhon A, Tiessen C, Leonard T, Herzog W, Conference of the Canadian Society for Biomechanics, Edmonton AB, August 19-22, 2024 -Podium Presentation (2024).

“Direct Functionalization of Polyethylene Surfaces with High-Density Polymer Brushes”; Anna E. Ringuette, Gozde Aktas Eken, Amaya B. Garnenez, Adriana I. Palmieri, Christopher K. Ober, Geoffrey W. Coates, & Brett P. Fors, Journal of the American Chemical Society, Volume 146, Issue 30 (July 17, 2024) (2024).

“Doping Profile Extraction for Predictive Modeling of Single Photon Avalanche Diodes”; Andrea Bonzi, Gabriele Laita, Ivan Rech, Angelo Gulinatti, IEEE Journal of Selected Topics in Quantum Electronics, Volume 30, NO. 1, January/February 2024 DOI: 10.1109/JSTQE.2023.3341349 (2024).

“Double Quantum Spin Hall Phase in Moiré WSe2”; Kaifei Kang, Yichen Qiu, Kenji Watanabe, Takashi Taniguchi, Jie Shan, And Kin Fai Mak, ACS Nano Letters Volume 24, Issue 46 November 6, 2024 (2024).

“Dynamic Sorption and Interfacial Assembly of Polysaccharide on Hydrophobic V. Hydrophilic Surfaces”; Behrooz Azimzadeh, Carmen Enid Martinez, Chemrxiv 19 November 2024 DOI:10.26432/Chemrxiv-2024-Cfqrr (2024).

“Dysregulation of Extracellular Vesicle Protein Cargo in Female Myalgic Encephalomyelitis/Chronic Fatigue Syndrome Cases and Sedentary Controls in Response to Maximal Exercise”; Ludovic Giloteaux, Katherine A Glass, Arnaud Germain, Carl J Franconi, Sheng Zhang, Maureen R Hanson, Journal of Extracellular Vesicles. 2024 Jan 13; (1): E12403. Doi:10.1002/Jev2.12403 (2024).

“Effect of Co-Reactants on Interfacial Oxidation in Atomic Layer Deposition of Oxides on Metal Surfaces”; Jay V. Swarup, Heng-Ray Chuang, Amy L. You, And James R. Engstrom, ACS Applied Materials & Interfaces. Volume 16, Issue 13, March 20, 2024 (2024).

“Effective Integration of Vision Foundational Models for Semantic Segmentation to Quantify Grape Foliage Powdery Mildew Infection”; Yiyuan Lin, Anna Underhil, Lance Cadle-Davison, Ana Jimenez, Summaira Riaz, Yu Jiang, ASABE Paper No. 2401108, 2024 ASABE Annual International Meeting, Anaheim, CA, USA (2024).

“Effects of ALD Chemistry on Process Windows, Thin Film Composition and Modification of the Underlying Substrate Surface”; Jay Swarup, American Vacuum Society 70th International Symposium and Exhibition Conference, 2024 (2024).

“Efficient Data Processing Using Tunable Entropy-Stabilized Oxide Memristors”; Sangmin Yoo, Sieun Chae, Tony Chiang, Matthew Webb, Tao Ma, Hanjong Paik, Yongmo Park, Logan Williams, Kazuki Nomoto, Huili G. Xing, Susan Trolier Mckinstry, Emmanouil Kioupakis, John T. Heron, Wei D. Lu, Natural Electronics Volume 7, Issue 6, Pp. 466-474, June 2024 (2024).

“Electronic Capacitance in Tunnel Junctions for Protected Charge-Parity Qubits”; B. Cole, Contributed Talk: American Physical Society March Meeting, Minneapolis, MN, March 6, 2024 (2024).

“Electronically Actuated Artificial Hinged Cilia for Efficient Bidirectional Pumping”; Wei Wang, Ivan Tanasijevic, Jinsong Zhang, Eric Lauga, And Itai Cohen, Royal Society of Chemistry DOI: 10.1039/D4LC00513A (Paper) Lap Chip, 2024, 24, 4549-4557 (2024).

“Electronically Configurable Microscopic Metasheet Robots”; Qingkun Liu, Wei Wang, Itay Griniasty, Jason Z. Kim, Jacob T. Pelster, Paragkumar Chaudhari, Michael F. Reynolds, Michael C. Cao, David A. Muller, Alyssa B. Apsel, Nicholas L. Abbott, Hadas Kress-Gazit, Paul L. Mceuen & Itai Cohen, Nature Materials 24, 109-115 (2024).

“Electron-Induced Chemical Transformations in Polymer Films: Understanding the Role of Electrons in EUV Lithography”; Mueller, Maximillian W, San Jose State University Proquest Dissertations & Theses, 2024. 31488889 (2024).

“Electrospray Emitters, Associated Methods for Their Use, And Associated Methods and Devices for Their Fabrication”; Sobhani, S., Petro, E. M., & Chamieh, S., U.S. Patent Application No. 18/407,219. (2024).

“Emergence of Ferromagnetism on the Onset of Moiré Kondo Breakdown”; W. Zhao, B. Shen, Z. Tao, S. Kim, P. Knuppel, Z. Han, Y. Zhang, K. Watanabe, T. Taniguchi, D. Chowdhury, J. Shan, K. F. Mak, Nat. Phys. 20, 1772–1777 (2024).

“Engineering Bacterial Biomanufacturing: Characterization and Manipulation of Sphingomonas Sp. LM7 Extracellular Polymers”; Ellen W. Van Wijngaarden, Alexandra G. Goetsch, Ilana L. Brito, David M. Hershey, And Meredith N. Silberstein, Soft Matter, 2024, 20, 6399-6410 (2024).

“Engineering Bacterial Polymers for Biomanufacturing: Characterization of a Novel Polysaccharide”; Ellen Van Wijngaarden, Goetsch, A., Brito, I., Hershey, D., Silberstein, M., Society for Experimental Mechanics, Vancouver, WA, US (2024).

“Engineering Biomaterial Interfaces for Microbial Control”; Yikang Xu, Syracuse University Dissertations & Theses (2024).

“Enhanced Magnetic Anisotropy for Reprogrammable High-Force-Density Microactuators”; Yulan Chen, Karthik Srinivasan, Marcus Choates, Ludovico Cestarollo, Amal El-Ghazaly, Advanced Funtional Materials Volume 34, Issue 2, 9 January 2024 – 2305502 (2024).

“Enhanced Trapped-Ion Quantum Gate Operations and Laser Cooling in Structured Light Fields”; Karan K. Mehta, Invited Talk, APS Division of Atomic, Molecular, and Optical Physics Meeting. Fort Worth TX 6/5/2024 (2024).

“Enhancement of Spin-Orbit Torque Generation from Antiferromagnetic Ordering in PdCr02”; Daniel Pharis, Xiaoxi Huang, Qi Song, Thow Min Jerald Cham, Rakshit Jain, Maciej Olszewski, Darrell Schlom, Daniel Ralph , March 8, 2024, APS March Meeting (2024).

“Enhancing Extracellular Vesicle Detection Via Cotargeting Tetraspanin Biomarkers”; Jesus M. Lopez Baltazar, Wenchao Gu, Qiuming Yu, Analytical Chemistry 2024, 96, 41, 16406-16414 (2024).

“Entangling Interactions Between Artificial Atoms Mediated by a Multimode Left-Handed Superconducting Ring Resonator”; T. Mcbroom-Carroll, A. Schlabes, X. Xu, J. Ku, B. Cole, S. Indrajeet, M.D. Lahaye, M.H. Ansari, And B.L.T. Plourde, PRX Quantum 5, 020325-1 May 2024 (2024).

“Epitaxial AlBN/β-Nb2N Ferroelectric/Superconductor Heterostructures”; Chandrashekhar Savant, Thai-Son Nguyen, Saurabh Vishwakarma, Joongwon Lee, Anand Ithepalli, Yu-Hsin Chen, Kazuki Nomoto, Farhan Rana, David J. Smith, Huili Grace Xing, Debdeep Jena, Physica Status Solidi (RRL) 2400157 (2024).

“Epitaxial Growth of Aluminium Scandium Nitride Films on Silicon Substrates”; Rishabh Singh, IWN Conference 2024 November (2024).

“Epitaxial Growth Of α-(AlxGa1−X)2 O3 by Suboxide Molecular-Beam Epitaxy at 1 μm/h”; Jacob Steele, Kathy Azizie, Naomi Pieczulewski, Yunjo Kim, Shin Mou, Thaddeus J. Asel, Adam T. Neal, Debdeep Jena, Huili G. Xing, David A. Muller, Takeyoshi Onuma, and Darrell. G. Schlom, 14-Mar-24 (2024).

“Evaluation of Microscopic Broadband Local Dielectric Spectroscopy Theory Using Thin Film Semiconductors and Interdigitated Electrodes”; Azreial Finsterer, Rachael Cohn, Virginia Mcghee, Chris Petroff, David T. Moore, Roger F. Loring, And John A. Marohn, CNF Annual Meeting Poster Session 17 September 2024 (2024).

“Exchange Bias Between Van Der Waals Materials: Tilted Magnetic States and Field-Free Spin–Orbit-Torque Switching”; T.M.J. Cham, R.J. Dorrian, X.S. Zhang, A.H. Dismukes, D.G. Chica, A.F. May, X. Roy, D.A. Muller, D.C. Ralph, Y.K. Luo, Advanced Materials Volume 36, Issue 13 Doi: 10.1002/Adma.202305739 (2024).

“Fabricate, Customize, and Utilize: Preparing Micron-Scale Cantilevers for Magnetic Resonance Force Microscopy”; George R. Du Laney, Peter Sun, Malcolm Thomas, John A. Marohn, (September 17, 2024) 2024 CNF Annual Meeting: Poster Session (2024).

“Faster Sperm Selected by Rheotaxis Leads to Superior Early Embryonic Development in Vitro”; Mohammad Yaghoobi, Abdallah Abdelhady, Amirhossein Favakeh, Philip Xie, Stephanie Cheung, Amir Mokhtare, Yoke Lee Lee, Ann V. Nguyen, Gianpiero Palermo, Zev Rosenwaks, Soon Hon Cheong and Alireza Abbaspourrad, Lab Chip, 2024, 24, 210-223 (2024).

“Ferroelectric AlBN Films by Molecular Beam Epitaxy; Chandrashekhar Savant”; Ved Gund; Kazuki Nomoto; Takuya Maeda; Shubham Jadhav; Joongwon Lee; Madhav Ramesh; Eungkyun Kim; Thai-Son Nguyen; Yu-Hsin Chen; Joseph Casamento; Farhan Rana; Amit Lal; Huili Grace Xing; Debdeep Jena, Applied Physics Letters Volume 125, Issue 7, 12 August 2024 (2024).

“Fiber-Robot with Adjustable Electrodes for Long Term Neural Recording”; Pelster, J. Et Al., Bulletin of the American Physical Society (2024).

“First Arrival Differential LiDAR”; A. Veeraraghavan, A. Molner, M. White, T. Zhang, A. Dave, A. Raghuram, and S. Ghajari, U.S. Patent 20240393465, November (2024).

“First-Ever Measurement of Hole Velocity Vs. Electric Field in Polarization-Induced Two-Dimensional Hole Gases in GaN/AlN Heterojunction”; Joseph Dill, 2024 APS March Meeting, Abstract: D13.00005 (2024).

“Fluorinated Ether as an Electrolyte Additive for Lithium-Air Batteries”; Bryan Junsuh Kim, Cornell NanoScale Science & Technology Facility (CNF) iREU Program Report (2024).

“Fully Transparent Epitaxial Oxide Thin-Film Transistor Fabricated at Back-End-Of-Line Temperature by Suboxide Molecular-Beam Epitaxy”; Felix V.E. Hensling, Patrick Vogt, Jisung Park, Shun-Li Shang, Huacheng Ye, Yu-Mi Wu, Kathleen Smith, Veronica Show, Kathy Azizie, Hanjong Paik, Debdeep Jena, Huili G. Xing, Y. Eren Suyolcu, Peter A. Van Aken, Suman Datta, Zi-Kui Liu, Darrell G. Schlom, Advanced Electronic Materials. 2400499. 11 September 2024 (2024).

“Functional Polymer Films Manufactured Using Electrospray Deposition”; Kingsley, Bryce James, State University Of New York At Binghamton ProQuest Dissertations & Theses, 2024. 31556478. (2024).

“Functionalization of Polymer Substrates from C-H Bonds”; Anna Ringuette, Provisional Patent 10827-01-US (2024).

“Functionalized Nanowires for Mirna-Mediated Therapeutic Programming of Naïve T Cells”; Kristel J Yee Mon, Sungwoong Kim, Zhonghao Dai, Jessica D West, Hongya Zhu, Ritika Jain, Andrew Grimson, Brian D Rudd, Ankur Singh, Nat Nanotechnol. 2024 Aug;19(8): 1190-1202 Dio: 10.1038/S41565-024-01649-7 -29 April 2024 (2024).

“Fusion Peptide-Cholesterol Interactions of the SARS CoV-2 Spike Protein are Mediated Through Specific Phenylalanine Residues; Pachaury, A., Park, S., Whittaker, G., Abbott, N., Daniel, S., ASV, Columbus, Ohio (2024).

“Gaining New Understanding of Sarcomere Length Non-Uniformities in Skeletal Muscles”; Meng Li, T. R. Leaonard, S. W. Han, E. Moo, W. Herzog, Frontiers in Physiology-Striated Muscle Physiology 14: 1242177. Doi: 10.3389/Fphys.2023.1242177 (2024).

“Generation of Buffered Surface-Active Block Copolymer Thin Films for Interruption of Marine Fouling”; Emma G. Hester, Zhengling Zhang, John A. Finlay, Anthony S. Clare, Aloysius Yi Jie Teow, Serena Lay-Ming Teo, Christopher K. Ober, ACS Fall 2024, Denver, CO, USA (2024).

“Genetically Engineering Bacterial Polysaccharide Properties”; Ellen Van Wijngaarden, Brito, I., Silberstein, M., Engineered Living Materials Institute Symposium, Ithaca, NY, US (2024).

“Geometry of Braided DNA Dictates Supercoiling Partition”; Yifeng Hong, Seong Ha Park, Hanjie Wang, Michelle D Wang, Biorxiv 2024 Oct. 11:2024.10.08.617221 (2024).

“Getting Microbes into Materials and Keeping Them Alive”; Hernandez, C.J., Engineered Living Materials Symposia. Saarbrucken, Germany (2024).

“Giant Spin Hall Effect in AB-Stacked MoTe2/WSe2 Bilayers”; Z. Tao, B. Shen, W. Zhao, N.C. Hu, T. Li, S. Jiang, L. Li, K. Watanabe, T. Taniguchi, A.H. Macdonald, J. Shan and K.F. Mak, Nat. Nanotechnol. 19, 28–33 (2024).

“Gram-Positive Bacterial Membrane-Based Biosensor for Multimodal Investigation of Membrane–Antibiotic Interactions”; Samavi Farnush Bint-E-Naser, Zeinab Jushkun Mohamed, Zhongmou Chao, Karan Bali, Róisín M. Owens, And Susan Daniel, Biosensors 2024, Volume 14, Issue 1, Doi: 10.3390/Bios14010045 (2024).

“Harnessing Magnetic-Field Driven Actuation for Microscale Motion in MEMS-Inspired Device”; L. Cestarollo, A. El-Ghazaly, Intermag Conference, Rio De Janeiro, Brazil (2024).

“Heterologous Expression of Dictyostelium Discoideum NE81 in Mouse Embryo Fibroblasts Reveals Conserved Mechanoprotective Roles of Lamins”; Jacob Odell, Ralph Graf, Jan Lammerding, Molecular Biology of the Cell. 2024 Jan 1;35(1): Ar7. Doi: 10.1091/Mbc.E23-05-0193 (2024).

“HfO2-Based Platform for High-Index-Contrast Visible/UV Integrated Photonics”; Oscar Jaramillo, Vighnesh Natarajan, Hamin Mahmud Rivy, Joshua Tensuan, Leonardo Massai, Karan K. Mehta, arXiv:2412.09421 12 December 2024 (2024).

“High Growth Rate Metal Organic Chemical Vapor Deposition Grown Ga2O3 (010) Schottky Diodes”; Sudipto Saha, Lingyu Meng, Dong Su Yu, A. F. M. Anhar Uddin Bhuiyan, Hongping Zhao, Uttam Singisetti, Journal of Vacuum Science & Technology A Volume 42, Issue 4, July 2024 (2024).

“High Performance and Efficient Circuits for Next Generation Wireless Communication”; Shimin Huang, Cornell University Proquest Dissertations & Theses, 2024. 31242891. (2024).

“High Power Chip-Scale Laser”; Yair Antman, Andres Gil-Molina, Ohad Westreich, Xingchen Ji, Alexander L. Gaeta, And Michal Lipson, Optica Publishing Group: Optics Express; Volume 32, Issue 26, Pp. 47306-47312 (2024).

“High Signal-To-Noise Ratio Event-Driven MEMS Motion Sensing”; Mohammad Mousavi, Mohammad Alzgool, Benyamin Davaji, Shahrzad Towfighian, Nano Micro Small, Volume 20, Issue 10, March 8, 2024 – 2304591 (2024).

“High Voltage Gallium Oxide (Ga2O3) Trench MOS Barrier Schottky and Methods of Fabricating Same (Active)”; Whenshen Li, Zongyang Hu, Kazuki Nomoto, Debdeep Jena, Huili Grace Xing, US11894468B2 (2024).

“High-Field Large ΦB Ga2O3 Schottky Diodes”; Bennett Cromer, WOCSEMMAD 2024, Las Vegas NV (2024).

“High-Performance 2D Electronic Devices Enabled by Strong and Tough Two-Dimensional Polymer with Ultra-Low Dielectric Constant”; Qiyi Fang, Kongyang Yi, Tianshu Zhai, Shisong Luo, Chen-Yang Lin, Qing Ai, Yifan Zhu, Boyu Zhang, Gustavo A Alvarez, Yanjie Shao, Haolei Zhou, Guanhui Gao, Yifeng Liu, Rui Xu, Xiang Zhang, Yuzhe Wang, Xiaoyin Tian, Honghu Zhang, Yimo Han, Hanyu Zhu, Yuji Zhao, Zhiting Tian, Yu Zhong, Zheng Liu, Jun Lou, Nature Commun. 2024 Dec. 30; 15(1):10780. Doi: 10.1038/S41467-024-53935-6 (2024).

“High-Remanence Magnetic Nanostructures for Microactuators”; A. El-Ghazaly, Y. Chen, L. Cestarollo, Functional Nanomaterials Session, The Minerals, Metals, & Materials Society (TMS) Annual Meeting, Orlando, Florida, March 6, 2024 (2024).

“High-Resolution, Low-Loss Phase Shifting Reflectors”; B. Govind, Alyssa Apsel, Provisional US Patent 63/633,380 (4/24) (2024).

“Human Ocular Fluid Drainage on Chip”; Renhao Lu, Esak Lee, Appl No. 63/571,529. (2024).

“Hybrid Magnonic System with Strongly Coupled Superconducting LC Resonator and Organic Ferrimagnet C[TCNE]”; Srishti Pal, 2024 Annual CCMR Symposium (2024).

“Hydrogen Sulfide Formation in Canned Wines: Variation Among Can Sources”; Sheehan MJ, Suarez JHR, Benefeito MM, Goddard JM, Sacks GL, American Journal of Enology and Viticulture. 75:0750003 2024 DOI: 10.5344/Ajev.2023.23069 (2024).

“Hydrophilic and Hydrophobic Zwitterion Functionalized Siloxane-Based Polymers for Interruption of Ph-Dependent Marine Settlement”; Emma G. Hester, Zhengling Zhang, John A. Finlay, Anthony S. Clare, Aloysius Yi Jie Teow, Serena Lay-Ming Teo, Christopher K. Ober, International Conference on Bioinspired and Zwitterionic Materials (2024).

“Ice Formation and its Elimination in Cryopreservation of Oocytes”; Abdallah W Abdelhady, David W Mittan-Moreau, Patrick L Crane, Matthew J Mcleod, Soon Hon Cheong, Robert E Thorne, Scientific Reports 2024 Aug 13; 14 (1) DOI: 10.1038/S41598-024-69528-8 (2024).

“Imaging Antiferromagnetic Order at the Nanoscale Using a Scanning Nitrogen-Vacancy-Center Microscope”; Qiaochu “Nicole” Guo, Cornell University PhD Theses (2024).

“Immunoassays for Extracellular Vesicle Detection Via Transmembrane Proteins Using Surface Plasmon Resonance Biosensors”; Jesus M. Lopez Baltazar, Wenchao Gu, Markéta Bocková, Qiuming Yu, ACS Sensors Volume 9, Issue 7, June 24, 2024 (2024).

"Immunoengineering Can Overcome the Glycocalyx Armour of Cancer Cells"; Sangwoo Park, Marshall J. Colville, Justin H. Paek, Carolyn R. Shurer, Arun Singh, Erica J. Secor, Cooper J. Sailer, Ling-Ting Huang, Joe Chin-Hun Kuo, Marc C. Goudge, Jin Su, Minsoo Kim, Matthew P. Delisa, Sriram Neelamegham, Jan Lammerding, Warren R. Zipfel, Claudia Fischbach, Heidi L. Reesink & Matthew J. Paszek, Nature Materials 23, 429-438 (2024).

"Impacts of Device Processing on Contact Interfaces to (010) β-Ga2O3"; Kathleen T. Smith, Cameron A. Gorsak, Avijit Kalra, Bennett J. Cromer, Debdeep Jena, Hari P. Nair, Huili G. Xing, Oxide-Based Materials and Devices XV. SPIE (2024), Vol. 12887, Pp. 25-33 (2024).

"Improvement in Structural Quality of Transition Metal Nitride Films Grown on Miscut Sapphire Substrates Using Molecular Beam Epitaxy"; Anand Ithepalli, 2024 ICMBE, Matsue, Japan (2024).

"In Situ Cryo 4D STEM of CDW Phase Transition in Layered Materials"; Judy Cha, Materials Research Society (MRS) 2024 Spring Meeting (4/2024, Seattle, WA) (2024).

"In Situ Cryo 4D STEM of CDW Phase Transition"; Judy Cha, Cryo-EM (ICE) Workshop for Advanced Materials, Oak Ridge National Lab (7/2024, TN) (2024).

"In Situ Cryogenic Cooling, Electric Biasing, and 4D-STEM of the 1T-Tas2 Charge Density Wave Transition"; James L Hart, Saif Siddique, Noah Schnitzer, Stephen Funni, Lena F Kourkoutis, & Judy J. Cha, Microscopy and Microanalysis, 30 (Suppl 1), 2024, 1370–1372 Https://Doi.Org/10.1093/Mam/Ozae044.673 (2024).

"In Situ Etching of β-Ga2O3 Using Tert-Butyl Chloride in an MOCVD System"; Cameron A. Gorsak, Henry J. Brown, Katie R. Gann, Joshua T. Buontempo, Kathleen T. Smith, Pushpanshu Tripathi, Jacob Steele, Debdeep Jena, Darrell G. Schlom, Huili Grace Xing, Michael O. Thompson, Hari P. Nair, Applied Physics Letters, Volume 125, Issue 24 (2024).

"In Situ FTIR Spectroscopy to Probe Effects of LiNO3 on First Cycle SEI Formation and Electrolyte Decomposition in Li-Metal Batteries"; Ben Hodder Alexander, Cornell NanoScale Science & Technology Facility (CNF) iREU Program Report (2024).

"In Situ Electric-Field Control of Ferromagnetic Resonance in the Low-Loss Organic-Based Ferrimagnet V[TCNE]X□2"; Seth W. Kurfman, Andrew Franson, Piyush Shah, Yueguang Shi, Hill Fung Harry Cheung, Katherine E. Nygren, Mitchell Swyt, Kristen S. Buchanan, Gregory D. Fuchs, Michael E. Flatte, Goplan Srinivasan, Michael Page, Ezekiel Johnston-Halperin, APL Materials Volume 12, Issue 5, May 14, 2024 (2024).

"Increasing Magnetic Anistropy at the Nanoscale for Micromagnetic Actuators"; A. El-Ghazaly, Y. Chen, L. Cestarollo, Materials Research Society Spring Meeting, Seattle (2024).

"Infrared Spectroscopy of Live Cells Using High-Aspect-Ratio Metal-On-Dielectric Metasurfaces"; Aditya Mahalanabish, Steven H. Huang, Dias Tulegenov & Gennady Shvets, ACS Nano Letters Vol. 24, Issue 37 (2024).

"Inorganic Trench-Masked Josephson Junctions"; Tathagata Banerjee & Valla Fatemi, 11168; 63/692,308. (2024).

"Interaction of Charge Density Waves with Defects in Rare-Earth Tritellurides"; Saif Siddique, James L Hart, Drake Niedzielski, Ratnadwip Singha, Myung-Geun Han, Noah Schnitzer, Michael Colletta, Mehrdad T Kiani, Stephen D Funni, Natalie Williams, Lena F Kourkoutis, Yimei Zhu, Leslie M Schoop, Tomás A Arias, Judy J Cha, Microscopy And Microanalysis, Volume 30, Issue Supplement_1, July 2024, Ozae044.728 Https://Doi.Org/10.1093/Mam/Ozae044.728 (2024).

"Interfacing Superconducting Qubits with Cryogenic Digital Circuits"; Britton Plourde, Invited Talk: Electrical and Computer Engineering Seminar, University of California, Riverside, April 2024 (2024).

"Interfacing Superconducting Qubits with Cryogenic Digital Circuits"; Britton Plourde, Invited Talk: Electron Devices Society Seminar, Cornell University, Ithaca, NY, February 2024 (2024).

"Interrupting Marine Fouling with Active Buffered Coatings"; Riddhiman Medhi, Alexandra D Handlin, Amanda K Leonardi, Giancarlo Galli, Elisa Guazzelli, John A Finlay, Anthony S Clare, Matteo Oliva, Carlo Pretti, Elisa Martinelli, Christopher K Ober, The Journal of Bioadhesion and Biofilm Research. 2024 Aug;40 (7):377-389. Doi. 10.1080/08927014.2024.2367491 (2024).

"Inverted Scanning Microwave Microscopy of Gan/AIN High-Electron Mobility Transistors"; X. Wang, K. Nomoto, G. Fabi, R. Al Hadi, M. Farina, D. Jena, H. G. Xing, And J. C. M. Hwang, In 2024 103rd ARFTG Microw. Meas. Symp. (ARFTG), Washington, DC, USA, June 2024, Pp. 1-4, Doi: 10.1109/ARFTG61196.2024.10660702 (2024).

"Inverted Transflection Spectroscopy of Live Cells Using Metallic Grating on Elevated Nanopillars"; Aditya Mahalanabish, Steven H. Huang, & Gennady Shvets, ACS Sensors Vol. 9, Issue 3 March 12, 2024 (2024).

"Investigating Segmental Mechanics of Titin in Immunofluorescent-Labelled Myofibrils"; Tiessen C, Sekhon A, Leonard T, Herzog W, 68th Meeting of the Biophysical Society, Philadelphia PA, Feb 10-14 -Poster Presentation (2024).

"Investigating the Effects of Calcium on Titin Force Regulation in Skeletal Muscle Myofibrils"; Desai D, Sekhon A, Herzog W, Conference of the Canadian Society for Biomechanics, Edmonton AB, August 19-22, 2024 -Podium Presentation (2024).

"Investigating the Magnetization and Behavior and Interactions in Magnetic Nanoparticles and Nanochains"; Yulan Chen, A. El-Ghazaly, African Materials Research Society (AMRS) Conference, Kigali, Rwanda (2024).

"Investigating VEGF-A Induced Lymphatic Vessel Remodeling and Its Implications for Immune Cell Trafficking in Pancreatic Cancer Using Tumor-On-Chip and Kaede Transgenic Mouse Model"; Kolarzyk A., Carter E., Leddon SA., Cano I., Lu R., Fowell D., Lee E., Gordon Research Conference (GRC Lymphatics, Ventura, CA (2024).

"Is Ba3In2O6 a High-Tc Superconductor"; F V E Hensling, D Dahliah, M A Smeaton, B Shrestha, V Show, C T Parzyck, C Hennighausen, G N Kotsonis, G-M Rignanese, M R Barone, I Subedi, A S Disa, K M Shen, B D Faeth, A T Bollinger, I Božović, N J Podraza, L F Kourkoutis, G Hautier And D G Schlom, Journal of Physics: Condensed Matter 36 315602, Doi: 10.1088/1361-648X/ad42f3 (2024).

"Is Drosophila Indirect Flight Muscle a Good Model to Investigate Residual Force Enhancement with Minimal Sarcomere Length Non-Uniformities"; Liu S, Joumaa V, Leonard T, Herzog W, 68th Meeting of the Biophysical Society, Philadelphia PA, Feb 10-14, 2024 -Poster Presentation (2024).

"Joint Microfluidic Assessment of Local Shear and Shear Historical Effects on Thrombosis: Applications to Heart-Assist Devices and Hyperinflammatory States"; Kang, Junhyuk, Cornell University ProQuest Dissertations & Theses, 2024. 31146693 (2024).

"Key Points to Design a Low Noise Velocity Sensitive Microphone "; Karimi, Morteza, State University Of New York At Binghamton ProQuest Dissertations & Theses, 2024. 31765330 (2024).

"Kilovolt Pyroelectric Voltage Generation and Electrostatic Actuation with Fluidic Heating; Di Ni, Ved Gund, Landon Ivy, Amit Lal, arXiv:2411.02295 (2024).

"Lactic and Acetic Acids in Sour Beers Promote Corrosion During Aluminum Beverage Can Storage"; Sheehan M, Montgomery A, Goddard JM, Sacks GL, Journal of the American Society of Brewing Chemists. Volume 83, Issue 1 (2024).

"Lester Eastman and the Monolithic Microwave Integrated Circuit Technology"; James C. M. Hwang, IEEE Microwave Magazine, Volume 25, Issue 6, Pp. 132-135, June 2024, Doi: 101109/MMM.2024.3379103 (2024).

"Leucine Zipper-Based SAIM Imaging Identifies Therapeutic Agents to Disrupt the Cancer Cell Glycocalyx for Enhanced Immunotherapy"; Sangwoo Park, Justin H. Paek, Marshall J. Colville, Ling-Ting Huang, Audrey P. Struzyk, Sydney J. Womack, Sriram Neelamegham, Heidi L. Reesink, Matthew J. Paszek, Biorxiv Doi:10.1101/2024.12.05.627089 (2024).

"Levitated Nanoparticles and Super-Resolution Spectroscopy as Tools for Optical Nanothermometry"; Z. Ye, B. Harrington, D.K. Bommidi, and A.D. Pickel, IMECE. Portland, OR. November 17 – 21, 2024. Contributed Talk (2024).

"Light-Harvesting Microelectronics Devices for Wireless Electrochemical Synthesis"; Bartosz Gorski, Jonas Rein, Samantha Norris, Yanxin Ji, Paul L. Mceuen, Song Lin, Sterochemistry Gordon Research Conference Poster Presentation, 21-26 July 2024, Newport, US. (2024).

"Lithiation in 2H-Mote 2 Nanoflakes"; Shiyu Xu, Natalie L. Williams, Sihun Lee, Jason J. Huang, Saif Siddique, Andrej Singer, Judy J. Cha, Research Gate Chemistry of Materials 36(20) DOI: 10.1021/Acs.Chemmater.4c01517 (2024).

"Lithiation Induced Phases in 1T′-MoTe 2 Nanoflakes"; Shiyu Xu, Kenneth Evans-Lutterodt, Shunran Li, Natalie L. Williams, Bown Hou, Jason J. Huang, Matthew G. Boebinger, Sihun Lee, Mengjing Wang, Andrej Singer, Peijun Guo, Diana Y. Qiu, & Judy J. Cha, ACS Nano Volume 18, Issue 26 June 18, 2024 (2024).

"Local Magnetic Response of Superconducting Sr2RuO4 Thin Films and Rings"; G. M. Ferguson, Hari P. Nair, Nathaniel J. Schreiber, Ludi Miao, Kyle M. Shen, Darrell G. Schlom, Katja C. Nowack, Arxiv:2403.17152, March 25, 2024 (2024).

"Localized Measurements of Water Potential Reveal Large Loss of Conductance in Living Tissues of Maize Leaves"; Piyush Jain, Annika E. Huber, Fulton E. Rockwell, Sabyasachi Sen, N. Michele Holbrook, Abraham D. Stroock, Plant Physiology Volume 194, Issue 4, April 2024, Pp. 2288-2300 (2024).

"Low-Frequency Wave Generation Via Optical Frequency Division"; Yun Zhao, Jae K. Jang, Yoshimoto Okawachi, Bok Young Kim, Alexander L. Gaeta, Michal Lipson, US Patent appl. 20240402571 appl# 18/309572, December 5, 2024 (2024).

"Low-Loss D-Band SIW Power Divider for Integrated Systems"; W. Wu, X. Wang, L. Li, J. C. M. Hwang, And P. Fay, In 2024 USNC-URSI Natl. Radio Sci. Meet. (NRSM), Boulder, CO, USA, Jan. 2024, Pp. 1-3 (2024).

"Lymphatic and Blood Endothelial Cell Contractility-Mediated Vascular Junction Formation Regulates Tumor Interstitial Fluid Pressure and Immune Response"; Haryy Peng, Gordon Research Conference, Ventura CA (Poster Presentation), March 3-8, 2024 (2024).

"Machine Learning with Complex Wave Propagation in Inverse-Designed Photonic Device"; Stein, M., Onodera, T., Ash, B. A., Sohoni, M. M., Bosch, M., Yanagimoto, R., … & Mcmahon, P. L., SPIE Photonics West 2024 In AI And Optical Data Sciences V (2024).

"Magnetic Decoupling for Programmable Microscopic Self-Limiting Assembly"; Liang, Zexi, Et Al, 98th ACS Colloid & Surface Science Symposium, Seattle, USA (2024).

"Magnetic Decoupling for Programmable Self-Limiting Assembly"; Liang, Zexi., Et Al., Poster Presentation, The 8th International Soft Matter Conference (2024).

"Magnetically Programmed Diffractive Robotics"; Conrad L Smart, Tanner G Pearson, Zexi Liang, Melody X Lim, Mohamed I Abdelrahman, Francesco Monticone, Itai Cohen, Paul L Mceuen, Science. 2024 Nov 29;386(6725):1031-1037. Doi:10.1126/Science. Adr2177. Epub 2024 November 28 (2024).

"Manipulating Chiral-Spin Transport with Ferroelectric Polarization"; Xiaoxi Huang, Xianzhe Chen, Yuhang Li, John Mangeri, Hongrui Zhang, Maya Ramesh, Hossein Taghinejad, Peter Meisenheimer, Lucas Caretta, Sandhya Susarla, Rakshit Jain, Christoph Klewe, Tianye Wang, Rui Chen, Cheng-Hsiang Hsu, Hao Pan, Jia Yin, Padraic Shafer, Ziqiang Qiu, Davi R. Rodrigues, Olle Heinonen, Dilip Vasudevan, Jorge Iniguez, Darrell G. Schlom, Sayeef Salahuddin, Lane W. Martin, James G. Analytis, Daniel C. Ralph, Ran Cheng, Zhi Yao, Ramamoorthy Ramesh, Nature Materials 23, 898-904 (2024) Arxiv:2306.02185 15 April 2024 (2024).

"Materials and Devices for Integrated Atomic Quantum Systems"; Karan K., Mehta Invited Talk, Fronties in Optics, Denver, CO 9/25/2024 (2024).

"Mechanical Compression Regulates Tumor Spheroid Invasion into a 3D Collagen Matrix"; Mrinal Pandey, Young Joon Suh, Minha Kim, Hannah Jane Davis, Jeffrey E Segall, & Mingming Wu, Physical Biology, Volume 21, Number 3, DOI: 10.1088/1478-3975/Ad3ac5 (2024).

"Metal Core Substrate for Advanced Packaging"; Shane Mcmahon, Graeme Housser, Gomactech 2024 Conference Paper and Poster Presentation March 18-21, 2024 - Charleston, SC (2024).

"Metal Core Substrate for Advanced Packaging"; Shane Mcmahon, Graeme Housser, Imaps 2024 Boston Conference Presentation September 28-October 3, 2024 - Boston MA (2024).

"Metal Substrates with Structures Formed Therein and Methods of Making Same"; Chad B. Moore, Graeme F. Housser, Shane T. McMahon, U.S. Patent US12087670B1 Assignee: Lux Semiconductors, Inc - 9/10/2024 (2024).

"Metasurface-Enhanced Mid-Infrared Microscopy for Vibrational Imaging in Fixed and Living Cells"; Steven H. Huang, Po-Ting Shen, Giovanni Sartorello, Aditya Mahalanabish, & Gennady Shvets, Proc. SPIE PC12855, Advanced Chemical Microscopy for Life Science and Translational Medicine 2024, PC1285503 (13 March 2024) (2024).

"Microbes and Biomechanics"; Hernandez, C.J., UC-Wide Bioengineering Meeting. La Jolla, CA, USA (2024).

"Micron-Scale Topographies Affect Phagocytosis of Bacterial Cells on Polydimethylsiloxane Surfaces"; Yikang Xu, K. Scott Phillips, Dacheng Ren, Acta Biomaterialia Volume 187, 1 October 2024, Pp. 253-260 (2024).

"Microphysiological System to Address the Opioid Crisis: A Novel Multi-organ Model of Acute Opioid Overdose and Recovery"; A Patel, S. Poddar, D. Nierenberg, S. Lang, H. Wang, C. P. Pires Demello, J. Gamarra, A. Colon, P. Kennedy, J. Roles, J. Klion, W. Bogen, C. Long, X, Guo, P. Tighe, S. Schmidt, M.L Shuler, J.J. Hickman, Current Research In Toxicology 8, 100209 (2024).

"Microresonator-Frequency-Comb-Based Platform for Clinical High-Resolution Optical Coherence Tomography"; Michal Lipson, Xingchen JI, Alexander Klenner, Xinwen Yao, Yu Gan, Alexander L. Gaeta, Christine P Hendon, US11859972B2. (2024).

"Microresonator-Frequency-Comb-Based Platform for Clinical High-Resolution Optical Coherence Tomography"; Michal Lipson, Xingchen JI, Alexander Klenner, Xinwen Yao, Yu Gan, Alexander L. Gaeta, Christine P. Hendon, US20240302157A1. (2024).

"Micro-Scale Topographies Affect Phagocytosis of Bacterial Cells on Polydimethylsiloxane Surface"; Yikang Xu, Zehui Han, K. Scott Phillips, Dacheng Ren, Biomedical Engineering Society (BMES) 2024 Annual Meeting (2024).

"Micro-Scale Topographies Affect Phagocytosis of Bacterial Cells on Polydimethylsiloxane Surface"; Yikang Xu, K. Scott Phillips, Dacheng Ren, Acta Biomaterialia. 2024 Aug 28;300(5):107231. (2024).

"Microscopic Magneto-Elastic Multi-State Machines"; Lim, Melody X. Et Al., Poster Presentation, The 8th International Soft Matter Conference (2024).

"Mimicking Kidney Flow Shear Efficiently Induces Aggregation of LECT2, a Protein Involved in Renal Amyloidosis"; Jeung-Hoi Ha, Yikang Xu, Harsimranjit Sekhon, Wenhan Zhao, Stephan Wilkens, Dacheng Ren and Stewart N Loh., J Biol Chem. 2024 Mar 26;300(5):107231. (2024).

"Mineralized Collagen Alters Osteoclast Differentiation to Mediate Tumor Cell Invasion"; K. Persson, S. Sutter, M. Whitman, M. Tran, S. Choi, L. Estroff, And C. Fischbach, (Poster Presentation) Signal Transduction by Engineered Extracellular Matrices Gordon Research Conference, Manchester NH, July 21-26, 2024 (2024).

"Mineralized Collagen Alters Osteoclast Differentiation to Mediate Tumor Cell Invasion"; C. Fischbach, ATCC, Baltimore, September 30, 2024 (2024).

"Mineralized Collagen Alters Osteoclast Differentiation to Mediate Tumor Cell Invasion"; C. Fischbach, GRC Signaling by Adhesion Receptors, July 16, 2024 (2024).

"Mist-CVD NiO/Ga2O3 Schottky Diodes and Conduction Non-Idealities for kV Devices"; Bennett Cromer, GOX-Workshop 2024, Columbus OH (2024).

"Mitigating Phonon-Mediated Quasiparticle Poisoning of Superconducting Qubits"; Britton Plourde, Invited Talk: Radiation Impact on Superconducting Qubits Workshop, Femi National Accelerator Lab, Batavia, IL, May 2024 (2024).

"Modeling and Imaging of GHz Ultrasonic Impedance of C. Elegans"; Anuj Baskota, Hsin-Yun Chang, Amaresh Chaturbedi, Justin Kuo, Serhan Ardanuc, Siu Sylvia Lee, Amit Lal (2024).

"Modeling Particle Impacts and Quasiparticle Poisoning in Superconducting Qubit Arrays"; E. Yelton, Contributed Talk: American Physical Society March Meeting, Minneapolis, MN, March 4, 2024 (2024).

"Modeling Phonon-Mediated Quasiparticle Poisoning in Superconducting Qubit Arrays"; E. Yelton, C.P. Larson, V. Iaia, K. Dodge, G.La Magna, P.G. Baity, I.V. Pechenezhskiy, R. Mcdermott, N.A. Kurinsky, G. Catelani, And B.L.T. Plourde, Physical Review B 110, 024519-30 July 2024 (2024).

"Modeling the Synovium on a Chip for Studying the Interactions Between Lymphatic Vasculature and Synoviocytes in Rheumatoid Arthritis; Kraus S., Lee E., Biomedical Engineering Society (BMES) Annual Meeting, Baltimore, MD (2024).

"Modification of the Niobium Oxide Surface for Superconducting Radio-Frequency Applications"; N. Sitaraman Et Al., Oral Presentation at Applied Superconductivity Conference 2024, Salt Lake City, UT, September 2024 (2024).

"Monomeric and Oligomeric Amyloid-Beta Cause Distinct Alzheimer's Disease Pathophysiological Characteristics in Astrocytes in Human Glymphatics-On-Chip Models"; Aria R. Yslas, Rena Park, Nozomi Nishimura, Esak Lee, Lab on a Chip. 2024 July 16; 24, 3826-3839 (2024).

"Multimode Metamaterial Ring Resonator as an Entangling Bus for Artificial Atoms"; Tianna Mcbroom-Carroll, Syracuse University Dissertations and Theses. 1898., February 2024 (2024).

"Multiscale Analysis of Klf10's Impact on the Passive Mechanical Properties of Murine Skeletal Muscle"; Y. Tatarenko, M. Li, P. Pouletaut, M. Kammoun, J. R. Hawse, V. Joumaa, W. Herzog, S. Chatelin, S. F. Bensamoun, Journal of the Mechanical Behavior of Biomedical Materials 150: 106298. Doi: 10.1016/J.Jmbbm.2023.106298 (2024 Feb) (2024).

"n Situ Derivatization of Unsaturated Mid-Chain Alcohols with Pyridine During Direct Analysis in Real Time Mass Spectrometry (DART-MS)"; Scott Z*, Kalenak AP, And Sacks G., 2nd Annual Conference of the American Society for Mass Spectrometry. Anaheim, CA. (June 2024) (2024).

"Nanoengineering Spikey Surfaces: Investigation of Reversible Organizational Control of Surface-Tethered Polypeptide Brushes"; Yuming Huang, Hyunseok Kim, Luis Adrian Padilla Salas, Warren R. Zipfel, Su-Mi Hur, and Christopher K. Ober, ACS Publications, Langmuir. 2024 Nov 12;40 (45): 24045-24061. Doi: 10.1021/Acs.Langmuir.4c03345 (2024).

"Nanomolding of Two-Dimensional Materials for Next-Generation Electronics"; Quynh Sam, CNF Annual Review (2024).

"Nanoscale Characterization of a Novel Electro-Chemical Memory Device by STEM-EELS"; Stephen D. Funni, Longlong Xu, Bilge Yildiz, and Judy Cha, Microscopy and Microanalysis, 30 (Suppl 1), 2024, 1130-1132 Https://Doi.Org/10.1093/Mam/Ozae044.562 (2024).

"Nanoscale Physical Barrier by Cellular Mucin Protects Cancer Cells from Immune Cell Attack"; Sangwoo Park, 2024 8th New England Glyco-Chemistry Meeting, Brandeis University, Waltham, MA, USA, June 8, 2024 (2024).

"Nanostructured Polymer Thin Films for Tailoring Surface Topography and Functionalities"; Yuming Huang, Cornell University PhD Thesis (2024).

"Nanowired to Regulate Cellular Fate Trajectories of T Cells"; Z. Dai, S. Grier, Z. Zhong, Z. Tong, A. Singh, Biomedial Engineering Society (BMES) Annual Meeting Balitmore, MD (Oral Presentation) (2024).

"Near-Unity-Efficiency Frequency Conversion on a Silicon-Nitride Chip"; Yun Zhao, Karl J. Mcnulty, Michal Lipson, & Alexander L. Gaeta, In CLEO 2024 (2024), Paper Sth1f.5. CLEO: Science and Innovations, Optica Publishing Group, P. Sth1f.5. (2024).

"Neural Inspired Behaviors in Electronics"; Taghavi Nezam Abad, Milad, Cornell University ProQuest Dissertations & Theses, 2024. 30993704 (2024).

"New Approaches to Dissect Leaf Hydraulics Reveal Large Gradients in Living Tissues of Tomato Leaves"; Piyush Jain, Annika E. Huber, Fulton E. Rockwell, Sabyasachi Sen, N. Michele Holbrook, Abraham D. Stroock, New Phytologist Volume 242, Issue 2, April 2024, Pp. 453-465 (2024).

"New Insights into Nuclear Mechanobiology in Physiology and Disease"; Jan Lammerding, Invited Platform Presentation at the Keen-On Healing Fibrosis Symposium at the Keenan Research Centre in Toronto. Toronto, Canada (19 October 2024) (2024).

"Nonlinear Dynamics of Coupled-Resonator Kerr-Combs"; Swarnava Sanyal, Yoshitomo Okawachi, Yun Zhao, Bok Young Kim, Karl J. Mcnulty, Michal Lipson, Alexander L. Gaeta, arXiv:2409.17343 (25 September 2024) (2024).

"Nonlinear Mid-Infrared Meta-Membranes"; Giovanni Sartorello, Joshua Bocanegra, David Knez, Daniil M. Lukin, Joshua Yang, Jelena Vučković, Dmitry A. Fishman, Gennady Shvets and Maxim R. Shcherbakov, Nanophotonics Volume 13, Issue 18, July 24, 2024 (2024).

"Normalizing Lymphatic Drainage Potentiates Immunotherapy in Breast Cancer"; Harry Peng, Biomedical Engineering Society Annual Conference, Baltimore MD (Oral Presentation), October 23-26, 2024 (2024).

"Normalizing Tumor Lymphatic Drainage Potentiates Immunotherapy in Breast Cancer"; Peng H., Lu R., Lee E., Biomedical Engineering Society (BMES) Annual Meeting, Baltimore, MD (2024).

"Novel Materials for Beam Acceleration"; S. Seddon-Stettler Et Al., (Nathan Sitaraman), In Proc. IPAC'24 Nashville, TN, May 2024, Pp. 2730-2732 Doi:10.18429/Jacow-IPAC2024-WEPS15 (2024).

"N-Terminal Tags Impair the Ability of Lamin a to Provide Structural Support to the Nucleus"; Jacob Odell, Jan Lammerding , Journal of Cell Science Volume 137, Issue 16, 28 August 2024 (2024).

"Nuclear Mechanobiology in Physiology and Disease"; Jan Lammerding, Squish and Squeeze-Invited Seminar as the Distinguished Keynote Speaker at the Graduate Research Symposium in The Biomedical Engineering Department at Boston University. Boston, MA (13 December 2024) (2024).

"Nuclear Mechanobiology in Physiology and Disease"; Jan Lammerding, Squish and Squeeze-Invited Seminar at the Mechanobiology Institute, National University of Singapore. Singapore (15 January 2024) (2024).

"Nuclear Mechanobiology of Cancer Cells- The Effects of Cells Squeezing Through Tight Spaces and Other Lessons Learned"; Jan Lammerding, Invited Platform Presentation at the Ushma Mahajani Symposium on Mollecular Medicine 'Physical Forces and the Hallmarks of Cancer' Co-Hosted by the UCSD, The Salk Institute, and The Sanford Burnham Prebys Medical Discovery Institute. La Jolla, CA (6 September 2024) (2024).

"Nuclear Mechanobiology of Confined Cell Migration"; Jan Lammerding, Invited Virtual Platform Presentation at the 8th CRCL Scientific Day "When Fighting Cancer Becomes Physical", Organized by the Cancer Research Center or Lyon (CRCL), France (14 June 2024) (2024).

"N-Way Frequency Beamsplitter for Quantum Photonics"; Richard Oliver, Miri Blau, Chaitali Joshi, Xingchen Ji, Ricardo Gutierrez-Jauregui, Ana Asenjo-Garcia, Michal Lipson, Alexander L. Gaeta, arXiv:2405.02453 (3 May 2024 (V1), Last Revised 15 May 2024 (V2) (2024).

"Observation of Double Quantum Spin Hall Phase Spin-Chern Insulators in Moiré WSe2"; K. Kang, Y. Qiu, K. Watanabe, T. Taniguchi, J. Shan and K.F. Mak, Nano Lett. 24, 46, 14901–14907 (2024).

"Observation of Spin Polarons in a Frustrated Moiré Hubbard System"; Z. Tao, W. Zhao, B. Shen, P. Knüppel, K.Watanabe, T. Taniguchi, J. Shan, And K. F. Mak, Nat. Phys. 20, 783–787 (2024).

"Observation of the Fractional Quantum Spin Hall Effect in Moiré MoTe2"; K. Kang, B. Shen, Y. Qiu, Y, Zeng, Z. Xia, K. Watanabe, T. Taniguchi, J. Shan and K.F. Mak, Nature 628, 522–526 (2024).

"Optical Probe for Measuring Photon Density"; Thomas Dunbar, Internation Patent Publication 11-7-2024 -WO 2024/229409. (2024).

"Optical Probe for Measuring Photon Density"; Thomas Dunbar, US Patent Application Publication 11-7-24 - US 2024/0369405 A1. (2024).

"Optical Readout of the Chemical Potential of Two-Dimensional Electrons"; Z. Xia, Y. Zeng, K. Watanabe, T. Taniguchi, J. Shan, and K.F. Mak, Nat. Photon. 18, 344–349 (2024).

"Optical Super-Resolution Nanothermometry Via Stimulated Emission Depletion Imaging"; Z. Ye, B. Harrington, And A.D. Pickel, 7th ASME Micro/Nanoscale Heat and Mass Transfer International Conference. Nottingham, United Kingdom. August 5-7, 2024. Contributed Talk. (Best Presentation Award) (2024).

"Optical Super-Resolution Nanothermometry Via Stimulated Emission Depletion Imaging"; Z. Ye, B. Harrington, and A.D. Pickel, MECE. Portland, OR. November 17 – 21, 2024. Invited Poster Presentation For 2024 ASME Rising Stars of Mechanical Engineering (2024).

"Optical Super-Resolution Nanothermometry Via Stimulated Emission Depletion Imaging of Upconverting Nanoparticles"; Z. Ye, B. Harrington, And A.D. Pickel, UPCON: 4th Conference on Properties, Design, and Applications of Upconversion Nanomaterials. Montréal, Canada. April 7-12, 2024. Contributed Talk (2024).

"Optical Super-Resolution Nanothermometry Via Stimulated Emission Depletion Imaging of Upconverting Nanoparticles"; Z. Ye, B. Harrington, and A.D. Pickel, Science Advances 10, Eado6268 (2024).

"Optical Torque Calculations and Measurements for DNA Torsional Studies"; Yifeng Hong, Fan Ye, Jin Qian, Xiang Gao, James T. Inman, & Michelle D. Wang, Biophysical Journal (2024).

"Optically Transparent 4-Port UWB Antenna for MIMO Applications"; Rabia Yahya, Haosen Yin, David Bertuch, A. El-Ghazaly, International Microwave and Antenna Symposium (IMAS), Marrakesh, Morocco (2024).

"Ordinary and Extraordinary Permittivities of 4H SiC at Different Millimeter-Wave Frequencies, Temperatures, and Humidities"; Tianze Li, Xiaopeng Wang, James C. M. Hwang, Shana Yanagimoto, IEEE Journal of Microwaves, Volume 4, Issue 4, Pp. 666-674, Oct. 2024, Doi: 10.1109/JMW.2024.3453325 (2024).

"Over 6 MV/Cm Operation in β-Ga2O3 Schottky Barrier Diodes with IrO2 and RuO2 Anodes Deposited by Molecular Beam Epitaxy"; Cromer, B.; Saraswat, D.; Pieczulewski, N.; Li, W.; Nomoto, K.; Hensling, F. V. E.; Azizie, K.; Nair, H. P.; Schlom, D. G.; Muller, D. A.; Jena, D; Xing, H. G., Sci. Technol. A 42 033206 (2024).

"Over 6 MV/Cm Operation in β-Ga2O3 Schottky Barrier Diodes with IrO2 and RuO2 Anodes Deposited by Molecular Beam Epitaxy"; B. Cromer, D. Saraswat, N. Pieczulewski, W. Li, K. Nomoto, F.V.E. Hensling, K. Azizie, H.P. Nair, D.G. Schlom, D.A. Muller, D. Jena, H.G. Xing, JVSTA, Volume 42, Issue 3, May 2024 (2024).

"Overcoming Stress Limitations in SiN Nonlinear Photonics via a Bilayer Waveguide"; Karl J. Mcnulty, Shriddha Chaitanya, Swarnava Sanyal, Andres Gil-Molina, Mateus Corato-Zanarella, Yoshitomo Okawachi, Alexander L. Gaeta, Michal Lipson, Arxiv:2409.08358 (12 September 2024) (2024).

"Overcoming Thermal Effects with Kerr Solition Combs in Compact Photonic Structures"; Garrett Beals, Yun Zhao, Karl Mcnulty, Sai Kanth Dacha, Michal Lipson, In 2024 Conference on Lasers and Electro-Optics (CLEO). 2024, Pp. 1-2 (2024).

"Passivation and Suppression of Oxides on Nb via Au and Zr Capping Layers"; N. Sitaraman Et Al., Oral Presentation to Working Group 1: Progress on High-G and High-Q Activites at TESLA Technology Collaboration Meeting, Lund, Sweden, November 2024 (2024).

"Passive Control of Capillary Rise Dynamics in Micro-Channels"; Aniruddah Saha, Joshua Krsek, Giancarlo D'Orazio, Sadaf Sobhani, 77th Annual Meeting of the Division of Fluid Dynamics (2024).

"Passive Control of Capillary Rise Dynamics in Micro-Channels"; Saha, A., Krsek, J., D'Orazio, G., & Sobhani, S, Bulletin of the American Physical Society (2024).

"Passive Post-Resonance Tuned Reflectors to Achieve Both 10-Bit Phase-Shifting Resolution and Low Insertion Loss Across 20–30 GHz"; B. Govind, Alyssa Apsel, IEEE Transactions on Circuits (2024).

"Performance Limiting Factors of 15-GHz Ku-Band FBARs"; Wenwen Zhao, Rishabh Singh, Saurabh Vishwakarma, Jimy Encomendero, Kazuki Nomoto, Lei Li, David J. Smith, James C. M. Hwang, Huili G. Xing, Debdeep Jena, IEEE Transactions on Electron Devices, Volume 71, NO. 8, August 2024, Doi: 1109/TED.2024.3418722 (2024).

"Phase-Matched Third-Harmonic Generation in Silicon Nitride Waveguides"; Surendar Vijayakumar, Kaustubh Vyas, Daniel H. G. Espinosa, Orad Reshef, Meiting Song, Kashif Masud Awan, Saumya Choudhary, James Cardenas, Robert W. Boyd, & Ksenia Dolgaleva, DE GRUYTER Nanophotonics 2024; 13(18): 3385-3393 (2024).

"Phonon-Mediated Quasiparticle Poisoning and Correlated Errors in Superconducting Qubit Arrays"; Britton Plourde, Invited Talk: Conference on New Frontiers in Scaling Quantum, ICTP, Trieste, Italy, January 2024 (2024).

"Photophysical Properties of Exciton–Polaritons in CdSe Nanocrystal–Cavity Systems"; Morshed, Ovishek, University of Rochester ProQuest Dissertations & Theses, 2024. 31558345 (2024).

"Physical Neural Networks Using Acoustics and Photonics"; Stein, M. M., Cornell University PhD Thesis (2024).

"Picosecond Volume Expansion Drives a Later-Time Insulator–Metal Transition in a Nano-Textured Mott Insulator"; Anita Verma, Denis Golež, Oleg Yu. Gorobtsov, Kelson Kaj, Ryan Russell, Jeffrey Z. Kaaret, Erik Lamb, Guru Khalsa, Hari P. Nair, Yifei Sun, Ryan Bouck, Nathaniel Schreiber, Jacob P. Ruf, Varun Ramaprasad, Yuya Kubota, Tadashi Togashi, Vladimir A. Stoica, Hari Padmanabhan, John W. Freeland, Nicole A. Benedek, Oleg G. Shpyrko, John W. Harter, Richard D. Averitt, Darrell G. Schlom, Kyle M. Shen, Andrew J. Millis & Andrej Singer, Nature Physics 20, 807-814 (2024).

"pid Analysis of Free and Total Volatile Phenols by Sorbent Sheet Extraction–Direct Analysis in Real Time Mass Spectrometry (SPMESH-DART-MS)"; Kalenak AP*, Bates TL, Bergmann B, And Sacks GL., 1st Annual Conference of the American Society for Mass Spectrometry. Houston, TX. R (June 2024) (2024).

"Piezo1 Regulates Meningeal Lymphatic Vessel Drainage and Alleviates Excessive CSF Accumulation"; Dongwon Choi, Eunkyung Park, Joshua Choi, Renhao Lu, Jin Suh Yu, Chiyoon Kim, Luping Zhao, James Yu, Brandon Nakashima, Sunju Lee, Dhruv Singhal, Joshua P. Scallan, Bin Zhou, Chester J. Koh, Esak Lee, And Young-Kwon Hong, Nature Neuroscience, 2024 Mar 25, 27, 913-926 (2024).

"Plasmonic Nanostructure and Associated Cellular Imaging Systems and Methods"; Aditya Mahalanabish, He Huang, Gennady Shvets (2024).

"Polarity-Dependent Structural and Electronic Properties of MBE Grown NbN/GaN Structures"; Anand Ithepalli, 2024 EMRS Fall, Warsaw, Poland (2024).

"Polyimide Films Manufactured Using Partially Wet Electrospray Deposition"; Bryce J. Kingsley, Paul R. Chiarot, ProQuest Dissertations & Theses, 2024. 31556478. (2024).

"Polymer Brushes and Synthetic Receptors: A Dynamic Duo in Sensing Technologies"; Gozde Aktas Eken Et Al., ACS Spring 2024, March 20, 2024 (2024).

"Polypeptoids with Defined Sequences Facilitating Stochastics Control and Discovery of Phenol-Based EUV Patterning Mechanism"; Chenyun Yuan, Cameron P. Adams, Rika Marui, Rachal A. Segalman, Christopher K. Ober, 2024 New York State Nanotechnology Network (NNN) Symposium, Rochester, NY, USA (2024).

"Populating and Feeding Rigid Engineered Living Materials"; Hernandez, C.J., MRS Fall Meeting. Boston, MA, USA (2024).

"Post-Resonance Reflections Break the Loss-Vs-Phase-Resolution Trade-Off in Microwave Electronics"; Bala Govind, Andreia Cathelin, Alyssa Apsel, Eess-arXiv:2407.16016 (2024).

"Preferential Electrospray Deposition of Polymer Films on Multi-Material Surfaces"; Bryce J. Kingsley, Paul R. Chiarot, Progress in Organic Coatings. Volume 200, 109086. (2024).

"Programmable Plants and the Internet of Living Things"; Abraham Stroock, Netflex Workshop: Advancing Electronics Packaging of Hybrid Electronics for Industrial and Medical Applications. University of Binghampton. April 2024 (2024).

"Programmable Viscosity Metamaterials: Designing Fluid Properties Using Temporal Superposition of Shear and Acoustics"; Prateek Sehgal, Meera Ramaswamy, Edward YX Ong, Christopher Ness, Itai Cohen, Brian J Kirby, Physical Review Research Volume 6, Issue 4, Pp. 043107 (2024).

“Protecting Qubits from High-Energy Impacts”; Britton Plourde, Invited Talk: R.G. Herb Condensed Matter Seminar, University of Wisconsin-Madison, March 2024 (2024).

“Pulse Coupled Oscillators for Micromachines”; Taghavi M, Wang W, Cohen I, Et Al., Bulletin of The American Physical Society (2024).

“Purcell Enhancement and Spin Spectroscopy of Silicon Vacancy Centers in Silicon Carbide Using an Ultra-Small Mode-Volume Plasmonic Cavity”; Jae-Pil So, Jialun Luo, Jaehong Choi, Brendan Mccullian, Gregory D. Fuchs, Nano Letters 24, 11669 (2024).

“Putting Magnets to Work”; A. El-Ghazaly, EE Colloquium, University of Buffalo, April 4, 2024 (2024).

“Quantitative Comparison of Simulation and Experiment Enabling a Lithography Digital Twin”; Yutong Xie, Benyamin Davaji; Ivan Chakarov; Sandy Wen; Michael Hargrove; David Fried, IEEE Transactions on Semiconductor Manufactoring, Volume 37, Issue 4, Pp. 546-552 DOI: 10.1109/TSM.2024.3427409 (2024).

“Quantitative Scanning Microwave Microscopy for Transfer Characteristics of GaN High-Electron-Mobility Transistors”; Xiaopeng Wang, Kazuki Nomoto, Gianluca Fabi, Marco Farina, Debdeep Jena, & Huili Grace Xing, IEEE DOI: 10.1109/TMTT.2024.3449128, 5 September 2024 (2024).

“Quantitative Scanning Microwave Microscopy of Nanoelectronic Materials and Devices”; X. Wang, Phd Thesis, May 2024 (2024).

“Quantitative Scanning Microwave Microscopy Transfer Characteristics of GaN/AIGaN High-Electron-Mobility Transistors”; X. Wang, K. Nomoto, G. Fabi, M. Farina, D. Jena, H. G. Xing, And J. C. M. Hwang, In SRC TECHCON, Austin, TX, USA, Sep. 2024 (2024).

“Quantum State Tomography in a Third-Order Integrated Optical Parametric Oscillator”; Roger Alfredo Kogler, Gabriel Couto Rickli, Renato Ribeiro Domeneguetti, Xingchen Ji, Alexander L. Gaeta, Michal Lipson, Marcelo Martinelli, And Paulo Nussenzveig, Optica Publishing Group: Optics Letters; Volume 49, Issue 11, Pp. 3150-3153 (2024).

“Quasiparticle Poisoning in Superconducting Qubit Arrays from Controlled Gamma Irradiation”; C. Larson, Contributed Talk: American Physical Society March Meeting, Minneapolis, MN, March 6, 2024 (2024).

“Quasiparticle Poisoning of Fluxonium Qubits”; Presenter: Kesavan Manivannan - Authors: Kesavan Manivannan, Ben Byrd, Ivan V. Pechenezhskiy, 2024 APS March Meeting; Minneapolis & Virtual S48.00008 (2024).

“Quasiparticle Poisoning of Superconducting Qubits from Resonant Absorption of Pair-Breaking Photons”; C.H. Liu, D.C. Harrison, S. Patel, C.D. Wilen, O. Rafferty, A. Shearrow, A. Ballard, V. Iaia, J. Ku, B.L.T. Plourde, R. Mcdermott, Physical Review Letters 132, 017001-2 January 2024 (2024).

“Quasi-True Time Delay”; B. Govind, T. Tapen, A. Apsel, US Patent appl. 18/908,585 (filled 10/24) (2024).

“Radiation Resilience of β-Ga2O3 Schottky Barrier Diodes Under High Dose Gamma Radiation”; Saleh Ahmed Khan, Sudipto Saha, Uttam Singisetti, A. F. M. Anhar Uddin Bhuiyan, Journal of Applied Physics Volume 136, Issue 22, 14 December 2024 (2024).

“Rapid Analysis of Aldehydes and Volatile Phenols Following in Situ Derivatization with Sorbent Sheets Coupled to Direct Analysis in Real Time Mass Spectrometry (DART-MS)”; Kalenak AP*, Bates TL, Bergmann B, and Sacks GL., Vino Analytica Scientia. Davis, CA July 2024 (2024).

“Rapid Analysis of C 6 Aldehydes by Solid-Phase Microextraction Sheets and Direct Analysis in Real-Time Mass Spectrometry (SPMESH-DART-MS)”; Terry L. Bates, Gavin L. Sacks, ACS – Food Science & Technology. 4, 9, Pp 2115–2123. (2024).

“Realignment and Suppression of Charge Density Waves in the Rare-Earth Tritellurdes R Te 3 (R = La, Gd, Er) ”; Saif Siddique, James L. Hart, Drake Niedzielski, Ratnadwip Singha, Myung-Geun Han, Stephen D. Funni, Michael Colleta, Mehrdad T. Kiani, Noah Schnitzer, Natalie L. Williams, Lena F. Kourkoutis, Yimei Zhu, Leslie M. Schoop, Tomas A. Arias, And Judy J. Cha, Phys. Rev. B 110, 014111 – Published 25 July, 2024 (2024).

“Realization of a Dual-Rail Photonic Cluster State”; Miri Blau, Richard Oliver, Xingchen Ji, Michal Lipson, And Alexander L. Gaeta, In CLEO 2024, Paper FM1K.5. CLEO Fundamental Science, Optica Publishing Group, P. FM1K.5 (2024).

“Realization of the Haldane Chern Insulator in a Moiré Lattice”; W. Zhao, K. Kang, Y. Zhang, P. Knüppel, Z. Tao, L. Li, C. Tschirhart, E. Redekop, K. Watanabe, T. Taniguchi, A. Young, J. Shan, And K.F. Mak, Nat. Phys. 20, 275–280 (2024).

“Real-Space Visualization of a Defect-Mediated Charge Density Wave Transition”; James L. Hart, Haining Pan, Saif Siddique, Noah Schnitzer, Krishnanand Mallayya, Shiyu Xu, Lena F. Kourkoutis, Eun-Ah Kim, & Judy J. Cha, PNAS August 6, 2024 (2024).

“Rear Cortex Contraction Aids in Nuclear Transit During Confined Migration by Increasing Pressure in the Cell Posterior”; Jeremy Keys, Brian C.H. Cheung, Margaret A. Elpers, Mingming Wu, Jan Lammerding, Journal of Cell Science Volume 137, Issue 12, June 2024 (2024).

“Recreating the Biological Steps of Viral Infection on a Cell-Free Bioelectronic Platform to Profile Viral Variants of Concern”; Zhongmou Chao, Ekaterina Selivanovitch, Konstantinos Kallitsis, Zixuan Lu, Ambika Pachaury, Roisin Owens, & Susan Daniel, Nature Communications 15, Article Number: 5606 (2024).

“Remote Imprinting of Moiré Lattices”; J. Gu, J. Zhu, P. Knüppel, K. Watanabe, T. Taniguchi, J. Shan, And K. F. Mak, Nat. Mater. 23, 219–223 (2024).

“Resistivity Scaling of Porous Mop Narrow Lines”; Han Wang, Gangtae Jin, Quynh P. Sam, Stephen D. Funni, Roberto R. Panepucci, Astrid D. Kengne, Saif Siddique, Nghiep Khoan Duong, Yeryun Cheon, Mehrdad T. Kiani, Judy J. Cha, APL Materials Volume 12, Issue 12 December 2024 (2024).

“RF Operation of AIN/AI0.25Ga).75N/AIN HEMTs With fT/fmax of 67/166 GHz”; E. Kim, J. Singhal, A. Hickman, L. Li, R. Chaudhuri, Y. Cho, J. C. M. Hwang, D. Jena, And H.G. Xing, In IPC APEX EXPO Electron. Circuits World Conv. (ECWC16), Anaheim, CA, USA, Apr. 2024 (2024).

“Robust Microstructure of Self-Aligning Particles in a Simple Shear Flow”; Neeraj S. Borker, Abraham D. Stroock, Donald L. Koch, APS Physical Review Fluids, 9 (4), P. 043301, 24 April 2024 (2024).

“Role of Heterointerface in Lithium-Induced Phase Transition in Td-WTe2 Nanoflakes”; Shiyu Xu, Mengjing Wang, Maria Bambrick-Santoyo, Kenneth Evans-Lutterodt, Natalie L. Williams, & Judy J. Cha, ACS Applied Electronic Materials Volume 6, Issue 2 February 14, 2024 (2024).

“Room Temperature Optically Detected Magnetic Resonance of Single Spins in Gan”; Gregory Fuchs, International Workshop on Nitrides, Honolulu, HI (2024).

"Room Temperature Optically Detected Magnetic Resonance of Single Spins in GaN"; Jialun Luo, Yifei Geng, Farhan Rana, Gregory D. Fuchs, Nature Materials 23, 4, 512-518-12 February 2024 (2024).

"Sarcomere Length and Force Behavior in Skeletal Muscle Myofibrils"; Ino T, Jinha A, Leonard T, Herzog W, Conference of the Canadian Society for Biomechanics, Edmonton AB, August 19-22, 2024 -Poster Presentation (2024).

"Scaling On-Chip Photonic Neural Processors Using Arbitrarily Programmable Wave Propagation"; Tatsuhiro Onodera, Martin M. Stein, Benjamin A. Ash, Mandar M. Sohoni, Melissa Bosch, Ryotatsu Yanagimoto, Marc Jankowski, Timothy P. Mckenna, Tianyu Wang, Gennady Shvets, Maxin R. Shcherbakov, Logan G. Wright, Peter L. Mcmahon, arXiv:2402. 17750 [Physics Optips] (2024).

"Scanning SQUID Microscopy on Van Der Waals Heterostructure with in Situ Uniaxial Strain Tuning"; Ruiheng Bai, Kaifei Kang, Bowen Shen, Brian T. Schaefer, Alexander Jarjou, Takashi Taniguchi, Kenji Watanabe, Kin Fai Mak, Jie Shan, Katja Nowack (2024).

"Schottky Barrier Height Dependence on Polarity and Doping Density of GaN in Epitaxially Grown NbN/GaN Structures"; Anand Ithepalli, 2024 ICPS, Ottawa, Canada (2024).

"Self-Timed and Spatially Targeted Delivery of Chemical Cargo by Motile Liquid"; Crystal, Xin Wang, Yu Yang, Sangchul Roh, Sarah Hormozi, Nathan C. Gianneschi, Nicholas L. Abbott, Advanced Materials, Volume 36, Issue 28 (July 11, 2024) 2311311 (2024).

"Sequence Control in Polypeptoid Photoresists and its Effect on Patterning Performance"; Chenyun Yuan, Cameron P. Adams, Rika Marui, Brett A. Helms, Rachel A. Segalman, Christopher K. Ober, 2024 EUVL Workshop and Supplier Showcase, Berkeley, CA, USA (2024).

"Sequence-Defined Metal-Organic Polypeptoids as Photoresists with Molecular Precision for EUV Lithography"; Chenyun Yuan, Erina Yoshida, Cameron Adams, Rachel A. Segalman, Christopher K. Ober, Advances Pattering Materials and Processes XLI, San Jose, CA, USA (2024).

"Serial Synchrotron Crystallography Sample Holding System"; R. E. Thorne, D. Closs, R. Jayne, and B. Apker, US 12, 007, 343 Issued: June 11, 2024 (2024).

"Shear Histories Alter Local Shear Effects on Thrombus Nucleation and Growth"; Junhyuk Kang, Anjana Jayaraman, James F Antaki, Brian Kirby, Annals of Biomedical Engineering Volume 52, Issue 4, Pp. 1039-1050 (2024).

"Silk Textiles as a Biosorbent and Oil-Water Separator"; B. Mori, AATCC Textile Summit, Savannah, Georgia (6-8 October 2024) (2024).

"Simulation, Generation, and Detection of Low Emittance Electron Beams for Ultrafast Science"; Kaemingk, Michael, Cornell University ProQuest Dissertations & Theses, 2024. 31562486 (2024).

"Single Spin Defects Hosted in Gallium Nitride"; Jialun Luo, Cornell University PhD Thesis (2024).

"Slow Light in Superconducting Metamaterial Transmission Lines with Left-Handed Dispersion"; Manabputra, Contributed Talk: American Physical Society March Meeting, Minneapolis, MN, March 8, 2024 (2024).

"Soft Elastomeric Nanofibers with Coaxially Embedded Liquid Metal Particles as a Conductive Filler for Soft Bioelectronic"; Dorsainvil, J. S., Tabor, C., Koh, A., BMES Annual Meeting, Baltimore, October 2024, Onsite Poster Presentation (2024).

"Soft Elastomeric Nanofibers with Coaxially Embedded Liquid Metal Particles as a Conductive Filler for Soft Bioelectronic"; Dorsainvil, J. S., Tabor, C., Koh, A., MRS Fall Meeting, Boston, December 2024, Onsite Poster Presentation (2024).

"Sonic Fourier Transform Imaging Using GHz Ultrasonic Transducer Array"; J. Hwang, J. Kuo, A. Naskota, And A. Lal, In 2024 IEEE 37th International Conference on Micro Electro Mechanical Systems (MEMS), 2024, Pp. 128-131 (2024).

"Spectrally Flat Normal-GVD Kerr Combs Via Opposite-Polarity Comb Synchronization"; Swarnava Sanyal, Bok Young Kim, Yoshitomo Okawachi, Yun Zhao, Karl J. Mcnulty, Michal Lipson, In 2024 Conference on Lasers and Electro-Optics (CLEO). 2024, Pp. 1-2 (2024).

"Spin Dynamics and Exchange Interactions from a Van Der Waals Antiferromagnet"; Thow Cham, Focus Session Invited Talk - American Physical Society (APS) March Meeting, Minneapolis, MN (2024).

"Spin Dynamics in Antiferromagnetic Van Der Waals Heterostructures"; Cham, T.M.J., Ph.D. Dissertation, Cornell University, Ithaca, USA (2024).

"Spin Physics from Topological Insulators and Spin Split Antiferromagnets"; R. Jain, 2024 March Meeting of the American Physical Society March 4-8, 2024, Minneapolis, MN (2024).

"Spin Qubits-Past, Present, and Applications"; Gregory Fuchs, 0 Years of Spin Plenary Session, Intermag 2024, Rio De Janeiro, Brazil (2024).

"Spin-Filter Tunneling Detection of Antiferromagnetic Resonance with Electrically-Tunable Damping; Thow Min Jerald Cham, Daniel G. Chica, Kenji Watanabe, Takashi Taniguchi, Xavier Roy, Yunqu Kelly Luo, Daniel C. Ralph, Materials Science arXiv: 2407.09462 12 July 2024 (2024).

"Spin-Orbit Torque in Magnetic Heterostructures: Exchange Interactions and Ultrasensitive Sagnac Magneto-Optic Interferometry"; Thow Cham, Invited Talk - Symposium on Low-Dimensional Magnetic Quantum Materials, Materials Research Society Spring Meeting & Exhibit, Seattle (2024).

"Spin-Orbit Torque in Magnetic Heterostructures: Exchange Interactions and Ultrasensitive Sagnac Optical Interferometry"; Y. Luo, 2024 March Meeting of the American Physical Society March 4-8, 2024, Minneapolis, MN (2024).

"Spontaneous Supercrystal Formation During a Strain-Engineered Metal–Insulator Transition"; Oleg Yu. Gorobstov, Ludi Miao, Ziming Shao, Yueze Tan, Noah Schnitzer, Berit Hansen Goodge, Jacob Ruf, Daniel Weinstock, Mathew Cherukara, Martin Victor Holt, Hari Nair, Long-Qing Chen, Lena Fitting Kourkoutis, Darrell G. Schlom, Kyle M. Shen, Andrej Singer, Advanced Materials Volume 36, Issue 32, August 8, 2024, 2403873 (2024).

"Stable Modelocking of Coupled Resonator Normal-GVD Kerr-Combs"; Swarnava Sanyal, Yoshitomo Okawachi, Yun Zhao, Bok Young Kim, Karl J. Mcnulty, Michal Lipson, and Alexander L. Gaeta, In CLEO 2024 (2024), Paper Fth4f.2. CLEO: Fundamental Science, Optica Publishing Group, P. Fth4f.2. (2024).

"Staphylococcus Aureus Colonization of Nanoscale Channels During Chronic Bone Infections"; Defrates, K., Lee, J., Jimenez, G., Hernandez, C.J., Biomedical Engineering Society, Baltimore, MD, USA (2024).

"Staphylococcus Aureus Does Not Use Durotaxis to Penetrate Osteocyte Canaliculi-Like Channels"; Defrates, K., Lee, J., Jimenez, G., Hernandez, C.J., American Society for Bone and Mineral Research, Toronto, Ontario, Canada (2024).

"Stomatal and Non-Stomatal Mechanisms Controlling Plant-Atmosphere Coupling"; Abraham Stroock, Harvard Workshop on Continental Climate. Harvard University. June 13-14, 2024 (2024).

"Strain-Balanced AlScN/GaN HEMTs with fT / fMAX of 173/321 GHz"; T.S. Nguyen and K. Nomoto and W. Zhao and C. Savant and H.G. Xing and D. Jena, 2024 International Electrong Devices Meeting (IEDM), Paper ID #: 922, Session Number: 9-5 (2024).

"Stroboscopic X-Ray Diffraction Microscopy of Dynamic Strain in Diamond Thin-Film Bulk Acoustic Resonators for Quantum Control of Nitrogen-Vacancy Centers"; Anthony D'Addario, Johnathan Kuan, Noah F. Opondo, Ozan Erturk, Tao Zhou, Sunhil A. Bhave, Martin V. Holt, & Gregory D. Fuchs, Physical Review Applied 22, 024016-7 August 2024 (2024).

"Study of Epitaxial Growth, Magnetic and Electric Properties, and Spin Transport in Room-Temperature Multiferroic Bismuth Ferrite Thin Films & Study of Room-Temperature Bistability of Antiferromagnetic and Ferromagnetic Phases in Iron-Rhodium Thin Films"; Yongjian Tang Cornell University May 2024 (2024).

"Superconducting Metamaterials for Quantum Simulations and Qubit Addressability in Quantum Processors"; Britton Plourde, US 12,069,966 (2024).

"Superconductivity in 3.6-Degree Twisted Bilayer Wse2"; Yiyu Xia, Gordon Research Conference (Two Dimensional Electronics Beyond Graphene) (2024).

"Superconductivity in the Parent Infinite-Layer Nickelate NdNiO2"; C. T. Parzyck, Y. Wu, L. Bhatt, M. Kang, Z. Arthur, T. M. Pedersen, R. Sutarto, S. Fan, J. Pelliciari, V. Bisogni, G. Herranz, A. B. Georgescu, D. G. Hawthorn, L. F. Kourkoutis, D. A. Muller, D. G. Schlom, K. M. Shen, arXiv: 2410.02007, 2 October 2024 (2024).

"Superconductivity in Twisted Bilayer WSe2"; Yiyu Xia; Zhongdong Han, Kenji Watanabe, Takashi Taniguchi, Jie Shan, Kin Fai Mak, Nature. 637, 833-838. Doi: 10.1038/S41586-024-08116-2. Epub 2024 Oct 30 (2024).

"Symmetry-Controlled Orbital Hall Effect in IrO2"; Michael Patton, Dongwook Go, Daniel A. Pharis, Xiaoxi Huang, Gautam Gurung, Evgeny Y. Tsymbal, Daniel C. Ralph, Mark S. Rzchowski, Yuriy Mokrousov, Chang-Beom Eom, Materials Science arXiv: 2410.02996 3 October 2024 (2024).

"Synthetic High Angular Momentum Spin Dynamics in a Microwave Oscillator"; Valla Fatemi, Nov 4-8, 2024: Spin Qubit, Sydney, Australia (2024).

"Synthetic High Angular Momentum Spin Dynamics in a Microwave Oscillator"; Saswata Roy, Alen Senanian, Christopher S. Wang, Owen C. Wetherbee, Luojia Zhang, B. Cole, C. P. Larson, E. Yelton, Kartikeya Arora, Peter L. Mcmahon, B. L. T. Plourde, Baptiste Royer, Valla Fatemi, May 24, 2024, arXiv:2405.15695. Doi: 10.48550/Arxiv.2405.15695 (2024).

"Systems, Compositions, and Methods for Manufacture of Sequence-Defined, Stochastic-Controlled, PAG-Free Polymeric EUV Photoresist Platforms"; Chenyun Yuan, Christopher K. Ober, Rachel Segalman, Cameron Adams, US Provisional Patent Application (2024).

"Telecom-To-Visible Frequency Conversion in a Sin Microresonator"; Sidarth Raghunathan, Richard Oliver, Yun Zhao, Karl Mcnulty, Michal Lipson, Alexander Gaeta, In 2024 Conference on Lasers and Electro-Optics (CLEO). 2024 Conference on Lasers and Electro-Optics (CLEO), Pp. 1-2 (2024).

"Temperature-Dependent Measurement of Hole Velocity Vs. Electric Field in Polarization-Induced Two-Dimensional Hole Gases in GaN/AlN Heterojunction"; Joseph Dill, 2024 Electronic Material Conference (2024).

"The Development of Complex Biomembrane Platforms to Investigate the Impact of Membrane Disrupting Agents on Membrane Biophysical Properties"; Bint E. Naser, Samavi Farnush, Cornell University ProQuest Dissertations & Theses (2024).

"The Effect of Nitrogen on the Stability of the Beta Phase in W Thin Films During Thermal Annealing"; Zhao Y. & Baker S.P., TMS 2024 Annual Meeting & Exhibition, Orlando, FL, United States (2024).

"The Effect of Nitrogen on Thermomechanical Behavior During the Beta-A Phase Transformation in W Thin Films"; Zhao Y., Morgan-Smith Myers, H.E., & Baker S.P, TMS 2024 Annual Meeting & Exhibition, Orlando, FL, United States (2024).

"The Lungs of Our Planet Engineering to Discovery in Plant Leaves"; Abraham Stroock, Institute Lecture, IIT Delhi, March 20, 2024 (2024).

"The Lungs of Our Planet Engineering to Discovery in Plant Leaves"; Abraham Stroock, Keynote at Azeotropy Conference. IIT Bombay. March 16, 2024 (2024).

"The Mechanics of Tumor Spheroids Revealed by a 3D Microfluidic Rheometer"; Young Joon Suh, Mrinal Pandey, Tao Luo, Jeffrey E Segall & Mingming Wu, 2024 CNF Annual Meeting (Poster Presentation), Ithaca, NY, September 17, 2024 (2024).

"The Mechanics of Tumor Spheroids Revealed by a 3D Microfluidic Rheometer"; Young Joon Suh, Mrinal Pandey, Tao Luo, Jeffrey E Segall & Mingming Wu, 6th Annual Mechanobiology Symposium (Poster Presentation), University of Pennsylvania, Philadelphia, PA. March 5-6, 2024 (2024).

"The Mechanics of Tumor Spheroids Revealed by a 3D Microfluidic Rheometer"; Young Joon Suh, Mrinal Pandey, Tao Luo, Jeffrey E Segall & Mingming Wu, American Physical Society March Meeting (Oral Presentation), Minneapolis, MN. March 3-8, 2024 (2024).

"The Planetary Origins and Evolution Multispectral Monochrometer (POEMM) "; Gordon J. Stacey, Dana Anderson, Richard Arendt, Andrea Banzatti, Jochem Baselmans, Edwin Bergin, Jennifer Bergner, Gordon Bjoraker, Christine Chen, Lauren Cleeves, Nicholas F. Cothard, Shahab Dabironezare, Lorenza Ferrari, Matthew Greenhouse, Willem Jellema, Attila Kovacs, Alexander Kutyrev, Meredith Macgregor, Gary J. Melnick, Stephanie N. Milam, Thomas Nikola, Klaus Pontoppidan, Isabel Rebollido Vazquez, Karwan Rostem, H. Phillip Stahl, Alexander E. Thelen, Volker Tolls, Leon Trapman, Edwin J. Wollack, Ke Zhang, Poster Presentation (2024).

"The Role of Rolling Friction in the Rheology of a Dense Suspension of Rings"; Lalieu J., Koch D., & Hormozi S., Bulletin of the American Physical Society (2024).

"The Role of the Lysine Deacetylase Sirtuin 1 in Regulating RNA Stability and the Production of a Secretome That Promotes Breast Cancer"; Fangyu Wang, Cornell University PhD Thesis (2024).

"Thermal Adaptive Laboratory Evolution of Bacteria in a Microfluidic System"; A. Karimi, Ab-On-A-Chip and Microfluidics World Congress, November 2024, Laguna Hills, CA (2024).

"Thermometric Control of the Resonance Frequency of a High-Q Si3N4 Microresonator"; Sai Kanth Dacha, Yun Zhao, Karl J. Mcnulty, Michal Lipson, Alexander L. Gaeta, In 2024 Conference on Lasers and Electro-Optics (CLEO). 2024, Pp. 1-2 (2024).

"Thin Channel Ga2O3 MOSFET with 55 GHz fMAX and >100 V Breakdown"; Chinmoy Nath Saha, Abhishek Vaidya, Noor Jahan Nipu, Lingyu Meng, Dong Su Yu, Hongping Zhao, Uttam Singisetti, Applied Physics Letters Volume 125, Issue 6, August 5, 2024 (2024).

"Three-Dimensional Lymphatics-On-A-Chip Reveals Distinct, Size-Dependent Nanoparticle Transport Mechanisms in Lymphatic Drug Delivery"; Renhao Lu, Benjamin J. Lee, and Esak Lee, ACS Biomaterials Science & Engineering. 2024 Sep 9;10(9):5752-5763. Doi:10.1021/Acsbiomaterials.4c01005. (2024).

"Threshold Voltage Instability in Vertical β-Ga2O3 finFETs Investigated by Combined Electrical and Optical Techniques"; Fregolent, C De Santi, F Piva, W Li, K Nomoto, Z Hu, D Jena, HG Xing, G Meneghesso, E Zanoni, M Meneghini, 5th International Workshop on Gallium Oxide and Related Materials May 2024 (2024).

"Titin Immunoglobulin Domain Refolding Contributes to Energy Recovery in Passively Stretched Skeletal Muscle"; Tiessen C, Leonard T, Sekhon A, Herzog W, Conference of the Canadian Society for Biomechanics, AB, August 19-22 -Podium Presentation (2024).

"Tochastics-Controlled, PAG-Free, Water-Developable EUV Photoresists Based on Sequential Polypeptoids"; Chenyun Yuan, Cameron P. Adams, Rachel A. Segalman, Christopher K. Ober, ACS Fall 2024 Meeting, Denver, Co, USA (2024).

"Torsion is a Dynamic Regulator of DNA Replication Stalling and Reactivation"; Xiaomeng Jia, Xiang Gao, Shuming Zhang, James T Inman, Yifeng Hong, Anupam Singh, Smita Patel, Michelle D Wang, PMCID: PMC11507786 PMID: 39464009 (2024).

"Towards Epitaxial Superconductor-Semiconductor Hybrid Systems on Wide Bandgap Gan Platform"; Anand Ithepalli, 2024 CCMR Symposium on Hybrid Superconductivity (Poster) (2024).

"Tumor Spheroid Mechanics and Invasion Revealed by a Microfluidic Rheometer"; Young Joon Suh, Mrinal Pandey, Tao Luo, Jeffrey E Segall & Mingming Wu, IUTAM Symposium on Theoretical and Numerical Developments in Cellular Mechanobiology (Oral Presentation), Etsi, Seville, Spain. June 5, 2024 (2024).

"Tunable Elliptical Cylinders for Rotational Mechanical Studies of Single DNA Molecules"; Yifeng Hong, Fan Ye, Xiang Gao, James T. Inman, & Michelle D. Wang, Science Advances Volume 10, Issue 50 (2024).

"Tunable Transport in Bidisperse Porous Materials with Vascular Structure"; Oliver Vincent, Theo Tassin, Erik J. Huber, And Abraham D. Stroock, APS Physical Review Fluids, 9 (6), P. 064202, 6 June 2024 (2024).

"Tuning Charge Density Wave States in Lanthanum Tritelluride Through Lithium Intercalation"; Natalie L. Williams, Shiyu Xu, Saif Siddique, Ratnadwip Singha, Leslie M. Schoop, Judy J. Cha, 2024 New York State Nanotechnology Network (2024).

"Tuning Exciton Emission Via Ferroelectric Polarization at a Heterogeneous Interface Between a Monolayer Transition Metal Dichalcogenide and a Perovskite Oxide Membrane"; Jaehong Choi, Kevin J. Crust, Lizhong Li, Kihong Lee, Jialun Luo, Jae-Pil So, Kenji Watanabe, Takashi Taniguchi, Harold Y. Hwang, Kin Fai Mak, Jie Shan, Gregory D. Fuchs, arXiv:2404.12490-18 April 2024 (2024).

"Tuning the Dimensional Order in Self-Assembled Magnetic Nanostructures: Theory, Simulations, and Experiments"; Yulan Chen, Hanyu Alice Zhang and Amal El-Ghazaly, Nanoscale, 2024, 16, 8868-8879 (2024).

"Tuning the Electronic and Magnetic States of Ca2RuO4 with Proton Evolution"; Di Tian, Ludi Miao, Liang Si, Nathaniel J. Schreiber, Shengchun Shen, Jianbing Zhang, Xinyu Shu, Xiaochao Wang, Hari P. Nair, Jacob P. Ruf, Darrell G. Schlom, Kyle M. Shen, and Pu Yu, APS Physical Review Materials 8, 074408-22 July 2024 (2024).

"Ultrabroadband, High Color Purity Multispectral Color Filter Arrays"; Jiewei Xiang, Meiting Song, Yi Zhang, Jennifer Kruschwitz, & Jaime Cardenas, ACS Photonics Volume 11, Issue 3 Article February 29, 2024 (2024).

"Ultra-Compact Quasi-True Time Delay for Boosting Wireless Channel Capacity"; Bala Govind, Thomas Tapen, & Alyssa Apsel, Nature 627, Pp. 88-94 (2024).

"Ultrahigh Reflectivity Photonic Crystal Membranes with Optimal Geometry"; F. Zhou, Y. Bao, J. J. Gorman, & J. R. Lawall, APL Photonics 9, 076120 (2024).

"Ultrawide Bandgap Semiconductor Heterojunction P–N Diodes with Distributed Polarization-Doped P-Type Algan Layers on Bulk Aln Substrates"; Shivali Agrawal, Len Van Deurzen, Jimy Encomendero, Joseph E. Dill, Hsin Wei (Sheena) Huang, Vladimir Protasenko, Huili (Grace) Xing, Debdeep Jena, Applied Physics Letters Volume 124, Issue 10, 4 March 2024 (2024).

"Understanding Magnetic Nanochain Interactions for Reconfigurable Soft Actuators"; Y. Chen, K. Srinivasen, M. Choates, L. Cestarollo, A. El-Ghazaly, Materials Research Society Spring Meeting, Seattle (2024).

"Using Both Faces of Polar Semiconductor Wafers for Functional Devices"; Len Van Deurzen, Eungkyun Kim, Naomi Pieczulewski, Zexuan Zhang, Anna Feduniewicz-Zmuda, Mikolaj Chlipala, Marcin Siekacz, David Muller, Huili Grace Xing, Debdeep Jena & Henryk Turski, Nature 634, 334-340 (2024).

"Valley-Coherent Quantum Anomalous Hall State in AB-Stacked MoTe2/WSe2 Bilayers"; Z. Tao, B. Shen, S. Jiang, T. Li, L. Ma, W. Zhao, J. Hu, K. Pistunova, K. Watanabe, T. Taniguchi, T. F. Heinz, K. F. Mak, J. Shan, Phys. Rev. X 14, 011004 (2024).

"Van Der Waals Magnets and Antiferromagnets Interacting with Electron Spins"; D. Ralph, Altermagnets, Zoom Workshop Organized by Suyang Xu, Harvard University September 20, 2024, Philadelphia, PA (2024).

"Van Der Waals Magnets and Antiferromagnets Interacting with Electron Spins"; D. Ralph, U.Penn Condensed and Living Matter Seminar September 25, 2024, Philadelphia PA (2024).

"Vascular Plants Engineers of Porous Media"; Abraham Stroock, Department of Chemical Engineering, IIT Bombay, March 15, 2024 (2024).

"Virtually Image Phrased Array (VIPA): Demonstration of the Next Generation Direct Detection Spectrometer for Velocity Resolved Spectroscopy in the Far-Infrared"; Nikola, Thomas; Zou, Bugao; Stacey, Gordon J.; Connors, Jake A.; Cothard, Nicholas F.; Kutyrev, Alexander S.; Mentzell, Eric; Rostem, Karwan; Wollack, Edward J.; Jellema, Willem; Kao, Tsung-Yu; Lee, Alan W. M., Millimeter, Submillimeter, and Far-Infrared Detectors and Instrumentation for Astronomy XII. Vol. 13102. SPIE (2024).

"Voltage Control of Multiferroic Magnon Torque for Reconfigurable Logic-In-Memory"; Yahong Chai, Yuhan Liang, Cancheng Xiao, Yue Wang, Bo Li, Dingsong Jiang, Pratap Pal, Yongjian Tang, Hetian Chen, Yuejie Zhang, Hao Bai, Teng Xu, Wanjun Jiang, Witold Skowroński, Qinghua Zhang, Lin Gu, Jing Ma, Pu Yu, Jianshi Tang, Yuan-Hua Lin, Di Yi, Daniel C Ralph, Chang-Beom Eom, Huaqiang Wu, Tianxiang Nan, Nat Commun. 2024 July 16; 15:5975 Doi: 10.1038/S41467-024-50372-3 (2024).

"Wafer-Scale Millimeter-Wave Metasurface Antenna Fabrication for CubeSat-Based Remote Sensing"; Kevin Gu, Poster Presentation, CUNY ASRC Nanofabrication Research Showcase, New York, NY, October 17, 2024 (2024).

"Waste Bombyx Mori Silk Textiles as Efficient and Reuseable Bio-Adsorbents for Methylene Blue Dye Removal and Oil–Water Separation"; Hansadi Jayamaha, Isabel Schorn, & Larissa M. Shepherd, Fibers 2024, 12(11), 99, Doi:10.3390/Fib12110099 (2024).

"Wireless Electrosynthesis"; Song Lin, American Chemical Society Fall National Meeting in Denver (August 2024) (2024).

"Wireless Electrosynthesis"; Song Lin, Heterocyclic Compounds, Gordon Research Conference (2024).

"Wireless Electrosynthesis"; Song Lin, Natural Products and Bioactive Compounds, Gordon Research Conference (2024).

"Wth of Wurtzite AlScN Thin Films on Commercial Silicon and SOI (111) Substrates Using PAMBE"; Rishabh Singh, APS March Meeting (2024).

"Zwitterionic Polymer Coatings with Compositional Gradient for Stable and Substrate-Independent Biofouling Deterrence via All-Dry Synthesis"; Pengyu Chen, Harry Shu, Wenjing Tang, Chirstina Yu, Rong Yang, arXiv.2410.23552 [Chemical Physics] (2024).

2024-2025

Cornell NanoScale Facility (CNF)

RESEARCH ACCOMPLISHMENTS

Tunable Elliptical Cylinders for Rotational Mechanical Studies of Single DNA Molecules

CNF Project Number: 1738-08

Principal Investigator(s): Michelle D. Wang
User(s): Yifeng Hong

Affiliation(s): Department of Electrical and Computer Engineering, Cornell University, Department of Physics, Cornell University, Howard Hughes Medical Institute

Primary Source(s) of Research Funding: Howard Hughes Medical Institute

Contact: mdw17@cornell.edu, yh874@cornell.edu

Research Group Website: http://wanglab.lassp.cornell.edu/

Primary CNF Tools Used: ASML DUV Stepper, Oxford 81 Etcher, Oxford 82 Etcher, Oxford PECVD, SC4500 Odd-Hour Evaporator, CVC SC4500 Evaporators, Zeiss Supra SEM, Zeiss Ultra SEM

Abstract:

The angular optical trap (AOT) is a powerful technique for measuring the DNA topology and rotational mechanics of fundamental biological processes. Realizing the full potential of the AOT requires rapid torsional control of these processes. However, existing AOT quartz cylinders are limited in their ability to meet the high rotation rate requirement while minimizing laser-induced photodamage. In this work, we present a trapping particle design to meet this challenge by creating small metamaterial elliptical cylinders with tunable trapping force and torque properties. The optical torque of these cylinders arises from their shape anisotropy, with their optical properties tuned via multilayered SiO2 and Si3N4 deposition. We demonstrate that these cylinders can be rotated at about three times the rate of quartz cylinders without slippage while enhancing the torque measurement resolution during DNA torsional elasticity studies. This approach opens opportunities for previously inaccessible rotational studies of DNA processing.

Summary of Research:

We have achieved our goal by creating smaller elliptical cylinders with tunable trapping force and torque properties[1]. Instead of using optical birefringence for optical torque generation as with the quartz cylinders, these elliptical cylinders experience an optical torque via their shape anisotropy because the major axis of their elliptical cross-section tends to align with the laser's linear polarization (Fig. 1, A and B). These cylinders are made of a metamaterial that affords an effective index of refraction higher than quartz via alternating layers of SiO2 and Si3N4 (Fig. 1C).

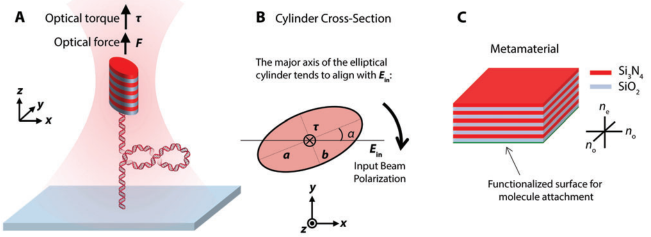

Figure 1: Operational principle of a metamaterial elliptical cylinder in an AOT. (A) experimental configuration of DNA torsional mechanics measurements using a meta-material elliptical cylinder in an AOT. (B) Optical torque generation of a dielectric elliptical cylinder. (C) The metamaterial.

We optimized the optical force, torque, and trapping stability by tuning the size, shape, and composition of these particles via an established COMSOL simulation platform[1,2]. Then, we nanofabricated the metamaterial elliptical cylinders with the targeted dimensions obtained from simulations via a top-down, DUV lithography-based process (Fig. 2A). The liftoff method for cylinder collection resulted in more uniform metamaterial elliptical cylinders with ~ 4-times volume

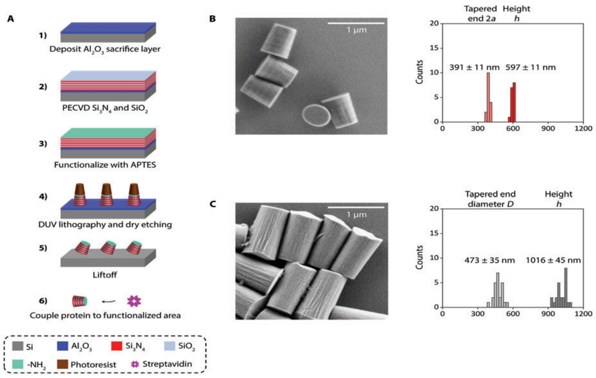

Figure 2: Nanofabrication of metamaterial elliptical cylinders. (A) Fabrication process flow of metamaterial elliptical cylinders. (B) An SEM image of nanofabricated metamaterial elliptical cylinders. The size and uniformity characterization is also shown. (C) An SEM image of nanofabricated quartz cylinders. The size and uniformity characterization is also shown.

reduction compared with the conventional quartz cylinders (Fig. 2, B and C).

We validated the trapping properties of these nanofabricated metamaterial elliptical cylinders with the AOT. We showed that our metamaterial elliptical cylinders can generate a maximum force and a maximum torque comparable to the quartz cylinders (Fig. 3, A and B). In addition, we measured the rotational motion of metamaterial elliptical cylinders and found they show a threefold reduction in γθ: 3.2 ± 0.3 pN·nm·s/turn (mean ± SD, n = 17), in comparison to 9.4 ± 1.7 pN·nm·s/turn (mean ± SD, n = 14) of the quartz cylinder (Fig. 3A). The reduced γθ of the metamaterial elliptical cylinders resulted in ~ 3- times faster cylinder rotation rate without slippage (Fig. 3B).

Moreover, the reduced γ_θ of the metamaterial elliptical cylinders also had an extra benefit of a greater signal-to-noise ratio (SNR) in the torque measurement of a DNA molecule. This threefold reduction in γθ should provide a 1.7-fold reduction in the noise of the measured torque of a DNA molecule, which was experimentally validated via the DNA torsional measurements (Fig. 4, A, B, and C).

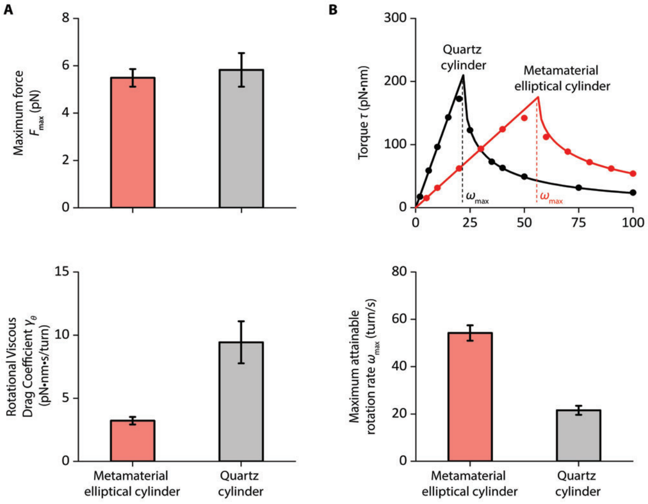

Figure 3: Trapping properties and maximum rotation rate of metamaterial elliptical cylinders. (A) Measurements of the maximum trapping force Fmax (top panel) at 30 mW laser power before the objective and rotational viscous drag coefficient γθ (bottom panel). (B) Method to determine the maximum trapping torque τmax (top panel) and the maximum rotation rate ωmax (bottom panel) without slippage at 30 mW laser power before the objective.

Conclusions and Future Steps:

We demonstrated, both theoretically and experimentally, that our small-size biocompatible metamaterial elliptical cylinders can permit cylinder rotation about three times the rate of the quartz cylinders while providing high force and torque for DNA torsional mechanics studies with enhanced torque resolution. Moreover, our methodology offers versatility in tuning the refractive index, shape anisotropy, and cylinder size to optimize the trapping properties. We anticipate that using these cylinders can enable previously inaccessible rotational studies of DNA-based biological processes.

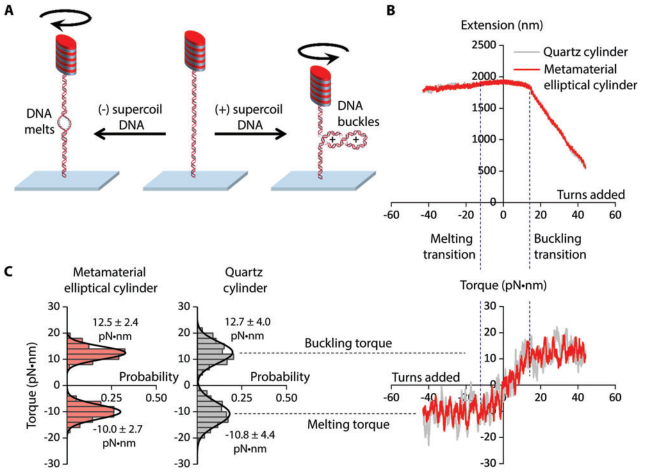

Figure 4: DNA torque measurements using a metamaterial elliptical cylinder, in comparison with those from a quartz cylinder. (A) experimental configuration for the measurements. (B) Measured DNA extension and torque as a function of turns added to DNA under 1 pN force. (C) Histograms of measured torque upon (+) DNA buckling and (−) DNA melting. Each histogram is fit by a Gaussian, with the mean and the SD of the fit shown.

References:

[1] Hong, Y.; Ye, F.; Gao, X.; Inman, J. T.; Wang, M. D. Tunable Elliptical Cylinders for Rotational Mechanical Studies of Single DNA Molecules. Sci. Adv. 10 (50), eadr4519. 2024 https://doi.org/10.1126/sciadv.adr4519.

[2] Hong, Y.; Ye, F.; Qian, J.; Gao, X.; Inman, J. T.; Wang, M. D. Optical Torque Calculations and Measurements for DNA Torsional Studies. Biophys. J. 2024. https://doi.org/10.1016/j.bpj.2024.07.005.

Building Microfluidics Devices to Study Zinc Metal Homeostasis in E. Coli Communities

CNF Project Number: 1844-09

Principal Investigator(s): Peng Chen
User(s): Felix Alfonso

Affiliation(s): Department of Chemistry and Chemical Biology, Cornell University

Primary Source(s) of Research Funding: National institute of health and the national institute of general medical sciences

Contact: pc252@cornell.edu, fsa33@cornell.edu

Research Group Website: http://chen.chem.cornell.edu/

Primary CNF Tools Used: Heidelberg DWL2000 Mark Writer, SUSS MA6-BA6 Contact Aligner, Oxford Cobra ICP Etcher, Plasma-Therm Deep Silicon Etcher, and P7 Profilometer

Abstract:

Bacterial organisms have developed sophisticated biochemical mechanisms to absorb vital nutrients from their surroundings while expelling surplus materials to avoid toxic accumulation. This research seeks to understand how single microbial units contribute to maintaining metal equilibrium within larger bacterial populations. To accomplish this objective, we created a specialized microfluidic system that enables precise cultivation of Escherichia coli colonies in carefully designed microscopic compartments. The size of these compartments was deliberately calibrated to match E. coli cell dimensions, creating controlled spatial restrictions that serve as a fundamental component of the experimental approach. The microfluidic platforms utilized in this work provide sophisticated environmental regulation capabilities, offering exceptional opportunities to examine and comprehend microbial behavior. Through this technology, we could examine in detail how these microscopic bacterial communities maintain equilibrium in their zinc metabolism processes. We utilized cutting-edge genetic engineering methods to develop E. coli variants containing luminescent protein indicators. This specialized genetic alteration enabled the observation and measurement of the activity of genes associated with complex ion transport systems, particularly focusing on zinc-specific pathways. The findings from this investigation may significantly advance our comprehension of microbial communities and their environmental relationships.

Summary of Research:

As an essential trace element, zinc plays a critical role in the survival of all life forms (1). This micronutrient performs crucial tasks in enzymatic processes, protein structure formation, and transcriptional control (2,3). When zinc concentrations become unbalanced significant disruptions occur in intestinal microbial communities, leading to detrimental health outcomes (4, 5). Throughout evolutionary history, microorganisms have evolved sophisticated molecular systems that enable efficient nutrient uptake from their surroundings while simultaneously expelling surplus amounts to avoid cellular damage. Bacterial cells control these export mechanisms by regulating the production of transport proteins through metal-sensitive transcriptional controllers. These regulatory elements monitor intracellular metal ion concentrations, directing cellular processes toward optimal metal balance. This research aims to investigate and measure zinc ion (Zn^{2+}) management within microbial communities, illuminating how single bacterial cells contribute to maintaining metal equilibrium across entire populations. We selected Escherichia coli as our experimental model to examine the intricate mechanisms of community-based zinc regulation. The inherent mobility of E. coli and its weak surface adhesion properties create obstacles for extended microscopic observation studies. Nevertheless, microfluidic technology provides an elegant solution by creating controlled experimental conditions suitable for bacterial community research (6). These microfluidic systems enable precise regulation of nutrient delivery and have proven successful in long-term imaging investigations (7).

Our experimental microfluidic apparatus incorporates two essential elements: flow channels, and microscopic cultivation chambers. The depth of these cultivation chambers is specifically designed to correspond with E. coli cell diameter (approximately 1 micrometer), enabling effective bacterial colony containment.

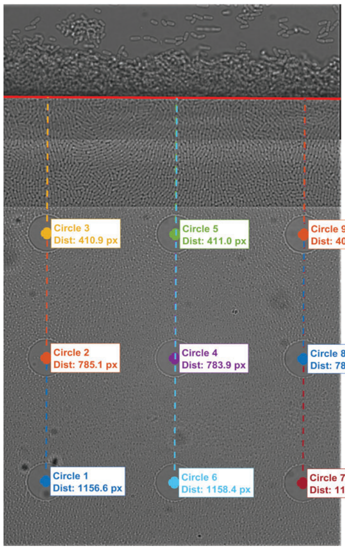

Figure 1: Monolayer of E. coli cells grown in microfluidic microchamber under 10 micromolar zinc exposure. The red line indicates the beginning of the chamber. Support posts within the chamber prevent ceiling collapse and serve as fiducial markers for distance calibration.

In Figure 1, we can observe a single layer of E. coli cultivated under 10 micromolar zinc conditions. The red marking indicates the chamber boundary, within which support pillars are positioned to prevent structural collapse while serving as reference points for distance measurements from the pillar to the chamber opening. Through time-lapse fluorescence microscopy, we can monitor the activation of the ZntA efflux protein during continuous exposure to 10 micromolar zinc concentration. The resulting curve displays initial S-shaped kinetics followed by sharp increases in later time periods (Figure 2). By utilizing spatial coordinates from the reference markers, we can organize our data according to distance from the channel entrance, providing insights into how gene expression varies with spatial position. This visualization is achieved through a two-dimensional histogram plotting distance (y-axis) versus time (x-axis) with concentration values as binned data (Figure 3). This microfluidic platform enables comprehensive spatial-temporal analysis of efflux protein and channel gene expression, potentially establishing a foundation for understanding metal homeostasis mechanisms and developing therapeutic strategies that target bacterial metal regulation systems.

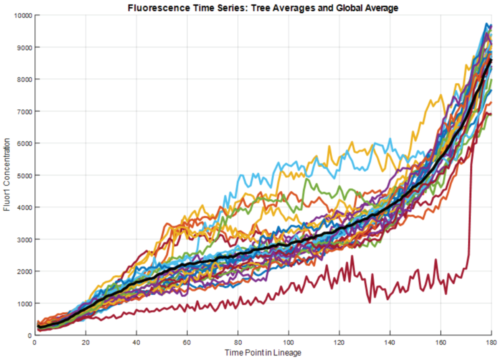

Figure 2: Time-course induction of ZntA efflux protein (nanomolar) expression under constant 10 micromolar zinc exposure measured by time-lapse fluorescent microscopy.

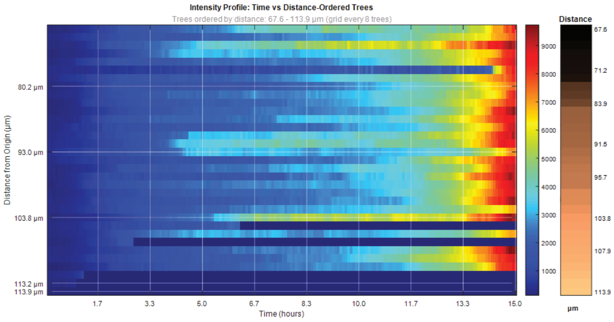

Figure 3: Two-dimensional histogram showing ZntA protein concentration (nanomolar) as a function of distance from channel entrance (y-axis) and time (x-axis).

Microfluidic device fabrication uses standard silicon nanofabrication. Silicon wafers are cleaned with piranha solution, coated with photoresist, and patterned using a custom photomask and Karl SUSS MA6-BA6 Contact aligner. Chambers are etched ~1µm deep using Oxford Cobra ICP Etcher. Channels are formed via SU-8 photolithography, cured at 95°C, then hard baked at 200°C for 10 minutes. The silicon template is coated with FOTS for easy PDMS removal. Completed devices are bonded to coverslips, loaded with bacterial cells, and imaged using appropriate microscopy equipment.

References:

[1] R. R. Robert B. Saper, Zinc: An Essential Micronutrient. Am. Fam. Physician. 79, 768 (2009).

[2] S. Tan, D. Guschin, A. Davalos, Y.-L. Lee, A. W. Snowden, Y. Jouvenot, H. S. Zhang, K. Howes, A. R. McNamara, A. Lai, C. Ullman, L. Reynolds, M. Moore, M. Isalan, L.-P. Berg, B. Campos, H. Qi, S. K. Spratt, C. C. Case, C. O. Pabo, J. Campisi, P. D. Gregory, Zinc-finger protein-targeted gene regulation: genomewide single-gene specificity. Proc. Natl. Acad. Sci. U. S. A. 100, 11997–12002 (2003).

[3] C. Andreini, I. Bertini, in Encyclopedia of Metalloproteins (Springer, New York, NY, 2013), pp. 2549–2554.

[4] S. R. Gordon, S. Vaishnava, Zinc supplementation modulates T helper 17 cells via its effect on gut microbiome. The Journal of Immunology. 204, 83.18–83.18 (2020).

[5] O. Koren, E. Tako, Chronic Dietary Zinc Deficiency Alters Gut Microbiota Composition and Function. Proc.AMIA Annu. Fall Symp. 61, 16 (2020).

[6] F. Wu, C. Dekker, Nanofabricated structures and microfluidic devices for bacteria: from techniques to biology. Chem. Soc. Rev. 45, 268–280 (2016).

[7] D. Binder, C. Probst, A. Grünberger, F. Hilgers, A. Loeschcke, K.-E. Jaeger, D. Kohlheyer, T. Drepper, Comparative Single-Cell Analysis of Different E. coli Expression Systems during Microfluidic Cultivation. PLoS One. 11, e0160711 (2016).

Microfabricated Nanogrooves to Promote in Vitro Muscle Fiber Differentiation and Maturation

CNF Project Number: 2065-11

Principal Investigator(s): Jan Lammerding
User(s): Eitan Jentis, Maggie Elpers, Sarah Henretta, Anna Hazelwood

Affiliation(s): Meinig School of Biomedical Engineering, Weill Institute for Cell and Molecular Biology, Cornell University

Primary Source(s) of Research Funding: National Institutes of Health award R01 HL082792; National Institutes of Health award R35 GM153257; National Institutes of Health award R01AR084664

Contact: ej225@cornell.edu, mae228@cornell.edu, sjh333@cornell.edu, alh333@cornell.edu

Research Group Website: http://lammerding.wicmb.cornell.edu/

Primary CNF Tools Used: Plasma-Therm Unaxis DRIE, Oxford Cobra etcher, Heidelberg DWL 2000 Mask Writer, GCA AS200 i-line Stepper, Karl Suss MA6 Contact Aligner, Anatech SCE-110-RF Resist Stripper, P-7 Profilometer, MVD-100; Oxford 81 etcher; Unaxis 770 Deep Silicon Etcher; BLE150 Hotplate; EcoClean Asher; PDMS spin coater

Abstract:

Muscular dystrophy encompasses a group of devastating diseases affecting skeletal muscle in young children and resulting in reduced mobility and premature death. Gaining a better understanding of the underlying disease mechanism is crucial for developing effective therapies, which are currently lacking. One challenge in studying the pathogenesis of muscular dystrophies is that common in vitro models based on the differentiation of skeletal muscle stem cells (myoblasts) do not match the form and function of skeletal muscle tissue in vivo, including the highly aligned and organized muscle fibers. Culturing myoblasts on nanostructured surfaces that provide physical cues for the differentiating muscle cells has been shown previously to promote the formation of mature and highly aligned muscle fibers. Here, we demonstrate the use of microfabricated silicon wafers that serve as molds to generate polydimethylsiloxane (PDMS) membranes with ~700 nm wide and ~1300 nm deep nanogrooves. These PDMS substrates, when coated with Matrigel extracellular matrix, enable the differentiation of primary mouse myoblasts into mature and well-aligned skeletal muscle fibers, which we are now using as a model system to study Emery-Dreifuss muscular dystrophy and other muscle diseases caused by mutations in the LMNA gene.

Summary of Research:

Mutations in the LMNA gene, which encodes the nuclear envelope proteins lamin A and C (lamin A/C), cause Emery-Dreifuss muscular dystrophy, congenital muscular dystrophy, and dilated cardiomyopathy. Although lamin A/C is expressed in nearly every tissue, most LMNA mutations primarily affect striated muscle, i.e., skeletal and cardiac muscle. Both the molecular mechanism underlying the muscle-specific defects and the pathobiology of the disease remain incompletely understood, presenting a major obstacle in the development of effective therapies. While animal models for these diseases are available, they are limited in their ability to allow detailed cell and molecular level observations of the disease progression, which is required to identify pathogenic mechanisms. In vitro models, on the other hand, are well suited for imaging but do not capture the structure and function of mature muscle tissue, limiting their usefulness. To overcome this challenge, we developed PDMS-based in vitro cell culture substrates with nanostructured ridges that are ~700 nm wide, ~1300 nm tall, and separated by ~700 nm wide gaps, to resemble in vivo tissue architecture and promote muscle cell differentiation and alignment.

We first fabricate silicon wafers to serve as molds to cast the nanostructured PDMS substrates (Figure 1). Oir620-7i photoresist is spin-coated onto a 4-inch wafer and exposed to UV light using the GCA AS200 i-line stepper to imprint the pattern into the photoresist layer. After developing the photoresists using the 726 MIF, we perform a silicon etch with the Unaxis 770 Deep Silicon Etcher, removing silicon in the regions not covered by photoresist. After etching, the remaining photoresist is stripped, and a hydrophobic Teflon coating is applied to the wafer to prevent PDMS from sticking, thus making the wafer suitable as a mold to cast thin sheets of PDMS containing the desired nanostructures. We confirmed the desired dimensions of the ridges on the silicon wafer using the Zygo Optical Profiler and scanning electron microscopy (Figure 2). Subsequently, PDMS is spin-coated onto the silicon wafer and cured by baking for >2 hours at 60°C. The PDMS sheets are then removed from the wafer and coated with Matrigel, an extracellular matrix molecule that supports muscle cells in vivo. Primary mouse myoblasts are cultured on the nanostructured PDMS substrate and induced to differentiate into muscle fibers, starting one day after plating. We use an Airyscan LSM900 confocal microscope to observe the cells and assess their alignment and maturity based on their sarcomeric structures. Figure 3 shows a representative image of wild-type muscle cells differentiated into >400 µm long muscle fibers with the characteristic striated sarcomere patterning and high alignment between muscle fibers.

Having established this experimental platform, we are now using it to compare LMNA mutant and wild- type muscle cells and determine the molecular mechanism responsible for the muscle defects. In addition to promoting muscle differentiation and alignment, the flexible PDMS substrate also enables us to apply mechanical strain to the muscle fibers, allowing us to test the hypothesis that the LMNA mutant muscle cells are more sensitive to mechanical stress, which could explain the muscle-specific defects of many laminopathies.

Taken together, this application illustrates new uses of the available nanofabrication technologies to create improved in vitro models to study normal muscle differentiation and muscle disease.

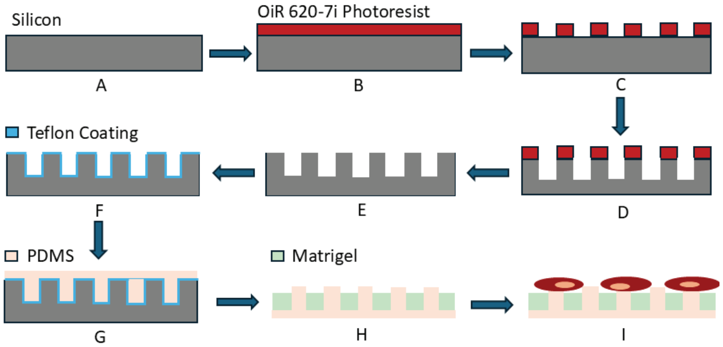

Figure 1: Nanofabrication process for nanostructured surfaces. A 4-inch n-type silicon wafer (A) is spin coated with OiR620-7i photoresist to 0.72 µm thickness (B), followed by exposure and development of the photoresist using the AutoStep 200 DSW i-line Stepper to create the desired patterns (C), which are then etched 1.3 µm deep into the silicon wafer using the Unaxis 770 system (D). After stripping the photoresist (E), a thin Teflon coating is applied (F) to prevent PDMS from sticking when cast onto the wafer (G). After removal of the PDMS substrate from the wafer, extracellular matrix, Matrigel, is applied to the wafer (H). Finally, primary muscle stem cells (myoblasts) are cultured on the substrate (I) and induced to differentiate into skeletal muscle fibers.

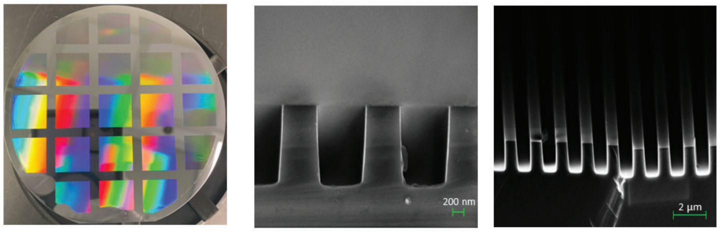

Figure 2: Characterization of the nanostructured silicon wafer. Photograph of the final wafer, with arrays of 1 cm × 1 cm squares containing the nanostructured ridges visible (left). Scanning electron microscope (SEM) images of the cross-section of the wafer are shown at high (center, scale bar = 200 nm) and low resolution (right, scale bar = 2 µm). The width of each ridge is around 660 nm, and the depth is 1.3 µm. The SEM images were taken on the Zeiss Ultra SEM.

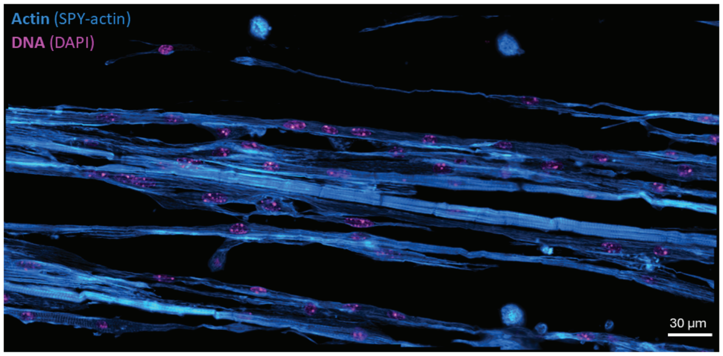

Figure 3: Differentiated skeletal muscle fibers on nanostructured substrate. Fluorescence microscopy image of primary mouse myoblast differentiated into muscle fibers and stained for DNA (DAPI) and actin (SPY-actin 555) to visualize sarcomeres, the contractile units of striated muscle.

Microfluidic Flow Cells for Time-Resolved Fluorescence-Based Studies of Biomolecules

CNF Project Number: 2158-12

Principal Investigator(s): Lois Pollack
User(s): Scout Fronhofer

Affiliation(s): Cornell University, Applied and Engineering Physics

Primary Source(s) of Research Funding: National Institutes of Health

Contact: lp26@cornell.edu, shf56@cornell.edu

Research Group Website: https://pollack.research.engineering.cornell.edu/

Primary CNF Tools Used: Heidelberg DWL2000, Oxford PECVD, ABM mask aligner, Oxford 80 RIE, Unaxis 770 Deep Silicon Etch, Suss SB8e Substrate Bonder, DISCO dicing Saw

Abstract:

We report the fabrication of microfluidic flow cells for time-resolved fluorescence measurements of biological molecules. These silicon and glass devices improve upon our previous design by allowing the CNF-fabricated flow cell to be combined with multiple types of microfluidic mixers. The simplified design will enable time-resolved studies of interactions between biological molecules such as nucleic acids and proteins.

Summary of Research:

Single-molecule fluorescence techniques are useful tools for studying dynamic, flexible biological molecules including single-stranded nucleic acids. One such method is fluorescence correlation spectroscopy (FCS) which can provide information about the size and interactions of molecules in solution by measuring the fluctuations in emitted photons from fluorescently labeled molecules in solution as they diffuse in and out of a laser confocal volume [1]. Another useful technique is Förster resonance energy transfer (FRET), which takes advantage of the distance dependence of energy transfer between pairs of fluorescent dyes to measure inter- and intra-molecular distances. At the single molecule level, these measurements provide insight into the dynamics and distribution of conformations in heterogeneous samples such as disordered single-stranded RNA [2]. Microfluidic devices enable time-resolved versions of these experiments, where a biological interaction is initiated and probed as a function of time as the molecules flow along a channel.

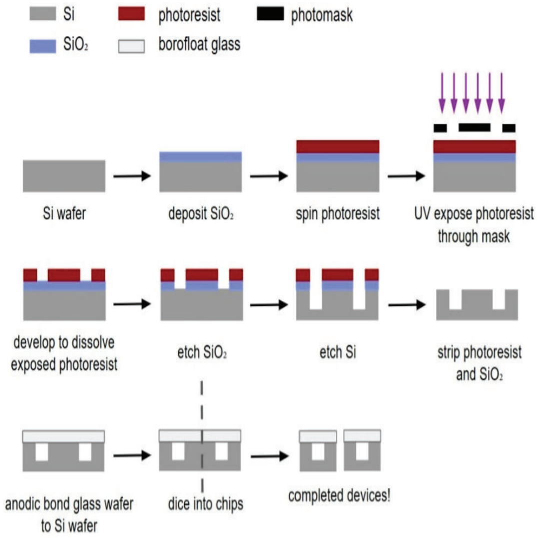

Figure 1: Fabrication process for making many silicon and glass flow cells out of a single wafer.

Here we describe the fabrication of durable, reusable microfluidic channels that can interface with our lab-built confocal fluorescence microscope as well as different types of microfluidic mixers, providing flexibility in terms of the techniques we can use and the biological systems we can investigate. The design is based on our previously established protocol for fabricating microfluidic mixing devices for time-resolved fluorescence measurements [3]. We now improve upon the earlier design by fabricating a simplified flow cell which can be interfaced with different microfluidic mixers depending on the properties of the system being studied. The flow cell consists of a channel etched into silicon, sealed by borofloat glass to make it compatible with a water immersion objective lens. The fabrication process, outlined in Figure 1, consists of several steps making use of the photolithography, etching, and bonding tools at the CNF. First, a layer of silicon dioxide is deposited onto a silicon wafer using the Oxford PECVD tool. This oxide layer serves as a hard mask for deep etching of the silicon. Next, a layer of photoresist is spun and baked onto the wafer before being exposed through a mask using the ABM contact aligner. After developing to remove the exposed photoresist, we etch

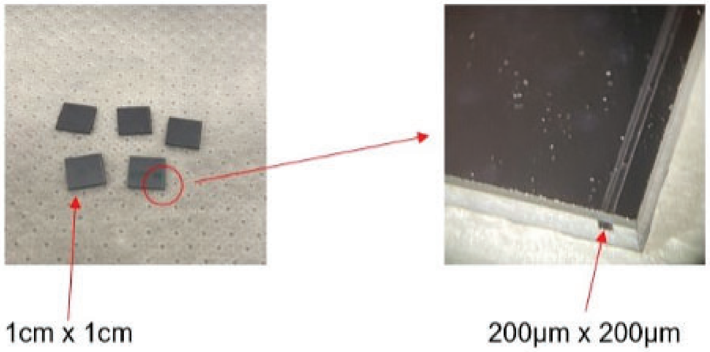

Figure 2: The image on the left shows several flow cells at the end of the fabrication process, after the bonded silicon and glass wafers have been diced. The image on the right is a stereoscope view of one flow cell, with a square opening at the front and the channel visible through the layer of glass.

first through the oxide using the Oxford 81/82, then into the silicon using the Unaxis deep silicon etcher, creating channels that are 200 µm wide and 200 µm deep. To seal the top of the channels, a 200um thick borofloat glass wafer is anodically bonded to the silicon using the Suss SB8E substrate bonder. Finally, the bonded wafers are diced into 1 cm x 1 cm chips. One wafer processed in this way results in about 40 individual chips, each of which contains a 200 µm x 200 µm square channel, sealed on four sides and open on the ends to allow for flow through the channel. A diced wafer and an individual chip are shown in Figure 2.

The completed chips, or flow cells, can then be coupled with a microfluidic mixer to perform time-resolved experiments. The simplicity of the design means that the mixer upstream of the flow cell can be customized for each experiment. Depending on the sizes of the biological molecules being mixed and the timescales of interest, a suitable mixer can be built to efficiently mix the reactant molecules and flow them through the observation channel where fluorescence measurements are recorded. For example, a system in which a small molecule is reacting with a large molecule might employ a coaxial diffusive mixer, while fast mixing of two large molecules requires a different method of mixing such as chaotic advection in a 3D printed mixer [4].

Conclusions and Future Steps:

We have fabricated versatile flow cells which, when paired with microfluidic mixers, will allow us to use time-resolved fluorescence techniques to study a variety of dynamic biological molecules. Future experiments will use these devices to investigate systems such as nucleic acid-protein and nucleic acid-nucleic acid interactions. These experiments will complement the structural information that can be obtained from other techniques, particularly x-ray scattering.

References:

[1] Elson, Elliot L. "Fluorescence correlation spectroscopy: past, present, future." Biophysical journal 101.12 (2011): 2855-2870

[2] Wang, Tong, et al. "Sequence-dependent conformational preferences of disordered single-stranded RNA." Cell Reports Physical Science 5.11 (2024).

[3] Plumridge, Alex (2020) Discovering Design Principles to Re-Engineer Functional RNA Elements Using Computational and Microfluidic Approaches.

[4] Zielinski, Kara A., et al. "Chaotic advection mixer for capturing transient states of diverse biological macromolecular systems with time-resolved small-angle X-ray scattering." IUCrJ 10.3 (2023): 363-375.

Metabolic Labeling of Mucin-Induced Extracellular Vesicles Isolated from Suspension-Adapted Cell Culture

CNF Project Number: 2272-14

Principal Investigator(s): Matthew Paszek
User(s): Erik Chow

Affiliation(s): Department of Biomedical Engineering, Cornell University

Primary Source(s) of Research Funding: NIH

Contact: paszek@cornell.edu, ec829@cornell.edu

Primary CNF Tools Used: Malvern NS300 Nanosight

Abstract:

Extracellular vesicles (EVs) are lipid-membrane-bound secreted nanoparticles which transport DNA, RNA, and proteins between cells and therefore have great potential as tools for disease diagnosis and treatment. The significance of the glycocalyx in EV biogenesis and function is largely unexplored, and the capacity to effect EV production and properties through rational manipulation of the glycocalyx remains poorly understood. We have previously demonstrated that overexpressing the transmembrane mucin glycoprotein Muc1 in the glycocalyx drives EV secretion in adherent MCF10A cells. Here, we expand these findings to suspension-adapted HEK293F cells and utilize metabolic labeling of inherent EV Muc1 biopolymer coatings as a proof-of-concept for engineering EVs with designed molecular payloads.

Summary of Research:

Extracellular vesicles (EVs) have rapidly garnered attention in biomedical engineering research for their ability to transport DNA, RNA and proteins, making them promising candidates as tools for disease diagnosis and treatment. The glycocalyx is a polymer meshwork of proteins, nucleic acids, and glycans which governs numerous intercellular interactions, but its role in regulating EV biogenesis and function remains poorly understood. It has been previously shown that engineering the glycocalyx via the overexpression of mucin can result in membrane morphologies which are favorable for the formation of EVs1. This report summarizes research from the last year characterizing "mucin-induced" EVs isolated from suspension-adapted cell culture and demonstrating the efficacy of bio-orthogonal labeling of EV mucin coatings as a strategy for engineering EV payloads. HEK293F cells were genetically engineered to express tetracycline-inducible Muc1 biopolymer. To induce Muc1 overexpression, cells were treated with 1 ug/mL doxycycline (dox) for 24 h.

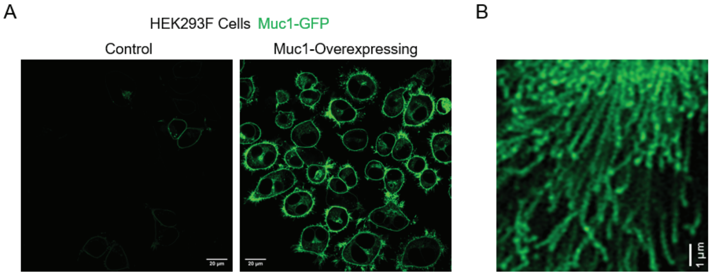

Figure 1: Induced expression of Muc1 biopolymer at the surface of HEK293F cells. A) Confocal fluorescence microscopy images of inducible Muc1-GFP expressed in engineered HEK293F cells. Cells samples were seeded onto poly-L-lysine coated glass-bottom dishes. Non-induced cells (Left) exhibit low leaky expression, while induced cells (Right) exhibit dramatic cell-surface Muc1 expression. Scale bar is 20 µm for both images. B) Pearled cell membrane tubules were observed on the surface of Muc1-overexpressing HEK293F cells. Individual pearls appear to be approximately 200-300 nm in diameter, consistent with structures observed in similarly engineered MCF10A cells. Scale bar is 1 µm.

Additionally, N-azidoacetylgalactosamine (GalNAz) was added to HEK293F culture media at a final concentration of 50 µM at the same time as dox induction. The cells were further incubated at 37 , 5% CO2 for 2 d. EV-containing media was then harvested, and the EVs were isolated by PEG-enrichment according to an existing protocol2. EVs from non-induced cells and EVs from induced cells lacking GalNAz were used as negative controls. EV particle size and concentration were measured by nanoparticle tracking analysis (NTA) using the Malvern NS300 Nanosight.

Expression of cell-surface Muc1 biopolymer in induced HEK293F cells was verified by confocal fluorescence microscopy (Fig 1A). Notably, pearling membrane structures were observed similar to those previously reported on similarly engineered MCF10A cells, suggesting that cell-surface Muc1 could have a similar effect on EV secretion in different cell types (Fig 1B). Indeed, EV secretion was dramatically increased in Muc1-overexpressing HEK293F cells compared to non-induced control (Figure 2A). Additionally, Muc1 expression resulted in a modest increase in median EV hydrodynamic diameter, consistent with Muc1 biopolymer coatings on the surfaces of mucin-induced EVs (Figure 2B). Metabolic incorporation of GalNAz into the glycans of EV Muc1 biopolymer coatings was confirmed by Western blot. Briefly, mucin-induced EVs from HEK293F cells with or without GalNAz incorporation were treated with DBCO-AzDye 568 dye (Click Chemistry Tools), allowing for bio-orthogonal click conjugation of fluorescent reporter to EVs containing GalNAz in their Muc1 surface coatings. Lysates from metabolically labeled and click-conjugated EVs were run on 7% Tris-Acetate SDS-PAGE gels. Western blot confirmed the presence of Muc1 in mucin-induced EV lysates, and further demonstrated successful bio- orthogonal conjugation of fluorescent dye specific to the EVs from HEK293F cells treated with GalNAz (Figure 3).

Conclusions and Future Steps:

These studies reinforce the role of the glycocalyx in EV secretion by demonstrating that the glycocalyx mucin Muc1 drives EV secretion in different cell types. These mucin-induced EVs carry innate mucin biopolymer surface coatings. EV mucin coatings can be further engineered using a combination of endogenous and exogenous modifications to design EV payloads, as demonstrated by the successful bio-orthogonal conjugation of fluorescent reporter molecules to metabolically labeled EVs.

References:

[1] Shurer, C. R. et al. (2019). Physical Principles of Membrane Shape Regulation by the Glycocalyx. Cell, 177(7), 1757–1770. https://doi.org/10.1016/j.cell.2019.04.017

[2] Rider, M. et al. (2016). ExtraPEG: A Polyethylene Glycol-Based Method for Enrichment of Extracellular Vesicles. Sci Rep 6, 23978. https://doi.org/10.1038/srep23978.

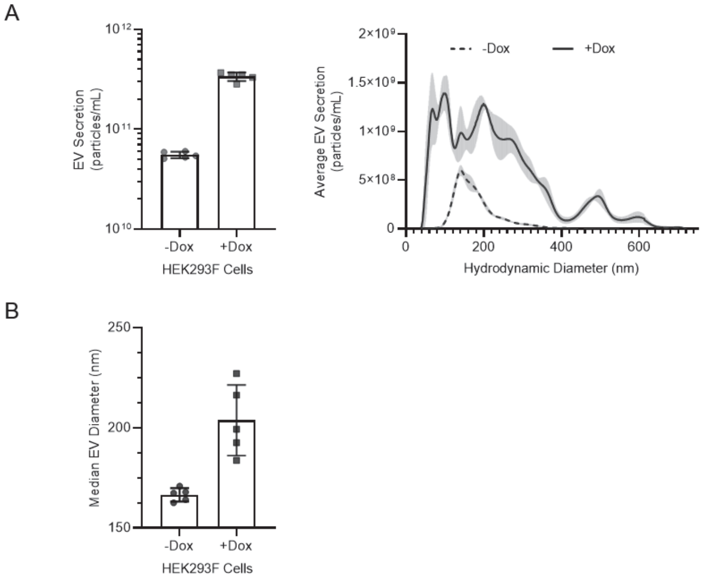

Figure 2: Nanoparticle tracking analysis of mucin-induced EVs isolated from HEK293F cells. A) Comparison of EV secretion from HEK293F cells with low (-Dox) and high (+Dox) Muc1 expression. Bar plot (Left) depicts the average +/- SD from 5 technical replicates.
Histogram (Right) shows the average secretion +/- SEM from 5 technical replicates for vesicles ranging in size from 0 to 750 nm. B) Comparison of median hydrodynamic diameter (HDD) of EVs from HEK293F cells with low (-Dox) or high (+Dox) Muc1 expression. Bars represent the average +/- SD from 5 technical replicates.

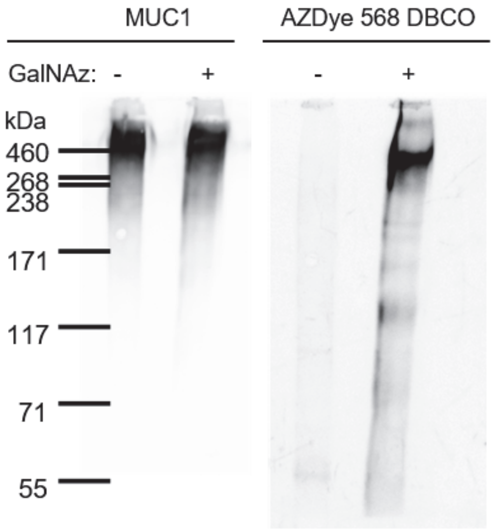

Figure 3: Bio-orthogonal click conjugation of mucin-induced EVs. Western blot detection of Muc1 (Left) and DBCO-AzDye 568 (Right) in lysates of mucin-induced EVs with or without N- azidoacetylgalactosamine (GalNAz) metabolically incorporated into the glycans of EV Muc1 biopolymer coatings.

Platform for Live Cells Infrared Chemical Imaging

CNF Project Number: 2472-16

Principal Investigator(s): Gennady Shvets
User(s): Dias Tulegenov, Steven Huang

Affiliation(s): Applied and Engineering Physics, Cornell University

Primary Source(s) of Research Funding: National Cancer Institute of the National Institutes of Health award number R21 CA251052. National Institute of General Medical Sciences of the National Institutes of Health award number R21 GM138947

Contact: gs656@cornell.edu, dt483@cornell.edu, hh633@cornell.edu

Research Group Website: http://shvets.aep.cornell.edu

Primary CNF Tools Used: JEOL 9500, CVC SC4500 Evaporator, Zeiss Ultra Scanning Electron Microscope, Oxford PECVD, PlasmaTherm 740, Glen Resist Strip, DISCO dicing saw, Heidelberg MLA 150, Schott IR inspector

Abstract:

Our group has been developing infrared spectroscopy and microscopy for live cells analysis by engineering nanostructured antennas on infrared transparent materials and coupling antenna resonances to molecular vibrations. The standard techniques and materials (e.g. e-beam lithography, calcium fluoride substrates, antenna made of gold) used in our device are not scalable due to usage of expensive tools/materials and CMOS incompatible metals. In this report, we focus on replacing our standard substrate, calcium fluoride, used in previous studies with a silicon wafer.

Summary of Research:

Infrared (IR) spectroscopy is a common non-destructive, label-free technique to identify chemical substances. Previously, we have demonstrated devices (MEIRS [1], 3D-ITS [2], 3D-MEIRS [3]) which are based on coupling plasmonic resonances of nanoantennas to molecular vibrations of chemical components. This allows us to monitor live cell activities such as intracellular activities, cholesterol depletion and cell adhesion. Additionally, by using a mid-IR quantum cascade laser (QCL) light source, our group designed a laser-scanning inverted confocal microscope. The QCL emission is focused on a diffraction-limited spot and scanned across the metasurface through movement of a motorized microscope stage. A liquid-nitrogen-cooled mercury-cadmium-telluride (LN-MCT) mid-IR detector collects modulated reflection from the interaction of the analyte with the metasurface near-fields [4]. Recently we utilized this technique to study metabolic cell differentiation [5]. The vibrational contrast from amide II and lipids (Figure 1) clearly show the high surface sensitivity of our device.

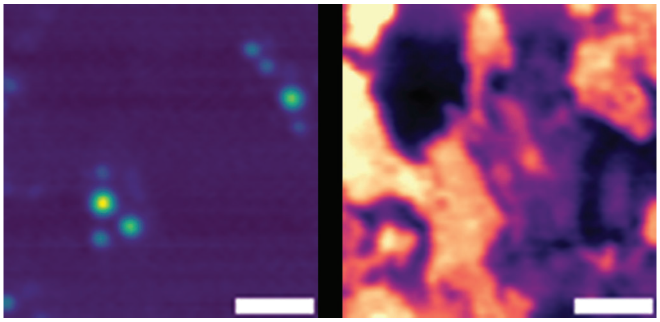

Figure 1: Vibrational contrast of 3T3-L1 at 12C=O ester (left) and amide II (right) bands (scale bar: 40µm).

However, the current substrate (CaF2) is very fragile and poses difficulty if one wants to use larger microplates, typically used for drug discovery studies. This work focuses mostly on replacing CaF2 with a simple silicon wafer with an oxide layer.

The device is made of gold nanoantennas on a double-side polished 4-inch Si wafer with a silicon dioxide spacer. First, the RCA cleaned silicon wafers were deposited by a 2 µm thick silicon dioxide layer. To pattern nanoantennas, a thin layer of PMMA was spin-coated followed by the e-beam exposure with JEOL9500. After developing, SC4500 evaporator was used to deposit a 5nm Ti adhesion layer followed by 70nm layer of gold to form antennas. Since we use the backside of the substrate to focus IR light, back etched marks located exactly under the metasurface arrays were made by backside alignment using Heidelberg MLA 150 for patterning and PT740 for etching. The last step is to lift-off gold by soaking the wafer/pieces into acetone overnight. Schott IR inspector was used to observe both sides of the wafer, top side having metasurfaces and bottom one having marks (Figure 2).

The metasurfaces are then brought to the lab where we culture cancer cells on top of them and acquire images and spectrum. Figure 3 shows the IR spectra of cells in newly fabricated metasurface. The absorbances magnitudes (vibrational contrast) of amide peaks are comparable to our previous designs, thus making it possible to replace fragile and expensive CaF2 with an unexpensive and easy to make SiO2-on-Si substrates.

Conclusions and Future Steps:

TWe have demonstrated that our plasmonic metasurface-based devices can also be made with simple Si unlike a standard IR-transparent CaF2 which paves the way for scaling up. We plan to replace expensive e-beam lithography with cheaper and more scalable photolithography (e.g. ASML DUV stepper) for metasurface patterning to large-area microplates. Plus, gold is not a compatible CMOS metal, so we also envision to consider different metals like Ti or Al.

References:

[1] Huang, S. H. et al. Metasurface-enhanced infrared spectroscopy in multiwell format for real-time assaying of live cells. Lab Chip 23, 2228-2240 (2023).

[2] Mahalanabish, A. Huang, S. H. Shvets, G. Inverted Transflection Spectroscopy of Live Cells Using Metallic Grating on Elevated Nanopillars. ACS Sens 9 (3), 1218–1226 (2024).

[3] Mahalanabish, A., Huang, S. H., Tulegenov, D., and Shvets, G. Infrared Spectroscopy of Live Cells Using High-Aspect-Ratio Metal-on-Dielectric Metasurfaces, Nano Lett. 24, 11607–11614 (2024).

[4] Huang S. H., Shen, PT., Mahalanabish, A., Sartorello, G., Li, J., Liu, X., and Shvets, G. Mid-infrared chemical imaging of living cells enabled by plasmonic metasurfaces, bioRxiv, 2024.09.17.613596.

[5] Huang, S.H., Tulegenov, D., and Shvets, G. Combining quantum cascade lasers and plasmonic metasurfaces to monitor de novo lipogenesis with vibrational contrast microscopy, Nanophotonics (2025).

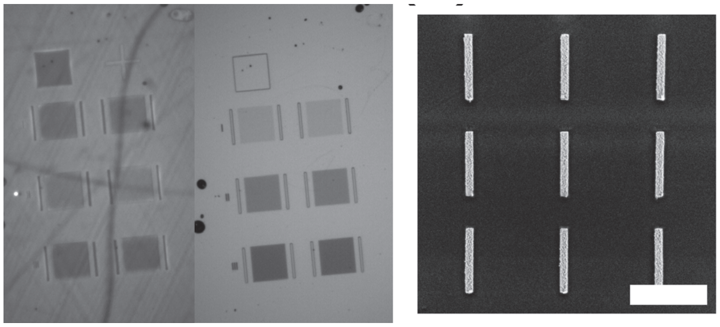

Figure 2: Left and middle figures show the bottom and top side of the wafer, respectively. SEM image of the antennas (right figure, scale bar: 3 µm).

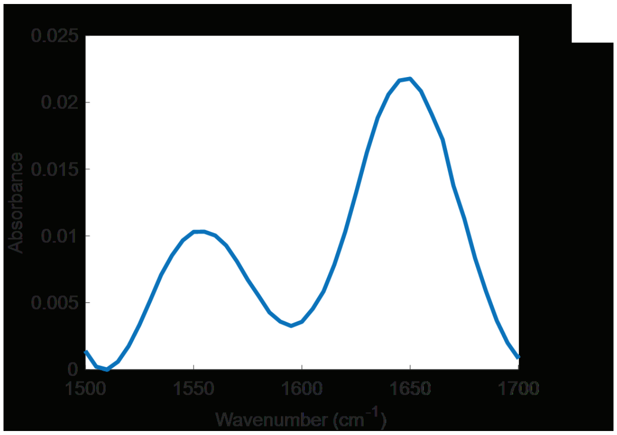

Figure 3: Absorbance spectrum of 3T3-L1 cell measured on the metasurface

Circulating Extracellular Vesicles and Physical Stress in ME/CFS

CNF Project Number: 2590-17

Principal Investigator(s): Maureen R. Hanson
User(s): Ludovic Giloteaux

Affiliation(s): Department of Molecular Biology and Genetics, Cornell University, Ithaca NY

Primary Source(s) of Research Funding: NIH U54

Contact: mrh5@cornell.edu, lg349@cornell.edu

Research Group Website: https://neuroimmune.cornell.edu/research/vesicles-and-signaling/

Primary CNF Tools Used: Malvern NS300 NanoSight

Abstract:

Myalgic Encephalomyelitis/Chronic Fatigue Syndrome (ME/CFS) is a debilitating and complex multisystem illness that affects millions in the United States. Individuals with ME/CFS suffer from persistent fatigue, cognitive impairment, unrefreshing sleep, and post-exertional malaise (PEM), a worsening of symptoms following physical or mental exertion. Growing evidence suggests that extracellular vesicles (EVs), membrane-bound particles released by all cells, play a role in mediating intercellular communication and may contribute to disease pathology. In this project, we used the Malvern NanoSight NS300 Nanoparticle Tracking Analysis (NTA) system to measure concentration of plasma-derived EVs from ME/CFS patients and matched controls across multiple time points surrounding a cardiopulmonary exercise test (CPET). Accurate quantification of EVs is essential not only to assess physiological responses to exercise but also to normalize downstream EV cargo analyses, including surface protein profiling using flow cytometry and RNA-based studies.

Summary of Research:

We used the Malvern NS300 NanoSight NTA instrument to characterize EV populations in plasma samples collected from 28 individuals with ME/CFS and 26 healthy controls. Blood samples were taken before, shortly after, and 24 hours following a CPET. EVs were isolated using standardized protocols to ensure consistency across samples.

Nanoparticle tracking analysis was performed to determine the concentration of EVs in each sample. The resulting data (Figure 1) demonstrate that there is no significant difference in baseline EV concentrations between ME/CFS patients and healthy controls. However, a significant increase in EV concentration was observed in both groups shortly after CPET. This was followed by a marked decrease in EV levels during the recovery phase (24 hours post- exercise), suggesting dynamic regulation of EV release in response to physical exertion in both healthy and diseased states.

Quantification data from the NTA are also being used to normalize EV input for multiplex surface marker profiling using flow cytometry kits and for RNA cargo analysis. This normalization step is crucial for ensuring meaningful biological comparisons across subjects and time points.

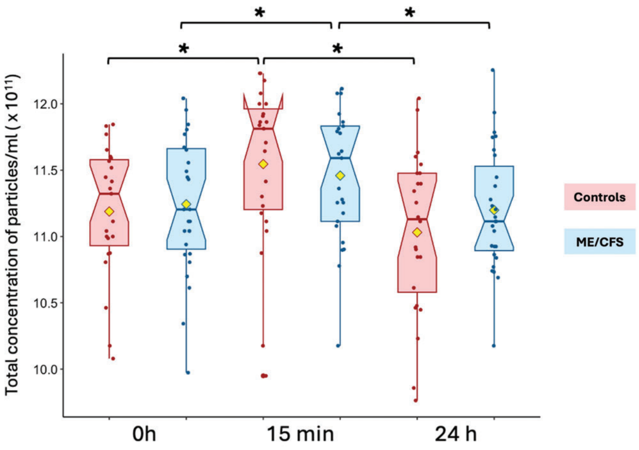

Figure 1: Characterization of extracellular vesicles by Nanoparticle Tracking Analysis. Total concentration of particles per mL of plasma across three time points: before exercise (0h), 15 minutes post-exercise, and 24 hours post-exercise.

Conclusions and Future Steps:

Our findings reinforce that EV concentrations increase after exercise and subsequently decline during recovery in both ME/CFS and control groups. This exercise-responsive EV dynamic highlights the utility of NTA for identifying physiologically relevant changes and enabling normalization across sample sets. Ongoing studies are expanding the dataset with additional subjects to improve statistical power. Future work will focus on integrating surface protein signatures from immunophenotyping using flow cytometry and RNA cargo analysis, allowing us to correlate EV content with exercise response and clinical severity in ME/CFS. These efforts aim to uncover biomarkers of PEM and dysfunctional intercellular signaling in ME/CFS, ultimately improving our understanding of disease mechanisms and therapeutic targets.

References:

[1] Giloteaux Ludovic and Maureen R. Hanson. Post-exercise changes in mitochondrial DNA of extracellular vesicles in myalgic encephalomyelitis/chronic fatigue syndrome. Poster presentation by L. Giloteaux at the International Society of Extracellular Vesicles (ISEV) 2025 conference held in Vienna, Austria, April 23rd-27th.

Broadband Electrical Impedance Spectroscopy of Single Cells for Viability Assessment

CNF Project Number: 2827-19

Principal Investigator(s): Alireza Abbaspourrad
User(s): Amirhossein Favakeh, Amir Mokhtare, Mohammad Javad Asadi, James C. M. Hwang

Affiliation(s): Department of Food Science, Cornell University, Ithaca 14853, New York, USA; School of Electrical and Computer Engineering, Cornell University, Ithaca, New York 14853, USA; School of Electrical and Computer Engineering, Cornell University, Ithaca, New York 14853, USA

Primary Source(s) of Research Funding: US Army research, development and engineering command

Contact: am2964@cornell.edu, ma2297@cornell.edu, jch263@cornell.edu

Primary CNF Tools Used: Heidelberg DWL2000 Mask Writer, ABM Contact Aligner, SUSS MA6 Contact Aligner, Oxford 82 Etcher, SCVC Even-Hour Evaporator

Abstract:

Single-cell analysis plays an important role in disease diagnosis. However, many characterization methods are labor-intensive, costly, and time-consuming. Electrical impedance spectroscopy (EIS) offers a label-free, non-invasive method for probing the biophysical characteristics of cells and assessing their viability. Here, we have designed and fabricated a coplanar waveguide (CPW) integrated with microfluidics that can precisely capture a single cell between the gaps of the CPW electrodes. By sweeping the frequency from low (30 kHz) to high (6 GHz) through the cell, we successfully extracted the cellular bilayer electrical properties in real-time monitoring and assessed the cell viability through modeling each layer of the cell with a suggested electrical equivalent circuit.

Summary of Research:

To fabricate the electrode (Figure 1a), first, we spin-coated AZ nLOF 2020 photoresist on a 4-inch fused silica wafer with a thickness of 500 µm. We created the photomask using Heidelberg DWL2000 Mask Writer. Then, we patterned the design using the SUSS MA6 Contact Aligner on the photoresist of the fused silica wafer. After developing with AZ 726 MIF, we removed residual resist by descumming the wafer using the Oxford 82 Etcher. Next, metal layers (20 nm titanium and 500 nm gold) were deposited onto the substrate using an electron beam evaporator. This was followed by a lift-off process to remove unwanted metal and remaining photoresist (Figure 1b).

Photolithography was used to fabricate the microfluidic channel. First, we used SU8-2025 negative photoresist to spin-coat a 20-micron-thick layer onto a silicon wafer. After soft baking, exposure was done using the ABM contact aligner, followed by post-baking and developing with SU8 developer. We then hard-baked the pattern. Afterward, the PDMS was poured over the master mold and placed in the oven at 65°C for 2 hours. Next, we peeled the PDMS off and bonded the microfluidic channel with the CPW intersection gap, ensuring a leak-proof seal. Finally, the CPW input and output were terminated with SMA coaxial connectors (Figure 1c).

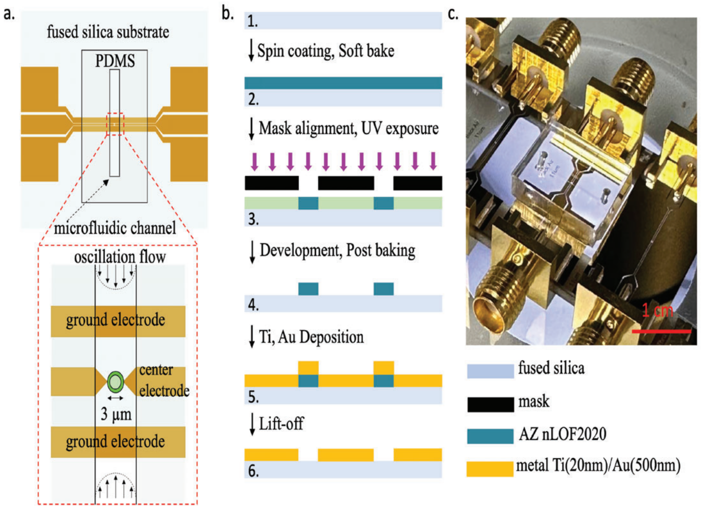

Figure 1: Electrical-impedance microfluidic platform to probe the single-cell biophysical characteristics. (a) Coplanar waveguide (CPW) design. (b) CPW fabrication process. (c) Photograph of the assembled platform.

The platform was connected to the vector network analyzer (VNA), and yeast cells suspended in a low-conductivity 8.5% sucrose solution were injected through the microchannel for final measurements.1 Using dielectrophoresis (DEP), we captured a single cell at 4 MHz and 0 dBm power between the CPW gap (Figure 2a). With EIS, most of the electric field passes through the cell; 2 therefore, by switching the trapping mode to characterization mode from 30 kHz to 6 GHz and using -18 dBm power, we successfully probed the cell's intracellular properties. Using a two-port measurement, we measured both the membrane and cytoplasm electrical properties, and we assessed cell viability through scattering (S) parameter measurement. The impedance data were then validated by fitting

S-parameters to the proposed equivalent circuit for the cell (Figure 2b) via Advanced Design System (ADS) software.

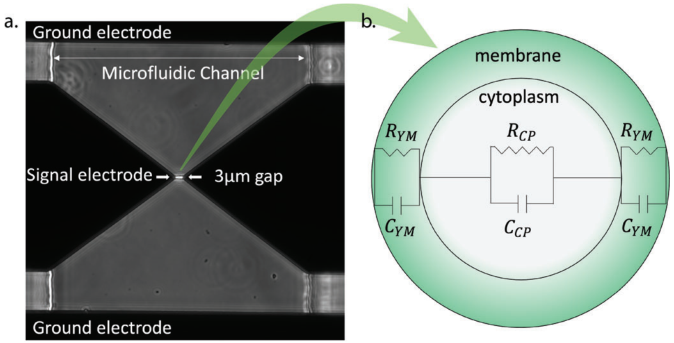

Figure 2: Microwave sensing of a single yeast cell. (a) Trapped single yeast cell between the coplanar waveguide (CPW) electrode gap. (b) Suggested equivalent circuit for each layer of the cell.

Conclusions and Future Steps:

We introduced a high-throughput electrical-impedance microfluidic platform that successfully measures the intracellular electrical properties of single cells. It can distinguish cell viability at high frequencies (3 GHz), where cytoplasm capacitance is dominant. The system enables real-time differentiation between live and dead cells with high accuracy, demonstrating a cytoplasmic capacitance of 3.6 fF for live cells. This platform is fast, accurate, non-invasive, and label-free, enabling real-time monitoring of single cells. It can be used for different electrode configurations and cell types, including mammalian and reproductive cells, for precise single-cell analysis. Future work will focus on EIS measurements of oocytes using this platform to select the best oocyte candidate for assisted reproductive technology (ART) purposes.

References:

[1] A. Favakeh, A. Mokhtare, M. J. Asadi, J. C. M. Hwang and A. Abbaspourrad, Lab Chip, 2025, 25, 1744–1754.

[2] J. C. M. Hwang, IEEE Microwave Mag., 2021, 22, 78–87.

Microfluidic-Based Analysis and Selection of Mammalian Spermatozoa

CNF Project Number: 2827-19

Principal Investigator(s): Alireza Abbaspourrad
User(s): Ali Karimi

Affiliation(s): Department of Food Science, College of Agriculture and Life Sciences, Cornell University

Contact: alireza@cornell.edu, ak2429@cornell.edu

Research Group Website: https://abbaspourradlab.com

Primary CNF Tools Used: ABM Mask Aligner

Abstract:

Successful fertilization depends on sperm navigating the complex, dynamic female reproductive tract shaped by geometry and fluid flow. We used microfluidic platforms to study bovine sperm migration under two levels of structural and hydrodynamic complexity. First, we examined rheotactic swimming through tapered microchannel strictures, finding narrower angles (45°) enhance upstream progression while wider angles (90°) impede it. Second, modeling and experiments revealed a novel behavior, rotary rheotaxis, where sperm follow stable, curved upstream paths in outward radial flow. We harnessed this in a microfluidic device combining radial flow and strictures to isolate highly motile sperm from raw semen, advancing sperm–fluid–structure interaction understanding and assisted reproduction technologies.

Summary of Research:

Spermatozoa transverse through and interact with the female reproductive tract (FRT) where they are exposed to a complex microenvironment on their way to the oocyte. Rheotaxis is the reorientation of sperm in a shear flow. We used two level of flow and geometrical complexity on rheotactic sperm navigation: obstructed pathways and radial flows. The microenvironments are fabricated by manufacturing microfluidic devices using conventional soft lithography technique. We used bovine sperm as a model for mammalian sperm.

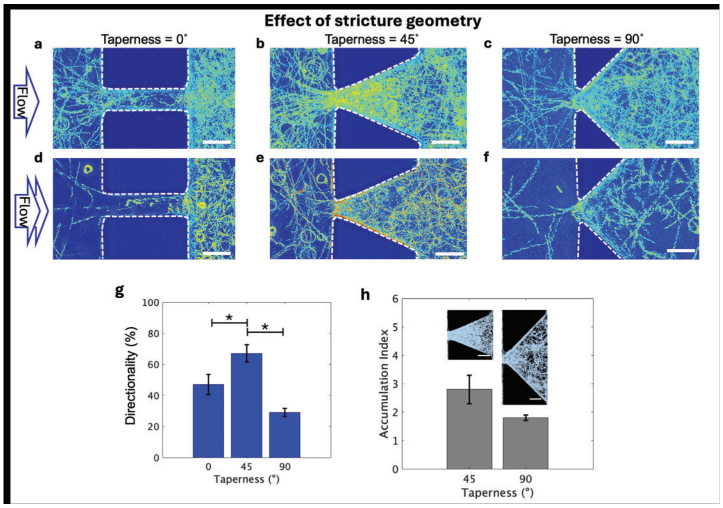

Figure 1: Obstructed pathways mimicking the female reproductive tract, showing sperm trajectories in straight barriers (a, d), tapered barriers with β = 45° (b, e) and β = 90° (c, f) under average shear rates of 8 and 12 s-1. Trajectories are colorized by grayscale intensity. Scale bar: 100 µm. (g) Average directionality across three barrier types under identical flow ($p < 0.0001$, one-way ANOVA). (h) Accumulation index decreases with increased taper angle from β = 45° to β = 90°. Overlaid images represent 5-second sperm motion; blue pixels mark sperm presence.

During their journey in the female reproductive tract (FRT), sperm interact hydrodynamically with complex microstructures formed by the epithelial surfaces of the fallopian tubes. Spatial heterogeneity and muscle contractions cause spatiotemporal geometry changes. Although several studies simulate the FRT using simple sperm passage channels, none clarify how geometry alterations affect upstream sperm navigation. Previous work showed gate-like behavior of strictures in sperm migration. We systematically studied how barrier geometry affects sperm navigation, mimicking fallopian tube structure (Fig. 1(a–f)). We found that 45° tapered barriers increased navigation by 20% (Fig. 1(g)), while increasing taper to 90° obstructed sperm passage. As shown in Fig. 1(h), accumulation at the barrier apex decreases as taper increases from 45° to 90° under the same shear rate.

We observed that sperm interact and cooperate while passing through the barrier port, forming train-like groups (Fig. 2(a)). This cooperation occurs in three phases: (1) Initial Alignment: temporary orientation at the port entrance due to tapered geometry; (2) Cooperative Train Formation: flagellar synchronization in the high-shear port enhances swimming efficiency; and (3) Dispersal: group disbands upon exiting into the upstream reservoir as shear decreases. To quantify this behavior, we measured inter-sperm distances (Δr) and

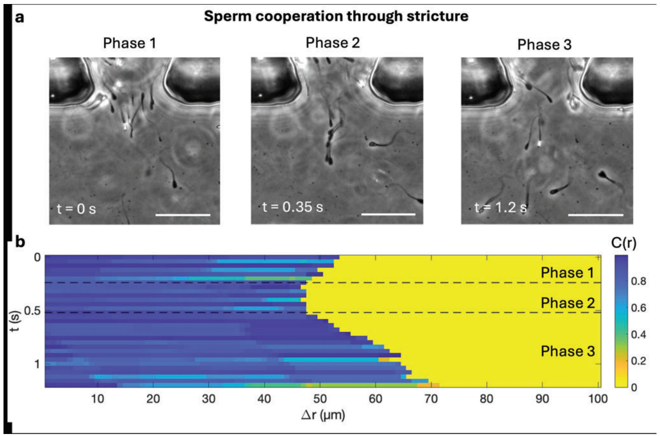

Figure 2: Sperm cooperation in the β = 45° barrier. (a) Stages: Phase 1—alignment by taper, Phase 2—cooperative train through high-shear port, Phase 3—dispersal upstream. (b) Heatmap of correlation function C(r) over distance and time, showing phase transitions. Color bar: correlation values.

orientation differences (Δθ) during a six-sperm event. The correlation function C(r), calculated across distance and time, captures the spatiotemporal dynamics of sperm cooperation (Fig. 2(b)).

We demonstrated that sperm navigate outward radial flow gradients (Fig. 3(a), (b)), showing distinct rheotactic behaviors based on flow rate. At moderate rates, sperm migrated toward the center; at higher rates, they exhibited a rotary rheotaxis, spiraling inward (Fig. 3(c)). This inspired the design of the SUN chip, which combines controlled radial flow with geometric strictures to enhance sperm selection (Fig. 3(e)). Stricture geometry, based on prior work, maximizes upstream navigation while maintaining high shear rates suitable for selecting motile sperm (Fig. 3(f)). Experiments confirmed effective navigation and radial flow directing sperm toward the origin (Fig. 3(g)). The SUN chip processes raw bull semen at various flow rates, isolating highly motile (>95%) and viable sperm (Fig. 4(a)). Selected sperm showed ~50% higher average path velocity (VAP) than raw semen (Fig. 4(b)). Amplitude of head oscillation (ALH) and beat cross frequency (BCF) increased significantly at most flow rates, indicating more progressive sperm behavior under low to moderate flow (Fig. 4(c)).

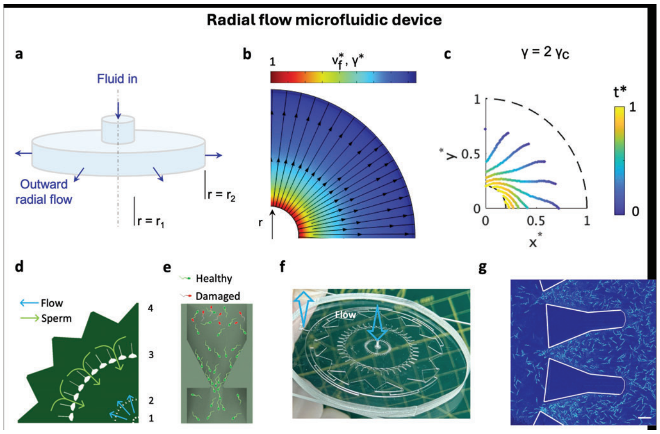

Figure 3: SUN chip design. (a) Radial flow generated by pressure difference between inner (r_1) and outer (r_2) radii. (b) Normalized velocity (v) decays with r; streamlines/arrows indicate flow direction. (c) Sperm trajectories at shear rate γ = 2γc. Time and dimensions normalized for clarity. (d) Schematic of one-quarter of the chip showing flow direction and regions I–IV. (e) Sperm migration through a stricture. (f) SUN chip image. (g) Sperm navigation in region II.*

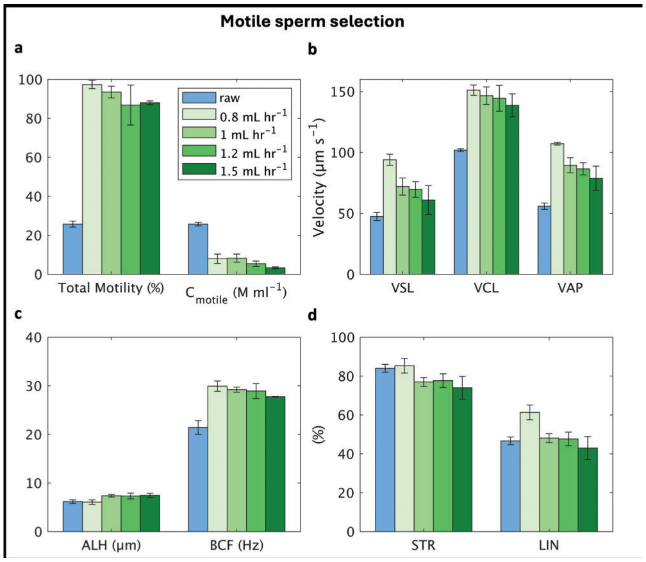

Figure 4: Motility profiles of sperm extracted via SUN chip under flow rates 0.8–1.5 mL/h vs. raw bovine semen. (a) Total motility and motile sperm concentration. (b) VSL, VCL, VAP. (c) ALH and BCF. (d) STR and LIN. SUN chip-processed samples show enhanced motility over raw semen.

Conclusions and Future Steps:

We developed microfluidic devices to study sperm migration in complex environments, focusing on obstructed pathways and radial flow. Our results show that pathway geometry, especially constriction angles, significantly influences rheotactic sperm behavior. Combining geometric strictures with radial flow, we created the SUN chip, which processes 150 µL. This work enhances understanding of microswimmer navigation in dynamic environments and lays groundwork for studying other motile microorganisms. Future efforts should scale processing volume and add automation for clinical use, particularly in IVF. The SUN chip's larger features ease fabrication for mass production, though automation and commercialization challenges remain.

References:

[1] Suarez, S. S.; Pacey, A. A. Sperm Transport in the Female Reproductive Tract. Hum. Reprod. Update 2005, 12 (1), 23–37.

[2] Zaferani, M.; Palermo, G. D.; Abbaspourrad, A. Strictures of a Microchannel Impose Fierce Competition to Select for Highly Motile Sperm. Sci. Adv. 2019, 5 (2), eaav2111.

[3] Karimi, A.; Yaghoobi, M.; Abbaspourrad, A. Geometry of Obstructed Pathway Regulates Upstream Navigational Pattern of Sperm Population. Lab. Chip 2025, 25 (4), 631–643.

Fabrication of Microchip Devices for Organ-on-a-Chip and Lab- on- a-Chip Applications

CNF Project Number: 2857-19

Principal Investigator(s): Esak (Isaac) Lee
User(s): Wukun Ouyang, Renhao Lu, Yansong Peng

Affiliation(s): Meining School of Biomedical Engineering, Cornell University

Primary Source(s) of Research Funding: R01 CA279560; R01 HL165135

Contact: el767@cornell.edu, wo55@cornell.edu, rl839@cornell.edu, yp255@cornell.edu

Research Group Website: https://leelab.bme.cornell.edu/

Primary CNF Tools Used: Heidelberg DWL2000 Mask Writer, ABM Contact Aligner, MVD100, SU-8 hotplate

Abstract:

Organ-on-a-chip is a microfluidic cell culture platform, integrated circuit (chip) that simulates the activities, mechanics, and physiological response of an entire organ or an organ system. Our lab aims to create organ-on-a-chip devices to study the mechanism of various diseases. In the past year, we mainly focused on three projects: (1) Astrocyte-driven vasoconstriction impairs glymphatic clearance in a human tauopathy-on-chip model; (2) Monomeric and oligomeric amyloid-β cause distinct Alzheimer's disease pathophysiological characteristics in astrocytes in human glymphatics-on-chip models; (3) Three-Dimensional Lymphatics-on-a-Chip Reveals Distinct, Size-Dependent Nanoparticle Transport Mechanisms in Lymphatic Drug Delivery.

Summary of Research:

Project 1: Astrocyte-driven vasoconstriction impairs glymphatic clearance in a human tauopathy-on-chip model [1]

The glymphatic system is a critical pathway for clearing metabolic waste from the brain by mediating cerebrospinal fluid and interstitial fluid exchange. In Alzheimer's disease (AD), tau protein accumulation is strongly associated with impaired glymphatic clearance, yet the underlying mechanism remains poorly defined. In this study, we employed a three-dimensional human glymphatics-on-chip model to investigate fluid transport and mass clearance in a brain-mimetic extracellular matrix containing engineered blood vessels (BV) surrounded by primary astrocytes. We found that phosphorylated tau (p-tau) induced morphological transformation of astrocytes into a hypertrophic, hypercontractile state, leading to astrocyte-mediated vasoconstriction and impaired glymphatic clearance. Notably, p-tau did not affect blood endothelial cells directly, implicating astrocyte-dependent mechanisms in glymphatic deregulation. Pharmacological inhibition of non-muscle myosin II with blebbistatin reversed astrocytic hypercontractility, restored BV diameters, and rescued glymphatic function. These findings elucidate a glial-specific mechanism of tau-induced glymphatic dysfunction and underscore astrocytic contractility as a promising therapeutic target in AD.

Project 2: Monomeric and oligomeric amyloid-β cause distinct Alzheimer's disease pathophysiological characteristics in astrocytes in human glymphatics-on-chip models [2]

Alzheimer's disease (AD) is marked by the aggregation of extracellular amyloid-β (Aβ) and astrocyte dysfunction. For Aβ oligomers or aggregates to be formed, there must be Aβ monomers present; however, the roles of monomeric Aβ (mAβ) and oligomeric Aβ (oAβ) in astrocyte pathogenesis are poorly understood. We cultured astrocytes in a brain-mimicking three-dimensional (3D) extracellular matrix and revealed that both mAβ and oAβ caused astrocytic atrophy and hyper-reactivity, but showed distinct Ca2+ changes in astrocytes. This 3D culture evolved into a microfluidic glymphatics-on-chip model containing astrocytes and endothelial cells with the interstitial fluid (ISF). The glymphatics-on-chip model not only reproduced the astrocytic atrophy, hyper-reactivity, and Ca2+ changes induced by mAβ and oAβ, but recapitulated that the components of the dystrophin-associated complex (DAC) and aquaporin-4 (AQP4) were properly maintained by the ISF, and dysregulated by mAβ and oAβ. Collectively, mAβ and oAβ cause distinct AD pathophysiological characteristics in the astrocytes.

Project 3: Three-Dimensional Lymphatics-on-a-Chip Reveals Distinct, Size- Dependent Nanoparticle Transport Mechanisms in Lymphatic Drug Delivery

Although nanoparticle-based lymphatic drug delivery systems promise better treatment of cancer, infectious disease, and immune disease, their clinical translations are limited by low delivery efficiencies and unclear transport mechanisms. Here, we employed a three-dimensional (3D) lymphatics-on-a-chip featuring an engineered lymphatic vessel (LV) capable of draining interstitial fluids including nanoparticles. We tested lymphatic drainage of different sizes (30, 50, and 70 nm) of PLGA-b-PEG nanoparticles (NPs) using the lymphatics-on-a-chip device. In this study, we discovered that smaller NPs (30 and 50 nm) transported faster than larger NPs (70 nm) through the interstitial space, as expected, but the smaller NPs were captured by lymphatic endothelial cells (LECs) and accumulated within their cytosol, delaying NP transport into the lymphatic lumen, which was not observed in larger NPs. To examine the mechanisms of size-dependent NP transports, we employed four inhibitors, dynasore, nystatin, amiloride, and adrenomedullin, to selectively block dynamin-, caveolin-, macropinocytosis-mediated endocytosis-, and cell junction-mediated paracellular transport. Inhibiting dynamin using dynasore enhanced the transport of smaller NPs (30 and 50 nm) into the lymphatic lumen, minimizing cytosolic accumulation, but showed no effect on larger NP transport. Interestingly, the inhibition of caveolin by nystatin decreased the lymphatic transport of larger NPs without affecting the smaller NP transport, indicating distinct endocytosis mechanisms used by different sizes of NPs. Macropinocytosis inhibition by amiloride did not change the drainage of all sizes of NPs; however, paracellular transport inhibition by adrenomedullin blocked the lymphatic transport of NPs of all sizes. We further revealed that smaller NPs were captured in the Rab7-positive late-stage lymphatic endosomes to delay their lymphatic drainage, which was reversed by dynamin inhibition, suggesting that Rab7 is a potential target to enhance the lymphatic delivery of smaller NPs. Together, our 3D lymphatics-on-a-chip model unveils size-dependent NP transport mechanisms in lymphatic drug delivery.

References:

[1] Park R, Peng Y, Yslas AR, Lee E. Astrocyte-driven vasoconstriction impairs glymphatic clearance in a human tauopathy-on-chip model. APL Bioeng. 2025 Jun 16;9(2):026126. doi: 10.1063/5.0261875. PMID: 40530247; PMCID: PMC12173474.

[2] Yslas AR, Park R, Nishimura N, Lee E. Monomeric and oligomeric amyloid-β cause distinct Alzheimer's disease pathophysiological characteristics in astrocytes in human glymphatics-on-chip models. Lab Chip. 2024 Aug 6;24(16):3826-3839. doi: 10.1039/d4lc00287c. PMID: 39037244; PMCID: PMC11302770.

[3] Lu R, Lee BJ, Lee E. Three-Dimensional Lymphatics-on-a-Chip Reveals Distinct, Size-Dependent Nanoparticle Transport Mechanisms in Lymphatic Drug Delivery. ACS Biomater Sci Eng. 2024 Sep 9;10(9):5752-5763. doi: 10.1021/acsbiomaterials.4c01005. Epub 2024 Aug 23. PMID: 39176471.

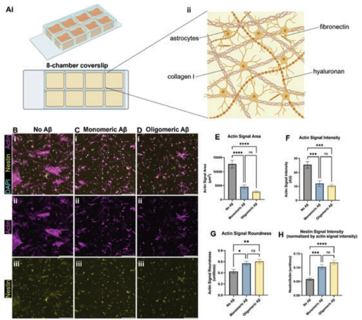

Figure 2: Astrocytic atrophy and reactivity changes in astrocytes exposed to monomeric and oligomeric Aβ. (A) A schematic of our initial 3D culture of astrocytes. (Ai) Human astrocytes were cultured in 3D ECM in chambers on a glass coverslip, (Aii) with brain-mimicking ECM components including collagen I, hyaluronan, and fibronectin. (B) Immunostaining astrocytes with phalloidin (F-actin staining), anti- nestin antibodies, and DAPI. The astrocytes were exposed to either no Aβ (B), monomeric (C), or oligomeric Aβ (D). (E) Changes in actin signal area per cell by monomeric or oligomeric Aβ. (F) Changes in total actin signal intensity by monomeric or oligomeric Aβ. (G) Changes in roundness by monomeric or oligomeric Aβ. (H) Changes in astrocytic reactivity by monomeric or oligomeric Aβ, as measured by nestin signal intensity relative to actin signal intensity. Scale bars (B– D) = 200 μm. * ($p < 0.05$), ** ($p < 0.01$), *** ($p < 0.001$), and **** ($p < 0.0001$) indicate statistical significance. ns = not significant.

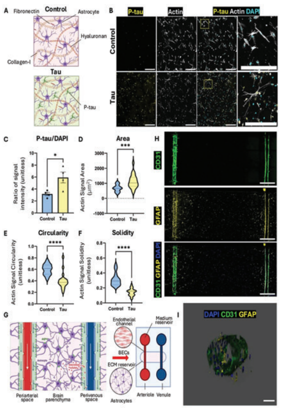

Figure 1: Human glymphatics-on-chip model recapitulates 3D neurovascular architecture with astrocytic reactivity to tau. (a) A schematic representation of the ECM components (astrocytes, fibronectin, collagen I, and hyaluronan) and experimental groups (control, red; tau-treated, green). (b) Immunofluorescence staining of phosphorylated tau (p-tau, yellow), actin (gray), and nuclei (DAPI, cyan) in control and tau-treated astrocytes. Zoomed insets highlight structural changes. (c) Quantification of p-tau signal intensity, normalized to DAPI (N¼ 4). (d) Violin plot showing astrocyte area under control and tau-treated conditions (N¼ 30–40). (e) Violin plot representing astrocyte circularity (N¼ 30–40). (f) Violin plot for astrocyte solidity, showing reduced compactness in tau-treated astrocytes (N¼ 30–40). (g) A schematic of the in vivo glymphatic system alongside the glymphatics-on-chip platform, depicting the arrangement of astrocytes and blood vessel channels. (h) Immunofluorescence images showing endothelial marker CD31 (green), astrocytic marker GFAP (yellow), and DAPI (blue) within the glymphatics-on-chip platform. (i) A representative, 3D-rendered blood vessel surrounded by astrocytes. Scale bars: 300 lm (b), 1 mm (h), and 100 lm (i). Statistical significance: ($p < 0.05$), ($p < 0.001$), and ($p < 0.0001$).

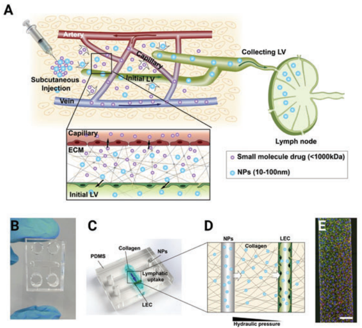

Figure 3: 3D lymphatics-on-a-chip modelto decipher size-dependent nanoparticle (NP) transportinto lymphatic vessels (LVs). (A) Schematic of the NP drug delivery system. Upon subcutaneous injection, water-soluble molecules (<1000 kDa) are collected by the blood capillary; however, NPs(10−100nm) are preferably drained into the lymphatic vessels via their permeable junctions and reach draining lymph nodes. (B,C) Picture and schematic of the lymphatics-on-a-chip model. The collagen bulk (blue) represents the 3D interstitial space, with ECM proteins penetrated by two hollow channels. (D) One of the channels seeded with lymphatic endothelial cells (LECs) forms an engineered LV. The second, cell-free channel allows the introduction of excess fluid to form an interstitial fluid pressure gradient between the acellular and lymphatic channels. Simulating subcutaneous NP injection, excess media, including NPs, are loaded into the acellular channel. NPs transport through the interstitial ECM space, reach the engineered LV, and drain into the LV. Drained and remaining NPs are collected from the 4 circular reservoirs for analysis. (E) Representative image of an engineered LV stained with anti-VE-cadherin (adherens junction, green) antibodies, phalloidin (F-actin, red), and DAPI (nucleus, blue). Scale bar in (E): 100 μm.

Nanofabrication of Metallic Barriers for Single Molecule Imaging

CNF Project Number: 2927-21

Principal Investigator(s): John Brooks Crickard
User(s): David Moraga, Ilayda Korkmaz, Mitchell Woodhouse

Affiliation(s): Molecular Biology and Genetics University: Cornell University

Primary Source(s) of Research Funding: NIGMS/Start-UP

Contact: jbc287@cornell.edu, dlm345@cornell.edu , ik353@cornell.edu, mvw25@cornell.edu

Research Group Website: https://blogs.cornell.edu/crickardlab/

Primary CNF Tools Used: Zeiss Supra with Nabity system for lithography, CVC SC4500 Even/Odd hour evaporator

Abstract:

DNA curtains are a powerful single-molecule technique that can analyze interactions between proteins and DNA in a high-throughput manner. This approach has transformed single-molecule fluorescence microscopy by combining statistical power with the ability to observe proteins moving along individual DNA strands. While other approaches can achieve this statistical power, they generally lack away to control the organization of DNA within a flow cell. We achieve this by nanofabricating chrome barriers onto microscope slides. This allows the alignment of hundreds of individual DNA molecules that can be visualized using total internal reflection fluorescence microscopy (TIRFM). The addition of fluorescently labelled proteins then allows us to monitor specific binding, protein-protein interactions, and the rate of protein movement along DNA. This powerful approach is made possible by equipment maintained in the center for nanofabrication at Cornell.

Summary of Research:

Our research focuses on the application of the DNA curtain technology. We use this approach to perform visual biochemistry approaches and monitor enzymes that function in DNA repair pathways(Figure 1A and Figure 2AB). Our specific work over the last period has focused on how related DNA motor proteins use translocation activity to facilitate the DNA repair process. Below, I will detail two specific projects that have utilized DNA curtains and our specific interactions with the CNF.

Rdh54 reduces Break induced replication during HR:

Rdh54 is a conserved DNA translocase, known as RAD54B in humans, and is a paralog of Rad54/RAD54L. Rdh54 is semi-redundant with Rad54, but its biological role is still unclear. The dominant hypothesis is that Rdh54 reduces Rad51 binding to dsDNA, increasing pools of Rad51 available to promote recombination. However, the role of Rdh54/RAD54B during HR is poorly understood. To improve our knowledge, we investigated the role of phosphorylation in activating Rdh54. Our conclusions from this study are that the effector kinase Rad53 regulates the clustering activity of Rdh54 through a kinase site on the C-terminus of the protein. The kinase activity helps prevent the onset of a mutagenic type of repair, break-induced replication (BIR). This complemented our earlier study, which illustrated that Rdh54 acted to stabilize HR intermediates and provided a novel

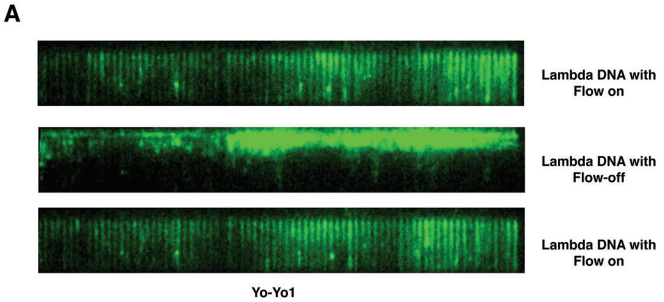

Figure 1: ***DNA curtains***
(A)*. Example of DNA curtains. Each green line represents an individual molecule of lambda phage. DNA (48.5 kbp). Flow turns on an off to extend or retract the DNA. The figure is taken from citation E.*

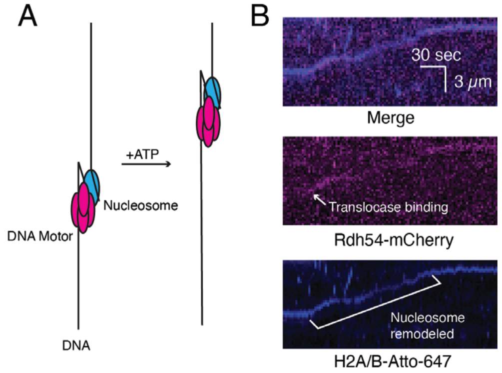

Figure 2: ***Rdh54 pushes nucleosomes on DNA***
(A)*. Cartoon illustrating Rdh54 moving nucleosomes.* ***(B).*** *Direct visualization of Rdh54 moving nucleosomes on DNA. This figure is form citation D.*

mechanism by which Rdh54 improves the fidelity of the strand exchange reaction. Our biochemical studies have been welcomed in the field because of the general challenges in understanding the role of this protein. Studies to understand the biological role of Rdh54 in the template-switching process are ongoing.

The activity of Rad54 as a regulator of crossover/NCO outcomes:

Rad54 is a Snf2 DNA motor protein that remodels DNA and works with Rad51-ssDNA filaments during recombination to catalyze strand exchange. A wealth of information exists on the biochemistry of Rad54 proteins, and we have identified several novel hypomorphic alleles, which allowed us to connect in vitro observations with tangible in vivo phenotypes. Generally, mutations or deletions of Rad54 have resulted in severe sensitivity to genotoxins, which has made developing more refined models for Rad54 function in vivo difficult. We have generated a genetic tool to dissect Rad54's function in all organisms by identifying and developing these hypomorphic alleles. These mutations slow translocation along DNA and in S. cerevisiae cause elevated genetic crossovers between homologous chromosomes during mitotic growth. A key finding from this study is that Rad54 is likely to improve the fidelity of the repair.

Interactions with CNF:

Our interactions with CNF are limited to the nanofabrication of flow cells, which we use to make flow cells (Figure 3AB). This involved electron beam lithography and chrome deposition to make barriers on the glass slide. These methods require us to train biochemistry and biology students to use the equipment in the cleanroom. These students would not have any interactions with this type of equipment or lithography applications otherwise. This cross-disciplinary training is a part of my research program but is made possible by the CNF.

Conclusions and Future Steps:

In the future we will continue to train students to make microscope slides.

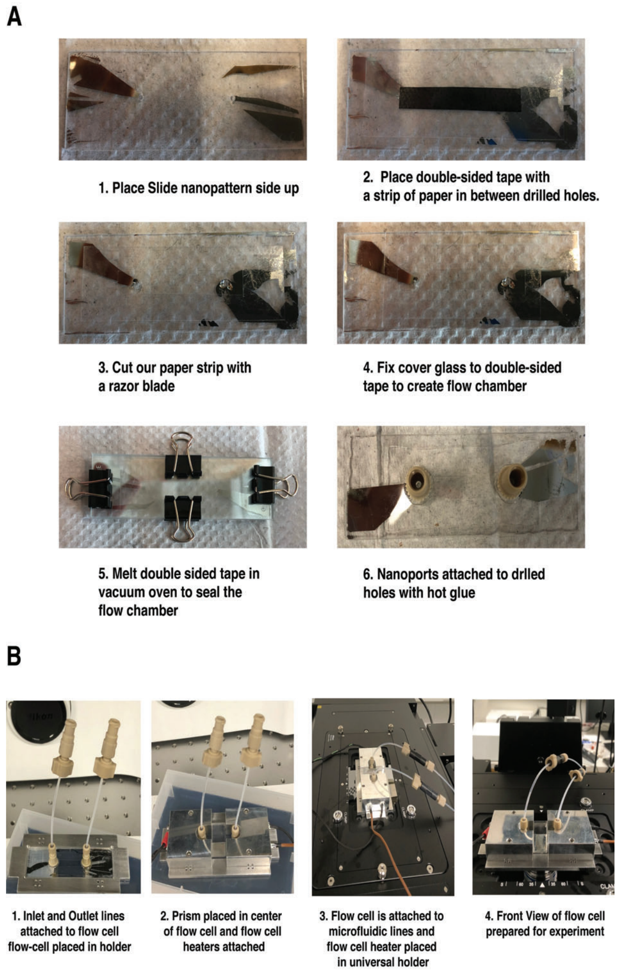

*Figure 3: **Assembly of flow cell for DNA imaging (A)**. Assembly steps for a flow cell. **(B)**. Assembly of a flow cell on the microscope. This figure is from citation E.*

References:

[1] Keymakh M*, Dau J, Ferlez B, Lisby M, Crickard JB. Rdh54 stabilizes Rad51 at displacement loop intermediates to regulate genetic exchange between chromosomes. (2022) PLOS Genetics PMID:36099310.

[2] Hu J, Ferlez B, Dau J, and Crickard JB. Rad53 regulates Rdh54 at homologous recombination intermediates. (2023) Nucleic Acids Research PMID: 37850655.

[3] Sridalla K&*, Woodhouse M&, Hu J, Scheer J*, Ferlez B, Crickard JB. The DNA strand opening activity of Rad54 reduces crossover outcomes during homologous recombination. Nucleic Acids Research (2024) PMID: 38828785.

[4] Woodhouse M, Crickard JB. DNA curtains to visualize chromatin interactions. Methods. 2023 Sep;217:36-42. doi: 10.1016/j.ymeth.2023.07.001. Epub 2023 Jul 10. PubMed PMID: 37437647; PubMed Central PMCID: PMC10529070.

[5] Crickard JB. Single Molecule Imaging of DNA-Protein Interactions Using DNA Curtains. Methods Mol Biol. 2023;2599:127-139. doi: 10.1007/978-1-0716-2847-8_10. PubMed PMID: 36427147; PubMed Central PMCID: PMC10082465.

Fabrication of Microelectrode Arrays for Oxygen Generation to Support Cellular Growth in Implantable Devices

CNF Project Number: 3066-23

Principal Investigator(s): Ahyeon Koh
User(s): Samavi Farnush Bint E Naser, Suk-Heung Song, Jafar Batayneh, Mousa Aldosari

Affiliation(s): Department of Biomedical Engineering, Binghamton University

Primary Source(s) of Research Funding: Advanced Research Projects Agency for Health (ARPA-H), Resilient Extended Automatic Cell Therapies (REACT)

Contact: akoh@binghamton.edu, sbintenaser@binghamton.edu, ssong@binghamton.edu, jbatayneh@binghamton.edu, maldosari@binghamton.edu

Primary CNF Tools Used: AJA Sputterer-1, Oxford 81/82, ABM Contact Aligner, YES Polyimide Bake Oven, P7 Profilometer

Abstract:

This project aims to develop a microelectrode array for wireless generation of oxygen to support cell culture in implantable, therapeutic devices. To achieve this goal, we have fabricated Platinum (Pt) microelectrodes using tools available at Cornell Nanofabrication Facility (CNF). The microfabricated electrodes are electrochemically coated with Iridium oxide (IrOx) films following transfer to flexible substrates (e.g., PDMS thin films). IrOx catalyzes water splitting, leading to oxygen evolution at a lower potential (~1.2 V) compared to bare Pt (~1.7 V). Based on the oxygen generation performance of the Pt/IrOx electrodes, the microelectrode design will be revised to optimize oxygen generation for cell growth. In future, the Pt/IrOx electrodes will be integrated with NFC chips to allow for wireless operation of the devices.

Summary of Research:

The Ti/Pt microelectrode array is fabricated following the steps in the schematic in Figure 1.1,2 The Si wafers are cleaned and primed with HDMS using the YES vapor prime oven at CNF prior to coating with 50 nm PMMA (495 PMMA A5, Kayaku Advanced Materials) and 1.75 µm polyimide (PI 2545, HD microsystems). The lift-off process was employed to create the Pt electrodes with LOR 10B as the lift-off resist and Microposit S1813 to define the microelectrode arrays. The AJA sputtering tool was used to deposit 20 nm Ti as the adhesion layer followed by a 100 nm thick Pt layer on the resist bilayer stack. Lift-off was achieved using Remover PG and mild oxygen descum (Oxford 81) post lift-off was used to remove residual resists. Next, a polyimide insulation layer was patterned using photolithography, followed by oxygen etching (Oxford 81) to open active sites on the metal electrodes. A Chromium (Cr) protection layer was used to prevent PI etching from undesired areas, which was removed after the PI etching step, rendering the Tt/Pt microelectrodes ready for the transfer printing step (Figure 2).

Contact profilometry was employed to confirm the final thicknesses of the deposited metal and PI encapsulation layers (Figure 3).

The PMMA layer was dissolved in acetone and water-soluble tapes were used to pick up the electrodes from the wafer (Figure 4A). A 200 nm SiO2 layer was deposited on the electrodes to promote adhesion to final substrates (e.g. PDMS thin films, Figure 4B).

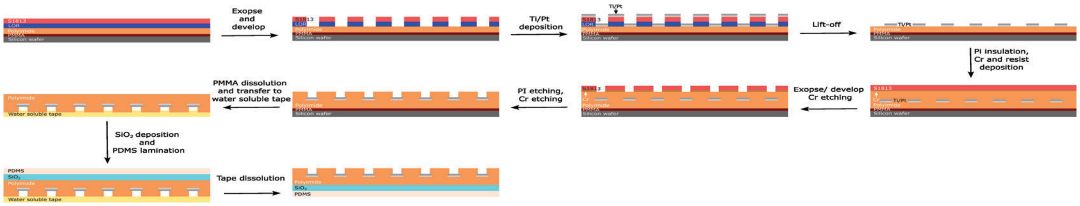

Figure 1: Schematic diagram for fabricating Pt microelectrodes of flexible support.

Flexible gold wires are used to connect these microelectrodes to electrochemical stations for targeted compound deposition, such as IrOx, and characterization of oxygen evolution.

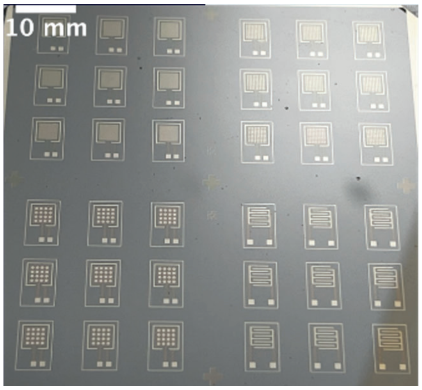

Figure 2: Pt microelectrodes fabricated on polyimide (PI) film supported on Si wafer using sputtering and lift-off. Images were taken at the end of the fabrication process after PI etching to expose the active electrode areas prior to transfer printing.

Conclusions and Future Steps:

Based on our preliminary experiments using the microfabricated devices, the designs are being updated to enhance performance. Our group is currently working on evaluating and establishing protocols for the IrOx deposition on microelectrode systems. We are exploring and investigating micro-coil antenna designs to integrate the microelectrodes into a wireless oxygen generation system.

References:

[1] Brown, M. S., Browne, K., Kirchner, N. & Koh, A. Adhesive-Free, Stretchable, and Permeable Multiplex Wound Care Platform. ACS Sens 7, 1996–2005 (2022).

[2] Lee, I. et al. Electrocatalytic on-site oxygenation for transplanted cell-based- therapies. Nat Commun 14, 7019 (2023).

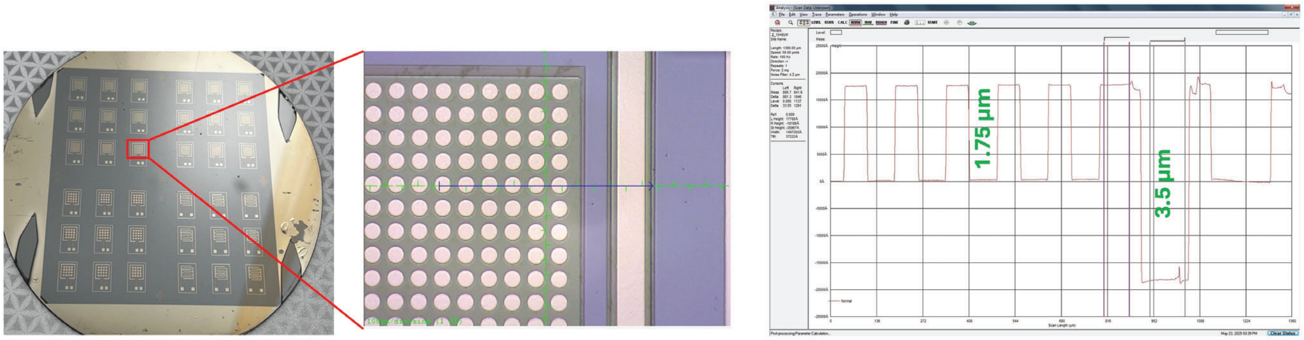

Figure 3: Profilometry performed using the P7 profilometer following the PI etching and Cr removal shows a 1.75 µm PI insulation layer patterning the 100 µm circular features and a 3.5 µm stack of the transferable electrode arrays patterned on the flexible PI supported on Si wafer.

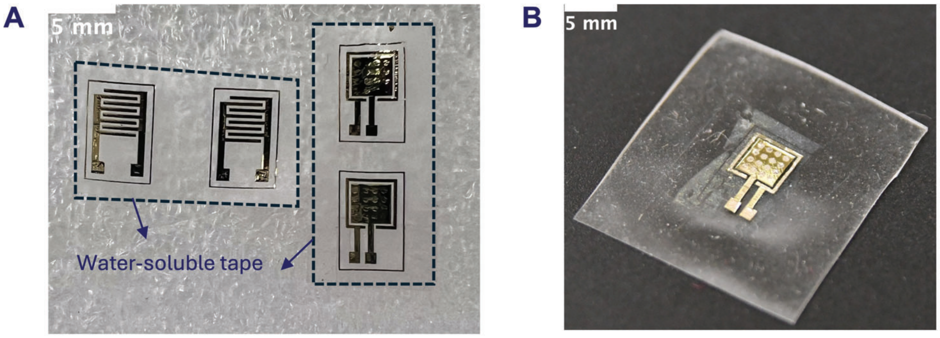

Figure 4: Pt microelectrode arrays (A) after 'pick-up' from the wafer to water-soluble tape and (B) after transferring to PDMS following the SiO2 deposition.

Generating Dendritic Cell-Mimetic Artificial Antigen Presenting Cell for Optimized T Cell Activation

CNF Project Number: 3089-23

Principal Investigator(s): Negin Majedi
User(s): Yan Zeng

Affiliation(s): Mechanical and Aerospace Engineering, Cornell University

Primary Source(s) of Research Funding: PI startup funds

Contact: fm457@cornell.edu, yz2898@cornell.edu

Primary CNF Tools Used: Hitachi TM3000 SEM, Malvern Nano ZS Zetasizer

Abstract:

This project aims to develop dendritic cell-mimetic artificial antigen-presenting cells using wrinkled polystyrene particles and chemically treated sunflower pollens to enhance T cell activation. Polystyrene particles are fabricated via solvent evaporation-induced interfacial instability, while pollen shells are prepared through acid-base treatment. Both are coated with polydopamine and conjugated with activation antibodies. Particle size and morphology are characterized using CNF tools: the Zetasizer and Hitachi TM3000 SEM. Future work will focus on improving surface morphology and antibody accessibility to enhance T cell stimulation.

Summary of Research:

Mechanical cues such as substrate stiffness and surface topography are important in regulating T cell activation [1]. This project aims to generate dendritic cell-mimetic artificial antigen presenting cells for optimized T cell activation using synthetic polystyrene particles and natural sunflower pollens respectively. The resulting protruding morphology facilitates the formation of an interaction area between naïve T cells and artificial T cells that mimics the natural immune synapse, which enhances T cell activation and proliferation.

The polystyrene particles are generated using interfacial instability of emulsion droplets during solvent evaporation using the method similar to the method described by Liu et al [2]. Polystyrene emulsion droplets are via homogenization, where the organic phase has polystyrene and 1- hexadecanol dissolved in chloroform, while the continuous phase has sodium dodecyl sulfate and glycerol dissolved in deionized water. The droplet size is optimized by tuning the polymer concentration and homogenization speed. After homogenization, the droplets are solidified under controlled solvent evaporation condition to trigger interfacial instability and form wrinkled surfaces. The solidified wrinkled polystyrene particles are incubated with deionized water and ethanol respectively to remove residual chloroform, sodium dodecyl sulfate, glycerol, and 1-hexadecanol. Clean particles are coated with polydopamine and conjugated with activation antibodies for T cell activation.

Sunflower pollens are first defatted and then incubated with acid and base respectively to obtain clean, hollow pollen shell for biomedical applications combining the protocols in previous literatures [3], [4]. For the defatting, sunflower pollens are washed subsequently with deionized water, acetone, and cyclohexane. Defatted sunflower pollens are incubated with phosphoric acid and then potassium hydroxide to remove the internal cytoplasmic contents. Clean pollen shells are also coated with polydopamine and then conjugated with activation antibodies for T cell activation.

Both dendritic cell-mimetic artificial antigen presenting cells are co-cultured with native CD4 T cells extracted from mice for three days. After the three-day activation, T cells are stained and examined under flow cytometry to check for activation markers.

Two CNF tools are used to characterize the polystyrene particles and sunflower pollens: Malvern Nano ZS Zetasizer is used for dynamic light scattering measurements to measure the diameter of polystyrene particles generated under different homogenization conditions. Hitachi TM3000 SEM is used to characterize the morphology of polystyrene particles and sunflower pollens.

Conclusions and Future Steps:

For the polystyrene artificial antigen presenting cells, the effect of homogenization speed on particle diameter is shown in Figure 1. The optimal particle diameter is 4-5 microns, which is similar to that of naïve T cells. A lower homogenization speed of 2.8k rpm generates particles with a diameter of 1.14 µm, which is larger compared to those generated at a homogenization speed of 5.2k rpm. To further increase the particle diameter, polymer concentration is further increased. The resulting particles are characterized with instruments outside of CNF and the results are not shown here. The largest polystyrene particles have a diameter of approximately 4-5 um.

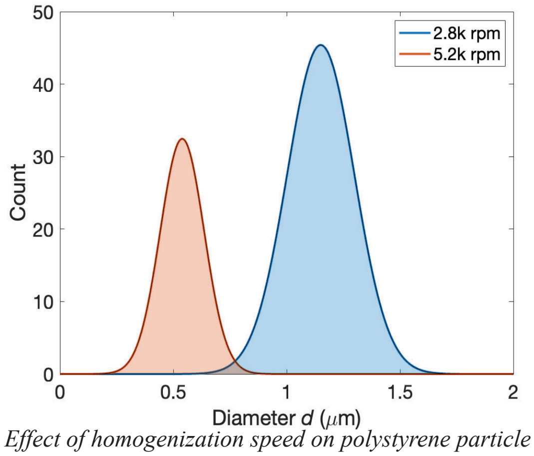

Figure 1: Effect of homogenization speed on polystyrene particle diameter obtained by dynamic light scattering.

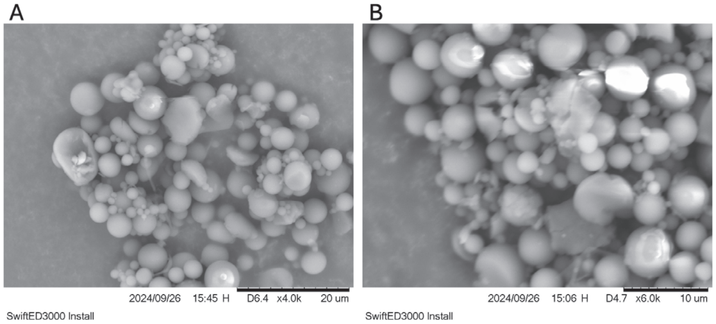

Figure 2: Effect of dialysis against ethanol on polystyrene particle morphology. After (A) 4 days,
(B) 6 days dialysis.

The wrinkling is first assumed to happen during the ethanol wash when 1-hexadecanol leaves the droplet, and the ethanol wash is first done via dialysis instead of direct incubation. Figure 2 shows the morphology of polystyrene particles sampled after 4 days and 6 days of dialysis against ethanol respectively. Particles with a diameter of 4-5 um is difficult to image clearly using the tabletop SEM. There's no significant difference in morphology between particles sampled after 4 days and 6 days of dialysis against ethanol, suggesting that wrinkling is not due to 1-hexadecanol leaving the structure. Alternatively, we assume that wrinkling happens during solidification instead of the ethanol wash, which is later confirmed by Gemini SEM results. For easier imaging, we later switched to Gemini SEM, and the results are not shown here.

The morphology of untreated pollens, acid treated pollens and acid and base treated pollens are shown in Figure 3. Pollens remain intact after acid treatment and base treatment and the spiky features are preserved. Acid treatment opens the apertures on pollen surface, suggesting removal of internal components.

Future work will focus on optimizing the accessibility of conjugated antibodies on pollen shells for more effective activation and increasing the percentage of wrinkled polystyrene particles.

References:

[1] K. Lei, A. Kurum, and L. Tang, "Mechanical Immunoengineering of T cells for Therapeutic Applications," Acc. Chem. Res., vol. 53, no. 12, pp. 2777–2790, Dec. 2020, doi: 10.1021/acs.accounts.0c00486.

[2] S. Liu, R. Deng, W. Li, and J. Zhu, "Polymer Microparticles with Controllable Surface Textures Generated through Interfacial Instabilities of Emulsion Droplets," Adv. Funct. Mater., vol. 22, no. 8, pp. 1692–1697, Apr. 2012, doi: 10.1002/adfm.201103018.

[3] J. M. Ageitos, S. Robla, L. Valverde-Fraga, M. Garcia-Fuentes, and N. Csaba, "Purification of Hollow Sporopollenin Microcapsules from Sunflower and Chamomile Pollen Grains," Polymers, vol. 13, no. 13, Art. no. 13, Jan. 2021, doi: 10.3390/polym13132094.

[4] [4] P. Gonzalez-Cruz, M. J. Uddin, S. U. Atwe, N. Abidi, and H. S. Gill, "A chemical treatment method for obtaining clean and intact pollen shells of different species," ACS Biomater. Sci. Eng., vol. 4, no. 7, pp. 2319–2329, Jul. 2018, doi: 10.1021/acsbiomaterials.8b00304.

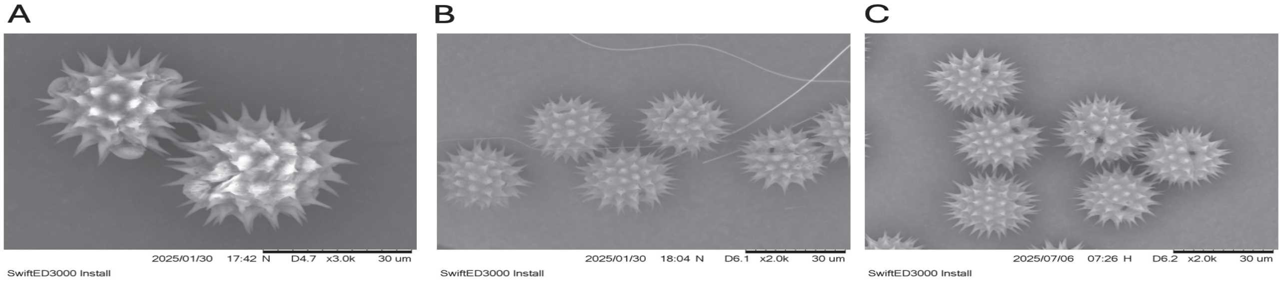

Figure 3: Effect of chemical treatment on pollen morphology. (A) Untreated pollens, (B) Acid treated pollens, (C) Acid and base treated pollens.

Exploring Microfabrication Parameters of Template-Based Carbon Nanotube Arrays for Gene Transfer

CNF Project Number: 3106-23

Principal Investigator(s): Michael Schrlau
User(s): Mujtaba YK Siddiqui

Affiliation(s): Department of Mechanical Engineering, Kate Gleason College of Engineering, Rochester Institute of Technology

Primary Source(s) of Research Funding: : National Institutes of Health R41 GM150320-01 and R43 MH133247-01

Contact: mgseme@rit.edu, mys8553@rit.edu

Research Group Website: https://people.rit.edu/mgseme/Site/Home.html

Primary CNF Tools Used: AJA Ion Mill, PT 740 RIE

Abstract:

Carbon nanotube (CNT) arrays are a promising new technology which can greatly reduce the costs of novel gene therapies for fighting cancer. It has been fabricated at the Cornell Nanoscale Facility (CNF) using a template-based manufacturing technique. Exploration of the various manufacturing parameters involved in the fabrication would allow for the development of a streamlined and optimized recipe. CNF tools were utilized to study various manufacturing recipes to gain insight into how they affect the surface structure of the device.

Summary of Research:

Carbon nanotube (CNT) arrays are a promising technology towards developing safer, more economically and technologically accessible method for the transfection of genetic and biomolecular load into cells. Current treatments for diseases like cancer require dangerous and toxic processes. Novel treatments for leukaemia involve gene therapies, the introduction of proteins into white blood cells modifying them to identify cancer. CNT arrays can be used to transfer these proteins into cells. [1–6]

CNT arrays are manufactured from an initial Anodic Aluminum Oxide (AAO) template. Aluminum forms a self-aligned hollow honeycomb-like porous surface when oxidized anodically, allowing AAO to be a commonly used mask for microfabrication at the nanoscale for freestanding nanostructures. Carbon is coated into the pores by means of a chemical vapor deposition (CVD) process. Carbon coated AAO templates are processed at the CNF using the AJA ion mill and PT 740 reactive ion etching (RIE) tools. [7-9] Resulting in a CNT array device with tips of carbon tubes exposed on the surface.

Previous research at the CNF was focused on the scale up of the CNT array manufacturing process. In that work, the manufacturing process was altered by introducing ion milling and employing a larger carrier wafer for producing devices at a larger scale. The work done since that report has built further upon the initial improvements. Exploring alternative starting templates and exploring manufacturing parameters were steps taken towards optimizing the manufacturing process.

The current standard for AAO templates is 13mm diameter disks, this limits the number of cells which can be cultured on each device. A 47 mm diameter template provides a much larger surface area for cell transfer. Figure 1 shows a silicon water affixed with 6 carbon-coated 47mm templates. Fabrication of these devices at the CNF confirmed the capabilities of the current tools and manufacture larger devices. However, the following standard recipe for 13mm did not produce devices with exposed tubes, due to insufficient carbon deposition during the CVD step.

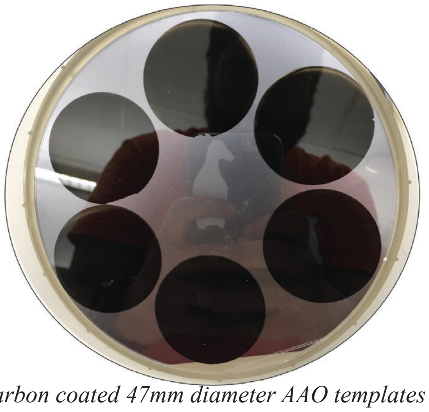

Figure 1:Carbon coated 47mm diameter AAO templates on a carrier wafer.

Alternative 13mm diameter templates were tested. A template with smaller pore diameters and larger pore density resulted in devices with thicker nanotubes when undergoing the standard fabrication process. Due to a smaller starting diameter and constant carbon mass flow rate during CVD. Templates of similar properties from other manufacturers were also tested and showed similar surface parameters as standard devices when undergoing the standard fabrication process.

A parametric study of the RIE process time and power was conducted, these parameters are likely to produce the largest impact on the final device. An initial test was conducted to determine the maximum tube height over etch time, as longer etch time is expected to lead to linear growth in exposed tube heights. Followed up by a study of RIE power to determine how increasing power affects tube height. The standard values for RIE etch were 2 hours at 50W power, the experiments covered increasing etch time to 3,4,5 hours and increasing power to 150W and 250W.

Figure 2 and Figure 3 show the results of these experiments; the measurable outputs were the tube height and tube thicknesses of the exposed CNT tips. As shown in the figures, tube heights increase as power and time increase, while tube thickness is maintained until a noticeable drop in thicknesses at larger parameter values. Micrographs showed that at higher powers and etch time the nanotubes tended collapse upon themselves due to lateral etching thinning them down.

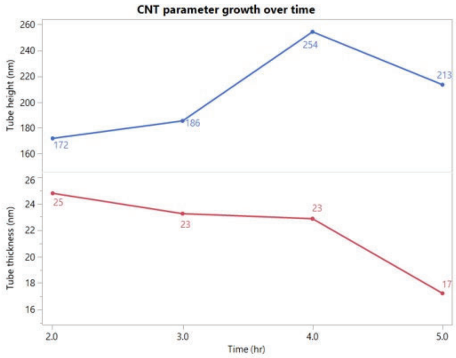

Figure 2: CNT parameters over time.

Conclusions and Future Steps:

Exploring alternative starting templates gives an insight into how to scale up the CNT arrays further while making them more useful for researchers and healthcare companies.

Determining the effects of RIE parameters would help establish upper and lower boundaries for future experiments to optimize the process. Next steps would include optimizing the process for 13 mm diameter devices and establishing a working recipe for 47mm diameter AAO templates.

References:

[1] “Leukemia Treatments.” [Online]. Available: https://www.hopkinsmedicine.org/kimmel- cancer-center/cancers-we-treat/blood-bone-marrow-cancers/leukemia-program/current-treatments. [Accessed: 04-Apr-2025].

[2] “Leukemia: Symptoms, Signs, Causes, Types & Treatment,” Cleveland Clinic. [Online]. Available: https://my.clevelandclinic.org/health/diseases/4365-leukemia. [Accessed: 04- Apr-2025].

[3] “Leukemia - Diagnosis and Treatment - Mayo Clinic.” [Online]. Available: https://www.mayoclinic.org/diseases-conditions/leukemia/diagnosis-treatment/drc- 20374378#. [Accessed: 04-Apr-2025].

[4] 2019, “Advances in Leukemia Research - NCI.” [Online]. Available: https://www.cancer.gov/types/leukemia/research. [Accessed: 04-Apr-2025].

[5] “CAR T Cells: Engineering Immune Cells to Treat Cancer - NCI.” [Online]. Available: https://www.cancer.gov/about-cancer/treatment/research/car-t-cells. [Accessed: 04-Apr-2025].

[6] “CAR T Cell Therapy,” MD Anderson Cancer Center. [Online]. Available: https://www.mdanderson.org/treatment-options/car-t-cell-therapy.html. [Accessed: 04- Apr-2025].

[7] Li, Z. P., Xu, Z. M., Qu, X. P., Wang, S. B., Peng, J., and Mei, L. H., 2017, “Fabrication of Nanopore and Nanoparticle Arrays with High Aspect Ratio AAO Masks,” Nanotechnology, 28(9), p. 095301. https://doi.org/10.1088/1361-6528/aa585c.

[8] Poinern, G. E. J., Le, X. T., O’Dea, M., Becker, T., and Fawcett, D., 2014, “Chemical Synthesis, Characterisation, and Biocompatibility of Nanometre Scale Porous Anodic Aluminium Oxide Membranes for Use as a Cell Culture Substrate for the Vero Cell Line: A Preliminary Study,” Biomed Res Int, 2014, p. 238762. https://doi.org/10.1155/2014/238762.

[9] Golshadi, Masoud, "Carbon Nanotube Arrays for Intracellular Delivery and Biological Applications" (2016). Thesis. Rochester Institute of Technology. Accessed from: https://repository.rit.edu/cgi/viewcontent.cgi?article=10360&context=theses.

[10] Wiesinger, M., März, J., Kummer, M., Schuler, G., Dörrie, J., Schuler-Thurner, B., and Schaft, N., 2019, “Clinical-Scale Production of CAR-T Cells for the Treatment of Melanoma Patients by mRNA Transfection of a CSPG4-Specific CAR under Full GMP Compliance,” Cancers (Basel), 11(8), p. 1198. https://doi.org/10.3390/cancers11081198.

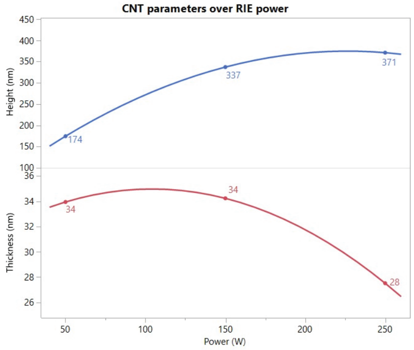

Figure 3: CNT parameters over power.

Microfluidic Chip Fabrication Using CNF Facilities

CNF Project Number: 3193-24

Principal Investigator(s): Anne Meyer
User(s): Danielle Bennett

Affiliation(s): University of Rochester

Primary Source(s) of Research Funding: : The Department of Energy, the University of Rochester

Contact: anne@annemeyerlab.org, dbenne15@ur.rochester.edu

Research Group Website: https://sites.google.com/site/annemeyerlab/home

Primary CNF Tools Used: Heidelberg DWL2000, GCA AS200 i-line Stepper, Oxford PECVD, Oxford 81 RIE

Abstract:

This project aimed to enable long-term fluorescence microscopy imaging of Shewanella oneidensis interactions with CdSe quantum dots by immobilizing motile bacteria physically within a channel instead of through chemical binding. To achieve this, we designed a custom "mother machine" microfluidic device composed of parallel microchannels branching from a main fluid channel. These side channels were aimed to be dimensionally matched to the diameter of individual bacteria, allowing for their physical confinement while maintaining media exchange, thus facilitating continuous observation over time. Fabrication of the device required high-resolution soft lithography using polydimethylsiloxane (PDMS) cast from a silicon mold. The Cornell NanoScale Science and Technology Facility (CNF) was essential for the creation of this master silicon mold. We used the Heidelberg DWL2000 laser writer for mask patterning, followed by photolithographic processing with the GCA AS200 i-line Stepper. Feature development and refinement were carried out using the Oxford PECVD for surface passivation and the Oxford 81 RIE system for precise etching. This platform aimed to allow us to resolve real-time nanoscale interactions between fluorescent nanoparticles and live bacteria, offering new insight into quantum dot– microbe dynamics. The machinery at the CNF facility was required to obtain the small diameter (below 0.7 µm) of the channel features, which was not attainable using our equipment or any commercial equipment.

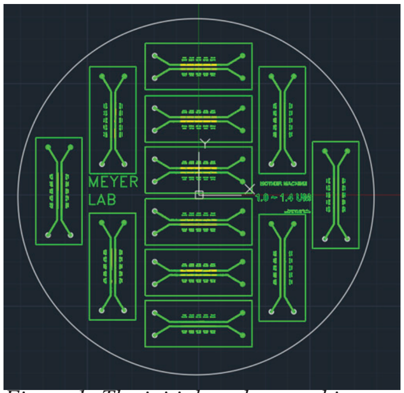

Figure 1: The initial mother machine chip design featuring sharp rectangular channels.

Summary of Research:

This microfluidics chip was designed to address the challenge of imaging interactions between motile Shewanella oneidensis bacteria 1,2 and CdSe quantum dots, which are used in our broader research on nanoparticle-based catalysis. Traditional imaging platforms require timescales too long to monitor these highly motile cells over time, so we engineered an ultraminiaturized "mother machine" to trap individual bacteria in channels that are significantly smaller than those used in previous designs3—pushing the limits of soft lithography resolution.

The design of the microfluidic chip centered on creating a high-resolution "mother machine" with sub-micron precision, featuring narrow side channels approximately 0.7 µm wide branching off a main flow channel approximately 25 µm wide. The chip was constructed from PDMS cast on a silicon mold, with SU-8 photoresist features forming the mold's surface relief. The layout was designed in KLayout software with extensive support from CNF staff, particularly Garry Bordonaro and Aaron Windsor, who provided critical guidance on optimizing the design for photolithography and transitioning from square to rounded channel geometries. This design adjustment, made between Figure 1 and Figure 2, significantly improved fluid dynamics by reducing backflow and enhancing media exchange across the confined bacteria. Fabrication at CNF involved multiple cleanroom steps, including photomask writing with the Heidelberg DWL2000, mask alignment and exposure using the GCA AS200 i-line Stepper, and multilayer etching using the Oxford 81 RIE system. Due to the chip's extremely fine features, the etch process required a two-step

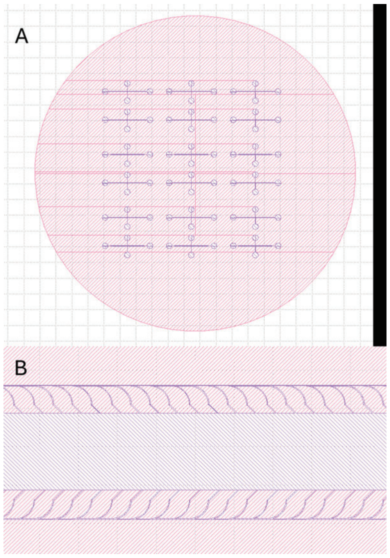

Figure 2: The mother machine design revised with the assistance of CNF staff featuring curved channels. Part A shows the full chip design and part B shows a closer view of the main channel and branching channels.

approach developed with the help of Jeremy Clark, who also provided expertise on the Oxford PECVD system for wafer preparation. Extensive cleanroom training and tool-specific instruction were essential to successfully executing this complex fabrication process.

To test the chip, PDMS was cast onto the fabricated silicon master and cured to form the microfluidic structure, which was then plasma treated and bonded to a glass coverslip to seal the channels. Fluidic testing involved introducing S. oneidensis cells into the device using a syringe pump to establish controlled flow through the microchannels. This functional testing revealed two key issues: first, the side channels were not sufficiently narrow to trap individual bacteria effectively, as shown in Figure 3; and second, leakage occurred at higher flow rates, suggesting inadequate bonding or minor defects at the PDMS–glass interface. These outcomes highlighted the need for tighter feature tolerances and improved sealing, prompting a redesign of the channel dimensions and further optimization of the fabrication protocol.

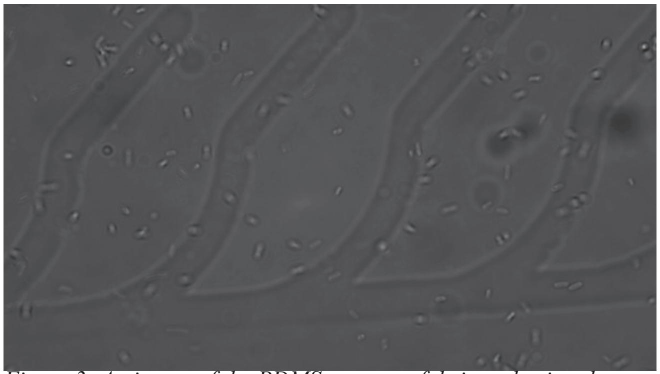

Figure 3: An image of the PDMS structure fabricated using the mask. Bacteria can be observed outside of the microchannels due to leakage at higher flow rates, and the side channels were slightly too large to trap the bacteria.

Conclusions and Future Steps:

Although the initial version of the microfluidic chip did not fully meet the functional requirements for long-term bacterial confinement, the fabrication process validated several critical aspects of the design and demonstrated the capabilities of CNF's advanced lithographic and etching tools. The pattern transfer from the KLayout design to the silicon mold using the Heidelberg DWL2000 and GCA AS200 i-line Stepper was highly successful, yielding clean and reproducible features at both the sub-micron and tens-of-micron scale. The two-step etching process developed with guidance from CNF staff, particularly Jeremy Clark, allowed for precise control over feature depths, which is essential for the multi-scale structure of the chip. While the final PDMS device exhibited some leakage at higher flow rates and did not achieve full bacterial trapping due to overly large side channels, these outcomes provided direct feedback that will inform future improvements.

The ability to prototype a custom-designed, high-resolution microfluidic device at this level would not have been possible without access to CNF's advanced photolithography and etching infrastructure, nor without the expert technical support provided throughout the process. This project has laid the groundwork for developing a next- generation mother machine capable of precisely trapping S. oneidensis for extended imaging of nanoparticle–microbe interactions. Moving forward, refined designs will incorporate narrower channel geometries and optimized bonding techniques to address current limitations. At this point no publications have been drafted.

References:

[1] Edwards, E. H.; Jelusic, J.; Kosko, R. M.; McClelland, K. P.; Ngarnim, S. S.; Chiang, W.; Lampa-Pastirk, S.; Krauss, T. D.; Bren, K. L. Shewanella Oneidensis MR-1 Respires CdSe Quantum Dots for Photocatalytic Hydrogen Evolution. PNAS 2023, 120, 17. https://doi.org/10.1073/pnas.

[2] Bennett, D. T.; Meyer, A. S. Robust Measurement of Microbial Reduction of Graphene Oxide Nanoparticles Using Image Analysis. Appl Environ Microbiol 2025, 0 (0), 9–11. https://doi.org/10.1128/aem.00360-25.

[3] Yang, D.; Jennings, A. D.; Borrego, E.; Retterer, S. T.; Männik, J. Analysis of Factors Limiting Bacterial Growth in PDMS Mother Machine Devices. Front Microbiol 2018, 9 (MAY), 1–12. https://doi.org/10.3389/fmicb.2018.00871.

Microfluidic Systems for Studying Bacteria Mechanobiology

CNF Project Number: 3229-24

Principal Investigator(s): Christopher J. Hernandez
User(s): Jay VanDelden

Affiliation(s): UC San Francisco, UC Berkeley

Primary Source(s) of Research Funding: : NSF 2135586, 2125491

Contact: christopher.hernandez@ucsf.edu, jvd@eigenphase.com

Research Group Website: hernandezresearch.com

Primary CNF Tools Used: AJA Sputter Deposition, 2 Gamma tool, ASML tool, Oxford 81 or Oxford 82 PT770, Oxford, 100, Versalaser

Abstract:

In this project we seek to understand the biomechanical properties of individual bacteria as well as bacterial mechanobiology (the response of living bacteria to mechanical stimuli). We have four goals in this project: 1) to determine mechanical properties of bacterial cell envelope of various species; 2) to understand how to embed and maintain viable bacteria within rigid materials, the so-called "engineered living material." 3) to utilize mechanical stimuli to promote biomineralization of ureolytic bacteria; and 4) to understand how bacteria grow into constricted space.

Summary of Research:

Currently, we are working on to demonstrate that mechanical stimuli can be used to promote biomineralization of ureolytic bacteria by using microfluidic device and genetically modifying a bacterial strain to link mechanosensitive gene to biomineralization gene. Additionally, we are working on to analyze how S. aureus grow and devide in a constricted space using the microfluidic devices manufactured at CNF. Since the inception of this project number we have been manufacturing devices with the help of Jay VanDelden (Eignphase).

Silicon Nitride Cantilevers for Muscle Myofibril Force Measurements

CNF Project Number: 3236-52

Principal Investigator(s): Walter Herzog
User(s): Andrew Sawatsky

Affiliation(s): Faculty of Kinesiology, University of Calgary, Calgary, Canada

Primary Source(s) of Research Funding: : Canadian Institutes of Health Research

Contact: wherzog@ucalgary.ca, ajsawats@ucalgary.ca

Research Group Website: https://kinesiology.ucalgary.ca/research/labs-and-centres/human-performance-lab

Primary CNF Tools Used: GCA 5X Stepper, SUSS MA6-BA6 Contact Aligner, Photolith spinners, Oxford 81 ion etcher, Reynolds Tech KOH Hood, Heidelberg DWL2000, MRL E4 LPCVD CMOS Nitride

Abstract:

Measurement of nano-Newton forces produced by individual sarcomeres and isolated myofibrils is possible using custom silicon-nitride cantilever pairs [1]. Advanced imaging techniques, including phase-contrast and immunofluorescent microscopy, allow for the correlation of visible physiological features with mechanical properties – at the level of the sarcomere. Recent advances in our lab have enabled, for the first time, fluorescent labelling of the giant spring-like protein titin without compromising mechanical properties of the sarcomere. Thus, the purpose of this study was to 1: identify the position of select antibody labels on titin during sarcomere elongation and 2: confirm if eccentric calcium-activation causes titin-actin binding, as has been widely suggested [2]. Using myofibrils isolated from rabbit psoas, we performed labelling of titin using N2A (anti-TTN-N2A, Myomedix, Germany) and F146.9 (anti-TTN-F146.9B9, Myomedix, Germany) primary antibodies followed by AlexaFluor488 (A32723 ThermoFischer Scientific, Illinois, United States) and AlexaFluor647 (A21449. A21244, ThermoFischer Scientific, Illinois, United States) secondary fluorophore conjugated antibodies. Chosen N2A and F146.9 primary antibodies flank titin's extensible PEVK segment, which is primarily responsible for titin elongation at physiological sarcomere lengths. Simultaneous measurement of the length of titin's PEVK segment during sarcomere elongation showed similar behavior to non-simultaneous previous experiments [3]. Post eccentric activation, measured PEVK segments were ~50nm longer than isometrically activated controls, suggesting increased force on titin caused by a proximal binding site. In all experiments tested, antibody labels had no effect on mechanical force production compared to protocol-matched unlabelled controls. In conclusion, for the first time, we labelled the sarcomeric protein titin without compromising mechanical function of the sarcomere. This novel labelling system allowed us to confirm both the behavior of titin's PEVK segment during sarcomeric extension and show evidence for titin-actin binding caused by eccentric activation.

Summary of Research:

Imaging of isolated myofibrils was performed using an inverted Olympus IX83 microscope, and analysis performed using CellSens® Dimensions software. Both phase contrast (PC) and fluorescent channels (AF488, AF647) were collected simultaneously, allowing for the identification of Z-lines (PC), M-lines (PC), TTN-N2A (AF488), and TTN-F146.9 (AF647) within myofibrils (Figure 1). Isolated myofibrils were attached to a glass needle and custom silicon nitride cantilever pairs. Stretching protocols were performed using the glass needle, moved using a piezoelectric motor. Force measurements were performed using optically measured

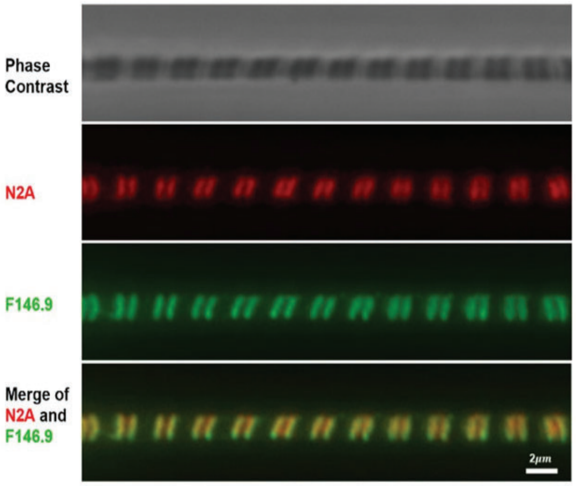

Figure 1: Isolated rabbit psoas myofibril visualized in phase contrast and fluorescent channels. Titin N2A labels are visualized in red (AlexaFluor647); Titin F146.9 labels are visualized in green (AlexaFluor 488). PEVK lengths were measured as the distance between Titin N2A and Titin F146.9 label centroids.

displacement of custom silicon-nitride cantilever pairs with known spring constants.

The introduction of titin labels (N2A and F146.9) did not compromise passive force production during passive sarcomere extension (Figure 2). Since titin is primarily, if not completely, responsible for the production of passive force during sarcomere extension, we concluded that our labelling system did not affect the mechanical behaviour of titin.

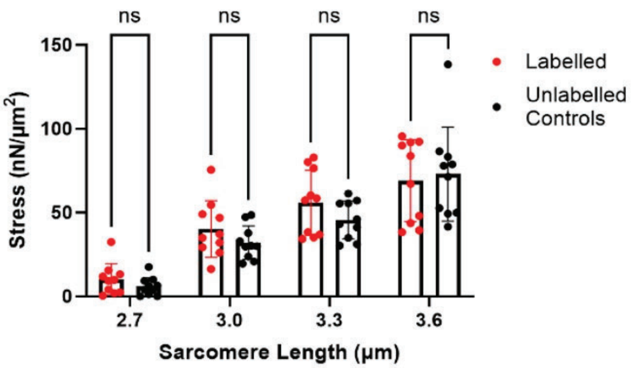

Figure 2: Passive stress production of Labelled myofibrils (n=10) is identical to unlabeled controls (n=10), (2-way ANOVA with Tukey's multiple comparisons test, ±SD)

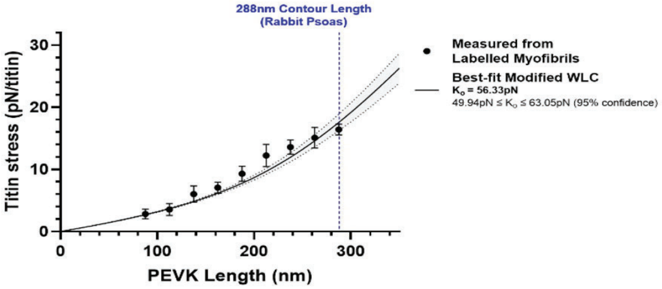

Figure 3: Stress-length relationship of titin's PEVK during passive extension. Data points are means of 25nm length bins, each containing ≥ 11 sarcomeres ± SEM. Data fit using a modified WLC model showing 95% confidence interval.

We captured the passive extension of titin's PEVK segment in labelled myofibrils (n=10, Figure 3). Extension of the PEVK segment was well modeled using the existent modified worm-like chain model for titin's PEVK region [3]. Thus, we found that in-situ extension of titin's PEVK, when titin is in its natural configuration inside a sarcomere, largely reproduces previously shown extension of isolated titin molecules.

It has been long theorized that titin-actin binding may occur during eccentric activation of muscle, thus leading to 'over-extension' of titin, and sustained increased force production termed residual force enhancement [2]. In 26 sarcomeres, from n=7 myofibrils, we measured the length of titin's PEVK post eccentric stretch. Titin's PEVK was significantly longer post-eccentric stretch compared to isometrically activated controls, thus providing strong evidence for titin-actin binding proximal to the PEVK region (Figure 4).

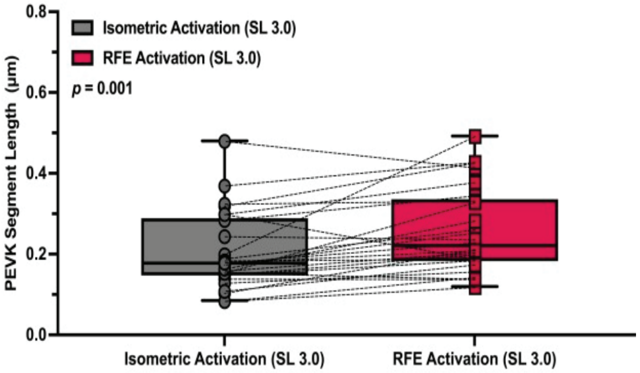

Figure 4: Titin's PEVK is significantly longer post-eccentric activation (RFE activation) compared to isometric controls (Isometric activation) (p =0.001, paired T-test).

Conclusions and Future Steps:

In conclusion, simultaneous measurement of forces produced by single sarcomeres and immunofluorescent imaging of titin allowed for the identification of in-situ behavior of the titin filament and showed strong evidence for titin-actin interactions during eccentric sarcomere activation. These findings support future advanced microscopy for subcellular biomechanics.

References:

[1] M. E. Fauver, et al. IEEE Trans Biomed Eng 45(7):891-898, 1998.

[2] Walter Herzog. J Exp Biol 15; 217(16): 2825–2833, 2014.

[3] W. Linke et al. PNAS 95(14): 8052-8057, 1998.

Identifying Sources of Per- and Polyfluoroalkyl Substances in Photolithography Wastewater

CNF Project Number: 2938-21
Principal Investigator(s): Damian Helbling
User(s): Vie Villafuerte

Affiliation(s): Civil and Environmental Engineering, Cornell University

Primary Source(s) of Research Funding: Semiconductor Research Corporation

Contact: deh262@cornell.edu, vav27@cornell.edu

Research Group Website: https://helbling.research.engineering.cornell.edu/

Primary CNF Tools Used: Suss Gamma Resist Cluster, ASML DUV Stepper, Oxford 100 ICP Dielectric, PlasmaTherm Versaline Deep Silicon Etch

Abstract:

Per- and polyfluoroalkyl substances (PFASs) are contaminants of concern to environmental and human health.1 Organofluorine-containing chemicals are widely used in semiconductor manufacturing processes such as lithographic patterning, etching, and stripping, among others; 2however, their release from specific fabrication processes is not well understood. While previous work focused on PFASs in wastewater and photolithography materials, putative sources such as plasma etching processes and scrubber blowdown have been underexplored. This study investigated PFAS formation during plasma etching of silicon wafers using various fluorinated etch gases. We performed nine plasma etch experiments and collected aqueous blowdown samples from a plasma-wet scrubber connected to two plasma etch tools. The samples were analyzed for total fluorine (TF), adsorbable organic fluorine (AOF), and 24 target PFASs. The goal of this project was to demonstrate if plasma etching processes are a significant source of PFASs and other organofluorine compounds in semiconductor fabrication facilities (fabs) emissions.

Summary of Research:

A variety of PFASs and other organofluorine-containing compounds are used during semiconductor manufacturing, 2and emissions of PFASs from fabs are of emerging concern. While most previous studies have focused on PFASs in fab wastewater samples or specific materials used during photolithography,[3,4]other potential PFAS sources, such as plasma etching processes and air scrubber blowdown, remain underexplored.

Fluorine inputs to plasma etch processes include both organofluorine-containing materials coated on the wafers (e.g., photoresists) and fluorinated gases. Hydrofluorocarbons (HFCs) and perfluorocarbons (PFCs), commonly used for silicon wafer etching, introduce fluorine into the system. The exhaust gas from these processes is treated with wet scrubbers, where PFASs can partition into aqueous scrubber blowdown. We hypothesize that fluorine-containing gases used in plasma etch processes generate fluorine radicals that react with organic chemicals deposited on the wafer surface to form PFASs, which are then released in the exhaust, likely a key source of PFASs measured in fab effluent.

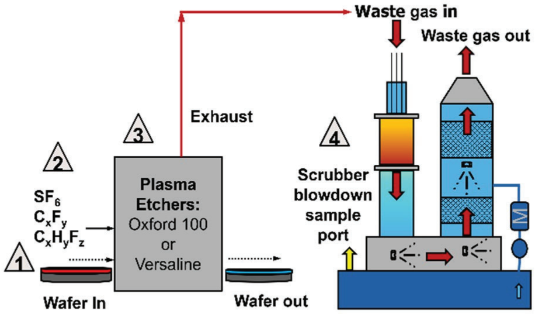

Figure 1: Schematic of the plasma etching and scrubbing process. The resulting exhaust from a plasma etch is routed to a scrubber system. Scrubber blowdown is collected for PFAS analysis.

We designed experiments to (1) demonstrate the formation of PFASs during plasma etching and transport to aqueous scrubber blowdown; and (2) identify the specific process conditions influencing PFAS formation. Four key process variables were investigated: (1) photoresist type, (2) choice of fluorinated etch gas, (3) plasma etching tool, and (4) use of plasma-enabled vs. non-plasma scrubber (Figure 1). We coated 4-inch silicon wafers with 500 nm of UV™ 210 Positive DUV photoresist using the Gamma Photoresist Cluster. The ASML DUV Wafer Stepper was used for edge-bead removal. Etching experiments used six fluorinated gases including CH_2F_2, CHF_3, C_4F_8, C_4F_6, SF_6, and $C_3H_2F_4$ (a low global warming potential alternative gas that demonstrated to meet semiconductor manufacturing performance objectives). [5]The etching experiments were conducted on both bare silicon and photoresist-coated wafers in each etching tool: the PlasmaTherm Versaline Deep Silicon Etch, which uses the Bosch process, and the Oxford 100 ICP Dielectric tool, with each listed gas. Finally, duplicate blowdown samples were collected immediately after the completion of each etching experiment from the GST Durian "plasma-wet" scrubber with the plasma feature deactivated, to isolate PFAS contributions of the etching process alone. The plasma scrubber feature was activated only during the first Versaline experiment. Additionally, duplicate baseline samples were collected from the scrubber water tank before any etching to account for background PFAS concentrations.

We analyzed the scrubber blowdown and baseline samples for TF, AOF, and 24 target PFASs. The baseline-corrected TF concentrations ranged from below the limit of quantification (<LOQ) to 506 mg/L, while the AOF concentrations from 0.3 to 91 µg F/L. Summed concentrations of target PFASs ranged from 0.02 to 3.4 µg/L for the baseline samples and from 0.2 to 12.8 µg/L in the post-etching samples (Figure 2). Perfluorocarboxylic acids (PFCAs), a PFAS class of regulatory concern, dominated the target PFAS profiles in all etching-related scrubber samples, comprising over 94% of the total target PFASs. Target PFASs accounted for 8-32% of the total AOF in the samples, suggesting the presence of additional unidentified organofluorine compounds (Table 1). These findings highlight the role of plasma etching processes as a source of organofluorine compound in fab emissions.

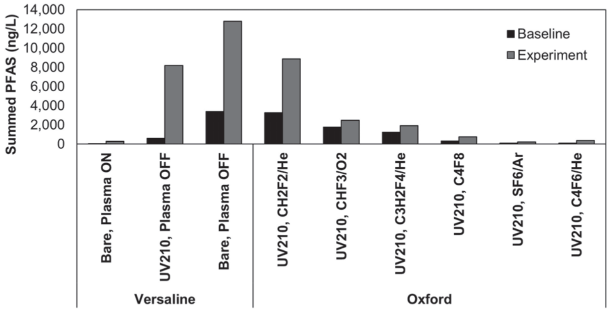

Figure 2: Summed PFAS concentrations for each etching experiment. "Baseline" refers to the sample before etching and "experiment" to the samples collected after etching experiments.

Sample Name	Etcher	PR, Plasma, Gas	AOF (µgF/L)	ΣPFAS (µgF/L)	ΣF in target PFAS (µg F-/L)	% Unexplained	% Explained
3a	Versaline	Bare, Plasma ON	<LOQ	0.27	0.18		
7a		UV210, Plasma OFF	61.97	7.57	5.17	92%	8%
9a		Bare, Plasma OFF	91.07	90.93	9.44	90%	10%
11a	Oxford	UV210, CH2F2/He	13.74	5.62	3.86	72%	28%
13a		UV210, CHF3/O2	2.19	0.70	0.48	78%	22%
16a		UV210, C3H2F4/He	1.79	0.70	0.47	74%	26%
18a		UV210, C4F8	1.32	0.44	0.29	78%	22%
20a		UV210, SF6/Ar	0.27	0.13	0.09	68%	32%
22a		UV210, C4F6/He	1.96	0.29	0.20	90%	10%

Table 1: Summary results for AOF and target PFASs in scrubber blowdown samples from the CNF.

Conclusions and Future Steps:

We conclude that (1) PFASs are formed during plasma etching processes and are captured in the scrubber blowdown from exhaust gases; and (2) target PFASs quantified in these samples can only explain up to 32% of the total AOF. Future steps will focus on: (1) conducting nontarget PFAS analysis in an effort to identify other PFASs that explain the remaining portion of the total AOF; (2) determining a more stable baseline between etching experiments; (3) conducting more etching experiments while modifying process variables such as testing other photoresist formulations and utilizing the new Oxford Cobra etcher.

References:

[1] Wang, Z.; DeWitt, J. C.; Higgins, C. P.; Cousins, I. T. A Never-Ending Story of Per- and Polyfluoroalkyl Substances (PFASs)? Environ Sci Technol 2017, 51 (5), 2508–2518. https://doi.org/10.1021/acs.est.6b04806.

[2] Ober, C. K.; Käfer, F.; Deng, J. Review of Essential Use of Fluorochemicals in Lithographic Patterning and Semiconductor Processing. Journal of Micro/Nanopatterning, Materials, and Metrology 2022, 21 (01). https://doi.org/10.1117/1.JMM.21.1.010901.

[3] Jacob, P.; Barzen-Hanson, K. A.; Helbling, D. E. Target and Nontarget Analysis of Per- and Polyfluoralkyl Substances in Wastewater from Electronics Fabrication Facilities. Environmental Science & Technology 2021, 55 (4), 2346–2356. https://doi.org/10.1021/acs.est.0c06690.

[4] Jacob, P.; Helbling, D. E. Exploring the Evolution of Organofluorine-Containing Compounds during Simulated Photolithography Experiments. Environmental Science & Technology 2023, 57 (34), 12819–12828. https://doi.org/10.1021/acs.est.3c03410.

[5] Windsor, A. J.; Clark, J. C.; McMurdy, G.; Joseph, E. A.; Syvret, R. G.; Olson, R. J.; Cha, J. J. Viability of HFO-1234ze(E) (Trans -1,3,3,3-Tetrafluoropropene) as a Low Global Warming Potential Silicon Dioxide Etch Gas. Journal of Vacuum Science & Technology B 2025, 43 (2). https://doi.org/10.1116/6.0004194.

New High Resolution Resists for EUV Lithography

CNF Project Number: 3137-23
Principal Investigator(s): Christopher Kemper Ober
User(s): Dr. Madan Rajendra Biradar, Dr. Gokhan Sagdic

Affiliation(s): Department of Materials Science and Engineering, Cornell University

Primary Source(s) of Research Funding: DuPont and SK hynix Inc.

Contact: cko3@cornell.edu, mrb348@cornell.edu, gs767@cornell.edu
Research Group Website: https://ober.mse.cornell.edu/index.html

Primary CNF Tools Used: ASML PAS 5500/300C DUV Wafer Stepper, JEOL 6300 E-Beam Lithography, P10 Profilometer, Optical Microscope, Veeco Icon Atomic Force Microscope

Abstract:

The semiconductor industry relies heavily on photoresists for fabricating advanced chips. With the growing need for higher resolution and pattern fidelity, EUV lithography presents unique challenges due to the limited number of EUV photons. This necessitates the use of highly sensitive resists such as chemically amplified resists (CAR) and novel double amplification resists (DAR). In DAR systems, ionizing radiation activates photoacid generators (PAGs), which produce acids that depolymerize the polymer backbone into monomers. Each acid can trigger multiple depolymerization events, enabling a double amplification effect. Due to their higher sensitivity of DAR resists compared to CAR, DAR systems require precisely tuned PAGs to control depolymerization kinetics. To address this, we designed and synthesized non-ionic PAGs to be utilized with DAR resists. This report details the design and synthesis of these PAGs and demonstrates their performance with Br-PPA polymer using DUV lithography. The resulting patterns were characterized by AFM microscopy.

Summary of Research:

To fabricate high-performance integrated circuits, the semiconductor industry relies heavily on chemically amplified resists (CARs), which typically comprise a polymer resin, a photoacid generator (PAG), a quencher, and various additives. [1]Most commercial CAR formulations use ionic PAGs because of their high sensitivity and efficient acid generation.[2-3]However, to meet the evolving demands for finer resolution and greater pattern fidelity, there is a growing need to develop next-generation high-performance resist systems. Polyphthalaldehyde (PPA) based resists belong to the class of double amplification resists (DARs), having self-immolative nature.[4-5]Upon acid activation, the polymer undergoes complete depolymerization into monomers, enabling sharp pattern formation and providing an efficient amplification mechanism, as illustrated in Figure 1. However, the higher sensitivity of DAR systems demands the use of optimized PAGs. [6]Non-ionic PAGs have gained importance due to their improved solubility in organic solvents, superior thermal stability during pre- and post-exposure bake steps, and reduced dark loss. By advancing both Br-PPA polymers and non-ionic PAG formulations, it is possible to achieve significant improvements in the performance of next-generation EUV photoresists.

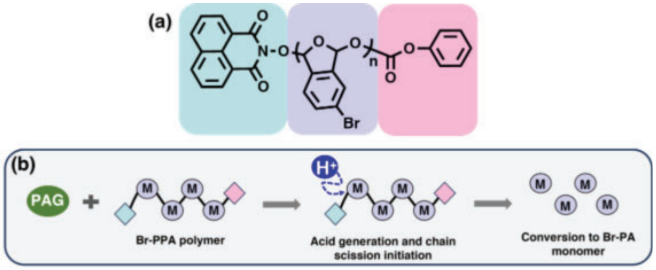

Figure 1: (a) Molecular design of Br-PPA polymer; (b) depolymerization mechanism of Br-PPA resist.

Results and Discussion:

Different functionalized non-ionic PAGs were designed using computational chemistry, synthesized, and characterized by ^{1}H and ^{13}C NMR spectroscopy. Br-PPA polymer was also synthesized and confirmed by ^{1}H NMR. Gel permeation chromatography was used to determine the molecular weight of polymer. A resist formulation, consisting the Br-PPA polymer and 20 wt% PAG in cyclohexanone, was spin-coated onto silicon wafers (2000 rpm, 60 s). These wafers were exposed to DUV radiation using an ASML PAS 5500/300C DUV wafer stepper. Further, pre- and post-exposure baking (90°C), followed by development in isopropyl alcohol (60 s) yielded line-space patterns, which were analysed by using atomic force microscopy as shown in Figure 2. The initial testing of a non-ionic PAG and Br-PPA as DAR resist yielded promising results, demonstrating

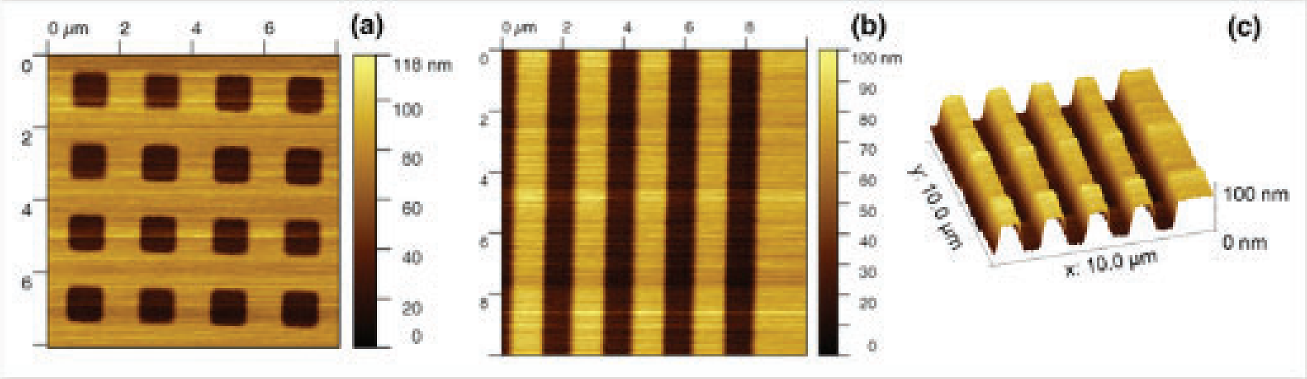

Figure 2: AFM images of 1 µm x 1 µm square hole pattern for DAR resist (a); 1 µm line patterns for DAR resist (b); (c) 3D height image of (b).

the fabrication of 1 µm × 1 µm square hole and line patterns.

Conclusions and Future Steps:

In this work, we developed a series of non-ionic PAGs incorporating various functional groups to evaluate their acid generation efficiency, sensitivity, and acid diffusion behavior, which are key factors affecting overall resist performance. DUV lithography experiments were conducted to evaluate the patterning performance of the DAR resists, and characterized by using AFM and SEM imaging. Further optimization studies, along with E-beam and EUV lithography evaluations, are currently in progress.

References:

[1] Cen, J.; Deng, Z.; Liu, S. Emerging Trends in the Chemistry of Polymeric Resists for Extreme Ultraviolet Lithography. Polym. Chem., 2024, 15 (45), 4599–4614. https://doi.org/10.1039/d4py00957f.

[2] Crivello, J. V. Cationic Polymerization — Iodonium and Sulfonium Salt Photoinitiators. Advances in Polymer Science, 1–48. https://doi.org/10.1007/bfb0024034.

[3] Komoto, K. Photopolymerization of Vinyl Ether by Hydroxy- and Methylthio-Alkylphosphonium Salts as Novel Photocationic Initiators. Polymer, 1994, 35 (1), 217–218. https://doi.org/10.1016/0032-3861(94)90077-9.

[4] Snyder, R.; Baranowsky, P.; Flajslik, K.; Kang, D.; Li, M.; Litchfield, B.; Yamada, S.; Zhang, W.; Oh, K. H.; Ban, C.; et al. Next-Generation EUV Photoresists-Based on Chain-Unzipping Polymers. Advances in Patterning Materials and Processes XLII, 2025, 5. https://doi.org/10.1117/12.3050849.

[5] Deng, J.; Bailey, S.; Jiang, S.; Ober, C. K. Modular Synthesis of Phthalaldehyde Derivatives Enabling Access to Photoacid Generator-Bound Self-Immolative Polymer Resists with Next-Generation Photolithographic Properties. J. Am. Chem. Soc., 2022, 144 (42), 19508–19520. https://doi.org/10.1021/jacs.2c08202.

[6] Biradar, M. R.; Oh, K. H.; Ban, C.; Kim, J. H.; Snyder, R.; Li, M.; Hernandez, K.; Kiliclar, H. C.; Sagdic, G.; Ober, C. K. Non-Ionic Photo-Acid Generators for next-Generation EUV Photoresists. Advances in Patterning Materials and Processes XLII, 2025, 73. https://doi.org/10.1117/12.3050818.

Isotropic Plasma ALE of Nitride Semiconductors

CNF Project Number: 280019
Principal Investigator(s): Huili Grace Xing
User(s): Rafael Panagiotopoulos

Affiliation(s): Department of Materials Science and Engineering
Primary Source(s) of Research Funding: SUPREME
Contact: grace.xing@cornell.edu
website: https://jena-xing.engineering.cornell.edu/
Primary CNF Tools Used: Takachi ALE

Abstract:

This study demonstrates the successful atomic layer etching of aluminum nitride and gallium nitride using sequential exposures to SF_6 plasma for surface fluorination, followed by Cl_2/BCl_3 plasma to remove the altered layer at 100 °C. We investigated the etch rates, the self-limiting behavior of the reactions, and their combined effect, aiming to better understand the underlying etching mechanism. A range of analytical tools was employed, including in-situ spectroscopic ellipsometry, X-ray photoelectron spectroscopy (XPS), and atomic force microscopy (AFM).

Summary of Research:

Gallium nitride (GaN) and aluminum nitride (AlN), both belonging to the III–V semiconductor group, play a pivotal role in modern electronic and photonic technologies. Their wide bandgaps, strong thermal stability, and intrinsic piezoelectric properties make them particularly suitable for fabricating high electron mobility transistors (HEMTs), which are commonly used in radio-frequency (RF) and power electronics applications[1–3]. Additionally, due to their outstanding optical characteristics, GaN and AlN are also emerging as key materials for photonic integrated circuits and light-emitting diodes (LEDs)[4,5].

As device architectures continue to evolve in complexity and scale, there is a growing demand for more sophisticated processing techniques. One such advancement is the development of enhancement-mode (E-mode) HEMTs, which are especially desirable for applications such as power conversion and industrial power systems[6,7]. The fabrication of efficient and robust E-mode HEMTs often requires the formation of recess gate structures[8,9]. However, traditional dry etching methods have notable limitations, often inducing damage to the surface and the two-dimensional electron gas (2DEG), which negatively impacts device performance[10]. To address these challenges in next-generation devices, atomic layer etching (ALE) has emerged as a promising alternative to conventional etching techniques[11],[12].

ALE operates on the principle of dividing the etching process into a series of self-limiting, sequential steps. This separation allows for precise control over the formation and transport of reactive species, enabling improved process uniformity and avoiding the surface damage typically associated with reactive ion etching. The ALE cycle generally comprises two distinct phases: a surface modification step that lowers the material's surface binding energy, followed by a removal step[13],[14].

Utilizing SF6 plasma for surface modification and Cl_2/BCl_3 plasma for removal, we achieved etch rates of 4.4 Å/cycle and 5.7 Å/cycle for AlN and GaN respectively, which correspond approximately to one unit cell per cycle. Etch rates were monitored with in situ ellipsometry as seen in Figure 1. This approach displayed very controlled results, as well as self-limiting behavior when the duration of the removal step was changed, demonstrated in Figure 2. In order to prove that the ALE recipe obeys the fluorination and ligand exchange mechanism similar to thermal ALE, XPS spectra were utilized at different points of the cycle. During surface modification, a significant Al-F peak emerges, indicating the formation of AlF3. During removal, the peak reduces in intensity, indicating the formation of volatile AlCl3. The spectra are displayed in Figure 3. This ALE approach also achieves surface planarization, leading to a 21% roughness reduction as seen in Figure 4 for AlN.

References:

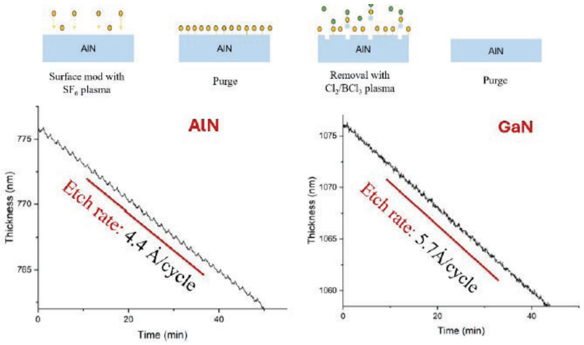

Figure 1: ALE cycle and etch rates for AlN and GaN

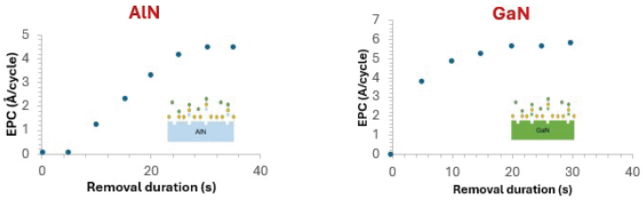

Figure 2: Removal step saturation curves for AlN and GaN displaying self-limiting behavior

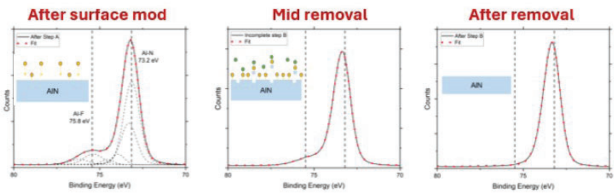

Figure 3: XPS spectra demonstrating fluorination and ligand exchange mechanism

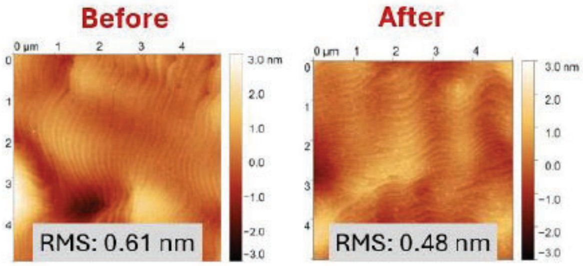

Figure 4: Surface morphology before and after etching for AlN

1 U. Mishra, P. Parikh, and Y.-F. Wu, “Algan/gan hemts-an overview of device operation and applications,” Proceedings of the IEEE 90, 1022–1031 (2002).

2 E. A. Jones, F. F. Wang, and D. Costinett, “Review of commercial gan power devices and gan-based converter design challenges,” IEEE Journal of Emerging and Selected Topics in Power Electronics 4, 707–719 (2016).

3 A. L. Hickman, R. Chaudhuri, S. J. Bader, K. Nomoto, L. Li, J. C. M. Hwang, H. Grace Xing, and D. Jena, “Next generation electronics on the ultrawide-bandgap aluminum nitride platform,” Semiconductor Science and Technology 36, 044001 (2021).

4S . Nakamura and M. R. Krames, “History of gallium–nitride-based light-emitting diodes for illumination,” Proceedings of the IEEE 101, 2211–2220 (2013).

5 C. Xiong, W. H. P. Pernice, X. Sun, C. Schuck, K. Y. Fong, and H. X. Tang, “Aluminum nitride as a new material for chip-scale optomechanics and nonlinear optics,” New Journal of Physics 14 (2012).

6 T. Imada, M. Kanamura, and T. Kikkawa, “Enhancement-mode gan mis-hemts for power supplies,” in The 2010 International Power Electronics Conference - ECCE ASIA - (2010) pp. 1027–1033.

7 H. W. Then, M. Radosavljevic, Q. Yu, A. Latorre-Rey, H. Vora, S. Bader, I. Momson, D. Thomson, M. Beumer, P. Koirala, J. Peck, A. Oni, T. Hoff, R. Jordan, T. Michaelos, N. Nair, P. Nordeen, A. Vyatskikh, I. Ban, A. Zubair, S. Rami, and P. Fischer, “Enhancement-mode

3 00-mm gan-on-si(111) with integrated si cmos for future mm-wave rf applications,” IEEE Microwave and Wireless Technology Letters 33, 835–838 (2023).

8 H. Lee, H. Ryu, J. Kang, and W. Zhu, “High temperature operation of e-mode and d- mode algan/gan mis-hemts with recessed gates,” IEEE Journal of the Electron Devices Society 11, 167–173 (2023).

9 T.-H. Hung, P. S. Park, S. Krishnamoorthy, D. N. Nath, and S. Rajan, “Interface charge engineering for enhancement-mode gan mishemts,” IEEE Electron Device Letters 35, 312–314 (2014).

10 T. Palacios, C.-S. Suh, A. Chakraborty, S. Keller, S. DenBaars, and U. Mishra, “High- performance e-mode algan/gan hemts,” IEEE Electron Device Letters 27, 428–430 (2006).

11 T.-Y. Yang, H.-Y. Huang, Y.-K. Liang, J.-S. Wu, M.-Y. Kuo, K.-P. Chang, H.-T. Hsu, and E.-Y. Chang, “A normally-off gan mis-hemt fabricated using atomic layer etching to improve device performance uniformity for high power applications,” IEEE Electron Device Letters 43, 1629–1632 (2022).

12 J. Guo, K. Wei, S. Zhang, X. He, Y. Zhang, R. Zhang, J. Wang, K. Wang, S. Huang, Y. Zheng, X. Wang, and X. Liu, “Low damage atomic layer etching technology for gate recessed fabrication,” Vacuum 217, 112591 (2023).

13 K. J. Kanarik, S. Tan, and R. A. Gottscho, “Atomic layer etching: Rethinking the art of etch,” The Journal of Physical Chemistry Letters 9, 4814–4821 (2018).

14 K. J. Kanarik, T. Lill, E. A. Hudson, S. Sriraman, S. Tan, J. Marks, V. Vahedi, and R. A. Gottscho, “Overview of atomic layer etching in the semiconductor industry,” Journal of Vacuum Science Technology A 33, 020802 (2015).

High Frequency Micro-Patterned Fe65Co35 Thin Film with Tunable FMR and Permeability for RF Passives

CNF Project Number: 286520
Principal Investigator(s): Amal El-Ghazaly
User(s): Haosen Yin

Affiliation(s): Electrical and Computer Engineering

Primary Source(s) of Research Funding: National Science Foundation

Contact: ase63@cornell.edu

website: https://vesl.ece.cornell.edu/

Primary CNF Tools Used: Microwave Small-Signal Probe Station and Electronics, Heidelberg MLA 150 Maskless Aligner, Keyence VHX-7100 Digital Microscope, SC4500 Odd-Hour Evaporator, AJA Sputter 3

Abstract:

This work presents a unique design method and optimization of high frequency magnetic patterns with controllable effective permeability and ferromagnetic resonance behavior for integrated microwave devices. Thin-film micro-patterned FeCo array with initial permeability of 42.7 has been fabricated to achieve a high FMR of 18.1 GHz. Independent control of magnetic properties of the pattern array has been realized by changing pattern spacing, showing a FMR tuning range of 2.20 GHz, with little change in effective permeability. Noise suppression and inductance enhancement at high frequencies (> 10 GHz) have been demonstrated for RF applications by integrating the proposed magnetic pattern array with coplanar waveguides (CPW). Our method shows a high degree of freedom and flexibility for designing high frequency integrated magnetic microwave components.

Summary of Research:

Fast growing demand of higher data rate, low latency, high quality of service in wireless communication systems calls for RF front-end devices that are frequency agile, miniaturized and multifunctional. Novel materials, structures and technologies have been explored to improve performance and bring new functionality for RF devices. Integrating high-performance novel magnetic materials into on-chip RF devices shows promising results in enhancing inductance, miniaturizing devices, suppressing interference and achieving non-reciprocity and tunability. Previous works have demonstrated the application of integrated magnetic materials in inductors, isolators, antennas, filters, and noise suppressors.

However, integrating magnetic materials for high frequency applications is particularly challenging. Limited by the relatively low ferromagnetic resonance (FMR) frequency, radio-frequency (RF) devices (e.g., on-chip inductors) integrated with common ferromagnetic materials consistently operate only at sub-GHz or up to a few GHz. While the FMR frequency can be increased by applying bias magnetic fields, this approach reduces the permeability of magnetic materials due to an intrinsic FMR-permeability tradeoff, therefore limiting the device performance. In addition, integrating large, localized bias magnetic fields with monolithic microwave circuits is highly impractical. Finally, the high loss of most ferromagnetic materials, especially near FMR frequency presents additional challenges for their device integration. Thus, novel magnetic materials with controllable high frequency characteristics are highly desired in microwave applications.

Previous work has shown promising results of improving FMR to a few GHz by patterning ferromagnetic thin films, yet no control of magnetic properties or design optimization of the magnetic pattern array has been proposed. In this work, we dramatically increase the FMR frequency of ferromagnetic patterns at zero field bias to 18.1 GHz, while maintaining a high broadband permeability of 42.7. An analytical model has been established to independently control and optimize the magnetic properties (ω_{FMR} and μ_r) of the patterned array by changing pattern spacing along two orthogonal axes. The proposed magnetic pattern array was integrated with CPWs to demonstrate its high frequency RF application for noise suppression and inductance enhancement. Our optimization approach allows for the facile design of integrated microwave magnetic components.

Conclusions and Future Steps:

In this work, we demonstrate design, tuning and optimization of patterned ferromagnetic thin film arrays for high frequency MMIC applications. The

FMR frequency of high permeability ferromagnetic patterns was increased to around 18 GHz (Ku band) for the first time. An analytical model was established, and a design method is proposed to independently tune the FMR, effective permeability of the magnet pattern array for optimal integrated device operation. The proposed pattern arrays were integrated with CPWs to experimentally demonstrate their RF applications as noise suppressors and inductors. Our method is highly versatile and provides a high degree of freedom for designing high frequency tunable magnetic properties for integrated microwave systems. In the future, we will implement a magnetic fully integrated inductor that works that high frequencies, and achieve tunability via magnetoelectric coupling.

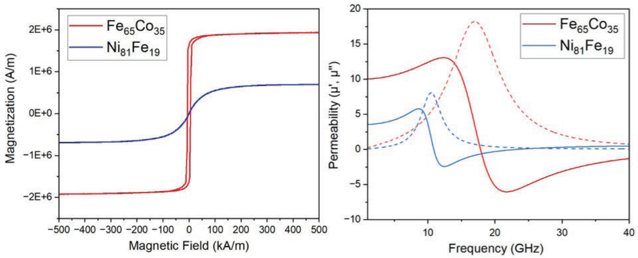

Fig. 1. Magnetic characterization M-H loops (left) of Fe65Co35 compared with Ni81Fe19 and frequency dependent permeability (right) calculated from the Landau-Lifshitz-Gilbert (LLG) model. The solid line and dash line represent the real part and imaginary part, respectively.

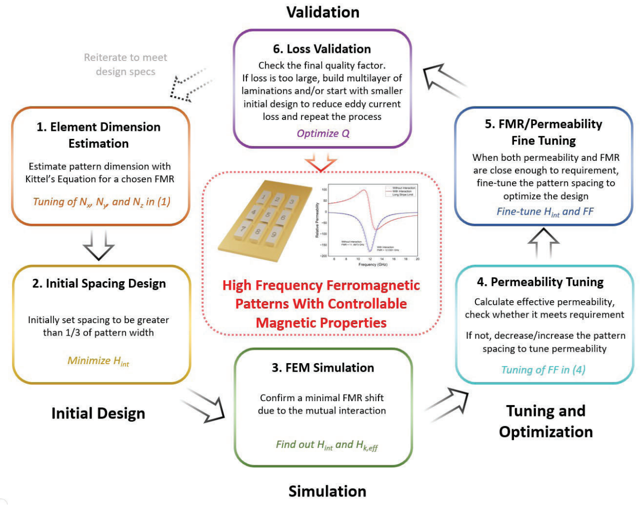

Fig. 2. Design flowchart for high frequency ferromagnetic patterns with controllable magnetic properties.

References:

[1] A. El-Ghazaly, R. M. White, and S. X. Wang, "Gigahertz-Band Integrated Magnetic Inductors," IEEE Trans Microw Theory Tech, vol. 65, no. 12, pp. 4893–4900, 2017, doi: 10.1109/TMTT.2017.2728040.

[2] M. Yamaguchi et al., "Performance of integrated magnetic thin film noise suppressor applied to CMOS noise test chips," in 2011 41st European Microwave Conference, 2011, pp. 49–52. doi: 10.23919/EuMC.2011.6101991.

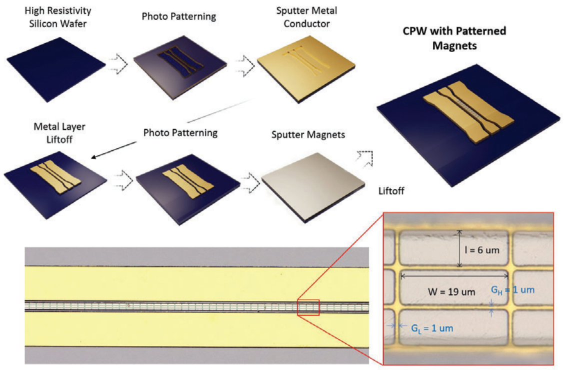

Fig. 3. Fabrication process and microscopic image of the Fe65Co35 magnet patterned CPW.

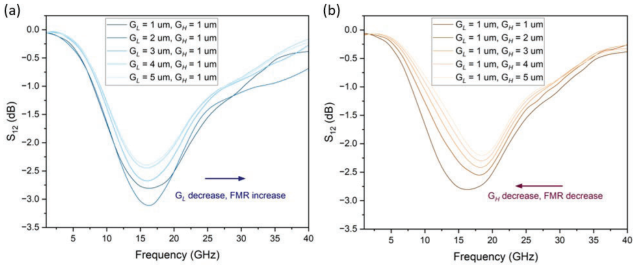

Fig. 4. Measured S12 parameters of noise suppressors when changing gaps of magnets along the (a) longitudinal (b) horizontal direction.

[3] Y. Zhang et al., "Nonreciprocal Isolating Bandpass Filter With Enhanced Isolation Using Metallized Ferrite," IEEE Trans Microw Theory Tech, vol. 68, no. 12, pp. 5307–5316, 2020, doi: 10.1109/TMTT.2020.3030784.

[4] Y. He et al., "Integrated Tunable Bandstop Filter Using Self-Biased FeGaB/Al2O3 Multilayer Thin Film," IEEE Trans Magn, vol. 54, no. 9, pp. 1–4, 2018, doi: 10.1109/TMAG.2018.2851579.

[5] H. Chen et al., "Integrated Tunable Magnetoelectric RF Inductors," IEEE Trans Microw Theory Tech, vol. 68, no. 3, pp. 951–963, 2020, doi: 10.1109/TMTT.2019.2957472.

[6] D. S. Gardner, G. Schrom, F. Paillet, B. Jamieson, T. Karnik, and S. Borkar, "Review of On-Chip Inductor Structures With Magnetic Films," IEEE Trans Magn, vol. 45, no. 10, pp. 4760–4766, 2009, doi: 10.1109/TMAG.2009.2030590.

[7] T. Wang et al., "Integrating Nanopatterned Ferromagnetic and Ferroelectric Thin Films for Electrically Tunable RF Applications," IEEE Trans Microw Theory Tech, vol. 65, no. 2, pp. 504–512, 2017, doi: 10.1109/TMTT.2016.2616869.

[8] J. A. Osborn, "Demagnetizing Factors of the General Ellipsoid," Physical Review, vol. 67, no. 11–12, pp. 351–357, Jun. 1945, doi: 10.1103/PhysRev.67.351.

[9] W. R. Eisenstadt and Y. Eo, "S-parameter-based IC interconnect transmission line characterization," IEEE Transactions on Components, Hybrids, and Manufacturing Technology, vol. 15, no. 4, pp. 483–490, 1992, doi: 10.1109/33.159877.

Supramolecular Control of Ionic Retention in Hybrid Bilayer Synaptic Transistors

CNF Project Number: 306423
Principal Investigator(s): Yu Zhong
User(s): Haolei Zhou, Kaushik Chivukula, Qiyi Fang

Affiliation(s): Department of Materials Science and Engineering, Cornell University,

Primary Source(s) of Research Funding: Cornell Startup Account

Contact: yz2833@cornell.edu

Website: https://zhong.mse.cornell.edu

Primary CNF Tools Used: ABM Contact Aligner, SC4500 Odd/Even-Hour Evaporator

Abstract:

The rise of big data and AI has exposed von Neumann architecture's limitations, spurring interest in computing paradigms that merge memory and processing. Artificial synapses, especially those based on electrolyte-gated transistors (EGTs) with ion-trapping layers, offer low voltage operation, robustness, and tunable retention. However, the molecular basis of ionic retention in these devices remains poorly understood.

Summary of Research:

Here, we report a supramolecular strategy to elucidate the molecular origin of ion retention in electrolyte-gated synaptic transistors. We designed a bilayer device comprising monolayer molybdenum disulfide (MoS_2) as the semiconducting channel and a polymeric ion-trapping layer incorporating dibenzo-18-crown-6 (DC), a cyclic host molecule known for its strong and size-selective binding to alkali metal ions (Fig. 1).1-2 Although crown ethers and their derivatives have been widely studied in ion recognition and transport, their potential to modulate ion retention dynamics in EGTs has been rarely explored.3-7 We fabricated the bilayer device using the following steps: To fabricate pre-patterned substrates, a 2-stage photolithography/e-beam deposition step was carried out on a 1 inch x 1 inch Si/SiO_2 piece to deposit source/drain electrodes and an SiO_2 insulating layer. Following this, we sequentially transfer a monolayer MoS_2 layer and DC-based thin film, thus yielding the final bilayer EGT device.

We show that ion retention in the DC layer is governed kinetically by ion concentration (Fig. 3) and thermodynamically by the competition between ion–host binding and ion solvation (Fig. 4), which can be tuned by solvent polarity. In particular, we demonstrate that the dielectric constant of the electrolyte plays a critical role in modulating the retention time, ranging from rapid ion relaxation to effectively permanent trapping within the crown ether layers. Experimental measurements and density functional theory (DFT) calculations reveal that these parameters reshape the free energy landscape of ion-DC binding versus solvation, thereby tuning the effective k1/k-1 ratio and controlling the rate of ion release. By selecting intermediate solvent conditions, we achieve memory retention dynamics suitable for emulating key short-term and long-term synaptic functions (Fig. 5).

Conclusions and Future Steps:

In conclusion, we constructed a bilayer EGT with a polymeric ion trapping layer to elucidate the molecular origin of ionic retention in such devices. Ion concentration and solvent polarity emerged as critical factors governing the kinetic and thermodynamic control of ionic retention. In particular, the solvent's dielectric constant played a pivotal role in modulating the balance between ion binding to crown ether units and ion solvation, leading to behaviors ranging from effectively permanent trapping to rapid ion relaxation. Intermediate solvent conditions allowed for the emulation of key short-term and long-term plasticity functions, thereby demonstrating a proof-of-concept neuromorphic device. These results highlight key strategies for controlling ion relaxation dynamics, providing valuable insights for the design of ionic–electronic artificial synapses.

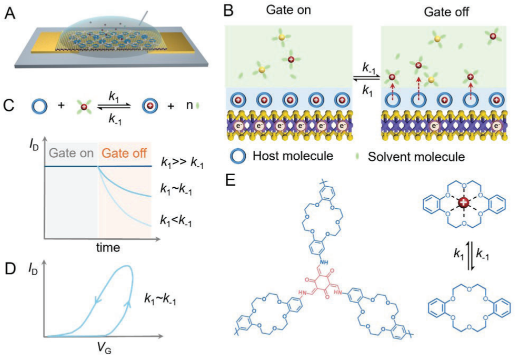

Figure 1: Working mechanism of the hybrid bilayer electrolyte-gated transistor.(A) Schematic of the bilayer transistor.(B) Illustration of ion capture/release in DCP film driven by gate-voltage.(C) A simplified schematic illustrating ion capture/release reaction rates (top), and the effect of these reaction rates on the dynamics of source-drain current (ID) (bottom). (D) Transfer characteristics of the bilayer transistor with comparable ion capture and release rates. (E) Structure of the ion trapping layer functionalized with 18-crown-6 building unit (left), and ion trapping/release reactions with crown ether units

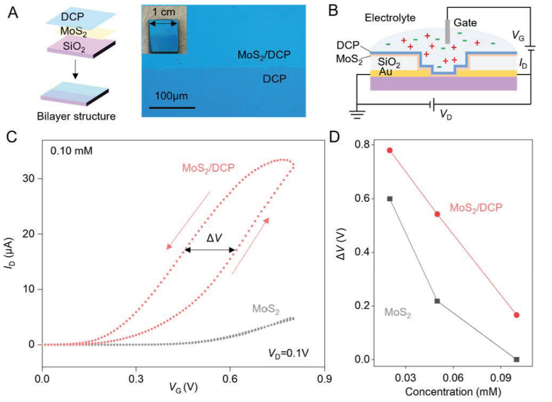

Figure 2: Electrical characterization of the hybrid bilayer electrolyte-gated transistor. (A) Schematic illustration of the stacking of bilayer structure (left) and optical image of the MoS2/DCP bilayer (right). Inset: Photo of the bilayer structure. (B) Schematic of the electrical characterization setup. (C) Transfer characteristics of the MoS2/DCP and MoS2 based transistors. (D) Hysteresis as a function of electrolyte concentration.

References:

(1) Steed, J. W. First- and Second-Sphere Coordination Chemistry of Alkali Metal Crown Ether Complexes. Coord. Chem. Rev. 2001, 215 (1), 171–221. https://doi.org/10.1016/S0010-8545(01)00317-4.

(2) Liou, C.-C.; Brodbelt, J. S. Determination of Orders of Relative Alkali Metal Ion Affinities of Crown Ethers and Acyclic Analogs by the Kinetic Method. J. Am. Soc. Mass Spectrom. 1992, 3 (5), 543–548. https://doi.org/10.1016/1044-0305(92)85031-E.

(3) Chiriac, A.-P.; Damaceanu, M.-D. A Novel Approach towards Crown-Ether Modified Polyimides with Affinity for Alkali Metal Ions Recognition. J. Mol. Liq. 2021, 322, 114929. https://doi.org/10.1016/j.molliq.2020.114929.

(4) Wang, J.; Jiang, N.; Wang, L.; Wang, D.; Chen, X.; Huang, D.; Wang, L. Selective Ion Transport in Two-Dimensional Ti3C2Tx Nanochannel Decorated by Crown Ether. Langmuir 2023, 39 (20), 7167–7174. https://doi.org/10.1021/acs.langmuir.3c00631.

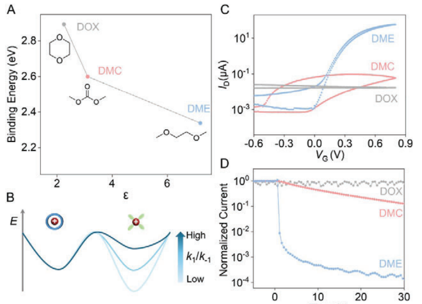

Figure 3: The effect of solvent in determining ion capture/ release dynamics. (A)Ion-host binding energy as a function of the solvent's dielectric constant. (B) Energy diagram of the ion-interaction between host molecules and solvate molecules as a function of trapping dynamics. Effect of solvent on (C) the transfer characteristics of the bilayer transistor, and (D) Ion-retention dynamics measured in terms of normalized source-drain current after gate voltage application

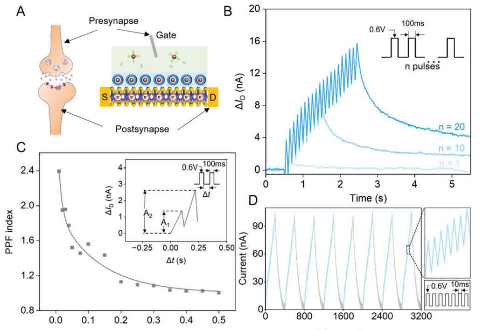

Figure 4: Emulation of short-term and long-term synaptic functions in the bilayer transistor. (A) Schematic illustration of the analogy between a biological neuron and the bilayer transistor (B) Short-term to long-term memory transition induced by the application of many gate pulses. (C) Paired pulse facilitation showing the relative magnitude of current increment as a function of the time-interval between two consecutive gate pulses. (D) Long-term potentiation and depression achieved by the application of a train of gate pulses.

(5) Sun, Z.; Barboiu, M.; Legrand, Y.-M.; Petit, E.; Rotaru, A. Highly Selective Artificial Cholesteryl Crown Ether K+-Channels. Angew. Chem. Int. Ed. 2015, 54 (48), 14473–14477. https://doi.org/10.1002/anie.201506430.

(6) Warnock, S. J.; Sujanani, R.; Zofchak, E. S.; Zhao, S.; Dilenschneider, T. J.; Hanson, K. G.; Mukherjee, S.; Ganesan, V.; Freeman, B. D.; Abu-Omar, M. M.; Bates, C. M. Engineering Li/Na Selectivity in 12-Crown-4–Functionalized Polymer Membranes. Proc. Natl. Acad. Sci. 2021, 118 (37), e2022197118. https://doi.org/10.1073/pnas.2022197118.

(7) Wang, B.; Li, R.; Cui, Z.; Wang, Z.; Fu, W.; Yan, J.; Jiang, C.; Wu, L.; Xu, T.; Wang, Y. Facile Design of a Crown Ether-Functionalized Polymeric Membrane for Highly Efficient Lithium and Magnesium Separation during Electrodialysis. Chem. Eng. Sci. 2025, 302, 120865. https://doi.org/10.1016/j.ces.2024.120865.

Imaging Radiation Detectors for Synchrotron X-Ray Sources and Electron Microscopes

CNF Project Number: 306523
Principal Investigator(s): Julia Thom-Levy
User(s): Sixuan Li, Nicholas Brown, Mark Tate

Affiliation(s): Cornell University, Laboratory of Atomic and Solid-State Physics

Primary Source(s) of Research Funding: United States Department of Energy

Contact: jt297@cornell.edu

Primary CNF Tools Used: Cadence Virtuoso

Abstract:

Advances in the brilliance of synchrotron x-ray sources and electron microscopes have outpaced the ability of radiation detectors to efficiently capture high-resolution diffraction data. This is especially true for ptychography, a promising method that allows detailed atomic structural determination of samples even for non-periodic samples. Ptychographic diffraction data are characterized by an enormous dynamic range, with low-angle scatter often millions of times more intense than high angle data; both low- and high-angle data are required for ptychographical reconstructions. In consequence, there is need for radiation detectors that can simultaneously capture quantitative images containing very intense low-angle scatter and quantum limited single x-ray or electron data at high angles. Ptychography requires the sequential acquisition of many diffraction patterns to make a full data set; hence, a very fast image frame rate is also required. The goal of our research is to explore detector integrated circuit structures that would allow the fabrication of imaging radiation detectors to meet these challenges.

Summary of Research:

The imaging detectors being explored are Pixel Array Detectors (PADs). PADs consist of a silicon diode sensor array bump-bonded pixel-by-pixel to a pixelated Application Specific Integrated Circuit (ASIC). Each pixel in sensor layer detects incident radiation and produces an electrical signal whose charge is proportional to the integrated x-ray energy. This is conveyed by microlithographic solder connection "bump" to electronics in the corresponding ASIC pixel for processing (Figure 1).

The approach being explored is to advance the charge-pump amplifier arrangement pioneered in our laboratory [1] to provide both sensitivity and dynamic range at higher frame rates than existing detectors. The integrating amplifier that receives the sensor signal must balance two conflicting requirements: It must have a high signal-to-noise ratio for unambiguous detection of single x-ray or electron quanta, thereby requiring a small feedback capacitor to provide high gain. At the same time a large dynamic range dictates use of a large feedback capacitor to integrate the signal from many quanta during an image exposure. The charge-pump circumvents these constraints by preventing the amplifier from reaching saturation. It does this via circuitry that constantly monitors the output of the amplifier. When the amplifier signal approaches saturation, corresponding to integration of many tens or hundreds of radiation quanta, a charge removal circuit is engaged that removes a fixed quantity of charge from the feedback amplifier capacitor and adds a bit to a digital counter. This process occurs without interrupting continued incident charge integration. At the end of the radiation exposure, the digital sum is scaled and added to the digitized value of any signal remaining on the feedback capacitor to provide the total integrated signal.

Research for the current project involved a cycle of redesign, simulation, fabrication, and testing to produce ASIC circuit structures with extended dynamic range, frame rate, and radiation hardness relative to prior designs.

Conclusions and Future Steps:

The next step is to combine the advanced circuits that were studied to produce a miniature detector to test actual radiation imaging performance. This will involve layout and fabrication of a 16x16 pixel test ASIC that will be bump-bonded to a sensor. It will also require the construction of accompanying external readout circuitry, cooling and vacuum housing and development of firmware to coordinate the many signals required to read out an image. This small prototype detector will then be tested for image acquisition performance with x-rays and in an electron microscope.

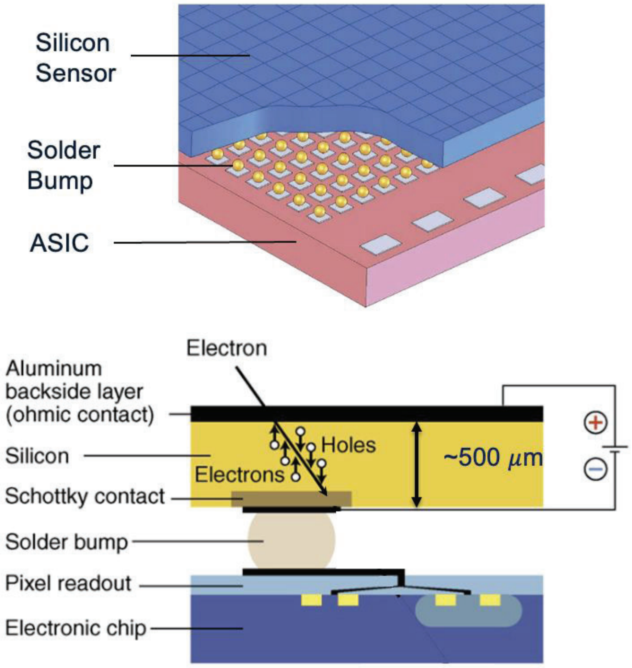

Figure 1: Simplified block diagram of a Pixel Array Detector

References:

[1] D. Schuette (2008). A mixed analog and digital pixel array detector for synchrotron x-ray imaging. PhD thesis, Dept. of Physics, Cornell University, Ithaca, NY 14853

SUPREME Tasks 6/7

CNF Project Number: 307823
Principal Investigator(s): James Hwang
User(s): Yunjiang Ding, Jin Hong Joo, Chunyi Li

Affiliation(s): Department of Materials Science and Engineering, Cornell University

Primary Source(s) of Research Funding: SRC/DARPA

Contact: jch263@cornell.edu

Primary CNF Tools Used: ABM Contact Aligner, SUSS MA6-BA6 Contact Aligner, Unaxis 770 Deep Silicon Etcher, AJA Ion Mill, AJA Sputter Deposition, Veeco Savannah ALD, Electroplating Hood – Au/Cu, P7 Profilometer, Zygo Optical Profilometer,HFTL DC Probe Station, HFTL Small-Signal Probe Station

Abstract:

For heterogeneous integration of millimeter-wave transceiver frontends, we compare the millimeter-wave loss of coplanar interconnects fabricated on Si interposers with different resistivities. Coplanar interconnects 2146-µm long are laid out on two types of Si substrates: HR Si (resistivity > 1 kΩ·cm, thickness = 155 µm) and doped Si (resistivity < 10 Ω·cm, thickness = 205 µm). Small-signal measurements from 1 GHz to 40 GHz indicate the advantages of high-resistivity (HR) Si interposers for heterogeneous integration of millimeter-wave circuits.

Summary of Research:

The width of the center electrode of the coplanar interconnect and its gap to the ground electrode are 30 µm and 16 µm, respectively, resulting in a characteristic impedance ≈ 50 Ω. The ground electrodes are grounded by a high density of through-silicon vias (TSVs) to suppress higher-order modes. To mitigate the residual stress from thermal expansion mismatch, TSVs are metallized with Al having an annular structure (Fig. 1) [1]. Front-side wafer fabrication comprises mainly sputtering of 20-nm Ti and 1.5-µm Al and patterning by liftoff. The most critical steps of backside fabrication involve etching and metallizing 50-µm-diameter TSVs. Using the Bosch process [2] with a 200-nm Al2O3 hard mask, the substrates are deep etched from the backside at an etch rate of 27 nm/s. TSV metallization is then carried out by depositing 50-nm Pt using atomic layer deposition [3], followed by 70-nm Ti and 2-µm Al using sputtering (Fig. 2) [4]. DC measurements confirm a TSV series resistance on the order of 1 Ω. Small-signal millimeter-wave on-wafer measurements (Fig. 3) show the coplanar interconnect fabricated on HR Si have an insertion loss of 0.7 dB/mm at 40 GHz (Fig. 4), an order of magnitude better than the same coplanar interconnect fabricated on doped Si. The return loss of the coplanar interconnect fabricated on HR Si is always greater than 20 dB between 1 and 40 GHz.

Conclusions and Future Steps:

The above result confirms that it is necessary to use HR Si (as opposed to doped Si) as an interposer for heterogeneous integration of millimeter-wave transceiver frontend. In the future, HR Si of different resistivities will be compared to determine the optimum resistivity level.

References:

[1] M. Leskela and M. Ritala, Thin Solid Films 409, 138 (2002).
[2] F. Laermer et al., IEEE Microelectromech. Syst. 211 (1999).
[3] X. Sun et al., IEEE Electron Packag. Technol. 76 (2011).
[4] S. M. Rossnagel, IBM J. Res. Dev. 43, 163 (1999).

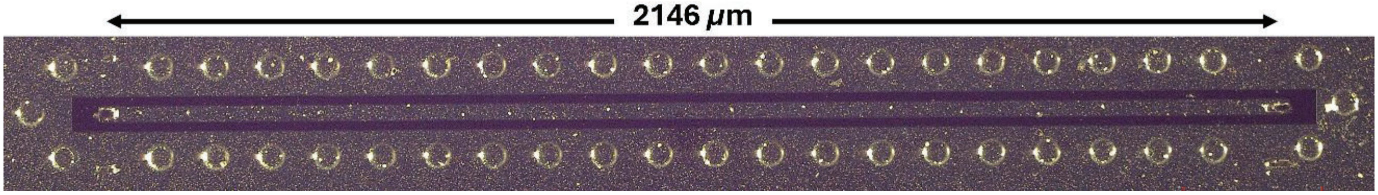

Fig. 1. Micrograph showing a 2146-µm-long grounded coplanar interconnect within two parallel rows of TSVs to prevent higher-order modes from propagating.

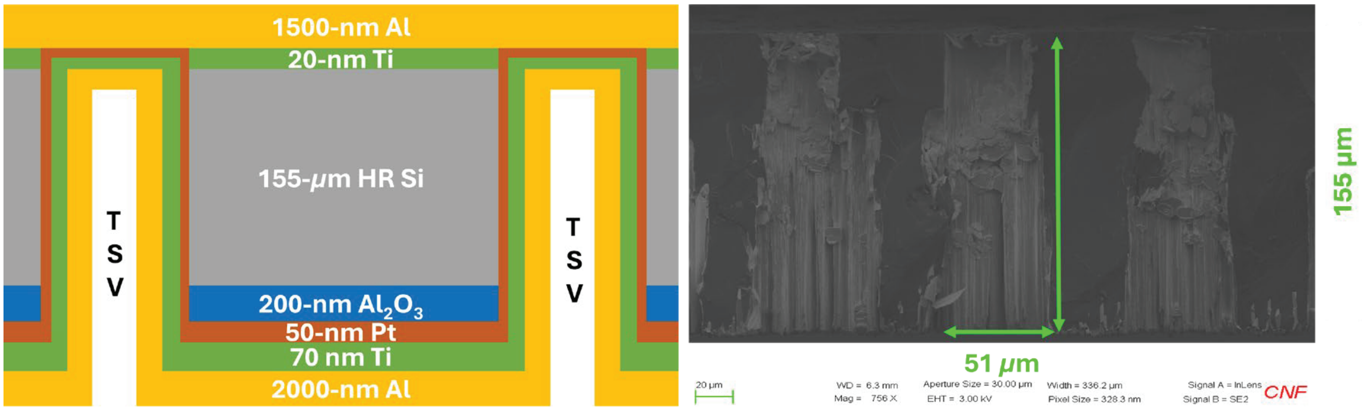

Fig. 2. Cross-section (a) schematic and (b) SEM image of a metallized through-Si via (TSV).

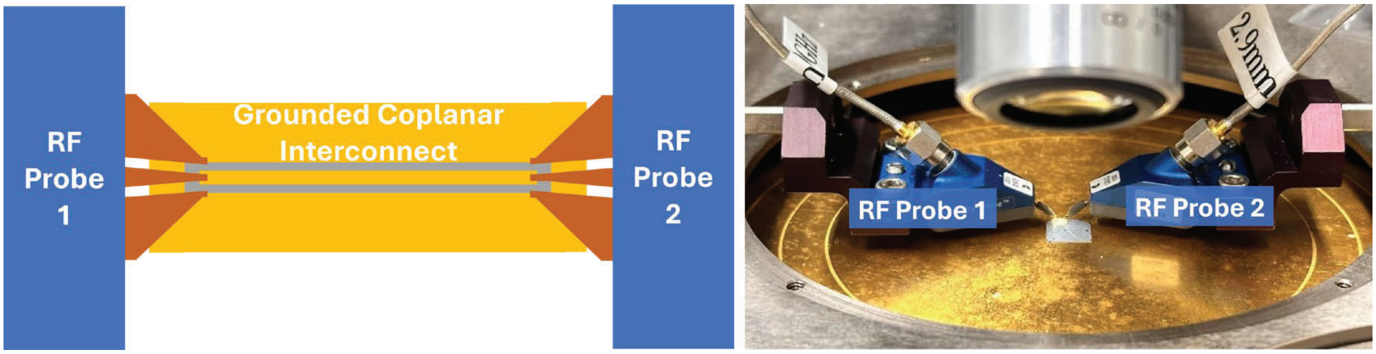

Fig. 3. (a) Schematic and (b) photograph of coplanar interconnect under millimeter-wave test.

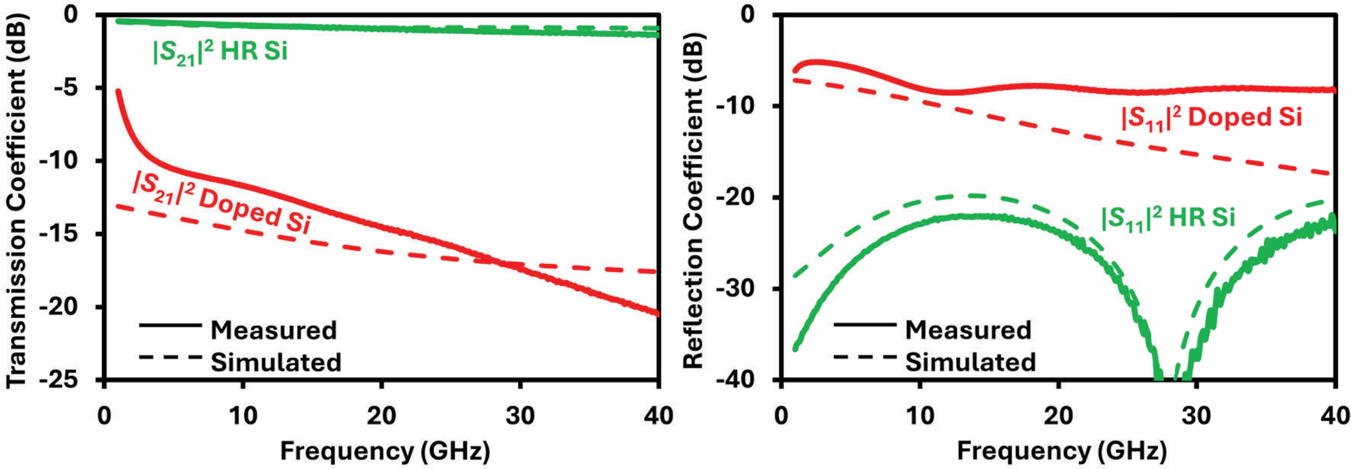

Fig. 3. (a) Schematic and (b) photograph of coplanar interconnect under millimeter-wave test.

Nanoelectronic Artificial Intelligence Processors

CNF Project Number: 316924
Principal Investigator(s): Peter McMahon
User(s): Guilherme Marega, Ruomin Zhu, Yongqi Zhang

Affiliation(s): Applied & Engineering Physics department, Cornell University

Primary Source(s) of Research Funding: the David & Lucile Packard Foundation, Cornell AEP

Contact: pmcmahon@cornell.edu

Website: https://mcmahon.aep.cornell.edu/index.html

Primary CNF Tools Used: Westbond 7400A Ultrasonic Wire Bonder, KLA P7 Profilometer, YES EcoClean Asher, Oxford 81 RIE, Suss MA6|BA6 Aligner, Hamatech Hot Piranha, Oxford PECVD, Oxford 100 ICP Dielectric, Woollam RC2 Spectroscopic Ellipsometer, Zeiss Ultra SEM, Oxford 82 RIE

Abstract:

Resistive crossbar arrays co-locate memory and analog computation to overcome the von Neumann “memory wall,” where data movement can dominate energy costs. By encoding weights in multi-level resistive cells and performing parallel dot-product operations directly within a 16 × 16 array fabricated at the Cornell Nanoscale Facility, we demonstrate up to 60.9 TOPS/W and four decades of linear dynamic range [1]. This in-memory computing platform offers a compelling path toward dramatically lower-power AI inference, as well as efficient signal and image processing.

Summary of Research:

The explosive growth of AI services is driving data-center electricity demand toward unsustainable levels. The International Energy Agency projects global data-center energy use to exceed 945 TWh by 2030—more than double current levels—and U.S. data centers, already consuming 4.4 % of national electricity in 2023, may account for up to 12 % by 2028 [4][5]. Even a single Artificial Intelligence query carries a measurable footprint: a typical ChatGPT interaction consumes roughly 0.3 Wh, equivalent to running an LED bulb for several minutes [6].

Conventional von Neumann architectures exacerbate this burden via the “memory wall,” in which moving a 64-bit word from Dynamic Random Access Memory (DRAM) to the Central processing unit (CPU) costs on the order of 1,000 pJ—about 50× the energy of a 64-bit floating-point add [7]. Across real workloads, data transfers can account for 60–70 % of total system energy, severely limiting both performance and efficiency.

Resistive crossbar arrays address this challenge by performing matrix-vector multiplications in situ: voltages applied to row lines induce column currents proportional to conductance-encoded weights, realizing massively parallel dot products in one step. Hardware demonstrations include 60.9 TOPS/W for binary neural inference in oxide-based devices [1], 405 TOPS/W in magnetoresistive prototypes at 0.8 V [2], and 3.6 TOPS/W in designs with nonlinear Analog Digital Converters (ADCs) for specialized preprocessing [3].

Since the first memristor crossbar proposal in 2008, the field has advanced rapidly: writes as low as 6 fJ per cell for sparse coding [8], 24 TOPS/W in XNOR-RRAM arrays monolithically integrated with 90 nm CMOS [9], and area efficiencies exceeding 130 TOPS/mm² alongside the aforementioned TOPS/W milestones [2].

In our work, we aim to fabricate resistive crossbar arrays with AI model encoded on them to save energy for AI computing. As a first step, we have fabricated 16 × 16 arrays using a CMOS-compatible process and measured their analog performance at Cornell Nanoscale Facility. By encoding image-processing kernels as conductance matrices and feeding input voltages corresponding to grayscale images, we obtained output currents that reproduce digital convolution outputs with high fidelity (Fig. 4), validating hardware-in-the-loop processing as a viable digital alternative.

Conclusions and Future Steps:

We have shown that resistor-based crossbar arrays can achieve state-of-the-art energy efficiency for low-precision AI and image-processing tasks. To scale this approach, we plan to:

- Increase array dimensions from 16 × 16 to 128 × 128, enabling higher-resolution kernels and larger neural-network layers.

- Expand application domains to voice-signal processing, discrete Fourier transforms and AI computing, leveraging the same in-memory dot-product primitive.

These developments will bring in-memory computing closer to deployment in edge AI accelerators and high-throughput signal-processing hardware.

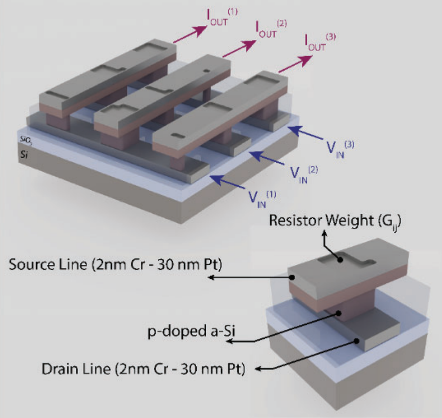

Figure 1: Structure of resistive crossbar arrays.

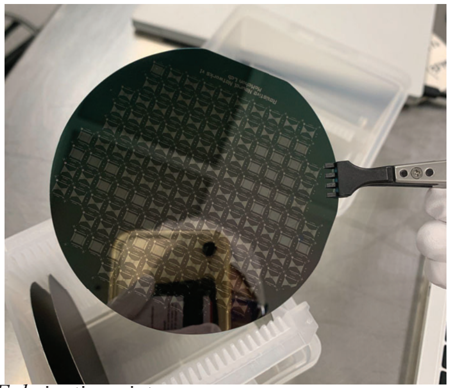

Figure 2: Fabrication picture.

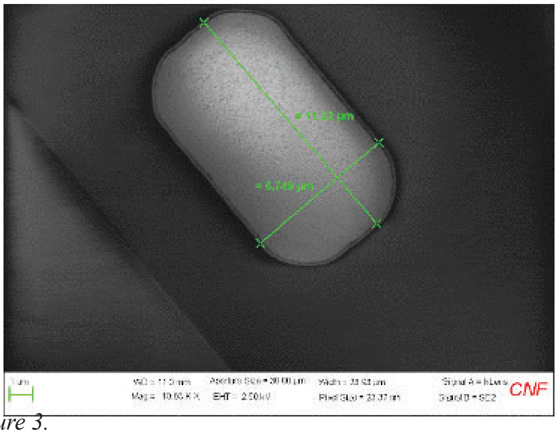

Figure 3.

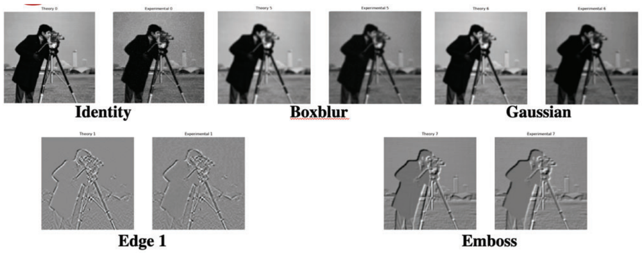

Figure 4: Digital and Hardware processing results.

References:

[1] Li H, Wang S, Zhang X, Wang W, Yang R, Sun Z, Feng W, Lin P, Wang Z, Sun L, Yao Y. Memristive crossbar arrays for storage and computing applications. Advanced Intelligent Systems. 2021;3(9):n/a. doi:10.1002/aisy.202100017.

[2] Jung S, Lee H, Myung S, Kim H, Yoon S-K, Kwon S-W, Ju Y, Kim M, Yi W, Han S, Kwon B, Seo B, Lee K, Koh G-H, Lee K, Song Y, Choi C, Ham D, Kim S-J. A crossbar array of magnetoresistive memory devices for in-memory computing. Nature. 2022;601:211–216. doi:10.1038/s41586-021-04196-6.

[3] Yang J, Mao R, Jiang M, Cheng Y, Sun P-S V, Dong S, Pedretti G, Sheng X, Ignowski J, Li H, et al. Efficient nonlinear function approximation in analog resistive crossbars for recurrent neural networks. Nat Commun. 2025;16:1136. doi:10.1038/s41467-025-56254-6.

[4] International Energy Agency. AI is set to drive surging electricity demand from data centres while offering the potential to transform how the energy sector works. IEA; 10 April 2025.

[5] Pomerleau S, Luna A. AI Data Centers: Why Are They So Energy Hungry? American Action Forum. July 15, 2025.

[6] You J. How much energy does ChatGPT use? Gradient Updates, Epoch AI; 07 Feb 2025.

[7] Leland RL, Murphy R, Hendrickson B. Large-Scale Data Analytics and Its Relationship to Simulation. Executive Office of the President; January 2014.

[8] Agarwal S, Quach T-T, Parekh O, Hsia AH, DeBenedictis EP, James CD, Marinella MJ, Aimone JB. Energy scaling advantages of resistive memory crossbar based computation and its application to sparse coding. Frontiers in Neuroscience. 2016;9:484. doi:10.3389/fnins.2015.00484.

[9] Yin S, Sun X, Yu S, Seo J-S. High-Throughput In-Memory Computing for Binary Deep Neural Networks with Monolithically Integrated RRAM and 90 nm CMOS. arXiv preprint arXiv:1909.07514; 2019. doi:10.48550/arXiv.1909.07514.

Validation of a First Digitho Programmable Photomask Prototype

CNF Project Number: 318324
Principal Investigator(s): Richard Beaudry
User(s): Guilherme Marega, Richard Beaudry

Affiliation(s): Digitho Technologies inc.

Primary Source(s) of Research Funding: NRC-IRAP, private funds and Fabric Program from ISED

Contact: richard@digitho.com

Website: https://mcmahon.aep.cornell.edu/index.html

Primary CNF Tools Used: GCA 5X g-line Stepper, GCA AS200 i-line Stepper

Abstract:

This report outlines the validation of a novel programmable photomask concept leveraging liquid crystal display (LCD) technology for dynamic UV lithography. Conducted at the Cornell NanoScale Facility, the evaluation focused on assessing the system's compatibility with standard g-line and i-line steppers, as well as its ability to support reconfigurable exposure processes. The results highlight the potential of LCD-based photomasks to serve as flexible, low-cost alternatives to conventional chrome masks, opening pathways for rapid prototyping and adaptive lithographic workflows in microfabrication.

Summary of Research:

The growing demand for reconfigurable and cost-effective lithographic tools has prompted exploration of alternatives to static, photolithography-grade chrome masks. In this context, the programmable photomask evaluated in this project integrates an LCD panel capable of modulating UV light in real time, combined with an embedded photodiode for synchronized exposure control. This approach seeks to enable dynamic patterning, reduce reliance on mask fabrication cycles, and facilitate multi-step or adaptive processes within research and development environments. An overview of the photomask structure and components is provided in Figure 1.

The prototype was tested using both g-line and i-line stepper systems at CNF to determine its operational compatibility with established lithography platforms. These tests demonstrated that the system could be integrated without requiring modification to tool workflows or introducing risk to equipment. The ability to maintain wireless communication and reliably update displayed images in response to UV exposure pulses marks a key step toward practical deployment in cleanroom settings.

In addition to confirming mechanical and communication compatibility, the campaign evaluated the core optical performance of the mask with the g-line stepper. Measurements confirmed sufficient UV transmittance (~20% for white pixels, 6–8% for black pixels) and contrast (>60%) for lithographic patterning, with successful image cycling and exposure repeatability demonstrated on resist-coated wafers. Results from these exposure tests are illustrated in Figure 2, while microscopy analysis of the patterned resist confirms a minimum resolved feature size below 100 µm, as shown in Figure 3.

The system also showed the ability to perform basic grayscale patterning through modulated exposures, reinforcing its suitability for early-stage prototyping and multi-depth resist structuring. These findings position LCD-based programmable photomasks as promising enablers of adaptable lithography workflows, with ongoing improvements aimed at enhancing resolution, synchronization robustness, and spectral compatibility.

Conclusions and Future Steps:

The successful validation of the LCD-based programmable photomask under real-world lithographic conditions marks a promising step toward more agile and cost-efficient fabrication workflows. By demonstrating compatibility with both g-line and i-line steppers, maintaining stable wireless communication, and delivering consistent image cycling during UV exposures, this system underscores the feasibility of deploying reconfigurable photomasks in advanced microfabrication environments.

While the current implementation relies on an LCD panel, which is limited to g-line and unsuitable for i-line exposure due to its lack of transparency below 400 nm, future versions of the system are expected to incorporate MEMS-based modulators. These alternatives offer the potential for higher optical performance, broader spectral compatibility—including true i-line transparency—and improved spatial resolution. Such advances would enable programmable photomasks to reach application domains currently limited to traditional chrome masks.

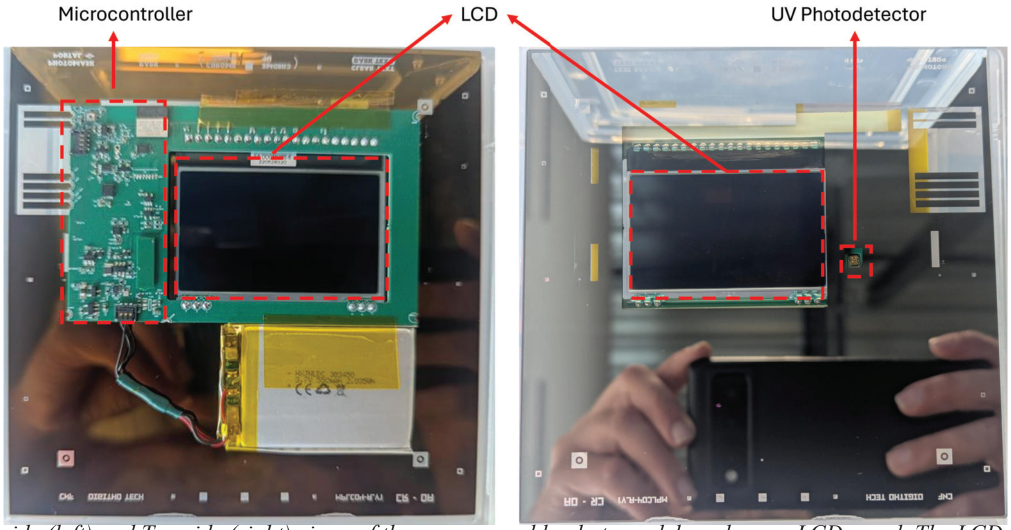

Figure 1: Bottom -side (left) and Top-side (right) views of the programmable photomask based on an LCD panel. The LCD (central red box) modulates UV light during exposure, while the integrated photodiode (rightmost red box) detects UV flashes to trigger image updates. The Bottom side includes control electronics and a rechargeable battery for wireless operation.

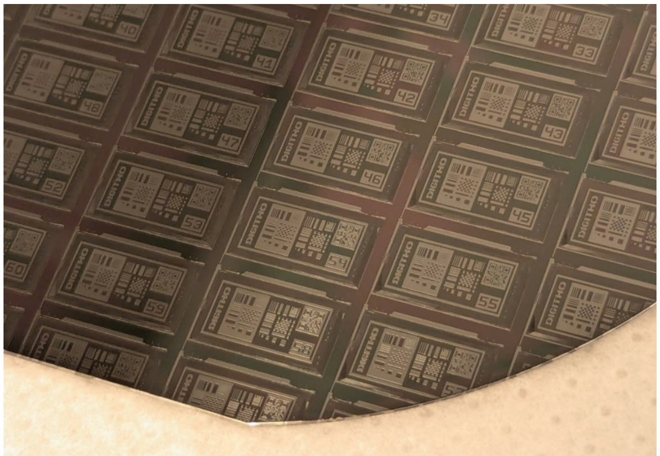

Figure 2: Photograph of a silicon wafer coated with photoresist and exposed using the programmable LCD photomask. Each rectangular field corresponds to a different image in the programmed sequence, demonstrating successful image cycling and pattern transfer during exposure.

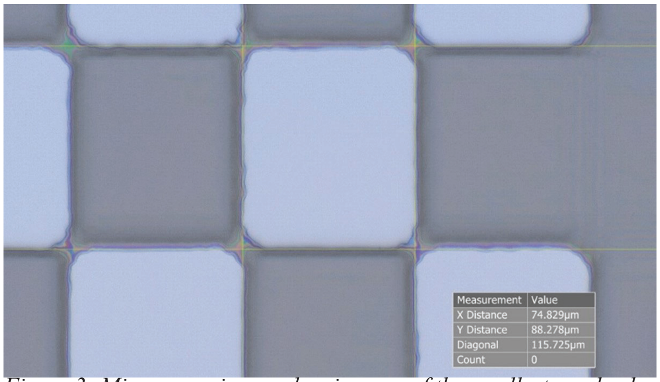

Figure 3: Microscopy image showing one of the smallest resolved features obtained using the programmable photomask. The measured dimensions are approximately 74.8 μm × 88.3 μm, confirming lithographic resolution below 100 μm consistent with LCD pixel limitations.

Microchannel Fabrication on Silicon Wafer and Development of Heating Elements on Silicon and Sapphire

CNF Project Number: 319424
Principal Investigator(s): Srikanth Rangarajan
User(s): Pranay Nirapure

Affiliation(s): Binghamton University

Primary Source(s) of Research Funding: National Science Foundation, Semiconductor Research Corporation

Contact: srangar@binghamton.edu

Website: https://mcmahon.aep.cornell.edu/index.html

Primary CNF Tools Used: Lesker PVD75 Sputter, CVC SC4500 Odd-hour evaporator, MRL A1 General Anneal

Abstract:

This project reports on the fabrication and post-deposition treatment of a transparent heater using a 600 nm thick Indium Tin Oxide (ITO) film sputtered onto a sapphire substrate. Following ITO deposition, a thin metal contact layer composed of 2 nm titanium and 150 nm gold was evaporated to facilitate electrical probing. ITO was deposited using the Lesker PVD 75 sputtering tool at 100 degrees Celsius, and post-annealing was conducted in ambient air at 500 degrees Celsius for 45 minutes. The device is designed to retain high optical transmittance while enabling Joule heating and low-resistance contact.

Summary of Research:

The objective of this project was to develop a transparent, electrically conductive heater using ITO on a sapphire substrate, integrated with metal contacts for reliable electrical interfacing. Transparent heaters are essential to study the bubble nucleation in boiling phenomena. Transparent heaters allow for both optical access and local heating, making them ideal for this study.

Sapphire substrates were selected for their desirable thermal properties, along with optical clarity and mechanical robustness. ITO was chosen as the heater material due to its high transmittance in the visible spectrum and relatively desirable sheet resistance when properly processed.

The ITO layer was deposited using the Lesker PVD 75 RF magnetron sputtering system. Deposition was carried out at a substrate temperature of 100 degrees Celsius under an argon ambient. The resulting film thickness was 600 nanometers.

Post-deposition annealing trials are being conducted in ambient air to improve crystallinity, reduce resistivity, and maintain high optical transmission. Annealing is to be performed in a tube furnace at 400 degrees Celsius for 45 minutes. This air anneal condition is supposed to provide a good balance between transmittance and electrical performance. While forming gas anneals can further reduce sheet resistance, they were not used in this iteration.

To enable low-resistance electrical contacts, a bi-layer metal stack was deposited using the CNF Odd-Hour. A 2 nm titanium adhesion layer was deposited directly on the ITO, followed by 150 nm of gold. Titanium provides good adhesion to both ITO and the underlying sapphire, while gold serves as a chemically inert, low-resistance contact layer suitable for wire bonding or probing.

The annealed ITO films exhibited an estimated average visible transmittance of 80 to 85 percent, with peak transmittance near 550 nanometers. The sheet resistance was estimated to be between 10 and 15 ohms per square, depending on grain structure, carrier mobility, and stoichiometry. These values are within expected ranges for ITO processed under similar conditions. [1] [2] [3]

The completed heater consists of a transparent region for optical access and well-defined metal pads for electrical interfacing, please refer to Fig. 1. The heater is compatible with applications requiring simultaneous thermal and optical functions. Future work will include photolithographic patterning of heater geometries and optimization of contact pad layouts.

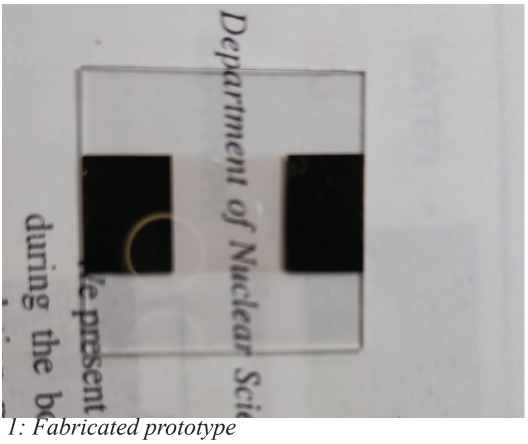

Figure 1: Fabricated prototype

References:

[1] Hamberg, M., and Granqvist, C. G., "Evaporated Sn-doped indium oxide films: Basic optical properties and applications to energy-efficient windows," Journal of Applied Physics, vol. 60, 1986.

[2] Ashour, A., "Physical properties of ITO thin films deposited by spray pyrolysis technique," Materials Letters, vol. 57, no. 2, pp. 452–460, 2003.

[3] Sharma, A. K., et al., "Post-deposition annealing effect on ITO films," Journal of Materials Science, vol. 45, pp. 1260–1266, 2010.

Interconnect-Based Temperature Sensing Array for IC Thermal Management

CNF Project Number: 321024
Principal Investigator(s): Ping-Chuan Wang and Graham Werner
User(s): Ping-Chuan Wang, Graham Werner

Affiliation(s): SUNY New Paltz Division of Engineering Programs

Primary Source(s) of Research Funding: SUNY New Paltz Research and Creative Projects Award (RCPA)

Contact: Wangp@newpaltz.edu, Wernerg1@newpaltz.edu

Website: https://mcmahon.aep.cornell.edu/index.html

Primary CNF Tools Used: Heidelberg MLA 150, Hamatech Wafer Processor, CVC SC4500 Odd-hour evaporator, YES EcoClean Asher Filmetrics Reflectometer

Abstract:

Excessive self-heating in integrated circuits (ICs) is a major barrier to performance and reliability within the semiconductor industry and necessitates innovation in thermal management [1,2], prompting detailed measurements of IC temperature with adequate spatial and temporal resolutions in designing and characterizing innovative cooling devices. This project presents the fabrication of an in-line spatial and temporal temperature mapping system designed to interface directly between an IC and its cooling device, consisting of a dense array of 64 aluminum Resistance Temperature Detector (RTD) sensors. The RTD array was successfully fabricated at CNF using a single-layer lift-off process on an oxide-coated silicon wafer, before integration into a measurement system. Our project validates the design, fabrication, and characterization of an aluminum RTD sensor array system for in-situ, high resolution thermal mapping, contributing to the experimental evaluation of IC thermal management solutions.

Summary of Research:

Resistance Temperature Detectors (RTDs) were chosen due to their straightforward device physics, use of a single conventional conductor, and fabrication simplicity through a single lithography step [3,4]. The RTD structure consisted of 64 individual serpentine-pattern sensors, spaced evenly to cover a 25 mm x 25 mm sensing area (Figure 1), with two arrays fabricated on a single 4-inch wafer. Fabrication employed a lift-off process on silicon wafers first passivated with thermally grown SiO2 (Figure 2). A bi-layer of lift-off resist and positive tone photoresist were spin-coated before pattern development. The Heidelberg MLA 150 maskless direct-write tool was used to expose the RTD design. The exposed photoresist was then developed in a Hamatech-Steag wafer processor, followed by dry-oxygen plasma descum using an Anatech plasma asher to remove resist residues.

Following development, metallization was performed, where A 100 Å titanium adhesion layer was followed by deposition of 2000 Å of aluminum using electron beam physical vapor deposition (EB-PVD). Lift-off was performed with an automated tool, and SiO2 passivation was applied atop metal pattern using PECVD after optimizing pre-cleaning to avoid damage to the aluminum, providing necessary electrical and mechanical insulation. After dicing and packaging, the calibrated system performed real-time measurements by multiplexing continuously across the sensor array to perform 4-point resistance measurements.

Once calibrated, the sensor array showed minimal sensor-to-sensor temperature variation under ambient conditions, with 0.18% variability at room temperature. During thermal transients, spatial temperature variations were resolved within 0.1 °C.

Conclusions and Future Steps:

The fabricated RTD sensor array successfully demonstrated ambient and transients with suitable spatiotemporal resolution for non-uniform thermal gradients during heating and cooling cycles. The measured average sensitivity was 0.197 ± 0.004 mV/°C, consistent with design expectations. Limitations include aluminum's inferior thermal properties compared to platinum for RTDs, and a lower spatial resolution of 10 sensors/ cm², which may be insufficient in some applications. Future work will focus on validating the system through numerical modelling or thermal finite element analysis (FEA) to ensure accuracy in detecting spatial temperature variations.

References:

[1] International Technology Roadmap for Semiconductors 2.0, 2015 ed., Executive Report (https://www.semiconductors.org/wp-content/uploads/2018/06/0_2015-ITRS-2.0-Executive-Report-1.pdf, accessed May 8, 2025)

[2] L. Shang and R. P. Dick, "Thermal Crisis: Challenges and Potential Solutions," IEEE Potentials, vol. 25, no. 5, pp. 31-35, (2006) (doi: 10.1109/MP.2006.1692283)

[3] G. Werner, "Development of IC-based Temperature Monitor with Spaciotemporal Resolution," M.S. thesis, State University of New York at New Paltz, 2025.

[4] G. Werner, P.-C. Wang, O. Trzcinski, and W. Cui, “Interconnect-Based Sensor Array for Characterizing Thermal Management of IC Chips,” 2025 TMS Annual Meeting, Las Vegas, NV, March 2025

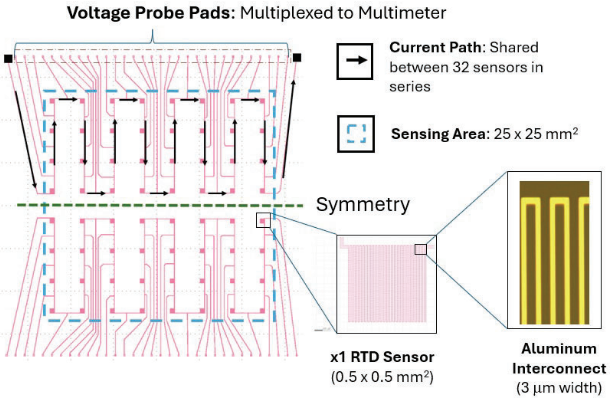

Figure 1: Layout of RTD sensor array.

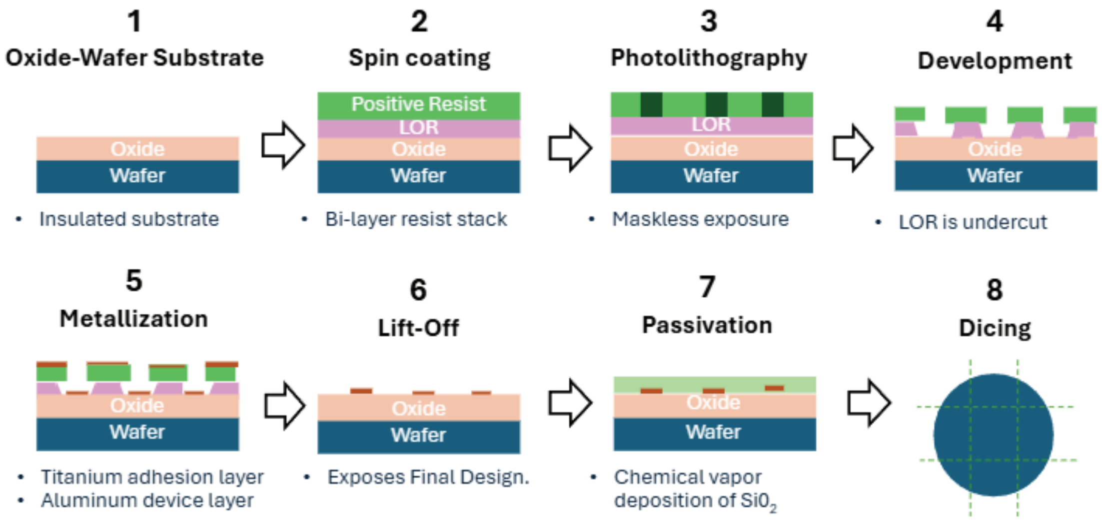

Figure 2: Lift-off fabrication steps.

Aluminum CMP Planarization for Graphene FETs

CNF Project Number: 321524
Principal Investigator(s): Ivan Puchades
User(s): William Huang

Affiliation(s): Department of Microsystems Engineering, Rochester Institute of Technology, Department of Electrical and Microelectronics Engineering, Rochester Institute of Technology.

Primary Source(s) of Research Funding: Rochester Institute of Technology

Contact: ixpeme@rit.edu

Primary CNF Tools Used: Logitech Orbis CMP / Aluminum

Abstract:

As silicon CMOS technology approaches its scaling limits, graphene offers a compelling alternative due to its high carrier mobility, atomically thin profile, offering strong electrostatic control and promising high-frequency performance. However, roadblocks such as device-to-device variation, high contact resistance, poor dielectric interfaces, and non-uniform graphene quality have limited the adoption of graphene field - effect transistors (GFETs). In this work, we directly compare two GFET structures through a controlled, side-by-side process split to evaluate the impact of gate electrode topography (raised vs. recessed buried local gate) in terms of device performance and device-to-device variation. While the top performing devices remained similar across the three proposed structures, very significant differences are seen in terms of yield and device-to-device variation in the proposed variations. The device-to-device variation of the hole mobility dropped from 36% to 19%, device yield increased from 54.4% to 65.1%, Dirac voltage was reduced from 1.2 V to 0.7 V when a recessed local-back gate is used as opposed to a raised local-back gate. As such, this study shows that a direct comparison of process conditions can help identify favorable process conditions to improve the manufacturability of graphene-based transistors.

Summary of Research:

The integration of a planarization process for the fabrication of GFETs with hBN dielectrics, results in both a smoother transition from channel to gate as shown in schematically in Figure 1, and Figure 2. The planarization process provides a statistical improvement in the performance and variability of graphene transistors in terms of Dirac point and mobility when compared to a raised gate architecture as shown in Figure 3 and Figure 4. Hysteresis measurements (not shown) also indicate that the level of traps in the hBN/graphene interface is similar between the raised and recessed process. When compared to other dielectrics such as Al2O3 [1], hBN also offers advantages in terms of yield and contact resistance when used in a local-back gate process. In addition, the observed parameter variability is much reduced with the use of hBN as a dielectric due to better material compatibility during processing, which along with other process improvement and considerations, could lead to the needed improvement in yield and reliability [2], [3], [4]

Conclusions and Future Steps:

While prior studies have aimed to improve GFET performance or reduce variability, most work has typically done so in evaluating disparate device structures, materials, or fabrication flows, and focusing only on "hero" devices that do not reflect broader statistical trends. In contrast, our work systematically integrates monolayer hBN as a gate dielectric and a CMP-recessed aluminum gate within a unified fabrication platform, enabling direct, controlled comparisons across design variations. This approach not only enhances key performance metrics, such as contact resistance, mobility, and cutoff frequency, but also dramatically reduces device-to-device variation and increases yield. By analyzing full device distributions rather than peak values alone, this study offers critical insights into how dielectric choice and gate geometry together influence reproducibility. Demonstrating a substantial reduction in device variability, the standard deviation of extracted hole mobility decreased from 36% to 18%, while device yield improved significantly from 54.4% to 65.1%. The Dirac point shifted closer to 0 V (from ~1.2 V to 0.7 V), and the contact resistance was reduced from 0.75 kΩ to 0.67 kΩ. Ultimately, our findings establish practical design and process guidelines for realizing scalable, high-performance graphene electronics to bridge gaps between isolated breakthroughs and manufacturable, wafer-level technologies. The reduction in device-to-device variation indicates that a process induced variation may be mitigated through the presented work.

The finding implies that extending the process flow to further large-scale integration may support a more uniform device array and a scalable, multi-user circuit design platform. By analyzing full device distributions rather than peak metrics alone, this study reveals how dielectric selection and gate geometry directly influence reproducibility. The observed consistency suggests that this hBN/ recessed gate structure is a strong candidate for an optimal platform of scalable, and high-performance GFET fabrication.

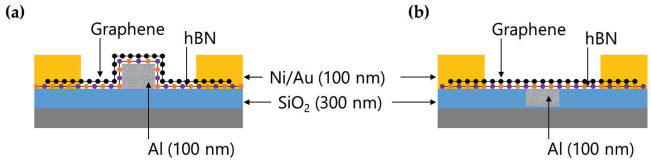

Figure 1: Device cross-section for (a) raised Al gate with hBN gate dielectric and (b) recessed Al gate with hBN gate dielectric.

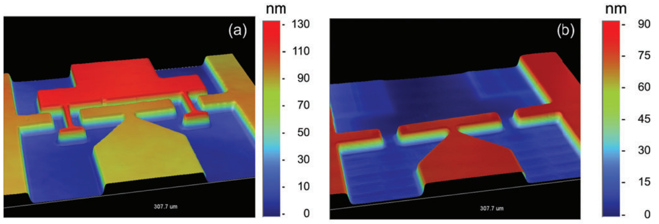

Figure 2: Three-dimensional white light interferometry scans of fabricated (a) raised and (b) recessed Al/hBN/graphene field effect transistors.

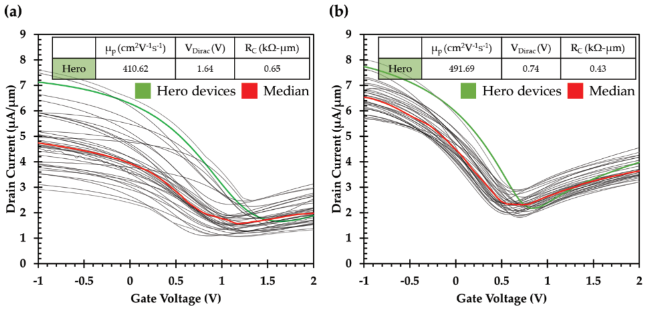

Figure 3: Transfer characteristics overlay at VDS = 0.1 V of fabricated graphene FETs with a gate length of 10 μm drain current normalized to its width of 20 μm and contact resistance (RC) normalized to its width (a) raised Al gate with monolayer hBN gate dielectric and (b) recessed Al gate with monolayer hBN gate dielectric.

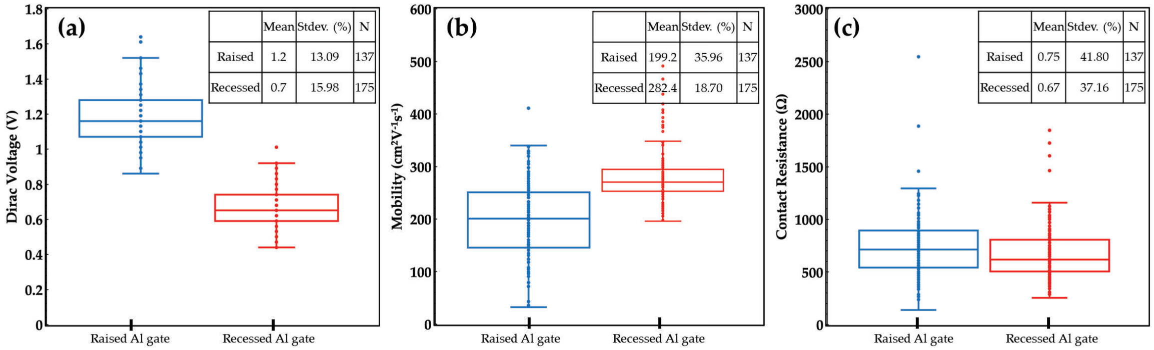

Figure 4: Box and whisker comparison of performance and variation of fabricated devices with raised and recessed aluminum gates in relation to (a) mobility, (b) Dirac voltage, and (c) contact resistance. Within each box and whisker plots, inset indicate the average, % standard deviation and number of working devices for each group.

References:

[1] T. J. Huang, A. Ankolekar, A. Pacheco-Sanchez, and I. Puchades, “Investigating the Device Performance Variation of a Buried Locally Gated Al/Al2O3 Graphene Field-Effect Transistor Process,” Applied Sciences (Switzerland), vol. 13, no. 12, Jun. 2023, doi: 10.3390/app13127201.

[2] S. Fukamachi et al., “Large-area synthesis and transfer of multilayer hexagonal boron nitride for enhanced graphene device arrays,” Nature Electronics 2023 6:2, vol. 6, no. 2, pp. 126–136, Feb. 2023, doi: 10.1038/s41928-022-00911-x.

[3] W. Zheng, “Scalable Production of Two-Dimensional Materials Based Microchips Containing Highly-Reliable Transistors,” 2025. Accessed: Jul. 24, 2025. [Online]. Available: http://hdl.handle.net/10754/705175

[4] “IRDSTM 2023: Beyond CMOS and Emerging Materials Integration - IEEE IRDSTM.” Accessed: Jul. 24, 2025. [Online]. Available: https://irds.ieee.org/editions/2023/20-roadmap-2023-edition/126-irds%E2%84%A2-2023-beyond-cmos-and-emerging-materials-integration

GALLO

CNF Project Number: 323825
Principal Investigator(s): Jon McCandless
User(s): Kazuki Nomoto

Affiliation(s): Gallox Semiconductors Inc.

Primary Source(s) of Research Funding: National Science Foundation, Breakthrough Energy

Contact: jon@galloxsemi.com

Primary CNF Tools Used: GCA AutoStep 200 DSW i-line stepper, JEOL 6300 E-beam, SEM, PT770 etcher, O2 Asher, Oxford RIE Etcher, AJA sputter system, E-beam evaporator, Oxford PECVD, RTA AG610

Abstract:

Gallium oxide (Ga_2O_3), an ultra-wide bandgap semiconductor, offers strong potential for highpower, high-voltage power electronics due to its large bandgap and high critical electric field strength. This research focuses on the design, fabrication, and testing of Ga_2O_3)-based diodes and transistors, with iterative improvements guided by performance data. Current efforts emphasize electric field management and thermal mitigation to enhance device performance and support future commercialization.

Summary of Research:

Gallium oxide (Ga_2O_3) is an ultra-wide bandgap (~4.8 eV) semiconductor [1]. Its large bandgap and high critical electric field strength make it well suited for high-power, high-voltage power electronics applications [2].

To commercialize Ga_2O_3-based transistors and diodes, devices must be carefully designed, fabricated, and tested. Effective electric field management and thermal mitigation strategies are essential to achieving the material's full potential.

We have designed, fabricated, and tested both diodes (Fig. 1) and transistors (Fig. 2) to evaluate the device performance (Fig. 3), and we continuously iterate: fabrication, testing, and data analysis to inform subsequent design improvements.

Conclusions and Future Steps:

We are working to introduce additional electric field management strategies, and to implement efficient heat removal strategies.

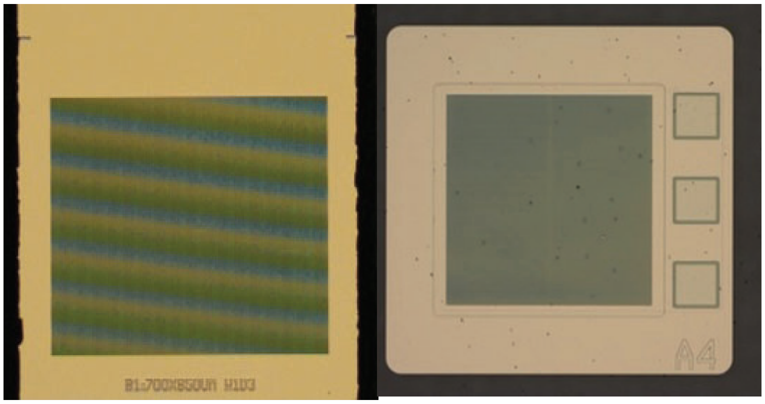

Fig. 1 (Left). A Schottky barrier diode is shown. Fig. 2 (Right). A field effect transistor is shown.

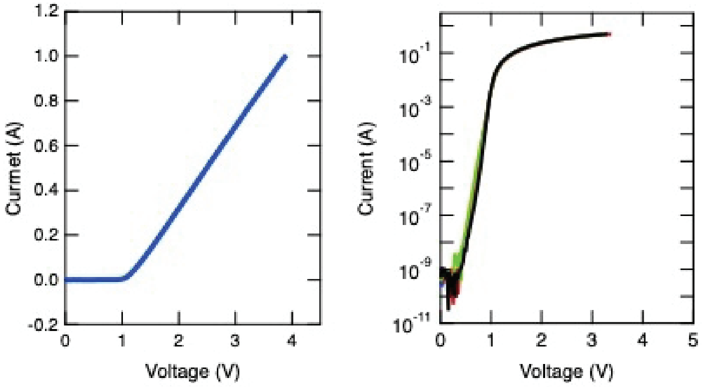

Fig. 3. Schottky barrier diode performance is characterized, and performance is assessed in order to optimize and iterate on the devices design. Current vs voltage measurements are obtained and plotted on a (left) linear scale and (right) log scale.

References:

[1] T. J. Huang, A. Ankolekar, A. Pacheco-Sanchez, and I. Puchades, "Investigating the Device Performance Variation of a Buried Locally Gated Al/Al2O3 Graphene Field-Effect Transistor Process," Applied Sciences (Switzerland), vol. 13, no. 12, Jun. 2023, do

Circuit Integration and Chip Design

CNF Project Number: 325925
Principal Investigator(s): Dr. Younes Ra'di
User(s): Pardha Sourya Nayani, Morteza Moradi

Affiliation(s): Department of Electrical Engineering and Computer Science, Syracuse University, Syracuse, NY, USA

Primary Source(s) of Research Funding: Syracuse University

Contact: yradi@syr.edu

Primary CNF Tools Used: Heidelberg MLA150 MasklessAligner, SC4500 Odd-Hour Evaporator, DISCO Dicing Saw and Westbond 7400A Ultrasonic Wire Bonder

Abstract:

This project focused on the design, fabrication, and testing of a compact circuit integrated into a packaged chip, optimized for impedance behavior analysis. The circuit, composed of capacitors, inductors, and resistors, was carefully designed and laid out for on-chip integration. The inductors were implemented using meander line structures, while the capacitors were realized as interdigitated fingers, together replicating the desired impedance characteristics. The fabricated chips are currently in the testing phase.

Summary of Research:

In this research, we developed a new circuit model consisting of capacitors, inductors, and resistors, which when configured as shown in Fig. 1a produce a desired impedance profile. The initial stage of the project involved theoretical analysis to extract the target circuit parameters, including the required capacitance, inductance, and resistance values. Subsequently, the focus shifted to translating these theoretical values into a practical layout by designing the individual passive components. Rather than designing the complete circuit in a single step, we adopted a modular approach: capacitors and inductors were designed separately and later integrated and optimized to match the desired impedance response. The layout designs were carried out using Keysight ADS, where we explored various geometries and material configurations. Specifically, capacitors and inductors were designed with different dimensions and using various metal layers, such as gold and aluminum, to achieve the same target values. Finally, the individual components were integrated into a complete layout, and the design was optimized to ensure that the overall impedance closely matched the theoretical predictions. The finalized designs were then exported as GDS files, ready for fabrication as seen in Fig. 1b.

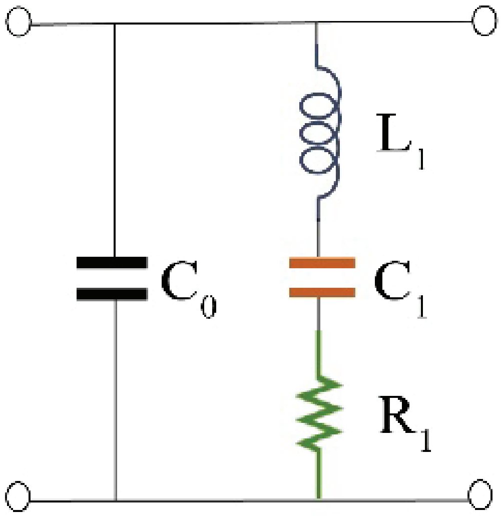

Figure 1a Topology of designed circuit.

At CNF, the fabrication process began with the selection of a 100 mm, prime-grade, n-type silicon wafer. Standard photolithography steps were followed, starting with spin-coating the wafer with a positive photoresist. Maskless lithography was then performed using the Heidelberg MLA 150 system, which enabled direct laser exposure of the desired pattern onto the photoresist without the use of a physical mask. Following exposure, the wafer was developed using an appropriate solvent, resulting in the transfer of the designed pattern onto the photoresist layer. After development, a metal deposition was carried out using the SC4500 Odd-Hour Evaporator. Two different metal stacks were deposited on separate wafers: one with a 1 µm-thick gold layer and the other with a 100 nm-thick aluminum layer. Upon completion of metal deposition, the wafers underwent a lift-off process (refer to Fig. 2a and 2b) to remove the remaining photoresist and define the final patterned metal structures. After the metal deposition and completion of the lift-off process, the wafer was diced into individual dies corresponding to the various unit cell designs developed during the initial design phase as seen in Fig. 3a. These discrete unit cell dies

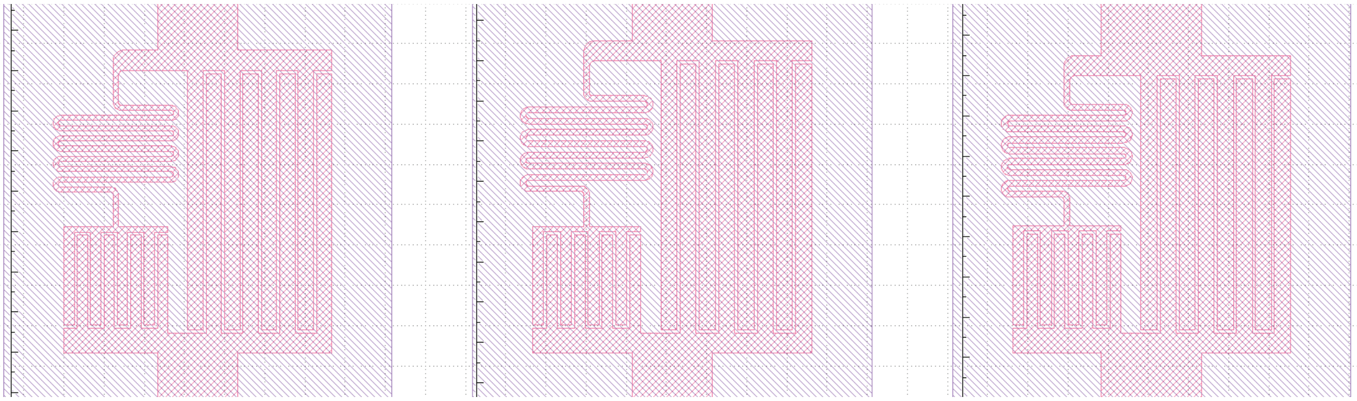

Figure 1b Layout of three different designs.

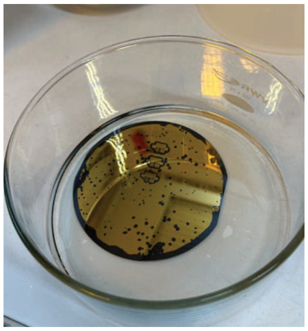

Figure 2a Lift-off process.

Figure 2b Wafer after Lift-off with designed metallic patterns.

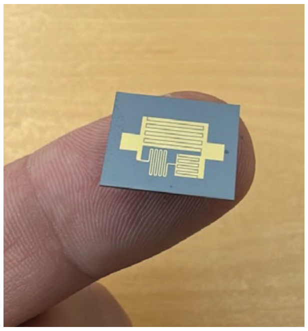

Figure 3a Diced unit cell.

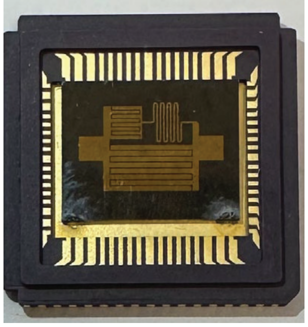

Figure 3b The fabricated circuit in a package.

were subsequently mounted and wire-bonded onto chip carriers for packaging shown in Fig. 3b. The packaged devices are currently in the final stages of preparation for preliminary measurements. We will characterize the fabricated devices by extracting key parameters such as S-parameters and impedance (Z) parameters, and compare the measured data against theoretical predictions. Based on any observed discrepancies, we will iteratively refine the initial designs and adjust intermediate fabrication steps to optimize performance. This cycle of design, fabrication, measurement, and analysis will be repeated until the desired device specifications are met.

Conclusions and Future Steps:

Based on the measurement results obtained, we will fine-tune specific design parameters to enhance alignment with theoretical predictions. Thus far, we have successfully designed and fabricated a single-order circuit unit cell. Moving forward, we plan to extend this work by developing and vertically stacking multiple unit cells to realize higher-order circuit architectures, which will also be fabricated on-chip. This work establishes a systematic design-to-fabrication workflow for custom impedance-engineered circuits at the microscale. The approach enables rapid prototyping and experimental validation of novel circuit topologies directly in integrated form. As the project progresses, further optimization and scaling of the architecture will be explored, with potential applications in compact RF front-ends, and on-chip electromagnetic systems.

Towards Quantitative Comparisons of Bulk and Local Optoelectronic Properties of Emerging Solar Cell Materials with Interdigital Electrodes

CNF Project Number: 86300
Principal Investigator(s): John A. Marohn
User(s): Azriel Finsterer

Affiliation(s): Cornell University Chemistry and Chemical Biology

Primary Source(s) of Research Funding: NSF Award DMR-2113994gy

Contact: john.marohn@cornell.edu

Primary CNF Tools Used: Hamatech Hot Piranha Cleaner, Class II Resist Spinners, Edge Bead Removal System, ABM Contact Aligner, Hamatech Wafer Processor, Oxford Plasma Etchers (81 and 82), SC4500 Odd-Hour Evaporator, SC4500 Even-Hour Evaporator, Disco Dicing Saw

Abstract:

Gold interdigitated electrodes with varying electrode length and separation have been fabricated using a simple photolithography procedure. Fabricated electrodes were used in space charge-limited current experiments with a thin film of N,N'-Bis(3-methylphenyl)-N,N'-diphenylbenzidine embedded in a polystyrene matrix. Future work aims to combine such experiments with scanned-probe microscopy experiments to quantitatively compare bulk and local optoelectronic properties.

Summary of Research:

Gold interdigitated electrodes have been fabricated with a simple photolithography procedure, shown in Figure 1. Four-inch, standard-thickness quartz wafers were purchased from Mark Optics and were cleaned using the Hamatech hot piranha cleaner. Cleaned wafers were dehydrated at 180□ for 10 minutes and introduced to the spin coater, where they were coated with LOR resist. LOR was dispensed dynamically at 400 rpm for 4 seconds before coating at 4000 rpm for 45 seconds. The layer was soft-baked for 20 minutes at a wafer temperature of

180□ before S1805 resist was deposited statically with a coating speed of 4000 rpm for 60 seconds with an acceleration of 1000rpm/s. The film was soft-baked at 115□ for 3 minutes. The edge bead was removed with the edge bead removal system.

Figure 2 depicts the exposure array used to determine the optimum dose for wafer patterning. An octagonal mask with an opening was placed between the light source and the wafer on the ABM contact aligner. The experiment tested 8 distinct exposure conditions, varying the exposure time from 1 second to 4.5 seconds in 0.5-second increments. The wafer was developed with 726 metal ion-free developer sprayed in a single puddle for sixty seconds post-exposure. Optical microscopy revealed that 3.5 seconds of exposure—corresponding to a dose of 41.7-53.6 mJ/cm2—was sufficient for producing the desired pattern and undercut.

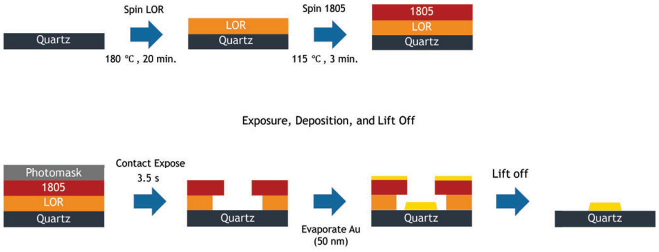

Figure 1: Schematic representation of the fabrication of gold interdigitated electrodes. Specific parameters are provided where possible.

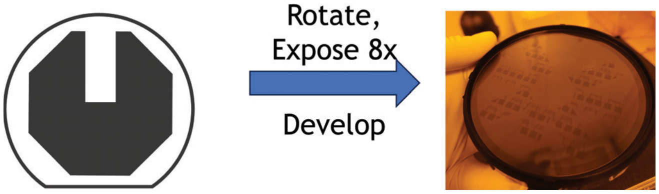

Figure 2: Schematic of the exposure array. Each region of the wafer was patterned using a distinct exposure dose. Determination of the ideal exposure dose was performed with optical microscopy.

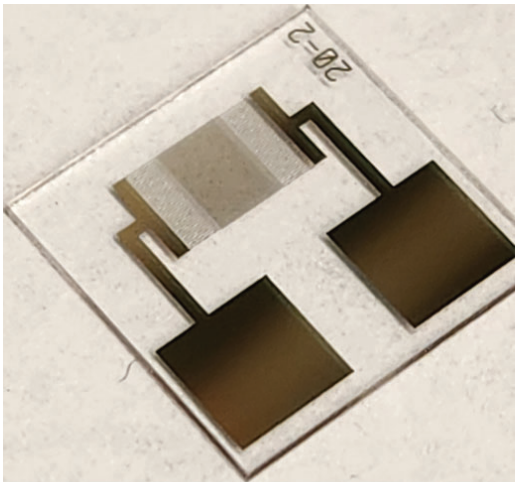

Figure 3: A successfully fabricated gold interdigitated electrode. The two numbers to the right of the electrode represent the separation of each digit in microns, while the second number signifies the length of each digit in millimeters.

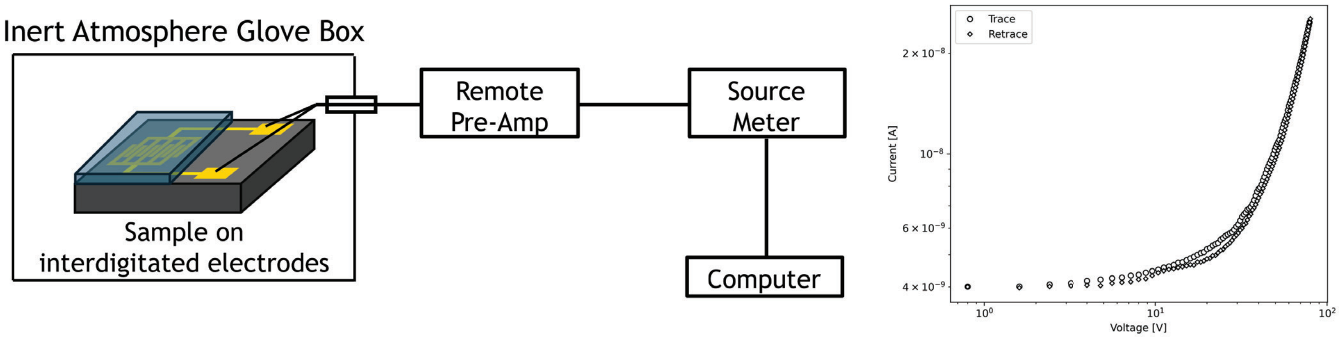

Figure 4: Block diagram of the space charge limited current experiment with a sample current voltage curve. The observed non-linearity in the current voltage curve is direct evidence of space charge-limited current injection.

Patterned wafers were placed in the Oxford 81 plasma etcher for a light oxygen plasma descum with a forward power of 50 mW for 45 seconds before being directly introduced into the Odd Hour Evaporator. When the bell jar pressure was ~ 2x10-6 Torr, 5 nm of chromium was deposited at a rate of ~1.4 Å/s, followed by the deposition of 50 nm of gold at a rate of 0.4 Å/s. The wafer was removed, and the metal was lifted off with Remover PG before being diced in the disco dicing saw. A representative electrode produced from the protocol is shown in Figure 3.

Electrodes were used in charge injection experiments involving the molecularly doped polymer system N,N'-Bis(3-methylphenyl)-N,N'-diphenylbenzidine in polystyrene. This system is known to produce space charge-limited current and provides a baseline for testing the electrodes1. A block diagram of the charge injection experiment and current-voltage curve is shown in Figure 4. The non-linearity of the current-voltage curve is direct evidence of space charge-limited current injection into the thin film. The bulk charge mobility of the film can be determined from the current-voltage data and can be subsequently compared to local mobility values determined with scanned-probe microscopy experiments[2].

Conclusions and Future Steps:

Gold interdigitated electrodes were fabricated using a simple photolithography procedure. These were implemented in space charge-limited current experiments involving a molecularly doped polymer, where space charge-limited current was directly observed as a non-linearity in the current-voltage curve. Using an established theory for space charge-limited current injection, the bulk charge mobility in the film can be determined.

Future work aims to incorporate the current-voltage curve experiment into a scanned probe microscopy experiment, where an oscillating cantilever charged with a frequency and amplitude modulated AC voltage will be brought over conductive thin films deposited on interdigitated electrodes operating in the space charge regime. Measuring the frequency shift as a function of the frequency modulation frequencies will yield a spectrum that can be used to quantitatively extract the charge density, charge mobility, and conductivity of the film. By modifying the amount of voltage applied to the electrode, measurements can be taken when the electrodes are operating under ohmic and space charge-limited current conditions, allowing for a robust test of the theory used to quantitatively extract key local optoelectronic properties.

References:

[1] Silveira, W. R.; Marohn, J. A. Microscopic View of Charge Injection in an Organic Semiconductor. Phys. Rev. Lett. 2004, 93 (11), 116104. https://doi.org/10.1103/PhysRevLett.93.116104.

[2] Murgatroyd, P. N. Theory of Space-Charge-Limited Current Enhanced by Frenkel Effect. J. Phys. D: Appl. Phys. 1970, 3 (2), 151. https://doi.org/10.1088/0022-3727/3/2/308.

Optimizing Silicon Chip Thickness and Pixel Activation Threshold in Scanning Transmission Electron Microscope Detectors

CNF Summer Student: Himani Anilkumar Mishra
Student Affiliation: School of Applied and Engineering Physics, Cornell University

Summer Program(s): 2025 Cornell NanoScale Facility Research Experience for Undergraduates (CNF REU) Program, SUPREME REU

Principal Investigator(s): David A. Muller, School of Applied and Engineering Physics, Cornell University

Mentor(s): Steven E. Zeltmann, Platform for the Accelerated Realization, Analysis, and Discovery of Interface Materials (PARADIM), Cornell University

Primary Source(s) of Research Funding: National Science Foundation under Grant No. NNCI-2025233, SUPREME

Contact: ham74@cornell.edu, steven.zeltmann@cornell.edu, david.a.muller@cornell.edu

Summer Program Website(s): https://cnf.cornell.edu/education/reu

Research Group Website: https://muller.research.engineering.cornell.edu/

Abstract:

Electron ptychography is a scanning transmission electron microscopy (STEM) technique used to achieve high-quality three-dimensional characterization of rapidly shrinking semiconductor devices[1]. We aim to design dose-efficient STEM detectors that use the maximal amount of generated signal. In STEM, a focused beam of electrons are either transmitted and/or scattered by our material of interest. The transmitted electrons then encounter a pixel array detector that is composed of a sensor layer, which is bump-bonded to an ASIC[2,3]. The silicon sensor layer is divided into pixels that record the amount of energy deposited by the electrons. Each pixel has a threshold of activation. If an electron deposits energy greater than the threshold, the pixel is activated. The problem lies in when the electron lands on the intersection of pixels. If the threshold is low, all pixels are triggered, leading to overcounting, but if the threshold is high, no pixels are triggered, leading to undercounting. Therefore, we must find the optimal pixel activation threshold value. We also test different thicknesses for the sensor layer to avoid the problem of oversaturation. We use a Monte Carlo simulation to track the trajectories and energies deposited by an incident beam of electrons in the sensor layer. From this, we analyze energy distributions and calculate the modulation transfer function (MTF) and detective quantum efficiency (DQE)[4,6] to evaluate the performance of different thickness levels and pixel activation thresholds. Careful thresholding in conjunction with thickness optimization will enable dose-efficient STEM for the high-quality characterization of next-generation semiconductors.

Summary of Research:

The pixel array detector is a type of electron microscope detector that offers high-speed data collection due to its parallel pixel readout and sensitivity to signal changes. It is composed of two layers: a sensor layer and CMOS Integrated Chip. The sensor layer is sectioned into square pixels. This layer is then bump-bonded to the IC. When the energy deposited in a given pixel by an electron is greater than the pixel activation threshold value, the pixel is activated. The problem lies in when an electron lands on the intersection of pixels. A low pixel activation threshold will lead to the electron depositing enough energy in all the pixels and activating all of them, resulting in overcounting. A high threshold will lead to the electron not depositing enough energy in any of the pixels and activating none of them, resulting in undercounting.

To study the relationships between sensor layer thickness and pixel activation threshold on the modulation transfer function (MTF) and detective quantum efficiency (DQE) of our system, we modeled the spread of electrons using a Monte Carlo simulation in a 500-micron deep silicon layer. We set varying initial beam voltages, from 60keV to 300keV. We created lateral and depth energy spread distributions, tracking electron energy at each location.

Summing over the Y and Z direction (Z direction is the beam direction, X-Y is the lateral plane) of the silicon, we created a line spread function, plotting the energy as a function of X position. Taking the Fourier transform of the LSF produces the MTF3. Then, we analyze the relationship between different silicon thickness and activation thresholds, performing the simulation for different pairs and plotting the MTF at Nyquist frequency (contrast for the smallest features) and DQE at 0 frequency (noise for the largest features).

We are also interested in studying the behavior of the Timepix4, a thinner detector, with a 300µm-deep Si layer. Using this depth and a 150 keV threshold, we analyze the relationship between beam radius and pixel size. We choose this threshold because it produces a good MTF. A 150 keV threshold corresponds to around 72.7% of the total energy deposition. This energy is contained in a radius of around 244µm, or 4.5 pixels. We map counts for each triggered pixel.

The origin receives the most energy, resulting in the greatest counts. Fewer pixels are triggered near the edge. At a low threshold, a higher ratio of beam radius to pixel width is favored and at high threshold, a lower ratio of beam radius to pixel width is favored. I also create a pixel activation map for a 300-micron-deep silicon layer (depth of the Timepix4 sensor layer)[5], and 150keV threshold and look at the relationship between the initial beam spread and the pixel width.

Conclusions and Future Steps:

Higher initial beam voltages have LSF's with broad tails, as the electrons spread further, both laterally and in depth. Smaller initial beam voltages have sharper LSF's, as the electrons don't have as much lateral or depth spread. Lower beam energies are closer to the ideal MTF because they trigger fewer pixels, producing greater contrast. Lower sensor layer thickness and higher threshold (up to an optimal point) favor higher MTF for the same reason.

Lower thicknesses obtain a better MTF for low thickness, because the electrons' spread is limited, resulting in a smaller radius of energy deposition. Each electron activates only a few pixels, resulting in better contrast. The optimal threshold for a good MTF appears to be around 125 keV for 100, 200, 400 and 500-µm depth, after which point the MTF decreases for higher thresholds. 300-um depth seems to have the optimal MTF around 150keV. Thus, there is an optimal point for the threshold, around 100-150keV, for most thicknesses between 100 to 500 µm.

Meanwhile, DQE is favored by higher sensor layer thickness, because a greater depth allows us to capture the entire spread of the electron, resulting in greater signal acquisition. A higher DQE is also favored by a lower pixel activation threshold because it allows each electron to consistently activate many pixels, producing less noise. At a low threshold, a higher ratio of beam radius to pixel width is favored and at high threshold, a lower ratio of beam radius to pixel width is favored. Thus, MTF and DQE are favored by opposite trends in thickness and threshold. It is important to assess these metrics for each distinct detector design to find the optimal conditions for both metrics. In the future, we will perform the Monte Carlo simulation with more electrons (at least 100,000) for a more detailed understanding of the relationship between thickness and threshold.

We may also consider how detectors with fewer pixels can attain maximal signal capture, as MTF and DQE may be easier to optimize for fewer pixels. Additionally, we can quantify the maximal usable imaging speed (MUIS), in addition to MTF and DQE, to assess different detector designs.

Acknowledgements:

Thank you to my mentor, Steven E. Zeltmann, and Principal Investigator, Professor David Muller for their support and guidance on this project. Thank you to the NSF/SRC SUPREME REU Program and the Cornell Nanoscale Facility (NNCI-2025233) for funding and supporting this project.

References:

[1] S. Karapetyan, S. Zeltmann, T.-K. Chen, V. D. H. Hou, and D. A. Muller, Visualizing Defects and Amorphous Materials in 3D with Mixed-State Multislice Electron Ptychography, Microscopy and Microanalysis 30, (2024).

[2] H. T. Philipp et al., Very-High Dynamic Range, 10,000 Frames/Second Pixel Array Detector for Electron Microscopy, Microsc Microanal 28, 425 (2022).

[3] M. W. Tate et al., High Dynamic Range Pixel Array Detector for Scanning Transmission Electron Microscopy, Microsc Microanal 22, 237 (2016).

[4] G. McMullan, S. Chen, R. Henderson, and A. R. Faruqi, Detective quantum efficiency of electron area detectors in electron microscopy, Ultramicroscopy 109, 1126 (2009).

[5] N. Dimova et al., Measurement of the Resolution of the Timepix4 Detector for 100 keV and 200 keV Electrons for Transmission Electron Microscopy, Nuclear Instruments and Methods in Physics Research Section A: Accelerators, Spectrometers, Detectors and Associated Equipment 1075, 170335 (2025).

[6] A. Gnanasambandam and S. H. Chan, Exposure-Referred Signal-to-Noise Ratio for Digital Image Sensors, arXiv:2112.05817.

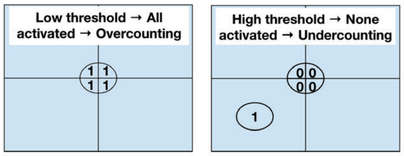

Figure 1: When an electron lands on intersection of pixels, there may be overcounting if the pixel activation threshold is too low and undercounting if the threshold is too high.

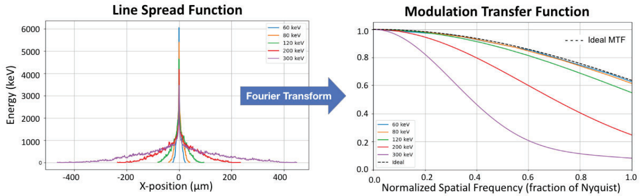

Figure 2: This line spread function (LSF) sums all the energy deposited from 1000 electrons in the Y and Z directions and plots the energy distribution as a function of X position. The Fourier transform of the LSF is the MTF.

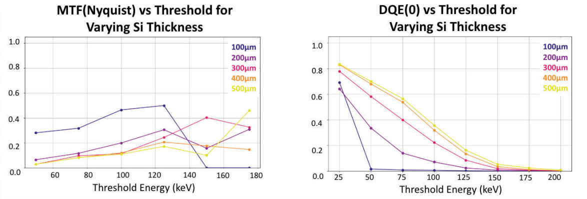

Figure 3: MTF at Nyquist frequency and DQE at zero frequency for varying silicon thicknesses and pixel activation thresholds.

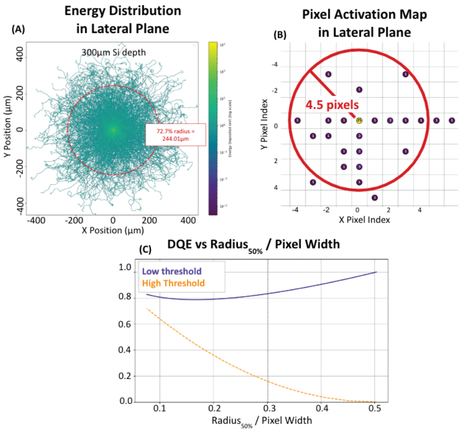

Figure 4: (A) Radius of energy distribution that corresponds to a 150keV threshold. (B) Pixel activation map for 300-µm thick silicon layer. (C) Relationship between ratio of radius where 50% of energy is distributed to pixel width and DQE.

Initiated CVD (iCVD) Polymerization in Liquid Crystal to Synthesize Polymer Particles

CNF Summer Student: Eva Reed
Student Affiliation: Chemical Engineering, Princeton University

Summer Program(s): 2025 Cornell NanoScale Facility Research Experience for Undergraduates (CNF REU) Program, SUPREME REU

Principal Investigator(s): Nicholas Abbott, Rong Yang

Mentor(s): Shiqi Li

Primary Source(s) of Research Funding: Future Manufacturing award to Cornell Chemical Engineering, FMRG: Cyber: Scalable Precision Manufacturing of Programmable Polymer Nanoparticles Using Low-temperature Initiated Chemical Vapor Deposition Guided by Artificial Intelligence, funded by the National Science Foundation under award CMMI-2229092

Contact: ryang@cornell.edu, nla34@cornell.edu, er564@cornell.edu, sl2869@cornell.edu

Summer Program Website(s): https://cnf.cornell.edu/education/reu

Research Group Website: https://theyanglab.com/

Primary CNF Tools Used: Leica 300 CPD, Zeiss Supra SEM

Abstract:

Synthesis schemes targeting specific nanoscale polymer architectures have the potential to advance the efficacy of polymer materials for applications in biomaterials and beyond as tunable material solutions [1]. In our current work, we expand previous investigations of the synthesis pathway of divinylbenzene (DVB) via initiated chemical vapor deposition (iCVD) templated in nematic liquid crystals to begin to explore polymerization with alternative monomers and process conditions. Understanding the effect of tuning the precursor concentrations and substrate properties on the resultant polymer architectures will empower future efforts to produce shape-controlled polymer particles within this synthesis pathway.

Summary of the Research:

Many existing methods to control polymer microparticle architectures involve physical manipulations, which are difficult to scale [1]. Initiated chemical vapor deposition (iCVD) within a liquid crystal (LC) template provides a pathway to construct polymer nanoscale and microparticles with specific architectures achievable based on the reaction conditions [2]. In iCVD, the polymer precursors–the monomer and initiator–are delivered continuously in vapor phase into a chamber alongside an inert carrier gas. A superheated filament radicalizes the initiator to allow the polymerization reaction to proceed. As the monomer and initiator molecules adsorb onto the substrate, free-radical polymerization occurs. iCVD eliminates the need for solvent-mediated reactions, which can result in impure polymer products, impacting the functionality and applicability of functionalized polymeric materials [3].

The innovation that inspired this project is the use of a liquid crystal (E7, a commodity liquid crystal containing a eutectic mixture of cyanobiphenyls and terphenyls) as a templating material rather than an isotropic (disordered) liquid. Liquid crystals are a phase of matter in between liquid and crystalline solids that acquire exciting and useful properties from heightened orientational and positional ordering of their constituent molecular subunits [5]. Researchers have taken advantage of the molecular level organization in these materials in iCVD systems to guide the polymerization process and control the particles' final conformation [2]. The identity of the substrate on which the film is prepared controls the properties and orientation of the mesogens within the LC thin-film. At the LC-air interface E7 adopts a perpendicular anchoring scheme while at the interface with untreated glass the mesogens will be anchored planarly in multi-domains. Chemical treatments octadecyltrichlorosilane (OTS) and Dimethyloctadecyl(3-(trimethoxysilyl)propyl)ammonium chloride (DMOAP) result in planar anchoring at the LC-substrate surface as well as inducing a single homeotropic domain across the LC film [1]. Representative illustrations of the different anchoring conditions are included in Figure 1. These treatment schemes offer the researcher an additional layer of control to the polymer template during the reaction. In addition to comparing polymer products on substrates with homolayers of OTS, and DMOAP treatments, gradient substrates prepared by the Genzer group at NC State–gradients of OTS to glass, DMOAP to glass,

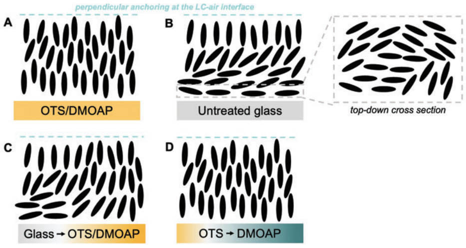

Figure 1: Illustration of anchoring effects on E7 for different substrate types.

and OTS to DMOAP counter gradients–were reacted to provide a comparison of both anchoring condition and the impact of anchoring strength and surface energy [5].

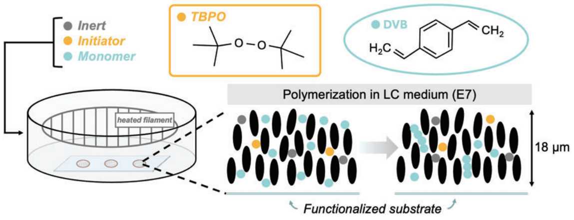

Figure 2: Schematic of in-lab set up for iCVD. Adapted from [1]: Jain, A. Science Advances 2024, 10 (45). https://doiorg/10.1126sciadv.adp5573.

Our experimental system, illustrated in Figure 2, reacts with controlled amounts of vaporized monomer and initiator tert-butyl peroxide (TBPO). The reaction takes place in a TEM grid containing nematic phase liquid crystal films (E7, TNI=60-63°C) mounted on a range of untreated and treated substrates. The chamber pressure is regulated to 150 mTorr and the sample stage is maintained at 20 °C. The reaction process is monitored in situ by a long focal length set up of a Keyence VHX 970F microscope and after reaction progress has been halted by SEM, confocal imaging, and microscopy on an Olympus BX41 microscope equipped with 4× and 20× objectives. Reactions were carried out at both high initiator to monomer ratios (~0.7 Monomer/Initiator) and low ratios (~0.15) at times ranging from 75 to 140 minutes. Critical point drying was employed to remove liquid crystal films while preserving the particles formed for imaging by SEM [1].

Conclusion and Future Steps:

Optical micrographs of films prepared on glass and homolayers of OTS and DMOAP showed that arrays of polymer nanospheres formed with greater regularity and covered a higher percentage of the available film area on DMOAP and glass than the OTS substrate (Figure 3). Analysis of particle sizes showed little significant variation in particle diameter between homolayer substrates: an observation confirmed with SEM imaging of representative polymer particles and particle clusters (Figure 4). Reactions performed on gradient films mirror this trend, with the sections of the film treated with DMOAP displaying a greater proportion of particle arrays than OTS. Analysis of reactions on the OTS to DMOAP gradient film further confirmed this trend, indicating that the anchoring orientation did not impact the formation of particle arrays. An implication of this finding is that the polymerization process occurs in the bulk LC or at the LC-air interface rather than on the LC-substrate interface. This hypothesis was supported by confocal microscopy which revealed that the nanosphere particles were positioned along a single focal plane within the LC bulk.

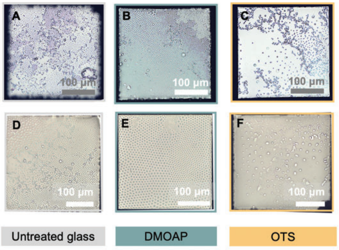

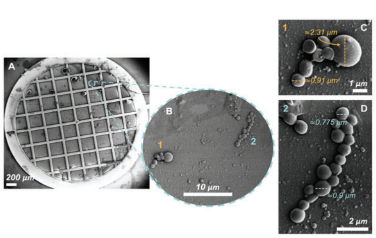

Figure 3 (Left) : White balanced optical micrographs showing the polymer products formed from high initiator to monomer ratio conditions (17.1 mTorr P(TBPO)/25.1 mTorr P(DVB)) (A-C) and low initiator to monomer ratio conditions (10.6 mTorr P(TBPO)/69 mTorr P(DVB)) (D-F). The DMOAP treated films (B,E) create more regular particle arrays than the untreated glass films (A,D) or the OTS treated films (C,F).
Figure 4 (Right): SEM images showing polymer nanoparticles. Low magnification (A) and high magnification are shown (B) alongside measurements of the range of particle diameters are also displayed (C, D).

Determining the location of particle formation during the initiation and growth processes deepens knowledge of the dynamics of the polymerization reaction and, in turn, will offer researchers greater insight into controlling the polymer architectures formed within the LC films. Future work will bring in more advanced imaging and characterization techniques, including AFM and advanced confocal microscopy, to detail this polymerization process and allow our understanding to empower iCVD studies of other monomer systems.

Acknowledgements:

This work was performed in part at the Cornell NanoScale Facility, a member of the National Nanotechnology Coordinated Infrastructure (NNCI), which is supported by the National Science Foundation (Grant NNCI-2025233). This work is further funded by a Future Manufacturing award to Cornell Chemical Engineering, FMRG: Cyber: Scalable Precision Manufacturing of Programmable Polymer Nanoparticles Using Low-temperature Initiated Chemical Vapor Deposition Guided by Artificial Intelligence, funded by the National Science Foundation under award CMMI-2229092 and finally the NIH S10RR025502 grant to the BRC for the Zeiss LSM 710 confocal microscope.

References:

[1] Jain, A et al., Single-step synthesis of shaped polymeric particles using initiated chemical vapor deposition in liquid crystals. Sci. Adv. 2024 10, eadp5573. DOI:10.1126/sciadv.adp5573..

[2] Cheng, Z.; Lee, H.; Kim, T.; et al. Templated Nanofiber Synthesis via Chemical Vapor Polymerization into Liquid Crystalline Films. Science 2018, 360 (6391), 804–808. https://doi.org/10.1126/science.aar8449

[3] Bradley, L. C.; Gupta, M. Microstructured Films Formed on Liquid Substrates via Initiated Chemical Vapor Deposition of Cross-Linked Polymers. Langmuir 2015, 31 (29), 7999–8005. https://doi.org/10.1021/acs.langmuir.5b01663.

[4] De Luna, M. S.; Torres, C. A.; Chen, H.; et al. Interactions between Polymers and Liquids during Initiated Chemical Vapor Deposition onto Liquid Substrates. Mol. Syst. Des. Eng. 2020, 5 (1), 15–21. https://doi.org/10.1039/c9me00087a.

[5] Clare, B. H.; Efimenko, K.; Fischer, D. A.; Genzer, J.; Abbott, N. L. Orientations of Liquid Crystals in Contact with Surfaces That Present Continuous Gradients of Chemical Functionality. Chem. Mater. 2006, 18 (9), 2357–2363. https://doi.org/10.1021/cm052537n.

Computer Vision Applied to Polymer Particles in Liquid Crystal (LC) to Enable On-the-Fly Characterization of their Morphology and Size Distribution, Among Other Properties

CNF Summer Student: William Sober
Student Affiliation: Physics, Amherst College

Summer Program(s): 2025 Cornell NanoScale Facility Research Experience for Undergraduates (CNF REU) Program, SUPREME REU

Principal Investigator(s): Nicholas Abbott, Fengqi You

Mentor(s): Soumyamouli Pal

Primary Source(s) of Research Funding: National Science Foundation award NNCI- 2025233, Center for Energy Efficient Magnonics (DE-AC02- 76SF00515), Department of Energy Office of Science, Basic Energy Sciences (DE-SC0019997)

Contact: nla34@cornell.edu, fengqi.you@cornell.edu, willsober@gmail.com

Summer Program Website(s): https://cnf.cornell.edu/education/reu

Abstract:

Monitoring polymerization reactions in-situ provides many advantages like real-time feedback for tuning conditions and viewing undisturbed growth. However, image quality can be reduced due to difficulties in viewing the reaction such as vibrations and long working distances with a microscope. This project explores approaches to enhance lower quality in-situ microscope images of polymers in liquid crystal from an initiated chemical vapor deposition (iCVD) reactor by using an enhanced super resolution generative adversarial network (ESRGAN). To train ESRGAN, polymer test systems were set up in an iCVD reactor, and low-quality in-situ images of the polymers were taken along with corresponding high-quality ex-situ images. We cropped matching single-cluster images and applied different pre-processing techniques while varying hyperparameters such as learning rate and weight decay. The accuracy of these methods was evaluated with the Structural Similarity Index Measure (SSIM) and visually compared to the reference high-quality images. We found that overall, ESRGAN has strong potential for polymer image enhancement, and changeable hyperparameters gives it versatility for different images. However, further model optimization is needed before it is adapted for real polymerization images. The adaptability of ESRGAN makes this approach applicable for more varied use like new types of polymers or different microscope setups.

Summary of Research:

Initiated chemical vapor deposition (iCVD) in liquid crystal (LC) has the capability to produce tunable polymer growths like nanospheres with potential for use in drug delivery or separations for chromatography1. In-situ monitoring of the reaction is possible through a window with a long-distance focal length lens Keyence VHX 970F microscope. However, issues with vibrations and external noise are compounded by the viewing distance, so the images from the microscope are blurry and low-quality. The samples can be high-quality ex-situ imaged by an Olympus BX41 microscope although this requires stopping the reaction to remove samples, which can also disturb polymers.

With the assistance of a machine learning-based approach, we can enhance the in-situ images to more closely match the quality of the high-quality ex-situ images. Previous preliminary research has found that the enhanced super-resolution generative adversarial networks (ESRGAN) model outperforms other models for this purpose.

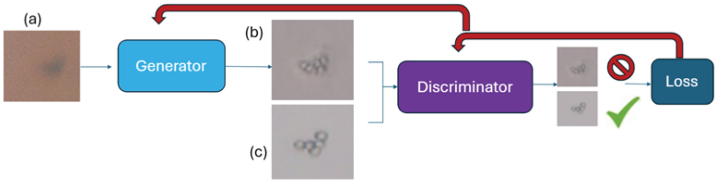

Figure 1: Diagram of ESRGAN structure. The generator takes low-quality images (a) and enhances them (b). The discriminator detects real (c) from fake images and then model updates from loss functions.

ESRGAN has two key components: the generator and the discriminator (Figure 1). For training, the generator takes a low-quality image and tries to enhance it to look like a high-quality image. The discriminator is then given that enhanced image along with the actual high-quality image and tries to determine which is the real one. Then the model calculates loss functions for how poorly the generator and discriminator performed so that the generator and discriminator can improve their weights. This process is iterative, with the generator and discriminator improving each other thousands of steps. In addition to the images used for training, many are set aside solely for testing the performance of the model to limit overfitting.

We tried multiple configurations of ESRGAN by varying hyperparameters, which are parameters in ESRGAN that can be adjusted to change how the model learns. We mainly looked at learning rate (.0001-.001), weight decay (0 or .0001), and number of epochs(10-300).

A test system was created using commercially available 5µ polystyrene spheres dispersed in the liquid crystal, allowing for fixed particle sizes and faster data collection compared to growing polymers.

Training the model with images of the entire LC grid causes complications with identifying the same polymer across low and high-quality images, therefore we used 64x64 pixel cropped patches, 32x32 pixel downscaled cropped patches, and 64x64 images where the contour of the particle was cropped and the background was replaced with white (Figure 2).

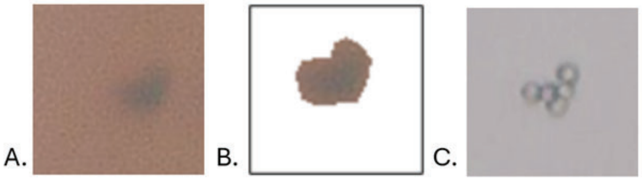

Figure 2: A. Low quality cropped polymer cluster, with B. its contour cropped and C. their high-quality reference. These images were used as three different training inputs for ESRGAN.

Conclusions and Future Steps:

As an exploratory project, a main goal of this project was to explore the feasibility of different approaches. Weight decay stabilized training of the 64x64 images and produced best overall results. Conversely, with 32x32 images, removing weight decay allowed the model to make riskier, but successful, improvements. While contour cropping the particles was not effective, ESRGAN was generally robust against noise. The main limitation was particle size estimation accuracy (Figure 3), likely due to inconsistent scaling during preprocessing. Remaking the dataset may resolve this issue. Overall, these findings establish a strong foundation for adapting ESRGAN for polymerization imaging.

For future development, ESRGAN should be adapted to work on real polymerization images, and polymers of different sizes. Training on lower magnification images would be more effective at capturing more polymers in the frame, fitting six full grids into the frame instead of one. Implementing the model with video capabilities would aid in faster and more convenient analysis during reactions. Applying a different de-noising program to the low and high quality images could also potentially increase the ground truth image quality and accelerate training.

References:

[1] Apoorva Jain et al., Single-step synthesis of shaped polymeric particles using initiated chemical vapor deposition in liquid crystals. Sci. Adv. 10,eadp5573(2024).DOI:10.1126/sciadv.adp5573

AJA Sputter 1 & 2 Materials Characterization

CNF Summer Student: Irwin Wang
Student Affiliation: Department of Engineering, Cornell University

Summer Program(s): 2025 Cornell NanoScale Facility Research Experience for Undergraduates (CNF REU) Program
Mentor(s): Tom Pennell, Cornell NanoScale Science and Technology Facility, Cornell University
Primary Source(s) of Research Funding: National Science Foundation under Grant No. NNCI-2025233,
Contact: iw87@cornell.edu, tjp83@cornell.edu

Abstract:

The application of sputtering for thin-film deposition has been a staple technique for decades, and its importance is growing with the expansion of nanotechnology. As new materials are developed to address unique challenges, their characterization within sputtering tools becomes increasingly essential. This study investigates the effects of various sputtering conditions on key film properties. The primary objective was to understand the relationship between sputtering parameters and both film Deposition Rate and Film Stress, while also measuring secondary characteristics such as Sheet Resistance and Index of Refraction. Depositions were performed using AJA 1 and AJA 2 Sputtering machines. The primary variable was chamber pressure, tested at three levels: 3 mTorr, 7 mTorr, and 20 mTorr. Deposition times were controlled to achieve a target film thickness between 100-300 nm for all samples. For a range of previously uncharacterized materials (Zr, Nb, Ru, Si3O4, Hf, NiO), trends for deposition rate and film stress were consistent with existing data. Specifically, increased chamber pressure generally resulted in a lower deposition rate. Film stress, as plotted and recorded against pressure, also matched general trends found with similar elements on other sputtering tools under different conditions. The key finding of this research was the consistency of these trends. The results suggest that the trends in film stress are element-specific and predictable. This research provides a foundation for future studies, allowing researchers to more accurately predict and plan for the effects of deposition parameters when working with novel materials.

Summary of Research:

Sputtering is a common deposition technique used to create the thin films necessary for building devices. Materials are selected based on their desired electrical, physical, or chemical properties. To ensure these desired effects are achieved, a standard table of characterization data is crucial, especially since sputtering tools can differ from each other even under "identical" conditions. Additionally, secondary effects like film stress are key considerations, as they can lead to device or film failure.

This research focused on collecting comprehensive data for a set of new materials on the AJA 1 and AJA 2 sputtering machines. The experimental process involved the following steps:

1. Wafer Preparation: Wafers underwent a MOS clean to remove organic contaminants and unwanted metals.
2. Native Oxide Removal: Prior to deposition, wafers were submerged in a two-minute buffered oxide etch to remove the native oxide layer.
3. Deposition: Experimental conditions were varied, with deposition times estimated to achieve a target thin-film thickness of 100-300 nm.
4. Data Collection: A patterned chip, or "witness sample," was attached to the carrier during deposition. After liftoff, a profilometer was used to measure the film height, assuming uniform deposition. This data was then used to measure film stress using a Flexus tool. Additional measurements were taken using a four-point probe for sheet resistance and an ellipsometer for refractive index.

Conclusions and Future Steps:

Analysis of the data reveals consistent trends between sputtering pressure and the resulting film properties, particularly for deposition rate and film stress. For most materials, an increase in chamber pressure correlated with a decrease in deposition rate, a widely observed phenomenon in sputtering processes. Similarly, film stress exhibited predictable, element-specific responses to pressure changes, with a clear shift from tensile to compressive stress in several cases (e.g., Zr, Nb) and a general trend of becoming less compressive with increasing pressure (e.g., Si3N4, Hf, Ti). These consistent, predictable trends suggest that film properties can be reliably tuned by controlling chamber

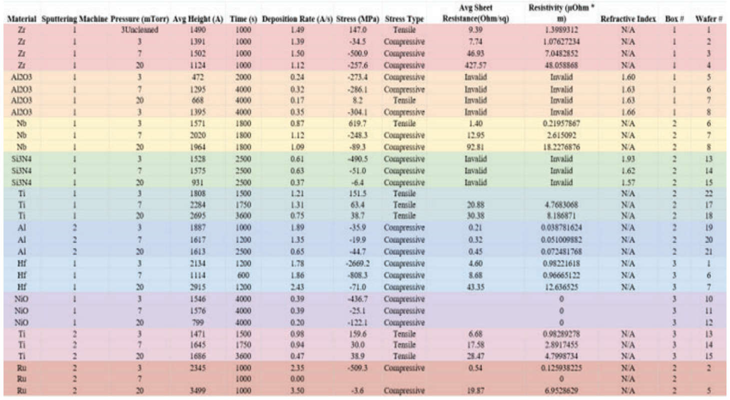

Material	Sputtering Machine	Pressure (mTorr)	Avg Height (A)	Time (s)	Deposition Rate (A/s)	Stress (MPa)	Stress Type	Avg Sheet Resistance(Ohm/sq)	Resistivity (µOhm * m)	Refractive Index	Box #	Wafer #
Zr	1	3Uncleaned	1490	1000	1.49	147.0	Tensile	9.39	1.3989312	N/A	1	1
Zr	1	3	1391	1000	1.39	-34.5	Compressive	7.74	1.07627234	N/A	1	2
Zr	1	7	1502	1000	1.50	-500.9	Compressive	46.93	7.0482852	N/A	1	3
Zr	1	20	1124	1000	1.12	-257.6	Compressive	427.57	48.058868	N/A	1	4
Al2O3	1	3	472	2000	0.24	-273.4	Compressive	Invalid	Invalid	1.60	1	5
Al2O3	1	7	1295	4000	0.32	-286.1	Compressive	Invalid	Invalid	1.63	1	6
Al2O3	1	20	668	4000	0.17	8.2	Tensile	Invalid	Invalid	1.63	1	7
Al2O3	1	3	1395	4000	0.35	-304.1	Compressive	Invalid	Invalid	1.66	1	8
Nb	1	3	1571	1800	0.87	619.7	Tensile	1.40	0.21957867	N/A	2	6
Nb	1	7	2020	1800	1.12	-248.3	Compressive	12.95	2.615092	N/A	2	7
Nb	1	20	1964	1800	1.09	-89.3	Compressive	92.81	18.2276876	N/A	2	8
Si3N4	1	3	1528	2500	0.61	-490.5	Compressive	Invalid	Invalid	1.93	2	13
Si3N4	1	7	1575	2500	0.63	-51.0	Compressive	Invalid	Invalid	1.62	2	14
Si3N4	1	20	931	2500	0.37	-6.4	Compressive	Invalid	Invalid	1.57	2	15
Ti	1	3	1808	1500	1.21	151.5	Tensile			N/A	2	22
Ti	1	7	2284	1750	1.31	63.4	Tensile	20.88	4.7683068	N/A	2	17
Ti	1	20	2695	3600	0.75	38.7	Tensile	30.38	8.186871	N/A	2	18
Al	2	3	1887	1000	1.89	-35.9	Compressive	0.21	0.038781624	N/A	2	19
Al	2	7	1617	1200	1.35	-19.9	Compressive	0.32	0.051009882	N/A	2	20
Al	2	20	1613	2500	0.65	-44.7	Compressive	0.45	0.072481768	N/A	2	21
Hf	1	3	2134	1200	1.78	-2669.2	Compressive	4.60	0.98221618	N/A	3	1
Hf	1	7	1114	600	1.86	-808.3	Compressive	8.68	0.96665122	N/A	3	6
Hf	1	20	2915	1200	2.43	-71.0	Compressive	43.35	12.636525	N/A	3	7
NiO	1	3	1546	4000	0.39	-436.7	Compressive		0		3	10
NiO	1	7	1576	4000	0.39	-25.1	Compressive		0		3	11
NiO	1	20	799	4000	0.20	-122.1	Compressive		0		3	12
Ti	2	3	1471	1500	0.98	159.6	Tensile	6.68	0.98289278	N/A	3	13
Ti	2	7	1645	1750	0.94	30.0	Tensile	17.58	2.8917455	N/A	3	14
Ti	2	20	1686	3600	0.47	38.9	Tensile	28.47	4.7998734	N/A	3	15
Ru	2	3	2345	1000	2.35	-509.3	Compressive	0.54	0.125938225	N/A	2	2
Ru	2	7		1000	0.00				0	N/A	2	
Ru	2	20	3499	1000	3.50	-3.6	Compressive	19.87	6.9528629	N/A	2	5

Figure 1.

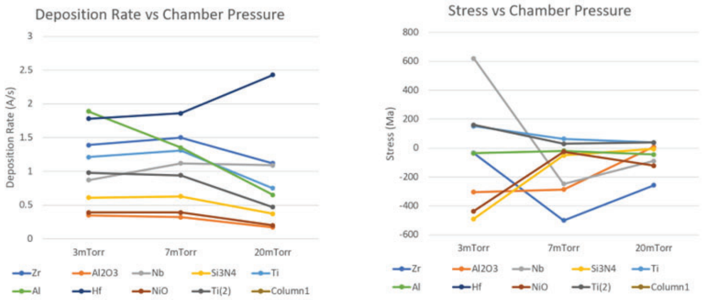

Figure 2.

pressure. The findings not only validate established sputtering principles but also provide a critical starting point for future researchers to optimize deposition conditions for a wide range of materials. In the future, this research hopes to expand its characterization by looking at film uniformity and roughness.

Acknowledgements:

Special thanks to Tom Pennell and the CNF staff for their support and mentorship throughout this whole research experience. I would like to acknowledge the CNF and their generosity for still offering a program after the 2025 AEOP program was canceled. This work was funded by the National Science Foundation via grants no. NNCI-2025233

Effects of Reactive Ion Etching on Conductivity of NbAs

CNF Summer Student: Iris You
Student Affiliation: Department of Materials Science and Engineering, Rutgers University

Summer Program(s): 2025 Cornell NanoScale Facility Research Experience for Undergraduates (CNF REU) Program, SUPREME REU
Principal Investigator(s): Judy J. Cha, Department of Materials Science and Engineering, Cornell University
Mentor(s): Yeryun Cheon, Department of Physics, Cornell University

Primary Source(s) of Research Funding: National Science Foundation under Grant No. NNCI-2025233, SUPREME Research Experience for Undergraduates #2349310

Contact: jc476@cornell.edu, yc2458@cornell.edu, icy2@scarletmail.rutgers.edu

Summer Program Website(s): https://cnf.cornell.edu/education/reu
Primary CNF Tools Used: Veeco Icon AFM, PT 720-740 RIE, Zeiss Supra SEM, Zeiss Ultra SEM

Abstract:

The continuation of Moore's Law has resulted in persistent downscaling of transistors and current copper (Cu) interconnects resulting in performance bottlenecks when interconnect dimensions are below the electron mean free path (~40 nm) of Cu [1]. Since Cu exhibits high resistance at such dimensionsscales, resistance-capacitance (RC) signal delay and high-power consumption result in lower overall performance [1]. Topological semimetals possess topologically protected conducting surface states that result in low resistivity at low dimensions [2]. Thus, they are of interest in the discovery of novel materials to replace Cu interconnects.

One such material is the Weyl semimetal niobium arsenide (NbAs). We have shown single crystal NbAs nanowires, produced by nanomolding, which has previously been shown to possess conductivity comparable to that of Cu at desirable length scales [3]. However, the promising resistivity trends of NbAs must be studied further as a function of size at sizes between these 10 nm and bulk crystals. has not been extensively studied aIn addition, nd the effects of surface damage on conductivity due to various processing techniques has not been reported must be explored.

In this work, we use reactive ion etching (RIE) to reduce the size of focused ion beam (FIB) produced NbAs nanoscale samples prepared by focused ion beam (FIB) milling and examine the trends in resistivity as a function of NbAs size and RIE conditions. We show that NbAs can be etched roughly linearlycontrollably and reliably under mild RIE conditions and resistivity continuously decreases as NbAs is reduced in size. This allows for greater understanding of resistivity scaling and its mechanisms in NbAs.

Summary of Research:

We etched fabricated single crystal NbAs nanoslabs using FIB milling and created electrical devices. A completed device is shown in Figure 1. Length and width measurements were extracted from scanning electron microscopy (SEM) images. Atomic force microscopy (AFM) was used to measure the height of the slabs. The cross-sectional area of the slabs was calculated from this data. Resistance measurements were acquired via 4-point probe current and voltage measurements. The measured resistance was converted to resistivity When combined with dimensional data, we were able to calculate the resistivity of our NbAs slabsfor the NbAs slabs.

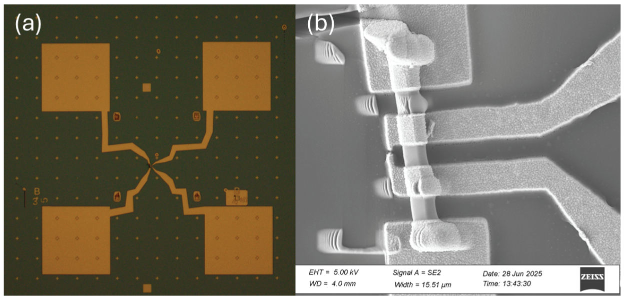

Figure 1: (a) Optical image of NbAs Device 3. (b) SEM image of Device 3.

The slabs were successively etched with RIE at 10 mTorr with 60 W of power using 30 sccm Cl_2 and 10 sccm CF_4 at varying etching times. Afterwards, AFM and resistance measurements were repeated to observe the changes in height and resistivity of the slabs. Figure 2 shows how uncertainty in the height measurements and thus etching calibration occurs due to the shape of the AFM tip as well as the geometry of the sample placed on the substrate. Additionally, we take into accountconsider the etching of the substrate when calculating the effects of etching. Overall, we are able to etched our devices at approximately 5-7 nm per minute.

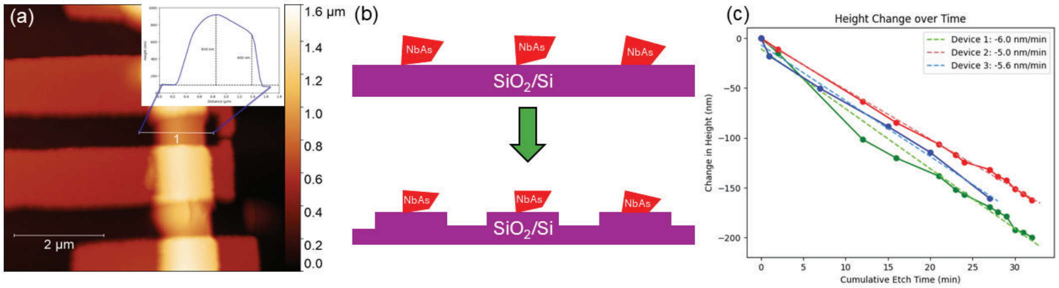

Figure 2: (a) AFM image with height profile of Device 3 pre-etching. (b) Schematic showing etching of substrate layer during RIE. (c) Plot of NbAs height change with respect to etching time.

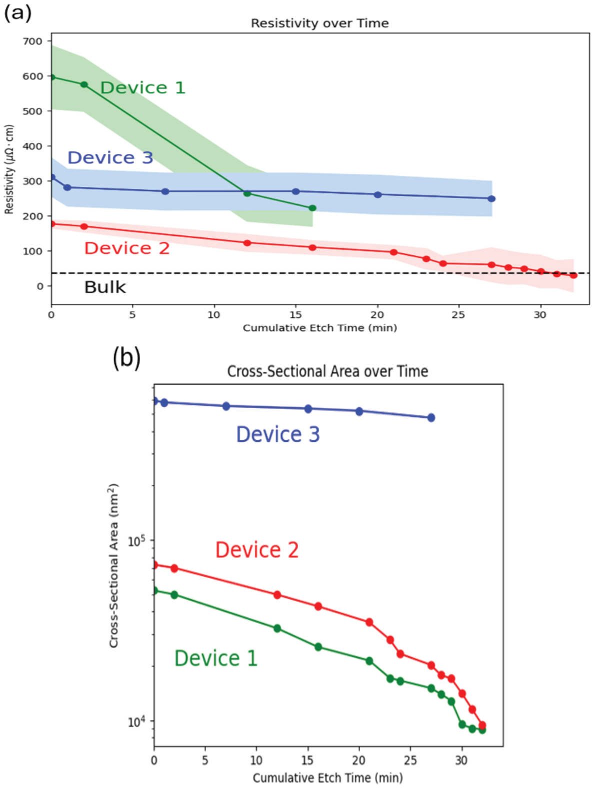

Figure 3: (a) Resistivity of NbAs devices as a function of total etch time. (b) Cross-sectional area of nanoslabs as a function of etch time.

There is a clear decreasing trend in resistivity as a function of cumulative etching time as shown in Figure 3. This supports the resistivity scaling trend of NbAs, and as the surface to volume ratio continuously increases from etching, the resistivity eventually falls below the bulk value while still decreasing.

SEM images in Figure 4 show considerable surface damage from RIE on the surface of the NbAs nanoslabs. However, the overall conductivity of the samples continues to exhibit decreasing behavior despite the surface damage.

Conclusions and Future Steps:

We progressively etched NbAs nanoslab devices through RIE at an etching rate of approximately 5-7 nm/min. We were further able to show that RIE is effective in reducing the size of NbAs without adversely affecting conductivity. We confirmed promising trend of decreasing resistivity for NbAs at decreasing dimensions in the nanoscale regime.

Future work would involve improving height measurements which are currently overestimated due to the geometry of the sample and FIB placement. Better methods to measure cross-sectional area would result in less overall error and a clearer understanding of our results. We would also like to continue investigating the surface contributions to the resistivity scaling of NbAs with RIE etching in future devices and investigate even less destructive methods of size reduction, whether it be through RIE or other means.

References:

[1] Joon-Seok Kim et al., Addressing interconnect challenges for enhanced computing performance. Science 386, eadk6189 (2024). DOI:10.1126/science.adk6189

[2] Asir Intisar Khan et al., Surface conduction and reduced electrical resistivity in ultrathin noncrystalline NbP semimetal. Science 387,62-67(2025). DOI:10.1126/science.adq7096

[3] Cheon, Y et al. https://arxiv.org/abs/2503.04621 (2025).

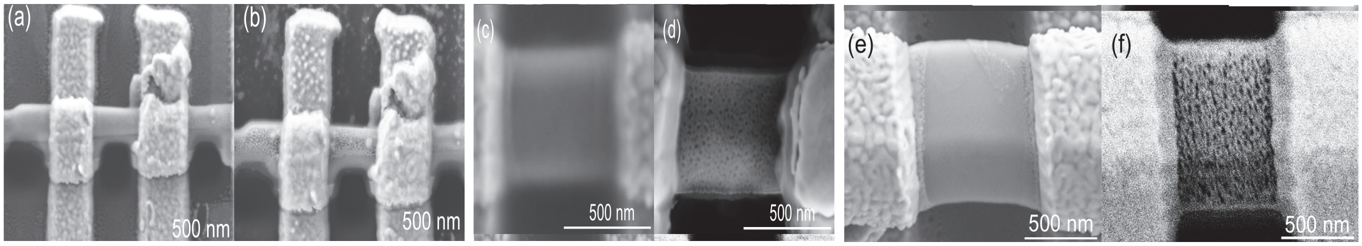

Figure 4: (a) Pre-etch SEM of Device 1. (b) Post-etch SEM of Device 1. (c) Pre-etch SEM of Device 2. (d) Post-etch SEM of Device 2. (e) Pre-etch SEM of Device 3. (f) Post-etch SEM of Device 3.

Synthesis of Temperature-Responsive Hydrogel Particles for Hydraulic Control of Cooled Short Circuits

CNF Project Number: 1356-05
Principal Investigator(s): Ulrich Wiesner
User(s): Danni Tang

Affiliation(s): Department of Materials Science and Engineering, Cornell University

Primary Source(s) of Research Funding: U.S. Department of Energy (DOE), Office of Energy Efficiency andRenewable Energy (EERE), Office of Technology Development, Geothermal Technologies Program (DE-EE0009786.000)

Contact: ubw1@cornell.edu, dt427@cornell.edu

Research Group Website: http://wiesner.mse.cornell.edu/

Primary CNF Tools Used: Heidelberg DWL2000, ABM Mask Aligner, AMST MVD100, PDMS Station

Abstract:

Enhanced geothermal systems (EGS) offer a promising pathway for harvesting subsurface heat from previously unsuitable regions of the planet. Their operational efficiency, however, is often compromised by the occurrence of “short circuits”, which arise from uneven permeability distributions within rock fracture networks. These short circuits can lead to preferential fluid flow through highly permeable regions, resulting in localized heat depletion, lower energy production efficiency, and even possible system failure. To mitigate this issue, temperature-responsive poly(N-isopropylacrylamide) (pNIPAM)-based hydrogel particles are designed to mitigate the issue by reducing the local permeability of “short circuit” regions. A parallel step emulsifier device is fabricated at CNF to produce particles with a narrow size distribution, and fundamental rheology tests will be conducted on the produced particles to understand their jamming behavior.

Summary of Research:

The “short circuit” issue arising from uneven permeability distributions within fracture systems is one of the major challenges in Enhanced Geothermal Systems (EGS). When a fluid gets injected underground, it preferably flows through highly permeable paths. As a result, these regions are rapidly drained of heat, leading to a premature thermal breakthrough and system failure [1]. To alleviate this problem, we designed temperature-responsive nanocomposite poly(N-isopropylacrylamide) (pNIPAM)-based microgel particles. As one of the most studied thermosensitive hydrogels, pNIPAM exhibits a reversible entropy-driven volume phase transition, leading to particle expansion at low temperatures and particle contraction at high temperatures [2]. With careful design, these pNIPAM-based particles can expand to up to several hundred times their original volume when the temperature of their local environment falls below a threshold. This could effectively diminish short circuits by decreasing local channel permeability.

To produce thermo-responsive microgels with a narrow size distribution, a parallel step emulsifier was fabricated and optimized at the Cornell Nanoscale Science and Technology Facility (CNF). As of the last reporting period, we started the fabrication of the emulsifier device. Specifically, an emulsifier device adapted from Stolovicki et al. was produced at CNF (Figure 1) [3]. Photolithography was used to make the device master mold. The mold was subsequently used to pattern the final poly(dimethylsiloxane) (PDMS) based device. This device was expected to produce pre-gel droplets with a target size of around 30 µm. The droplets will then be polymerized under a UV source to form the final crosslinked polymer particles.

During this reporting period, our efforts have been focused on further optimizing the device fabrication and droplet production process. A key challenge we encountered in the previous fabrication attempts was the inconsistent bonding of nozzles to glass slides. As illustrated in Figure 2a, the previous bonding process involved first cutting the PDMS into the desired shape and then bonding it to the glass slides. The major issue with this method is that the PDMS is extremely deformable, and therefore even small deformations of the PDMS material can result in insufficient bonding of the channel to the glass substrate, which leads to polydisperse droplet production (Figure 3a).

To address this problem, a new bonding process has been developed. Here, instead of cutting the PDMS into its final shape and directly bonding it to the glass slides, we first cut and bond the whole molded PDMS slab with another plain PDMS slab. Then, we cut the assembled

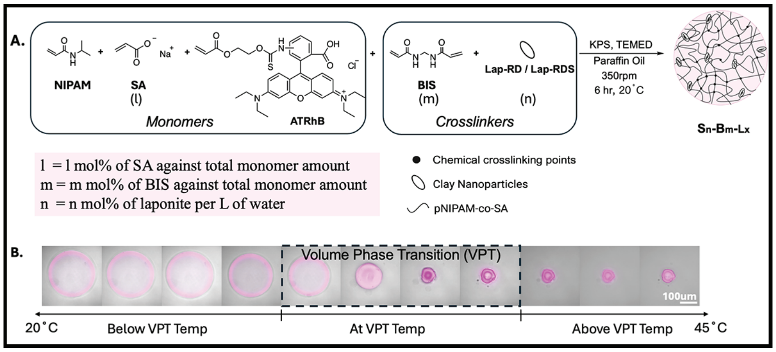

Figure 1: CAD design of the parallel step emulsifier device adapted from the Weitz group [1]. (A) Layer 1; (B) Layer 2; (C) merged images.

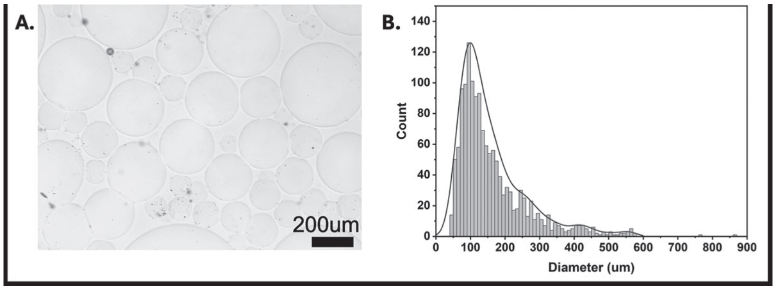

Figure 2: (A) Original PDMS device fabrication process (from the last reporting period) compared to optimized PDMS device fabrication process shown in (B).

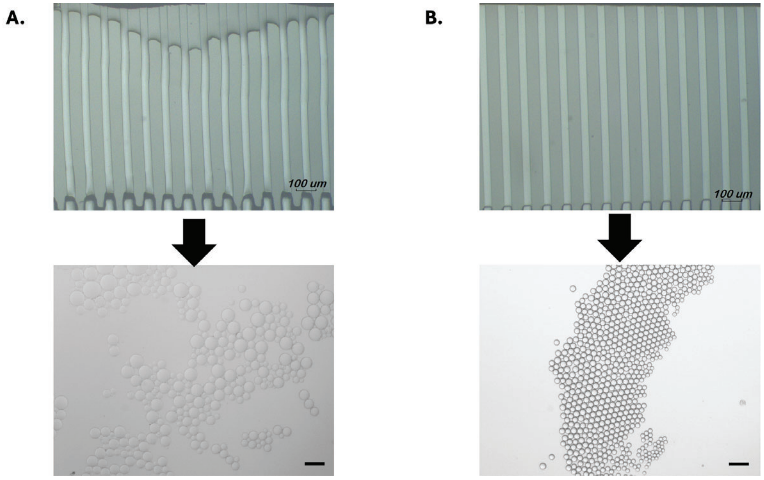

Figure 3: Typical optical images of the device nozzle areas (top) and resulting droplets (bottom) when using (A) the original PDMS device fabrication process (from the last reporting period) versus (B) the optimized PDMS device fabrication process. (Scale bar=100 µm)

PDMS slabs into the final shape of the device and bond it to the glass slides (Figure 2b). This method significantly improves the nozzle bonding quality and allows better production of monodisperse droplets. As shown in Figure 3b, the produced particles exhibit significantly reduced size variation, indicating improved monodispersity.

Conclusions and Future Steps:

In conclusion, we have successfully fabricated a microfluidic device to produce temperature-response polymeric particles for geothermal applications. With further optimization in the PDMS binding process, we were able to produce droplets with narrow size distributions. In the next step, particles with varying compositions will be produced using this device and studied for their rheological behaviors.

References:

[1] Oh, K. W.; Lee, K.; Ahn, B.; Furlani, E. P. Design of Pressure-Driven Microfluidic Networks Using Electric Circuit Analogy. Lab Chip 2012, 12 (3), 515–545. https://doi.org/10.1039/c2lc20799k.

[2] Hirotsu S.; Hirokawa, Y.; Tanaka, T. Volume-Phase Transitions of Ionized N-Isopropylacrylamide Gels. Journal of Chemical Physics 1987, 87 (2), 1392–1395. https://doi.org/10.1063/1.453267.

[3] Stolovicki, E.; Ziblat, R.; Weitz, D. A. Throughput Enhancement of Parallel Step Emulsifier Devices by Shear-Free and Efficient Nozzle Clearance. Lab on a Chip 2017, 18 (1), 132–138. https://doi.org/10.1039/C7LC01037k.

Design and Synthesis of Sequence-Defined Oligopeptoids for Potential Lithographic Use

CNF Project Number: 175709
Principal Investigator(s): Christopher Ober
User(s): Danya Liu, Seungjun Kim

Affiliation(s): Materials Science and Engineering, Cornell University

Primary Source(s) of Research Funding: department of materials science and engineering, National Science Foundation 23-552: Futre of Semiconductors (Fuse)

Contact: cko3@cornell.edu , dl957@cornell.edu, sk3434@cornell.edu

Research Group Website: https://ober.mse.cornell.edu/

Primary CNF Tools Used: AFM-Veeco Icon, ASML PAS 5500/300C DUV Wafer Stepper, and Woollam RC2 Spectroscopic Ellipsometer.

Abstract:

Extreme-ultraviolet (EUV) lithography underpins continued device miniaturization, yet conventional photoresists suffer from stochastic issues and the resolution-sensitivity-roughness trade-off at sub-10 nm dimensions.1, 2 Herein, we present a modular synthetic platform based on sequence-defined peptoids to overcome these limitations. In this work, two distinct oligopeptoid architectures were explored. The first employs a chemical amplification mechanism, using Boc-protected side chains to trigger solubility switching upon acid-catalyzed deprotection.3 Their lithographic performance, using either ionic or non-ionic photoacid generators (PAGs), was evaluated under deep-ultraviolet (DUV) exposure. The second is a creative innovation in which non-ionic PAGs were covalently tethered onto peptoid backbones via copper-catalyzed azide-alkyne cycloaddition, making the PAG itself the solubility-switch moiety and ensuring uniform acid distribution.

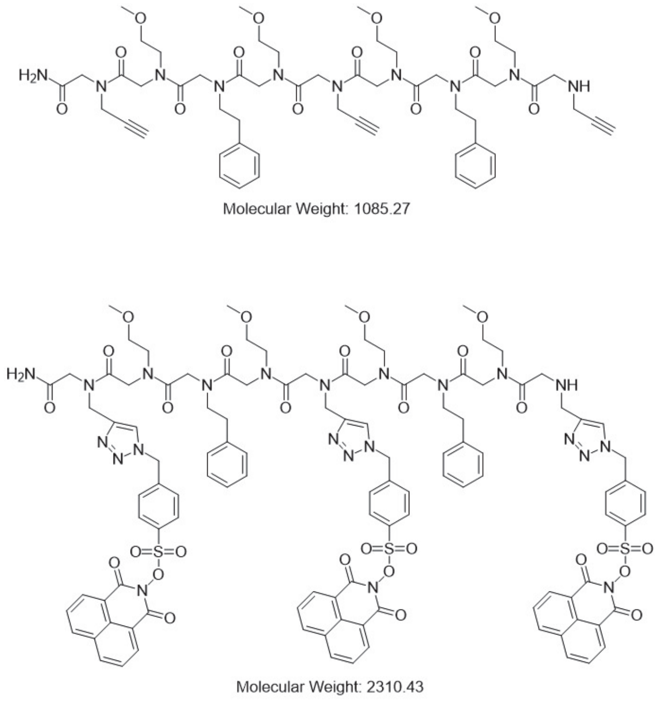

Figure 1: (a) Peptoid structure of PMFMPMFMP 9-mer, designed with propagyl amines as potential sties of click reaction and (b) PAG-incorporated peptoid by click reaction.

Summary of Research:

We designed and synthesized bioinspired, sequence-defined and length-controlled oligopeptoids incorporating both clickable sites and solubility-switch functional groups. Two distinct strategies were explored: one employing Boc-protected tyramines as acid-labile switches in a chemically amplified resist system, and the other utilizing tethered non-ionic PAGs directly integrated into the peptoid backbone.

Thermal stability studies of both the oligopeptoids and PAG components helped determining the suitable post-apply and post-exposure bake temperatures. Through systematic evaluation of key lithographic parameters—including developer composition, TMAH dilution ratios, and film thickness—a set of processing parameters was established to generate discernible patterns under DUV exposure. Intriguingly, a tone-switch behavior was observed in peptoid films formulated with ionic PAGs, wherein thinner films behaved as positive-tone resists while thicker films as negative-tone, highlighting the complex interplay between film morphology and development responses.

Furthermore, a brand new type of resist using tethered PAG as the solubility switch was invented. The CuAAC click reaction was used to tether azide-functionalized PAGs onto peptoid backbones, with LC-MS confirming efficient tri-site conjugation under optimized reaction

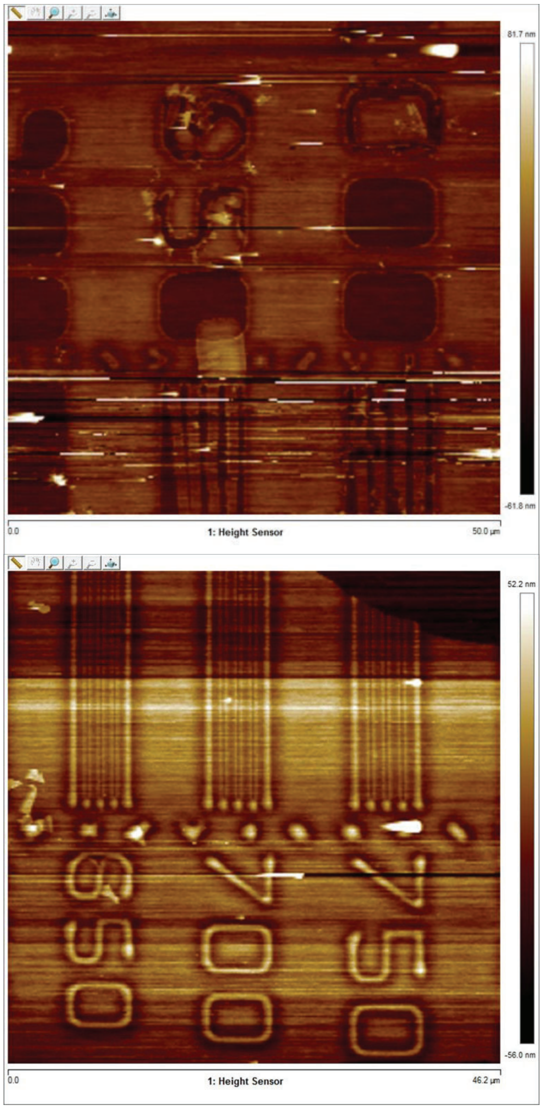

Figure 2: DUV (248 nm) 1:1 Line space pattern; dose 60 mJ/cm2; post-apply and post-exposure bake temperature 110 °C; 40 wt.% TPS-TF, developed in (a) undiluted AZ 726 for 3 seconds and (b) 50× diluted AZ 726 for 45 seconds, observed under AFM.

conditions. Comparative evaluation of purification methods revealed that bypassing the alumina column step significantly improved overall yield particularly due to the low amount of copper catalyst content.

Overall, this study demonstrates a modular synthetic framework for peptoid-based photoresists with tunable chemical functionality and processibility, paving the way for further investigations into their performance under EUV and electron beam lithographic conditions, advancing the development of next-generation organic resist materials.

References:

[1] Enomoto, S.; Machida, K.; Naito, M.; Kozawa, T. In Study of RLS trade-off mitigation utilizing an organotin-containing chemically amplified resist for high sensitivity patterning, International Conference on Extreme Ultraviolet Lithography 2022, SPIE: 2022; pp 101-105.

[2] Fonseca, C.; Head, B.; Shite, H.; Nafus, K.; Gronheid, R.; Winroth, G. In Understanding EUV resist dissolution characteristics and its impact to RLS limitations, Extreme Ultraviolet (EUV) Lithography II, SPIE: 2011; pp 343-353

[3] Tarascon, R.; Reichmanis, E.; Houlihan, F.; Shugard, A.; Thompson, L., Poly (t-BOC-styrene sulfone)-based chemically amplified resists for deep-UV lithography. Polymer Engineering & Science 1989, 29 (13), 850-855.

Broadband Waveguide

CNF Project Number: 212612
Principal Investigator(s): Gregory David Fuchs
User(s): Srishti Pal, Qin Xu

Affiliation(s): Department of Applied Physics & Engineering and Department of Physics, Cornell University
Primary Source(s) of Research Funding: Department of Energy (DOE) and Center for Molecular Quantum Transduction (CMQT)
Contact: gdf9@cornell.edu, sp2253@cornell.edu, qx85@cornell.edu
Research Group Website: https://fuchs.research.engineering.cornell.edu/
Primary CNF Tools Used: AJA Sputter Deposition, Heidelberg Mask Writer - DWL2000, GCA 6300 DSW 5X g-line Wafer Stepper, YES Asher, P7 Profilometer, Zeiss Supra SEM, Nabity Nanometer Pattern Generator System (NPGS), Dicing Saw – DISCO, Westbond 7400A Ultrasonic Wire Bonder.

Abstract:

We fabricate a broadband waveguide to test the magnetic properties of a low loss ferrimagnet vanadium tetracyanoethylene (V[TCNE]x) at cryogenic temperatures. We find that, in the temperature range between 0.44 K to 68.6 K, the linewidth of our V[TCNE]x sample increases with decreasing temperature. Below 0.44K, the resonance magnetic field decreases with decreasing temperature. These results are informative for the future applications of V[TCNE]x.

Summary of Research:

This research focuses on exploring exotic low-temperature broadband FMR response of the low-loss organic ferrimagnet V[TCNE]x.

The basic steps for patterning our broadband waveguide using photolithography are shown in Figure 1(a).First, we coat clean (with acetone followed by IPA) sapphire wafers with bilayer of LOR5A and S1813. The resist coated wafer is then exposed in 5X g-line Wafer Stepper to be patterned with the design written on a photomask using Heidelberg Mask Writer-DWL2000. The developed resist (in AZ726MIF) is descummed in YES Asher followed by deposition of 225 nm thick Ti/Cu/Pt tri-layer in the AJA sputter deposition tool. Finally, we lift-off the metal using 1165 and then dice the wafer using Dicing Saw–DISCO. For the magnon sub-system, we use the low-loss organic ferrimagnet V[TCNE]x with a low Gilbert damping α~10–4 offering long magnon lifetime and thus low Km. Using e-beam lithography in Nabity Nanometer Pattern Generator System (NPGS) connected to Zeiss Supra SEM, we pattern a 36 µm wide and 2 mm long bar on the 40 µm wide and 2 mm long central wire of the broadband chip using the steps shown in Figure 1(b). We then ship the exposed broadband chips to our collaborators in Ohio State University for V[TCNE]x growth and liftoff.

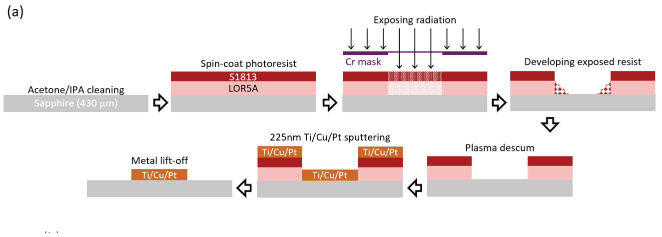

Figure 1: Process flow for (a) patterning the broadband chips with Ti/Cu/Pt tri-layer, and (b) e-beam patterning for V[TCNE]x deposition.

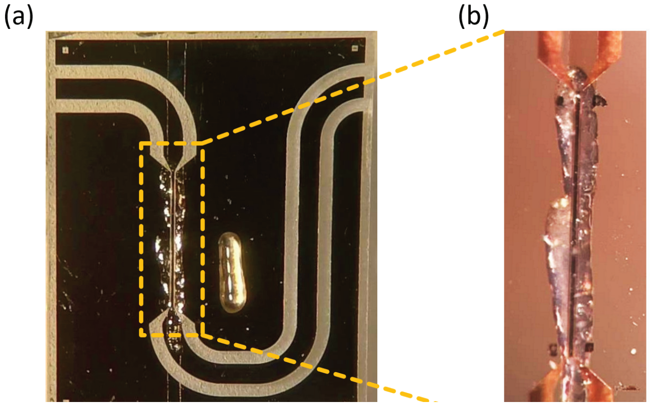

Figure 2: (a) Microscope image of broadband chip with patterned V[TCNE]x, ALD encapsulation, and protective grease layer. (b) Magnified microscope image of the region marked with yellow dashed rectangle in (a).

The V[TCNE]x is then encapsulated by ALD Alumina by our collaborators in Northwestern University to prevent degradation from air exposure and then sent back to us for measurement. We finally applied an additional layer of cryogenic grease for further protection of the V[TCNE]x film as shown in Figure 2.

For the FMR measurement setup, we first put the sample into a dilution refrigerator which has a base plate temperature of 15 mK. The broadband waveguide

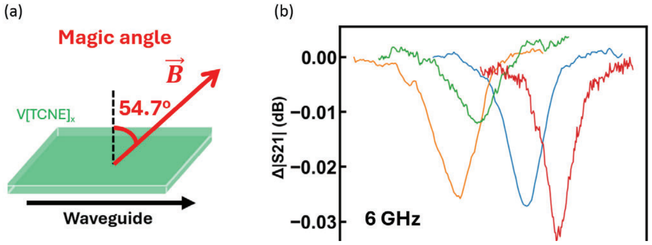

Figure 3: (a) Measurement setup scheme showing the orientation of the external field relative to the waveguide and the V[TCNE]x film. The external field is at 54.7•from the film normal of the V[TCNE]x film. (b) Microwave transmission spectrum vs the external magnetic field magnitude when the microwave frequency is 6 GHz. We can see the dip of the FMR resonance at different microwave excitation powers or temperatures. The 4 dips from left to right are obtained at –68 dBm microwave power at the sample in the dilution fridge; –58 dBm in the dilution fridge; –48 dBm in the dilution fridge; and –83 dBm at 0.44 K in the He-3 cryostat.

is connected to a vector network analyzer for the microwave transmission measurement. As shown in Figure 3(a), the external magnetic field is applied at 54.7• from the film normal (the magic angle) of the V[TCNE]x film. In this geometry, the inhomogeneous linewidth caused by the length of the V[TCNE]x is minimized.

Figure 3(b) shows the 6 GHz microwave transmission magnitude vs the external magnetic field magnitude at different driving powers. When the V[TCNE]x's Larmor frequency matches 6 GHz, it will absorb some of the microwave energy, thus causing a dip in the transmission spectrum. The 3 dips on the left are the transmission spectrums when the microwave powers at the sample are –68 dBm, –58 dBm and –48 dBm respectively. The dip shifts to a higher magnetic field when the excitation power is higher, which is later shown to be caused by the heating of the V[TCNE]x. In other words, the dip shifts to a higher magnetic field when the sample temperature is higher. Note that this shifting happens at all directions of the external magnetic field, which rules out temperature dependent changes in magnetic anisotropy.

Then, the sample chip was put into a He-3 cryostat that has a tunable temperature between 0.44 K and 70 K. The rightmost dip in figure 3(b) is got when the sample space temperature is 0.44 K with –83 excitation power, which proves that the resonance field shift is caused by the raising temperature. Figure 4 shows the linewidth of the V[TCNE]x at 6 GHz and 14 GHz. It shows that the linewidth of V[TCNE]x increases with decreasing temperature. Also, most of the linewidth is due to frequency-independent broadening.

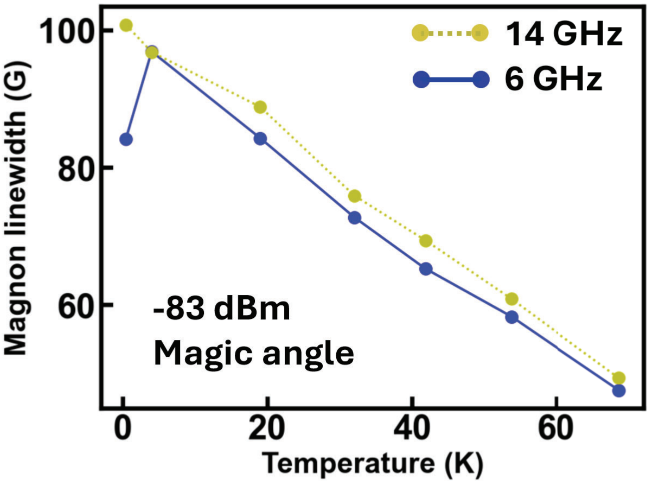

Figure 4: FMR linewidth of V[TCNE]x at 6 GHz and 14 GHz at different temperatures. The microwave power is -83 dBm.

Conclusions and Future Steps:

We fabricate a microwave frequency waveguide chip and use it to measure the broadband FMR of V[TCNE]x at cryogenic temperatures. We see an increase in FMR linewidth from 68.6 K to 0.44 K and a shift in resonance magnetic field vs temperature below 0.44K. More experiments are needed to fully characterize the sources of the observed linewidth and frequency changes.

References:

[1] H. F. H. Cheung, M. Chilcote, H. Yusuf, D. S. Cormode, Y. Shi, S. Kurfman, A. Franson, M. E. Flatté, E. Johnston-Halperin, and G. D. Fuchs, "Raman Spectroscopy and Aging of the Low-Loss Ferrimagnet Vanadium Tetracyanoethylene", The Journal of Physical Chemistry C 125, 20380 (2021).

[2] Q. Xu, H. F. H. Cheung, D. S. Cormode, T. O. Puel, S. Pal, H. Yusuf, M. Chilcote, M. E. Flatté, E. Johnston-Halperin, and G. D. Fuchs, "Strong Photon-Magnon Coupling Using a Lithographically Defined Organic Ferrimagnet", Advanced Science 11, 2310032 (2024).

Sequence-Defined Polypeptoids Enable Stochastics Control and Discovery of Novel Patterning Mechanism in Next-Generation EUV Resists

CNF Project Number: 273318
Principal Investigator(s): Christopher Ober
User(s): Chenyun Yuan, Rika Marui

Affiliations(s): Department of Materials Science and Engineering, Cornell University

Primary Source(s) of Research Funding: Center for High Precision Patterning Science (CHiPPS), an Energy Frontier Research Center funded by the U.S. Department of Energy.

Contact: cko3@cornell.edu, cy479@cornell.edu

Research Group Website: https://ober.mse.cornell.edu/

Primary CNF Tools Used: JEOL JBX-6300FS E-beam Lithography System, JEOL JBX- 9500FS E-beam Lithography System, ASML DUV Stepper, AFM - Veeco Icon, Zeiss Gemini SEM

Abstract:

As lithography continues to advance into the extreme ultraviolet (EUV) regime, stochastic effects are becoming an increasingly significant challenge. One key contributor to it is the chemical stochastics, which arises from molecular-level inhomogeneities within photoresist materials. Traditional polymer-based photoresists often exhibit variations in molecular weight, composition, and sequence. In the case of chemically amplified resists (CARs), unbound photoacid generator (PAG) molecules may distribute unevenly at the nanoscale, and the lateral acid diffusion after exposure are somehow uncontrolled, further adding to stochastics. In this project, we investigated a photoresist system built on sequence-defined polypeptoids, which can be precisely tailored in terms of length, composition, and sequence, using the solid-phase submonomer synthesis method. These polypeptoid resists can be patterned in negative tone using either electron beam or EUV exposure, without requiring any additional photoactive components. This results in a monomolecular resist formulation that greatly minimizes chemical stochastic effects. We explored the patterning mechanism through a variety of characterization techniques and propose that the solubility behavior is driven by a mechanism that is rarely considered in EUV photoresist design. Additionally, we investigated how variations in composition and sequence affect lithographic performance, revealing consistent trends. With EUV exposure, we achieved a resolution of 14 nm half-pitch.

Summary of Research:

We have developed a novel sequence-defined polypeptoid photoresist platform to address stochastics challenges in EUV lithography. Traditional polymeric photoresists struggle with chemical stochastics originating from the random nature of conventional polymers in terms of molecular weight, composition and sequence, as well as the random distribution of photoactive compounds and lateral acid diffusion in terms of CARs. There are also environmental concerns due to the use of PAGs which are mostly fluorinated compounds [1]. The new polypeptoid photoresist system, synthesized via solid-phase submonomer synthesis, features precisely positioned functional groups and exhibits uniform chain length, composition, and sequence [2-3]. These materials exhibit ultra-low dispersity and tunable properties, enabling intrinsic patternability under EUV and e-beam exposures without the need for PAGs. Their unique decarboxylation-based mechanism allows for high-resolution patterning (down to 14 nm half- pitch) and development in ultra-dilute (ppm level TMAH) or even aqueous developers, presenting a greener and more precise resist platform for next-generation lithography.

A representative sequence-defined polypeptoid, composed of six t-butyl ester and four phenol repeating units with a terminal carboxylic acid (Fig.1) was synthesized via solid-phase submonomer synthesis, purified by high-performance liquid chromatography (HPLC), and confirmed to be molecularly homogeneous by liquid chromatography-mass spectrometry (LC-MS). Its low molecular weight combined with a single molecular species enables high-resolution lithography. It is fully compatible with standard lithographic processes, forming homogeneous films via spin coating. Upon EUV or e-beam exposure, terminal carboxylic acids undergo decarboxylation, leading to CO2 outgassing and increased hydrophobicity. Patterns are developed without a post-exposure bake using a highly diluted (ppm-level) TMAH solution, or in some other sequences, deionized water, enabling an eco-friendly process.

These resists exhibit negative-tone behavior under both e-beam and EUV, and achieve resolutions 14 nm half-pitch under EUV (Fig. 2), demonstrating high patterning fidelity under both exposure methods. The decarboxylation-based mechanism has been confirmed with mass spectrometry analysis on post- exposure films and outgassing experiments.

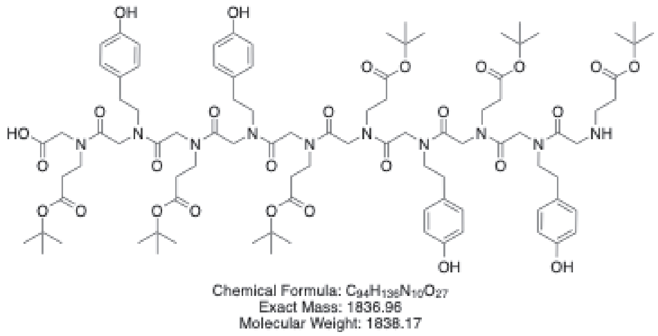

Figure 1: Molecular structure of the example polypeptoid sequence.

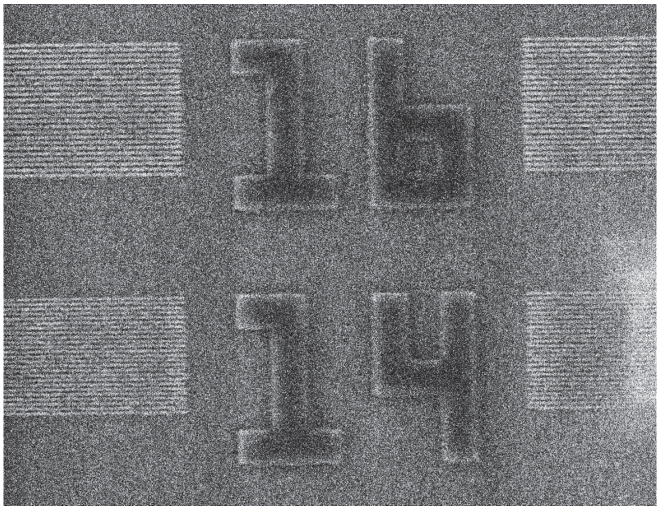

Figure 2: SEM image of EUV patterns showing 16- and 14-nm half-pitch line/space resolution.

Conclusions and Future Steps:

Our current research focuses on further improving patterning performance by screening libraries of selected polypeptoid sequences in which multiple carboxylic acid solubility-switch groups are positioned along the backbone, rather than one group exclusively at the chain end. We are also developing strategies to incorporate metal atoms with high EUV absorption into the polypeptoids to enhance sensitivity.

References:

[1] C. K. Ober, F. Käfer, J. Deng, Review of essential use of fluorochemicals in lithographic patterning and semiconductor processing. Journal of Micro/Nanopatterning, Materials, and Metrology 21, (2022). doi:10.1117/1.Jmm.21.1.010901

[2] R. N. Zuckermann, J. M. Kerr, S. B. H. Kent, W. H. Moos, Efficient method for the preparation of peptoids [oligo(N-substituted glycines)] by submonomer solid-phase synthesis. J. Am. Chem. Soc. 114, 10646-10647 (1992). doi:10.1021/ja00052a076

[3] C. P. Adams et al., Polymer Sequence Alters Sensitivity and Resolution in Chemically Amplified Polypeptoid Photoresists. ACS Macro Lett, 1055-1059 (2025). doi:10.1021/acsmacrolett.5c00320.

Two-Photon Printing of Polymer and Glass Electrospray Emitters

CNF Project Number: 295321
Principal Investigator(s): Elaine Petro, Sadaf Sobhani
User(s): Bryce Kingsley

Affiliation(s): Cornell University, Mechanical and Aerospace Engineering
Primary Source(s) of Research Funding: Government (DARPA)
Contact: epetro@cornell.edu, sobhani@cornell.edu, bjk234@cornell.edu
Research Group Website: https://www.sobhanilab.com, https://www.astralab.mae.cornell.edu
Primary CNF Tools Used: Nanoscribe GT2, Photolithography hoods, YES O2 Asher, DISCO Wafer Dicer

Abstract:

Advances in nano-scale additive manufacturing technologies have opened new possibilities for fabrication of precision components/parts with highly complex geometries. Within the field of space propulsion, these technologies are particularly relevant in the development and fabrication of electrospray thrusters – propulsion systems which utilize charged droplet/ion emission for thrust generation. A fundamental component of these thruster systems is the electrospray emitter, wherein performance depends heavily on the resolution and geometrical characteristics of the emitter structure. Conventional fabrication processes (MEMS techniques, micromachining, etc.) often lack the resolution, geometric flexibility, or material compatibility needed for optimal emitter design and fabrication. This work investigates an alternative technique of electrospray emitter fabrication using Two-Photon Polymerization printing, exploring its potential to produce intricate emitter architectures and integrated microfluidic structures that can enhance the performance of electrospray thrusters.

Summary of Research:

Two-Photon Polymerization (TPP) printing is an emerging nano-scale additive manufacturing process which utilizes a high-power laser to print 3D structures from photosensitive resin. Figure 1 shows a generalized schematic of a TPP printing system. A NIR (near infrared) laser is projected through a microscope objective and focused within a pool (dip) of photosensitive resin. Two-photon absorption near the focal region of the beam elevates the energy above the activation energy of the resin, resulting in cross-linking and solidification of the resin into a solid feature. Using precise positioning systems, the beam is drawn in XYZ space to fabricate 3D parts/components. In this work, we utilize the Nanoscribe Photonic Professional GT2 printer available in the CNF facilities. Using the GT2 system, we fabricate electrospray emitters from polymer (IP-Q) and glass (GP-Silica and POSS) resins.

The user-friendly nature of the GT2 printing system greatly simplifies the emitter fabrication process, as follows: (1) the emitter geometry is modeled using standard CAD software and exported to a mesh, (2) the emitter mesh is sliced using Nanoscribe's slicing software (Describe) and transferred to the GT2 system for printing, (3) a clean substrate (silicon) is loaded into the printer with the selected photosensitive resin (polymer/glass), (4) emitter geometry is printed (typically <10 minutes), (5) substrate and emitter removed from GT2 and developed to remove residual resin, and (6) thermal post-processing (glass resins only). This simplified fabrication process promotes rapid prototyping and development of novel emitter designs which would be difficult with conventional methods, such as chemical etching which would require multiple stages of etching and new masks developed for each new prototype [1]. Additionally, TPP printing enables emitter architectures that would be extremely challenging or impossible to achieve with traditional fabrication techniques. We leverage this capability by integrating microfluidic channels and structures within the body of the printed emitters to promote propellant transport to the emitter tip and improve performance. One such microfluidic structure we implement is the Triply-Periodic Minimal Surface (TPMS), which is a lattice structure that is generated from 3D mathematical equations. Figure 2 contains an SEM image of a polymer (IP- Q) emitter printed with the gyroid TPMS lattice structure. This structure contains a network of interconnected micro-pores (~8 µm) for propellant to transport from the base (where it is loaded) to the tip (the site of emission). We note that this work uses the 10X microscope objective for printing, which has a minimum TPMS pore size of approx. 6 µm. A higher objective (e.g., 25X) would be required for smaller pores, at the expense of longer print times.

As mentioned previously, glass emitters are fabricated using TPP printing with specialized photosensitive resins. Here, we use two formulations of glass resins:

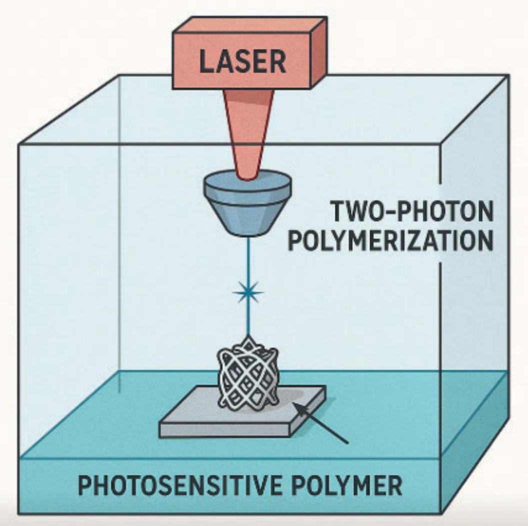

Figure 1: Schematic of two-photon polymerization (TPP) printing.

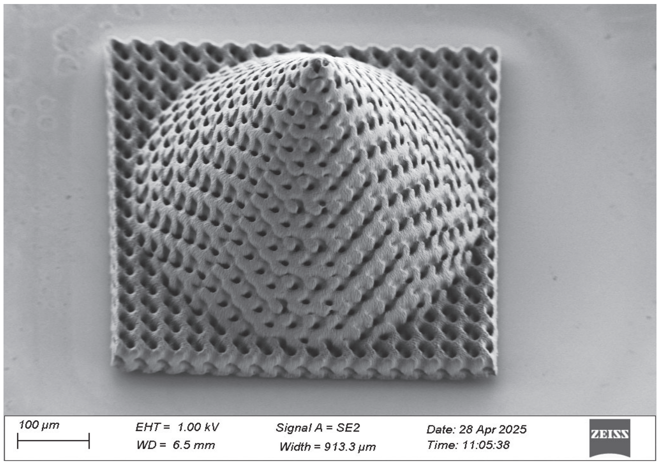

Figure 2: SEM of a polymer electrospray emitter TPP-printed with a TPMS lattice structure.

(1) the GP-Silica resin from Nanoscribe which contains silica nanoparticles that fuse together during thermal treatment, and (2) a POSS (polyhedral oligomeric silsesquioxane) formulation which chemically transforms into fused silica during thermal treatment [2]. For the application of electrospray emitters, glass/fused silica is advantageous over polymer materials due to its higher degree of wettability and stability (chemical, thermal, etc.). Figure 3 contains 3D optical profilometry scans of a TPP-printed glass emitter before (a) and after (b) thermal post-processing. As can be seen in the profilometry scans, thermal processing introduces significant shrinkage (~35-40%) of the emitter structure which must be accounted for during the design stage to achieve accurate geometry/dimensions.

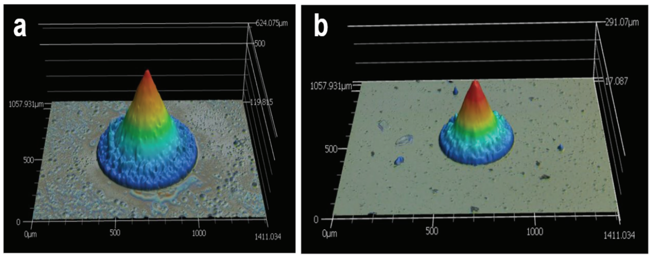

Figure 3: 3D optical profilometry scan of a TPP-printed glass emitter (a) before and (b) after thermal treatment.

Conclusions and Future Steps:

This work investigates a new/alternative technique of fabricating electrospray emitters using two-photon polymerization (TPP) printing. The unique capabilities and advantages of TPP printing enable highly complex emitter architectures that would be very challenging or impossible to fabricate with traditional emitter fabrication processes. Microfluidic channels and structures (TPMS) can be integrated directly into the body of the printed emitters to tailor fluid/propellant transport to the tip for optimized emission. TPP printing supports different materials systems, enabling emitters to be fabricated out of polymer or glass materials.

This work is ongoing and testing is currently underway to evaluate the emission performance of these printed emitters compared to standard electrospray emitters. Additionally, we have plans to scale-up to fabricating emitter arrays (i.e., gridded emitters) for implementation in electrospray thruster systems.

References:

[1] L. F. Velasquez-Garcia, A. I. Akinwande and M. Martinez-Sanchez, "A Planar Array of Micro-Fabricated Electrospray Emitters for Thruster Applications," Journal of Microelectromechanical Systems 15, 1272-1280 (2006), DOI: 10.1109/JMEMS.2006.879710

[2] J. Bauer, C. Crook and T. Baldacchini, “A sinterless, low-temperature route to 3D print nanoscale optical-grade glass,” Science 380, 960-966 (2023), DOI: 10.1126/science.abq3037.

A Brief Survey of Contact Angle Measurements for Predicting Fluid Flow in Electrospray Emitters

CNF Project Number: 295321

Principal Investigator(s): Sadaf Sobhani
User(s): Lindsay Wright

Affiliation(s): Sibley School of Mechanical and Aerospace Engineering

Primary Source(s) of Research Funding: RA Offer for the Defense Advanced Research Projects Agency, Account #E559359

Contact: sobhani@cornell.edu, law289@cornell.edu
Research Group Website: sobhanilab.com

Primary CNF Tools Used: VCA Optima Goniometer, spincoating fume hoods

Abstract:

Electrospray is a method of satellite propulsion and mass spectrometry that works by moving ionic liquid from a receptacle to emitter tips and then vaporizing and propelling the ions using strong alternating electric fields from an extractor. With recent advances in additive manufacturing, electrospray emitters can be custom manufactured for different surface properties to optimize fluid flow. However, fluid flow in electrospray emitters has mainly been parametrized using metrics such as permeability or impedance, without the level of detail necessary to design channel networks. Our work aims to model the effects of specific materials and surface treatments on the speed of fluid flow—to develop an accurate predictive framework, a study of different materials' surface properties is necessary. Thus, a series of samples have been fabricated in the Cornell Nanoscale Facility to obtain contact angle measurements.

Summary of Research:

Two Photon Polymerization was attempted to create contact angle measurements that matched the surface characteristics of additively manufactured electrospray emitters. Due to bumps and other surface texture discrepancies caused by stitching in larger print sizes, we opted for spin coating surfaces instead, curing them under UV to replicate the Two Photon Polymerization process with a more even surface.

The following recipes were created for spin coating:

GP Silica: Dispense approximately 1 mL of resin on 1" silicon wafer square. Then, ramp to 500 rpm at 100 rpm/sec, and hold for 5-10 seconds. Next, ramp to 1000 rpm/s at a rate of 300 rpm/sec, and hold for 30 seconds. Finally, soft bake for 6 mins at 65 degrees Celsius, then 20 mins at 95 degrees Celsius

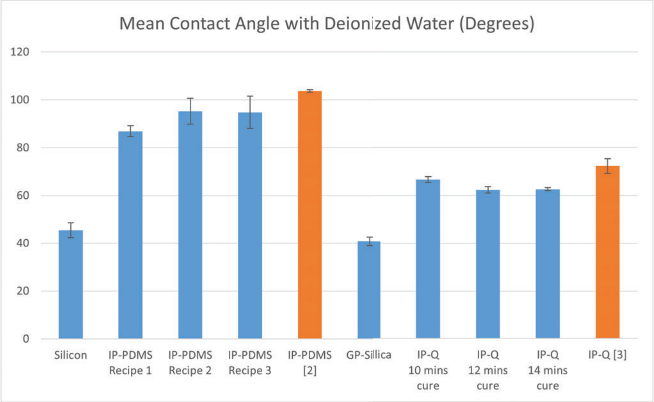

Figure 1: Contact Angles of Spin Coated Polymer Resin Recipes with Deionized Water

IP-PDMS Recipe 1 (created by collaborator at Rice University): Dispense approximately 1 mL of resin on 1" silicon wafer square. Next, ramp at 10 rpm/s to 500 rpm, and hold for 5 seconds. Finally, UV cure the sample for 10 minutes using an Aiffoto brand lamp [1].

IP-PDMS Recipe 2: Dispense approximately 1 mL of resin on 1" silicon wafer square. Next, ramp at 10 rpm/s to 500, and hold for 5 seconds. Then, UV cure samples for 30 minutes using the cylinder lamp at the Cornell Nanoscale Facility, reported to have an energy flux of 21 mW/cm^2 @ 405nm

IP-PDMS Recipe 3: Prime a 1" silicon wafer with 20% HMDS (first at 700 rpm, with a 1000 rpm/s ramp at 10 seconds duration; then, at 2500 rpm, with a 1000 rpm/s ramp and 60 seconds duration). Then, dispense approximately 1 mL of resin on 1" silicon wafer square. Ramp the spin coater at 10 rpm/s to 500 rpm and hold for 5 seconds. Next, UV cure samples for 30 minutes using the cylinder in the Cornell Nanoscale Facility. Finally, develop for 10 minutes in isopropanol.

IP-Q: Prime a 1" silicon wafer with 20% HMDS. Then, dispense approximately 1 mL of resin on 1” silicon wafer square. Ramp to 500 rpm at 100 rpm/sec and hold for 5 seconds. Next, ramp to 2500 rpm at 300 rpm/sec, for a total of 40 seconds. Then, UV cure samples to the desired time (10, 12, or 14 minutes) using the Cornell Nanoscale Facility lamp.

Finally, develop for 10 minutes in isopropanol.

Contact angle measurements of varying surface recipes with deionized water were measured with a Ramehart 500 Goniometer, except for IP-PDMS samples fabricated using Recipes 2 and 3, which were measured by processing iPhone 16 images with ImageJ. The data with standard error bars can be found in Figure 1, along with literature values for IP-PDMS and IP-Q to compare [2] [3].

A preliminary study of the contact angle measurements of ionic nanoparticle fluids suspended in polymer matrices was also conducted for silicon and IP-PDMS. Silicon had a contact angle of 48.3 degrees with water, 17.6 degrees with Jeffamine, and 13.4 degrees with NIMS 15 2:1, while Recipe 1 for IP-PDMS had a contact angle of 90.7 degrees with water, 37.7 degrees with Jeffamine, and 64.2 degrees with NIMS 15 2:1.

Conclusions and Future Steps:

A majority of the polymer resins used were weakly hydrophilic to water. GP-Silica, due to being a glass resin, is more strongly hydrophilic, while IP-PDMS is borderline hydrophobic. It will be interesting to continue to study the properties of ionic liquids and ionic nanoparticle fluids against different surfaces to determine whether more complex interactions are occurring that influence wettability.

IP-PDMS and IP-Q contact angle measurements were found to be consistently more hydrophilic than literature values, with the difference between literature and observations being more pronounced in IP-PDMS samples. It is noted that Govindarajan et al cured IP-PDMS using a 10W 395nm wavelength lamp [2]. Isaakidou used Two Photon Polymerization with a center wavelength of 780 nm, operating at 80 MHz at a duration of 100 fs to fabricate IP-Q samples [3]. The degree to which these differences affect the contact angle is a point to investigate.

A preliminary study of UV cure time and contact angle measurements was made for IP-Q, with the contact angle decreasing slightly over time from 10 to 12 to 14 minutes. Future steps would include experimenting with different treatments in addition to UV cure time. Experimentalists have found, for example, that UV-ozone treatment of PDMS can reduce the contact angle at controllable rates, which could be preserved by storage in distilled water [4]. Additional surface treatments could include etching, Atomic Layer Deposition, and Molecular Vapor Deposition to further manipulate the surface.

References:

[1] Amazon (n.d.). 3D Printing UV Resin Curing Light 405nm, Smart 3D Printer UV Resin Curing Light for Solidify Photosensitive Resin, Portable Timer Function DIY Curing Enclosure, 5V/2A Input USB Powered. https://www.amazon.com/dp/B0D5HKQ2DQ?ref_=ppx_hzsearch_conn_dt_b_fed_ asin_title_1

[2] Isaakidou, Aikaterini, Iulian Apachitei, Lidy Elena Fratila-Apachitei, and Amir Abbas Zadpoor. 2023. "High-Precision 3D Printing of Microporous Cochlear Implants for Personalized Local Drug Delivery" Journal of Functional Biomaterials 14, no. 10: 494. https://doi.org/10.3390/jfb14100494

[3] Srinivasaraghavan Govindarajan, Rishikesh & Sikulskyi, Stanislav & Ren, Zefu & Stark, Taylor & Kim, Daewon. (2023). Characterization of Photocurable IP-PDMS for Soft Micro Systems Fabricated by Two-Photon Polymerization 3D Printing. Polymers. 15. 10.3390/polym15224377.

[4] Kun Ma, Javier Rivera, George J. Hirasaki, Sibani Lisa Biswal, Wettability control and patterning of PDMS using UV–ozone and water immersion, Journal of Colloid and Interface Science, Volume 363, Issue 1, 2011,Pages 371-378, ISSN 0021-9797, https://doi.org/10.1016/j.jcis.2011.07.036.

Lithography on 2D Materials for Stressor Film Deposition

CNF Project Number: 296721

Principal Investigator(s): Judy Cha

User(s): Sihun Lee, Yu-Mi Wu

Affiliation(s): Department of Materials Science and Engineering, Cornell University

Primary Source(s) of Research Funding: The Gordon and Betty Moore Foundation's EpiQS Initiative (GBMF9062.01); Department of Energy, Basic Energy Sciences program Grant No. DE-SC0023905

Contact: jc476@cornell.edu, sl2859@cornell.edu, yw2658@cornell.edu

Research Group Website: https://cha.mse.cornell.edu

Primary CNF Tools Used: Heidelberg MLA 150 Maskless Aligner, SC4500 Evaporator, Zeiss Supra scanning electron microscope, Nabity Nanometer Pattern Generator System

Abstract:

To investigate the heterostrain-induced electronic properties in 2D materials, we fabricated stressor thin film Al2O3/SiO2/Al2O3 directly onto the target materials using lithographic patterning. Direct writing lithography tools were used to pattern the resist with stripes, followed by thin film deposition of stressors using e-beam evaporation. Subsequently, metal contacts were integrated for device characterization, revealing the effects of strain on the structural and electrical transport properties of MoS2.

Summary of Research:

Recent experimental advances in process-induced strain-engineering technique have enabled controlled strain application in 2D materials through lithographic patterning of stressor thin films [1], providing a versatile platform to engineer material properties. Here, utilizing the process- induced strain-engineering approach [2], we apply heterostrain to exfoliated MoS2 flakes by patterning evaporated thin film stressors, and fabricate biasing devices to characterize their resulting strain-induced electrical properties of MoS2.

The biasing devices were fabricated on conventional Si/SiO2 substrates. Figure 1 shows a cross- sectional schematic of the device design and a plan-view optical image of the device used for electrical transport measurements. First, the interdigitated electrode design with a 1 µm spacing, was patterned directly onto a Si/SiO2 substrate using photolithography with the MLA 150 direct writer. Cr/Au contacts were subsequently deposited using e-beam evaporation, followed by a lift-off process. Subsequently, the exfoliated MoS2 flakes were transferred onto the pre-patterned electrodes using a conventional polymer-assisted dry transfer technique. To introduce the local strain, the MLA 150 was used again to pattern a small stripe on top of the MoS2 flake (highlighted in red), where the Al2O3/SiO2/Al2O3 stressor films were deposited via e-beam evaporation. The draw-mode functionality of the MLA 150 facilitates the stressor patterning process without requiring any additional alignment steps, ensuring accurate overlay with the target flake region.

To investigate the structural effects of heterostrain at high resolution, we also fabricated samples on transmission electron microscopy (TEM) grids with freestanding membranes. Figure 2 shows optical images of the TEM grid overview and the fabrication process. Poly(methyl methacrylate) was used as the resist, and the patterning was conducted using e-beam lithography with the Nabity Nanometer Pattern Generator System on the Zeiss Supra scanning electron microscope. Manual alignment was employed to center the stripe patterns (~10 µm in width and spacing) onto the membrane region of the TEM grids. Following exposure, Al2O3/SiO2/Al2O3 stressor films were deposited via electron beam evaporation. The stripe-patterned stressor films were successfully deposited directly onto MoS2 flakes on the TEM grids, enabling subsequent structural characterization.

Next step, we investigated the local structural changes induced by heterostrain in MoS2 using scanning transmission electron microscopy (STEM). Figure 3 focus on a MoS2 flake under the patterned film stressor on the TEM grid. The white dotted line marks the boundary where the stressor film terminates. As shown in Fig. 3b and 3c, dislocations appear as bright lines in the low- angle annular dark-field STEM images due to the diffraction contrast. The observed diamond- shaped dislocation network in MoS2 likely originates from heterostrain-induced lateral displacement between layers. The strain transferred from the stressor film is primarily applied to the topmost few layers of MoS2, resulting in interlayer sliding and modified stacking configurations. This sliding induces a dislocation network that relieves the resulting lattice mismatch and reflect local structural relaxation mechanism in the system.

Conclusions and Future Steps:

DLS is a facile tool to characterize the emulsion condition of colloidal system. For emulsions with nanoparticles and multiple ingredients, it's a challenge to make ideally uniform nano-encapsulation environments. Concentration and temperature play critical roles and need to be modified systematically in the future.

References:

[1] Chenyun Yuan, Florian Kafer, and Christopher K. Ober. (2021). Polymer-Grafted Nanoparticles (PGNs) with Adjustable Graft-Density and Interparticle Hydrogen Bonding Interaction.

[2] Alicia Cintora, Florian Kafer, Chenyun Yuan, and Christopher K. Ober. (2021). Effect of monomer hydrophilicity on ARGET-ATRP kinetics in aqueous mini-emulsion polymerization.

[3] Roselynn Cordero, Ali Jawaid, Ming-Siao Hsiao, Zoe Lequeux, Richard A. Vaia, Christopher K. Ober, "Mini Monomer Encapsulated Emulsion Polymerization of PMMA in Aqueous ARGET ATRP", ACS Macro Letters, 7, 4, 459-463.

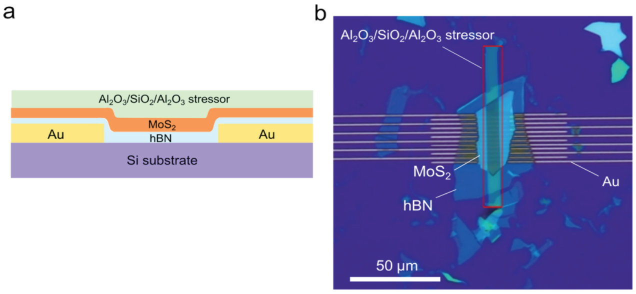

Figure 1: Figure 1. (a) Cross-sectional schematic of the device with stressor film. (b) Optical image of a biasing device fabricated for electrical transport measurements. The red outline shows where the stressor film was deposited. The MoS2 sits above the biasing electrodes and an insulating dielectric hBN layer.

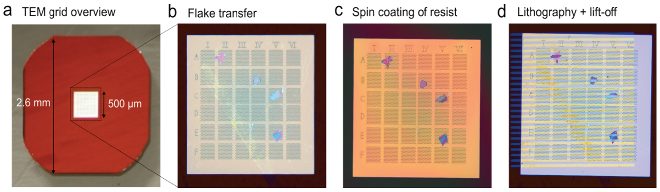

Figure 2: (a) Overview of the TEM grid with a 500 µm x 500 µm membrane where the material can be imaged with a TEM. (b-d) Zoomed-in images of the MoS2 flakes transferred onto a TEM grid, followed by the spin coating of the PMMA resist, then e-beam lithography patterning and lift-off, respectively. Stripes of the stressor film Al2O3 (10 nm)/SiO2 (30 nm)/Al2O3 (10 nm) are deposited on top of the MoS2.

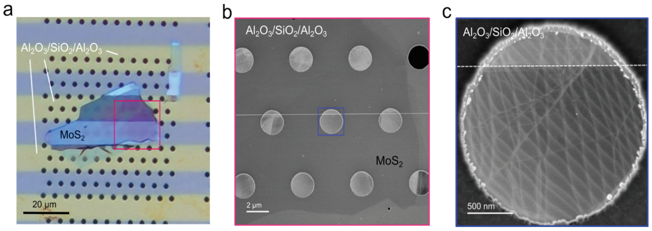

Figure 3: (a) An optical image showing a single MoS2 flake partially covered by a stressor film (yellow region on the TEM membrane). (b) Low magnification low-angle annular dark-field (LAADF) scanning transmission electron microscopy (STEM) image of MoS2 from the red box in (a). (c) LAADF STEM image of MoS2 over a single membrane hole from the blue box in (b), showing dislocations from the diffraction contrast.

Area Selective Deposition

CNF Project Number: 299021
Principal Investigator(s): James R. Engstrom
User(s): James T. Jensen, Jay V. Swarup

Affiliation(s): Chemical Engineering, Cornell University

Primary Source(s) of Research Funding: DOE

Contact: jre7@cornell.edu, jtj33@cornell.edu, jvs64@cornell.edu

Primary CNF Tools Used: Woollam RC2 Spectroscopic Ellipsometer, VCA Contact Angle, Oxford FlexAL

Abstract:

In this work, we describe our results aimed at developing the fundamental framework behind the use of small molecules to achieve area selective deposition (ASD), examining the atomic layer deposition (ALD) of Al2O3 on SiO2. We have examined 2 precursors, and 2 blocking molecules. For ASD, we have determined that the size of the precursor and blocking molecule strongly influence blocking efficacy, with bulkier precursors and long-chain self-assembled monolayers (SAM's) leading to increased blocking on SiO2.

Summary of Research:

We are developing the fundamental framework behind the use of small molecules to achieve ASD, examining the deposition of Al2O3 on SiO2. The overall approach is to examine explicitly the effects of the choice of the precursor and blocking molecules on blocking Al2O3 thin film growth on SiO2.

We have employed a quartz crystal microbalance (QCM) to monitor thin film deposition in situ and in real-time.1,2 In CNF, we coated Au QCM crystals with 20 nm of SiO2 to get a starting surface of SiO2 for ASD experiments. We exposed the SiO2 surface to the blocking molecule: (N,N-dimethylamino)trimethylsilane (DMATMS) in vapor phase and octadecyltrichlorosilane (ODTS) in solution phase. Water contact angles were used to assess changes in surface chemistry. The SiO2 surface becomes hydrophobic upon formation of the blocking molecule, and these changes are shown in Figures 1 and 2. Once the blocking molecule was formed, we performed ALD in our laboratory using 2 different precursors: trimethylaluminum (TMA) and bisdimethylamino-diamino-Aluminum (BDMADA-Al). A key difference between these precursors is that BDMADA-Al is larger and bulkier due to its more complex ligands compared to TMA. In Figure 3 we show QCM data for 40 cycles using BDMADA-Al as the precursor and H2O as the co-reactant at T = 120 °C on ODTS- and DMATMS-SiO2 QCM crystals. From the QCM results, the longer-chain ODTS blocking molecule resulted in prolonged attenuation of growth on SiO2. In Figure 4 we show a similar set of experiments but using TMA as the precursor. From these results, we again see longer attenuation of growth on ODTS compared to DMATMS, although the growth is larger than what was observed using BDMADA-Al as the precursor under

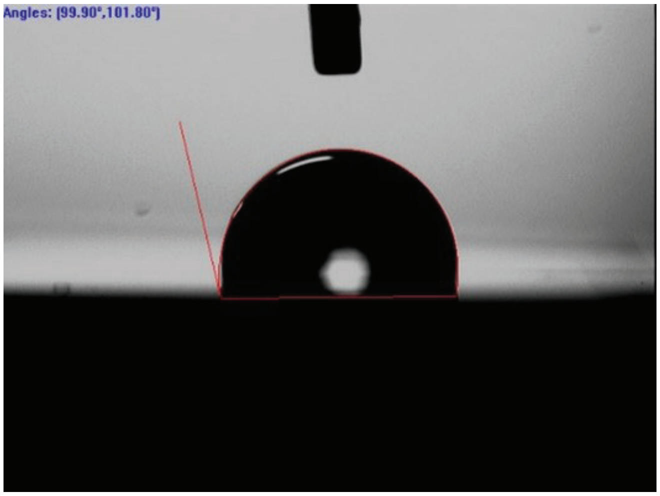

Figure 1: Water contact angle of DMATMS-passivated SiO2 is ~95°, which is significantly higher than Bare SiO2 which is ~15°.

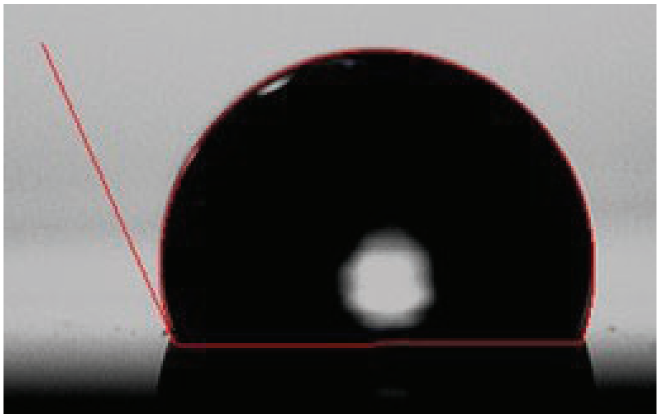

Figure 2: Water contact angle of ODTS-passivated SiO2 is ~110°, which is significantly higher than Bare SiO2 which is ~15°.

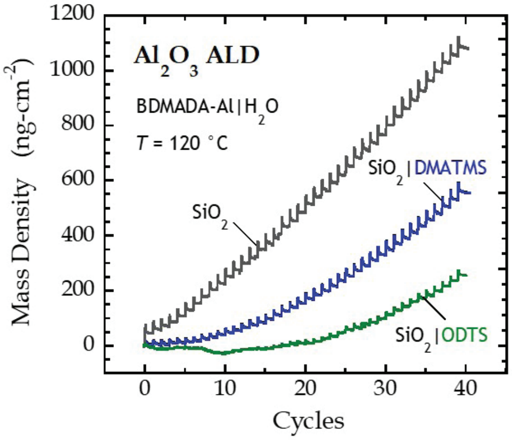

Figure 3: QCM data showing mass densities vs number of cycles for Al2O3 using BDMADA- Al|H2O process chemistry at T = 120 °C on SiO2 crystals passivated with either DMATMS or ODTS.

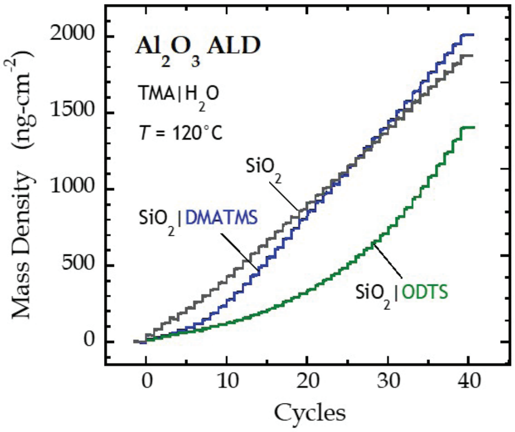

Figure 4: QCM data showing mass densities vs number of cycles for Al2O3 using TMA-Al|H2O process chemistry at T = 120 °C on SiO2 crystals passivated with either DMATMS or ODTS.

similar reaction conditions.

Conclusions and Future Steps:

We have shown that steric hindrance between the precursor and the blocking molecule plays an important role in blocking ALD growth on non-growth surfaces. Our future steps involve studying alternative precursors and blocking molecules to achieve ASD for a variety of thin films and surfaces.

References:

[1] Swarup, J. V; Chuang, H.-R.; You, A. L.; Engstrom, J. R. Effect of Co-Reactants on Interfacial Oxidation in Atomic Layer Deposition of Oxides on Metal Surfaces. ACS Appl Mater Interfaces 2024, 16 (13), 16983–16995. https://doi.org/10.1021/acsami.3c19033.

[2] Swarup, J. V; Chuang, H.-R.; Jensen, J. T.; Gao, J.; You, A. L.; Engstrom, J. R. Nonpyrophoric Alternative to Trimethylaluminum for the Atomic Layer Deposition of Al2O3. Journal of Vacuum Science & Technology A 2025, 43 (2), 022404. https://doi.org/10.1116/6.0004171.

Mapping Structure Evolution During Lithiation of 2D Materials

CNF Project Number: 303522
Principal Investigator(s): Judy Cha
Users(s): Natalie Williams, Sihun Lee

Affiliations(s): Department of Materials Science and Engineering, Cornell University; Department of Chemistry and Chemical Biology, Cornell University

Primary Source(s) of Research Funding: The Gordon and Betty Moore Foundation's EpiQS Initiative (GBMF9062.01); Department of Energy, Basic Energy Sciences program Grant No. DE-SC0023905

Contact: jc476@cornell.edu, nlw49@cornell.edu, sl2859@cornell.edu

Research Group Website: cha.mse.cornell.edu

Primary CNF Tools Used: Heidelberg DWL66FS, Heidelberg MLA 150 Maskless Aligner, SC4500 Odd-Hour & Even-Hour Evaporator

Abstract:

To study promising materials for lithium-ion batteries, it is essential to track complete phase evolutions throughout lithiation. Lithium intercalation, the process by which lithium ions are reversibly inserted into a host material, typically induces structural and electronic phase transitions in electrode materials [1], directly influencing battery capacity and cycling stability. Techniques such as in situ Raman spectroscopy, electrical transport, and x-ray diffraction provide valuable insights into structural transformations but lack the spatial resolution to visualize these changes at the nanoscale in real space. Among available experimental methods, scanning transmission electron microscopy (STEM) uniquely offers simultaneous imaging, diffraction, and spectroscopy at atomic- scale resolution. Here, we employ multimodal in situ 4D STEM, along with in situ Raman spectroscopy and electrochemical data using coin-type cells, to map nanoscale phase evolutions during lithium intercalation in the layered material $LaTe_3$.

Summary of Research:

Figure 1a illustrates the structure of $LaTe_3$, and Figure 1b depicts the geometry of our electrochemical cell, which varies slightly based on experimental requirements. In situ Raman spectroscopy identifies four distinct lithiation phases in LaTe3 (Figure 2b). The initial phase corresponds to the pristine state of $LaTe_3$ at open-circuit voltage (OCV). At the first phase transition, phonon modes associated with the charge density wave (CDW) of LaTe3 disappear and are replaced by new modes that evolve continuously throughout lithiation. Optical imaging reveals dark lines forming on the flakes during lithiation, which are wrinkles caused by strain relaxation from structure transformations (Figure 2a). A galvanostatic discharge curve from a LaTe3 coin-cell similarly portrays four distinct lithiation phases (Figure 2b).

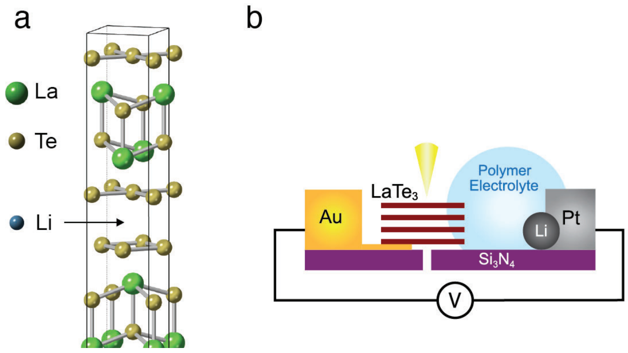

Figure 1: (a) Crystal structure of LaTe3. Li ions are intercalated electrochemically between the Te sheets. (b) Schematic of an electrochemical cell on a S/TEM e-chip for multimodal in situ STEM experiments.

To gain deeper insight into the lithiated phases, we performed an in situ lithiation experiment to acquire complementary datasets using STEM, including atomic-resolution and low-magnification STEM imaging, electron energy loss spectroscopy (EELS), and spatially resolved four-dimensional diffraction (4D STEM) using an Electron Microscopy Pixel Array Detector (EMPAD) [2]. Figure 3a shows electron diffraction acquired during in situ 4D STEM lithiation of $LaTe_3$. The original CDW is suppressed, as indicated by the disappearance of superlattice peaks at $q = 2/7c^*$ at the first phase transition, corroborating Raman results. A new lithium-induced superlattice emerges at $q = 1/3c^*$, accompanied by changes in $LaTe_3$ layer stacking, seen in the varying intensities of lithium ordering peaks. We also observe initial in-plane lattice expansion followed by relaxation, along with evolving lithium occupancy in the host lattice. Ultimately, as lithium becomes fully incorporated, all ordering peaks vanish. Concurrent in situ EELS confirms the emergence and gradual increase of lithium content during intercalation (Figure 3b).

Conclusions and Future Steps:

We have successfully mapped structural, chemical, and electronic transitions in $LaTe_3$ induced by lithium intercalation through combined in situ Raman spectroscopy, electrochemical data of coin-cells, and multimodal in situ STEM techniques (imaging, EELS, and 4D STEM). The observed lithiated phases of LaTe3 are new and have not been observed previously. Our methodology provides a robust framework applicable to future investigations of phase transformations in other intercalation materials.

References:

[1] 1. M. Wang, S. Xu, and J. J. Cha, "Revisiting Intercalation-Induced Phase Transitions in 2D Group VI Transition Metal Dichalcogenides," Advanced Energy and Sustainability Research, vol. 2, no. 8, p. 2100027, 2021, doi: 10.1002/aesr.202100027.

[2] M. W. Tate et al., "High Dynamic Range Pixel Array Detector for Scanning Transmission Electron Microscopy," Microscopy and Microanalysis, vol. 22, no. 1, pp. 237–249, Feb. 2016, doi: 10.1017/S1431927615015664.

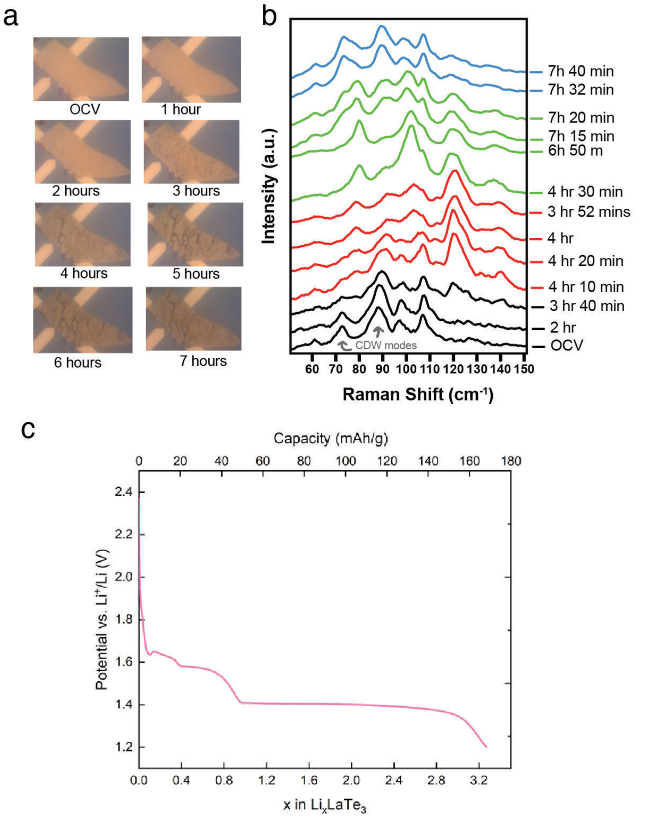

Figure 2: (a) Optical images and (b) in situ Raman spectra during lithiation of LaTe3. (c) Galvanostatic discharge curve of LaTe3 coin cell, suggesting three distinct lithated phases.

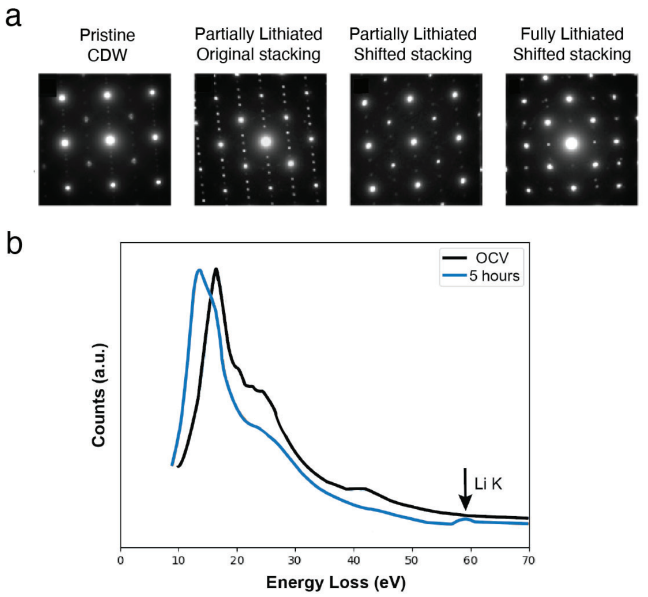

Figure 3: (a) Diffraction patterns of the four main structures acquired during in situ STEM of lithium intercalation into LaTe3. (b) Low loss EEL spectra from 2 points in the experiment, depicting the emerging Lithium K-edge edge in the host lattice.

Spore-Polymer Composite Materials

CNF Project Number: 308523

Principal Investigator(s): Meredith Silberstein
User(s): Ellen van Wijngaarden

Affiliation(s): Sibley School of Mechanical and Aerospace Engineering

Primary Source(s) of Research Funding: Office of Naval Research

Contact: silbersteinlab.com, mt845@cornell.edu, ewv8@cornell.edu

Research Group Website: silbersteinlab.com

Primary CNF Tools Used: Lyophilizer, PDMS Casting Station

Abstract:

Repeated loading on materials leads to fatigue cracking and eventually, catastrophic failure. Current methods for crack detection, such as visual inspection or ultrasonic testing are expensive, require equipment downtime and do not mitigate cracks that are detected. Living materials achieve novel functionalities through leveraging living organisms to sense and respond to changes in the environment, such as a crack. We designed a bacterial-polymer composite coating capable of detecting fatigue cracking and with the potential to regulate the crack conditions to mitigate cracking in the substrate. This study demonstrates crack detection for various substrate geometries and loading conditions. Ultimately, early crack detection will reduce material waste, increase product lifespan, and improve safety through preventing failure.

Summary of Research:

Fatigue cracking due to repeated loading, eventually leads to failure in all materials. Engineers are continuously looking to develop fatigue resistant materials and early crack detection methods to mitigate the safety risk.[1] Designing living materials presents a novel method of detecting cracks by leveraging living organisms' ability to sense and respond to the environment. Living materials combine conventional synthetic matrices with live organisms to expand the functionality of materials. Extensive progress has been made in developing bacteria-based materials that can self-heal and sense chemicals in the environment.[2,3] However, maintaining a viable living material remains a significant roadblock. Bacterial spores provide a robust option that enables bacteria cells to survive harsh conditions in a dormant, spore, state.[4] Bacterial spores are capable of surviving ultraviolet light exposure, drastic temperature shifts, and lack of nutrients. [5] We have integrated bacterial spores into a material system to produce a functional coating capable of detecting cracks via fluorescence. Our work explores the material coating design and material selection process. Lastly, we demonstrate the versatility of our coating for different geometries and loading conditions for in situ fatigue crack detection.

The tools and technical expertise provided at the CNF was essential to the rapid testing necessary for biological samples. Future work will investigate different polymer matrix options for obtaining varied material properties. We will also expand on our preliminary tests to include genetically modified spores to respond to specific germinants for sensing applications.

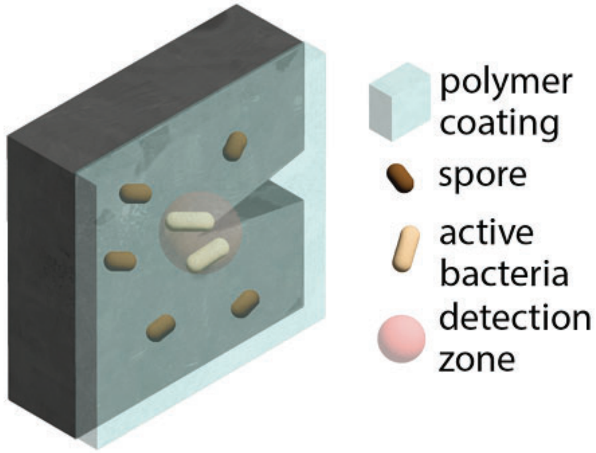

Figure 1: Bacteria-based fatigue crack detection and mitigation concept schematic.

References:

[1] P. Paris, M. Gomez, W. Anderson, Trends Engin. 1961, 13, 9.

[2] H. Jonkers, Self Healing Concrete: A Biological Approach, Vol. 100, Springer, Dordrecht, 2007.

[3] L. Gao, L. Feng, D. F. Sauer, M. Wittwer, Y. Hu, J. Schiffels, X. Li, Cell Rep. Phys. Sci. 2022, 3, 101054.

[4] F. Lyu, T. Zhang, M. Gui, Y. Wang, L. Zhao, X. Wu, L. Rao, X. Liao, CRFSFS 2023, 22, 2728.

[5] E. Black, P. Setlow, A. Hocking, C. Stewart, A. Kelly, D. Hoover, Compr. Rev. Food Sci. Food Saf. 2007, 6, 103.

Biphilic Porous Transport Layer Enabled High Efficiency and High-current Density Proton Exchanger Membrane Electrolyzer

CNF Project Number: 322324
Principal Investigator(s): Lenan Zhang
User(s): Paranut Aksornsiri

Affiliation(s): Sibley School of Mechanical and Aerospace Engineering, Cornell University
Primary Source(s) of Research Funding: Electricity Generating Authority of Thailand
Contact: lzhang@cornell.edu, pa379@cornell.edu
Research Group Website: https://sites.google.com/view/energy-research-lab/home

Primary CNF Tools Used: ABM Contact Aligner, Heidelberg MLA 150 Maskless Aligner

Abstract:

Green hydrogen is considered one of the most promising energy carriers for achieving carbon neutrality, offering a scalable solution for long-duration, high-energy-density energy storage. Among various production technologies, proton exchange membrane water electrolysis (PEMWE) stands out due to its high energy efficiency, compatibility with intermittent renewable energy sources, and ability to generate high-purity hydrogen.

However, at high current densities, PEMWE systems suffer from significant mass transport losses, particularly due to limitations in water and gas transport within the porous transport layer (PTL). [1,2]

This research proposes a novel design for the PTL aimed at enabling ultrahigh current density operation (>5 A/cm²) with enhanced energy efficiency. The design introduces a biphilic pattern (figure 1), comprising spatially alternating hydrophilic and hydrophobic regions, into the PTL to facilitate mass transport. Hydrophilic regions promote continuous water delivery to the catalyst layer, while hydrophobic regions facilitate oxygen gas removal. The biphilic pattern is fabricated using photolithographic techniques, followed by coating of hydrophobic particles. After development and photoresist removal, the resulting PTL exhibits distinct wetting regions. Preliminary analysis suggests that this design may double the energy efficiency under ultrahigh current density conditions.

Summary of the Research:

The proposed biphilic pattern is designed to enhance mass transport on the anode side of the PEM electrolyzer by facilitating the removal of oxygen bubbles through dry hydrophobic channels. These hydrophobic regions leverage capillary pressure in the PTL's microstructure to drive oxygen out of the cell, while hydrophilic regions ensure continuous water supply to the catalyst layer. This spatial separation of gas and liquid transport pathways minimizes bubble accumulation on the catalyst surface, therefore reducing overpotentials and enhancing overall electrochemical performance [3].

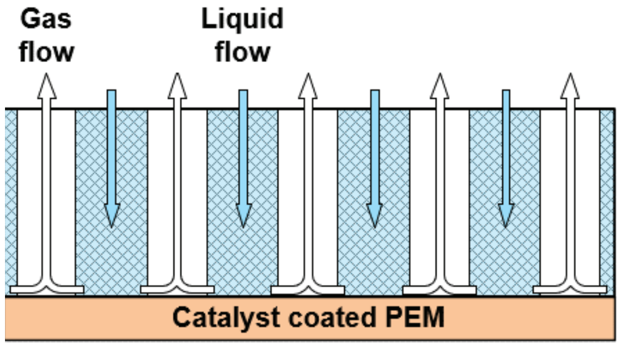

Figure 1: Figure 1: Schematic illustration of the biphilic porous transport layer (PTL) design.

To demonstrate the feasibility of the patterning approach, initial experiments were conducted on silicon wafers due to their flat geometry and ease of processing. A thin layer of P20 MICROPOSIT™ PRIMER was applied, followed by spin-coating of SHIPLEY MICROPOSIT™ S1827 photoresist. After soft baking, the samples were exposed to UV light using an ABM contact aligner and developed to define the desired pattern. The developed samples were then uniformly coated with hydrophobic particles. Finally, the photoresist was removed using MICROPOSIT™ REMOVER, leaving hydrophobic particles only on the exposed regions, thereby forming the intended biphilic pattern. As shown in Figure 2, water droplets deposited on each region exhibit distinctly different contact angles, confirming successful formation of a biphilic surface.

Subsequently, the fabrication was extended to titanium PTL substrates. The samples were diced to the desired size using a DISCO dicing saw. A simplified design—

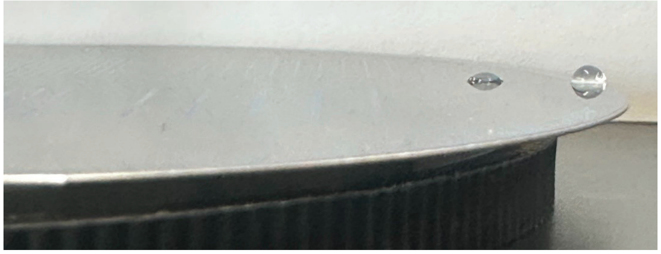

Figure 2: Water droplets on silicon wafer demonstrating biphilic pattern formation.

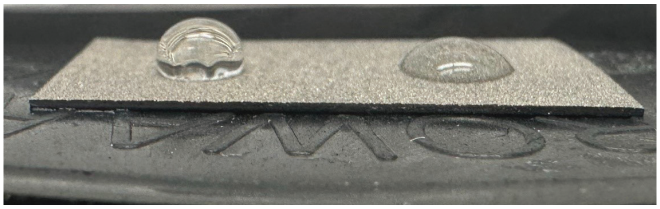

Figure 3: Water droplets on titanium porous transport layer with a simplified biphilic pattern.

comprising one large hydrophilic region adjacent to a large hydrophobic region—was fabricated to examine wetting contrast by following the same procedure as the silicon wafers. Figure 3 displays the resulting patterned PTL.

However, experimental observations revealed incomplete removal of hydrophobic particles from the photoresist-covered areas, resulting in partial hydrophobicity in regions intended to be hydrophilic. The final photomask design, generated using the Heidelberg Mask Writer DWL2000, was successfully used to produce high-resolution micro-patterns on titanium substrates, though the final coating step is pending resolution of the contamination issue.

Conclusions and Future Plans:

Microscale patterning was successfully achieved on both silicon and porous titanium substrates. However, the incomplete removal of hydrophobic particles remains a key challenge, affecting the fidelity of the biphilic pattern. Future work will focus on enhancing the contrast between hydrophilic and hydrophobic regions through optimized cleaning procedures, including alkaline treatment and plasma exposure. Additionally, further refinement of the photolithography parameters will be pursued to improve resist coating uniformity on the porous PTL surface and ensure pattern integrity. These steps are critical to fully realizing the potential of the proposed PTL design for high-efficiency PEMWE operation.

References:

[1] M. R. Domalanta et al., Pathways towards Achieving High Current Density Water Electrolysis: from Material Perspective to System Configuration, ChemSusChem, 16, e202300310, 2023.

[2] J. K. Lee et al., Critical Current Density as a Performance Indicator for Gas-Evolving Electrochemical Devices, Cell Reports Physical Science, 1, 100147, 2020.

[3] Y. Yang et al., Improving Mass Transfer with Surface Patterning of the Porous Transport Layer for PEM Water Electrolysis, Cell Reports Physical Science, 6, 102433, 2025.

Electrically Programmable Microvalve for On-Demand Drug Delivery

CNF Project Number: 241616
Principal Investigator(s): Itai Cohen
User(s): Jinsong Zhang, Wei Wang, Yanxin Ji, Jacob Pelster, Chibin Zheng

Affiliation(s): Laboratory of Atomic and Solid State Physics, Kavli Institute at Cornell for Nanoscale Science, Department of Physics

Primary Source(s) of Research Funding: National Science Foundation

Contact: itai.cohen@cornell.edu, ww459@cornell.edu; jz2325@cornell.edu; yj323@cornell.edu; jtp246@cornell.edu; cz553@cornell.edu

Research Group Website: https://cohengroup.lassp.cornell.edu/

Primary CNF Tools Used: Oxford 81/82 etcher, Oxford 100 ICP etcher, Oxford Cobra ICP; Xactix Xenon Difluoride, YES EcoClean Asher, Gamma Automatic Coat-Develop Tool, SC 4500 odd-hour evaporator, OEM M1 AlN Sputter, AJA Sputter Tool, Heidelberg DWL2000, ABM Mask Aligner, Oxford FlexAL, Oxford PECVD, Plasma-Therm Takachi HDP-CVD, DISCO Dicing Saw, Zeiss SEM, KLA P7 Profilometer, Keyence VHX-7100 Digital Microscope

Abstract:

We present a microactuator-integrated nanofluidic membrane system that enables actively programmable and reversible control of molecular transport for advanced drug delivery applications. This platform combines two key technologies: (1) electrostatically gated nanofluidic channels for charge-selective diffusion and (2) Pd/Ti bilayer microactuators for mechanically regulating bulk flow. The actuators, operating under low-voltage input (−1.2 V to +0.6 V), undergo reversible bending via hydrogen absorption without gas evolution, providing robust and fatigue- resistant control over valve states. Integrated with a hexagonal array of slit nanochannels, the system supports dynamic, spatially patterned gating of molecular transport. Unlike conventional controlled-release systems that rely on passive diffusion or fixed release profiles, our approach offers real-time, reconfigurable, and multiplexed control over drug dosing. Preliminary experiments demonstrate highly uniform actuator response, long-term durability over hundreds of cycles, and programmable region-specific valve activation. This technology provides a versatile foundation for implantable drug delivery systems with closed-loop feedback capability, and may be extended to broader microfluidic and bio-interfacing applications.

Summary of Research:

Precise, responsive drug delivery remains a central challenge in biomedical engineering, especially for chronic diseases requiring variable dosing over time [1, 2]. Conventional systems—such as polymer matrices, osmotic pumps, or diffusion-based capsules—typically offer fixed or pre- programmed release profiles, lacking adaptability to dynamic physiological conditions.

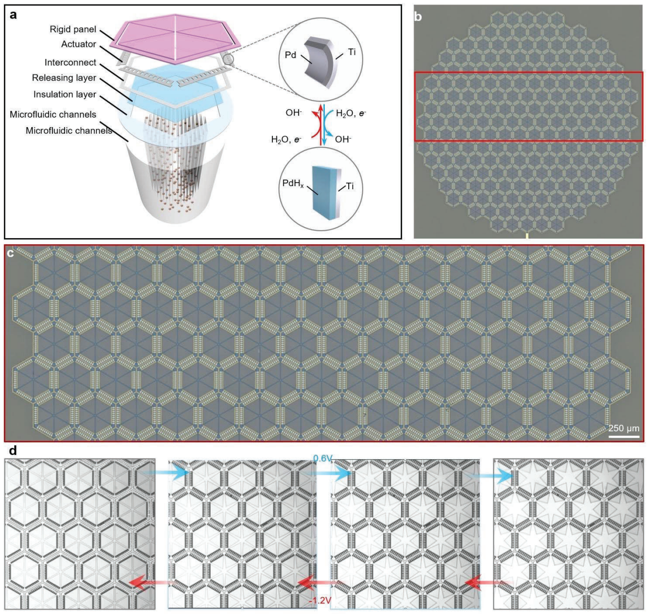

Figure 1: Integrated microactuator-nanofluidic membrane platform for voltage-controlled drug delivery. (a) Schematic diagram of the device architecture. A Pd/Ti bilayer microactuator is integrated on top of a nanofluidic membrane consisting of layered microfluidic channels, insulation, and releasing layers. When voltage is applied, the actuator bends due to hydrogen absorption in Pd, forming PdHx, enabling reversible switching between open and closed states without bubble formation. (b) Optical micrograph of a fabricated circular array containing hundreds of individual actuator units arranged in a hexagonal lattice. The red box outlines the region shown in (c). (c) Zoom-in view of the actuator array, showing the detailed tiling pattern of hexagonal units, each with a central membrane and six radial flaps. The actuators are fabricated with high uniformity across the array. Scale bar: 250 µm. (d) Sequential optical images showing voltage-controlled actuation: valves remain closed at 0 V, open at +0.6 V, and return to the closed state at −1.2 V. The actuation is robust and repeatable for over 300 cycles using 100 nm Pd / 100 nm Ti bilayer actuators.

Nanofluidic membranes offer electrostatic selectivity, but their functionality is limited to specific molecular charges [3]. To overcome these constraints, we propose a hybrid strategy that combines nanofluidic selectivity with actively reconfigurable microvalves for spatiotemporal control of molecular transport.

We have developed an electrically programmable microvalve array integrated with a nanofluidic membrane to enable real-time, spatially controlled drug delivery. The device combines Pd/Ti bilayer electrochemical actuators with dense arrays of nanoslits for charge-selective transport, enabling dual-mode regulation of molecular flow through both electrostatic and mechanical mechanisms.

Figure 1a illustrates the device architecture, where thin-film actuators are monolithically integrated atop nanofluidic membranes consisting of Si-based slit channels, insulation, and fluidic layers. Upon application of a voltage (−1.2 V to +0.6 V), the Pd layer undergoes hydrogen absorption, forming PdHx, which induces out-of-plane bending relative to Ti due to lattice expansion. This mechanical deformation allows each valve to reversibly switch between open and closed states (Figure 1d). The actuation process is stable, bubble-free, and repeatable across more than 300 cycles with minimal fatigue. The fabricated actuator array, arranged in a hexagonal tiling (Figure 1b–c), demonstrates high patterning fidelity and uniform performance. Each unit consists of six independent actuator flaps surrounding a central nanochannel inlet. Actuation behavior is highly robust, with >95% of flaps responding uniformly under each voltage sweep. Each device utilizes 100 nm Pd / 100 nm Ti bilayers.

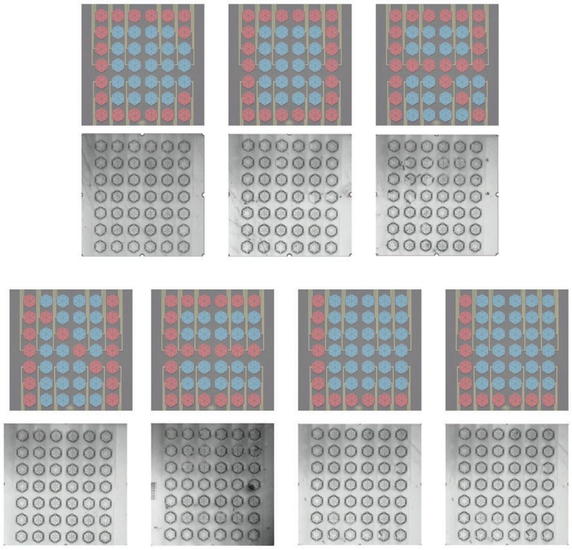

Figure 2: Spatially programmable microvalve actuation for pattern-defined molecular gating. Top two rows: Predefined activation patterns and corresponding optical micrographs demonstrating selective spatial control of microactuator arrays. Colored overlays (red and blue) represent distinct voltage-addressable regions activated under orthogonal driving signals. Each pattern corresponds to a unique flap-opening configuration across the array, allowing for reconfigurable and localized drug release profiles. Bottom two rows: Additional examples of spatially programmed actuation with varied addressable regions. Designed activation maps (top) are followed by corresponding actuation results (bottom), confirming high spatial fidelity and reproducibility across repeated cycles. The platform enables complex programmable gating geometries for multiplexed delivery zones or patterned molecular access.

To demonstrate spatial programmability, we designed multi-region addressable patterns using independently biased electrode zones (Figure 2). Simulated activation masks (colored blue and red) match closely with experimental actuation results across multiple configurations, confirming our ability to locally modulate flow through desired patterns. This programmable gating enables localized drug dosing, zonal delivery control, and dynamic therapeutic scheduling within a single device.

The hybrid system addresses limitations of current controlled-release platforms, which often rely on static polymer matrices, osmotic gradients, or diffusion-based mechanisms that lack real-time control [2,4]. In contrast, our platform enables both charge-selective gating through electrostatic interaction within the nanochannels and physical flow modulation via microactuation. This allows for transport of a wide range of molecules, including neutrals and cations, not previously accessible via electrostatic gating alone.

Conclusions and Future Work:

Future efforts will focus on packaging and biocompatibility, in vivo validation, and integration with real-time feedback systems for autonomous control. Ultimately, this microvalve-nanofluidic hybrid architecture could serve as the foundation for adaptive therapeutic implants, multi-analyte chemical release platforms, or sensor-responsive systems in closed-loop medical devices.

References:

[1] Del Bono F, Di Trani N, Demarchi D, et al. Active implantable drug delivery systems: engineering factors, challenges, opportunities[J]. Lab on a Chip, 2025.

[2] Di Trani N, Silvestri A, Sizovs A, et al. Electrostatically gated nanofluidic membrane for ultra- low power controlled drug delivery[J]. Lab on a Chip, 2020, 20(9): 1562-1576.

[3] Lei D, Zhang Z, Jiang L. Bioinspired 2D nanofluidic membranes for energy applications[J]. Chemical Society Reviews, 2024, 53(5): 2300-2325.

[4] Pons-Faudoa F P, Di Trani N, Capuani S, et al. Long-acting refillable nanofluidic implant confers protection against SHIV infection in nonhuman primates[J]. Science translational medicine, 2023, 15(702): eadg2887.

Programmable Magnetoelastic Energy Landscapes for Autonomous Microscopic Machines

CNF Project Number: 296421
Principal Investigator(s): Itai Cohen, Paul L. McEuen
User(s): Weiyi Li, Zexi Liang, Melody Xuan Lim

Affiliation(s): Kavli Institute at Cornell for Nanoscale Science, School of Applied and Engineering Physics, Laboratory of Atomic and Solid-State Physics, Department of Physics, Cornell University

Primary Source(s) of Research Funding: National Science Foundation, Alfred P. Sloan Foundation

Contact: itai.cohen@cornell.edu, plm23@cornell.edu, zl467@cornell.edu, mxl3@cornell.edu, wl689@cornell.edu

Primary CNF Tools Used: Oxford 81/82 etcher, YES EcoClean Asher, ASML DUV stepper, Gamma Automatic Coat-Develop Tool, JEOL 9500 EBL, SC 4500 odd-hour evaporator, AJA Sputter Deposition, Heidelberg DWL2000, PT770 ICP etcher (left side), Unaxis 770 Deep Silicon Etcher, Oxford FlexAL, Plasma-Therm Takachi HDP-CVD, Zeiss SEM, Veeco AFM.

Abstract:

The function of many microscopic machines is determined not only by their structure, but by conformational, dynamic changes in the shape of a device or molecule. Developing design paradigms for these microscopic machines requires the development of novel experimental platforms with controlled energy landscapes, and the ability to drive transitions between energy minima. Here, we introduce such a platform based on panels covered with programmable nanomagnetic domains, connected by flexible elastic hinges. We show that the combination of magnetic and elastic parameters gives rise to tunable energy minima, which can be accessed by applying an external magnetic field. Structuring the elastic or magnetic degrees of freedom of the device leads to the creation of multiple stable states, and as a first step we demonstrate a basic paradigm for three-state work cycles. We combine these principles to produce conformation-dependent locomotion via a magnetic walker with bistable energy landscape.

Research Summary:

The function of many biological and synthetic micromachines is realized by targeted conformational changes (1). Such functions include catalysis, sensing, force and torque generation creating concentration gradients, fluid pumping, light steering, and locomotion. However, the rational design of microscopic machines that undergo conformational change and transduce energy into mechanical work remains an outstanding goal. A key obstacle is the difficulty of modeling and designing the entire energy landscape of systems driven by electrostatic and chemical interactions, and furthermore to perform mechanical work by controllably actuating transitions between local energy minima (2).

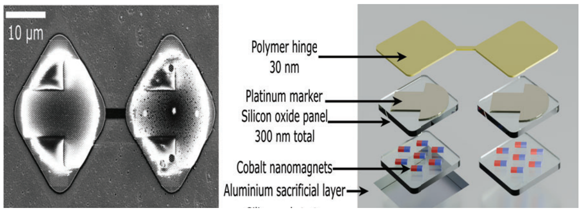

Figure 1: Scanning electron microscope image of the device, with schematic showing the device layer structure.

Here, we present a new experimental platform for programmable energy landscapes based on microscale magneto- elastic structures (Figure 1) (3,4,5). Competing elastic and magnetic interactions allow for the design and construction of energy landscapes with many potential minima, whose depth is controlled by device parameters. At the same time, transitions between these constructed energy minima can be actuated by applying directed torques in the form of external magnetic fields.

Combining magnetic and elastic design degrees-of-freedom allows for the construction of a two-state bistable shutter. Such a bistable shutter toggles between two states, here an "open" and a "closed" state, which can differentially control light transmission at the location of the free panel. In order to actuate transitions between local energy minima, we use an external magnetic field to apply a torque to the free panel. Once the panels are close enough, magnetic interactions between the panels stabilize the "closed state". To re-access the "open" state, we apply an increasing magnetic field, so that the stable state of the system switches to being aligned with the external magnetic field (Figure 2). This two-panel, one elastic degree-of- freedom device thus provides a minimal example of a bistable energy landscape with controlled minima depth, with a single actuated transition between the two stable states.

In addition to controlling an on/off state, many

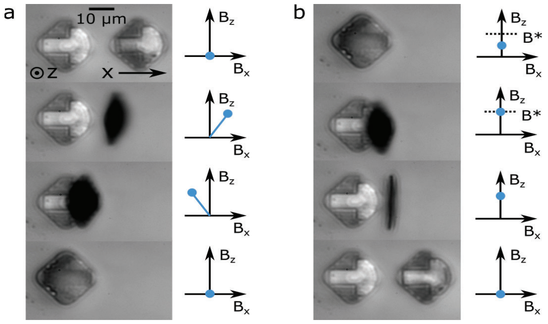

Figure 2: Using external magnetic fields to actuate a bistable shutter. (a) Sequence of images and accompany magnetic field magnitudes for closing a magnetic shutter. Magnetic interactions stabilize the closed position when the magnetic field is turned off. (b) Sequence of images showing the shutter re-opening upon the application of a finite magnetic field.

microscopic machines perform some work on the environment, such as pumping fluid, which requires a nonreciprocal cycle through configuration space. We construct such a nonreciprocal cycle by twisting the flexible elastic hinge to access a third stable state in the energy landscape (Figure 3). Each cycle of the machine pumps fluid in a rotational motion. This pumping is enabled by the difference in cross-sectional drag between the first and second steps of the work cycle, where the energy stored in the system by bending the hinge in-plane is released out-of-plane and transferred into rotational fluid flow.

The work generated (in the form of fluid flow) by this three-state device is realized by navigating between minima in an energy landscape. Such navigation requires a relatively complex control sequence in order to guide the free panel through the correct sequence of motions. In contrast, molecular motors convert a scalar energy input (ATP) to translate along a symmetry-broken direction. Similarly, we utilize a unidirectional magnetic field as our scalar energy input, and break the symmetry of the locomotion direction by bistability in the energy landscape of the magnetic device. In this case, devices operate within an energy landscape with multiple basins, where the initial condition of a device determines the basin about which it operates. The unidirectional magnetic field then serves as an energy source to drive work cycles within each basin, which translate to motion in opposite directions (Figure 4).

References:

[1] Alzgool, M., Tian, Y., Davaji, B., and Towfighian, S. (2023). Self-powered triboelectric MEMS accelerometer. Nano Energy, 109, 108282.

[2] M. Baroncini, L. Casimiro, C. De Vet, J. Groppi, S. Silvi, and A. Credi, Making and operating molecular machines: a multidisciplinary challenge, ChemistryOpen 7, 169 (2018).

[3] J. Cui, T.-Y. Huang, Z. Luo, P. Testa, H. Gu, X.-Z. Chen,B. J. Nelson, and L. J. Heyderman, Nanomagnetic encoding of shape-morphing micromachines, Nature 575, 164 (2019)

[4] C. L. Smart, T. G. Pearson, Z. Liang, M. X. Lim, M. I. Abdelrahman, F. Monticone, I. Cohen, and P. L. McEuen, Magnetically programmed diffractive robotics, Science 386, 1031 (2024).

[5] K. J. Dorsey, T. G. Pearson, E. Esposito, S. Russell, B. Bircan, Y. Han, M. Z. Miskin, D. A. Muller, I. Cohen, and P. L. McEuen, Atomic layer deposition for membranes, metamaterials, and mechanisms, Advanced Materials 31, 1901944 (2019).

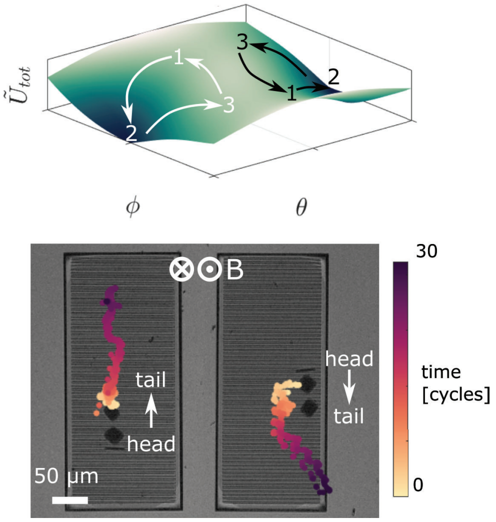

Figure 4: (a) Energy landscape with two minima, allowing for two independent work cycles, (b) Center-of-mass motion of two magnetic walkers with tails facing opposite directions, under the same magnetic actuation, with the time indicated by the shared color scale on the right.

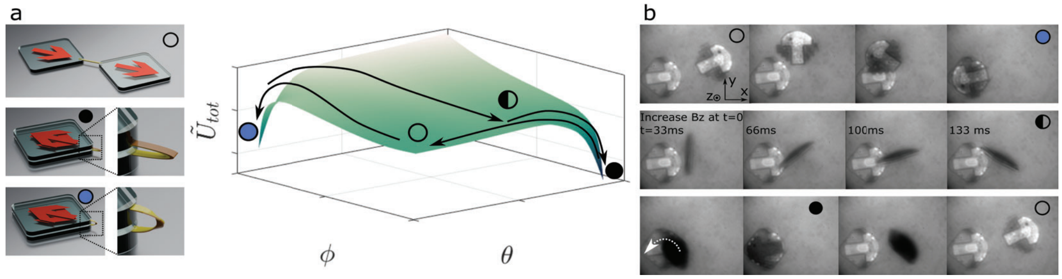

Figure 3: Creating a microfluidic rotary pump by navigating a multi-stable energy landscape. Diagram of the stable states of the system, together with the predicted energy landscape. (b) Series of optical microscope images showing a three-state work cycle, marked by symbols corresponding to the illustrations in (a).

Bioinspired Acoustic Particle Velocity Sensor

CNF Project Number: 322424

Principal Investigator(s): Jian Zhou

User(s): Xiangyu Wei, Wanyin Zheng

Affiliation(s): Department of Mechanical Engineering, Binghamton University

Primary Source(s) of Research Funding: Binghamton University startup, National Science Foundation

Contact: jianzhou@binghamton.edu, xwei2@binghamton.edu, wzheng7@binghamton.edu

Research Group Website: https://www.zhou-labs.com/

Primary CNF Tools Used: LPCVD silicon nitride deposition

Abstract:

Inspired by the velocity-sensitive ears of small animals [1, 2], vector acoustic sensing using viscous-driven mechanical structures is emerging as a promising alternative to traditional pressure-based sound detection. We have performed silicon nitride deposition using CNF, which serves as the structural layer for forming slender microbeams used in bioinspired acoustic particle velocity sensing. This vector sensing approach overcomes fundamental limitations of scalar pressure-based acoustic sensors, offering intrinsic advantages in directional sound detection, source localization, and noise rejection.

Research Summary:

We used CNF facilities for silicon nitride deposition on double-side- polished wafers. The deposited silicon nitride served as the structural layer for fabricating slender microbeams designed for bioinspired acoustic particle velocity sensing.

Conclusions and Future Steps:

We successfully fabricated slender silicon nitride microbeams (Figure 1) based on the deposition work performed at CNF, which are currently being characterized for their performance in acoustic particle velocity sensing. As a next step, we plan to use the Nanoscribe 3D printer at CNF to fabricate 3D microstructures on the silicon nitride beams. These structures aim to enhance acoustic performance by mimicking the 3D geometry of mosquito antennae, which are capable of detecting extremely weak sounds.

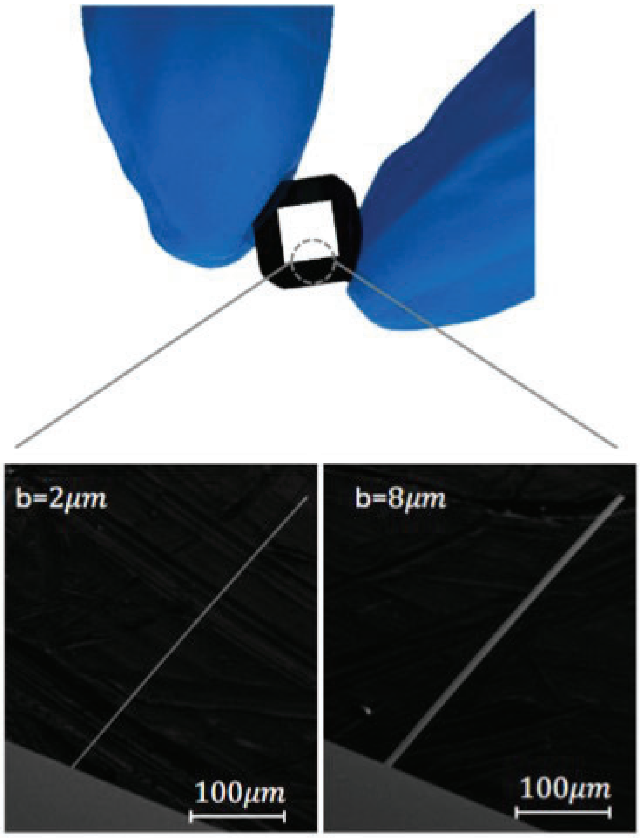

Figure 1: False-color scanning electron microscope image of a diffractive robot, consisting of (yellow) ALD silicon oxide hinges, (red) programmable cobalt nanomagnets, and (blue) rigid silicon oxide panels.

References:

[1] Zhou, Jian, Junpeng Lai, Gil Menda, Jay A. Stafstrom, Carol I. Miles, Ronald R. Hoy, and Ronald N. Miles. "Outsourced hearing in an orb-weaving spider that uses its web as an auditory sensor." Proceedings of the National Academy of Sciences 119, no. 14 (2022): e2122789119.

[2] Pantoja-Sánchez, Hoover, Brian C. Leavell, Bianca Rendon, WA Priyanka P. de-Silva, Richa Singh, Jian Zhou, Gil Menda et al. "Tiny spies: mosquito antennae are sensitive sensors for eavesdropping on frog calls." Journal of Experimental Biology 226, no. 24 (2023): jeb245359.

23dB On-Chip Interferometric Signal-to-Noise Enhancement via Weak Value Amplification

CNF Project Number: 2524-17
Principal Investigator(s): Jaime Cardenas
User(s): Yuhan Mei

Affiliation(s): Department of Physics and Astronomy, University of Rochester

Primary Source(s) of Research Funding: National Science Foundation

Contact: jaime.cardenas@rochester.edu, ymei7@ur.rochester.edu

Research Group Website: https://www.hajim.rochester.edu/optics/cardenas/

Primary CNF Tools Used: ASML stepper, Oxford 100 Inductively coupled plasma reactive ion etching (ICP-RIE), YES EcoClean Asher, Oxford PECVD, Furnace, JEOL-9500, Woollan RC2 Spectroscopic Ellipsometer, AJA Sputter, Unaxis 770 Deep Silicon Etch, Veeco Icon AFM, PT VLN Deep Silicon Etch, Xactix Xenon Difluoride etcher

Abstract:

We demonstrate a 23dB On-chip Interferometric Signal-to-Noise Enhancement in the phase response of an on-chip weak value interferometer compared to a standard Mach-Zehnder interferometer paving the way to ultrahigh sensitivity in classical interferometry.

Summary of Research:

Optical interferometry plays a critical role in precision metrology, gravitational wave detection, positioning and navigation, and environmental sensing. However, the sensitivity is fundamentally limited by quantum noises such as shot noise. Classical methods to improve the sensitivity of a measurement usually minimize electronic and technical sources of noise to operate in the shot noise limit. In this limit, the signal to noise ratio (SNR), and thus the sensitivity, can be enhanced by increasing the optical power that reaches the detector up to the point of detector saturation. Quantum strategies to improve the SNR use quantum squeezing to reduce the shot noise level, which, however, is difficult to implement in practice and very susceptible to loss.

Here, we show that weak value amplification (WVA) on a photonic chip is capable of record-breaking sensitivity enhancement by amplifying the signal without increasing the detected optical power. WVA enhances sensitivity by post-selecting photons for detection[1–3]. WVA has previously demonstrated measurements of optical beam displacements of a few femtometers[4] and object velocities as low as 400fm/s[5]. However, these demonstrations were shown on bulky tabletop experiments and can't access large amplifications. Previous on-chip demonstration of WVA showed an enhancement of 7dB[6]. In this work, we have successfully implemented WVA in an integrated photonic device, which offers a compact and stable solution for SNR improvement, achieving a 23dB SNR improvement that is robust against optical loss. The amplification surpasses the record 15dB tabletop quantum squeezing record to the best of our knowledge[7].

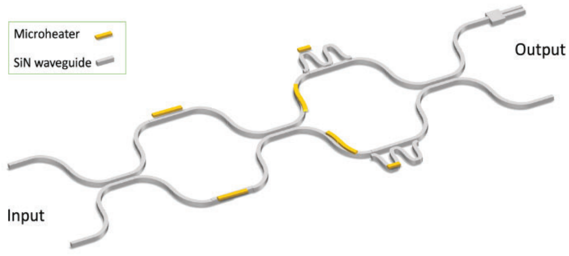

Figure 1: A schematic of A schematic of the integrated ultra-high weak value device.

We fabricate the device on a CMOS compatible silicon nitride platform. The device schematic is given in Figure 1. The fabrication process begins by depositing a 300 nm Si3N4 layer using LPCVD on top of a 4um thermal-grown SiO2 layer as shown in Figure 2. We deposit 400nm silicon dioxide by OXFORD PECVD on top of waveguide layer as a hard mask for following etching processes. We pattern the waveguides (single mode: 1.06 um wide, multi-mode: 2 um wide) with JEOL 9500 e-beam lithography and etch with OXFORD 100. The cladding is a 2um SiO2 layer deposited by OXFORD PECVD with TEOS recipe. Next, we pattern the microheaters with ASML DUV photolithography. Then, we sputter 10 nm Titanium as an adhesion layer and another 100 nm Pt (3 um wide, 100um long) with AJA sputter. The metal residues remaining on the photoresist are then removed using acetone to finalize the formation

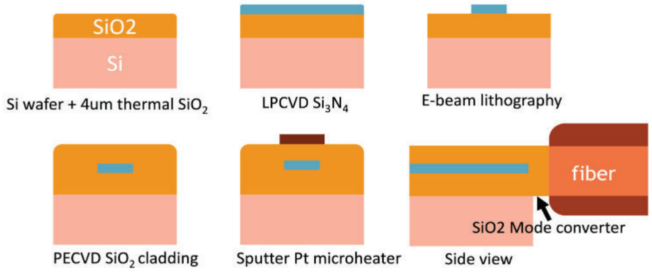

Figure 2: Main fabrication steps.

of microheaters on the chip. To improve fiber-chip coupling efficiency by matching the mode area in fiber (diameter = 10.4um), we pattern mode converters with ASML DUV photolithography at the end of inversed waveguide tapers (short sections of SiO2 measuring 10um in length and tapering from 20um to 11.5um in width suspended in the air).[8,9]We etch 6 um SiO2 with OXFORD 100 and then etch Si by 160um with Bosch process with VLN deep Silicon etcher. Finally, we undercut the silicon under the mode converter consist of silicon dioxide with Xactix Xenon Difluoride (XeF2) etcher.

Conclusions and Future Steps:

We have successfully tested 23dB SNR improvement by weak value amplification in fabricated integrated photonic devices. Our future research aims to apply this technique to capture phase signals from external information carriers, such as making a highly sensitive gyroscope.

References:

[1] Aharonov, Y. How the result of a measurement of a component of the spin of a spin-1/2 particle can turn out to be 100. Phys. Rev. Lett. 60, 1351–1354 (1988).

[2] Duck, I. M., Stevenson, P. M. & Sudarshan, E. C. G. The sense in which a ‘weak measurement’ of a spin-½ particle’s spin component yields a value 100. Phys. Rev. D 40, 2112–2117 (1989).

[3] Dressel, J., Malik, M., Miatto, F. M., Jordan, A. N. & Boyd, R. W. Colloquium : Understanding quantum weak values: Basics and applications. Rev. Mod. Phys. 86, 307–316 (2014).

[4] Dixon, P. B., Starling, D. J., Jordan, A. N. & Howell, J. C. Ultrasensitive Beam Deflection Measurement via Interferometric Weak Value Amplification. Phys. Rev. Lett. 102, 173601 (2009).

[5] Viza, G. I. et al. Weak-values technique for velocity measurements. Optics Letters 38, 2949–2952 (2013).

[6] Song, M. et al. Enhanced on-chip phase measurement by inverse weak value amplification. Nat Commun 12, 6247 (2021).

[7] Vahlbruch, H., Mehmet, M., Danzmann, K. & Schnabel, R. Detection of 15 dB Squeezed States of Light and their Application for the Absolute Calibration of Photoelectric Quantum Efficiency. Phys. Rev. Lett. 117, 110801 (2016).

[8] Nauriyal, J., Song, M., Yu, R. & Cardenas, J. Fiber-to-chip fusion splicing for low-loss photonic packaging. Optica, OPTICA 6, 549–552 (2019).

[9] Kumar, S., Nauriyal, J. & Cardenas, J. Low-Loss, High Extinction Ratio Fiber to Chip Connection via Laser Fusion for Polarization Maintaining Fibers. in 2023 Optical Fiber Communications Conference and Exhibition (OFC) 1–3 (2023). doi:10.1364/OFC.2023.M3C.1.

On-Chip Soliton Generation

CNF Project Number: 2524-17
Principal Investigator(s): Jaime Cardenas
User(s): Arunima Nauriyal and Sushant Kumar

Affiliation(s): University of Rochester, Institute of Optics
Contact: jaime.cardenas@rochester.edu, anauriya@ur.rochester.edu
Primary CNF Tools Used: PECVD, LPCVD Furnace, Electron beam lithography JEOL 9500, ASML, Oxford 100, Unaxis, dicing saw, Piranha, YES eco clean

Abstract:

Development of on chip soliton generation using dispersion management. Carefully designing the waveguides by manipulating the dispersion properties of silicon nitride. Improving fiber to chip coupling efficiency by integrating mode converters [Fig. 1] to improve on chip soliton properties.

Summary of Research:

We achieved our goal of getting high energy anomalous dispersion soliton on chip. For a smoother surface we deposited TEOS using PECVD followed by the twist and grow method [1] in E4 furnace for LPCVD of thick nitride to manage nitride stress. Double pass writing was used in JEOL 9500 for higher precision and Q factor. To ensure we have no air gaps between the ring resonator and the bus waveguide we deposit HTO in furnace followed by TEOS deposition in PECVD as the upper cladding. The next step was using ASML lithography to pattern mode converters [2] on our wafer to maximize chips to fiber coupling. Etching oxide and nitride layers were done using the OXFORD 100 standard recipes. Silicon etching was performed using the Unaxis as Versaline was down, this was then followed by undercutting the wafer using Xenon difluoride. Many of these devices are under testing so we do not have results on the device performance yet.

Conclusions and Future Steps:

Our novel method for generation of solitons on chips was carefully and successfully implemented by using the tool available to us by CNF. We will be working on improving the devices to achieve higher peak power solitons and help the academic industry grow in knowledge.

Figure 1: Mode converter Top view

Acknowledgements:

The authors wish to thank National Science Foundation funding (award CCF-1918549). PLM gratefully acknowledges financial support from a David and Lucile Packard Foundation Fellowship. The authors wish to thank NTT Research for their financial and technical support. We gratefully acknowledge the Air Force Office of Scientific Research for funding under Award Number FA9550-22-1-0378. This work was performed in part at the Cornell NanoScale Facility, a member of the NNCI, which is supported by NSF Grant NNCI-2025233.

References:

[1] Houssein El Dirani, Laurene Youssef, Camille Petit-Etienne, Sebastien Kerdiles, Philippe Grosse, Christelle Monat, Erwine Pargon, and Corrado Sciancalepore,,""Ultralow-loss tightly confining Si3N4 waveguides and high-Q microresonators,"," in Opt. Express 27, 30726-30740 (2019).

[2] Juniyali Nauriyal, Meiting Song, Yi Zhang, Marissa Granados-Baez, and Jaime Cardenas, ""Fiber array to chip attach using laser fusion splicing for low loss"," Opt. Express 31, 21863-21869 (2023).

Suspended Multimode SiN Platform for Strong Intermodal Brillouin Scattering

CNF Project Number: 2524-17
Principal Investigator(s): Jaime Cardenas
User(s): Jiewei Xiang

Affiliation(s): The Institute of Optics, University of Rochester

Contact: jaime.cardenas@rochester.edu, jxiang6@ur.rochester.edu

Primary CNF Tools Used: ASML stepper, Oxford 100 Inductively coupled plasma reactive ion etching (ICP-RIE), YES EcoClean Asher, Oxford PECVD, Furnace, JEOL-9500, Heidelberg Mask Writer-DWL2000, ABM Contact Aligner, Woollan RC2 Spectroscopic Ellipsometer, YES Ecoclean asher, Critical pointer dryer-Leica

Abstract:

We demonstrate forward intermodal Brillouin interactions with fundamental acoustic modes (FIM-FAM) in a suspended triple-core Si_3N_4 waveguide, achieving sub-50 kHz linewidths and a gain coefficient over 1100 $W^{-1}\cdot m^{-1}$. This platform enables narrowband RF filtering in a CMOS-compatible photonic circuit.

Summary of Research:

Microwave filters based on stimulated Brillouin scattering (SBS) in integrated photonic platforms offer the potential for ultra-narrowband, reconfigurable RF filtering with high spectral resolution and compact form factors[1–4]. While Brillouin interactions in silicon nitride (Si_3N_4) waveguides are attractive due to the material's low optical loss and CMOS compatibility, achieving high SBS gain has been hindered by low photoelasticity and weak acoustic confinement[5–7]. To overcome these challenges, we demonstrate an on-chip forward intermodal SBS platform based on a suspended triple-core Si_3N_4 waveguide structure. This design supports SBS interactions between the TE_1 and TM_0 optical modes, which collectively drive low-frequency fundamental acoustic modes, including both flexural-y and torsional modes, via radiation pressure.

The waveguide geometry is carefully optimized to support strong acoustic mode confinement through large impedance mismatch at air-Si_3N_4 interface and to ensure momentum matching by engineering the effective index difference between the interacting optical modes. Importantly, the suspended waveguide is fabricated with a central core and two symmetric outer cores, creating a spatially distributed radiation pressure profile that avoids destructive cancellation and enhances net optical force coupling.

Using phonon-mediated four-wave mixing spectroscopy, we measure a Brillouin gain coefficient exceeding 1100 $W^{-1}\cdot m^{-1}$ and linewidths as low as 45 kHz, representing a record performance for SBS in Si_3N_4 waveguides. The suspended region is defined using a combination of dry etching and buffered oxide undercut, followed by critical point drying to preserve mechanical integrity. The triple-core waveguide supports large acoustic impedance mismatch with the surrounding air, suppressing phonon leakage and maintaining long phonon lifetimes. The structure also enables the formation of an acoustic cavity, where coherent reflections at the suspended region boundaries discretize the phonon spectrum, contributing to reduced acoustic linewidth.

This platform provides efficient access to fundamental acoustic modes with long coherence times and enables RF filtering capabilities that are fully compatible with planar photonic integration. Compared to SBS in

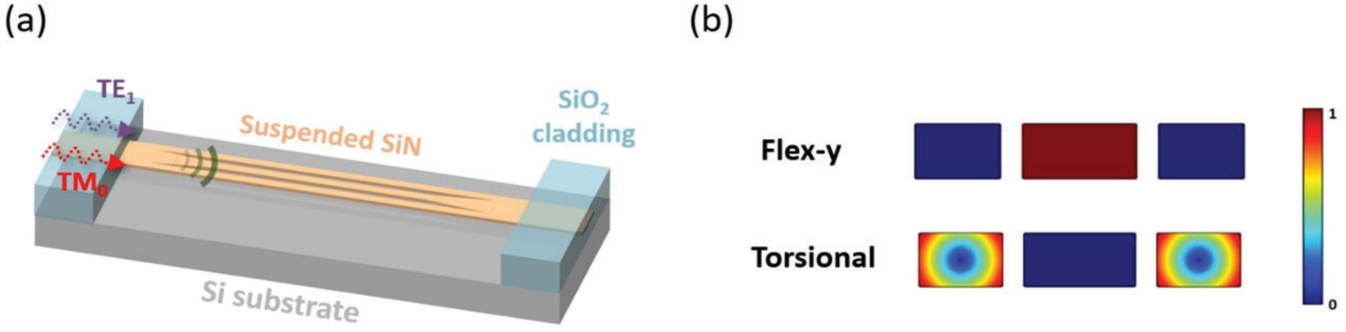

Figure 1: (a) Schematic of the suspended triple waveguide design (b) Simulated results for flexural-y and torsional acoustic modes.

optical fibers or hybrid materials, the demonstrated approach offers significant size reduction and process scalability, laying the foundation for on-chip microwave photonic filters with kHz-level resolution, high spectral selectivity, and low power operation.

Schematic plot of the suspended triple waveguide design and two fundamental acoustic modes confined in triple-core waveguide are shown in Fig. 1. The main fabrication steps for our design are illustrated in Fig. 2. The fabrication process begins with the deposition of a 4 µm thermal oxide bottom cladding layer, followed by a low-loss silicon nitride (Si_3N_4) core layer using low-pressure chemical vapor deposition (LPCVD). A PECVD oxide layer is then deposited to serve as an etch mask. Waveguides are defined using electron-beam lithography with a JEOL-9500 system and a negative-tone MaN resist. The pattern is transferred into the Si_3N_4 layer via inductively coupled plasma reactive ion etching (ICP-RIE) using an Oxford 100 system. Post-etching, the resist is stripped with a YES EcoClean plasma asher, and a top oxide cladding is deposited using PECVD.

To define the suspended region, a protective GKR resist layer is spun onto the chip, and an ASML stepper is used to expose the undercut windows. The top oxide thickness in the suspended area is partially reduced by another ICP etching step using the Oxford 100. The chip is then immersed in buffered oxide etchant (BOE) to selectively undercut the oxide beneath the waveguides, thereby achieving full suspension of the Si_3N_4 core. Finally, a critical point dryer (Leica CPD) is used to ensure structural integrity during the drying process. Fig. 3 shows the SEM image of the suspended Si_3N_4 waveguide, drying with the nitrogen gun and the critical point dryer.

Conclusions and Future Steps:

In conclusion, we demonstrate efficient on-chip forward intermodal stimulated Brillouin scattering (SBS) in a suspended triple-core silicon nitride waveguide, enabling strong interaction with low-frequency fundamental acoustic modes. Through careful mode engineering and acoustic confinement, we achieve a record Brillouin gain coefficient exceeding 1100 $W^{-1} \cdot m^{-1}$ with sub-50 kHz linewidths. This platform offers a compact, CMOS-compatible solution for narrowband microwave photonic filtering and establishes a scalable foundation for future low-power, high-resolution RF signal processing on chip.

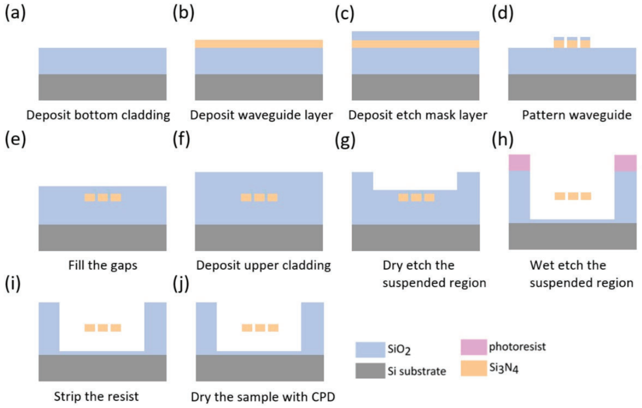

Figure 2: The main fabrication steps.

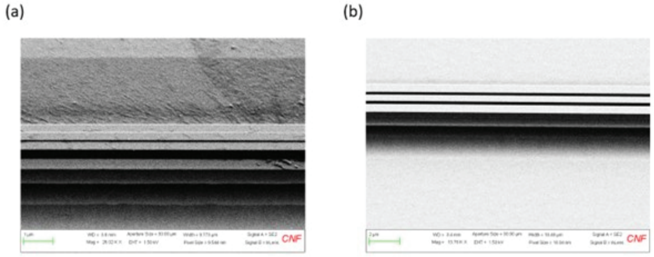

Figure 3: The SEM pictures of suspended Si3N4 waveguide. (a) Drying with the nitrogen gun (b) Drying with the critical point dryer.

References:

[1] Liu, Y. et al. Integration of Brillouin and passive circuits for enhanced radio-frequency photonic filtering. APL Photonics 4, 106103 (2019).

[2] Choudhary, A., Liu, Y., Marpaung, D. & Eggleton, B. J. On-Chip Brillouin Filtering of RF and Optical Signals. IEEE J. Sel. Top. Quantum Electron. 24, 1–11 (2018).

[3] Marpaung, D. et al. Low-power, chip-based stimulated Brillouin scattering microwave photonic filter with ultrahigh selectivity. Optica 2, 76–83 (2015).

[4] Eggleton, B. J., Poulton, C. G., Rakich, P. T., Steel, Michael. J. & Bahl, G. Brillouin integrated photonics. Nat.Photonics 13, 664–677 (2019).

[5] Klaver, Y. et al. Surface acoustic waves Brillouin photonics on a silicon nitride chip. Preprint at http://arxiv.org/abs/2410.16263 (2024).

[6] Botter, R. et al. Guided-acoustic stimulated Brillouin scattering in silicon nitride photonic circuits. Sci. Adv. 8, eabq2196 (2022).

[7] Gyger, F. et al. Observation of Stimulated Brillouin Scattering in Silicon Nitride Integrated Waveguides. Phys. Rev. Lett. 124, 013902 (2020).

Reducing the Operating Voltage of Deep-Ultraviolet Light Emitting Diodes

CNF Project Number: 2801-19
Principal Investigator(s): Debdeep Jena and Huili (Grace) Xing
User(s): Sheena (Hsin Wei) Huang

Affiliation(s): Electrical and Computer Engineering, Cornell University

Primary Source(s) of Research Funding: DARPA

Contact: djena@cornell.edu, hh494@cornell.edu

Research Group Website: https://jena-xing.engineering.cornell.edu/

Primary CNF Tools Used: PT770 ICP-RIE, Oxford PE-ALD, E-beam evaporator, AS 200 I-line stepper, Heidelberg MLA, Ultra SEM, PE-CVD, Woollam RC2 ellipsometer

Abstract:

Improving the electrical efficiency of deep-ultraviolet light emitting diodes (DUV- LEDs) based on the ultrawide bandgap material AlGaN is important for applications in disinfection, sensing, and lithography. Reducing the contact resistance of the device is crucial to improving the electrical efficiency. For high-performance electronic and optoelectronic devices, specific contact resistivities (p_c) on the order of 10^{-5}-10^{-6} Ωcm^2 are typically required. However, the ultrawide bandgap nature of AlGaN alloys poses intrinsic difficulties in achieving such low-resistance contacts. In this study, we investigate the co- optimization of p-InGaN and n-AlGaN contacts of DUV LEDs in monolithic integration.

These diodes are grown pseudomorphically on bulk AlN substrates by molecular beam epitaxy (MBE), resulting in low threading dislocation density and allowing for internal quantum efficiency (IQE), carrier injection efficiency (CIE), and lifetime of devices. The goal of this work is towards an electrically-injected DUV laser diode grown by MBE.

Summary of Research:

We find that using a thin $In_{0.07}Ga_{0.93}N$ cap is effective in achieving ohmic p-contacts with specific contact resistivity of 3.10×10^{-5} Ωcm^2. Upon monolithic integration of p- and n-contacts for DUV LEDs, we find that the high temperature annealing of 800 °C required for the formation of low resistance contacts to n-AlGaN severely degrades the p-InGaN layer, thereby reducing the hole concentration and increasing the specific contact resistivity to 9.72×10^{-4} Ωcm^2. Depositing a SiO_2 cap by plasma-enhanced atomic layer deposition (PE-ALD) prior to high temperature n-contact annealing restores the low p-contact resistivity, enabling simultaneous low-resistance p- and n-contacts.

DUV-LEDs emitting at 268 nm fabricated with the SiO_2 technique exhibit a 3.5 V reduction in operating voltage at a current level of 400 A/cm² and 1.9 mΩcm² decrease in differential ON-resistance. This study highlights a

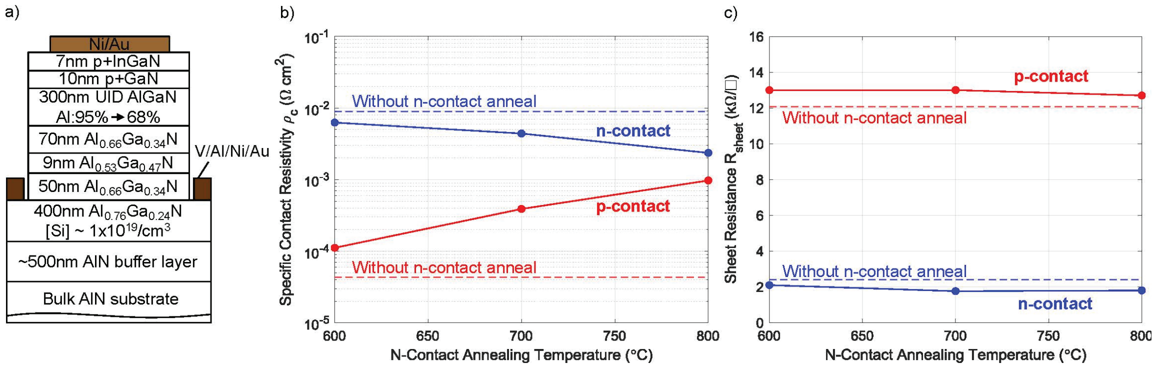

Figure1: (a) Heterostructure of the DUV LED samples used for this contact annealing temperature-dependent study. (b) Specific contact resistivity of n- and p-contact vs n- contact annealing temperature. P-contacts were subsequently annealed at 450 °C. All resistance values were extracted at 1 mA from CTLM-IV measurement. (c) Sheet resistance vs n-contact annealing temperature.

scalable route to high-performance, high-Al-content bipolar AlGaN devices.

Conclusions and Future Steps:

We are continuing to reduce the contact resistance of the p- and n-contacts through different metallization annealing conditions, metal stack, and acid treatment. We would also like to experiment with different capping materials like SiN and AlN to further reduce the degradation of p-InGaN during n-contact anneal.

References:

[1] Appl. Phys. Express 12, 124003 (2019)

[2] Advanced Electronic Materials 11, 2300840 (2025)

[3] Applied Physics Letters 124, 102109 (2024)

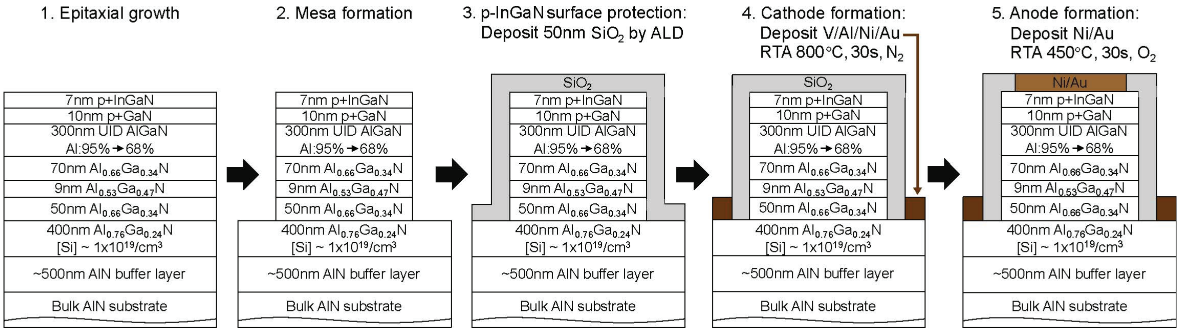

Figure 2: Schematic diagram illustrating the fabrication process of an LED with the SiO2 capping technique.

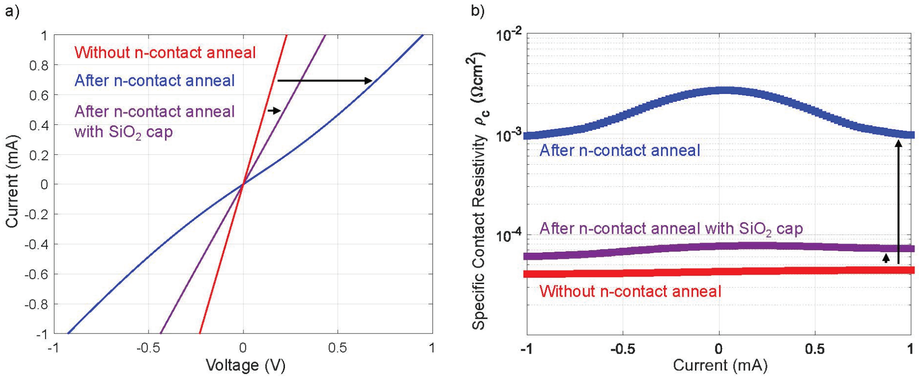

Figure 3: (a) CTLM-IV curves comparison of p-contact without undergoing n contact anneal, after undergoing n-contact anneal with SiO2 cap, and after undergoing n-contact anneal without SiO2 cap. IVs are plotted for 2 µm spacing. (b) Resistance vs metal electrode spacings for the data shown in (a).

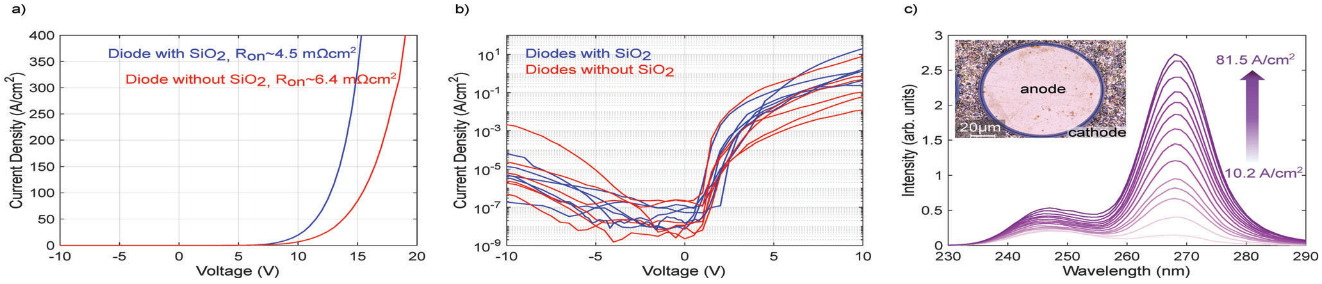

Figure 4: (a) Room temperature J-V characteristics of two LEDs, one with SiO2 capping method and one without. The diferential ON- resistance was extracted at 400A/cm2. (b) IV from batch test of LEDs with and without SiO2 capping. (c) Room temperature electroluminescence of an LED with the SiO2 capping method. Inset shows the microscopy image of a fabricated LED.

Towards Release-Free Intermodal Acousto-Optic Modulation at Visible and UV Wavelengths

CNF Project Number: 2985-21
Principal Investigator(s): Karan Kartik Mehta (2)
User(s): Oscar Jaramillo(1, 2)

Affiliation(s): School of Applied and Engineering Physics, Cornell University (2) School of Electrical and Computer Engineering, Cornell University

Primary Source(s) of Research Funding: NSF

Contact: karanmehta@cornell.edu, oj43@cornell.edu

Primary CNF Tools Used: Zeiss Ultra SEM, PT770 Etcher, Woollam RC2 Spectroscopic Ellipsometer, SC4500 Evaporator, Oxford PECVD, Keyence VHX-7100 Digital Microscope, Oxford FlexAL, OEM Endeavor M1, ASML Stepper

Abstract:

We present an inter-modal acousto-optic modulator designed to operate near λ~405 nm, leveraging acoustic modes confined and co-localized with a buried optical waveguide. We demonstrate the acoustic waveguiding concept, predicted to enable opto-mechanical coupling coefficient g ≈2 (sqrt(μW)mm)$^{-1}$.

Summary of Research, 2023-2024 Progress:

Acousto-optic modulators (AOMs) are widely used for frequency, phase, and amplitude control in a broad range of applications. Tabletop systems suffer from a relatively large footprint since the acoustic power is delocalized relative to the optical power. As a result, they typically consume on the order of 1-10 Watts, limiting their scalability and compatibility with multiplexed on-chip systems. Promising efficiencies of on- chip AOMs have been demonstrated at λ~780-1550 nm[1-4]. In certain cases, the use of non-standard CMOS materials and/or the fabrication complexity—such as released structures—pose challenges for large-scale integration. Furthermore, the materials employed to date are lossy in the UV and visible, essential for a variety of applications such as bio-chemical spectroscopy, and quantum control of trapped ions, neutral atoms, and solid-state quantum systems [5,6].

We present a design for robust, low-power, compact, and CMOS-compatible on-chip AOMs in the blue and UV, and demonstrate the fundamental waveguiding principle in our concept, towards scalable modulation for atomic systems. The concept leverages the high refractive index (RI) contrast offered by HfO2-Al2O3 composites [7], resulting in high opto-mechanical coupling coefficient g owing to n^3 scaling from photo-elasticity and ~$\varepsilon^2(\varepsilon_{clad}^{-1} - \varepsilon_{core}^{-1})$ core from waveguide boundary movement [1].

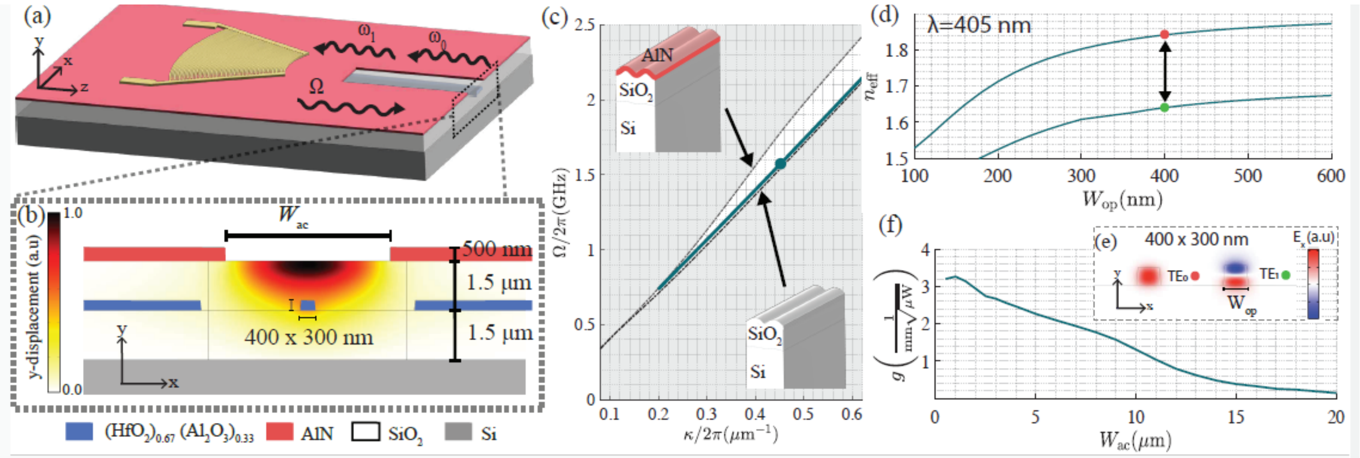

Figure 1: a) Schematic of a release-free AOM with co-confined acoustic and optical modes. (b) Cross section showing the dominant (y) displacement of a confined acoustic mode. c) Dispersion of guided mode with top (bottom) light-cone of a AlN+SiO$_2$ (SiO$_2$) RM. d) Effective index n$_{eff}$ of optical modes vs optical waveguide width W$_{op}$ with points representing modes used to calculate g. Gray modes are the non phase-matched modes. f) Simulated g for a 400 ×300 nm optical waveguide vs acoustic waveguide width (W$_{ac}$). Use of buried optical waveguides facilitates integration in CMOS- like stacks, along with integration of additional photonic waveguide layers for mode demultiplexing.

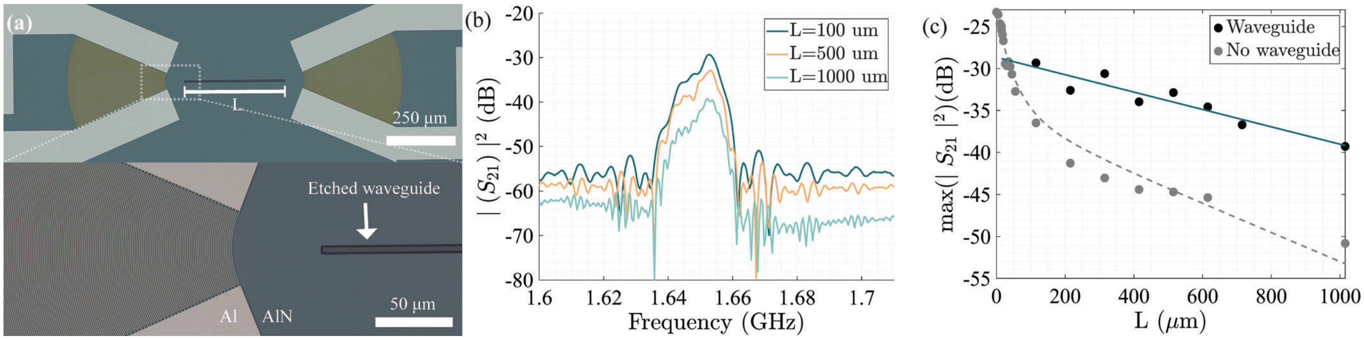

Figure 2: . a) Micrograph of a fabricated device with acoustic waveguide length L. b) Subset of representative |S12 |2 curves. c) Peak values for |S12|2 vs L for structures without and with the acoustic waveguide etched, indicating clear acoustic guiding.

Our AOM is composed of a $(\mathrm{HfO_2})_{.67}(\mathrm{Al2O_3})_{.67}$ multi-mode optical-waveguide buried in SiO2 and a 500 nm thick film of sputtered AlN used to launch a counter-propagating acoustic wave via a focusing inter- digitated transducer (Fig. 1a). The overall film stackup supports a RM (top inset of Fig. 1c), which together with an etched trench of width W_{ac} on AlN, creates a confined acoustic mode that overlaps with the buried optical waveguide (Fig. 1b). This mode is characterized by its dominant displacement along the y- direction, which shifts the top and bottom boundaries of the optical mode, coupling the TE_0 and the TE_1 modes at $\lambda = 405$ nm (Fig. 1d). As W_{ac} decreases, the acoustic energy overlap with the waveguide increases, resulting in a higher *g*. The acoustic wave induces oscillations in power between the optical modes, achieving full conversion from the TE_0 to the TE_1 mode at an acoustic power of $P_{\pi/2} = (\pi/(2gL_{\mathrm{eff}}))^2$, where $L_{\mathrm{eff}} = (1-\exp(-\alpha_{wg}L))/\alpha_{wg}$ is the effective length and α_{wg} is the acoustic waveguide loss.

To demonstrate the acoustic guiding principle, we design and fabricate the device from Fig. 1a without the optical waveguide. We sputter ~500 nm of AlN on 3 µm of thermal SiO2, pattern the electrodes with 100 nm of aluminum using a lift-off process and etch the waveguide with a dry etch process. A fabricated device with acoustic waveguide length L= 500 µm is shown in Fig. 2a. To estimate propagation loss ignoring reflections, we measure S21 for L varying from 100 to 1000 µm (Fig. 2b) and take the peak value as the transmission (Fig. 2c).A fit to $\max(|S_{12}|^2) = \eta^2\exp(-\alpha_{wg}L)$ indicates a transducer-WG coupling efficiency $|\eta| = -14.4 \pm 0.4$ dB and $\alpha_{wg} = 10.3 \pm 1.6$ dB/mm. Fig 2c also shows measurements of the same device prior to trench etching, demonstrating that as L increases, the transmission follows our model, which accounts for losses due to mode mismatch from defocusing, along with a Rayleigh-mode (RM) loss of approximately αRM ~9 dB/mm. With the etched waveguide, the transmission remains linear for an etched waveguide, indicating the functioning of the acoustic guiding. The measured transduction efficiency and acoustic waveguide loss project that a device with the $(\mathrm{HfO_2})_{.67}(\mathrm{Al_2O_3})_{.33}$ film should exhibit full mode-conversion in L= 100 µm with an RF driving power below 2.5 mW.

This work establishes an efficient platform for on-chip inter-modal acousto-optic modulation in a CMOS compatible and release-free configuration at blue and UV wavelengths. Realization of the full acousto- optic device leveraging the demonstrated optical and acoustic waveguides and transducers together is in progress. This platform may enable foundry-compatible efficient active control of UV and visible light in integrated systems.

References:

[1] C. J. Sarabalis et al., "Acousto-optic modulation of a wavelength-scale waveguide," Optica 8, 477–483 (2021).

[2] L. Zhang et al., "Integrated-waveguide-based acousto-optic modulation with complete optical conversion," Optica 11, 184–189 (2024).

[3] E. A. Kittlaus et al., "Electrically driven acousto-optics and broadband non-reciprocity in silicon photonics," Nat. Photonics 15, 43–52 (2021).

[4] Q. Lin et al., "Optical multi-beam steering and communication using integrated acousto-optics arrays," Nat. Commun. 16, 1–7 (2025).

[5] D. J. Blumenthal, "Photonic integration for UV to IR applications," APL Photonics 5 (2020).

[6] G. Moody et al., "2022 roadmap on integrated quantum photonics," J. Phys.: Photonics 4, 012501 (2022).

[7] O. Jaramillo et al., "$\mathrm{HfO_2}$-based platform for high-index-contrast visible and UV integrated photonics," Opt. Lett. 50, 3165–3168 (2025).

Programmable Poling for Electric Field Induced Second Harmonic Generation

CNF Project Number: 2971-21
Principal Investigator(s): Peter McMahon [1, 2]
User(s): Ryotatsu Yanagimoto [1, 3], Benjamin Ash [1, 3], Yiqi Zhao [1, 3]

Affiliation(s): [1] School of Applied and Engineering Physics, Cornell University, Ithaca, NY 14853, USA; [2] Kavli Institute at Cornell for Nanoscale Science, Cornell University, Ithaca, NY 14853, USA; [3] NTT Physics and Informatics Laboratories, NTT Research, Inc., Sunnyvale, CA, USA

Primary Source(s) of Research Funding: National Science Foundation (award CCF-1918549) PLM gratefully acknowledges financial support from a David and Lucile Packard Foundation Fellowship. The authors wish to thank NTT Research for their financial and technical support. We gratefully acknowledge the Air Force Office of Scientific Research for funding under Award Number FA9550-22-1-0378. This work was performed in part at the Cornell NanoScale Facility, a member of the National Nanotechnology Coordinated Infrastructure (NNCI), which is supported by the National Science Foundation (Grant NNCI-2025233)

Contact: pmcmahon@cornell.edu, ry338@cornell.edu, baa77@cornell.edu, yz2893@cornell.edu

Primary CNF Tools Used: Oxford PECVD, Oxford 100 ICP Dielectric, ASML DUV Stepper

Abstract:

Nonlinear photonics uses coherent interactions between optical waves to engineer functionality that is not possible with purely linear optics. Traditionally, the function of a nonlinear-optical device is determined during design and fixed during fabrication, which limits the scope and flexibility of its use. Here, we present a photonic device with an arbitrarily reconfigurable distribution of $\chi^{(2)}$ nonlinearity. To showcase the versatility of our device, we demonstrated spectral, spatial, and spatio-spectral engineering of second-harmonic generation by tailoring the quasi-phase-matching (QPM) grating structures in a two dimensional slab waveguied. Moreover, we have demonstrated record-breaking on-chip poling lengths by optimizing our poling pattern to a spiral waveguide geometry. Our work shows that we can transcend the conventional one-device–one-function paradigm, expanding the potential applications of nonlinear optics in situations where fast device reconfigurability is not merely practically convenient but essential—such as in programmable optical quantum gates and quantum light sources, all-optical signal processing, optical computation, and adaptive structured light for sensing.

Summary of Research:

Lithography-free photonics has attracted considerable attention in the field of programmable photonics because the large number of programmable parameters allows the device to move beyond the one-device–one-function paradigm. This means lithography-free devices can perform a large range of tasks and compensate for fabrication error [1]. Recent advances in lithography-free technology have enabled a device with real index of refraction modulation on-chip. In this device, a photoconductor and waveguiding layer with high native $\chi^{(2)}$ nonlinearity are stacked in series and placed under high voltage, allowing the two layers act as a voltage divider. Because the index of refraction of the waveguiding layer depends on the electric bias, the index of refraction can be spatially controlled by shining different patterns of light onto the photoconductor [2]. Using the same device concept, the core material can be replaced with silicon nitride, which possesses a large induced $\chi^{(2)}$ during an electric-field induced second harmonic (E-Fish) process.

By engineering $\chi^{(2)}$ quasi-phase matching (QPM) gratings on a two-dimensional slab waveguide, we realized versatile functions on a single device, flexibly controlling nonlinear- optical processes in the spectral, spatial, and spatio-spectral domains. The programmability of the device further enabled in-situ inverse designs and optimizations based on real-time experimental feedback, robustly achieving complex functions that are challenging on conventional non-programmable devices [3]. This approach can be extended to one-dimensional channel waveguide, where the loss of orthogonal spatial programmability is compensated by lower propagation loss, broader band operation, and longer interaction length. Preliminary studies show super-linear scaling of the nonlinear conversion efficiency with increased interaction length, paving a way for programmable nonlinear photonics on silicon nitride to one day rival lithium niobate.

Spatio-Spectral Engineering on Programmable Slab Waveguide:

To fabricate the nonlinear programmable slab waveguide, we started with a conductive P- type doped Si substrate with 1 µm of thermal SiO_2 and 2 µm of PECVD SiN_x provided by Silicon Valley Microelectronics. We then deposit 1 µm of PECVD SiO_2 followed by 12 µm of PECVD silicon-rich nitride (SRN), which acts as the photoconductive layer in the device.

Lastly, we sputter 30 nm of indium tin oxide (ITO) as our top electrode. After cleaving and polishing the waveguide facet, we couple an ELMO-HP pulsed laser from Menlo systems into the waveguide, apply high voltage to the stack, and project an image (generated by a spatial light modulator) onto device. The photoconductor and waveguide layers act as a voltage divider, so whenever the photoconductor becomes more conductive upon illumination, more voltage drops in the waveguiding layer, inducing a larger $\chi^{(2)}$ nonlinearity in the illuminated region. This process is shown in figure 1. The output of the waveguide is then imaged out to a grating, which separates the spectral components of each spatial position.

By sculpting the spatial $\chi^{(2)}(x, z)$ pattern, we can programmably phase match different processes at once. As figure 1 shows, we can engineer the output second harmonic wavefront in both the spatial and spectral domain by reprogramming the $\chi^{(2)}(x, z)$ pattern. Furthermore, because we can alter the nonlinearity distribution with no memory of the previous pattern, we can optimize the poling pattern to produce non-trivial spectral outputs. Figure 2 shows this concept, where we can use analytic poling patterns to produce easy spectral outputs, but more complicated outputs rely upon real-time feedback and optimization.

Super-linear Conversion Efficiency Scaling on Programmable Channel Waveguide:

Using the same principle as the slab waveguide, we fabricated a programmable channel waveguide using SiNx. To fabricate this device, we start with a conductive P-type doped Si substrate with 1 µm of thermal SiO_2. We then deposit 2 µm of PECVD SiNx and etch it using a $CHF_3/O_2/N_2$ chemistry and SiO_2 hard mask. We deposit an additional 1 µm of conformal PECVD SiO_2 followed by a 4 hour 1200 °C anneal to drive N-H bonds out of the film. We then follow the same process as the slab waveguide, depositing 12 µm of PECVD (SRN), sputtering, 30 nm of ITO, and cleaving the facets open.

With a finished device, we couple a Santec TSL-570 continuous-wave laser into a spiral structure and pole along the outer Archimedes spiral waveguide. By utilizing interference between different subdivisions of the spiral, the phase and poling period of each section can be optimized to achieve superliner scaling. Figure 3 shows the scaling of SHG signal measured with increasing poling distance (measured on a photomultiplier tube) and the loss of the device over the C-band, which shows the broadband potential of this device to be reprogrammed for efficient conversion.

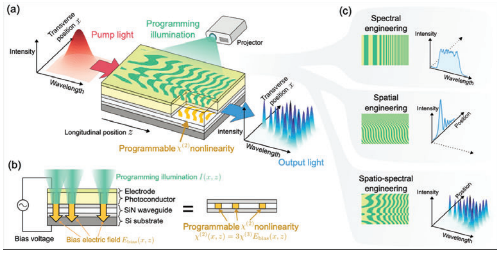

Figure 1: Overview of spatio-spectral engineering. a) Device operational overview. b) Schematic of how programmable illumination induces a programmable χ(2) nonlinearity. c) Experimental data showing how different programmed poling periods yield different beam outputs in the spatial and spectral domain,

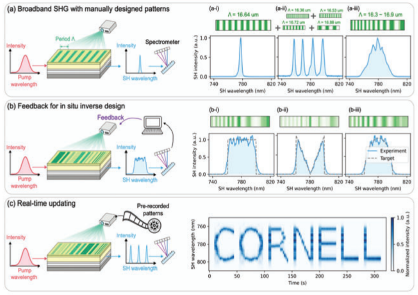

Figure 2: Real-time optimization of poling pattern. a) Output spectra from a single poling period, multiple poling periods added, and a chirped poling period. b) Different output spectra achieved through real-time optimization of the poling period. c) Output spectra changing in time to print the word "CORNELL".

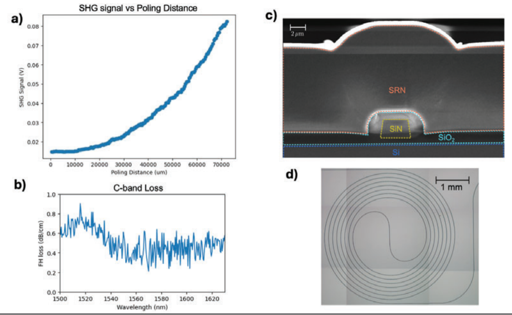

Figure 3: Early results on programmable channel waveguides. a) Super linear scaling of the second harmonic signal, as measured on a photomultiplier tube. The signal scaled with poling distance to the power of 2.5 and poling was done over a total of 7 cm. b) Loss measurement on device using cut-back method. c) SEM image of device cross-section with each material layer labeled. d) Microscope image of a device with a 7 cm spiral.

References:

[1] P. L. McMahon, Nature Reviews Physics 5, 717 (2023).

[2] T. Onodera, M. M. Stein, B. A. Ash, M. M. Sohoni, M. Bosch, R. Yanagimoto, M. Jankowski, T. P.McKenna, T. Wang, G. Shvets, M. R. Shcherbakov, L. G. Wright, and P. L. McMahon, Scaling on-chip photonic neural processors using arbitrarily programmable wave propagation (2024), arXiv:2402.17750

[3] Ryotatsu Yanagimoto, Benjamin A Ash, Mandar M Sohoni, Martin M Stein, Yiqi Zhao, Federico Presutti, Marc Jankowski, Logan G Wright, Tatsuhiro Onodera, Peter L McMahon, Programmable on-chip nonlinear photonics (2025), arXiv:2503.19861

Photonic Integrated Technologies for Low-SWaP, Narrow- Linewidth, and Tunable Laser Systems

CNF Project Number: 3041-22
Principal Investigator(s): Adam Heiniger
User(s): Mateus Corato Zanarella

Affiliation(s): TOPTICA Photonics Inc.

Primary Source(s) of Research Funding: Self-funded

Contact: Adam.Heiniger@toptica-usa.com, mateus.corato.zanarella@toptica-usa.com

Research Group Website: https://www.toptica.com/

Primary CNF Tools Used: AJA Sputter, DISCO Dicing Saw, Hamatech Hot Piranha, Heidelberg DWL2000, JEOL JBX-9500FS E-beam Lithography System, KLA P7 Profilometer, MOS Clean Bench & Tanks, MRL B3 LPCVD LTO, MRL B4 LPCVD Nitride, MRL E4 LPCVD CMOS Nitride, Oxford 100 ICP Dielectric, Oxford 80 RIE, PT Takachi HDP-CVD, Suss MA6|BA6 Aligner, Unaxis 770 Deep Silicon Etch, YES EcoClean Asher, YES Asher, Zeiss Ultra SEM, Woollam RC2 Spectroscopic Ellipsometer, Keyence VHX- 7100 Digital Microscope

Abstract:

As quantum technologies transition from laboratories to the world, their successful deployment critically relies on the size, weight, and power (SWaP) of the laser sources fueling them. Due to the stringent optical requirements of most of these systems, they still predominantly use bulky lasers made of free-space components. With the emergence of high-performance, chip-scale lasers based on photonic integrated circuits (PICs) [1], practical quantum systems that are compact and scalable are now within reach. However, to successfully realize a PIC-based laser module that meets both optical and functional requirements, a system-level approach for co-designing the optical source (gain medium and PIC), the driver electronics, and the control software needs to be adopted.

Summary of Research:

Our research comprises the design, fabrication, characterization, and packaging of PIC-based laser systems. The PIC components include the laser external cavity and any other desired light processing units to manipulate and deliver the light.

Conclusions and Future Steps:

We have successfully demonstrated a complete and compact PIC-based laser system around 780 nm wavelength targeting quantum applications. Our work was featured in the conference publications listed in References [2- 4]. Future steps include improving the current system, expanding to other wavelengths, and adding more optical components for light manipulation and delivery.

References:

[1] M. Corato-Zanarella, A. Gil-Molina, X. Ji, M. Chul Shin, A. Mohanty, M. Lipson, “Widely tunable and narrow-linewidth chip-scale lasers from near-ultraviolet to near-infrared wavelengths,” Nat. Photon. 17, 157–164 (2023).

[2] M. Corato-Zanarella, M. Lommel, D. Mayzlin, J. Nojic, A. Eras, C. Nölleke, B. Globisch, C. Haimberger, “Low-SWaP, Narrow-Linewidth, and Tunable Laser System For The Next Generation Of Quantum Technologies”, 2025 Conference on Lasers and Electro-Optics Europe & European Quantum Electronics Conference (CLEO/Europe-EQEC), Munich, Germany (2025).

[3] J. Nojic, A. Eras, L. Winkler, D. Mayzlin, M. Corato-Zanarella, M. Lommel, C. Nölleke , “Narrow-linewidth, Fully Integrated Chip-based Laser System in the Red Spectral Range”, 2025 Conference on Lasers and Electro-Optics Europe & European Quantum Electronics Conference (CLEO/Europe-EQEC), Munich, Germany (2025).

[4] S. Dadras, M. Corato-Zanarella, A. Heiniger, C. Haimberger, “PIC-based tunable diode lasers for fieldable quantum applications”, Proc. SPIE PC13563, Photonics for Quantum 2025, PC1356314 (18 July 2025); https://doi.org/10.1117/12.3065992.ff

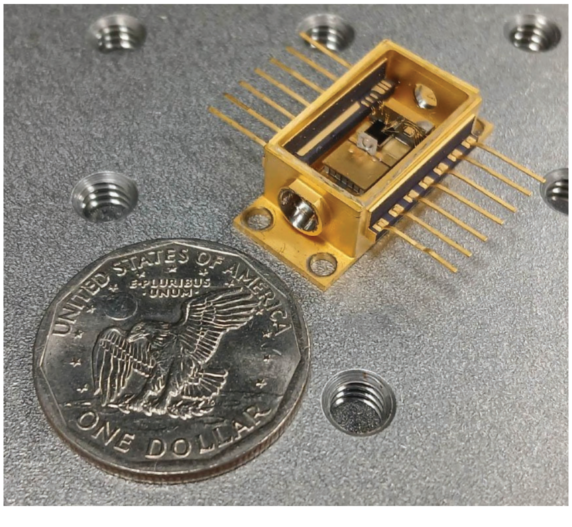

Figure 1: Low-SWaP, PIC-based laser.

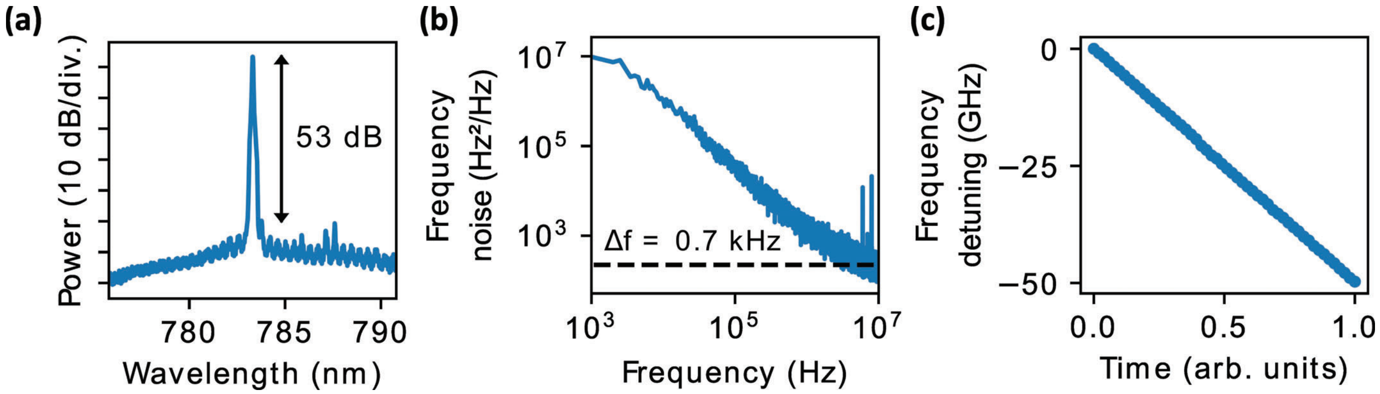

Figure 2: Example performance metrics of a PIC-based laser. (a) Side-mode suppression ratio. (b) Frequency noise. (c) Mode hop-free tuning range.

Design and Fabricate Robust Nanocavities

CNF Project Number: 3261-25
Principal Investigator(s): Wei Bao
User(s): Wei Li, Yilin Meng

Affiliation(s): Department of Materials Science and Engineering, Rensselaer Polytechnic Institute

Primary Source(s) of Research Funding: Army Research Office

Contact: baow2@rpi.edu, liw24@rpi.edu, mengy5@rpi.edu

Primary CNF Tools Used: Heidelberg MLA 150 Maskless Aligner

Summary of Research:

To realize tunable mid-infrared nanophotonic platforms with strong light–matter interaction, we are fabricating arrays of gold disks as the foundational step toward constructing epsilon-near-zero (ENZ) plasmonic nanocavities. As illustrated in Fig. 1a and 1b [Nat. Photonics 15, 125–130 (2021)], such nanocavities enable significant optical resonance and ultra-strong coupling with phonons. Gold is chosen as the cavity material due to its low intrinsic loss and chemical stability in the infrared range.

At Cornell CNF, we first spin-coated a UV photoresist and employed photolithography to define the gold disk array patterns. The primary lithography tool used was the Heidelberg MLA 150 Maskless Aligner. Subsequent processing was carried out at RPI, where we deposited a 3 nm titanium (Ti) adhesion layer followed by 100 nm gold (Au) using electron-beam evaporation. A standard lift-off process was then applied to form the final gold disk array. Characterization at RPI confirmed the fabrication results of the designed structures, as shown in Fig. 2a. The fabricated array features a periodicity of 4.77 µm and disk diameters of 1.76 µm. To evaluate the optical performance of the fabricated nanocavity structure, we conducted transmission measurements of the bare gold disk array. The resulting spectrum (Fig. 2b) demonstrates an optical resonance, showing that our lithography created the intended plasmonic modes. However, the observed quality factor of the resonance remained low, suggesting the presence of optical loss. Further investigation using scanning electron microscopy (SEM), as shown in Fig. 2c, revealed prominent lift-off wings around the edge of each disk, which, we believe, are responsible for the elevated loss.

To address this issue, our next fabrication iteration will adopt a bilayer resist strategy to promote clean undercut profiles and facilitate lift-off process.

Conclusions and Future Steps:

The plasmonic disk array has been successfully fabricated, but the observed optical modes exhibit high loss, likely due to lift-off artifacts. Moving forward, we plan to use ASML PAS 5500/300C DUV Wafer Stepper and Heidelberg MLA 150 Maskless Aligner to optimize our fabrication. With high-quality plasmonic resonance mode achieved, we will coat the structure with ENZ materials to investigate cavity–matter coupling and explore optical control of material excitations.

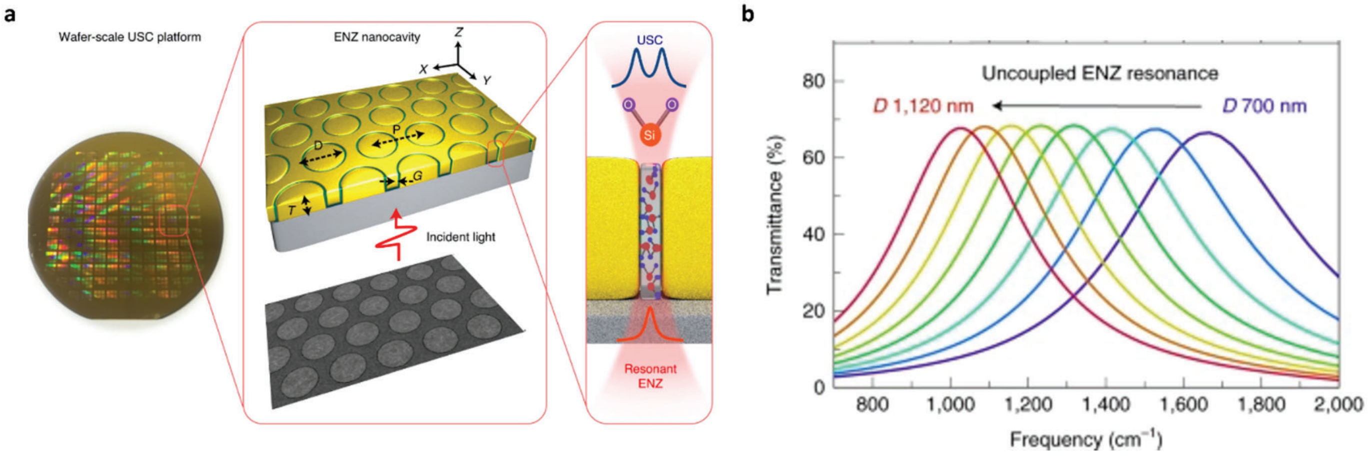

Figure 1: (a) Schematic of ENZ nanocavity and illustration of SiO2 phonons interacting with the nanocavity mode. (b) Transmission resonances of ENZ nanocavity with different aperture diameters. Image reproduced from Nat. Photonics 15, 125–130 (2021).

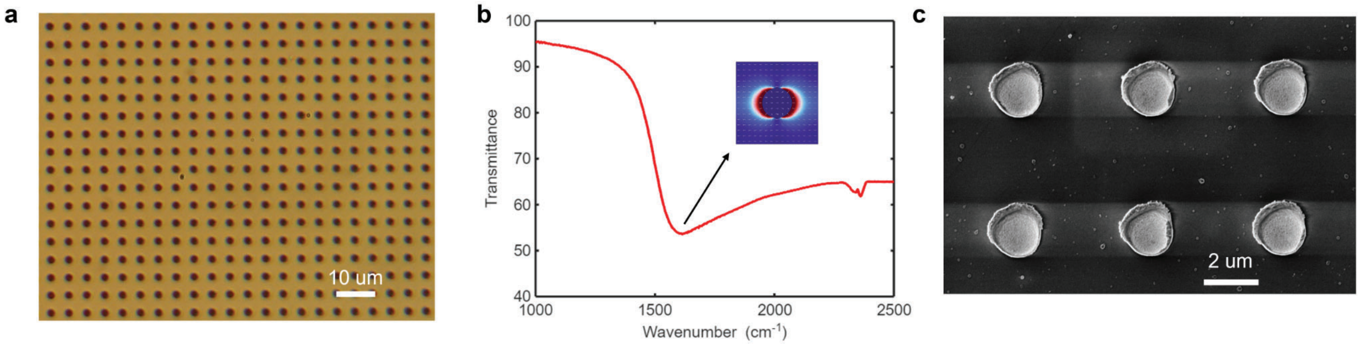

Figure 2: (a) Optical image of the fabricated gold disk array with a designed periodicity of 4.77 µm and disk diameters of 1.76 µm. (b) Measured transmission spectrum of the array, showing a resonance dip. The inset displays a simulated electric field profile of the resonance mode, indicating the dipolar resonance around the gold disk. (c) Scanning electron microscopy image reveals the presence of lift-off wings surrounding each gold disk.

Fabricating Dual-Gated 2D CrSBr Devices to Investigate Nonlinear Transport Effects

CNF Summer Student: Calvin Chiu
Student Affiliation: Physics, The University of Texas at Austin

Summer Program(s): 2025 Cornell NanoScale Facility Research Experience for Undergraduates (CNF REU) Program

Principal Investigator(s): Dan Ralph, Physics, Cornell University

Mentor(s): Bozo Vareskic, Physics, Cornell University

Primary Source(s) of Research Funding: Center for Energy Efficient Magnonics, funded by the U.S. Department of Energy, Office of Science, Basic Energy Sciences under Award #DE-AC02-76SF00515

Contact: dcr14@cornell.edu, bv227@cornell.edu, ckc2398@my.utexas.edu

Summer Program Website(s): https://cnf.cornell.edu/education/reu

Primary CNF Tools Used: Zeiss Supra SEM, Nabity NPGS Nanometer Pattern Generator System, CVC SC4500 Odd-Hour Evaporator, Oxford 81 RIE

Abstract:

The tremendous interest in 2D van der Waals (vdW) materials in condensed matter physics has led to studies on magnetic materials for potential applications in spintronics and quantum information. CrSBr is a magnetic semiconductor that has garnered interest due to its ability to be exfoliated to the 2D limit. However, transport effects in 2D CrSBr such as the nonlinear Hall effect have yet to be explored. In this project, we aim to fabricate functioning dual-gated CrSBr devices and investigate the existence of a nonlinear Hall effect when subjecting the devices to varying parameters.

Summary of Research:

Two-dimensional materials have generated enormous research interest, and the discovery of new materials and ordered phases continues to expand the scope of the field. One category of 2D materials includes van der Waals (vdW) magnets such as chromium sulfur bromide (CrSBr) [1]. CrSBr is particularly interesting from an experimental standpoint, as it is more air-stable compared to other 2D magnetic materials and can be exfoliated relatively easily to the monolayer limit [2].

CrSBr is a magnetic semiconductor exhibiting A-type antiferromagnetic structure; the magnetic moments within a layer are aligned ferromagnetically (same direction) in the plane, while the magnetic moments in adjacent layers are aligned antiferromagnetically (opposite direction). CrSBr also exhibits intriguing electronic and magnetic anisotropies. Due to CrSBr's electronic structure, particularly the orbital composition of its conduction band, electron transport is massively favored along one direction, with the conductivity along the b-axis (σb) being up to 10,000 times larger than σa [2, 3]. Moreover, 2D CrSBr can exhibit strong coupling between its electronic and magnetic structure, including exciton-magnon coupling in twisted bilayer CrSBr [2, 4].

Although various studies have been conducted on CrSBr, there has yet to be definitive measurements regarding a quantum nonlinear Hall effect (NLHE). NLHE is an extension of the classical Hall effect, where a transverse Hall voltage (VH) is induced when a material carrying current is exposed to a perpendicular magnetic field. However, in NHLE, an applied electric field can induce a nonlinear VH, even without introducing a magnetic field. NHLE has been observed and predicted in various materials [5, 6], but we aim to experimentally investigate the NHLE in few-layer CrSBr.

Methods. In this project, we focused on fabricating dual-gated CrSBr transistors for the purposes of investigating whether a nonlinear Hall effect exists, as well as its dependence on temperature, carrier density, and out of plane electric field. To do so, we conducted optimization trials and referenced previous research [5, 7, 8] to develop a working fabrication process, as outlined below:

1. Perform Scotch tape exfoliation onto blank silicon substrates for crystals of few-layer graphene (FLG) and hexagonal boron nitride (hBN). Search for clean ~40 µm x 10 µm FLG and ~50 µm x 50 µm x 70µm hBN flakes.

2. Utilize PDMS viscoelastic stamping to place FLG-hBN on pre-prepared silicon substrates, leaving a segment of FLG exposed for the bottom gate (if convenient).

3. Pattern inner electrodes (e.g. in a double Hall bar geometry) using KLayout and spin-coat substrates with PMMA A4 followed by PMMA A2.

4. Expose/develop samples and deposit 8 nm of platinum using CNF tools, including the Zeiss Supra SEM, Nabity NPGS, and SC4500 Evaporator. Perform lift-off in acetone and tip-based cleaning using an atomic force microscope (Fig. 1).

5. In an oxygen- and water-free glove box, exfoliate and search for ~10 µm x 5 µm few-layer CrSBr and more hBN flakes. Stamp CrSBr flakes such that the flake contacts all inner electrodes, and stamp hBN to cover all but the exposed FLG.

6. Pattern openings to the inner electrodes. Spin-coat and expose/develop. Etch the exposed segments to remove the hBN using the Oxford 81 RIE.

7. Pattern outer electrodes, a top gate, and bottom gate(s) to connect to the pre-prepared bonding pads. Spin-coat, expose/develop, deposit 10 nm Ti/90 nm Au, and perform lift-off (Fig. 2 - 4).

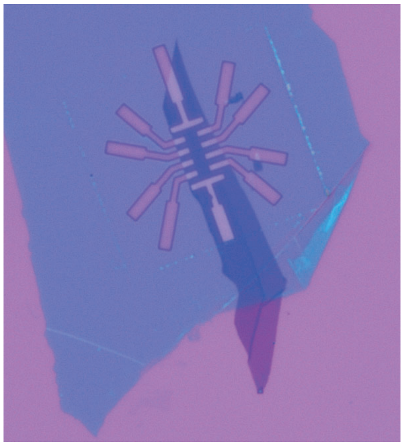

Figure 1: Image of an example of device after step 4 of the fabrication process.

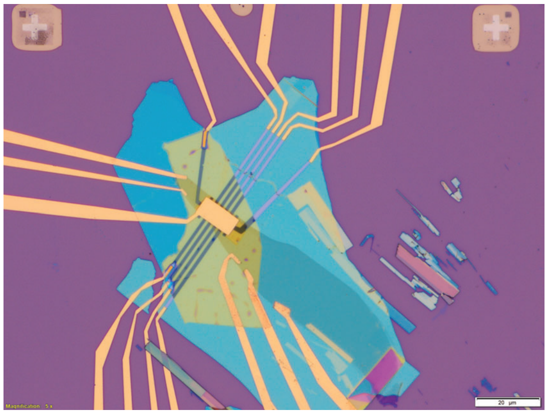

Figure 2: Image of an example device after the full fabrication process.

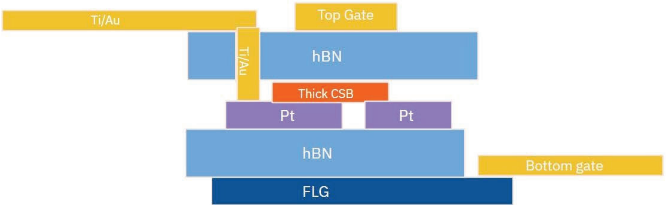

Figure 3: Transverse view of the device "stack", with colors corresponding to Figure 2.

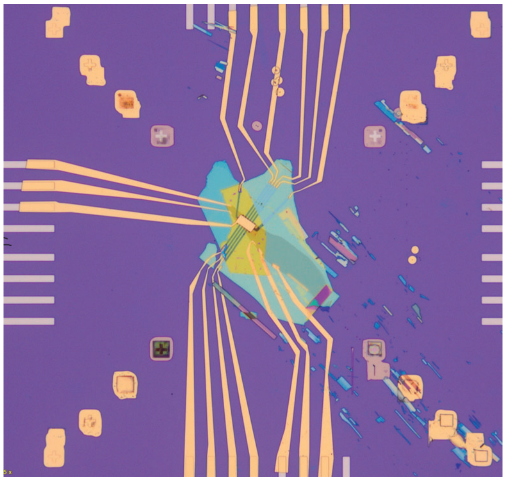

Figure 4: Zoomed-out image of Figure 2.

Conclusions and Future Steps:

Through extensive testing and trial-and-error, we have established a working fabrication process for creating dual-gated 2D CrSBr devices. Despite the supposed air stability of CrSBr, the exfoliation in the glove box and complete insulation by the top hBN were required to prevent the CrSBr from degrading and losing electrical contact after several hours. Our fabrication process may also apply to other air-sensitive 2D materials with transport properties of interest.

With our obtained measurements, we aim to extract the conductivity tensors of few-layer CrSBr in the near future. Further studies can be conducted to verify the obtained results improve the fabrication efficiency

Acknowledgements:

Many thanks to the 2024 Cornell NanoScale Facility Research Experiences for Undergraduates (CNF REU) Program funded by the National Science Foundation under Grant No. NNCI-2025233, and the National Nanotechnology Coordinated Infrastructure. Special thanks to Prof. Dan Ralph and Bozo Vareskic for all of their guidance and support.

References:

[1] Burch, K. S. et al. https://doi.org/10.1038/s41586-018-0631-z
[2] Michael E. Ziebel et al. DOI: 10.1021/acs.nanolett.4c00624
[3] Wu, F. et al. DOI: 10.1002/adma.202109759
[4] Sun, Y. et al. DOI: 10.48550/arXiv.2506.10080
[5] Chichinadze, D. V. et al. DOI: 10.48550/arXiv.2411.11156
[6] Min L et al. DOI: 10.1038/s41467-023-35989-0
[7] Sun, S. et al. DOI: 10.48550/arXiv.2507.15853
[8] Bhatia, P. et al. DOI: 10.1016/S0968-4328(24)00164-1

Fabrication of Manhattan-style Josephson Junctions

CNF Summer Student: Gabriele Di Gianluca
Student Affiliation: Physics, University of Florida

Summer Program(s): 2025 Cornell NanoScale Facility Research Experience for Undergraduates (CNF REU) Program
Principal Investigator(s): Valla Fatemi
Mentor(s): Simon Reinhardt, Maciej Olszewski, Lingda Kong
Primary Source(s) of Research Funding: NORDTECH (SQ Fab)
Contact: vf82@cornell.edu, digianlucag@ufl.edu
Summer Program Website(s): https://cnf.cornell.edu/education/reu
Research Group Website: https://fatemilab.aep.cornell.edu/
Primary CNF Tools Used: Angstrom-Q, JEOL 6300 E-beam Lithography System, Zeiss Ultra SEM, GCA AS200 i-line Stepper, Heidelberg DWL2000, AJA Sputter 1

Abstract:

Qubits based on superconducting quantum circuits are one of the most promising platforms for quantum computing [1]. The critical component of these superconducting qubits is the Josephson Junction. We use a Josephson Junction which is a superconductor-insulator-superconductor interface that relies on the tunneling of Cooper pairs through the thin insulating barrier [1]. Once below the critical temperature of the superconducting material, the Josephson Junction can now conduct a current without any applied voltage, exhibiting the Josephson Effect. This nonlinear current creates the key anharmonicity needed to create a qubit [2]. In this research, we fabricate Manhattan-style Josephson Junctions in the Angstrom-Q and characterize the oxidation process.

Summary of Research:

The main two types of Josephson Junctions are Dolan and Manhattan-style. Dolan-style junctions rely on a shadow evaporation method where Electron-Beam lithography on the JEOL 6300 is performed onto a PMMA/MMA resist stack. During this lithography, a bridge is defined, and two evaporations are performed at different angles with an oxidation in between. This overlap between the two evaporation defines our junction area, a key factor in determining the properties of the Josephson Junction. The main downside to this style is that the bridge used is fragile and can frequently collapse, therefore halting the fabrication process. Additionally, the bridge can vary between lithography runs due to resist thickness. This inconsistency in the bridge leads to an inconsistency in junction area, which changes the parameters of the qubit. In an effort to increase reproducibility in our qubit fabrication, we began to fabricate Manhattan-style Josephson Junctions using the new Angstrom-Quantum evaporator, designed specifically for this purpose. Manhattan-style junctions (Figure 1) are a bridge-less technique that use a similar PMMA/MMA resist stack, but instead rely on an evaporation into two different trenches [3]. As opposed to Dolan-style junctions, in this case, the area of our junctions is only determined by the lithography. This, coupled with the fact that there is no bridge involved, increases our reproducibility between fabrication runs.

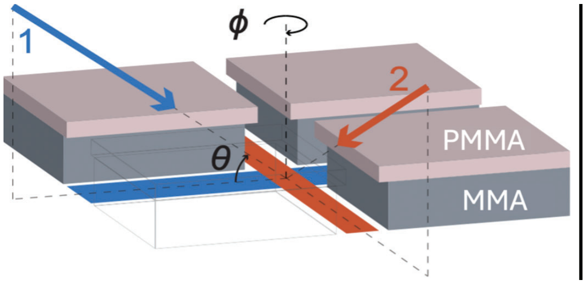

Figure 1:

The main reason we care about the area of our junction is that it affects critical current, I_c, the maximum current the junction can hold before returning to a non-zero resistance state. The critical current is given by the Ambegaokar–Baratoff relation (Figure 2a), in which the superconducting gap of Aluminum is known and the normal state resistance, R_n, can be obtained by a room temperature two-probe resistance measurement. From the critical current, we can then determine the Josephson Energy, E_J (Figure 2b). E_J is a key term in the Hamiltonian of our circuit and determines the circuit dynamics, primarily our qubit frequency, a critical

a)

$$I_c = \frac{\pi\Delta}{2eR_n}$$

$\Delta =$ Superconducting gap
$R_n =$ Normal state resistance

b)

$$E_J = \frac{\Phi_0}{2\pi} I_c \propto I_c$$

Magnetic flux quantum: $\Phi_0 = \frac{h}{2e}$ =constant

Figure 2:

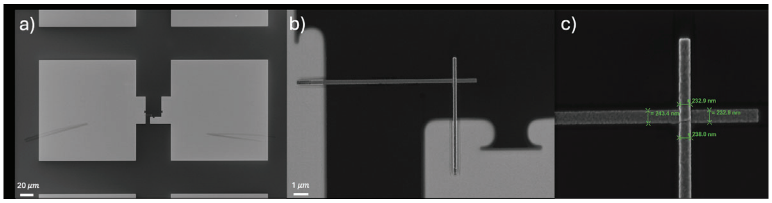

Figure 3:

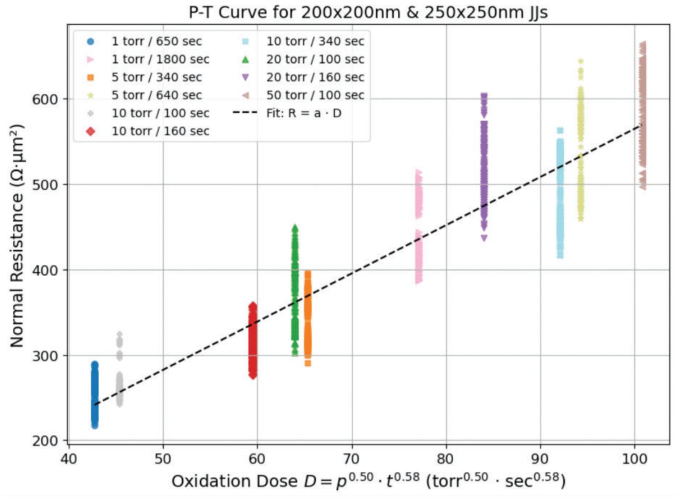

Figure 4:

number in benchmarking qubit performance [1].

Our fabrication process began by doing a standard HF clean of our 100mm Si wafer in order to remove the native oxide layer. Then we spun on a LOR 3A and S1813 photoresist stack before patterning bonds pads using the i-line stepper on a mask written in the Heidelberg DWL2000. After developing on a Hamatech automatic developer, we deposited Ti-seeded Pt using the AJA 1 Sputter tool. The 5nm of Ti acts as an adhesion layer for the 80nm of Pt which does not naturally oxidize, making it compatible with our probe station. After doing lift-off in Remover PG overnight, we spun on a PMMA/MMA e-beam resist stack. This allowed us to pattern our Josephson Junctions in the JEOL 6300 Electron-Beam Lithography system. Onto our wafer, we patterned 100 200x200nm and 100 250x250nm junctions. Before depositing, we cleaved our wafer into chips and developed them in IPA:DI (3:1) for 2 minutes. Once loaded into the Angstrom-Q, we do an in-situ argon milling to remove any unwanted oxide that could prevent poor contact. We then deposit 20nm of Al for our bottom electrode at a rate of 2 A/s and a chamber pressure <5e-8. Our oxidation step varies with pressures from 1 to 50 torr and 1 to 30 minutes. Our top electrode is 70nm of Al and is deposited at a similar chamber pressure as the bottom electrode. Before taking our sample out, we do a post-oxidation step instead of letting the sample oxidize arbitrarily in atmosphere. Then we do lift-off in heated DMSO at 80-90 C overnight. Finally, we measure room temperature resistance using a Keithley SourceMeter and a probe station with Tungsten tips. After probing resistance, SEM images were taken on the Zeiss Ultra SEM in order to calculate the area of our junctions and evaluate the success of lift-off (Figure 3).

We iterated on our fabrication many times in order to produce 20 data points across JJs with a 20nm bottom electrode. With this data, we plotted the normal resistance, resistance of our junctions times the area, versus the oxidation dose, a combination of the pressure and time of the oxidation. The value of the exponents assigned to pressure and time and the linear fit to our data was optimized (Figure 4). We observe our data aligns with our linear fit and with previous work [4]. We also compute the variability of junction resistance across a die and observe a variance <5%, which is acceptable for qubit devices.

Conclusions and Future Steps:

We successfully demonstrated the fabrication of Manhattan-style Josephson Junctions in the Angstrom-Q. We also characterized and optimized the fabrication process by constructing a pressure-time curve. This curve will allow us to determine the oxidation dose necessary to obtain a junction of a desired resistance with minimal trial and error.

The next step will be move away from Dolan-style junctions and incorporate Manhattan-style Josephson Junctions into our qubit fabrication process. As we do multiple fabrication runs, we will see whether the junction properties are reproducible and whether Manhattan junctions have any advantage over Dolan junctions. Another possibility will be to do an aging study of Josephson Junctions. This would involve measuring the resistance of junctions over at least a month and observing how the resistance changes over time.

References:

[1] Rasmussen et al., "Superconducting Circuit Companion---an Introduction with Worked Examples."

[2] Krantz et al., "A Quantum Engineer's Guide to Superconducting Qubits."

[3] Kreikebaum et al., "Improving Wafer-Scale Josephson Junction Resistance Variation in Superconducting Quantum Coherent Circuits."

[4] Zeng et al., "Direct Observation of the Thickness Distribution of Ultra Thin AlOx Barriers in Al/AlOx/Al Josephson Junctions."

Domain Switching in Twisted Double Bilayer Graphene

CNF Summer Student: Peter Golemis
Student Affiliation: Physics and Electrical & Computer Engineering, University of Illinois Urbana-Champaign

Summer Program(s): 2025 Cornell NanoScale Facility Research Experience for Undergraduates (CNF REU) Program
Principal Investigator(s): Kenji Yasuda
Mentor(s): Daniel Brandon
Primary Source(s) of Research Funding: National Science Foundation under Grant No. NNCI-2025233)
Contact: kenji.yasuda@cornell.edu, db923@cornell.edu, golemis3@illinois.edu
Summer Program Website(s): https://cnf.cornell.edu/education/reu
Research Group Website: https://www.yasudalab.org/home
Primary CNF Tools Used: Oxford 81 RIE, SC4500 Odd-Hour Evaporator, Zeiss Supra SEM, Nabity Nanometer Pattern Generator System

Abstract:

For over two decades, the properties of two-dimensional (2D) graphene films have been rigorously explored, exhibiting a variety of profound electronic phenomena [1]. Few-layer graphene has received great attention due to the wide range of electronic band structures realized across its various stacking orders [2]. Different coexisting stacking orders are obtained by precisely controlling the twist angle between two bilayer graphene flakes, generating Bernal (ABAB) and rhombohedral (ABCA) domains. In this work, we obtain transport measurements of small-angle twisted double bilayer graphene (TDBG) Hall bar devices with this domain structure, which exhibit gate-tunable domain switching. This platform enables the observation of the interplay between domain switching and the electronic properties of Bernal and rhombohedral graphene.

Summary of Research:

Device Fabrication:

Bernal (Fig. 1a) and rhombohedral (Fig. 1b) ordered graphene are two possible stacking configurations of four-layered graphene systems. Introducing a small twist angle between two bilayer graphene films enables the formation of large coexisting Bernal and rhombohedral domains. The electronic properties of small-angle TDBG are probed in double-gated stacks (Fig. 1c) constructed using a PDMS/PC dry transfer process. High- quality uniform gates consisting of a thin hexagonal boron nitride (hBN) dielectric and conducting graphite flake are used to tune the carrier density and out-of-plane displacement field through the TDBG. Initially, the bottom gate is stacked and placed onto a pre-patterned Si/SiO2 substrate (Fig. 1d). Mechanically exfoliated bilayer graphene flakes are then identified using optical microscopy and cut into two pieces by applying a high-frequency alternating voltage to a conductive atomic force microscope (AFM) tip [3].

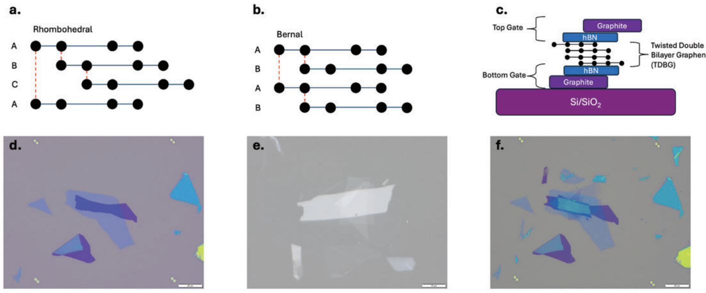

Figure 1: a,b, Visualization of rhombohedral and Bernal stacking orders in TDBG. c, Profile schematic of a double gated TDBG stack. d, Bottom gate placed on a pre-patterned chip. e, Complete top stack on PDMS/PC stamp. f, Complete stack consisting of a bottom gate (Fig. 1d) and top stack (Fig. 1e).

Scanning the conductive AFM tip over a graphene flake in a humid environment drives an anodic oxidation process to selectively remove regions of the flake with minimal induced strain on the crystal lattice. Implementing the dry transfer process, a top gate is fabricated separately by stacking graphite on top of a thin hBN flake. The first half of the bilayer graphene flake is stacked beneath the top gate, and the other half is rotated by θ = 0.03º. Finally, the rotated graphene is stacked beneath the graphene on the top gate (Fig. 1e), which is then released onto the bottom gate on the pre-patterned chip (Fig. 1f).

After stacking the double-gated TDBG structure, a Hall bar etching mask with 1D graphene contacts is designed on a clean region of the device. The device is coated with PMMA 950K

A4 resist, and the etching mask is written using e-beam lithography. Exposed graphite and hBN regions are etched completely using low-power O_2 and CHF_3/O_2 plasma, respectively. After the Hall bar geometry has been defined (Fig. 2a), the device is coated with PMMA 495K A4 and PMMA 950K A2 to write the electrode pattern connecting to the TDBG contacts. After writing the pattern using electron beam lithography, the exposed contact regions of the Hall bar are then etched completely to expose a 1D TDBG contact region.

Finally, chromium, palladium, and gold contacts are deposited onto the chip, and the remaining resist is removed in an acetone bath (Fig. 2b).

Results:

Sweeping the top and bottom gate voltages of the device at T = 1.5K gave rise to gate- dependent signatures in the hole-doped region (Fig. 3a). This implies a gate-induced change in the structure being measured, in which graphene layers slide between a Bernal and rhombohedral stack ordering. By applying an external magnetic field, the magnitude of the switching response varies dramatically from the B = 0T case. After applying an external field B = 2T, the switching response in the higher hole density region is emphasized, whereas the switching response closer to charge neutrality is emphasized in the zero-field case (Fig. 3a,c). Having defined part of the switching region, the measurement scheme demonstrated in Fig. 3b is conducted, in which the device switches deep into the rhombohedral phase. From the rhombohedral-dominated phase, two measurements of the switching response Rxx(n, D) are made by ramping Vtg (Vbg) and then sweeping Vbg (Vtg) to map out the entire switching region. The sum of these plots highlights multiple boundaries in the hole-doped region (Fig. 3d). These distinct equipotential lines correspond to the free energy required to overcome the domain wall pinning energy to switch from one order to another.

Conclusions and Future Steps:

These results demonstrate the transport behaviors of domain switching in multi-layer 2D materials. Domain switching can be used to gain new insights into exotic transport phenomena. Future experiments may involve domain switching in platforms with different stacking configurations, twist angles, and crystals. It would also be of great interest to explore emergent transport properties unique to these different stacking orders and their interactions in a domain switching platform.

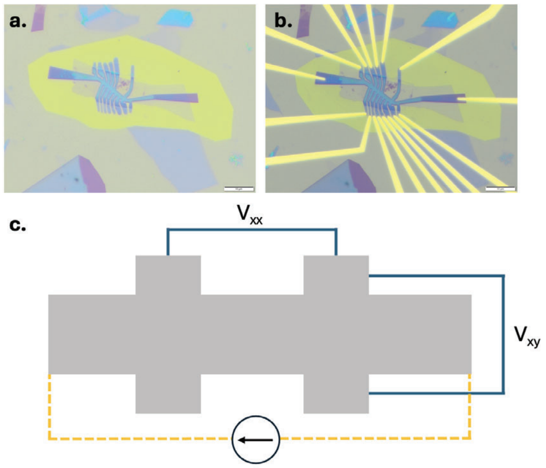

Figure 2: a, Complete stack (Fig. 1f) etched into a Hall bar geometry. b, Cr/Pd/Au contacts deposited on 1D TDBG contacts. c, Hall bar measurement configuration.

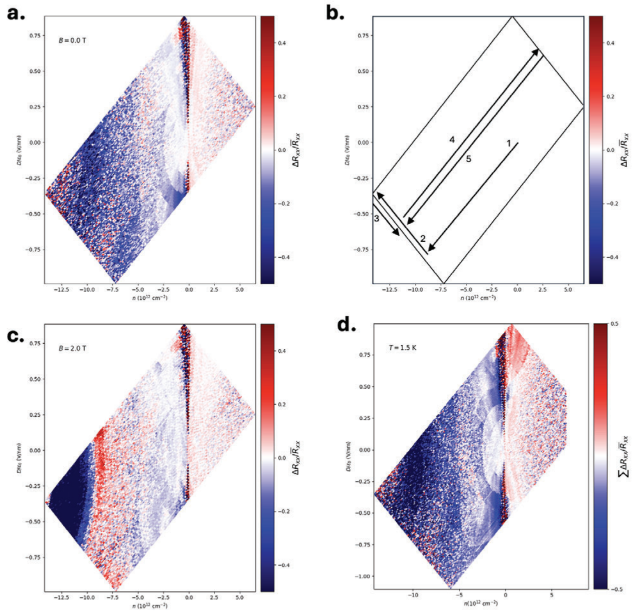

Figure 3: a, Switching boundary between Bernal and rhombohedral phases. This is defined by the mean normalized difference between the forward and backward bottom gate sweeps. b, Measurement scheme to define switching boundary in Fig. 3a. c, Same measurement as Fig. 3a under B = 2T. d, Sum of the mean normalized differences from the bottom and top gate sweeps. This plot maps the entire rhombohedral-Bernal switching region.

References:

[1] K. S. Novoselov et al., Electric Field Effect in Atomically Thin Carbon Films.Science306,666-669(2004). https://doi.org/10.1126/science.1102896

[2] Lui, C., Li, Z., Mak, K. et al. Observation of an electrically tunable band gap in trilayer graphene. Nature Phys 7, 944–947 (2011). https://doi.org/10.1038/nphys2102

[3] Electrode-Free Anodic Oxidation Nanolithography of Low-Dimensional Materials Li, H. et al. Nano Letters 2018 18 (12), 8011-8015 DOI: 10.1021/acs.nanolett.8b04166

Structure and Dynamics of the Compression Induced Polycrystalline-Glass Transition

CNF Summer Student: Sylvie Shaya
Student Affiliation: Wellesley College Department of Physics

Summer Program(s): 2025 Cornell NanoScale Facility Research Experience for Undergraduates (CNF REU) Program, SUPREME REU

Principal Investigator(s): Julia Dshemuchadse, Erin Teich

Mentor(s): Katherine Wang

Primary Source(s) of Research Funding: National Science Foundation award NNCI- 2025233

Contact: jd732@cornell.edu, et106@wellesley.edu, xw682@cornell.edu, ss131@wellesley.edu

Summer Program Website(s): https://cnf.cornell.edu/education/reu

Research Group Website: https://capecrystal.mse.cornell.edu/

Abstract:

When polycrystal grain size is sufficiently reduced, materials undergo a solid-to-glass transition that is distinct from the more commonly studied liquid-to-glass transition and is critical to understanding the behavior of ultrafine-grained polycrystals. These materials hold promise in microelectronics and thermoelectrics, yet their behavior at and beyond the glass transition is not well understood. We simulate a binary system of hard and soft particles under compression to investigate the structure and dynamics of the polycrystalline-to-glass transition. Our results reveal a strong relationship between local structural features and dynamical behavior and indicate that soft particles play an outsized role in the glass transition, as they are associated with areas of strong dynamics and disorder.

Summary of Research:

Background:

Polycrystals are known to exhibit Hall–Petch behavior, which describes how materials strengthen as grain size is reduced. As grain size is further decreased and grain boundary behavior dominates, polycrystals soften and become glassy [1]. Ultrafine-grained polycrystals display properties of interest for materials applications, including high electrical conductivity and reduced thermal conductivity, and understanding the polycrystalline-to-glass transition is critical for further development of these materials [2].

Simulation Methods:

We perform molecular dynamics simulations on a binary system of 6400 hard and 6400 soft discs using the simulation toolkit HOOMD-blue [3]. Particle interactions were defined by Weeks–Chandler–Andersen potentials shifted radially to ensure all particles have the same effective diameter of *d* = 1, with Lorentz–Berthelot mixing rules applied to cross-interactions, described in Fig. 1(b). Particle softness was denied via σ, which varies the shape of the potential well. Hard-particle softness was defined as σ = 0.2 and held constant for all systems, and soft- particle softness was varied between $\sigma_{soft} = 1$ and 5, as shown in Fig. 1(a).

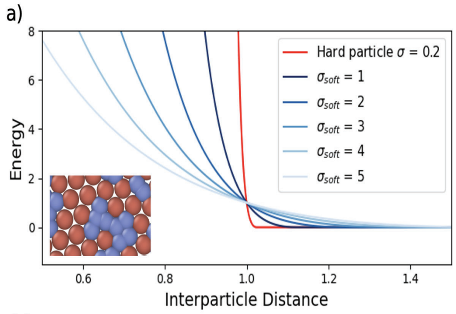

b)

$$U(r) = \begin{cases} 4\epsilon((\frac{\sigma}{r-\Delta})^{12} - (\frac{\sigma}{r-\Delta})^{6}) - \epsilon & r < 2^{1/6}\sigma + \Delta \\ 0 & r \geq 2^{1/6}\sigma + \Delta \end{cases} \quad (1)$$

$$\Delta = \frac{(d_{hard} + d_{soft})}{2} - \sigma \quad (2)$$

$$\sigma_{ij} = \frac{\sigma_{ii} + \sigma_{jj}}{2} \qquad \epsilon_{ij} = (\epsilon_{ii}\epsilon_{jj})^{1/2} \quad (3)$$

Figure 1: Model setup. (a) Particle interactions via Weeks–Chandler–Andersen potentials for various softnesses σ. (b) Equations describing particle interactions. 1.) Weeks–Chandler–Andersen potentials, shifted radially by a factor Δ, defined in equation 2.). 3.) Lorentz–Berthelot mixing rules.

The system was initialized at low density, then randomized and compressed to a density between $\phi = 0.8$ and $\phi = 1.1$. Following compression, the system was equilibrated to account for artifacts from the compression step, then run for 10^8 molecular dynamics timesteps to collect data. Simulation temperature was fixed at kT = 0.2.

Results:

To establish the system's glassiness, we investigate the mean squared displacement (MSD) and the non-Gaussian parameter α(t), an indicator of dynamical heterogeneity. Glassy systems feature a plateau in MSD and a peak in α(t) at intermediate time scales, due to particles being trapped in cages of their neighbors before moving collectively at long time scales [4]. At low σ_{soft}, the system is crystalline and shows neither of these features. We chose to focus on σsoft = 4, where we observe these behaviors at ϕ-values above 0.9, indicating that the system is glassy.

The compression of the system can be seen in the radial distribution functions (RDFs), where hard–soft and soft–soft RDF peaks are broader and located at smaller distances *r* than hard–hard peaks, seen in Fig. 2(a), as soft particles overlap under compression. There are clear peaks in the RDF at low ϕ, which disappear under compression, as shown in Fig. 2(b), reflecting the existence and subsequent breakdown of long-range order as the system transitions into a glass.

Lattice structure was characterized through the hexatic order parameter ψ_6. Global ψ_6 is maximal (at 1) when the system is crystalline, and decreases at higher ϕ, shown in Fig. 2(c). At high densities, the distribution of soft particle ψ_6 is flatter than that of hard particles, seen in Fig. 2(d), indicating that soft particles tend to be more disordered than hard particles.

To characterize the dynamics of the system, we calculate the Lindemann parameter *L*, a measure of the strength of particle dynamics, and D^2min, an indicator of irreversible rearrangements [1, 5]. At low densities, particles with large *L* and D2min exist primarily along grain boundaries. As density increases, high *L* and D^2min particles form clusters throughout the system, as seen in Figs. 3(a)-(b). The distribution of soft-particle *L*s and D^2min is higher than those of hard particles, seen in Figs. 3(d)-(e), indicating that soft particles display stronger dynamics than hard particles.

To understand the relationship between dynamical parameters and structure, we calculated the covariances of D2min with the number of soft neighbor particles and *L* with ψ_6, shown in Fig. 4(a)-(b). For $\sigma_{soft} = 4$, there is a peak at $\phi = 0.9$ for both covariances. The peak of the covariance of *L* and ψ^6 has been shown to correlate to the polycrystalline-to-glass transition [1]. We observe a peak in the same location in the covariance of D^2min and number of soft neighbors, in Fig. 4(b), demonstrating a clear relationship between structure and dynamics at the glass transition.

As σ_{soft} increases, the peak of the covariance, and in turn the glass transition, shifts lower in density, seen in Fig 4(b). The global average ψ_6 shifts similarly, as seen in Fig. 2(c), as the breakdown in structure associated with the glass transition shifts.

Conclusion and Future Steps:

Under compression, binary systems of hard and soft particles display interesting behavior as they undergo a polycrystalline-to-glass transition. There is a strong relationship between the structure and dynamics of the system, seen in the covariances of dynamical and structural properties. Soft- particle softness impacts the location of the glass transition in density space, and soft particles appear to play an outsized role in this transition, as they tend to have stronger dynamics and disorder than hard particles.

Future steps include improved characterization of the relationship between structure and dynamics through statistical analysis, and descriptions of the collective motion of particles. Qualitative observation of the system indicates the existence of string- and loop-like cooperative motion, which in future work could be related to the structure of the system.

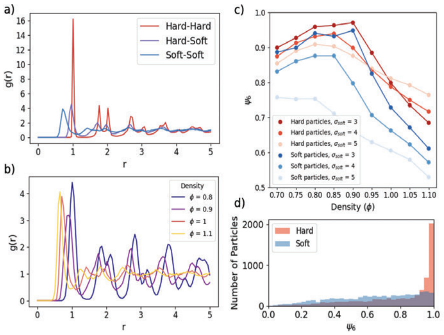

Figure 2: Structural parameters. (a) Type-wise RDFs for the 100th frame of simulations with $\sigma_{soft} = 4$ and $\phi = 1$. (b) Soft–soft RDFs for $\sigma_{soft} = 4$ over various ϕ values. (c) Global average ψ_6 for hard and soft particles. (d) Distributions of ψ6 by particle type at the 100th frame of simulations with σsoft = 4 and ϕ = 1.

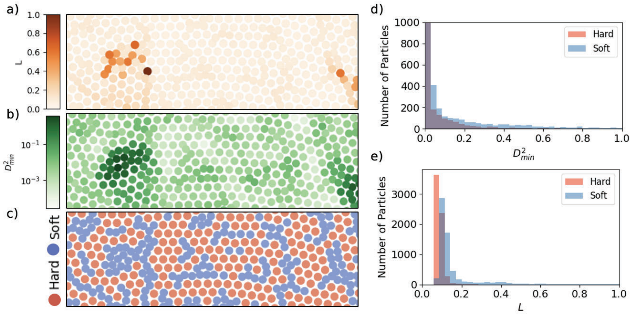

Figure 3: Dynamical characterizations, calculated over the first 100 frames of simulations with $\sigma_{soft} = 4$ and $\phi = 1$. (a) Heatmap of L. (b) Heatmap of D^2_{min} with a logarithmic colormap. (c) Particle identities at the 100th frame of simulation. (d) Histogram of L by particle type. (e) Histogram of D^2_{min} by particle type.

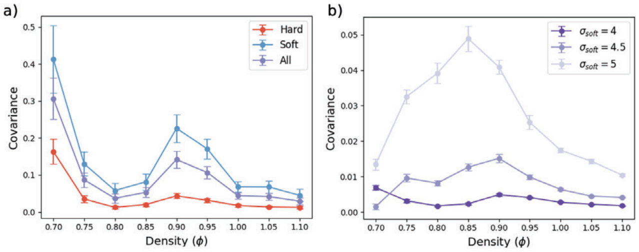

Figure 4: Covariances of dynamics and structure. (a) Typewise covariances of D^2_{min} and number of soft particle neighbors for $\sigma_{soft} = 4$. (b) All particle covariances of disorder, defined as $1 - \psi_6$, and L over various σsoft values.

References:

[1] Zhang, H. & Han, Y. Physical Review X 8, 041023 (2018).
[2] Lu, L. et al. Science 304, 422–426 (2004).
[3] Anderson, J.A. et al. Computational Materials Science 173, 109363 (2020).
[4] Teich, E.G. et al. Nature Communications 10, 64 (2019).
[5] Falk, M.L. & Langer, J.S. Physical Review E 57, 7192 (1998).

Probing Spin Dynamics in Exfoliated van der Waals Ferromagnet Fe_5GeTe_2 Using Superconducting Resonators

CNF Summer Student: Matthew Willard
Student Affiliation: Physics, SUNY Geneseo

Summer Program(s): 2025 Cornell NanoScale Facility Research Experience for Undergraduates (CNF REU) Program, SUPREME REU

Principal Investigator(s): Gregory D. Fuchs

Mentor(s): Julie Soho Shim

Primary Source(s) of Research Funding: National Science Foundation award NNCI- 2025233, Center for Energy Efficient Magnonics (DE-AC02- 76SF00515), Department of Energy Office of Science, Basic Energy Sciences (DE-SC0019997)

Contact: gdf9@cornell.edu, jss545@cornell.edu, mtw14@geneseo.edu

Summer Program Website(s): https://cnf.cornell.edu/education/reu

Primary CNF Tools Used: AJA Orion Sputtering Systems, Heidelberg MLA 150 Maskless Aligner, Oxford 81/82, PT770 Etcher, DISCO Dicing Saw, Westbond 7400A Ultrasonic Wire Bonder

Abstract:

Two-dimensional (2D) magnetic materials offer a rich landscape for exploring spin dynamics and topological textures, with tunable properties and compatibility with heterostructure engineering. Among these, a 2D ferromagnet Fe_5GeTe_2 (F5GT) has emerged as a promising candidate due to its high Curie temperature and low Gilbert damping. However, bulk measurements are often limited by structural inhomogeneities. Here, we present a single-flake ferromagnetic resonance (FMR) study of exfoliated F5GT nanoflakes using high-Q superconducting resonators ($Q > 10^4$) to probe intrinsic damping properties with enhanced sensitivity. We observed ferromagnetic resonance in an F5GT flake transferred onto a 4 GHz superconducting resonator, demonstrating magnetic coupling between the flake and the resonator. The extracted upper bound for the Gilbert damping parameter is slightly lower than bulk values, indicating reduced damping in exfoliated samples. To further resolve damping contributions, we have also fabricated quarter-wavelength resonators with overtone modes and Q-factors exceeding 10^6, enabling frequency-resolved separation of viscous and inhomogeneous linewidth broadening. This work can offer new insights into the dynamical properties of van der Waals magnets.

Experimental Procedure:

Two-dimensional (2D) magnets have garnered significant attention for hosting exotic magnetic phenomena and topological spin textures, arising from strongly enhanced intrinsic spin fluctuations [1]. Their magnetic properties are readily tunable through external fields, strain, or chemical modifications, and their cleavable nature enables seamless integration into engineered heterostructures [1]. These features position 2D magnets as versatile platforms for probing fundamental spin interactions and developing multifunctional devices that integrate electronic, optical, and magnetic properties. Despite their intriguing properties, many two-dimensional ferromagnetic materials exhibit Curie temperatures significantly below room temperature, restricting their practical use. Recently, a promising candidate—Fe_5GeTe_2 (F5GT)—has been identified [2], demonstrating a Curie temperature of up to 332 K in bulk [3] and 280 K in exfoliated thin flakes (~10 nm) [2]. A recent ferromagnetic resonance (FMR) study reported that bulk F5GT crystals exhibit effective Gilbert damping coefficient of $\alpha \approx 0.01$—comparable to permalloy (NiFe)—although the measurements revealed substantial inhomogeneous linewidth broadening beyond viscous (Gilbert) damping contributions [3].

To better assess the intrinsic damping properties, we perform FMR measurements at the single- flake level using exfoliated F5GT, which are expected to be more structurally pristine. For this purpose, we design and fabricate high-Q superconducting resonators ($Q > 10^4$) and transfer exfoliated F5GT flakes onto them, enabling sensitive detection of their dynamic magnetic response (Fig. 1).

Fabrication:

Niobium (Nb) films were sputtered onto high-resistivity Si (100) wafers using AJA Orion Sputtering Systems. Superconducting resonators were fabricated by patterning the Nb layer with the Heidelberg MLA 150 Maskless Aligner, followed by cleaning with Oxford 81/82 and dry etching using a PT770 Etcher. The patterned wafers were subsequently diced using a

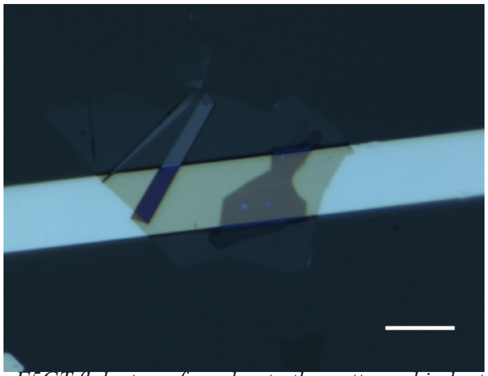

Figure 1: F5GT flake transferred onto the patterned inductor line of the 4 GHz superconducting resonator. A larger, close-to-transparent flake is the hBN flake capping the F5GT flake. The scale bar represents 10 µm.

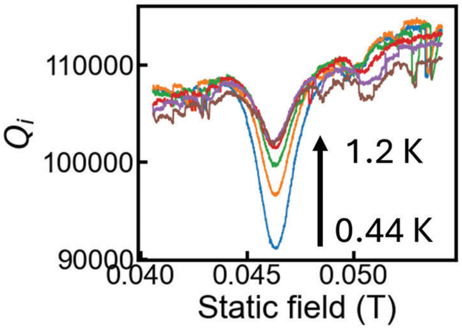

Figure 2: Ferromagnetic resonance (FMR) line at various temperatures.

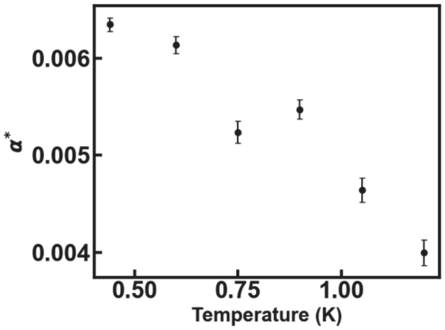

Figure 3: Estimated upper limit in Gilbert damping α at various temperatures..*

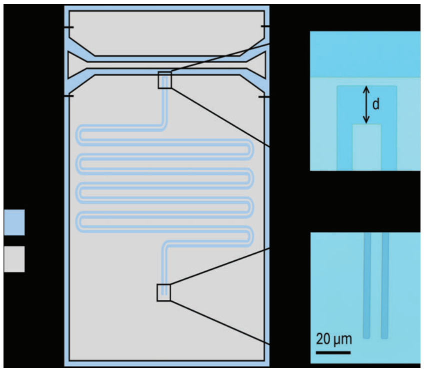

Figure 4: Schematic of the quarter-wavelength superconducting resonator. The zoomed-in optical images show the capacitive end and the inductive end of the resonator. The gap distance d in the capacitive end is 20 µm.

DISCO Dicing Saw. A nanoflake of Fe_5GeTe_2 (F5GT), capped with hexagonal boron nitride (hBN), was transferred onto the inductor line of the superconducting resonator (Fig. 1). For ferromagnetic resonance (FMR) measurements, the Westbond 7400A Ultrasonic Wire Bonder was used to wirebond the resonator to an electrical circuit component.

Conclusions and Future Steps:

We performed ferromagnetic resonance (FMR) measurements on a 25 nm F5GT flake capped with a 10 nm hBN flake that is transferred onto a 4 GHz lumped-element superconducting resonator. As shown in Fig. 2, we observe a decrease in the intrinsic Q-factor (Qi) at a static magnetic field of 0.046 T. This reflects that as the F5GT flake comes into resonance, it is drawing energy out of the superconducting resonator, which results in an apparent decrease in Qi. This measurement confirms the coupling between the flake and the resonator and demonstrates successful single- flake FMR detection.

To estimate an upper bound for the Gilbert damping parameter (α*), we analyze the FMR linewidth under the assumption of negligible inhomogeneous broadening. The extracted α* values are slightly lower but comparable to bulk values reported at 10 K ($\alpha \approx 0.007$), suggesting reduced damping in the exfoliated sample (Fig. 3). Interestingly, we observe that α decreases with temperature in the range of 0.4 – 1.2 K. To further investigate damping properties at the single-flake level, we have designed and fabricated quarter-wavelength superconducting resonators with optimized Q-factors, targeting values exceeding 106 (Fig. 4). A key advantage of this approach is that we will use the many overtone resonances, each as a separate frequency probe, which will allow us to distinguish viscous Gilbert damping from inhomogeneous linewidth broadening. The zoomed-in optical images show one representative device from a set of resonators we fabricated with varied gap distances, all of which are ready for FMR characterization. We plan to measure each resonator's Q-factor, transfer F5GT nanoflakes, and utilize overtone modes to extract the intrinsic damping parameters of F5GT with enhanced spectral resolution.

References:

[1] K. S. Burch, D. Mandrus, and J.-G. Park, Nature, 563, 47-52 (2018). J. M. Bartell, D. H. Ngai, Z. Leng, G. D. Fuchs, Nat. Commun., 6, 8460 (2015).

[2] A. F. May et al, ACS nano, 13, 4436-4442 (2019). C. Zhang, J. M. Bartell, J. C. Karsch, I. Gray, and G. D. Fuchs, Nano Lett., 21, 4966-4972 (2021).

[3] L. Alahmed et al, 2D Mater. 8, 045030 (2021).Mater. Quantum. Technol. 4(2), 025801 (2024).https://doi.org/10.1088/2633-4356/ad4b8c

[4] 1 M.P. Bland, F. Bahrami, J.G.C. Martinez, et al. "2D transmons with lifetimes and coherence times exceeding 1 millisecond," (2025).

Out-of-plane spin component produced by magnetic ordering

CNF Project Number: 598-96
Principal Investigator(s): Daniel C. Ralph
User(s): Xiaoxi Huang

Affiliation(s): Department of Physics, Cornell University
Primary Source(s) of Research Funding: Department of Energy
Contact: dcr14@cornell.edu, xh384@cornell.edu
Primary CNF Tools Used: Heidelberg MLA 150 Maskless Aligner, AJA Sputter Deposition

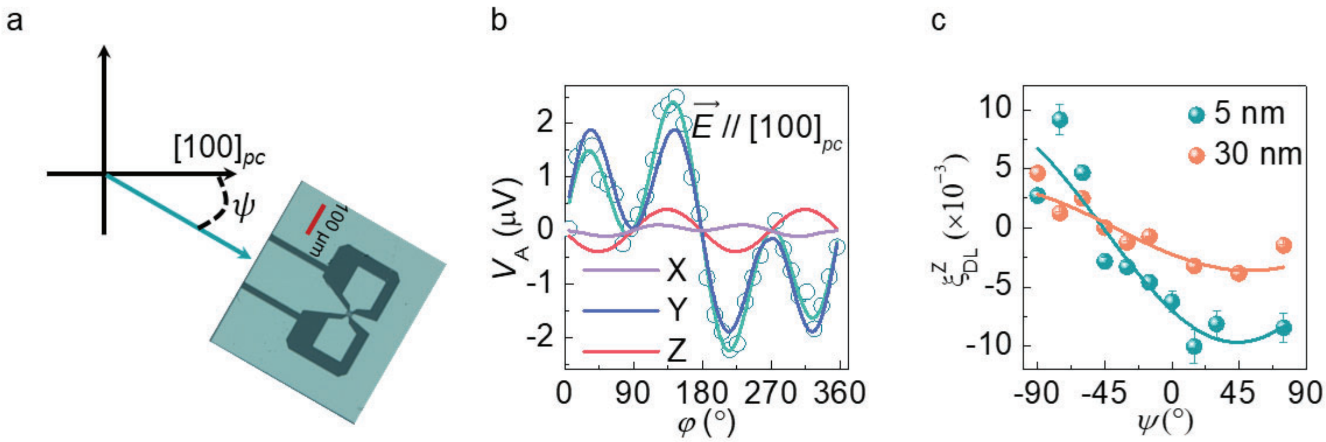

Figure 1:Out-of-plane anti-damping torque generation. a) A schematic demonstration of the in-plane crystallographic study. b) A signature of the out-of-plane anti-damping torque, sin2 Ψ component. c) $\xi z/DL$ as a function of in-plane electric field angle.
Figure 2 | Non-local excitation and detection of coherent magnons.

Abstract:

Micron-sized devices made with the Heidelberg MLA maskless laser direct writer and AJA sputter system were used to study spin currents and magnon currents generated as a consequence of magnetic ordering. We experimentally observed that a canted magnetic moment produces an out-of-plane damping-like torque from SrRuO3 thin films.

Summary of Research:

Magnetic materials with perpendicular magnetic anisotropy (PMA) are the most promising materials for high-density magnetic memory; and the efficient magnetization switching of PMA-magnets is enthusiastically pursued by Spintronics researchers because it has the potential to realize energy-efficient high-density information storage. Fortunately, an out-of-plane spin component borne by a spin current is theoretically predicted and experimentally demonstrated to be able to drive efficient anti-damping switching of the magnetization of a PMA magnet [1]. Our primary research goal is to find materials that efficiently produce spin currents or magnon currents with an out-of-plane spin component and ultimately to demonstrate the efficient switching of magnetization of PMA-magnet pillars with diameters as small as 100 nm. Our search for such materials has been centered around materials that have magnetic order, including both ferromagnetic and anti-ferromagnetic order. To detect spin current generation and the specific spin orientations that are allowed for these materials, micron-sized devices such as spin-torque ferromagnetic resonance (ST-FMR) devices and non-local magnon excitation and detection devices are patterned using these materials.

The ST-FMR device is shown in Fig. 1a. Bar structures with dimension of 20 µm ×70 µm are patterned with the Heidelberg MLA maskless laser direct writer. Then contacts made of Ti/Pt are deposited on the patterns in an AJA sputtering system. An example of spin current generated because of magnetic order is the unconventional spin-orbit torque generation from SrRuO3. SrRuO3 thin films when grown on (001)-oriented SrTiO3 substrates

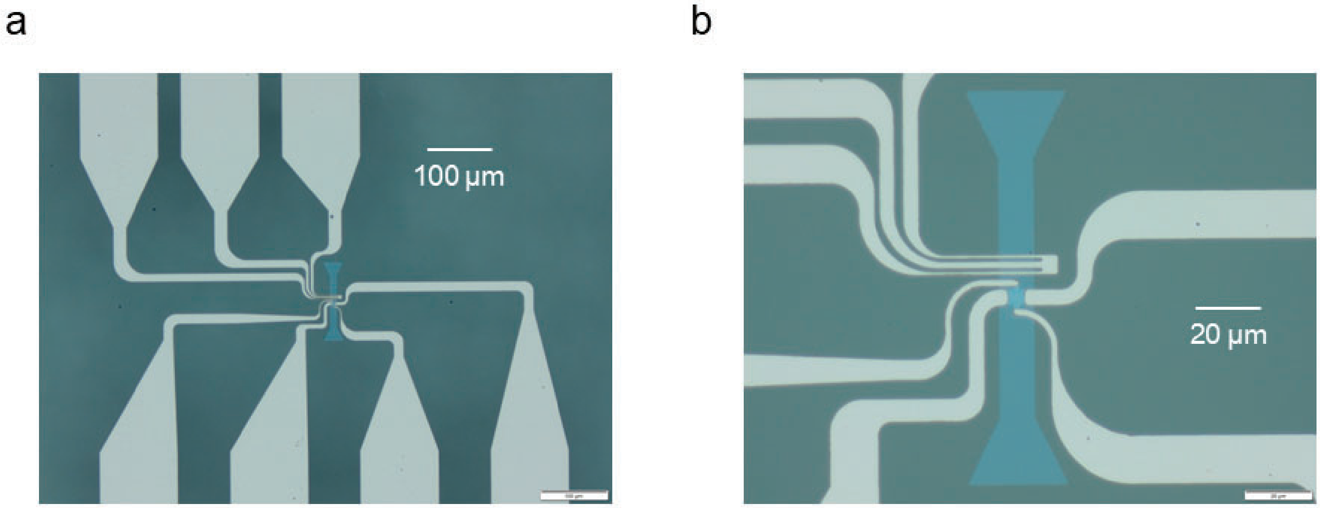

Figure 2:Non-local excitation and detection of coherent magnons.

exhibit canted magnetization and ferromagnets with magnetic moment canted out of the plane are predicted to be able to produce tilted spin currents with tilted spin polarization [2]. We measured the spin-orbit torque generated by SrRuO3 is on ST-FMR devices (Fig. 1a). When the rf current and oscillating magnetoresistance are mixed together, a dc mixing voltage is produced. The anti-symmetric component of the mixing voltage is contributed by the out-of-plane torques. A signature of the out-of-plane anti-damping torque is observed for electric field applied along [100]pc (Fig. 1b). To investigate the origins of out-of-plane anti-damping torque, the ST-FMR measurements were repeated on devices with intermediate Ψ angles for the orientation of the applied electric field relative to the [100]pc crystal direction (Fig. 1a). The out-of-plane anti-damping torque efficiency ξz/DL has the angular dependence shown in Fig. 1c, which indicates that two different mechanisms contribute to the out-of-plane toque (the spin anomalous Hall effect and the planar Hall spin current) This is the most exciting and important finding of our work so far and this work is currently under review.

Another pathway to produce out-of-plane spin component is to utilize coherent magnons, as a circularly polarized magnon in a magnetic material will have a net spin angular momentum aligned with magnetization [3]. We study the excitation and detection of coherent magnons on devices shown in Fig. 2, where coherent magnons are excited by a microwave-current-induced Oersted field and detected by spin-torque-induced harmonic Hall voltages. The ground-signal-ground waveguide on the excitation side has a minimum dimension of 1 µm and the Hall device on the detection side is of dimension 4 µm ×1 µm.

Conclusions and Future Steps:

Magnetic ordering plays a crucial role in producing out-of-plane damping-like torques. We plan to publish the work on SrRuO3 and to study the out-of-plane spin component produced by coherent magnons.

References:

[1] David MacNeill et al, Nat. Phys. 13, 300 (2017).
[2] Tomohiro Taniguchi et al, Phys. Rev. Lett. 3, 044001 (2015).
[3] Jiahao Han et al, Science 366, 1121 (2019).

Gate-tunable electroresistance in a sliding ferroelectric tunnel junction

CNF Project Number: 598-96
Principal Investigator(s): Daniel C. Ralph
User(s): Bozo Vareskic

Affiliation(s): Laboratory for Atomic and Solid State Physics, Cornell University

Primary Source(s) of Research Funding: National Science Foundation (NSF) grant DMR-2104268

Contact: dcr14@cornell.edu, bv227@cornell.edu

Primary CNF Tools Used: Zeiss Supra SEM, Nabity Nanometer Pattern Generator System, Angstrom E-Beam Evaporator, Oxford 81 Etcher

Abstract:

Ferroelectric tunnel junctions are an attractive platform next-generation memory applications due to their capacity for non-volatile operation and non-destructive readout of the electrical polarization. Generating a tunneling current that is sensitive to the polarization state requires a tunneling potential profile that is mirror asymmetric. This asymmetry has been engineered in previous work by using electrode layers with mismatched densities of states [1] or dielectric spacer layers directly within the tunnel barrier [2]. Here, we show that by fabricating ferroelectric tunnel junctions with an electrostatic gate, the tunneling conductance can be sensitive to the polarization state even when the two electrode layers are both monolayer graphene and there is no dielectric spacer layer. The magnitude and sign of the resulting tunneling electroresistance can be controlled by the bias and gate voltage of the junction.

Summary of Research:

In a ferroelectric tunnel junction (FTJ), two conducting layers sandwich an insulating ferroelectric tunnel barrier. Achieving appreciable readout currents with conventional ferroelectrics is challenging since depolarization fields, which increase with decreasing film thickness, can destabilize ferroelectric order in ultra-thin layers. Van der Waals ferroelectric materials, however, can sustain ferroelectric polarizations with no critical thickness limit. Recently discovered van der Waals sliding ferroelectrics offer a novel mechanism for ferroelectric switching that also promises higher endurance compared to non-sliding ferroelectrics [3-5].

In our devices, we mechanically assemble parallel bilayer boron nitride (P-BBN) with graphene electrodes on either side. The heterostructure is encapsulated by hexagonal boron nitride dielectric layers with a bottom graphitic gate. Figure 1 shows a schematic of the device geometry. To make electrical contact to the graphene electrode and graphite gate layers, we perform electron beam lithography (Zeiss Supra SEM and Nabity Nanometer Patter Generator System) and reactive ion etching (Oxford 81 Etcher) to first expose edges of the conducting layers. We then deposit Ti/Au contacts with electron beam deposition (Angstrom Evaporator). Figure 2 shows a micrograph of a completed device.

Transport measurements are performed at T = 4.2K. We measure the differential conductance dI/dV of the junction by applying a small AC bias (1 mV) as we sweep the DC bias, V, and read out the resulting AC current. The gate voltage, V_G, is fixed during each bias sweep. The left panel of Figure 3 shows the tunneling conductance on a forward and backward sweep of the DC bias. The tunneling conductance is nonlinear and increases with bias voltage, indicating that the P-BBN acts as a good insulating barrier. Step-like features in the conductance are likely due to inelastic electron tunneling assisted by phonons in the barrier or electrode layers. The tunneling conductance is hysteretic with the bias and can be quantified by the tunneling electroresistance $\mathrm{TER} = 100 \times \frac{G_f - G_b}{G_f + G_b}$ where $G_{f(b)}$ is the conductance of the forward (backward) bias sweep.

Notably, the magnitude and sign of the TER vary strongly with DC bias. At $V_G = -1.0$ V, Figure 3 right panel, a positive peak appears at negative bias while a negative peak is present at positive bias. By varying the gate, the bias dependence of the TER can be controlled. Figure 4 shows the same data as Figure 3 but now taken at $V_G = 5.4$ V. Now, a negative (positive) peak is present at negative (positive) bias, which is opposite the signal at $V_G = -1$ V (Figure 3 right panel).

In summary, we have shown that the conductance graphene/P-BBN/graphene tunnel junction is sensitive to the polarization state of ferroelectric P-BBN. The magnitude and sign of the resulting TER can be tuned by the bias and gate voltage.

References:

[1] M. Y. Zhuravlev, R. F. Sabirianov, S. S. Jaswal, and E. Y. Tsymbal, Physical Review Letters 94, 246802 (2005).

[2] M. Y. Zhuravlev, Y. Wang, S. Maekawa, and E. Y. Tsymbal, Applied Physics Letters 95, 052902 (2009).

[3] K. Yasuda, X. Wang, K. Watanabe, T. Taniguchi, and P. Jarillo-Herrero, Science 372, 1458 (2021).

[4] C. R. Woods, P. Ares, H. Nevison-Andrews, M. J. Holwill, R. Fabregas, F. Guinea, A. K. Geim, K. S. Novoselov, N. R. Walet, and L. Fumagalli, Nature Communications 12, 347 (2021).

[5] M. Vizner Stern, Y. Waschitz, W. Cao, I. Nevo, K. Watanabe, T. Taniguchi, E. Sela, M. Urbakh, O. Hod, and M. Ben Shalom, Science 372, 1462 (2021).

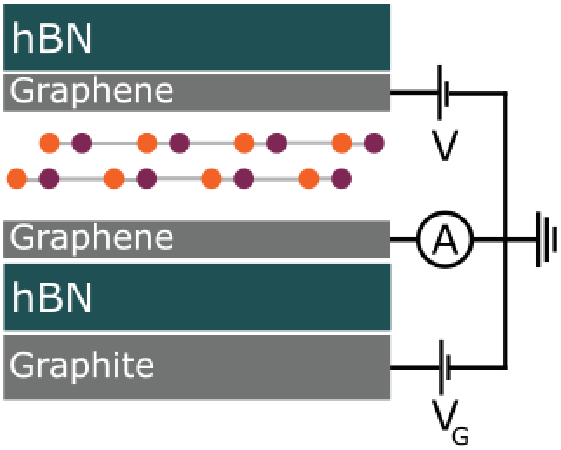

Figure 1:Device schematic of graphene/P-BBN/graphene tunnel junction. A bottom graphite gate is used to tune the carrier densities of the two graphene layers.

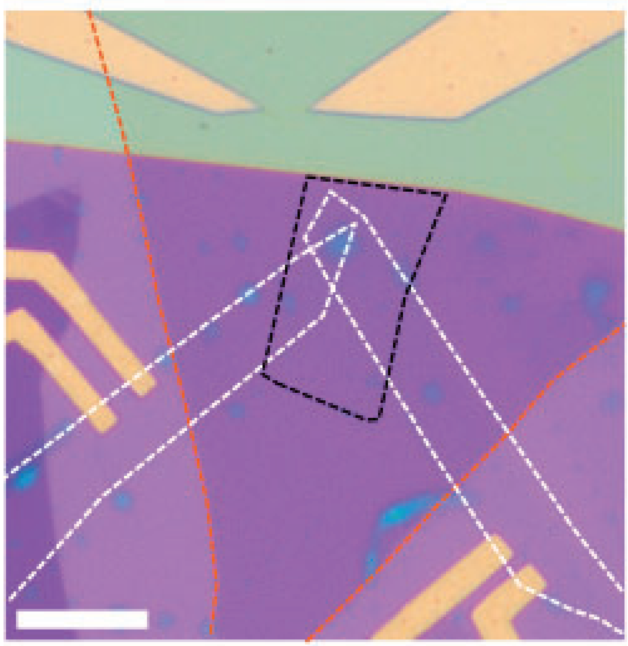

Figure 4:Same as Figure 3 but at V_G= −5.4 V.

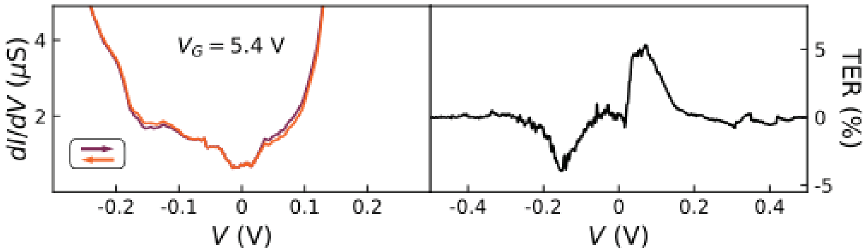

Figure 2:Micrograph of device. The graphene electrodes, P-BBN, and graphite gate electrode are outlined in dashed white, black, and orange lines, respectively. The scale bar is 10 μm

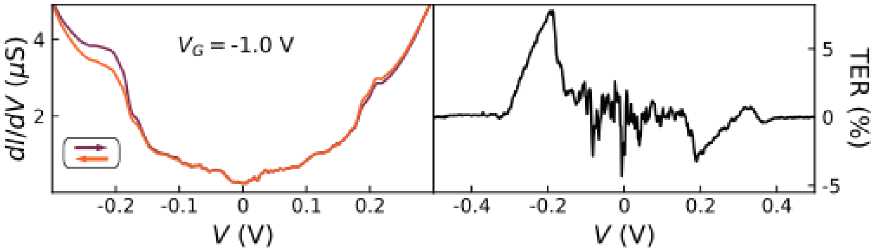

Figure 3: Left: Tunneling conductance as a function of bias voltage at constant gate voltage V_G= −1.0 V The forward (backward) sweep is shown in purple (orange). Right: TER calculated from the data on the left panel.

Quantum-Limited Measurement as a Tool for Entanglement in Superconducting Circuits

CNF Project Number: 173508

Principal Investigator(s): Ivan Pechenezhskiy, Britton Plourde

User(s): Jadrien Paustian

Affiliation(s): Syracuse University

Primary Source(s) of Research Funding: Syracuse University

Contact: ivpechen@syr.edu, jtpausti@syr.edu

Primary CNF Tools Used: Anatech Oxygen Descum, PlasmaTherm 770 Reactive Ion Etch, Photoresist Processing, DISCO Dicing Saw

Abstract:

As part of the Materials Characterization and Quantum Performance: Correlation and Causation project, we tuned up the niobium base layer recipes for fabrication of quantum superconducting devices while carefully documenting correlations between process changes and resonator internal quality factors. We find significant correlations between internal quality factors and the deposition conditions, the photoresist stripping chemistry, and the dose of post-fabrication hydrofluoric acid treatment.

Summary of Research:

We performed in-house photolithography before moving on to fabrication at the CNF, where we make use of the Anatech as an oxygen descum prior to a reactive ion etching with the PlasmaTherm 770 using a chlorine-based reactive ion etch. We then stripped off the photoresist in the hot strip baths in the photoresist section, before an additional descum with the Anatech tool and spinning protective resist on the sample for dicing. Dicing was performed using the DISCO dicing saw. Then, at Syracuse University, we performed additional HF treatments afterwards. The resonator devices are measured in an adiabatic demagnetization refrigerator. A packaged sample is shown in Figure 1. 20 minutes of buffered oxide etch provides the best quality factors for our samples, as shown in Figure 2. We solved significant issues created by the resist stripping process, demonstrating an optimal resist strip using AZ300T, shown in Figure 3. Additionally, after noticing anomalies in our temperature-dependent measurements, we began varying our sputter parameters. This altered our film stress by changing the deposition environment, and we found that film stress creates an anomalous increase in thermal losses, as shown in Figure 4.

Conclusions and Future Steps:

We observe that the interplay between treatments at different fabrication steps can have unintuitive effects on sample quality. We find distinct correlations between hydrofluoric acid treatment, resist stripping, and internal quality factors of superconducting resonators. We additionally find that sputter deposition parameters can alter the film stress, which can produce anomalous temperature dependence in loss.

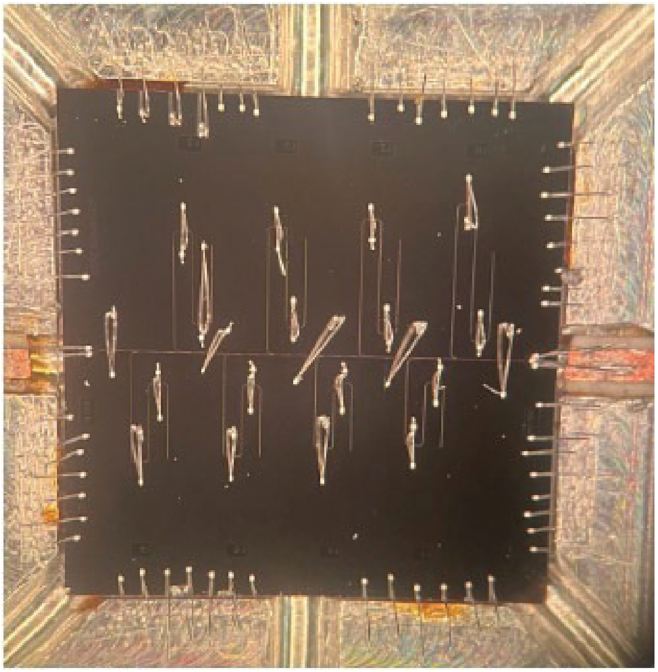

Figure 1: Fully packaged sample

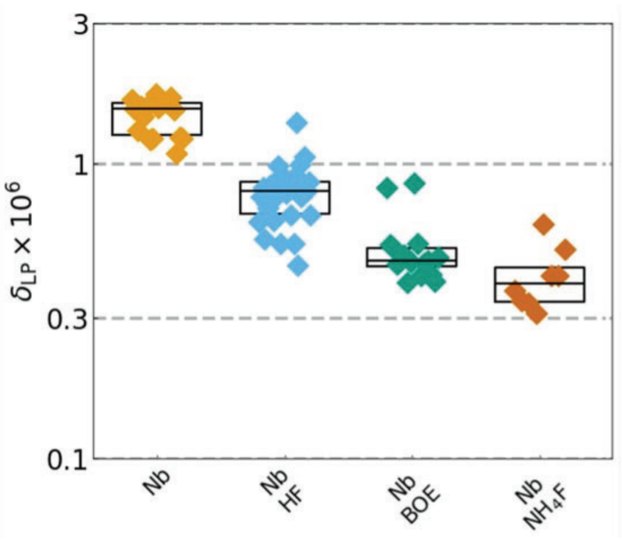

Figure 2: Loss tangents achieved with optimal HF treatment using buffered oxide etch, and a further improvement with ammonium fluoride.

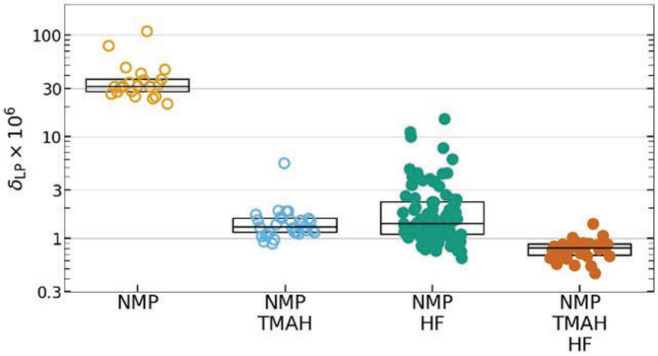

Figure 3: Loss tangents achieved with AZ300T resist stripping, a solution of n-methyl-2-pyrrolidone and tetramethyl-ammonium-hydroxide.

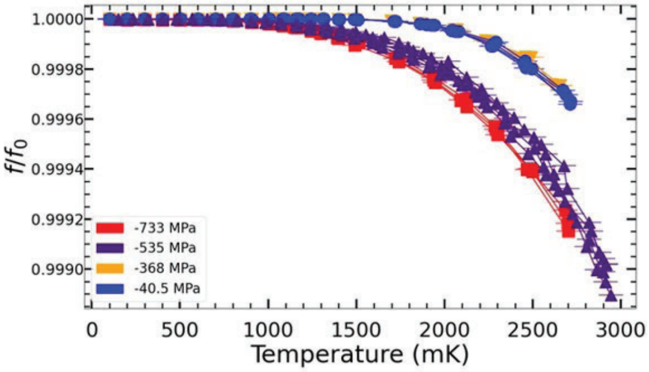

Figure 4: Relative resonator frequency shifts with anomalous temperature dependent frequency shifts for samples with average room temperature film stress beyond -500 MPa.

References:

[1] Maciej W. Olszewski et al. Low-loss Nb on Si superconducting resonators from a dual-use spin-tronics deposition chamber and with acid-free post-processing. 2025. arXiv: 2503.13285 [quant-ph]. url: https://arxiv.org/abs/2503.13285.

Deposition of Gold Films as a Sample Surface Coating for Magnetic Resonance Force Microscopy

CNF Project Number: 212512
Principal Investigator(s): John Marohn
User(s): George Du Laney

Affiliation(s): Chemistry & Chemical Biology, Cornell University

Primary Source(s) of Research Funding: National Institutes of Health, Cornell University

Contact: gdf9@cornell.edu, jam99@cornell.edu, grd44@cornell.edu
Website: https://marohn.chem.cornell.edu/

Primary CNF Tools Used: CVC SC4500 Odd-Hour E-beam evaporator

Abstract:

We employ e-beam evaporation of gold to prepare a surface noise-reducing coating for applications in magnetic resonance force microscopy. By transferring the deposited gold film from a sacrificial polymer to our samples of interest, we ensure we have a sample with the benefits of a gold coating while avoiding sample damage from direct exposure to e-beam evaporation.

Summary of Research:

Magnetic resonance force microscopy (MRFM) is a scanning-probe technique used to resolve the locations of nuclear and electronic spins using principles of magnetic resonance. To accomplish this, we bring an attonewton-sensitive magnet-tipped microcantilever in proximity to a spin-polarized sample. The sample's polarization is modulated and the resulting changes to the cantilever's vibrational amplitude and frequency are recorded as the signal. A challenge in MRFM is achieving an optimal cantilever–sample separation while avoiding surface noise-induced frequency fluctuations. It has been shown that applying a conductive layer over a polymer sample can reduce this surface noise. [1] Previous work has employed e-beam evaporated gold films to reduce surface noise in MRFM measurements. [2–4] Radical-doped polymer films which had gold directly e-beam evaporated onto them had a reduced electron spin resonance (ESR) signal due to a suspected "dead layer" within the sample from excess heating. [5] A novel film transfer approach was developed whereby the gold was e-beam evaporated onto a sacrificial layer and then transferred onto the sample obviated this issue, recovering a factor of 20 in enhancement was achieved. [6]

Despite this 20-fold enhancement, there is still a factor of 17 difference between experimental ESR-MRFM signal and predicted signal. As we adjust our experimental parameters to recover this remaining factor of 17, we continue to use this gold laminate coating to reduce sample surface noise.

Figure 1 shows a representative gold-laminate sample prepared for MRFM. The vertical column in the center is 20 nm of e-beam-evaporated gold sitting atop a ~520 nm film of tempamine-doped polystyrene. The ensemble of films sits atop the centerline of a custom-made waveguide for delivering radiofrequency and microwave radiation to the polystyrene film. A strip of gold was achieved by masking the sacrificial substrate with Kapton tape during e-beam evaporation. Masking allows the preparation of gold films that are small enough to stay over the centerline without covering the tapered regions of the waveguide, which would make the waveguide very lossy. To transfer the gold to the polymer-coated waveguide, the strip is aligned to the centerline, pressed together, and then the sacrificial substrate is allowed to dissolve, leaving the gold laminated to the polymer-coated waveguide.

This procedure of predefining the shape of the gold and aligning to the waveguide before dissolving the sacrificial polymer marks an improvement over a previously used version of this procedure, whereby strips were cut with a razor from a gold film that spanned the substrate, the sacrificial polymer was dissolved in water. [6] The cut-out flecks of gold were left to float on the water's surface, and the waveguide was stamped onto the flecks, which had a tendency to laminate imperfectly or in an incorrect location on the waveguide. This new transfer procedure affords the user more control over gold positioning, and

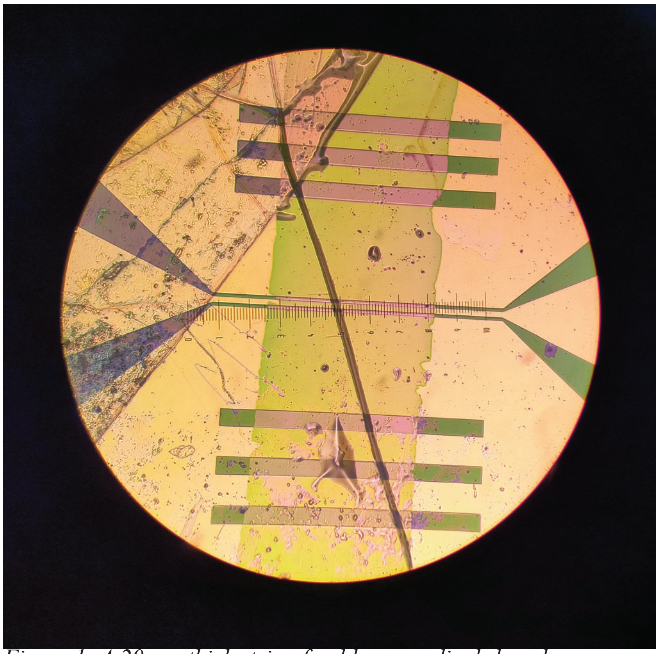

Figure 1: A 20 nm-thick strip of gold on a radical-doped polystyrene film, located over the centerline of a waveguide. Centerline dimensions are 10 µm by 500 µm. The roughness in the top left of the image is excess polystyrene film that did not laminate flatly during the transfer step. This image was taken using the Cornell Center for Materials Research's Olympus BH-2 optical microscope with IC20 objective. The graticule in the image is 500 µm across.

a single attempt is usually sufficient per waveguide.

Conclusions and Future Steps:

The implementation of e-beam evaporated gold films as a surface coating in our experiments continues to improve. Previous work developed a transfer procedure that avoided sample damage, and our latest procedure affords greater control over positioning the gold coating during the transfer. In the future, we may employ lithographically-defined masks to make precisely-defined regions of gold, but Kapton tape affords us the precision we need for the time being.

References:

[1] Kuehn, S.; Loring, R.F.; Marohn, J.A. Phys. Rev. Lett. 2006, 96 (15), 156103.

[2] Garner, S.R.; Kuehn, S.; Dawlaty, J.M.; Jenkins, N.E.; Marohn, J.A. Appl. Phys. Lett. 2004, 84 (25), 5091–5093.

[3] Moore, E.W.; Lee, S-G.; Hickman, S.A.; Wright, S.J.; Harrell, L.E.; Borbat, P.P.; Freed, J.H.; Marohn, J.A. Proc. Natl. Acad. Sci. U.S.A. 2009, 106 (52), 22251–22256.

[4] Hickman, S.A.; Moore, E.W.; Lee, S-G. Longenecker, J.G.; Wright, S.J.; Harrell, L.E.; Marohn, J.A. ACS Nano 2010, 4 (12), 7141–7150.

[5] Isaac, C.E. Ph.D. thesis, Cornell University/Cornell University, Ithaca, NY, 2018.

[6] Boucher, M.C.; Isaac, C.E.; Sun, P.; Borbat, P.P.; Marohn, J.A. ACS Nano 2023, 17 (2), 1153–1165.

Perfect Coulomb Drag in a Dipolar Excitonic Insulator

CNF Project Number: 263318
Principal Investigator(s): Jie Shan, Kin Fai Mak
User(s): Raghav Chaturvedi, Phuong X. Nguyen, Jinwoo Yu

Affiliation(s): Laboratory of Atomic and Solid State Physics, School of Applied and Engineering Physics; Cornell University

Primary Source(s) of Research Funding: DOE, NSF, AFOSR, Moore Foundation

Contact: jie.shan@cornell.edu, kinfai.mak@cornell.edu, rc669@cornell.edu, pxn2@cornell.edu, jy968@cornell.edu

Website: https://sites.google.com/site/makshangroup/

Primary CNF Tools Used: Zeiss Supra SEM, Nabity Nanometer Pattern Generator System (NPGS), Angstrom E-Beam Evaporator, SC4500 Odd/Even- Hour Evaporator, Oxford 81/82 RIE, YES Asher, Autostep i-line Stepper, Hamatech Wafer Processor Develop, Heidelberg Mask Writer - DWL2000, Photolithography Spinners, Dicing Saw - DISCO

Abstract:

Exciton is a quasiparticle made of one electron and one hole bound by Coulomb attraction. In systems where the exciton binding energy exceeds the single particle band gap, excitons spontaneously form, and the new ground state is an excitonic insulator (EI): conducting for excitons but insulating for free electrons or holes. In this work, we realize a dipolar EI in MoSe2/WSe2 double layers. The formation of excitons results in perfect Coulomb drag, that is, driving a charge current in one layer induces an equal and opposite drag current in the other layer. Upon increasing exciton density beyond the critical Mott density, excitons dissociate into an electron-hole plasma and the drag current becomes negligible. Our work opens pathways to realize exciton superfluidity and other exotic phases of correlated excitons.

Summary of Research:

Excitonic insulators (EIs) [1] form when the binding energy of bound electron-hole pairs exceeds the single particle bandgap in a semiconductor. Unlike charge insulators, where the charges are immobile, excitons can flow. However, excitons are charge neutral which makes driving an exciton current impossible in bulk EIs. Using van der Waals (vdW) semiconductors it's possible to fabricate independent electron and hole contacts by separating the electrons and holes to different layers of material. This approach has been used to flow an exciton current in coupled GaAs quantum wells [2] and graphene double layers [3], however, only in the quantum Hall regime. In our work, we use dipolar EIs observed in Coulomb-coupled double layers [4] to flow an excitonic current in the absence of magnetic field [5].

Figure 1A and 1B show a schematic cross-section and an optical image of our device, respectively. The device consists of WSe2/MoSe2 double layers separated by a thin hexagonal boron nitride (hBN) barrier. WSe2 and MoSe2 form a type-II band alignment as shown in Figure 1C, that is, the lowest (highest) energy conduction (valence) band lies in the MoSe2 (WSe2) layer. The double layer is further encapsulated by two gates made of hBN and graphite. We use Pt and Bi electrodes that make Ohmic contacts to holes in the WSe2 layer and electrons in the MoSe2 layer, respectively. An interlayer bias, V_b, is applied between the layers to tune electron-hole pair density, n_p, and the gate voltages allow to tune electron-hole density imbalance. Our experiment is performed at equal electron and hole densities.

Figure 2A shows the configuration for the Coulomb drag measurement. An electron current is driven in the MoSe$_2$ layer while WSe2 layer is connected to an ammeter. In this configuration, when an exciton current flows in the system, it's expected that the drive current in the MoSe$_2$ layer will induce an equal and opposite drag current in the WSe$_2$ layer. This is because a flowing electron in the MoSe$_2$ layer will drag along a hole in the WSe2 layer.

The results for the Coulomb drag measurement are shown in Figure 2B. Drive current in the MoSe$_2$ layer (black line) is observed when V_b crosses a threshold value and injects electron-hole pairs into the double layer. At low n_p, the drag current (red line) in the WSe$_2$ layer exactly traces the drive current. The ratio of the drag and drive current (blue line) persists to 1 for exciton density up to ~ 4 x 10^{11} cm^{-2}. Upon further increasing N_p beyond this density, the drag current abruptly drops to zero. This corresponds to the Mott limit, beyond which excitons unbind into an electron-hole plasma due to larger screening of the electron-hole interaction at higher densities.

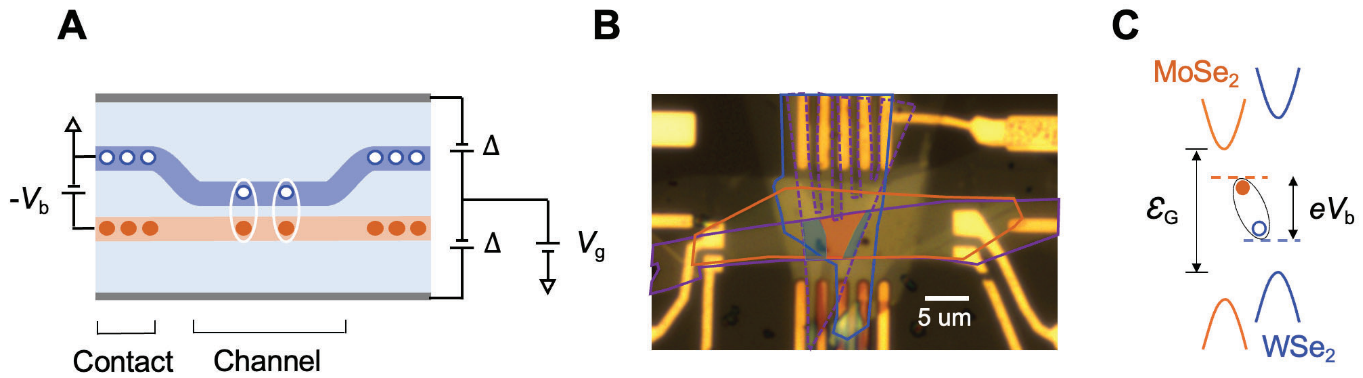

Figure 1: a, Schematic cross-section of the device. b, Optical microscope image of a double layer device. Scale bar is 5 μm. c, Type-II band alignment of $MoSe_2$ and WSe_2.

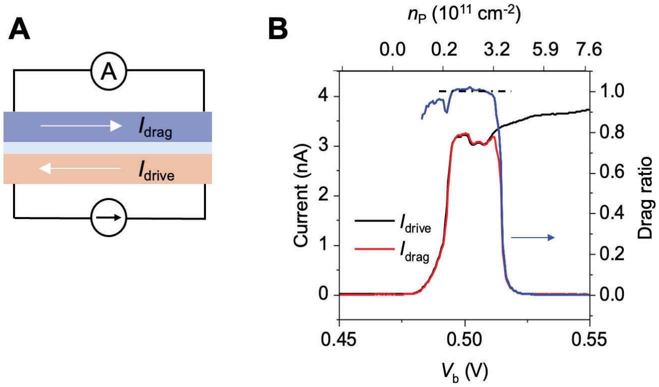

Figure 2: a, Circuit for Coulomb drag measurement. b, Drive (black line) and drag (red) currents in the MoSe2 and WSe2 layers respectively measured as a function of V_b. The ratio of the currents is plotted in blue. The black dashed line marks drag ratio = 1.

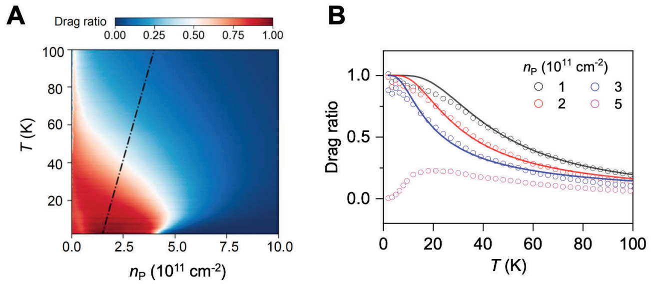

Figure 3: a, Drag ratio as a function of temperature and n_p . Black dashed line corresponds to the degeneracy temperature. b, Linecuts of drag ratio as a function of temperature for different n_p. Solid lines are fit to the Saha equation.v

We measure the temperature dependence of the drag ratio for varying n_p as shown in Figure 3. The drag ratio remains above 0.9up to 20 K at low n_p. When excitons are dissociated above the Mott limit, only frictional drag is observed with a characteristic quadratic temperature dependence as expected for two independent Fermi liquids. Furthermore, the temperature dependence of the drag ratio can be largely captured by a simple ionization model (solid lines in 3B) based on the Saha equation. We also plot the degeneracy temperature (black dashed line) obtained through compressibility measurements for each density in Fig 3A. Below the degeneracy temperature, the exciton fluid is expected to become a quantum fluid.

Our work successfully realizes exciton circuitry in the absence of a magnetic field and enables future studies of exciton transport, including a four-terminal measurement of the exciton chemical potential that can directly detect exciton superfluidity.

References:

[1] D. Jérome, T.M. Rice & W. Kohn, Excitonic Insulator, Physical Review 158, 462–475 (1967).

[2] D. Nandi, A. D. K. Finck, J. P. Eisenstein, L. N. Pfeiler & K. W. West, Exciton condensation and perfect Coulomb drag. Nature 488, 481–484 (2012).

[3] X. Liu, K. Watanabe, T. Taniguchi, B. I. Halperin & P. Kim, Quantum Hall drag of exciton condensate in graphene. Nat. Phys. 13, 746–750 (2017).

[4] L. Ma, P. X. Nguyen, Z. Wang, Y. Zeng, K. Watanabe, T. Taniguchi, A. H. MacDonald, K. F. Mak & J. Shan, Strongly correlated excitonic insulator in atomic double layers. Nature 598, 585–589 (2021).

[5] P. X. Nguyen, L. Ma, R. Chaturvedi, K. Watanabe, T. Taniguchi, J. Shan & K. F. Mak, Perfect Coulomb drag in a dipolar excitonic insulator. Science 388, 274–278 (2025).

Superconductivity in twisted bilayer WSe_2

CNF Project Number: 263318
Principal Investigator(s): Jie Shan, Kin Fai Mak
User(s): Zhongdong Han, Yiyu Xia, Yichi Zhang

Affiliation(s): Laboratory of Atomic and Solid State Physics, School of Applied and Engineering Physics; Cornell University

Primary Source(s) of Research Funding: DOE, NSF, AFOSR, Moore Foundation

Contact: jie.shan@cornell.edu, kinfai.mak@cornell.edu, zh352@cornell.edu, yx579@cornell.edu, yz2662@cornell.edu

Website: https://sites.google.com/site/makshangroup/

Primary CNF Tools Used: Zeiss Supra SEM, Nabity Nanometer Pattern Generator System (NPGS), Angstrom E-Beam Evaporator, SC4500 Odd/Even-Hour Evaporator, Oxford 81/82 RIE, YES Asher, Autostep i-line Stepper, Hamatech Wafer Processor Develop, Heidelberg Mask Writer - DWL2000, Photolithography Spinners, Dicing Saw - DISCO

Abstract:

Semiconductor moiré materials have emerged as a highly tunable platform for simulating the Hubbard model [1,2], which is believed to capture the essential physics of high-temperature superconductors [3]. However, the experimental evidence for superconductivity in these systems remains elusive. Here, we report the observation of robust superconductivity in twisted bilayers WSe_2. Our results reveal its unconventional nature rooted in strong electron correlations.

Summary of Research:

The Hubbard model [4], a simplest model describing interacting electrons on a lattice, provides profound insights into the physics of strongly correlated particles. Tuning the effective interaction strength to the moderate correlation regime is expected to stabilize a variety of exotic phases near the Mott transition. A well-known example is the idea that doping a Mott insulator captures the essential physics underlying high transition temperature (Tc) superconductors [5,6]. Developing a controllable platform to simulate Hubbard model physics and high-Tc phenomenology is highly desirable, as it could offer new perspectives on the high-Tc problem and guide the design of next-generation high-temperature superconductors.

In this study, we investigate the electrical transport properties of a 3.65° twisted bilayer WSe2 (tWSe2) device with tunable carrier density n and out-of-plane electric field E. Our measurements establish the electrostatic phase diagram for tWSe2 at moderate correlation regime. At half-band filling, a Mott insulator is observed, with its correlation strength effectively controlled by the electric field. Upon approaching the metal-insulator transition near zero E field—where the hopping amplitude t becomes comparable with the onsite interaction U—we observe robust superconductivity. The optimal superconducting temperature is about 200 mK, corresponding to about 1-2% of the effective Fermi temperature. This ratio is comparable to that of high-temperature cuprate superconductors and suggests strong pairing.

Figure 1 shows the device schematics (a) and its optical image (b). The encapsulated twisted bilayer WSe2 is directly transferred onto prepatterned Pt electrodes. The dual-gated geometry enables independent tuning of n and E. Additional contact and split gates, deposited atop the full stack, are implemented to achieve low contact resistances and eliminate unwanted parallel conduction channels. The Hall-bar geometry is defined by all four gates, including the top, bottom, contact and splitting gates. Electrical transport measurements are performed in a dilution refrigerator, equipped with low-temperature resistor-capacitor and radiofrequency filters mounted on the mixing chamber plate to attenuate electrical noise from about 65 kHz to tens of gigahertz. Low-frequency (5.777 Hz) lock-in techniques are employed to measure sample resistance using a small excitation current (<10 nA) to avoid sample heating.

Figure 2 shows the longitudinal resistance R measured as a function of moiré filling factor v and E (a) and a zoom-in phase diagram near half-band filling (v=1) and zero E field (b). In the electrostatic phase diagram, the layer-shared (inner) and layer-polarized (outer) regions are delineated by dashed lines. In the layer-shared region, the van Hove singularity (vHS), characterized by a diverging density of states (DOS), is identified as a high-resistance feature traced by the red curve. Overall, the phase diagram aligns well with the single-particle expectation, except for the correlated insulating states observed at commensurate fillings v=1/4,1/3,1. Notably, at v=1, a robust zero-resistance phase emerges at the verge of the correlated insulator near zero E field.

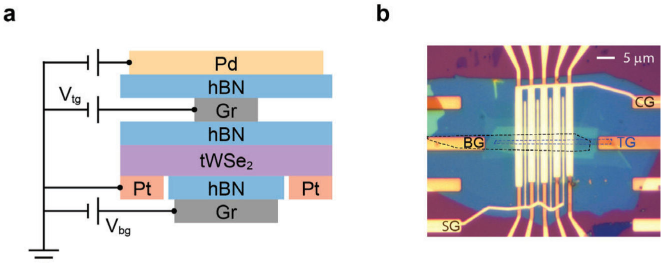

Figure 1: a, Schematic of the device structure. b, Optical microscope image of a 3.65° tWSe2 device. Scale bar is 4 μm .

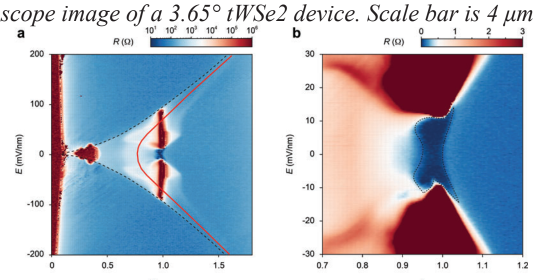

Figure 2: a, Longitudinal resistance R as a function of moiré filling factor v and electric field E. b, Zoom-in phase diagram near half-band filling and zero E field.

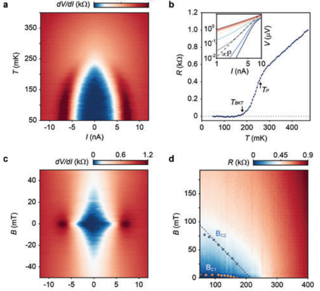

Figure 3: a, Differential resistance dV/dI as a function of current bias I and temperature T. b, Zero-bias resistance R as a function of T Insert: I-V characteristics at varying T c, Differential resistance dV/dI as a function of I and magnetic field B d, Zero-bias resistance R as a function of T and B.

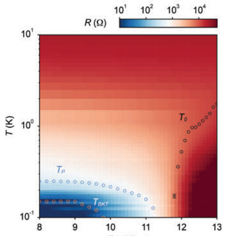

Figure 4: Zero-bias resistance R as a function of E and T, showing an electric-field–induced superconductor–insulator transition at v=1.

Figure 3 further investigates the differential conductance of the zero-resistance phase under applied perpendicular magnetic fields at elevated temperature. Figure 3a shows the differential resistance dV/dI as a function of bias current I and temperature T. The critical current is I_c=5 nA at T=50 mK and gradually decreased to zero near 250 mK. The corresponding zero-bias resistance R as a function of T is shown in Figure 3b, revealing a Berezinskii–Kosterlitz–Thouless (BKT) transition temperature T_{BKT}=180 mK and a pairing temperature T_P=250 mK. Figure 3c shows dV/dI as a function of I and magnetic field B. Figure 3d shows zero-bias resistance R as a function of B and T, from which the critical fields B_{c1} and B_{c2} are identified.

A linear fit to

$$B_{c2} = \frac{\Phi_0}{2\pi\xi^2}\left(1-\frac{T}{T_p}\right)$$

shown as the dashed line, gives rise to a superconducting coherence length ξ≈52 nm, which is about 10 times the moiré period a_M≈5 nm (Φ_0 denotes the magnetic flux quantum).

Figure 4 shows R as a function of E and T, revealing an electric-field-induced superconductor-insulator transition at v=1. The critical temperatures T_{BKT} and T_P are indicated on the superconducting side and the extracted thermal activation gaps T_0 are plotted on the insulating side. All characteristic temperature scales vanish continuously as E approaches the critical field E_c≈11.7 mV / nm, indicating a continuous quantum phase transition.

Conclusions and Future Steps:

We observe robust superconductivity in tWSe$_2$, emerging at the verge of correlated insulating state at v=1. The continuous superconductor-insulating transition highlights the delicate interplay between the kinetic energy t and on-site interaction U, resembling the physics of high-T_c cuperate superconductors.
A superconducting transition temperature to Fermi temperature ratio (T_c/T_f) of 1-2%, along with a short coherence length ξ/a_M≈10 (both comparable to values in cooperate superconductors), further suggest strong pairing. Our findings motivate further investigations into questions such as the superconducting pairing symmetry and underlying pairing mechanism.

References:

[1] Tang, Y. et al. Nature 579, 353-358 (2020)
[2] Regan, E. C. et al. Nature 579, 359-363 (2020)
[3] Anderson, P. W. Science 235, 1196-1198 (1987)
[4] Hubbard, J. Proc. R. Soc. A 276, 237-257 (1963)
[5] Lee, P. A., Nagaosa, N., Wen, X.-G. Reviews of Modern Physics 84, 1383-1417 (2012)
[6] Imada, M., Fujimori, A., Tokura, Y. Reviews of Modern Physics 70, 1039-1263 (1998)

Thermodynamic evidence of fractional Chern insulator in moiré $MoTe_2$

CNF Project Number: 263318
Principal Investigator(s): Kin Fai Mak, Jie Shan
User(s): Zhengchao Xia, Yihang Zeng, Kaifei Kang, Bowen Shen, Jiacheng Zhu, Patrick Knüppel, Chirag Vaswani

Affiliation(s): Laboratory of Atomic and Solid State Physics, School of Applied and Engineering Physics, Kavli Institute at Cornell for Nanoscale Science; Cornell University

Primary Source(s) of Research Funding: DOE, NSF, AFOSR, GBMF

Contact: jie.shan@cornell.edu, kinfai.mak@cornell.edu, zx287@cornell.edu, yz425@cornell.edu, kk726@cornell.edu, bs792@cornell.edu, jz969@cornell.edu, pk439@cornell.edu, cv246@cornell.edu

Website: https://sites.google.com/site/makshangroup/

Primary CNF Tools Used: Zeiss Supra SEM, Nabity Nanometer Pattern Generator System (NPGS), Angstrom E-Beam Evaporator, SC4500 Odd/Even-Hour Evaporator, Autostep i-line Stepper, Hamatech Wafer Processor Develop, Heidelberg Mask Writer - DWL2000, Photolithography Spinners, Dicing Saw – DISCO, Yes Asher

Abstract:

Fractional Chern insulators are the lattice analogues of the fractional quantum Hall effects, characterized by Hall conductance quantized to rational fractional multiples of e^2/h in the absence of external magnetic field or Landau levels [1, 2, 3]. By employing a new technique to optically readout the local thermodynamics [4], we discover thermodynamic evidence of both integer and fractional Chern insulators in a 3.4° twisted homo-bilayer $MoTe_2$ moiré device. Specifically, we obtain local electronic compressibility through a monolayer semiconductor sensor capacitively coupled to the tMoTe2 moiré and show that the correlated insulators at hole filling factors v = 1 and 2/3 spontaneously break time-reversal symmetry. We further demonstrate that they are integer and fractional Chern insulators with Chern numbers 1 and 2/3, respectively, from the dispersion of the insulating states in moiré filling with applied magnetic field. Our findings pave pathways for uncovering other new fractional topological phases and demonstrating the fractional statistics in moiré semiconductor materials.

Summary of Research:

Fractional topological phases represent a unique class of quantum states that combine strong interactions with nontrivial band topology. Transition-metal dichalcogenide (TMD) semiconductor moiré materials, which support tunable topological flat bands, provide a highly tunable platform for realizing fractional topological phases [5, 6]. Our experiment demonstrates that, in 3.4° tMoTe2 moiré, the correlated-insulating states at hole filling v = 1 and 2/3 are integer and fractional Chern insulators.

Figure 1 illustrates the schematic of a dual-gated 3.4° twisted homo-bilayer MoTe2 device with a monolayer WSe2 sensor for thermodynamic measurements. Inset shows the schematic of tMoTe2 lattices. The twisted bilayers form a honeycomb moiré superlattice, with two sublattices (red and blue) residing in two different layers. Mo atoms in the top layer are aligned with Te atoms in the bottom layer at the red sublattice sites, and the arrangement is reversed at blue sublattice sites.

We employ our newly developed technique to optically readout the local thermodynamics of tMoTe2 moiré. Figure 2(a) exhibits a simplified measurement scheme. A monolayer semiconductor sensor (green) is capacitively coupled to the sample (blue), allowing an interlayer bias Vs to be applied between sample and sensor. For each measurement, sensor chemical potential is actively adjusted through a feedback circuit to lock the reflection count at a chosen reference point. The amount of adjustment directly reads the chemical potential μ of the sample.

Figure 2(b) shows an example reflectance spectrum as a function of WSe_2 sensor chemical potential (tuned by V_{bg}). The neutral exciton resonance peak quenches rapidly upon electron doping near 4.69V. In Figure 2(c) the integrated photon count drops sharply upon electron doping, enabling accurate determination of WSe2 band edge, making it a natural reference point. During each measurement, V_{bg} is tuned through a feedback loop to lock the reflection count the chosen reference point (vertical dashed line). As shown in Figure 2(d), under this arrangement, sensor chemical potential (dashed green line) is kept at sensor conduction band edge, while sample chemical potential (dashed blue line) is at eVs below it, with μ=0 defined at the moiré band edge. Therefore, sample's chemical potential is given by

$$\mu/e =, \ (1+\frac{C_{bg}}{C_s})V_{S}, - \frac{C_{bg}}{C_s}V_{bg},$$

where C_{bg} and C_s are the bottom-gate-to-sensor and sensor-to-sample geometrical capacitances, respectively.

We apply this technique to the 3.4° $tMoTe_2$ moiré device shown in Figure 1. Figure 3(a) and (b) show moiré chemical potential (μ) and incompressibility (dμ/dv) as a function of doping density (ν), respectively, when the moiré is tuned to near zero interlayer potential dfference ($E \approx 0$). The steps in chemical potential, or peaks in incompressibility, correspond to insulating states at $\nu = 1, 2/3$ and 2. Figure 3(c) and (d) shows the magnetic circular dichroism (MCD) as a function of perpendicular magnetic field (B) at $\nu = 1$ (c), and $\nu = 2/3$ (d). Spontaneous magnetization and magnetic hysteresis can be clearly identified for both states, indicating that correlated insulators at $\nu = 1$ and 2/3 spontaneously break time reversal symmetry.

Figure 4(a) shows the electronic incompressibility as a function of ν and B at $E \approx 0$. We observed that the incompressible states at $\nu = 1$ and 2/3 disperse linearly with B. Empty circles denote the center of mass of the incompressibility peaks. Filled circles in Figure 4(b) mark the corrected dispersion with respect to a trivial Mott insulator at large E. Linear fits to the corrected dispersions are denoted by the solid lines in Figure 4(b), which yield the quantum numbers (t, s) according to the Diophantine equation

$$\nu = t\frac{e}{h}\frac{B}{n_M} + s$$

We conclude that for $\nu = 1$, $t = 1.0 \pm 0.1$ (corresponding to Chern number 1), while for $\nu = 2/3$, $t = 0.63 \pm 0.08$ (corresponding to Chern number 2/3).

Conclusions and Future Steps:

By employing the optical readout of local chemical potential on a 3.4° tMoTe2 device, we obtain thermodynamic evidence of fractional Chern insulators at $\nu = 2/3$, with Chern number 2/3. Our results indicate that TMD moiré flat bands can host topologically ordered states carrying fractionalized excitations in the absence of magnetic fields.

References:

1. Tang, Y. et al. Nature 579, 353-358 (2020) 2. Regan, E. C. et al. Nature 579, 359-363 (2020) 3. Anderson, P. W. Science 235, 1196-1198 (1987) 4. Hubbard, J. Proc. R. Soc. A 276, 237-257 (1963) 5. Lee, P. A., Nagaosa, N., Wen, X.-G. Reviews of Modern Physics 84, 1383-1417 (2012) 6. Imada, M., Fujimori, A., Tokura, Y. Reviews of Modern Physics 70, 1039-1263 (1998).

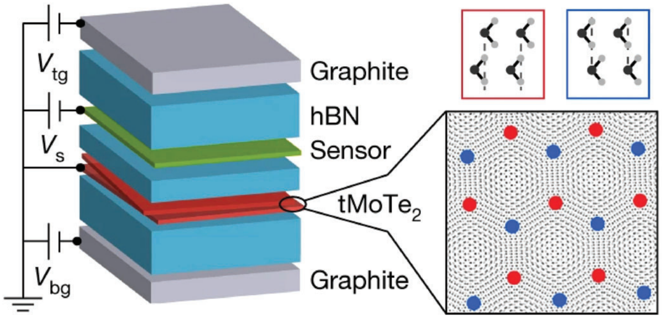

Figure 1: Device schematic. Inset: schematic representation for $tMoTe_2$ moiré lattice.

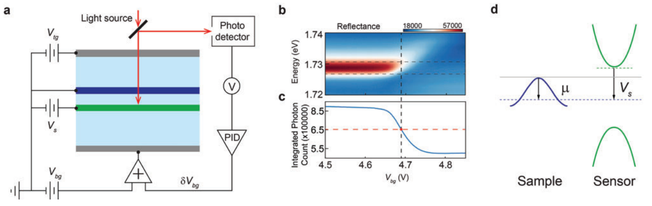

Figure 2: a, schematic for optical measurement of thermodynamics in a typical dual-gated device. b, V_{bg} dependence of reflectance contrast near monolayer WSe2 sensor's neutral exciton resonance. c, spectrally integrated photon counts over the window in b horizontal dashed lines) as a function of V_{bg}. d, schematic of the band alignment.

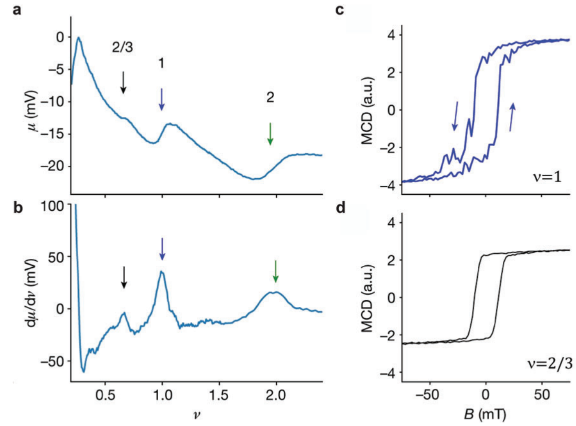

Figure 3: a, b, chemical potential (a) and charge incompressibility (b) as a function of $tMoTe_2$ moiré filling (ν). c, d, MCD as a unction of B at $\nu = 1$ (c) and $\nu = 2/3$ (d). All measurements performed at $E \approx 0$.

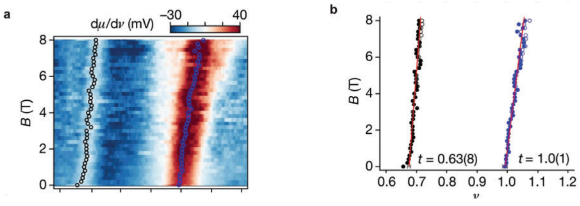

Figure 3: a, b, chemical potential (a) and charge incompressibility (b) as a function of $tMoTe_2$ moiré filling (ν). c, d, MCD as a unction of B at $\nu = 1$ (c) and $\nu = 2/3$ (d). All measurements performed at $E \approx 0$.

Investigating the Impact of an External Electric Field on Thermal Behavior

CNF Project Number: 275819
Principal Investigator(s): Zhiting Tian
User(s): Amelia Schaeffer, Aloyse Maille

Affiliation(s): Sibley School of Mechanical and Aerospace Engineering; Cornell University

Primary Source(s) of Research Funding: Office of Naval Research

Contact: zt223@cornell.edu, afs97@cornell.edu, aam299@cornell.edu

Website: https://ztgroup.org/

Primary CNF Tools Used: ABM Contact Aligner, SUSS MA6-BA6 Contact Aligner, SC4500 Odd-Hour Evaporator, Glen 1000 Resist Strip, Everbeing EB-6 DC Probe Station

Abstract:

As electronics continue to scale to smaller dimensions and increased power densities, understanding how electric fields impact the thermal properties of materials becomes important for accurate thermal budgeting. In this work, we fabricate structures to study how thermal properties of hexagonal boron nitride (hBN) change when a cross-plane electric field is applied to the material. Microscale capacitors with Ti/Au contacts were fabricated using dry transfer, contact photolithography, electron-beam evaporation, and liftoff processing. Thermal measurements of the devices under applied external fields are ongoing.

Summary of Research:

To perform thermal measurements, a lateral hBN flake dimension of at least 80 µm is desirable, and thicker flakes are selected to help limit the influence of the interfaces on thermal measurements. (Bulk samples are not used since a single-crystal domain is necessary to eliminate the effect of grain boundaries.) Compared to typical 2D material flakes used for device fabrication, these flakes have much larger lateral dimensions (~100 µm x ~100 µm) and are thicker (~100 nm or thicker). This, combined with the electrode dimensions, allows us to utilize contact photolithography to pattern our electrodes, a technique not typically used for 2D flakes.

Mask design, mask writing, and photolithography dose testing were all performed as initial steps in the device development process. To make a wafer of devices, the bottom electrodes are patterned, metal is deposited, and liftoff is performed. After the bottom electrode is set, dry transfer is used to precisely place hBN flakes. Then, the top electrode is patterned on top of the flake, and deposition and liftoff are repeated. Sonication cannot be used at any step once the flakes are placed, as it can lead to delamination. An example of a fully fabricated device is shown in Fig. 1.

Some iteration on this general process was necessary to ensure repeatable and high quality results. The initial wafer of devices run showed contaminants on the flake that affected the top electrode, and atypical aging of the gold used for both the top and bottom electrodes was observed. An oxygen plasma resist strip and a more aggressive substrate clean prior to processing resolved these two issues, respectively. A comparison of a device from the first wafer and one from the second wafer, after these changes have been implemented, is shown in Fig. 2.

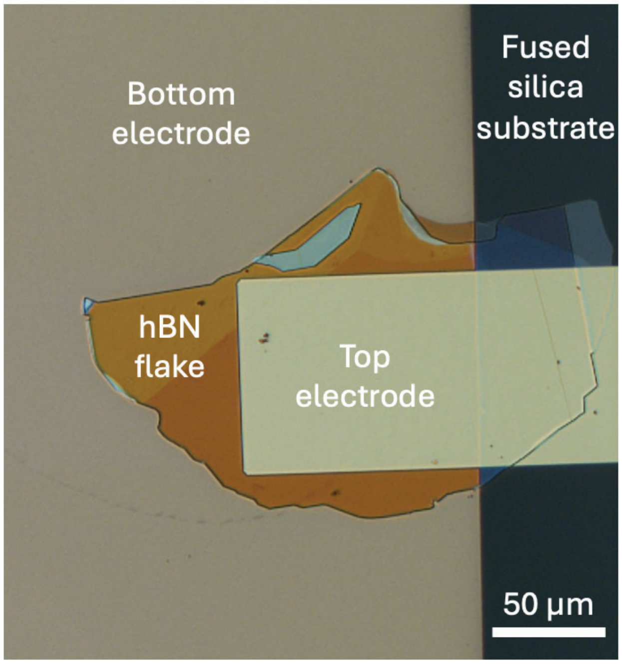

Figure 1: An optical microscope image of a fully-fabricated device with structures labelled for clarity. Both the top and bottom electrodes are Au with a Ti adhesion layer, but the difference in appearance is due to different thicknesses of Au.

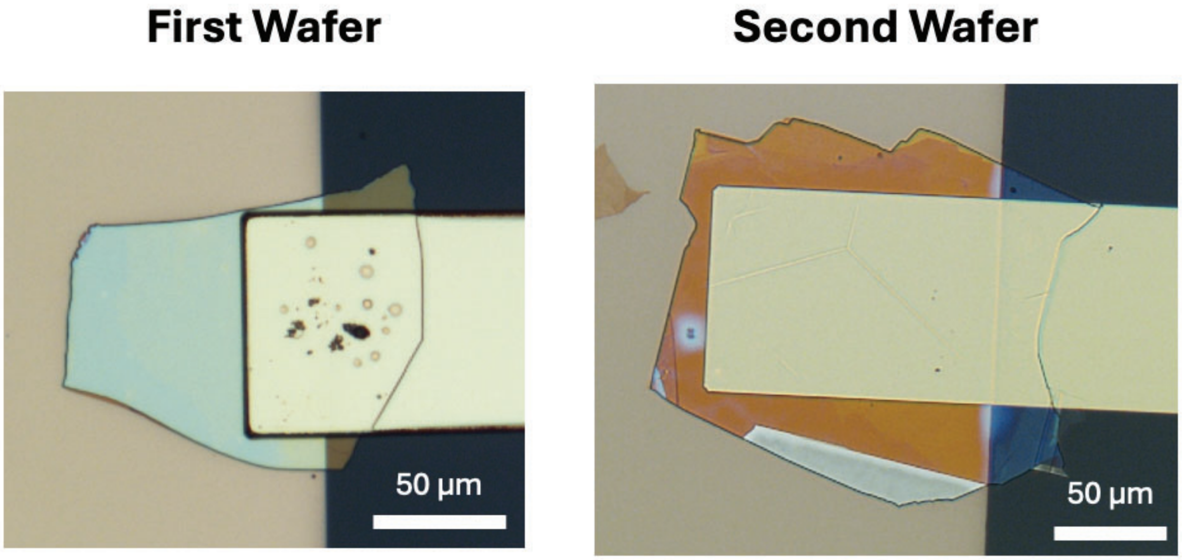

Figure 2: Two optical microscope images showing a device on the first wafer fabricated without additional cleaning steps and a device on the second wafer where more robust substrate cleaning and an oxygen plasma clean immediately prior to top electrode deposition helped to eliminate residues present on the first wafer.

Conclusions and Future Steps:

A repeatable and effective fabrication method has been developed for these devices that ensures well-defined contacts and clean surfaces. These devices are now undergoing thermal measurements while fields are applied, and future steps will be informed by the experimental results obtained from these measurements.

Thin-Film Deposition for Surface Characterization Studies for Superconducting Radio Frequency Cavity Application

CNF Project Number: 2779-19
Principal Investigator(s): Matthias Liepe
User(s): Nathan Sitaraman

Affiliation(s): Cornell Laboratory for Accelerator-based Sciences and Education, Cornell University

Primary Source(s) of Research Funding: The U.S. National Science Foundation under Award PHY-1549132, the Center for Bright Beams

Contact: mul2@cornell.edu, nss87@cornell.edu

Website: https://physics.cornell.edu/matthias-liepe

Primary CNF Tools Used: AJA Sputter Deposition 1 & 2

Abstract:

Superconducting radio-frequency (SRF) cavities are a key component of particle accelerators (with applications ranging from fundamental physics research to synchrotron X-ray sources, to e-beam microscopy and lithography) and are also being developed for applications in dark matter detection and quantum computing. We are developing next-generation surface treatments to enhance the performance of niobium superconducting surfaces. By using facilities at the CNF, we investigate the effect of metallic doping on the niobium surface. We highlight our recent success in growing Nb3Al and Nb-Zr superconducting alloys.

Summary of Research:

We used CNF's AJA sputter deposition tools to deposit zirconium on niobium samples for Nb-Zr alloy growth. This builds on our earlier development of a zirconium oxide capping layer recipe using the same CNF tool. We are still working to develop a recipe that achieves the optimal composition for superconducting performance. Additionally, we used the same tools to deposit aluminum on niobium samples for Nb3Al layer growth. We were able to verify the presence of Nb3Al on samples by Tc measurement and x-ray diffraction at CCMR.

Conclusions and Future Steps:

We prepared a large sample plate with Nb3Al, following the same recipe that was successful on small samples, and this sample plate has successfully been assembled into our RF testing setup for data collection. The results of this test will help guide future work on Nb3Al for SRF applications. In parallel, we will continue development of an Nb-Zr alloy recipe.

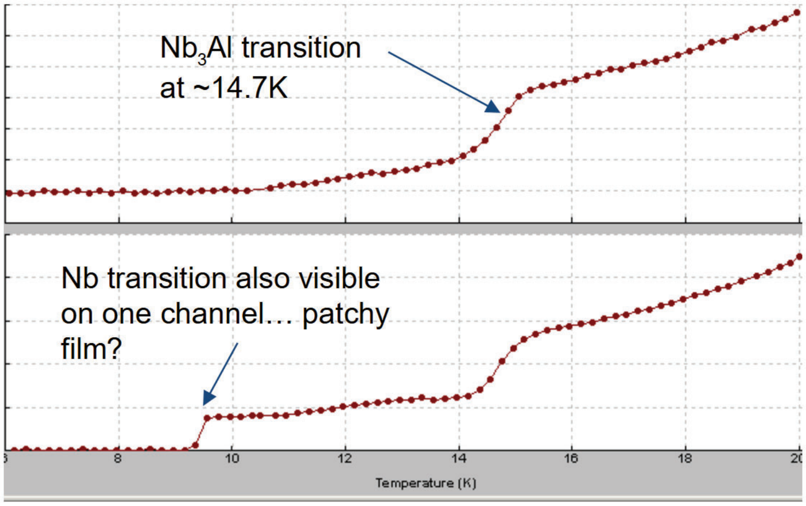

Figure 1: Resistance vs temperature data on first successful Nb3Al-on-Nb sample.

Enhancement of laser plasma driven ion acceleration using dielectric metasurfaces

CNF Project Number: 2979-21
Principal Investigator(s): Gennady Shvets
User(s): Samyobrata Mukherjee

Affiliation(s): School of Applied and Engineering Physics, Cornell University

Primary Source(s) of Research Funding: Carbon Ion Radiation Therapy (E903324), NSF project: "Interaction of Ultra-Intense Laser Pulses with Structured Targets in the Multi-Petawatt Regime" (E71-8417)

Contact: gshvets@cornell.edu, sm2575@cornell.edu

Website: http://shvets.aep.cornell.edu

Primary CNF Tools Used: JEOL 6300, SC4500 Evaporator, Unaxis 770 Etcher, SUSS MA6-BA6 Contact Aligner, Oxford 82 Etcher, Oxford PECVD, KLA P7 Profilometer, Zeiss Supra SEM, Heidelberg Mask Writer DWL-2000, Hamatech Mask Processor, E-beam and Photolithography Spin Coaters, Resist Hot Strip Bath, Hamatech Wafer Processor, Anatech Resist Strip, FilMetrics.

Abstract:

We aim to study the acceleration of heavy ions generated by the interaction of high-power ultrashort laser pulses with structured solid targets. We compare the yield of heavy ions produced by laser pulses incident on thin flat silicon oxide (SiO2) membranes with the yield from structured silicon metasurfaces resting on similar SiO2 membranes. Simulations as well as preliminary experiments carried out at the ALEPH laser facility in Colorado State University reveal that we obtain a greater flux of higher energy ions from the structured targets. Such high charge/flux heavy ion beams may have applications in diverse areas including cancer therapy and high-flux neutron generation.

Summary of Research:

Ultrashort, high intensity pulsed lasers have enabled the creation of tabletop ion accelerators which rely on a driving electron component and the resulting electric field created by charge separation. A typical mechanism involves target normal sheath acceleration (TNSA) where a laser beam incident on a solid thin foil target creates an electron sheath on the rear of the target which generates highly energetic ions. The incident laser pulse generates hot electrons which penetrate the foil and while a few electrons escape, the target's capacitance traps most of the electrons which end up forming a charge-separation field. At the rear surface, the electric field is strong enough to ionize atoms, and it accelerates the ions in a direction normal to the surface.

We are investigating a scheme to enhance the acceleration of the heavy ions compared to standard TNSA from a foil target by structuring the target. Specifically, we create arrays by patterning a silicon layer which lies on a thin (~1 µm) silicon oxide membrane. Blocks of silicon comprising the array are separated from each other by high aspect ratio trenches. A laser pulse polarized perpendicular to the trench will draw electrons out of the silicon blocks into the trench (see Fig. 1a) and accelerates them to relativistic energies which are far greater than the energies obtained in traditional TNSA, leading to a stronger sheath electric field [1]. Simulations predict that the structured targets will enhance both the energy and flux of the ions produced (see Fig. 1b).

Our targets are produced at the CNF. We start with a buried oxide silicon on insulator wafer and deposit 3 µm SiO2 on the handle layer which will be patterned as a hard mask to etch the substrate. We carry out e-beam lithography on PMMA deposited on the device layer and evaporate Al2O3 on the PMMA after development. The PMMA is then lifted off in acetone and the remaining Al2O3 acts as a hard mask for the anisotropic etching of the device silicon layer in the Unaxis 770 using a customized recipe based on a modified Bosch process. After that we remove the Al2O3 in Al etch and remove polymer coatings on the sidewall using EKC polymer strip. The SiO2 on the handle layer is then patterned via backside aligned photolithography on the MA6 mask aligner followed by etching in the Oxford 82. Finally, the substrate below the silicon arrays is etched on the Unaxis 770 using the standard Bosch process.

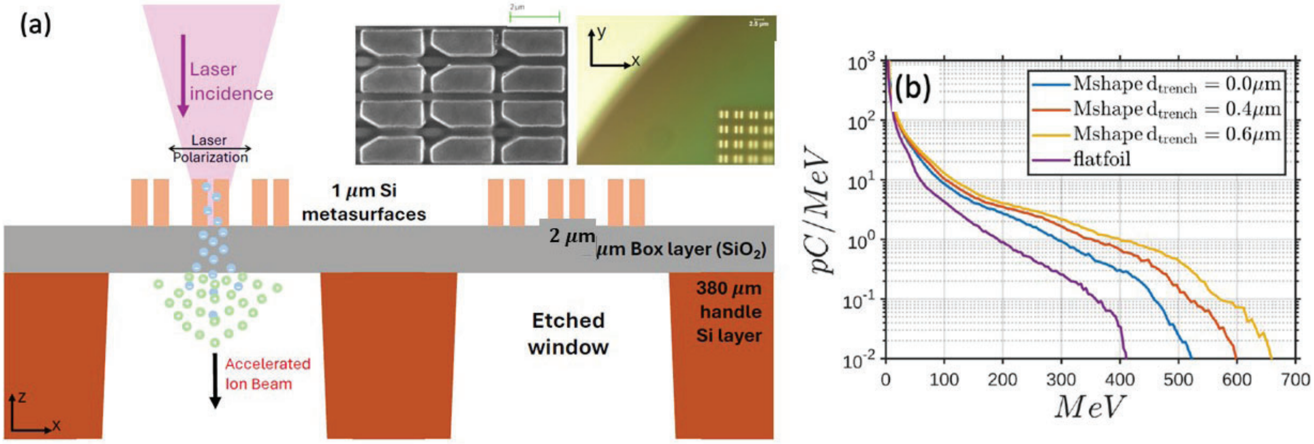

Fig. 1: (a) Schematic showing the laser incident on a structured target on a membrane. The insets show optical and SEM images of two different structured targets. (b) Simulation results predicting higher energy ions from structured targets.

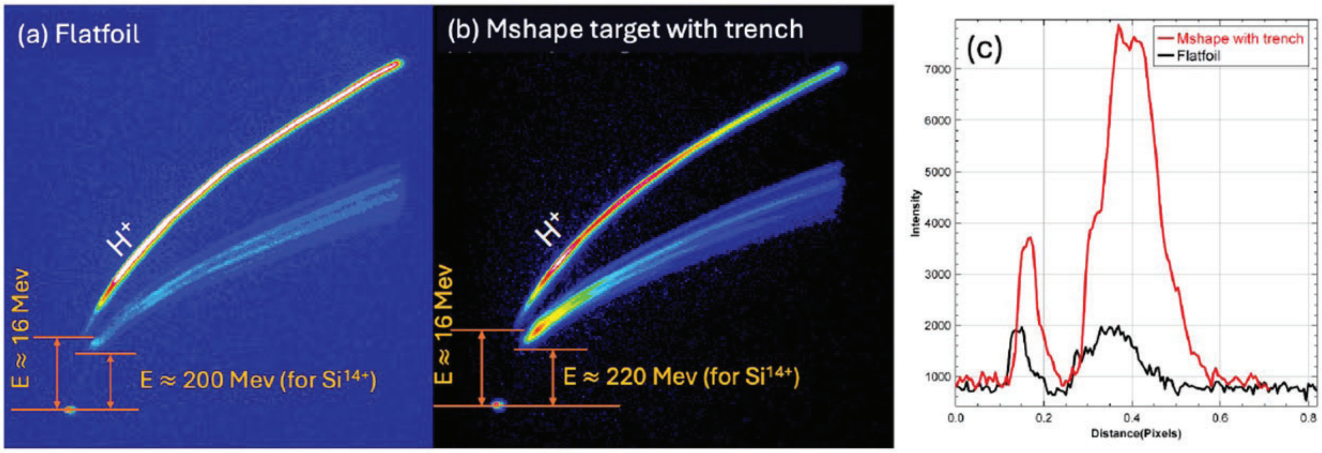

Fig. 2: Thompson parabola spectrometer output showing traces for different ion species with laser incident on (a) flat foil and (b) structured target. (c) Comparison of image intensity at a fixed energy.

Conclusions and Future Steps:

Our proposal was evaluated in a competitive process, and we were awarded beam time at multiple laser facilities across the US (ALEPH at Colorado State University, SCARLET at Ohio State and ZEUS at the University of Michigan). Preliminary results from experiments carried out at the ALEPH facility have shown that the structured targets produce a higher flux of heavy ions at higher energies as recorded on Thompson parabola spectrometers (see Fig. 2). We are currently preparing for further experimental campaigns to confirm our results. To this end we are also updating our target design based on feedback from previous experiments.

References:

[1] Shcherbakov, M. R. et al. Nanoscale reshaping of resonant dielectric microstructures by light-driven explosions. Nat Commun 14, 6688 (2023).

Sensing superconducting film loss via flip chip

CNF Project Number: 299822
Principal Investigator(s): Valla Fatemi
User(s): Haoran Lu

Affiliation(s): Applied and Engineering Physics, Cornell University
Primary Source(s) of Research Funding: AFOSR
Contact: vf82@cornell.edu, hl2396@cornell.edu
Website: https://fatemilab.aep.cornell.edu/
Primary CNF Tools Used: Heidelberg MLA 150 Maskless Aligner, DWL2000, PT770, ABM contact aligner, SC4500 Even-Hour Evaporator

Abstract:

Superconducting quantum circuits are a leading prospective platform for achieving quantum computation. One bottleneck is the low lifetimes of individual qubits, partially related to the microwave loss associated with the superconducting films. This project focuses on developing a benchmarking scheme that enables detecting the loss of different superconducting thin films (target film) without the involvement of the fabrication on the target film. The scheme is also capable of sensing specific losses in the metal-air interface and in the conductor itself (e.g., due to quasiparticles) before any fabrication steps are taken, thereby isolating these losses in the 'pristine' state of the material. This serves as a useful benchmark for subsequent work testing devices after nanofabrication.

Summary of Research:

Sensing resonator: In this project, we use a high quality factor superconducting resonator (sensing resonator) to probe a target film. The sensing resonator is fabricated from niobium or tantalum thin films at CNF.

SU8 pillar: To sense the loss of the target film, the sensing resonator must be a few microns away from the target film, with an uncertainty less than half a micron. In this project, we use 4 µm SU8 pillar. The resist coating, exposure, and development are done in CNF as well.

Target film and measurement: The target film involved in this study includes SiO2 layers on Nb films. The SiO2 layers are deposited using the even-hour evaporator. Preliminary data shows a similar power-dependent quality factor as resonators deposited directly onto SiO2. This is encouraging, as it indicates our novel approach will be able to sense any elevated losses in target films without exposing those films to fabrication processes.

Conclusions and Future Steps:

We developed a scheme combining SU8 and superconducting resonators for target film loss sensing. In the coming months, we will test different materials and share this technique to the community as a better platform to evaluate loss.

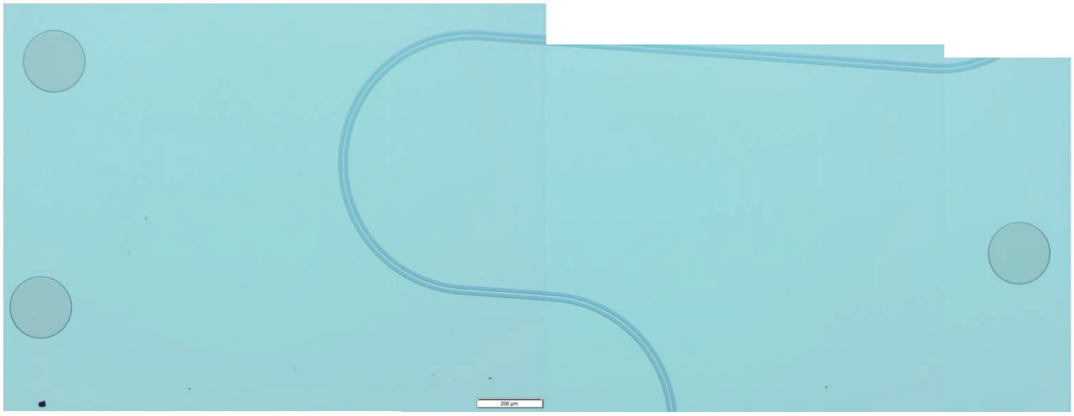

Figure 1: Resonator and pillar (partial).

Improving Quality Factors in Superconducting Resonators

CNF Project Number: 299822
Principal Investigator(s): Valla Fatemi
User(s): Maciej Olszewski (1), JT Paustian (2), Tathagata Banerjee (3), Haoran Lu (3)

Affiliation(s): (1) Cornell University Department of Physics, (2) Syracuse University Department of Physics, (3) Cornell University Applied and Engineering Physics

Primary Source of Research Funding: Air Force Research Laboratory, Laboratory for Physical Sciences

Contact: vf82@cornell.edu, mwo34@cornell.edu

Website: https://fatemilab.aep.cornell.edu/

Primary CNF Tools Used: G-Line Stepper, Oxford 81, PT 770, DISCO Dicing Saw, Heidelberg 2000 Mask WriterEven-Hour Evaporator

Abstract:

Superconducting microwave circuits are one of the leading candidate platforms for enabling quantum computing technology, and Nb on Si is a commonly implemented materials set. Currently one of the main bottlenecks for improving device performance and technological prospects is elimination of defects from the materials and interfaces within the superconducting circuits resulting from nanofabrication processing. In this report, we demonstrate compact (3 µm gap) coplanar waveguide resonators with low-power internal quality factors near one million. We achieve this using a resist strip bath with no post-fabrication acid treatment, which results in performance comparable to previous strip baths with acid treatments. Avoiding post-fabrication acid treatments reduces the aging in our devices by reducing oxide regrowth. We correlate improved performance with a reduction of post-etch contamination as shown by XPS. This work in based on our manuscript [1].

Summary of Research:

Superconducting transmon qubit fabrication involves many steps which have a profound impact on device performance. To better understand how each step impacts the final device quality we use superconducting coplanar resonators as a proxy for full qubit devices. Both devices share many fabrication steps including substrate preparation, superconductor growth, photolithography patterning, metal etching, photoresist removal, and device cleaning.

In this report, we focus on improving superconducting resonator performance by testing various solvents used for resist removal post dry reactive ion etching. To best isolate the impact of resist removal on resonator performance, we prepare devices with identical recipes, except we change the solvent used for resist removal. For this work we focus on comparing MICROPOSIT 1165 (1165) and Integrated Micro Materials AZ 300T (AZ 300T). Both solvents are N-methyl-2-pyrrolidinone based solvents while AZ 300T also contains propylene glycol and tetramethyl ammonium hydroxide (TMAH). Based on our discussions with the vendor, we believe that the addition of TMAH is the key difference in device performance.

After preparing devices with two different nanofabrication recipes, we test our resonators with cryogenic RF measurements at milli-Kelvin temperatures. We extract the internal loss tangents of resonators prepared with both methods. As shown in figure 1, we find a very significant difference in resonator performance between the samples prepared with 1165 and the ones with AZ 300T. This gap in performance is much larger than the fluctuations between devices and is statistically significant.

To better understand the reason behind this gap in performance, we look for physical differences between these devices. Using x-ray photoemission spectroscopy (XPS) we find that the two devices have significant differences in contaminants present on both niobium and silicon surfaces. As shown in figure 2, we find a significant difference in carbon contamination, as well as residue chlorine percentage. These indicate that AZ 300T is better at removing etch residue as compared to 1165, leading to better device performance.

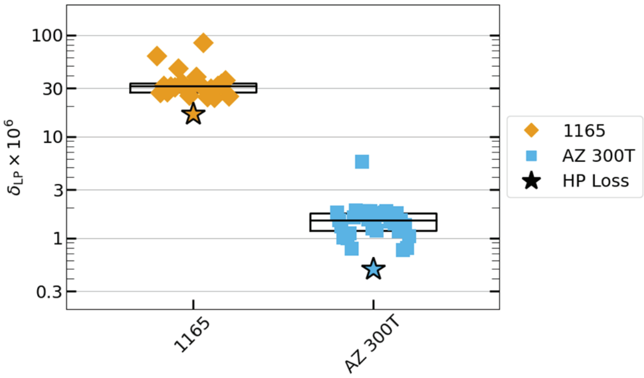

Figure 1 Caption: Boxplot comparing resonator performance with samples made with 1165 and samples made with AZ 300T, with otherwise identical fabrication.

Conclusions and Future Steps:

Our current fabrication procedure yields state of the art resonators as compared to other work in the literature. We plan to continue to further improve the quality of our devices by debugging other areas of our nanofabrication process, including using other materials, trying new etching recipes, and exploring new resist removers.

Further, we also plan on incorporating our improved devices into full transmon qubit devices by incorporating Josephson junctions into our recipe. The improvements in resonator performance should directly translate to better qubit performance, improving lifetimes. We plan to conduct a similar study on improving qubit performance through optimizing our nanofabrication procedure.

References:

[1] https://arxiv.org/abs/2503.13285

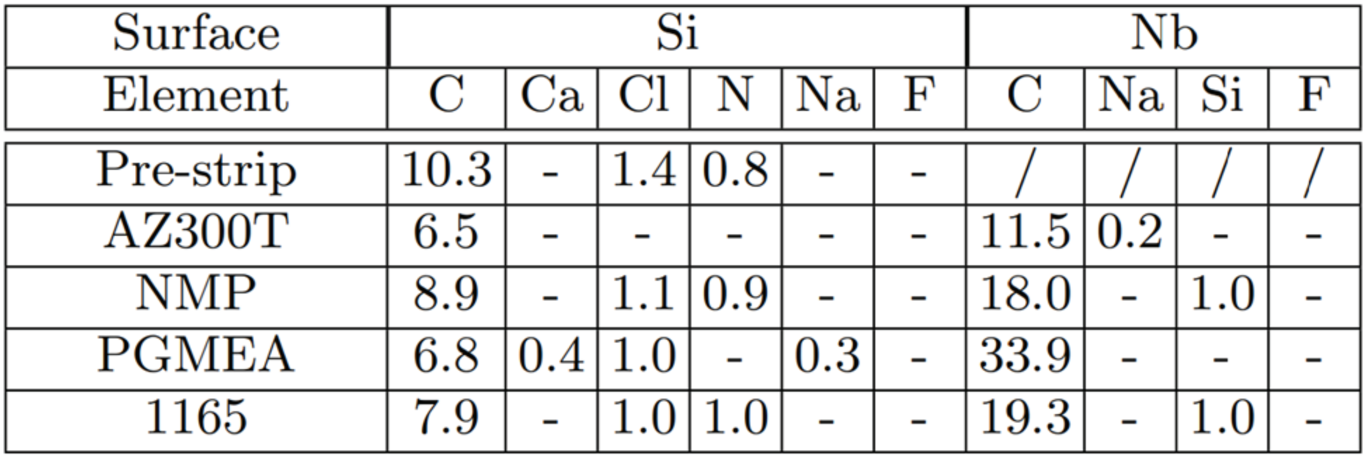

Surface	Si						Nb			
Element	C	Ca	Cl	N	Na	F	C	Na	Si	F
Pre-strip	10.3	-	1.4	0.8	-	-	/	/	/	/
AZ300T	6.5	-	-	-	-	-	11.5	0.2	-	-
NMP	8.9	-	1.1	0.9	-	-	18.0	-	1.0	-
PGMEA	6.8	0.4	1.0	-	0.3	-	33.9	-	-	-
1165	7.9	-	1.0	1.0	-	-	19.3	-	1.0	-

Figure 2 Caption: XPS data with contamination of various surfaces post-resist removal with various solvents

Manufacturing SiN Bullseye Cavities & SOI Photonic Crystal Nanobeam Cavities

CNF Project Number: 300822
Principal Investigator(s): Professor Pablo A. Postigo
User(s): Christopher (Christer) Everly, Martin Sanchez

Affiliation(s): Institute of Optics, University of Rochester

Primary Source of Research Funding: UoR Startup, URA Award 2023-2024 from University of Rochester

Contact: ppostigo@ur.rochester.edu, ceverly@ur.rochester.edu, msanch23@ur.rochester.edu

Website: https://www.postigolab.com

Primary CNF Tools Used: JEOL 6300, JEOL 9500, E-beam Spin Coaters, Olympus MX-50 Microscopes, Oxford 82, Oxford 100, PT770 RIE, Oxford Cobra ICP, Plasma Therm Tikachi HDP-CVD, Oxford PECVD, Primaxx Vapor HF Etcher, Yes EcoClean Asher, Yes Asher, Filmetrics systems, Zeiss Ultra SEM, Zeiss SEM Supra, Veeco AFM, Disco Dicer Saw

Abstract:

Our group is interested in quantum research on photonic platforms. Some topics we are currently exploring include: on-chip lasing and single-photon emission enhancement with circular Bragg gratings, and room temperature single phonon quantum sensing using phononic crystal enhanced optomechanical cavities. We have designed, fabricated, and tested Purcell enhanced Bragg cavities, as well as various photonic crystal optical nanocavities, and phononic crystal enhanced mechanical resonators.

Summary of Research:

Users have done diligent work to refine the fabrication process for the circular Bragg grating (CBG) cavity, colloquially referred to as a bullseye cavity. A deposition recipe was developed on the Oxford PECVD that achieves repeatable SiO2 followed by SiN deposition thicknesses. Experimentation was completed on different gas pressures during inductively coupled plasma (ICP) etching of silicon nitride in order to achieve the high aspect ratio, anisotropic etches required for the silicon nitride (SiN) bullseye cavities.

Additionally, the group has created our first fabrication procedure for creating suspended structures including: photonic crystal nanobeams, photonic crystal L and H cavities, and megahertz phononic crystal arrays. Due to the fine transverse structures required to make photonic crystal nanobeam cavities specifically, experimentation has been done with E-beam resist type, thickness, and dosage applied in lithography machines to match designed requirements. Experimentation was also completed on applying a varied bias to different regions in pattern files in order to account for reactive ion etch lag (RIE lag) affecting the transverse dimensions of nanostructures differently than larger structures. Different chemistries have been attempted in the lab to create anisotropic silicon etches during pattern transfer with great successes being achieved with a Hydrobromic Acid (HBr) inductively coupled plasma (ICP) etch, instead of the sulfur hexafluoride and oxygen (SF6/O2) chemistry frequently seen in literature for silicon etches. Finally, experimentation was completed with vapor hydrogen fluoride (HF) etching to successfully create suspended structures free of stiction. This was successful for suspended features in the tested range of tens to hundreds of microns. Photonic crystal cavities from these fabrications have been successfully tested and are undergoing further experiments.

Conclusions and Future Steps:

Optical characterization of bullseye cavities has been conducted with great success indicating that our fabrication process is adequate to achieve the desired sub 100nm dimensions required for our designed bullseyes cavities.

We are constantly modifying and improving our designs of the photonic crystal cavities for optomechanics. Many of these designs push the limits of transverse dimensions achievable these types of cavities. Next steps would include fabricating the modified photonic crystal cavities and testing the limits of transverse dimensions achievable in our transverse structures.

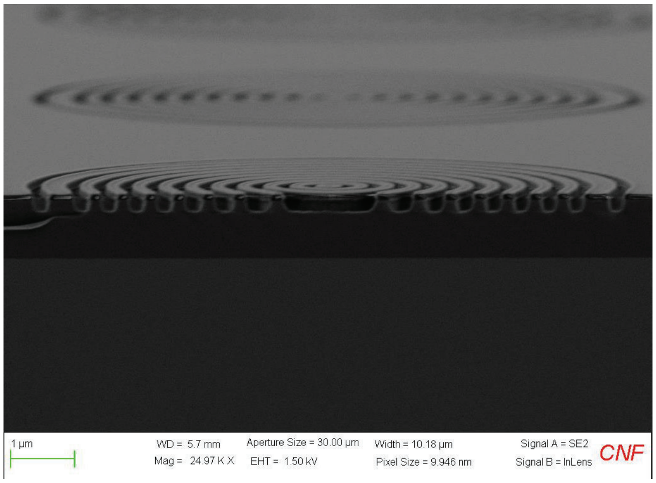

Figure 1: Cross-section of a bullseye cavity.

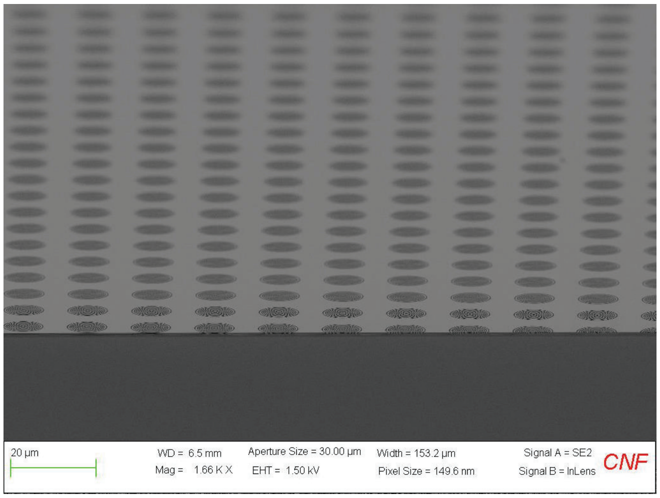

Figure 2: Array of bullseye cavities

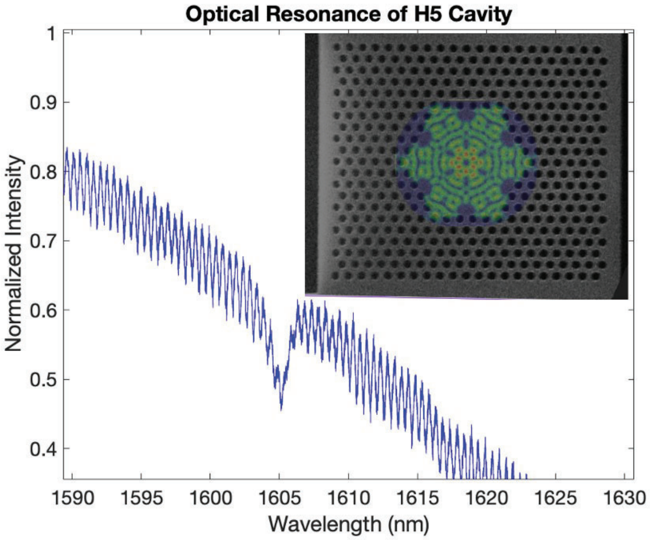

Figure 3: Resonant scatter spectrum plotted for measured photonic crystal H5 cavity, inset: microscope image of H5 cavity taken with Zeiss SEM Ultra, overlayed by simulated resonant mode profile of electromagnetic field norm.

References:

[1] Room-Temperature Lasing in Colloidal Nanoplatelets via Mie-Resonant Bound States in the Continuum

[2] Mengfei Wu, Son Tung Ha, Sushant Shendre, Emek G. Durmusoglu, Weon-Kyu Koh, Diego R. Abujetas, Jose A. Sánchez-Gil, Ramón Paniagua-Domínguez, Hilmi Volkan Demir, and Arseniy I. Kuznetsov Nano Letters 2020 20 (8), 6005-6011 DOI: 10.1021/acs.nanolett.0c01975

[3] Enhanced Emission from WSe2 Monolayers Coupled to Circular Bragg Gratings Ngoc My Hanh Duong, Zai-Quan Xu, Mehran Kianinia, Rongbin Su, Zhuojun Liu, Sejeong Kim, Carlo Bradac, Toan Trong Tran, Yi Wan, Lain-Jong Li, Alexander Solntsev, Jin Liu, and Igor Aharonovich ACS Photonics 2018, 3950-3955 DOI: 10.1021/acsphotonics.8b00865

[4] Exploring Regenerative Coupling in Phononic Crystals for Room Temperature Quantum Optomechanics Lukas M. Weituschat, Irene Castro, Irene Colomar, Christer Everly, Pablo A. Postigo, & Daniel Ramos Scientific Reports 14, Article number: 12330 (2024) DOI: https://doi.org/10.1038/s41598-024-63199-1

[5] Resolved-sideband cooling of a micromechanical oscillator A. Schliesser, R. Rivière, G. Anetsberger, O. Arcizet, & T.J. Kippenberg Nature Physics 4, 415-419 (2008) DOI: 10.1038/nphys939

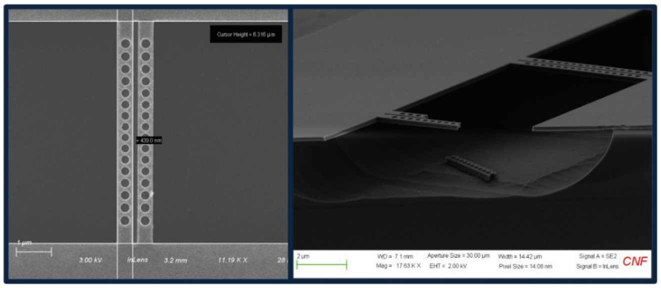

Figure 4: Microscope images taken with Zeiss SEM Ultra (left) image of dual nanobeams showing some transverse dimensions (right) dual nanobeams intentionally broken to show fully etched photonic crystal holes with intact suspended nanobeams in the background

Fabrication of Fluxonium-Like Qubits

CNF Project Number: 301022
Principal Investigator(s): Ivan Pechenezhskiy
User(s): Benjamin Byrd, Kesavan Manivannan

Affiliation(s): Department of Physics, Syracuse University
Primary Source of Research Funding: Syracuse University, Army Research Office
Contact:ivpechen@syr.edu
Website: https://www.postigolab.com, babyrd@syr.edu, kmanivan@syr.edu
Primary CNF Tools Used: ASML DUV Stepper, JEOL 6300, PT770 Plasma Etcher, Oxford81 Etcher, Heidelberg DWL2000 Mask Writer

Abstract:

We fabricate fluxonium qubits to probe the behavior of broken cooper pairs (quasiparticles) in superconducting circuits and to study the effect of measurement-induced state transitions (MIST) [1]. To probe the quasiparticle population in our qubits, we fabricate Josephson junctions on the perimeter of the devices, which are biased beyond their superconducting gap, controllably generating a reproducible population of quasiparticles in the sample. Probing the qubit state with large numbers of photons can force the qubit outside of it's computational subspace, inducing the aforementioned MIST. The fluxonia for this project are fabricated using a previously reported recipe [2].

Summary of Research:

A fluxonium qubit (Fig. 1) is a superconducting circuit which is comprised of a 2-D capacitor shunted by a small Josephson junction and a 2-D inductor formed of a chain of larger Josephson junctions (Fig. 2). This device forms a loop through which a magnetic field is applied. At specific amounts of magnetic flux passing through this loop, various loss mechanisms which negatively impact qubit performance are suppressed. These qubits are capacitively coupled to a microwave resonator, whose fundamental mode shifts conditional on the state of the qubit. We measure microwave transmission near this frequency as a proxy for the measurement of the qubit state. Our devices are fabricated on Si wafers. All large features, capacitors, coplanar waveguides, and microwave resonators, are patterned into a ~ 70nm niobium base layer using the ASML DUV stepper and the PT770. After initial processing, the devices are cleaned in the CNF hot strip bath, the Glen1000, then in a bath of buffered oxide etch. To form Josephson junctions for both the inductive shunt and the small junction, electron beam lithography using the JEOL 6300 is required. The small junctions for our fluxonia are on the order of ~ 100nm × 100 nm, and ~ 1um × 1um for 1 each of the ~ 200 junctions in the chain. After electron beam patterning is complete, the junctions are formed by electron beam evaporation using the Dolan bridge technique at Syracuse University.

In the last year, we developed a new fluxonium design with the primary goal of increasing readout fidelity enormously. These design changes are also intended to enable improved characterization of measurement-induced state transitions (MISTs) in our qubits by enabling discrimination between states outside of the typical computational subspace. To achieve this, we increased the coupling between the microwave resonators used for readout and the transmission line used for S21 measurements. We also increased the qubit/resonator coupling from previous generations of samples fabricated at the CNF. Both of these changes, in addition to minor tweaks to various other circuit parameters, were implemented on our most recent generation of devices. Fabrication quality plays a direct role in our understanding of MIST, in that defects referred to as two-level systems contribute strongly to MIST effects, and give us a window to compare our fabrication quality to the state-ofthe-art. To fully leverage the new design, additional fine-tuning of the fabrication and preliminary characterization are required.

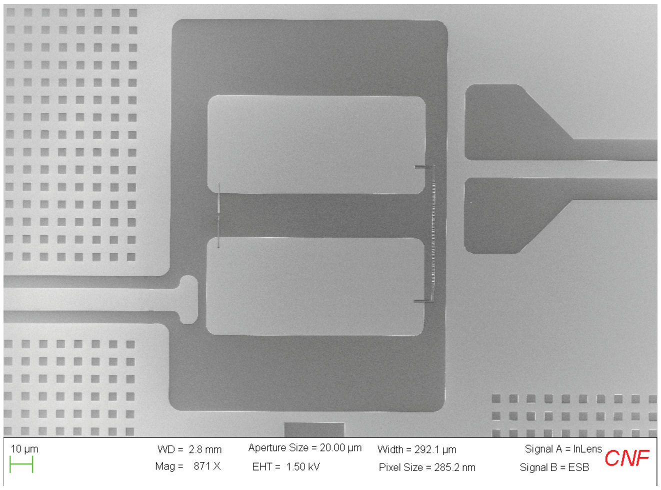

Figure 1: Scanning electron microscopy (SEM) image of one of the fluxonium qubits taken at CNF.

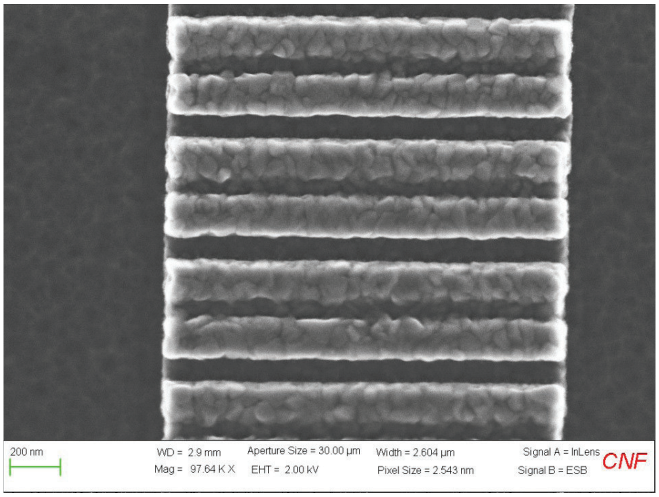

Figure 2: SEM image of a Josephson junction chain, taken at CNF.

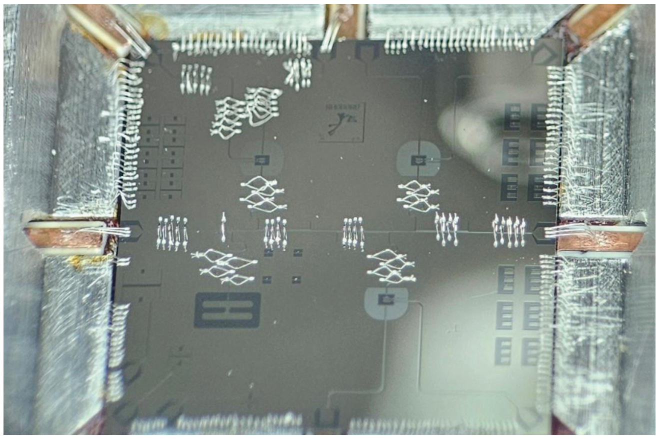

Figure 3: Photograph of a sample set into the holder wire-bonded for low-temperature measurements.

References:

[1] K. Nesterov et al. Measurement-Induced State Transitions in Dispersive Qubit-Readout Schemes. Phys. Rev. Appl. 22, 064038 (2024). https://doi.org/10.1103/PhysRevApplied.22.064038

[2] V. Iaia et al. Phonon downconversion to suppress correlated errors in superconducting qubits. Nature Communications 13, 6425 (2022). https://doi.org/10.1038/s41467-022-33997-0

[3] M. Randeria et al. Dephasing in Fluxonium qubits from Coherent Quantum Phase Slips. arXiv:2404.02989

[4] I. V. Pechenezhskiy et al. The superconducting quasicharge qubit. Nature 585, 368 (2020). https://doi.org/10.1038/s41586-020-2687-9

Weak Link Superconducting Quantum Interference Devices for High-Resolution Scanning Magnetometry

CNF Project Number: 301722
Principal Investigator(s): Katja Nowack
User(s): Alex Striff

Affiliation(s): Laboratory of Atomic and Solid State Physics, Cornell University

Primary Source of Research Funding: AFOSR MURI FY21 Tunneling, Phenomena in Interface Superconductors FA95502110429 (Subaward ID 134400-5118001)

Contact: kcn34@cornell.edu, abs299@cornell.edu

Website: https://nowack.lassp.cornell.edu/

Primary CNF Tools Used: AJA Sputter 1, Bruker DektakXT Profilometer, Heidelberg MLA 150 Maskless Aligner, JEOL JBX-6300FS, E-beam Lithography System, Oxford 82 RIE, SC4500 Even-Hour Evaporator, SC4500 Odd-Hour Evaporator, Unaxis 770 Deep Silicon Etch, Zeiss Gemini SEM, Zeiss Supra SEM, Zeiss Ultra SEM,

Abstract:

Magnetic imaging is a powerful tool for studying quantum materials. To make a sensitive magnetometer for use in a scanning probe microscope, a small superconducting loop is interrupted by two Josephson junctions to create a superconducting quantum interference device (SQUID), which converts the magnetic flux coupled into the loop into a measurable signal [1]. This research explores one way to increase the spatial resolution and maximum operating field of a SQUID, which is to replace conventional superconductor-insulator-superconductor (SIS) Josephson junctions with narrow constrictions (weak links) in the superconducting loop, which allow the size of the loop to be less than 1 µm [2]. Initial measurements have demonstrated the sensitivity of test SQUIDs to magnetic flux, with improvements in progress.

Summary of Research:

Figure 1(c) depicts a weak link SQUID, made of a patterned 50 nm niobium film on a silicon substrate with thermal oxide. For the weak links to behave like Josephson junctions, they must have dimensions comparable to the superconductor's coherence length [3], which necessitates the use of electron beam lithography to pattern a hard mask for the SQUID loop. A bilayer lift-off process patterns the SQUID loop in 20 nm of aluminum, and the pattern is then transferred to the niobium by dry etching in CF4 and O2. In order to raster the SQUID loop across the surface of a sample like in Figure 1(a), a Bosch process deep etch (Figure 1(b)) defines the corner of the scanning probe where the SQUID will be patterned. This approach has been successfully applied to scan conventional SQUIDs [4].

A key parameter for the performance of these SQUIDs is the maximum current that can flow through the weak links while they remain superconducting, which is known as the SQUID's critical current. Cryogenic measurements of several SQUIDs revealed an up to 50 variations in the patterned widths and lengths of the weak links. Since the critical current is expected to be a function of only the resistance of the weak link [3], the variation is likely due to differences in the thickness of the niobium grain where the weak link happens to be patterned. Such niobium grain size differences are depicted in Figure 2(a).

When a weak link SQUID is operated in the readout scheme used for conventional SQUIDs, heating of the weak links occurs, and as such the thermal as well as electrical characteristics of the SQUID become important to the design. As such, we are changing the silicon dioxide film under the niobium to be a bare silicon film instead, in order to increase the thermal conductivity from the SQUID to the substrate. Doing so required the development of a new dry etch that would not undercut the silicon or niobium weak links, as seen in Figure 2(b). Another avenue to reduce the noise and electrothermal behavior of these SQUIDs is to add an on-chip resistive shunt in parallel with the SQUID (Figure 3). As the shunt value must be comparable to the weak link resistance of a few Ohms, we optimized in-situ argon backsputtering in the AJA 1 sputtering system to completely remove the native niobium pentoxide layer before sputtering the platinum. Weakly cleaned shunts had insulating contacts at cryogenic temperatures, while partially cleaned shunts had a contact resistance of a few Ohms, and fully cleaned shunts could reach 100–200 mΩ. The addition of a resistive shunt is also expected to eliminate destruction of the weak links by electrostatic discharge, as in Figure 4.

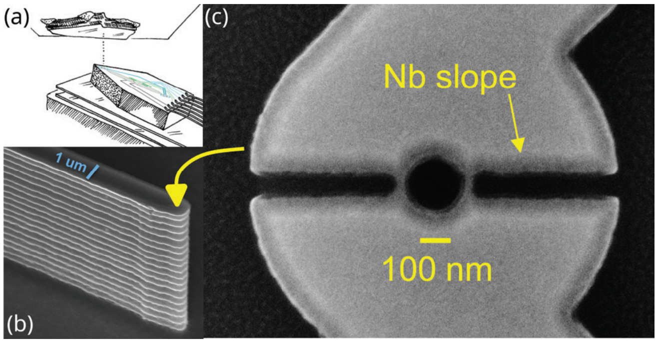

Figure 1: (a) A SQUID is a sensitive magnetometer that may be rastered over the surface of a sample. (b) By performing a deep silicon etch, a scanning probe at the etched tip may be brought within 1 µm of the sample. (c) Scanning electron microscope (SEM) image of a niobium (Nb) weak link SQUID. The narrow superconducting constrictions by the niobium slope make the device a sensitive tool for measuring the local magnetic flux through the loop.

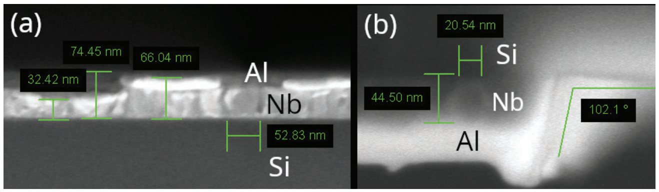

Figure 2: (a) SEM image of a cleaved niobium line, nominally 50 nm thick, with aluminum mask on top. Niobium grains as thin as 32 nm are visible. (b) Edge of an etched niobium line, with no undercutting of the niobium or silicon substrate, and little over-etching into the silicon.

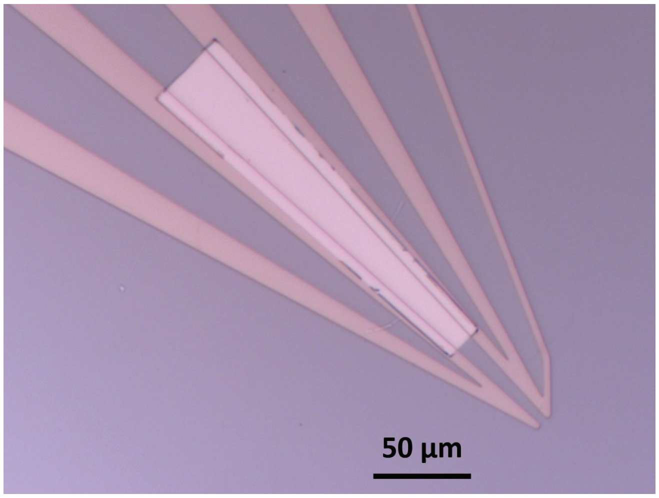

Figure 3: Bright-field microscope image of a platinum shunt center) on niobium traces. A SQUID would normally be patterned at the bottom right, but was omitted for testing the shunt. As the relevant contact occurs primarily through the covered niobium sidewall, the fencing along the perimeter of the platinum shunt has little impact on the shunt resistance.

Conclusions and Future Steps:

We are continuing to optimize the design and fabrication of these weak link SQUIDs. Future work will investigate managing a heat budget during the deposition of the platinum shunt and of the mask for deep silicon etching, as these process steps partially degrade the superconductivity of the niobium. Empirical optimization of the SQUID and shunt design is also in progress.

References:

[1] Huber, M. E., et al. Review of Scientific Instruments 79, 053704 (2008).

[2] Vasyukov, D., et al. Nature Nanotech 8, 639-644 (2013).

[3] Likharev, K. K. Rev. Mod. Phys. 51, 101-159 (1979).

[4] Pan, Y. P., et al. Supercond. Sci. Technol. 34, 115011 (2021).

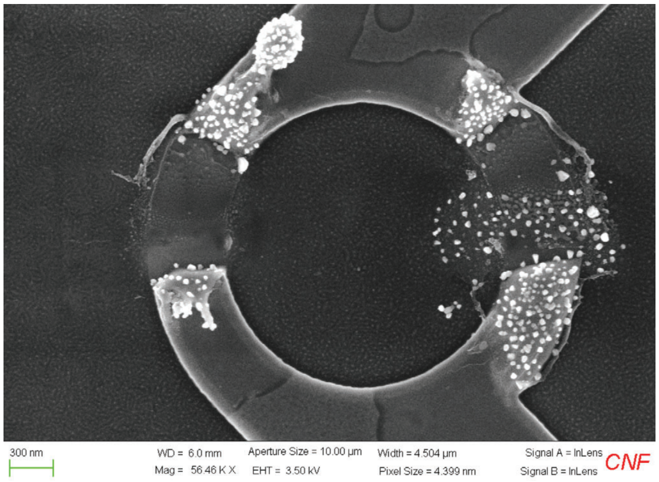

Figure 4: SEM image of a SQUID loop after a low-voltage electrostatic discharge event destroyed the weak links during electrical testing.

Resistivity scaling in Weyl semimetal NbAs nanowires and thin slabs

CNF Project Number: 303222
Principal Investigator(s): Judy Cha
User(s): Yeryun Cheon

Affiliation(s): Department of Physics, Cornell University

Primary Source of Research Funding: Semiconductor Research Corporation JUMP 2.0 SUPREME

Contact: jc476@cornell.edu, yc2458@cornell.edu

Website: https://cha.mse.cornell.edu/

Primary CNF Tools Used: Zeiss Supra SEM, Nabity NPGS Nanometer Pattern Generator System, Oxford 81 RIE, SC4500 Odd-Hour Evaporator, Westbond 7400A Ultrasonic Wire Bonder

Abstract:

Topological semimetals possess topologically protected surface states that can enhance electrical conduction at reduced dimensions. Theory predicts certain topological semimetals, such as niobium arsenide (NbAs), can exhibit unusual resistivity scaling, i.e., decreasing resistivity with decreasing size, highlighting their potential as next-generation interconnects. However, experimental studies over a wide size range remain limited, particularly for 1D-confined nanostructures relevant to practical applications. In this work, we synthesize NbAs nanowires and thin slabs using thermomechanical nanomolding and focused ion beam (FIB) milling, respectively. Electrical measurements on nanomolded NbAs nanowires show that 40 nm-diameter wires exhibit a room-temperature resistivity of 10.5 ± 2.4 μΩ·cm, which is ~3 times lower than bulk. This is attributed to the suppressed surface electron scattering, corroborated by theoretical simulations showing a substantially longer carrier lifetime for surface states than for bulk states. In contrast, FIB-prepared NbAs thin slabs with larger cross-section areas and ion-beam induced damage show higher resistivity, suggesting the impact of surface damage on electrical transport.

Summary of Research:

Previous approaches for synthesizing NbAs nanostructures have employed bottom-up methods such as chemical vapor deposition or molecular beam epitaxy, as well as top-down methods like FIB milling. However, these approaches have been limited in either crystal quality or accessible sample sizes. Here, we use thermomechanical nanomolding to synthesize single-crystal NbAs nanowires with diameters down to 40 nm. To test the electrical properties of NbAs nanowires, we fabricate four-terminal devices via standard e-beam lithography, using shared facilities in CNF. Notably, our NbAs nanowires exhibit decreasing resistivity with decreasing size, which is opposite to the trend observed in conventional metals such as Cu. Specifically, 40 nm diameter NbAs nanowires show a room-temperature resistivity of 10.5 ± 2.4 μΩ·cm, which is ~3 times lower than single-crystal bulk. Based on theoretical calculations, we attribute this resistivity reduction to a significantly longer carrier lifetime in surface states compared to bulk states.

Since the nanomolding process relies on interfacial diffusion, it becomes increasingly challenging to produce samples with large cross-section areas. To complement the nanowire study, we fabricate NbAs thin slabs using FIB milling and study their transport properties across different geometries and surface facets. Despite performing the final milling at a low accelerating voltage of 2 kV, Ga^+-induced damage leads to the formation of an Nb-rich surface shell, which causes a superconducting transition at ~2 K. In contrast to the nanomolded nanowires, these FIB-prepared slabs show higher resistivity than bulk, suggesting the absence of the surface-dominant transport observed in nanowires, possibly due to surface damage.

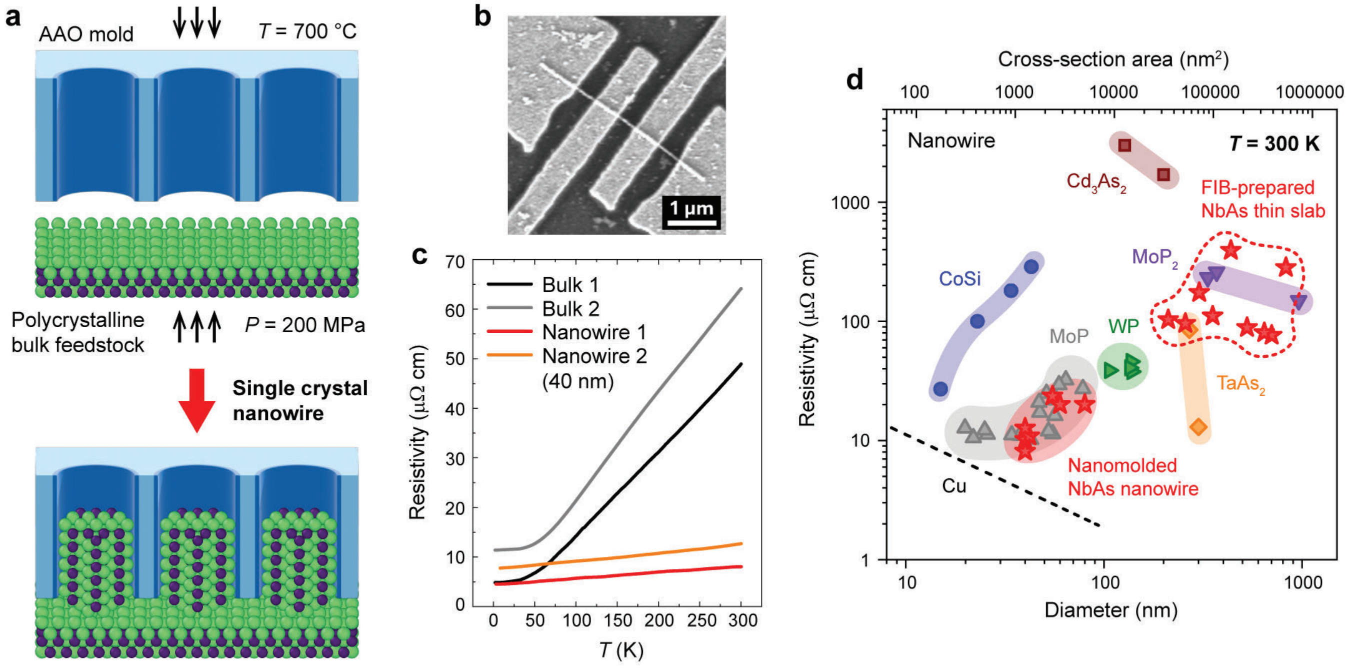

Figure 1. (a) Schematic of the thermomechanical nanomolding process. (b) Representative SEM image of a four-terminal NbAs nanowire device. (c) Temperature-dependent electrical resistivity of bulk single crystals and nanowires. (d) Room-temperature resistivity as a function of diameter (cross-section area) for NbAs nanowires, NbAs thin slabs, and various other topological semimetal nanowires.

Conclusions and Future Steps:

Our results demonstrate surface-dominant transport in NbAs nanowires, highlighting the significant role of topologically protected surface states at reduced dimensions. We will continue measuring nanowire and thin slab devices of varied sizes, with particular focus on further reducing nanowire diameters to enhance surface-state contributions. In addition, we plan to systematically investigate how the surface orientations of NbAs thin slabs influence transport behavior.

References:

[1] Cheon, Y. et al. Surface-dominant transport in Weyl semimetal NbAs nanowires for next-generation interconnects. arXiv:2503.04621 (2025).

Resistivity Scaling of CuAl2-x Nanowires for Post-Cu Interconnects

CNF Project Number: 303222
Principal Investigator(s): Jeeyoung Judy Cha
User(s): Quynh Sam

Affiliation(s): Department of Materials Science and Engineering, Cornell University

Primary Source of Research Funding: Semiconductor Research Corporation SUPREME JUMP2.0 Center

Contact: judy.cha@cornell.edu, qps2@cornell.edu

Website: https://cha.mse.cornell.edu/

Primary CNF Tools Used: Nabity, Zeiss Supra SEM, AJA Sputter 1 and 2, Odd-hour evaporator

Abstract:

The dimensions of copper interconnects in current microelectronic integrated circuits have decreased below copper's electron mean free path (40 nm), leading to high resistivity and thus detrimental increases in power dissipation and signal delays. To continue the downscaling of electronics while maintaining performance, a material with better resistivity is needed to replace copper in interconnects. CuAl2 is a promising candidate due to its low bulk resistivity (6.5 μΩ·cm),1 small mean free path (14 nm),1 and high electromigration resistance compared to copper.2 CuAl2 has demonstrated promising resistivity scaling in thin films,3 however, the scaling behavior of nanowires has not been studied. We report the resistivity of core-shell CuAl2-x nanowires with diameters ranging from 30 nm to 70 nm. The CuAl2-x nanowires are fabricated using thermomechanical nanomolding and possess a 5 – 10 nm thick CuAl shell with a CuAl2 core. At diameters below 45 nm, the resistivities range between 20 - 35 μΩ·cm while larger diameter nanowires show slightly higher resistivities. This scaling behavior along with improved electromigration resistance suggest that CuAl2 may be a promising post copper interconnect candidate.

Summary of Research:

We fabricated four-point probe devices on SiO2/Si substrates using the molded CuAl2-x nanowires as shown by the schematic in Figure 1a. Figure 1b shows a high angle annular dark field scanning transmission electron microscopy (HAADF-STEM) image of a nanowire device cross-section. There is a distinct contrast between the nanowire perimeter and core, revealing that the nanowires have a core-shell structure. STEM electron energy loss spectroscopy (EELS) composition mapping shown in Figure 1c shows that the core is CuAl2 while the shell is CuAl. Resistivity measurements are carried out in a cryogenic probe station at 10-6 mbar after annealing the devices at 400 K for 1 hour. A 4-point I-V curve is shown in Figure 2a, and size-dependent resistivity data for 10 nanowire devices is summarized in Figure 2b. The majority of the resistivity values of the CuAl2-x nanowires are much higher than that of bulk CuAl2 and effective Cu. Possible causes of the increased resistivity include surface roughness and compositional variations in the nanowires.

Conclusions and Future Steps:

We present the size-dependent resistivity scaling of core-shell CuAl2-x nanowires fabricated using thermomechanical nanomolding. The resistivity values are higher than that of bulk CuAl2 as well as effective Cu at comparable dimensions, possibly due to surface roughness as well as compositional variation throughout the nanowires that can increase scattering. Without these defects, it is possible that the resistivity and line resistance of stoichiometric CuAl2 nanowires could become competitive against effective Cu at nanoscale dimensions.

References:

[1] J. Appl. Phys. 136, 171101 (2024)
[2] J. Alloys and Compounds, 918, 165615 (2022).
[3] J. Vac. Sci. Technol. B 37, 031215 (2019).

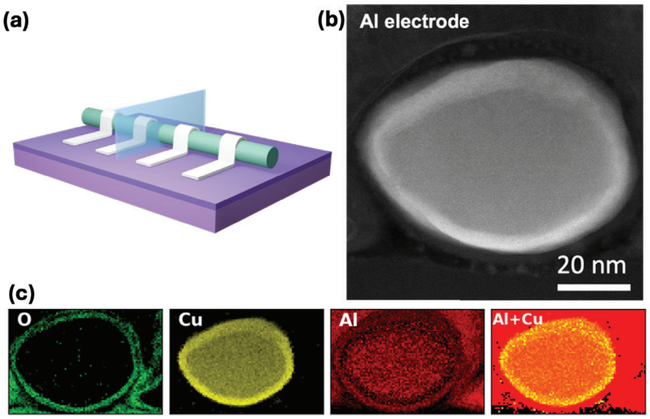

Figure 1. Cross-section analysis of core-shell CuAl2-x nanowire device. (a) Schematic showing CuAl2-x nanowire (teal) on SiO2/Si substrate (purple) with Al contacts (white). The blue plane denotes the cross-section plane of the STEM analysis. (b) HAADF-STEM image of the crosssection of CuAl2-x nanowire device. (c) STEM-EELS maps of cross-section showing O, Cu, Al, and Al and Cu elemental fractions.

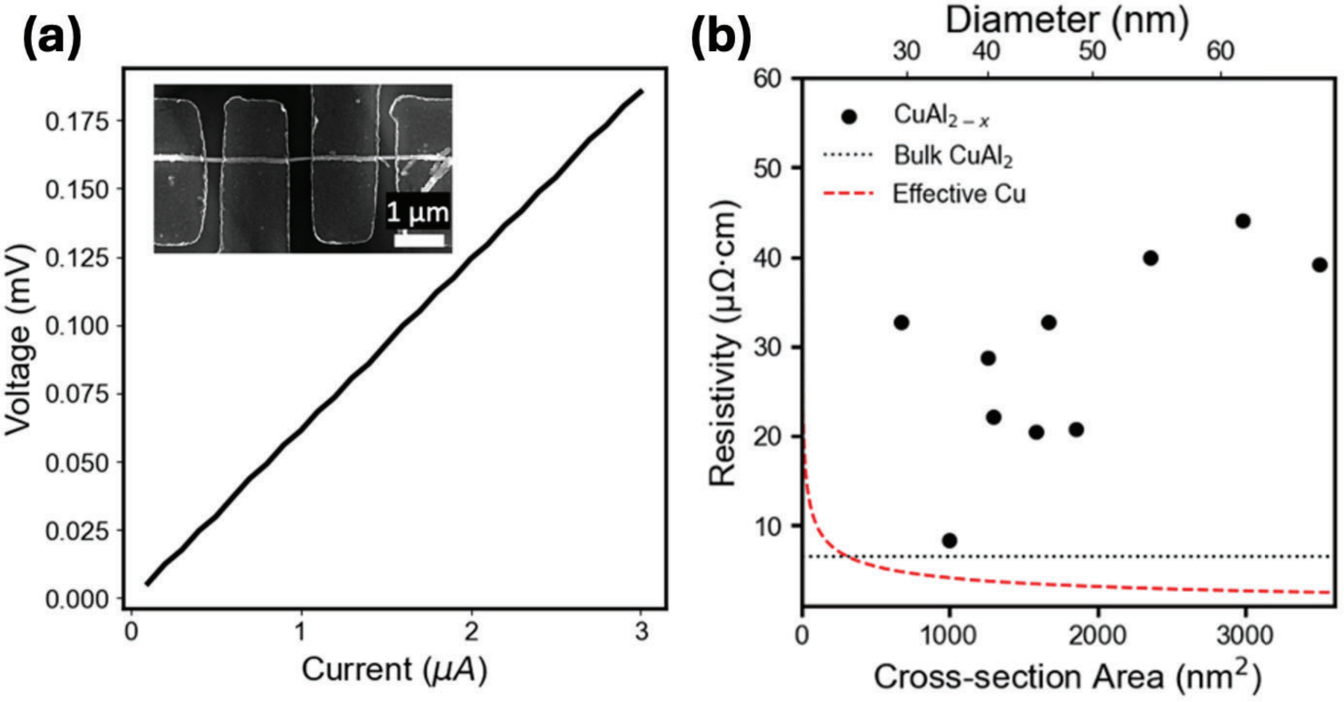

Figure 2. Transport data for CuAl2-x nanowire devices. (a) Four-point I-V curve of a CuAl2-x nanowire device. The inset shows an SEM image of the device. (b) Resistivity vs. size for ten CuAl2-x nanowire devices compared with bulk CuAl2 and effective Cu. The total core-shell cross-section area is used to calculate resistivity values.

Characterization of Fluxonium Qubits

CNF Project Number: 306723
Principal Investigator(s): Ivan Pechenezhskiy
User(s): Benjamin Byrd, Kesavan Manivannan

Affiliation(s): Syracuse University

Primary Source of Research Funding: Army Research Office

Contact: ivpechen@syr.edu, babyrd@syr.edu, kmanivan@syr.edu

Primary CNF Tools Used: ASML DUV Stepper, JEOL 6300, PT770 Plasma Etcher, Heidelberg DWL2000 Mask Writer

Abstract:

Quasiparticles are a significant intrinsic decoherence channel in superconducting qubits. Although their characterization and mitigation have been extensively studied in transmon qubits, their impact on fluxonia remains comparatively unexplored. To investigate this, we generate excess quasiparticles in fluxonia by injecting pair-breaking phonons and photons via on-chip injectors. In this controlled injection, we observe the qubit population dynamics that warrant separate extraction of qubit excitation and relaxation rates.

Summary of Research:

Superconducting quantum systems are among the leading platforms for implementing quantum computing. Josephson tunnel junctions provide the necessary nonlinearity for the spectral isolation of qubit computational states. The fluxonium qubit specifically comprises a small Josephson junction shunted by a capacitor and a large inductance realized with an array of Josephson junctions. This qubit design exhibits long coherence times and large anharmonicity [1, 2].

Figure 1a shows an SEM image of our recent design of a fluxonium qubit fabricated at the CNF. The two niobium capacitor pads (40 µm × 100 µm each) define the capacitive energy scale $E_C/h \sim 1.1$ GHz. The Al/AlOx/Al small Josephson junction (~100nm × 100 nm) between the pads sets the Josephson energy EJ/h ~ 2.1 GHz. The inductor formed by an array of ~ 200 Josephson junctions (~ 0.5 µm × 1 µm each) is associated with the inductive energy EL/h ~ 90 MHz.

Photolithography and electron-beam lithography were performed at the CNF, and electron-beam evaporation and sputtering were carried out at Syracuse University. The flux bias line can be seen on the right in Fig. 1a. Each qubit is capacitively coupled to a resonator for dispersive readout of the qubit state. Figure 1b displays the design of the injector Josephson junction, which is voltage biased to produce pair-breaking phonons and photons that subsequently produce quasiparticles at the qubit junctions [3].

The qubits are measured in a dilution refrigerator at 10 mK. Under certain injection biases, we observed an apparent increase in energy relaxation time T1 extracted from standard free decay measurements, as shown in Fig. 2a. This is because the excitation rate becomes comparable to or even exceeds the relaxation rate, causing the excited-state population to decay toward a steady state above the background. Fitting such dynamics to a simple exponential that neglects this offset can yield an apparent increase in the extracted T1, necessitating a direct extraction of the individual transition rates. In Fig. 2b, we show background and post-injection population dynamics after the qubit initialization to states |0> and |1>. We use this protocol to investigate the increase in transition rates caused by quasiparticle poisoning, including the effects arising from the efficient coupling of pair-breaking photons from the injector to the qubit, mediated by spurious antenna modes of the injector and qubit geometries [4].

References:

[1] A. Somoroff et al. Millisecond Coherence in a Superconducting Qubit. Phys. Rev. Lett. 130, 267001 (2023). https://doi.org/10.1103/PhysRevLett.130.267001

[2] L. Nguyen et al. High-Coherence Fluxonium Qubit. Phys. Rev. X 9, 041041 (2019). https://doi.org/10.1103/PhysRevX.9.041041

[3] V. Iaia et al. Phonon downconversion to suppress correlated errors in superconducting qubits. Nature Communications, 13, 6425 (2022). https://doi.org/10.1038/s41467-023-35986-3

[4] C. Liu et al. Quasiparticle Poisoning of Superconducting Qubits from Resonant Absorption of Pair-Breaking Photons. Phys. Rev. Lett. 132, 1 (2024). https://link.aps.org/doi/10.1103/PhysRevLett.132.017001

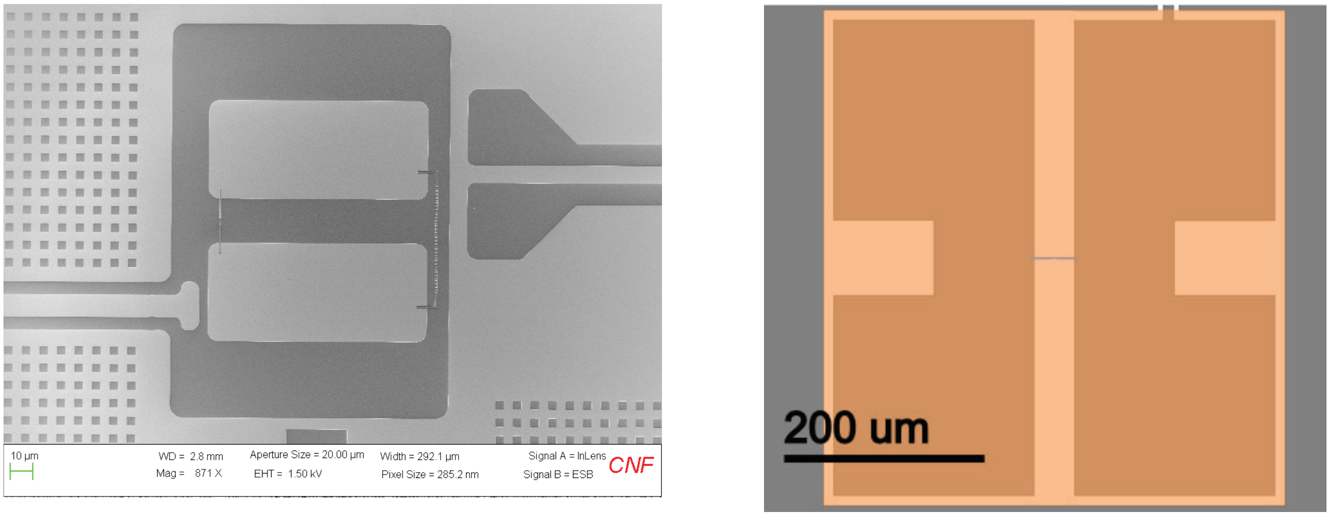

Figure 1: (a) Scanning electron micrograph of the fluxonium qubit showing the capacitor pads, single Josephson junction, and the chain of Josephson junctions. (b) Design of the Josephson junction injector.

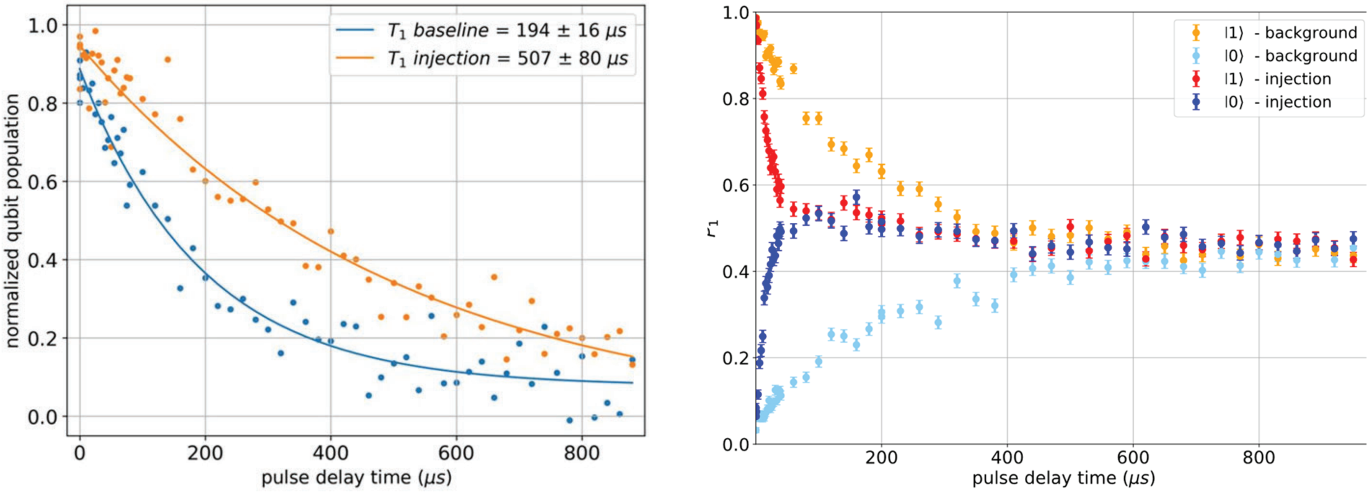

Figure 2: Two different measurement protocols for the baseline and injection cases. (a) Conventional free decay T1 measurement. (b) Qubit populations measured after initialization in the |0>and |1>states.

Epitaxial Nitride Josephson Junctions

CNF Project Number: 311723
Principal Investigator(s): Valla Fatemi
User(s): Benjamin Byrd, Kushagra Aggarwal

Affiliation(s): School of Applied and Engineering Physics, Cornell University

Primary Source of Research Funding: AFOSR

Contact: vf82@cornell.edu, ka543@cornell.edu

Website: https://fatemilab.aep.cornell.edu

Primary CNF Tools Used: Heidelberg MLA 150 Maskless Aligner, PT 770, ICP Etcher, JEOL-9500FS E-beam Lithography System, Zeiss Ultra SEM, SC4500 Even-hour Evaporator, AJA Sputter 1.

Abstract:

Superconducting quantum technologies have traditionally relied on aluminum-based devices because of the ease of fabrication and the self-limiting growth of aluminum oxide. However, aluminum has a relatively low critical temperature (1.2K) requiring helium-3 refrigeration, and it suffers from surface oxides and dielectric loss. In this work, we focus on fabricating Josephson junctions from nitride-based materials grown by molecular beam epitaxy (MBE). These crystalline materials are more resistant to surface oxidation and have the potential to reduce material-related losses in superconducting qubits, thereby enabling significantly improved coherence times.

Summary of Research:

A trilayer stack comprising NbN (7 nm) – AlGaN (3 nm) – NbN (7 nm) is grown using MBE. The Josephson junction is fabricated using a bottom-up approach, as shown in Figure 1. In a first step, the stack is etched to define the bottom layer. Then, a central region is defined as the junction and the top two layers are etched everywhere else, defining the bottom electrode. The top electrode is connected using an Nb wiring layer. Since there is a possibility of the top wiring layer getting connected to the bottom NbN, a spacer layer made of SiO2 acts as an electrical isolation between the top Nb and bottom NbN.

Conclusions and Future Steps:

In this work, we have completed the lithography steps of the junction with proper alignment and isolation achieved between the layers. In the next steps, we will work on removing the SiO2 to eliminate any source of dielectric losses and improving the quality of the MBE grown films.

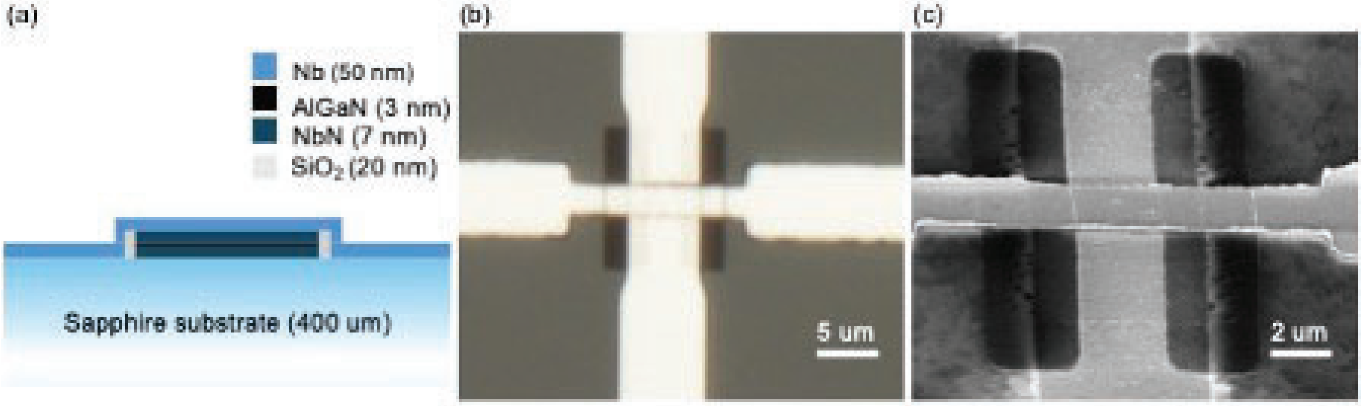

Fig. 1: Epitaxial nitride Josephson junction: (a) NbN (7 nm) – AlGaN (3 nm) – NbN (7 nm) stack grown using MBE on a sapphire substrate. (b) An optical image of the patterned junction. (c) A scanning electron microscope image showing the junction, where a top Nb wiring layer is connected and SiO2 isolates the Nb wiring layer from the bottom.

Fabrication of 2D Graphene Devices for Low Temperature Transport Measurement

CNF Project Number: 312523
Principal Investigator(s): Kenji Yasuda
User(s): Benjamin Byrd, Lujin Min, Zhen Yang

Affiliation(s): School of Applied and Engineering Physics, Department of Physics, Cornell University

Primary Source of Research Funding: Lab Start-up Fund

Contact: kenji.yasuda@cornell.edu, db923@cornell.edu, lm936@cornell.edu, zy467@cornell.edu

Website: sites.google.com/view/kenjiyasuda

Primary CNF Tools Used: Heidelberg MLA 150, Zeiss Supra SEM, Nabity Nanometer Pattern Generator System (NPGS), SC4500 Odd/Even-Hour Evaporator, Oxford PlasmaLab 80+ RIE System (Oxford 81)Lithography System, Zeiss Ultra SEM, SC4500 Even-hour Evaporator, AJA Sputter 1.

Abstract:

It can be said that many of the most exotic correlated many body states can be found in the phase diagram of magic angle twisted bilayer graphene (MATBG), including unconventional superconductivity [1] and the quantum anomalous hall effect (QAHE) [2]. In order to study the now broad range of emerging 2D materials, these devices must undergo a careful sample preparation and fabrication procedure. We report the successful fabrication and measurement of a variety of graphene based devices, including some twisted bilayer graphene (TBG).

Summary of Research:

By measuring the longitudinal and hall resistance of a material we can probe the most important aspects of its electronic properties. In a dual-gated hall bar device architecture, with the instruments available in our lab, it is possible to measure these two resistances versus a versatile 4D phase space of carrier density, electric displacement field, out of plane magnetic field, and temperature. We can search for and define interesting phenomena within this phase space, as well as characterize their properties. In this report we present data from two different TBG devices.

Before fabrication can be done, our samples must be stacked into the correct device architecture. A schematic of this device structure can be seen in Figure 1a. In short, we have a top and bottom graphite gate along with two pieces of hBN to act as the dielectric, with a middle device layer. An image of a TBG device in the middle of the stacking procedure can be seen in Fig 1b. Additionally, we can characterize the moiré pattern formed by the twisted bilayer graphene using an atomic force microscopy technique (AFM), torsional force microscopy (TFM), during this step as shown in Fig 1c.

Once the stacking procedure is complete we fabricate the resulting device into a hall bar shape and make electrical contacts. Figure 2a shows the device coated in Polymethyl methacrylate (PMMA), patterned into a hall bar shape with electron beam lithography (EBL). Figure 2b shows the final result after etching the device into a hall bar, followed by another round of EBL as well as metal deposition. Finally, the device can be installed onto our sample holder, wirebonded, and installed onto our low temperature probe for transport measurements, as seen in Fig 2c.

Figure 3 shows the longitudinal resistance measurement for two different devices at a temperature of 1.5K. Fig 3a shows the landau fan diagram of the TBG sample which is detailed in Fig 1 and 2.The full filling peak is very well developed and some landau fan features can be observed, including some coming from the full filling. However, the integer peaks are blurred, likely due to being far from the magic angle and the device angle not being homogeneous. Fig 3b shows the landau fan for another TBG device. This one seems to have many different peaks and landau levels. It is not clear whether these peaks correspond to the integer peaks, full filling from twist angle inhomogeneity, or hBN alignment in the device. None-the-less, low noise transport data resolving clearly the features of both devices are able to be taken.

Conclusions and Future Steps:

We have been able to implement a complete fabrication procedure in order to perform low temperature transport measurements on our devices. With these fabrication and measurement methods well established we are planning to expand our sample fabrication to a variety of materials and device structures in the search for interesting correlated and symmetry breaking phenomena.

References:

[1] Y. Cao, V. Fatemi, S. Fang, K. Watanabe, T. Taniguchi, E. Kaxiras, and P. Jarillo-Herrero, Unconventional superconductivity in magic-angle graphene superlattices, Nature 556, 43 (2018).

[2] M. Serlin, C. L. Tschirhart, H. Polshyn, Y. Zhang, J. Zhu, K. Watanabe, T. Taniguchi, L. Balents, and A. F. Young, Intrinsic quantized anomalous Hall effect in a moiré heterostructure, Science 367, 900 (2020).

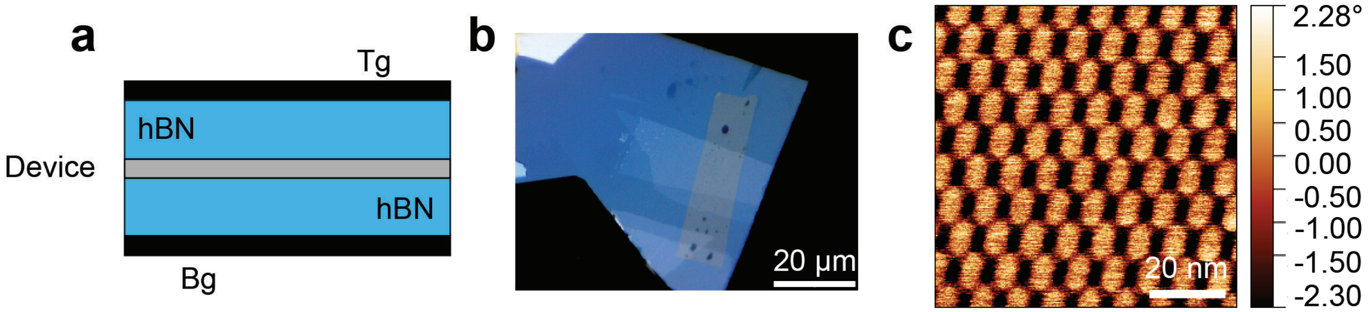

Figure 1: a. Device structure, including two graphite gates, hBN as the dielectric, and the device layer. b. Optical images of a partially stacked device. Scale bar - 20 µm. c. TFM-phase image of the moiré pattern formed by the twisted graphene layers. Scale bar - 20 nm.

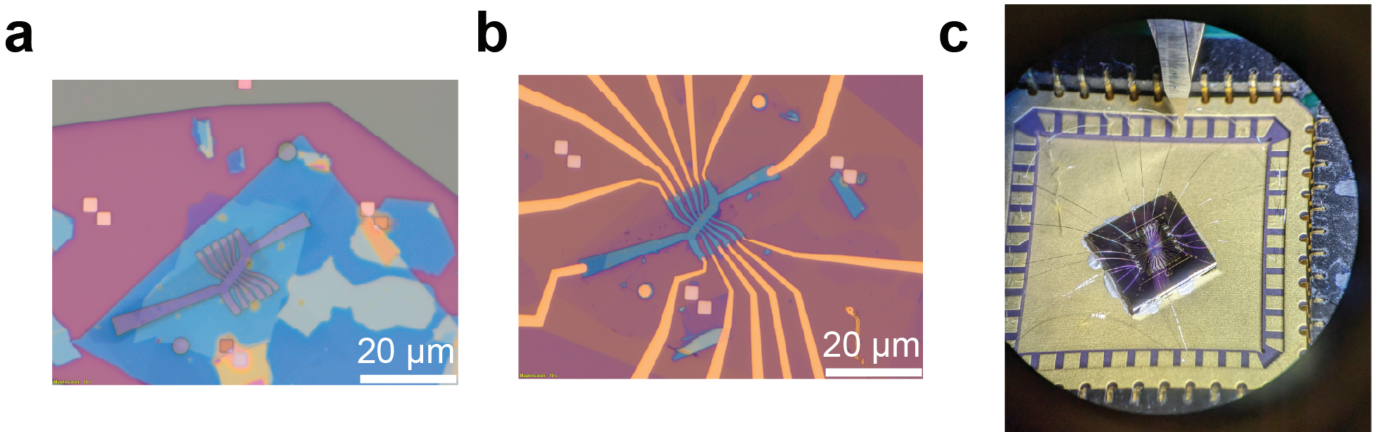

Figure 2: a. Optical image of the device after the shape defining EBL. b. Optical image of the device showing the electrical contacts defined using EBL. c. Image of the sample installed onto our sample holder with the pads being wirebonded for electrical contact.

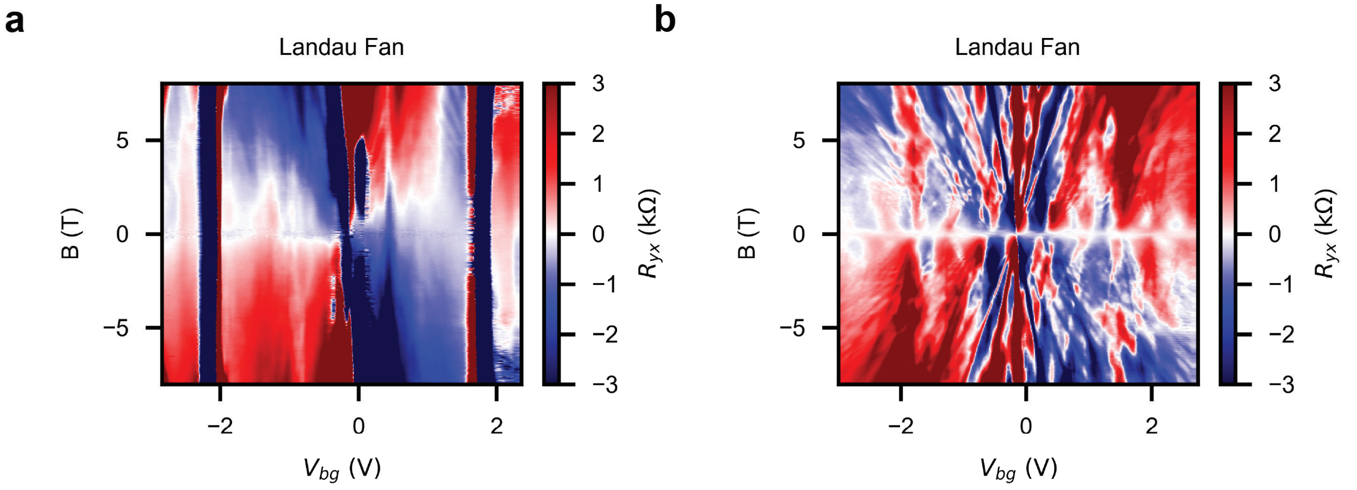

Figure 3: a. Ryx measured versus Vbg and B of a TBG device. b. Ryx measured versus Vbg and B of a different TBG device. Both are taken at 1.5K.

Electrical Transport in Graphene Heterostructures

CNF Project Number: 316224
Principal Investigator(s): Xiaomeng Liu
User(s): Jinghao Deng, Jiabin Xie, Chang Chang, Alexander Sanchez

Affiliation(s): Laboratory of Atomic And Solid State Physics, Department of Physics, Cornell University

Primary Source of Research Funding: National Science Foundation, College of Arts and Sciences

Contact: xiaomengliu@cornell.edu

Website: https://www.xiaomengliu.com/

Primary CNF Tools Used: Heidelberg DWL 2000, Photolithography Spinners, GCA AutoStep 200 DSW i-line Wafer Stepper, E-Beam Lithography Spinners, Zeiss Supra SEM, Nabity Nanometer Pattern Generator System, Oxford 81/82 Etcher, SC4500 Even/Odd, Oxford ALD Flexal

Abstract:

Graphene heterostructures continue to provide myriad opportunities for researching new strongly correlated and topological physics. We fabricate three different types of graphene heterostructure, to facilitate study of this physics. We will examine magic-angle twisted bilayer graphene in close proximity to few-layer graphene, an electronic double-layer of bilayer graphene separated by thin boron nitride, and rhombohedral stacked graphene. Each of these configurations is host to unique phenomena to be surveyed using low temperature electrical transport measurements. Imperative to our ability to process these graphene heterostructures into electronic devices which can be measured in a dilution refrigerator are a variety of tools available to us through the Cornell nano-scale science and technology facility.

Summary of Research:

We are conducting low temperature electrical transport measurements on three different categories of graphene heterostructures, magic-angle twisted bilayer graphene, insulated graphene bilayers, and rhombohedral-stacked graphene.

The pairing mechanism of superconductivity in magic-angle twisted bilayer graphene remains unclear, whether it be a conventional phonon-mediated pairing or a more exotic unconventional pairing. Previous work has used bilayer graphene in close proximity to but insulated from magic angle twisted bilayer graphene to tune the strength of the Coulomb interaction, thereby tuning the superconducting phase[3]. We will use multilayer graphene to further investigate the effect of Coulomb screening on magic angle twisted bilayer graphene. Figure 1 shows a graphene heterostructure device, intended to be used for this purpose.

Using bi-layer graphene separated by a thin piece of boron nitride, an exciton condensate phase has previously been demonstrated[2]. We have fabricated bi-layer graphene heterostructure devices to analyze this. Figure 2 shows a graphene heterostructure device for studying exciton condensation in a graphene bi-layer heterostructure. To prevent the formation of PN junctions between differently doped graphene bi-layers, we used the Oxford ALD Flexal to deposit an AL2O3 thin film on top of the graphene heterostructure, and then evaporated additional metal electrodes, to dope the graphene contacts.

Rhombohedral-stacked graphene's unique electronic properties promote the role of electron-electron interactions, giving rise to topological and strongly correlated quantum phases[4, 1]. These phases are not yet fully understood, but could have a variety of applications in future electronics. We have fabricated few-layer Rhombohedral-stacked graphene heterostructures and performed low temperature electronic transport measurements on them. A rhombohedral-stacked graphene heterostructure device is shown in Figure 3.

Crucial to our work studying graphene heterostructures has been the Cornell nano-scale science and technology facility. All of our graphene heterostructure devices use a similar nano fabrication procedure, which is carried out entirely within the Cornell nano-scale science and technology facility's clean room. First, a completed graphene/boron nitride heterostructure is deposited onto a silicon substrate outside the clean room, using transfer techniques standard to van der Waals heterostructure assembly[5]. Alignment markers are evaporated onto this substrate in the clean room before deposition, they are patterned using a quartz photomask prepared with the Heidelberg DWL200, and then exposed using the

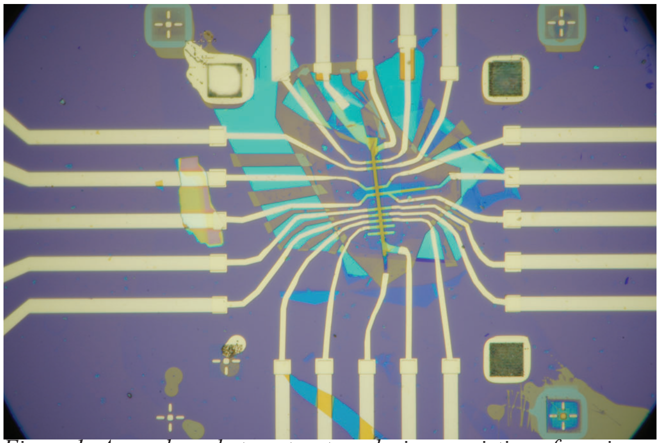

Figure 1: A graphene heterostructure device consisting of magic-angle twisted bilayer graphene in close proximity to few-layer graphene. The heterostructure has been etched into a Hall bar geometry using clean room tools.

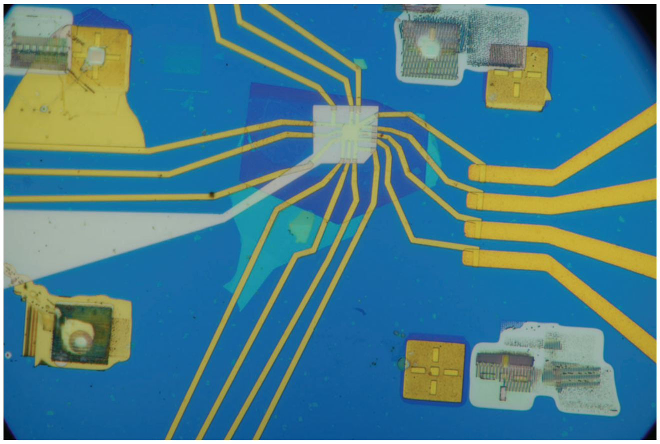

Figure 2: An electronic double layer device made with bilayer graphene separated by thin boron nitride. Al2O3 has been deposited on top of it, and gold has been evaporated to dope the graphene contacts.

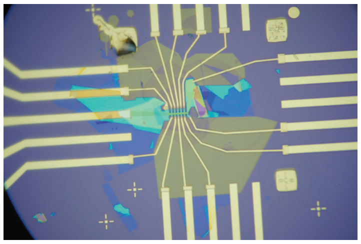

A rhombohedral-stacked multilayer graphene heterostructure which has been etched into a Hall bar geometry using nanofabrication facilities.

GCA AutoStep 200 DSW i-line wafer stepper. Using the E-Beam lithography spinners, PMMA A4-950 is spun onto the sample, and then the graphene/boron nitride heterostructure is patterned into an appropriate electrical geometry using successive electron beam lithography steps with the Zeiss Supra SEM and Nabity Nanometer Pattern Generator system and etching steps with the Oxford 81/82 Etchers, wherein O2 and CHF3 plasmas are used to etch. When the graphene/BN heterostructure has been patterned appropriately, the SC4500 Even/Odd-Hour evaporators are used to deposit chromium, palladium, onto the silicon substrate and create metal electrodes. To aid with lift-off after metal evaporation, layers of PMMA A4-495 and A4-950 are used, or M2-950.

Conclusions and Future Steps:

Our work studying magic-angle twisted bilayer graphene in close proximity to few-layer graphene, an electronic double-layer of bilayer graphene separated by thin boron nitride, and rhombohedral stacked graphene probes topological and strongly correlated physics. We have carried out measurements of completed rhombohedral stacked graphene heterostructure devices, but have not yet done so on the other two configurations of graphene device we have fabricated. Future work will include electrical measurements of these configurations, and further assemblage of graphene devices to improve measurement quality and certainty. The Cornell nano-scale science and technology facility provides access to tools essential to our continued research.

References:

[1] Tonghang Han, Zhengguang Lu, Zach Hadjri, Lihan Shi, Zhenghan Wu, Wei Xu, Yuxuan Yao, Armel A. Cotten, Omid Sharifi Sedeh, Henok Weldeyesus, Jixiang Yang, Junseok Seo, Shenyong Ye, Muyang Zhou, Haoyang Liu, Gang Shi, Zhenqi Hua, Kenji Watanabe, Takashi Taniguchi, Peng Xiong, Dominik M. Zumbühl, Liang Fu, and Long Ju. Signatures of chiral superconductivity in rhombohedral graphene. Nature, 643(8072):654–661, Jul 2025.

[2] Xiaomeng Liu, Kenji Watanabe, Takashi Taniguchi, Bertrand I. Halperin, and Philip Kim. Quantum hall drag of exciton condensate inÂ graphene. Nature Physics, 13(8):746–750, Aug 2017.

[3] Xiaoxue Liu, Zhi Wang, K. Watanabe, T. Taniguchi, Oskar Vafek, and J. I. A. Li. Tuning electron correlation in magic-angle twisted bilayer graphene using coulomb screening. Science, 371(6535):1261–1265, 2021.

[4] Zhengguang Lu, Tonghang Han, Yuxuan Yao, Aidan P. Reddy, Jixiang Yang, Junseok Seo, Kenji Watanabe, Takashi Taniguchi, Liang Fu, and Long Ju. Fractional quantum anomalous hall effect in multilayer graphene. Nature, 626(8000):759–764, Feb 2024.

[5] L. Wang, I. Meric, P. Y. Huang, Q. Gao, Y. Gao, H. Tran, T. Taniguchi, K. Watanabe, L. M. Campos, D. A. Muller, J. Guo, P. Kim, J. Hone, K. L. Shepard, and C. R. Dean. One-dimensional electrical contact to a two-dimensional material. Science, 342(6158):614–617, 2013.

Reliable Scanning Tunneling Microscopy Prepared Fabrication for 2D Quantum Material Device Research

CNF Project Number: 319924
Principal Investigator(s): Xiaomeng Liu
User(s): Yiming Sun, Jinghao Deng

Affiliation(s): Laboratory of Atomic And Solid State Physics, Department of Physics, Cornell University

Primary Source of Research Funding: The College of Arts & Sciences, Cornell University, National Science Foundation

Contact: xl956@cornell.edu

Website: https://www.xiaomengliu.com/

Primary CNF Tools Used: Heidelberg DWL 2000 Mask Writer, GCA AS200 i-line Stepper, Oxford Plasmalab 81/82 RIE, SC4500 Odd-Hour Evaporator, DISCO Dicing Saw

Abstract:

This report introduces a novel fabrication methodology enabling the reliable production of scanning tunneling microscopy (STM) prepatterned chips for micro-level 2D material flake identification. By integrating precision photomask design, optimized interfacial metal stacks, and defect-minimized processing, we achieved >95% yield in devices capable of targeting sub-5µm flakes. The process establishes a new baseline for reproducible quantum material research platforms.

Summary of Research:

STM achieves atomic resolution but suffers from an intrinsically small field of view (~1 µm), rendering navigation to specific micron-scale samples (e.g., 2D flakes) slow and prone to tip crashes. External localization aids are impractical in extreme environments [1, 2]. In CNF, we developed recipes for prepatterned chips with integrated registration markers to resolve this by enabling reliable STM navigation to target flakes without external systems.

1. Precision Photomask Engineering

Critical to pattern making was developing quartz 5-inch photomasks with alignment markers resolvable at 199 nm scales. Using the Heidelberg DWL 2000, AutoCAD-designed patterns underwent .dxf to .gds conversion in KLayout with manual correction of alphanumeric fiducials (design pattern see Fig. 1). This eliminated coordinate drift during stepper alignment, enabling consistent placement of µm level registration markers essential for 2D quantum device targeting. Post-write verification included Hamatech Process 2 cleaning and 60s Cr etching (Process 1) to ensure defect-free surfaces.

2. Lithography for Flake-Scale Features

A bilayer resist system (LOR3A/SPR700) was optimized for STM-specific undercut profiles, comprising an adhesion layer of P20 at 3000 rpm (15s), undercut control via LOR3A (4000 rpm, 180°C/5min bake), and an imaging layer of SPR700 (3000 rpm, 90°C/1min bake). GCA iline exposure at focus = -6, dose = 0.22 produced 800 nm apertures with tapered sidewalls (70° angle), verified by cross-section SEM. Post-development O_2 descum (Oxford RIE, 60W, 25s) prevented resist scumming around critical edges.

3. Interfacial Engineering for Flake Contact

Two metallization strategies enabled reliable flake-electrode interfaces: edge contacts with 3.5nm Cr / 15nm Pd evaporated at 0.5Å/s (1×10^{-6} Torr), and scanning pads with 50nm Cr at 4Å/s (4×10^{-6} Torr). The Cr/Pd bilayer provided oxidation-resistant surfaces while maintaining atomic-scale flatness, critical for STM tip stability during flake characterization.

4. Damage-Mitigated Device Release

Liftoff utilized inverted 1165 solvent immersion (3hr) to preserve delicate flake-search electrodes, followed by dicing protection via PMMA 495 A4 coatings (2000 rpm, 170°C bake) to reduce edge fractures, with back-polishing to manually remove the insulating SiO_2 layer. Cutting was conducted under a DISCO Dicing saw along predefined lines, and final plasma cleaning employed sequential 200W O_2 strips (Oxford RIE) to remove organics without ion bombardment damage.

Final chips showed >90% electrode integrity (Fig. 2) and have been used for more than 100 STM 2D quantum device making. Reliability validation involved ~200 STM_v2 chips processed across two wafer lots, demonstrating functionality in locating 2-10µm flakes (Fig. 3), zero registration failures during 2D material transfers, and half a year shelf-life stability (N_2 storage).

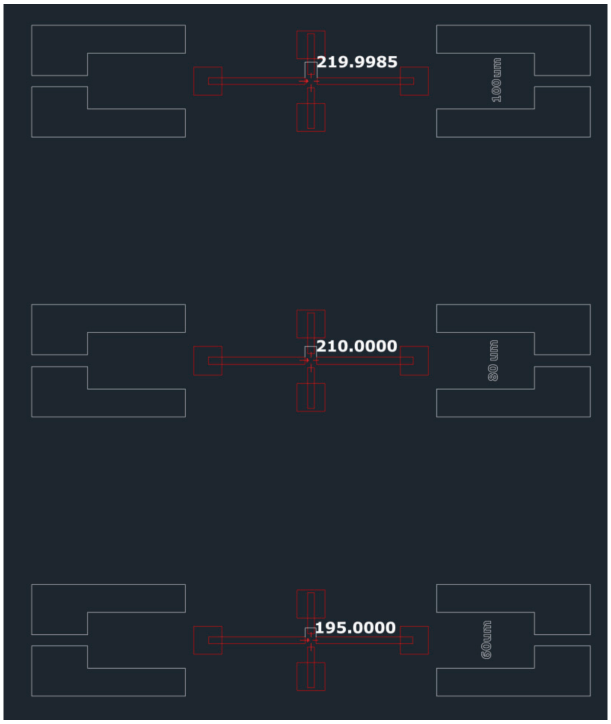

Fig. 1: STM_v2 mask design showing 3µm alignment markers.

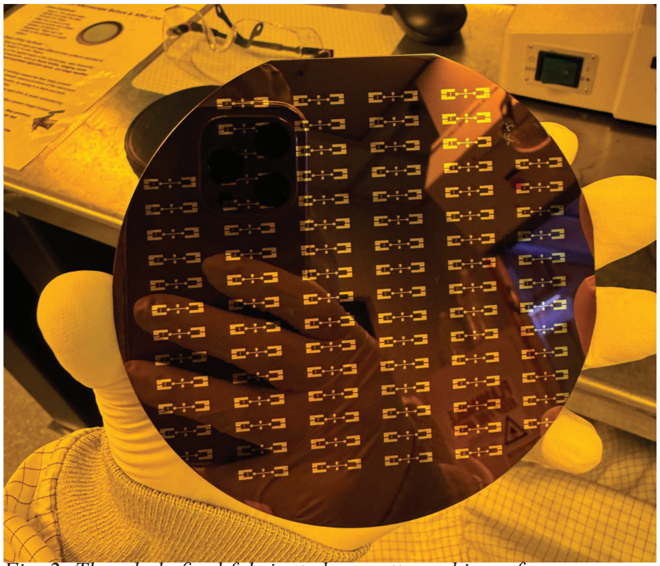

Fig. 2: The whole final fabricated prepattern chip wafer.

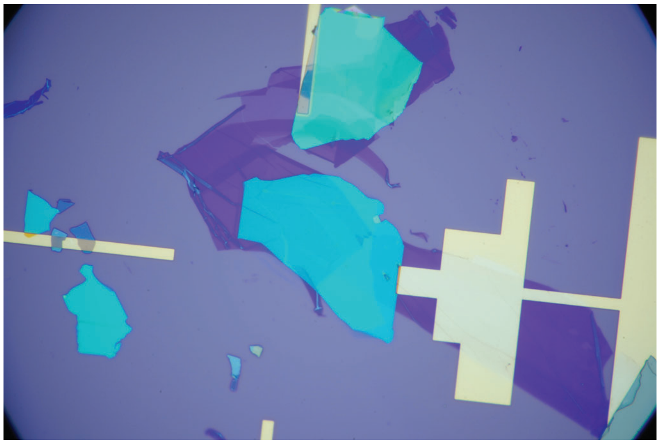

Fig. 3: Optical micrograph of a graphene-based 2D device on an STM prepattern chip.

Conclusions and Future Steps:

The established process enables reliable fabrication of STM prepatterned chips for microscale 2D flake discovery, achieving >95% yield in registration-critical devices. Future work will extend this methodology to air-sensitive materials (e.g., $CrPS_4$) via glovebox-compatible integration, requiring conductance-optimized electrodes through testing new electrode categories to minimize conductance reduction and geometric redesign through modifying pad geometries to prevent bonding-induced circuit shorts.

References:

[1] Li, G., Luican, A., & Andrei, E. Y. Rev. Sci. Instrum. 82, 073701 (2011)

[2] Liu, X., et al., Science 375, 321-326 (2022)

Sensor Development for Picosecond Timing

CNF Project Number: 321324
Principal Investigator(s): Marina Artuso
User(s): Bridget Mack

Affiliation(s): Department of Physics, Syracuse University

Primary Source of Research Funding: National Science Foundation

Contact: martuso@syr.edu

Website: https://hep.syr.edu/

Primary CNF Tools Used: DISCO Dicing Saw, Westbond 7400A Ultrasonic Wire Bonder

Abstract:

Future particle detectors will require fast timing capabilities to handle the high luminosities planned for collider experiments. Research and development into low gain avalanche diodes is needed to reach resolutions on the order of 10 picoseconds. Multiple fabrication parameters, including implantation energy, thickness, and mask area need to be optimized for sensing large quanties of particles in high radiation environments. Several of these design parameters are being tested, with goals to characterize design parameters of low gain avalanche diodes for precision timing applications in high energy particle detectors. Prototype development is currently underway; the first wafers will be ready within the next six months.

Summary of Research:

The future of particle physics as a field will rely on heavy research and development in instrumentation motivated by the physics goals of the next generation of experiments. Proposed future collider experiments boast higher luminosities, meaning – from a detector standpoint – large influxes of particles and radiation over short timescales. The ability to attach a precise time stamp on the order of 10 picoseconds to position or energy measurements becomes crucial, with broad potential to be transformative not only in particle physics instrumentation, but also in other research areas such as medical imaging [1-3].

Low Gain Avalanche Diodes are good candidates for use in both tracking detectors and hybrid calorimeters including layers with high granularity and timing resolutions. The added gain layer at the junction creates a high electric field, leading to charge multiplication and an amplified signal with a sharp rise time, yielding good timing resolution [4]. Multiple parameters – including active area, thickness, and gain – must be tailored to the specific granularity, radiation hardness, and acceptance requirements of a given detector system. Ten 4-inch wafers with arrays of silicon sensors are at various stages of production with varying fabrication parameters. Figure 1 shows a rough schematic of the masks used, which include sensors with active areas between 3 and 10 square millimeters.

Manufacture-side delays in wafer productions due to issues with contact metallization have limited production progress, thus limiting facility use. These technical hurdles are now resolved, and no further roadblocks are anticipated. A full set of pre-diced prototypes by the manufacturer are expected within the next six months; some smaller samples and partial wafers are already available and will need to be diced with the DISCO dicing saw. The Westbond 7400A Ultrasonic Wire Bonder has been used for wire bonding some of these samples to printed circuit boards.

Preliminary electrical testing of 3mm and 10mm square pads shows that increasing active area, and thus, capacitance, allows for more current to flow through the device, while the depletion voltage stays the same. Figure 2 shows a current vs voltage characterization curve that compares the two devices. In the coming weeks, the devices will be tested using transient current technique to study the differences in signal formation and to determine spatial and timing resolutions.

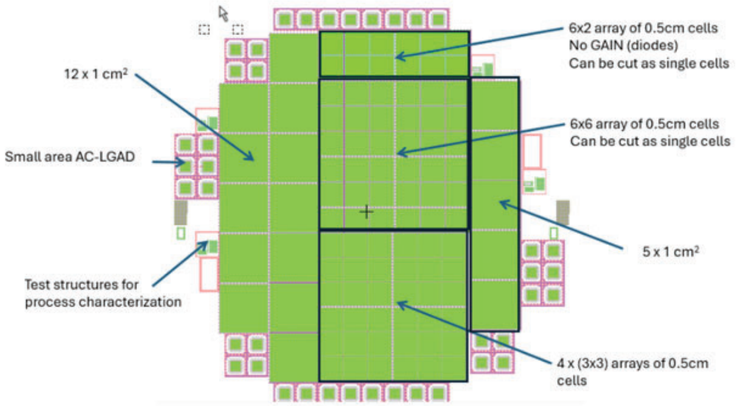

Figure 1: Rough schematic of masks used for wafer fabrication. Each wafer has a set of test structures, as well as diodes and low gain avalanche diodes of different sizes. Pairs of wafers are being fabricated with different implantation energies and epitaxial thicknesses.

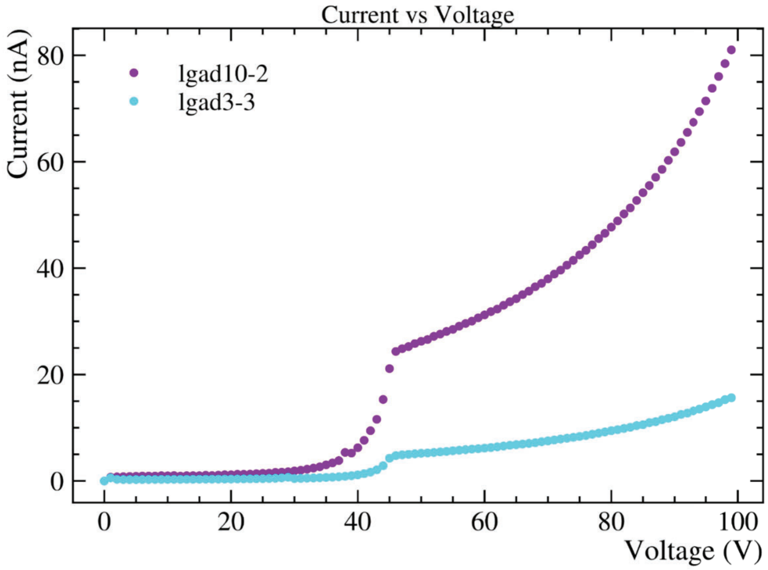

Figure 2: Current vs applied voltage for 10mm (lgad10-2; top curve) and 3mm (lgad3-3; bottom curve) devices. Both low gain avalanche diodes tested are from the same wafer and have the same epitaxial thickness and implantation energy.

Conclusions and Future Steps:

As more devices become available, they will be tested before being wire bonded at Syracuse University. For the periods of time in which the Syracuse wire bonder is down, the Westbond 7400A Ultrasonic Wire Bonder will be used. In addition to the prototypes from the manufacturer, several partial wafers from Hamamatsu with standard silicon diodes are being prepped to be diced using the DISCO Dicing Saw. After dicing, they will undergo electrical tests before they are also wire bonded to readout boards for further study. Comparisons between the low gain avalanche diodes and the standard silicon diodes will be made to further explore the capabilities and limitations of solid-state detectors for particle physics applications.

References:

[1] W. Krüger et al., "Lgad technology for hades, accelerator and medical applications", Nuclear Instruments and Methods in Physics Research Section A: Accelerators, Spectrometers, Detectors and Associated Equipment 1039, 167046 (2022).

[2] S. Dharani, "Particle Identification using Time of Flight in the International Large Detector ILD", Bachelorarbeit (Universit¨at Leipzig, 2018), p. 41, https://bib-pubdb1.desy.de/record/414330.

[3] S. V. Chekanov et al., "Physics potential of timing layers in future collider detectors", JINST 15, P09021 (2020), arXiv:2005.05221 [physics.ins-det].

[4] A. Apresyan et al., "Measurements of an AC-LGAD strip sensor with a 120 GeV proton beam", JINST 15, P09038 (2020), arXiv:2006.01999 [physics.ins-det].

Fabrication of superconducting qubits at CNF

CNF Project Number: 323724
Principal Investigator(s): Prof. Valla Fatemi
User(s): Simon Reinhardt, Maciej Olszewski, Lingda Kong, Gabriele Di Gianluca

Affiliation(s): Cornell Applied and Engineering Physics (AEP)
Primary Source of Research Funding: Nordtech (SQFAB)
Contact: vf82@cornell.edu
Website: https://fatemilab.aep.cornell.edu/
Primary CNF Tools Used: Angstrom-Q, JEOL 6300, Zeiss Ultra SEM, AJA-Q

Abstract:

We demonstrate fabrication of superconducting qubits using CNF tools. Josephson junctions of Dolan and Manhattan type are defined using shadow masks. Evaporation and in-situ oxidation are performed using the Angstrom Quantum evaporator.

Summary of Research:

The objective of this project is to demonstrate fabrication of state-of-the-art superconducting qubits at CNF. We fabricate transmon qubits on base layers of tantalum thin films on 100mm highly resistive silicon wafers. The fabrication of the tantalum base layer structures is covered in a separate report.

The main step in the fabrication of superconducting qubits is the deposition of Josephson junctions (JJs). The JJs are fabricated using shadow evaporation and liftoff. In a first step the shadow masks are defined using electron beam lithography (JEOL 6300) in a bilayer resist stack (MMA/PMMA). Using the JEOL6300 ebeam writer we perform lithography on 100mm wafers. The ebeam writer allows loading of two 100mm wafers for each writing session.

We demonstrate both Dolan-type JJs (Fig. 1) which use a suspended PMMA bride as well as Manhattan-type JJs without a suspended bridge (Fig. 2). Initially we used the AJA-Q evaporator for the deposition of Dolan-type JJs providing superconducting qubits with highly promising characteristics.

As part of the CNF-REU summer project we characterized the new Angstrom-Q tool, which is dedicated for the fabrication of Josephson junctions for superconducting qubits (REU student Gabriele Di Gianluca). The Angstrom-Q provides several benefits for the fabrication of JJs:

- fully programmable recipes, high degree of automation
- precise alignment of stage rotation and tilt, ideal for shadow deposition
- in-situ argon ion milling and oxygen plasma descum
- evaporation of ultra-clean aluminum films directly from the copper hearth, without graphite crucibles
- low base pressure $p < 1e-8$ torr after chamber baking and titanium gettering
- both static and dynamic in-situ oxidation with a tunable Ar/O2 pressure settings

After deposition the fabrication is finalized by a liftoff in a hot solvent. The JJs can be characterized at room temperature using a probe station. After optimization of the recipes in the REU project we obtain resistance variations as low as 2% over single dies. The JJs can be imaged using the Zeiss Ultra SEM , see images Fig. 1 and Fig. 2 below.

Acknowledgement:

Funding (or Partial funding) for shared facilities used in this prototype was provided by the Microelectronics Commons Program, a DoD initiative, under award number N00164-23-9-G061.

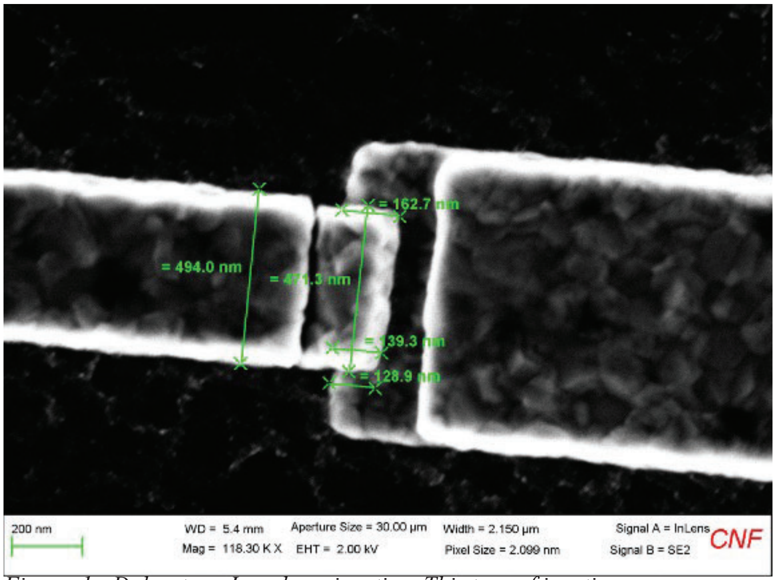

Figure. 1: Dolan-type Josephson junction. This type of junction uses a suspended bridge formed by electron beam lithorgaphy in MMA/PMMA resist. The evaporation of aluminum electrodes and in-situ oxidation is performed in the newly installed Angstrom-Q evaporator.

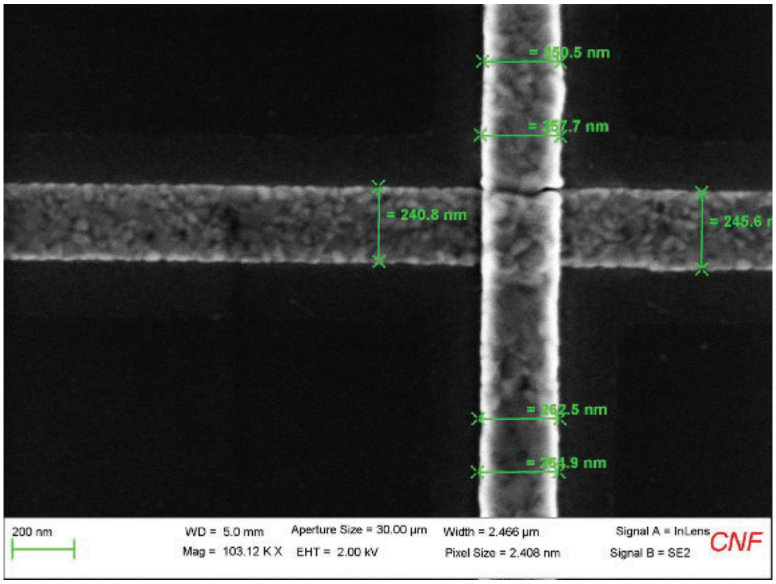

Figure. 2: Manhattan-type Josephson junction with an area of 250nm x 250nm. Lithography of the shadow mask is performed using the JEOL 6300 ebeam writer. The evaporation of aluminum electrodes and in-situ oxidation is performed in the newly installed Angstrom-Q evaporator.

Study of vortex dynamics in Josephson junction arrays

CNF Project Number: 326525
Principal Investigator(s): Katja Nowack
User(s): Cequn Li

Affiliation(s): Laboratory of Atomic and Solid State Physics, Cornell University

Primary Source of Research Funding: US Department of Defense

Contact: kcn34@cornell.edu

Website: https://nowack.lassp.cornell.edu/

Primary CNF Tools Used: JEOL JBX-6300FS, Heidelberg MLA 150 Maskless Aligner, Angstrom E-Beam Evaporator, AJA sputter, Zeiss Ultra SEM, Zeiss Supra SEM, Glen 1000 Resist Strip

Abstract:

An array of superconducting islands deposited on a normal metal film forms the so-called Josephson junction arrays, providing a tunable platform for studying quantum critical phenomena. This system enables the investigation of competing vortex states and the phase transitions [1-4]. Here, we fabricate Nb-Au Josephson junction arrays and study vortex dynamics by combining electrical transport measurements and scanning superconducting quantum interference device microscopy. Our preliminary data shows the presence of periodic vortex lattice formed in the square and hexagonal arrays. Experiments on the vortex dynamics driven by an external current will be studied.

Summary of Research:

We fabricated Nb-Au Josephson junction arrays (JJA) and studied the formation of periodic Josephson vortex lattices using electrical transport measurements and scanning superconducting quantum interference device (SQUID) microscopy at low temperatures. Figure 1 illustrates the process to fabricate Nb-Au JJAs. First, we patterned Au/Ti (40/5 nm) films on Si substrates using optical lithography and electron-beam evaporations. Then we performed electron-beam lithography and sputtered Nb/Ti (70/2 nm) on the pre-patterned Au/Ti. Figure 2 shows an optical image of an exemplary Nb-Au square JJA device. The Nb islands are only connected by the underneath Au films, forming superconductor-normal metal-superconductor networks.

The JJAs were characterized by low-temperature transport measurements. We confirmed the JJAs are superconducting with the critical temperatures ranging between 5 K and 7 K. Furthermore, we observed maxima in the critical currents as a function of the external magnetic fields, indicating the formation of periodic vortex lattices [2]. We also performed scanning SQUID measurements to visualize the vortex lattices at different magnetic fields.

Conclusions and Future Steps:

We successfully fabricated Nb-Au JJAs with the critical temperatures ranging between 5 K and 7 K. Through electrical transport measurements and scanning SQUID microscopy, we detected the presence of vortex lattice in the JJAs, leading to enhancements of the critical currents at specific magnetic fields. We will visualize the motion of vortices driven by an external current for the understanding of the vortex dynamics [3, 4].

References:

[1] S. Teitel and C. Jayaprakash, Josephson-junction arrays in transverse magnetic fields, Phys. Rev. Lett. 51, 1999 (1983).

[2] N. Poccia, T. I. Baturina, F. Coneri, et al., Critical behavior at a dynamic vortex insulator-to-metal transition, Science 349, 1202 (2015).

[3] C. Bøttcher, F. Nichele, M. Kjaergaard, et al., Superconducting, insulating and anomalous metallic regimes in a gated two-dimensional semiconductor–superconductor array. Nat. Phys. 14, 1138–1144 (2018).

[4] C. Bøttcher, F. Nichele, J. Shabani, et al., Dynamical vortex transitions in a gate-tunable two-dimensional Josephson junction array, Phys. Rev. B 108, 134517 (2023)

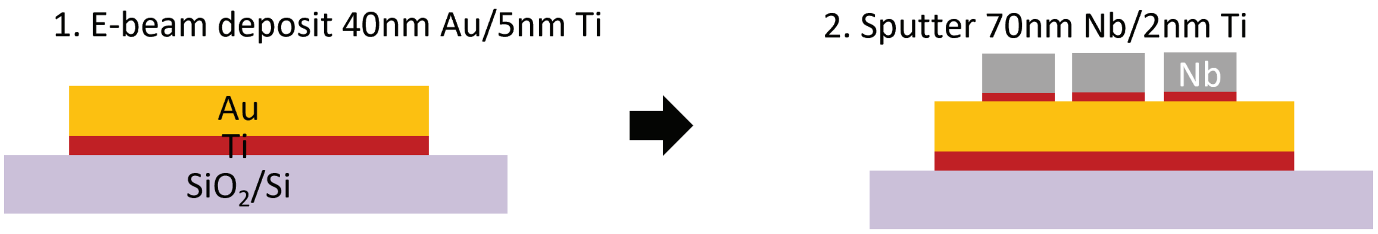

Figure 1: Schematics of fabrication process of Nb-Au Josephson junction arrays.

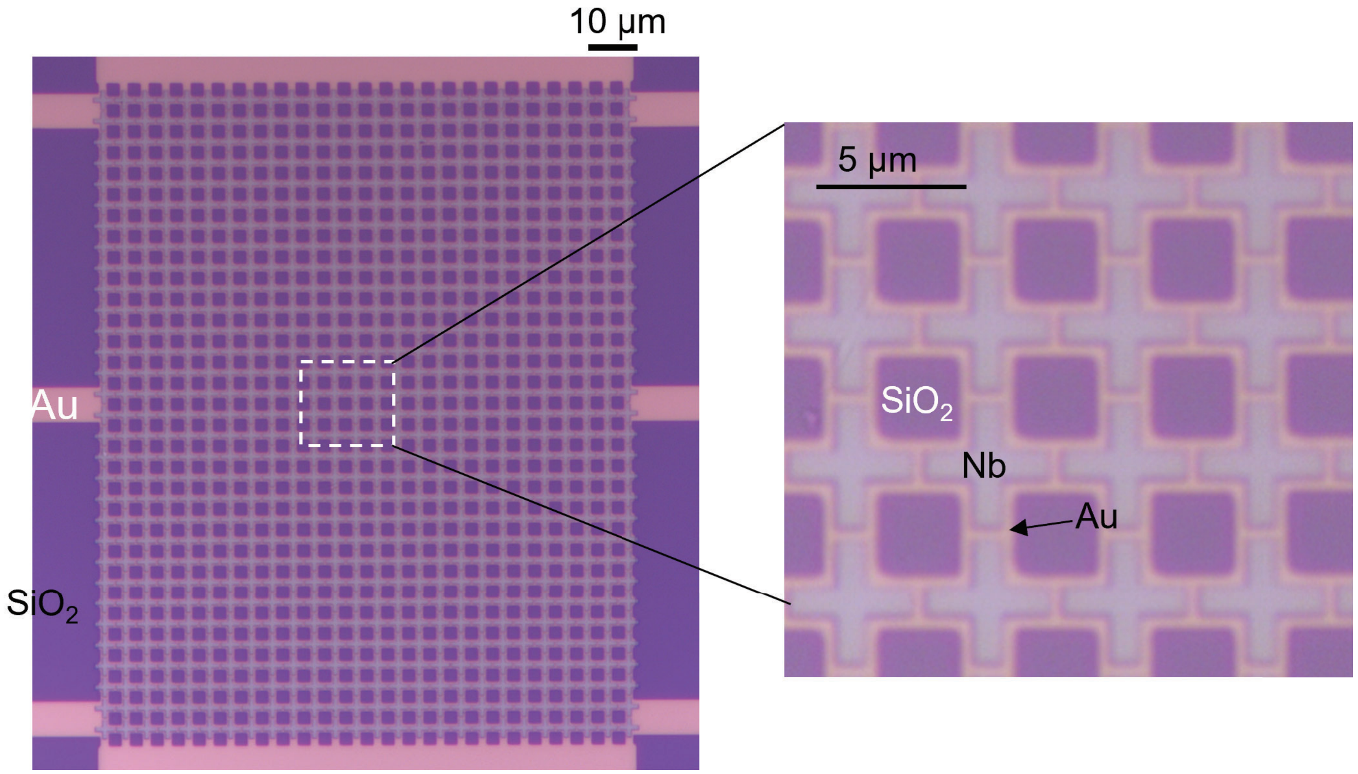

Figure 2: An optical image of an exemplary Nb-Au JJA device.

Silicon Carbide Nanophotonic Cavities for Integration with Color Centers

CNF Project Number: E718638
Principal Investigator(s): Greg Fuchs
User(s): Ying Yang

Affiliation(s): School of Applied and Engineering Physics, Cornell University

Primary Source of Research Funding: NSF

Contact: gdf9@cornell.edu

Primary CNF Tools Used: Oxford COBRA, Oxford 81 Etcher, JEOL 6300, Nabity, Dicing saw -- Disco, Glen 100, CVC SC4500 Odd hour Evaporator, Zeiss Supra SEM, Zeiss Ultra SEM, LPCVD HTO & LTO

Abstract:

Silicon carbide (SiC) has emerged as a promising platform for quantum photonics due to its excellent material properties and intrinsic color centers. We demonstrate the fabrication of two complementary cavity architectures in SiC: plasmonic silver nanopan cavities and dielectric ring-waveguide resonators on SiC-on-insulator (SiCOI). These structures are designed to provide cavity modes with field confinement and high-quality factor. The cavity modes are coupled with SiC color centers to enhance collection efficiency and emission rate through the Purcell effect. We report significant advances in addressing fabrication challenges including sidewall tapering through optimized e-beam lithography using dual PMMA layers and refined etching recipes.

Summary of Research:

Silicon carbide hosts optically addressable spin defects that exhibit excellent quantum properties, including long spin coherence times (>1 ms) and near-infrared emission compatible with telecommunication infrastructure (1,2). However, the collection efficiency of photons from these color centers is limited by their low Debye-Waller factor (5% for divacancies) and the high refractive index of SiC (n = 2.6), which causes most emitted light to undergo total internal reflection. Photonic cavities can overcome these limitations through Purcell enhancement, increasing both the emission rate and the fraction of photons collected into desired optical modes (3,4). Here, we develop two cavity platforms that leverage different enhancement mechanisms: plasmonic nanopan cavities offering ultrasmall mode volumes and dielectric ring resonators on insulator providing high quality factors.

For the plasmonic nanopan cavity fabrication in Figure 1, we begin with 8×8 mm pieces of 4H-SiC. Prior to any fabrication steps, samples undergo thermal annealing at 650°C in vacuum for 1 hour to remove inherent defects and damage. The process is given in Figure 1. It first employs electron beam lithography with a bilayer resist structure consisting of 220 nm PMMA 495 A4 (spun at 1600 rpm) and 120 nm PMMA 950 A4 (spun at 6000 rpm) to create undercut profiles that mitigate sidewall angles, and each baked at 170°C for 15 minutes. An e-spacer layer (~25 nm) is applied without baking to prevent charging. Circular patterns with diameters ranging from 200-800 nm are exposed using a Nabity at 10kV with doses of 400-850 µC/cm². After development in 1:3 MIBK:IPA for 60s, we deposit 100 nm of nickel using the CVC SC4500 evaporator at 1.3 Å/s with intermittent cooling (20 nm deposition followed by 77s pause). Lift-off is performed in acetone overnight, followed by 5s brief ultrasonication.

The etching process utilizes Oxford COBRA ICP-RIE with an SF_6/O_2 chemistry (30:15 sccm) at 2000W/40W and 8 mTorr pressure, achieving an etch rate of ~5.5 nm/s. We address the sidewall taper issue by utilizing the undercut profile from the PMMA495/PMMA950 bilayer, which provides better pattern transfer fidelity compared to MMA/PMMA495 bilayer in our previous recipe. After etching to depths of 400 nm, the nickel mask is removed using Type 1 nickel etchant at 40°C for 10s. The SiC nanopillars are then encapsulated with 500 nm of silver deposited by CVC SC4500 evaporator, creating the plasmonic cavity structure. The devices (Figure 2a-d) demonstrate strong out-of-plane field confinement in FDTD simulations in Figure 2e, enabling the efficient coupling to c-axis oriented VSi dipoles and realizing photoluminescence enhancement (5).

For the SiCOI ring-waveguide resonators in Figure 3, we use commercially available 4H-SiCOI pieces with 540 nm SiC, 3044 um SiO2 and 680 µm Si layers (6). The fabrication is given in Figure 3. It first employs the same dual PMMA resist approach. To remove the edge

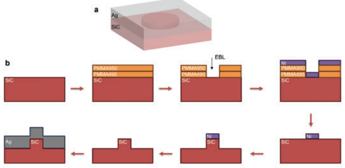

Figure 1: (a) Schematic of the SiC nanopan cavities. (b) Fabrication process flow for SiC nanopan cavities showing resist deposition, e-beam lithography, metal deposition, etching, and silver encapsulation steps.

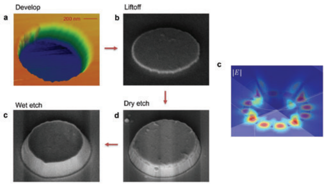

Figure 2: (a) AFM and SEM image of the fabricated SiC nanopan cavities of developing the resist, liftoff Ni mask, dry etching the SiC, wet etching the Ni mask. (b) FDTD simulation of SiC nanopan cavity's E field profile showing the whispering gallery mode TM12,0,0 the field concentration at SiC-silver interface. (c) Photoluminescence spectrum from silver nanopan cavity (red) compared to bare SiC substrate (black), showing enhancement of V1 and V1' emission lines around 860 nm.

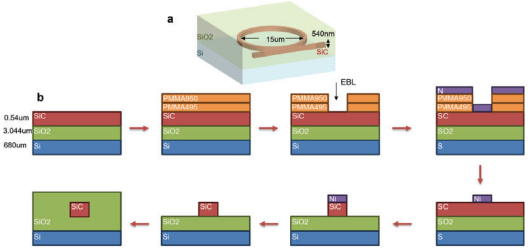

Figure 3: a) Schematic of the SiCOI ring-waveguide-grating devices. (b) Fabrication process flow for SiCOI ring-waveguide-grating devices showing resist deposition, e-beam lithography, metal deposition, etching, and silica cladding steps.

beads on the 5×5 mm SiCOI pieces, the sample piece is bond to the center of a dummy wafer and a dummy piece is bond side by side. Ring resonators with radii of 10-20 µm, waveguide width of 300-500 nm and grating couplers with of 2 µm width, 50% duty cycle and 420 nm pitch (7,8), are patterned by JEOL 6300 system in 10nA 60nm aperture with doses of 300-500 µC/cm². We deposit 100 nm nickel masks with the same duty-cycled evaporation to minimize thermal stress. The etching recipe was optimized to reduce the taper by adjusting SF_6/O_2 to 30:10 sccm.

The fabricated ring resonators exhibit smooth sidewalls. Coupling gaps of 300-700 nm between the ring and bus waveguides are achieved with good uniformity, to guarantee the critical coupling. After nickel mask removal, we deposit a SiO2 cladding layer using a two-step LPCVD process: first, 600 nm of high-temperature oxide (HTO) deposited at 1.5 nm/min to conformally cover the etched structures and fill narrow gaps, followed by 2 µm of low-temperature oxide (LTO) at 10 nm/min to provide a thick upper cladding for mode confinement and environmental protection. In Figure 4, preliminary transmission simulations show whispering gallery modes $TM_{m,0,0}$ with high quality factors due to the large refractive index mismatch of SiC and SiO2 layers. The grating coupler's simulated transmission gives a broad stop band centered at 860 nm close to V1 centers in SiC, which can provide good injection and reading of laser beam into the device.

Conclusions and Future Steps:

We have demonstrated two complementary approaches for creating photonic cavities in silicon carbide: plasmonic nanopan structures and SiCOI ring resonators for maximum field enhancement and high-Q operation. The optimized dual PMMA resist system and refined etching processes effectively address the sidewall taper challenges for us to tune the device performance. Future work will focus on precise spectral and spatial alignment of color centers with cavity modes through controlled ion implantation after cavity fabrication. We plan to perform detailed Purcell factor measurements using time-resolved photoluminescence and explore coherent control of cavity-coupled spins. Additionally, we will investigate hybrid integration approaches combining the high field enhancement of plasmonic structures with the low loss of dielectric cavities to approach the strong coupling regime necessary for deterministic quantum gates.

References:

[1] Castelletto, S. et al. Nat. Mater. 21, 67-73 (2022)
[2] Lukin, D. et al. Nat. Photonics 14, 330-334 (2020)
[3] Castelletto, S. et al. ACS Photonics, 9, 1434-1457 (2022)
[4] Ou, H. et al. Materials, 16, 1014 (2023)
[5] So, J. P. et al. Nano Letters, 24, 11669-11675 (2024).
[6] Yi, A. et al. Optical Materials, 107, 109990 (2020).
[7] Lukin, D. et al. arXiv preprint, 2504, 09324, (2025).
[8] Afridi, A. A. et al. Applied Physics Letters, 124 (2024).

Characterization of Silicon Carbide Wafers

CNF Summer Student: Tyrone Chen
Student Affiliation: Department of Material Science and Engineering , Cornell University College of Engineering

Summer Program(s): 2025 Cornell NanoScale Facility Research Experience for Undergraduates (CNF REU) Program
Mentor(s): Phil Infante, Cornell NanoScale Science and Technology Facility, Cornell University
Primary Source(s) of Research Funding: National Science Foundation under Grant No. NNCI-2025233,
Contact: tc724@cornell.edu, pi12@cornell.edu
Summer Program Website(s): https://cnf.cornell.edu/education/reu

Abstract:

This project focused on characterizing silicon carbide (SiC) thin films deposited using low pressure chemical vapor deposition (LPCVD). The films were grown from a mixture of dichlorosilane (DCS) and acetylene (C_2H_2) gas, with hydrogen gas as the carrier gas aiding deposition, at two deposition temperatures: 800°C and 850°C. To help isolate the electrical properties of the SiC layer itself, two types of substrates were used—plain silicon wafers and silicon wafers with a deposited layer of silicon oxide. All wafers were cleaned using a standard MOS process and loaded into the A4 SiC furnace for deposition, where the ratio of DCS to acetylene was systematically varied. After deposition, the films were analyzed for thickness, refractive index, intrinsic stress, and resistivity. A noticeable drop in stress or refractive index at certain gas ratios suggested a potential change in film crystalline structure In the final phase, ammonia (NH_3) was introduced during deposition to explore in-situ doping. Some of these doped films showed unexpectedly low stress and very high conductivity. One particular sample could not be accurately modeled using standard optical fitting tools, suggesting an unusual film structure or electronic behavior. While more work is needed, these results point toward new ways to engineer SiC films with customized electrical and mechanical properties.

Summary of Research:

This project focused on the low-pressure chemical vapor deposition (LPCVD) of silicon carbide (SiC) thin films using dichlorosilane (DCS) and acetylene (C_2H_2) gas. This work aimed to investigate the effects of deposition conditions—specifically gas ratios and temperature—on film characteristics such as thickness, refractive index, stress, and resistivity, with the broader goal of tailoring SiC films properties for potential semiconductor applications. A secondary goal was to explore the effect of ammonia (NH_3) doping on electrical and mechanical properties. The wafers used for deposition included both bare silicon wafers and silicon wafers with deposited silicon oxide layers. The oxide-coated wafers served to isolate the electrical properties of the SiC film by minimizing current leakage into the substrate. Prior to deposition, all wafers underwent a cleaning sequence beginning with a sodium hydroxide (NaOH) base bath, followed by a rinse, then an acid bath using hydrochloric acid (HCl), and a final rinse until the surface resistivity reached approximately 16 MΩ·cm. These wafers were then spun dry and ready for depositions. This surface preparation ensured minimal contamination and enabled consistent film growth.

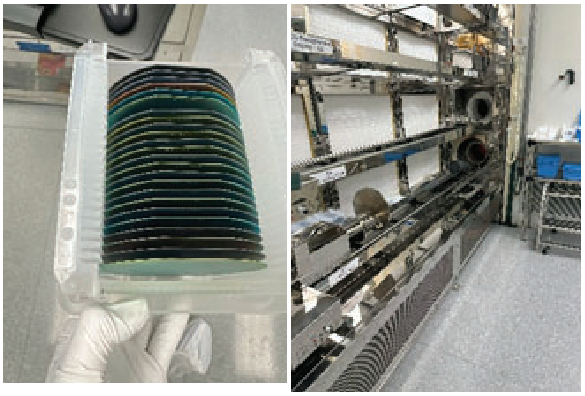

Figure 1: The picture on the right shows the furnace that was used for the deposition process. The picture on the left shows the resulted wafers that were deposited. As you can see the color of the wafers are an indicator of the thin film and this color may vary depending on the deposition conditions.

Deposition was carried out in the A4 SiC furnace under low-pressure conditions. The precursor gases—200 sccm of DCS and 50 sccm of acetylene had varying ratios where the DCS was kept at 31% max sccm while the acetylene ranged from 38% - 22% max sccm, while hydrogen was introduced as a helping gas. The hydrogen flow was found to be essential for achieving uniform films; wafers processed without it displayed black spots and non-uniform coverage. Depositions were performed at two temperatures: 800 °C and 850 °C. At 850 °C, deposition time was held around 70 minutes, while at 800 °C the process time was extended to approximately

140 minutes. These times were chosen to target a final film thickness of about 130 nm. Pressure within the furnace was actively controlled through a series of automated sequences including purging, pump-down, leak checking, and venting.

After deposition, multiple characterization techniques were used to assess the films. The RC Woollam ellipsometer was first used to measure the thickness and refractive index from the reflective surface of the wafer using a SiC optical model. The Filmetrics F50 tool was used to evaluate the thickness uniformity across the wafer surface. For stress analysis, the wafer backside was etched using the Oxford 82 system with a CF_4/O_2/Ar gas mixture to expose the front-side curvature. The curvature was then measured using the Flexus tool to calculate intrinsic film stress. Finally, the electrical resistivity of the SiC layers was measured using the Filmetrics R50 system, particularly on the oxide-coated wafers to ensure that the readings were specific to the film itself.

Across both the 800 °C and 850 °C deposition conditions, the silicon carbide thin films demonstrated consistent deposition rates, with no significant fluctuations observed as the gas flow ratio between dichlorosilane (DCS) and acetylene (C_2H_2) was varied. The refractive index of the deposited films remained relatively stable, ranging from 2.7 to 2.9 throughout all runs. In contrast, the resistivity of the films showed a clear downward trend as the DCS-to-acetylene ratio increased, indicating a correlation between gas ratio and film conductivity. Similarly, film stress exhibited a decreasing trend with increasing gas flow ratio at both temperatures. These trends were consistently observed across both sets of wafers and suggest reproducible control of key film properties through process parameter variation. These graphs are shown collectively in Figure 2.

In the doping experiment, ammonia (NH_3) gas was introduced in the deposition process at varying flow rates to explore its effect on the properties of the silicon carbide thin films. Across both 800 °C and 850 °C deposition temperatures, specific NH_3 gas flow settings resulted in films that exhibited high conductivity. At a deposition temperature of 800 °C, a flow rate of 20% max sccm resulted in a film that was highly conductive, as confirmed through resistivity measurements using the Filmetrics R50. Similarly, at 850 °C, a flow rate of 60% max sccm produced a film with high conductivity. These points of interest were repeated to confirm the observed results, and in each case, the outcome remained consistent. However, under these particular doping conditions, the RC Woollam ellipsometer was unable to return a valid model fit or measure the thickness of the films. This in turn resulted in no stress, refractive index, and deposition rate measurements for these wafers. Despite the incomplete optical characterization, the electrical measurements potentially indicate that NH_3 doping successfully altered the electronic properties of the silicon carbide films in certain cases.

Conclusions and Future Steps:

In conclusion this characterization demonstrates that the properties of SiC wafers can be tuned depending on gas ratios, temperatures and even external doping. As the acetylene gas concentration got lower, stress and resistivity also dropped. The introduction of ammonia gas can potentially lead to a more conductive wafer. Future work could focus on specific structural microscopy as the RC Woolam was not able to perfectly characterize some wafers. Other future work could also be in the introduction of ammonia and optimizing the conditions for the best conductivity.

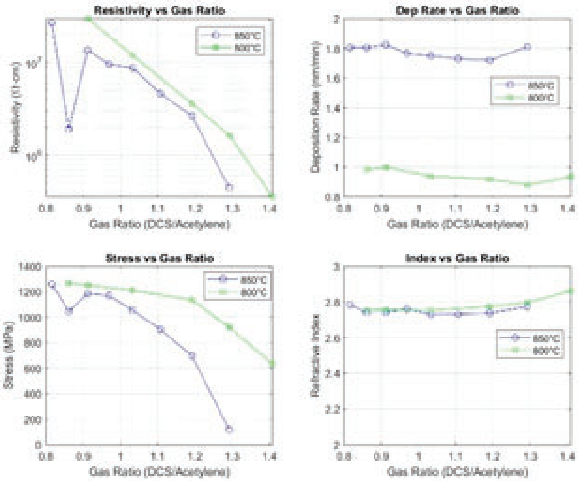

Figure 2: The graphs and their trends are shown above where blue represents 850 °C and green represents 800 °C.

Acknowledgements:

Special thanks to the 2025 Cornell Nanoscale Facility Research Experiences for Undergraduates (CNF REU) Program funded by the National Science Foundation (NSF). I would also like to thank the CNF staff, especially Phil Infante, for their incredible mentorship.

Baseline Etch Processes: Evaluating Etching and Stripping Tools

CNF Summer Student: Scott Coonrod
Student Affiliation: Cornell University College of Engineering

Summer Program(s): 2025 Cornell NanoScale Facility Research Experience for Undergraduates (CNF REU) Program

Mentor(s): Aaron Windsor, Cornell NanoScale Science and Technology Facility, Cornell University

Primary Source(s) of Research Funding: National Science Foundation under Grant No. NNCI-2025233,

Contact: windsor@cnf.cornell.edu, src252@cornell.edu

Summer Program Website(s): https://cnf.cornell.edu/education/reu

Primary CNF Tools Used: Oxford 81, Oxford 82, PT740, FilMetrics F50, P-7 Profilometer

Abstract:

Reactive Ion Etching is a technique that can achieve highly anisotropic etches, as well as high selectivity. Etching is performed by high energy ions as well as reactive species that interact with the surface, with an etch rate dependent on the recipe and the material being etched. Certain tools in the cleanroom, such as the PT740, Oxford 81, Oxford 82, and Glen 1000 all have stated etch rates for certain recipes. However, over time, these rates have changed from when the measurements were originally taken, meaning the manuals may no longer be accurate. The goal of this project is to measure the current etch rates of these machines across many recipes and materials to update the manuals, ensuring that future users will be able to more precisely etch their samples.

Summary of Research:

When measuring etch rates on the PT740, Oxford 81, and Oxford 82 tools, recipes stated in their respective manuals were used. Measurements of the samples before and after etching were performed by the FilMetrics F50 optical metrology tool, allowing for the characterization of etch rates across the sample. Silicon oxide wafers were deposited using 4 different PECVD methods; high rate, low rate, HDP, and TEOS deposition. Silicon Nitride wafers (figure 1) were produced with PECVD, LPCVD, HDP-CVD, as well as with the NIT N=2 recipe on the PT Takachi HDP-CVD. Carbide wafers were made by LPCVD. All aforementioned wafers were produced by Aaron Windsor. The Glen 1000 oxygen plasma tool was also characterized alongside the RIE machines. Three different resists were measured: Shipley 1813, nLof Az 2020, and SPR220-3.0. These were characterized using the RIE configuration of the Glen 1000 (figure 4), with etch rates measured using the P-7 profilometer. The final characterization that was performed was BARC (Bottom Anti-Reflective Coating) strip times. With a thin layer of BARC, incremental 1-minute runs on different machines were performed, until the coating was no longer measurable on the wafer. Two machines were able to remove the layer in under a minute; the Glen 1000 rack B (either 400 or 500 W), as well as the YES Ecoclean Asher using the recipe "0resist_strip_1min" (figure 2).

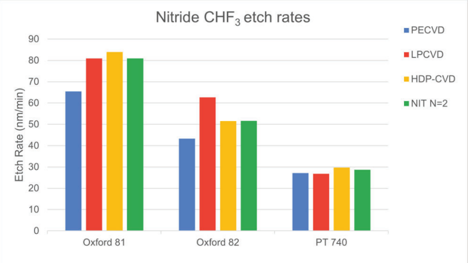

Figure 1

Figure 1: Etch rates over 3 tools and 4 deposition methods of silicon nitride, showing trend that the Oxford 81 is the fastest, followed by the Oxford 82, then the PT740.

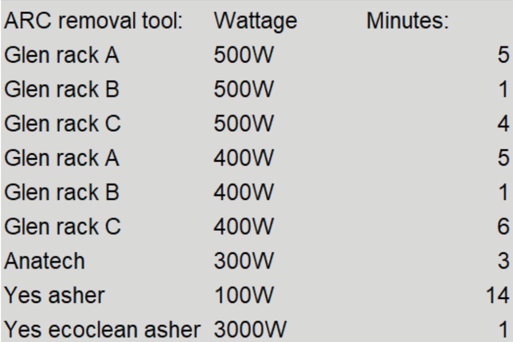

ARC removal tool:	Wattage	Minutes:
Glen rack A	500W	5
Glen rack B	500W	1
Glen rack C	500W	4
Glen rack A	400W	5
Glen rack B	400W	1
Glen rack C	400W	6
Anatech	300W	3
Yes asher	100W	14
Yes ecoclean asher	3000W	1

Figure 2

Figure 2: Time to remove ARC layer over different tools.

Etch/strip rates:

When comparing the measured etch rates with the etch rates stated in the manuals, two machines have changed considerably since the last time they were characterized.

The Oxford 82 recipe "CHF_3 / O_2 oxide etch" was stated to have an etch rate of 43 nm/min, however, the measured etch rate is only around 25 nm/min. The "CF_4 / O_2 oxide etch" also has decreased over time, as the stated etch rate is 42 nm/min, while the measured etch rate is

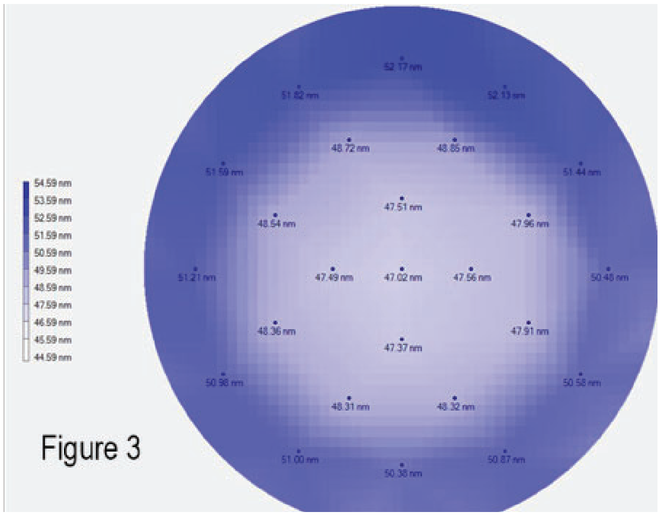

Figure 3

Figure 3: Difference map of before and after an etch with the PT740, showing a higher etch rate along the edge of the wafer.

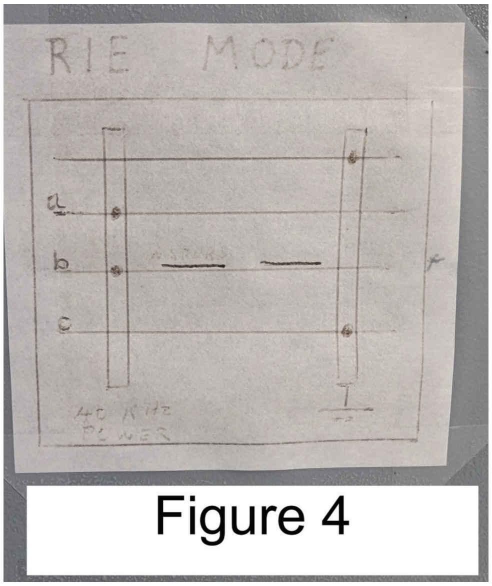

Figure 4

Figure 4: Design showing the configuration of the Glen 1000 during testing, with 1st and 4th rack being grounded, and the 2nd and 3rd rack attached to power.

closer to 21 nm/min. The Glen 1000, has significantly changed since the last characterization, which was taken around 2003. The old stated values for racks A, B, and C are respectively; 300nm/10min, 730nm/10 min, and 280nm/10 min. The current measured values are 92 nm/10 min, 410 nm/10 min, and 41 nm/10 min. The PT740 manual had one stated recipe that did not match the measured rate, that being the 'CHF_3 / O_2 nitride etch LSN", with the stated value being 19 nm/min, and the measured value 27 nm/min. However, this etch rate was characterized recently, and it is suspected that the etch rates of the PT740 vary due to other uncontrolled factors, so further testing would be required to definitively state whether this recipe needs to be updated.

Uniformity:

Tests were run on the RIE machines using 100mm wafers. The two Oxford 80 tools have similarly uniform etches, with a uniformity of around ± 2.5-3%. The Oxford 81 appears to etch slightly faster in the center than the outside, with the Oxford 82 being the opposite. With the PT740, however, it is clearly visible that the outside of the wafer etches with the highest rate, with the outside of the wafer (10mm from the edge) etching around 10% faster than the middle (figure 3). This machine has a uniformity across the wafer of around ± 5%.

Conclusions and Future Steps:

When etching Silicon compounds, the tool with the highest etch rate is the Oxford 81, followed by the Oxford 82 then the PT740. The fact that the two Oxford tools have differing etch rates is surprising, given that they are two identical instruments. The reason for this discrepancy is unclear, and determining and correcting the cause of this difference is a possible area for future work. Using this new data the recipes for the Oxford 82 stated in this report should be updated, as well as all the numbers on the Glen 1000. BARC stripping can now be suggested for some users with material restrictions to be done in the Glen 1000 rack B or the YES Ecoclean Asher could be used.

Acknowledgements:

Special thanks to Aaron Windsor and Lynn Rathbun for enabling me to have this amazing hands-on experience, as well as providing consistent support throughout this summer. I also would like to thank the rest of the Cornell NanoScale Science and Technology Facility for allowing me to perform this research.

References:

[1] Coburn, J.W., and Harold F. Winters. "Plasma etching—A discussion of mechanisms." Journal of Vacuum Science and Technology, vol. 16, no. 2, 1979. Accessed 4 8 2025.

[2] Link to data spreadsheet containing all measured etch rates: https://1drv.ms/x/c/402b9da0fc160dae/Efrv37R3g3JJlw8Ylu3WqJoBCddXBHjEDM6YexCmTonH5w?e=1vMcMx

Determining Out-of-Plane Structure via Electron Diffraction

CNF Summer Student: Tyler Hendee
Student Affiliation: Department of Engineering Physics, University of Wisconsin Platteville

Summer Program(s): 2025 Cornell NanoScale Facility Research Experience for Undergraduates (CNF REU) Program
Principal Investigator(s): Judy Cha, Department of Materials Science & Engineering, Cornell University
Mentor(s): Stephen Funni, Natalie Williams
Primary Source(s) of Research Funding: National Science Foundation under Grant No. NNCI-2025233
Contact: rjc476@cornell.edu, hendeet@uwpatt.edu, sdf68@cornell.edu, nlw49@cornell.edu
Summer Program Website(s): https://cnf.cornell.edu/education/reu
Research Group Website: https://cha.mse.cornell.edu/

Abstract:

In situ studies of phase transitions in materials are essential to understanding structure evolution, and thus engineering for novel or advanced applications [1]. This is especially true in battery materials where dramatic, intercalation-induced phase transitions impact safety, reliability, and performance [2]. Scanning transmission electron microscopy (S/TEM) provides simultaneous imaging, diffraction, and spectroscopy data from a single instrument. However, in situ intercalation experiments in the TEM are uncommon and often rely on highly specialized holders [3]. Here we characterize the complete lithiation-induced phase transition in the layered van der Waals (vdW) material, lanthanum tritelluride ($LaTe_3$), using a standard electrical biasing holder by fabricating electrochemical cells that are liquid-free.

Throughout lithiation of the $LaTe_3$ flake, we observed at least two distinct phase transformations, various $LaTe_3$ stackings, and an expansion and subsequent relaxation of the in-plane lattice. During this experiment, several types of data were acquired: atomic resolution and low-magnification STEM imaging, electron energy loss spectroscopy (EELS), and spatially resolved diffraction using four-dimensional STEM (4D STEM). The combined analysis of these datasets reveals the morphological, electronic, chemical and structural changes of the flake during intercalation. The experimental patterns observed were replicated by multislice simulations (abTEM [5]) from different 1x1x3 supercells with lithium ordering in vdW gap interstitials (Figure 2).

A later experiment includes 4D STEM data from convergent beam electron diffraction (CBED). This provides out-of-plane structure due to interactions with the higher order Laue zone (HOLZ) of the reciprocal lattice. Simulations confirm individual stackings are distinguishable from each other and from out-of-plane disorder. CBED analysis via Hough circle transforms [6] allows us to measure out-of-plane strain.

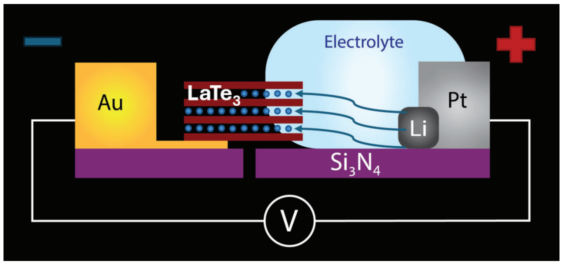

Figure 1: The all solid-state electrochemical cell, where the voltage bias controls lithium intercalation in the vdW gaps between $LaTe_3$ layers.

Summary of Research:

In each in situ experiment, we utilize an off-the-shelf electronic chip (e-chip) placed in a standard Protochips Fusion350 heating/biasing holder. The all solid-state electrochemical cell is displayed in Figure 1. At the start of the experiments, the $LaTe_3$ flake is in the pristine state, as shown in Figure 2a. EELS analysis tells us there is no detectable lithium in this phase. In the first experiment, after measuring an open circuit voltage of 2.3 V, we initiated intercalation by lowering the cathode potential to 0 V (vs Li anode). After 10 minutes, we observed an intercalation-induced new phase propagated across the flake, verified by low magnification STEM imaging. The EELS data taken 35 minutes after initiating intercalation showed an increase in intensity following the Li-K edge onset at 57 eV. Representative diffraction patterns in this phase revealed two lithiated structures with the same ordering: one maintaining the bulk stacking and one with a layer shifted by half the lattice (Figure 2b), as seen in the alignment of Te-nets across the vdW gap. 4D STEM analysis at this stage showed significant in-plane lattice expansion of approximately 1.5%.

After continuing intercalation at the 0 V cathode potential, the flake did not exhibit further significant changes. Approximately 4 hours into the experiment, we lowered the cell voltage to -9 V. By the 5.5-hour mark, we observed a second major phase transformation. The lithium-ordering superlattice disappeared (Figure 2c) and the previous in-plane lattice expansion had relaxed. Simulated diffraction of the proposed structures matches the experimental diffraction patterns from their respective lithiated phases (Figure 2). We attribute the in-plane strain relaxation to the addition of out-of-plane unit cell expansion. CBED simulations result in diffraction patterns containing HOLZ rings, whose radii we measure with Hough circle transforms. This analysis is robust to sample tilt, and the measured radius of HOLZ rings is inversely correlated with the out-of-plane strain of each stacking (Figure 3). The CBED patterns of different stackings are distinguishable from one another, which allows us to measure out-of-plane strain while preserving phase information.

We determined the optimal TEM parameters with more simulations, then ran the experiment again using scanning CBED. Preliminary analysis shows significant out-of-plane disorder in later stages of lithiation. This causes the HOLZ rings to blur, making them more challenging to measure with the Hough circle transform alone. We aim to increase the precision of our measurement method and subsequently pair it with a radial average integration technique. Currently, we are using simulations to investigate the resultant diffraction patterns caused by various types of disorder.

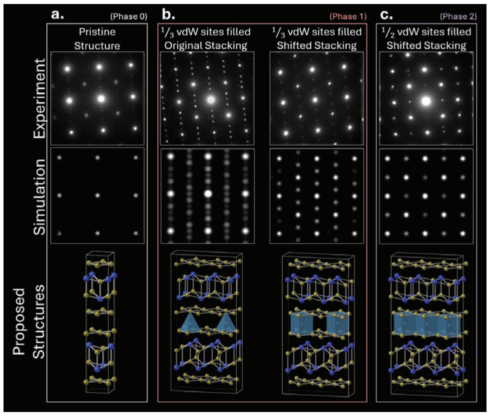

Figure 2: (a) The pristine structure, which contains no lithium, (b) the first phase transformation, where 1/3 of the vdW sites are filled and we observe the original as well as a shifted stacking, and (c) the second phase transformation, where 1/2 of the vdW sites are filled and we only observe shifted stacking.

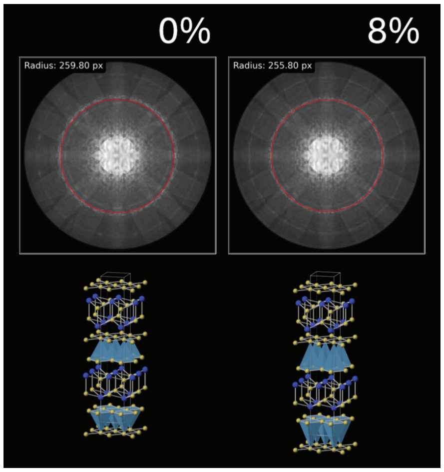

Figure 3: A demonstration of the inverse relationship between out-of-plane unit cell expansion and HOLZ ring radius.

Conclusions and Future Steps:

In situ experiments allowed us to identify two distinct phase transformations of $LaTe_3$ via multimodal STEM (imaging, EELS, and 4D STEM). To enable this complete characterization in a single experiment, we developed an all solid-state electrochemical cell on a standard Si_3N_4 membrane-style TEM e-chip. We developed techniques for mapping structural information during the intercalation process, including out-of-plane stacking and unit cell expansion. We perform these measurements over large fields of view using 4D STEM. With abTEM multislice simulations, we determined optimal CBED parameters and repeated the intercalation experiment. Looking forward, we aim to improve measurement precision, further investigate out-of-plane disorder, and complete the remaining analysis of our latest dataset. Our method should enable future investigations of other intercalation materials to directly and comprehensively observe their phase transformations.

References:

[1] M. Wang, S. Xu, and J. J. Cha, “Revisiting Intercalation-Induced Phase Transitions in 2D Group VI Transition Metal Dichalcogenides,” Advanced Energy and Sustainability Research, vol. 2, no. 8, p. 2100027, 2021, doi: 10.1002/aesr.202100027.

[2] M. Rajapakse et al., “Intercalation as a versatile tool for fabrication, property tuning, and phase transitions in 2D materials,” npj 2D Mater Appl, vol. 5, no. 1, pp. 1–21, Mar. 2021, doi: 10.1038/s41699-021-00211-6.

[3] C. Wang, R. Zhang, J. Li, and H. L. Xin, “Resolving electrochemically triggered topological defect dynamics and structural degradation in layered oxides,” Proceedings of the National Academy of Sciences, vol. 122, no. 3, p. e2409494122, Jan. 2025, doi: 10.1073/pnas.2409494122.

[4] M. W. Tate et al., “High Dynamic Range Pixel Array Detector for Scanning Transmission Electron Microscopy,” Microscopy and Microanalysis, vol. 22, no. 1, pp. 237–249, Feb. 2016, doi: 10.1017/S1431927615015664.

[5] J. Madsen and T. Susi, “The abTEM code: transmission electron microscopy from first principles,” Open Research Europe, vol. 1, p. 24, Mar. 2021, doi: 10.12688/openreseurope.13015.1.

[6] Xie, Yonghong, and Qiang Ji. "A new efficient ellipse detection method." Pattern Recognition, 2002. Proceedings. 16th International Conference on. Vol. 2. IEEE, 2002, doi: 10.1109/ICPR.2002.1048464

Silicon Interposer for Millimeter-Wave Heterogenous Integration: Doped vs. High Resistivity Substrates

CNF Summer Student: Kenta Lin
Student Affiliation: Ming Hsieh Department of Electrical and Computer Engineering; University of Southern California

Summer Program(s): 2025 Cornell NanoScale Facility Research Experience for Undergraduates (CNF REU) Program
Principal Investigator(s): James C. M. Hwang
Mentor(s): Jin Hong Joo
Primary Source(s) of Research Funding: National Science Foundation under Grant No. NNCI-2025233, SUPREME
Contact: jch263@cornell.edu, kentalin@usc.edu, jj593@cornell.edu
Summer Program Website(s): https://cnf.cornell.edu/education/reu
Research Group Website: https://cha.mse.cornell.edu/
Primary CNF Tools Used: SUSS MA6-BA6 Contact Aligner, AJA Sputter Deposition, UNAXIS 770 Deep Silicon Etcher, PlasmaTherm Versaline System, Veeco Savannah ALD, ReynoldsTech Cu ECD Hood, DC Probe Station, Microwave Small-Signal Probe Station

Abstract:

As the demand for heterogeneous-integrated RF chips increases, interposers for millimeter-wave circuits using through-silicon vias (TSVs) have become increasingly important due to their low loss and high- power capacity across a wide frequency range. For frequencies above 110 GHz, substrate-integrated waveguides (SIWs) are small enough to be integrated in Si interposers for high-power interconnects.

They can also be used to form high-quality passive devices such as filters and antennas, which have been difficult to integrate on-chip. This enables system-on-chip. In this study, we investigate the fabrication of SIWs and grounded coplanar waveguides (GCPWs) in silicon (Si) interposers with a thickness on the order of 200 um with resistivities ranging from 10 to 1 kΩ·cm. Thin Si wafers were patterned and etched using the Bosch deep reactive ion etching (DRIE) process to create TSVs. The TSVs are then metallized with platinum (Pt) using atomic layer deposition (ALD) and filled with copper (Cu) using electroplating deposition. DC measurements confirm a TSV series resistance of less than 1 Ω. Small-signal millimeter- wave on-wafer measurements show that the coplanar interconnects fabricated on high-resistivity (HR, resistivity > 1 kΩ·cm) Si have an insertion loss of 0.7 dB/mm at 40 GHz, an order of magnitude better than the same coplanar interconnects fabricated on doped Si (resistivity < 10 Ω·cm).

Summary of Research:

Si is the most extensively used material in semiconductor devices due to its exceptional electrical and mechanical properties, including a high dielectric constant, electrical resistivity, breakdown strength, and low loss tangent. These characteristics make it an attractive candidate for SIWs. However, its relatively low mechanical toughness and high thermal conductivity compared to materials like silicon carbide (SiC) pose challenges during processing, particularly in etching processes. Our group has previously demonstrated SiC as a viable substrate material for SIW processing. The methodology developed for SiC SIW fabrication is adapted as a proof of principle for Si SIW fabrication.

To develop a processing recipe for Si-based SIWs, we used a thinned HR Si wafer with a thickness of approximately 200 µm and resistivity greater than 1 kΩ·cm. Building on a similar methodology used for SiC SIWs while leveraging the more mature and faster etching processes available for Si, we began by depositing a 50 nm layer of aluminum oxide (Al2O3) on the wafer's backside using AJA Sputter

Deposition. Al2O3 was selected as the etch mask due to its excellent masking performance in the Bosch DRIE process for Si, providing a high selectivity greater than 1:1000.

The DRIE was performed using either the UNAXIS 770 Deep Silicon Etcher or the PlasmaTherm Versaline System. To ensure effective cooling during etching, the Si wafer was bonded to a sapphire carrier wafer using cool grease. The etching chemistry employed C4F8/SF6, which react with Si to anisotropically form vias. As shown in Figure 1, this process yielded 200 um-deep TSVs with a diameter of 50 um and sidewall angles ranging from 80° to 90°.

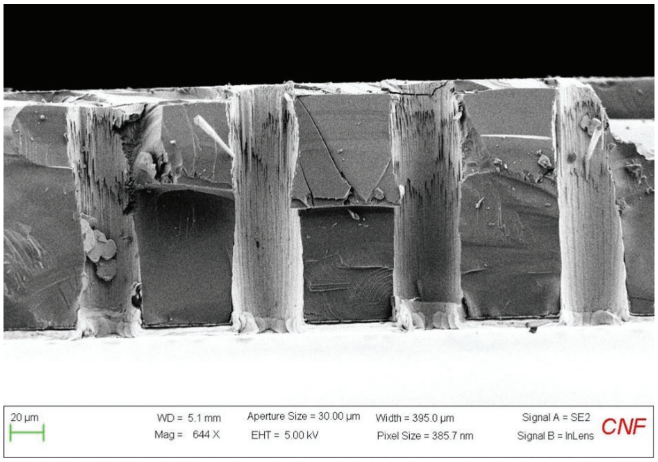

Figure 1: Cross-Sectional SEM Images of TSVs.

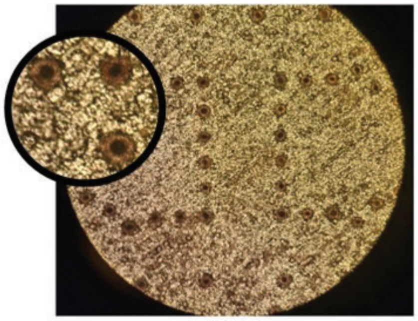

Figure 2: Top-View Optical Image of TSVs After Cu Electroplating.

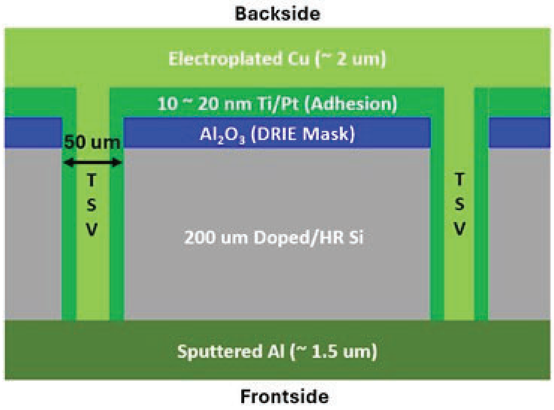

Figure 3: Schematic of Si Interposer Layout.

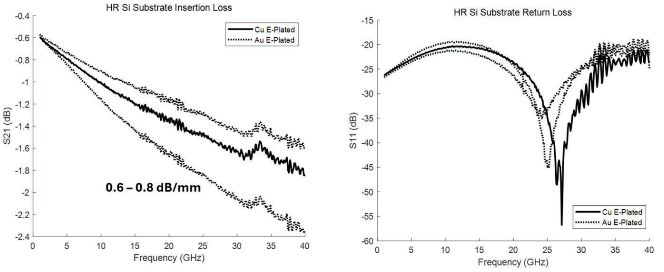

Figure 4: Measured Insertion Loss (S21) and Return Loss (S11) of HR Si Substrate Across 1 – 40 GHz.

After the TSVs were fully etched through, ALD was used to coat the TSV sidewalls with a Pt seed layer. Cu was then electroplated to fill the TSVs, initiating from the Pt seed layer, as illustrated in Figure 2.

Once the backside processing was completed, the front side was patterned with SIW and GCPW lines. A titanium/aluminum (Ti/Al) layer was subsequently deposited using AJA sputter deposition. The structural details and final device configurations are shown in Figure 3.

Both HR and doped Si devices were tested at the High Frequency Test Lab (HFTL) where TSV series resistance and GCPW line performance were evaluated. Using the DC probe station, I-V measurements showed that the TSV series resistance was typically below 1 Ω for both HR and doped Si substrates. RF measurements were then conducted over 1 – 40 GHz range using the small-signal probe station, as shown in Figure 4. For HR Si, insertion loss (S21) values ranged from 0.6 to 0.8 dB/mm, with return loss (S11) exceeding 20 dB. In comparison, doped Si devices exhibited insertion loss of approximately 3.2 dB/mm and return loss greater than 10 dB.

Conclusions and Future Steps:

The fabrication of Si interposers focused on optimizing Bosch DRIE of thinned Si wafers and refining metallization processes to achieve uniform anisotropic etching and consistent metal filling across the wafer. Measurements comparing HR and doped Si substrates revealed that HR Si exhibits insertion loss an order of magnitude lower than that of doped Si, highlighting its potential as a promising substrate material for millimeter-wave applications. Looking ahead, with updated tools and improved techniques for etching and metallization, fully metal-filled TSVs are expected to achieve insertion losses below 0.5 dB/mm at frequencies up to 220 GHz, utilizing the 220 GHz single-sweep probe station at HFTL.

References:

[1] M. J. Asadi, L. Li, K. Nomoto, Y. Tang, W. Zhao, P. Fay, D. Jena, H. G. Xing, and J. C. M. Hwang, “SiC Substrate Integrated Waveguides for High-Power Monolithic Integrated Circuits Above 110 GHz,” 2021 IEEE MTT-S Int. Microw. Symp. (IMS), Atlanta, GA, USA, 2021, pp. 669-672.

[2] D. Malta, E. Vick, S. Goodwin, C. Gregory, M. Lueck, A. Huffman, and D. Temple, “Fabrication of TSV-based silicon interposers,” 2010 IEEE International 3D Systems Integration Conference (3DIC), Munich, Germany, 2010, pp. 1–6.

[3] M. Leskela and M. Ritala, Thin Solid Films 409, 138 (2002).

[4] F. Laermer et al., IEEE Microelectromech. Syst. 211 (1999).

Alpha-Tantalum Thin Film Deposition on Pure Silicon Wafers with the Angstrom-Q

CNF Summer Student: Porter Rowbotham
Student Affiliation: Mechanical Engineering, Rochester Institute of Technology

Summer Program(s): Summer 2025 CNF NORDTECH Intern
Mentor(s): Aaron Windsor - Thin Film Process Engineer, CNF
Primary Source(s) of Research Funding: NORDTECH
Contact: pjr4887@rit.edu
Research Group Website: https://www.nordtechub.org
Primary CNF Tool Used: Angstrom-Q, Filmetrics R50, Zeiss Ultra SEM

Abstract:

Material choice in superconducting quantum circuits can greatly impact device coherence and losses. Recently, Tantalum thin films have shown great potential for transmon qubit fabrication, boasting high resonating times and high quality[1]. Tantalum's α crystal phase is especially important as it boasts a superconducting critical temperature of 4.2°K. Recent studies have shown that using a heated substrate can enable α-Tantalum thin film deposition [2,3,4]. The Cornell Nanoscale Facility recently introduced a new quantum-oriented electron beam evaporation tool witwh the capabilities to deposit these films, the Angstrom-Q. The project for this summer is to find the transition temperature where α-Tantalum can be deposited.

Summary of Research:

All samples for this project are deposited on 100mm undoped silicon wafers. All Tantalum depositions are completed at 1Å/s to a final thickness of 500Å.

Deposition Temperatures:

The temperature at which deposition takes place across different tools for α-Tantalum deposition can vary greatly based on the temperature measurement or deposition method. Sputtering an α-tantalum film may require a higher heat than evaporation as evaporation's particles carry heat onto the surface of the substrate. With studies showing α-Tantalum growth at 350°C [2], 400-500°C[3], and 600-650°C[4]. With this data, we chose to do a baseline run at room temperature, and then start at 350°C, moving at 50°C increments until the transition temperature is found, then move to 10°C increments.

Wafer cleaning:

One of the most important steps in creating a high quality α-Ta film is the cleaning. The wafers are RCA cleaned at the CNF MOS tanks, followed by a 60s bath in 20:1 HF to remove any surface oxides. This process remained until a water-streaked, highly non-uniform film began to appear at deposition temperatures above 425°C. We suspected that the HF bath in the MOS bath may be contaminated, or that the wafer was being oxidized by spending too long being rinsed in DI water. To correct this, we switched to removing the surface oxides by using 10:1 HF for 60s and 30s dip in DI water by hand. Additionally, it was found that the samples should spend less than one hour between the finish of the MOS clean and being processed.

Heated Deposition:

Once the wafer is fully cleaned and has its surface oxides stripped, it is placed in the Angstrom-Q load lock and put under vacuum. This is done in less than ten minutes to avoid the re-growth of surface oxides. Once in the machine, the wafer is heated to the desired deposition temperature, and then held at that temperature for 60 minutes to ensure even heating across the substrate. The wafer and carrier are allowed to cool and removed once reaching a temperature lower than 100°C.

Resistivity:

One convenient method to determine the crystallinity of a tantalum film is the film's resistivity. The room temperature resistivity of β-Ta is 150-200μΩ-cm and the resistivity of α-Ta is 15-20μΩ-cm [3]. We used the Filmetrics R50 four point probe to measure the sheet resistance of the film, then multiplied the sheet resistance by the thickness of the film to find the resistivity of the samples (Figure 1).

X-Ray Diffraction:

X-Ray Diffraction (XRD) scans were completed on all of the samples using the Rigaku SmartLab X-ray Diffractometer at the Cornell Center for Materials Research by Lingda Kong. Matching known scan peaks to our experimental runs shows what crystalline phase the sample is (Figure 2).

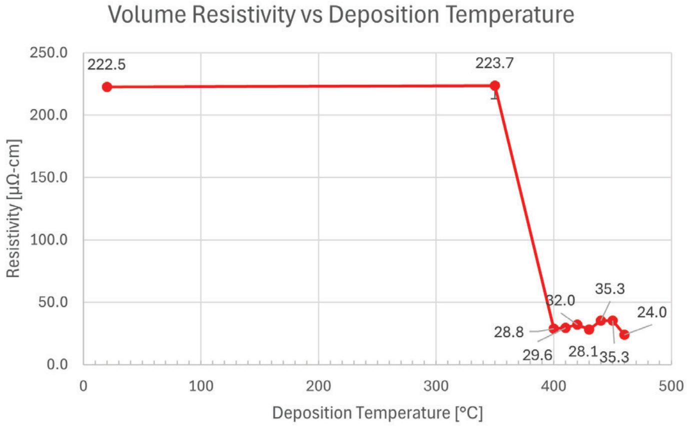

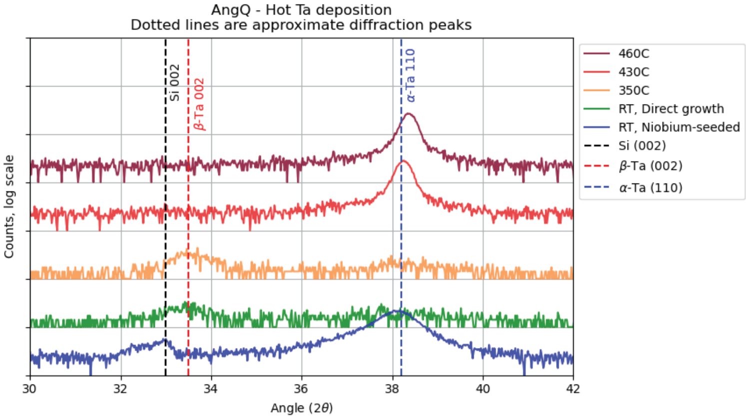

Figure 1 (Left): Volume Resistivity of Samples vs. their Deposition Temperature. Figure 2 (Right): X-Ray Diffraction Scans of Several Samples

Seed Layers:

A popular method for growing an α-Tantalum film is to use a thin layer of another material to avoid Tantalum-Silicon interactions and promote the correct crystalline phase. We did one Niobium seeded Tantalum deposition with 5Å of Niobium and 50Å of Tantalum, both deposited at 1Å/s at room temperature. The niobium seed layer sample had a RT resistivity of 60.8μΩ-cm. XRD scanning showed a peak around the α-Tantalum region without a peak in the α-Tantalum range (Figure 2).

Conclusions and Future Steps:

With this data, we can conclude that mostly pure α-Tantalum depositions on pristine silicon wafers at temperatures above 400°C, and that the transition temperature may lay in the 350-450°C range. Niobium seeded tantalum deposition shows α-Tantalum results at room temperature. Further depositions could be used to find the exact temperature range to form pure α-Tantalum. Additionally, films should be investigated to see if Tantalum Silicides (TaSi2) are being formed. Once completed, quantum computing components could be fabricated.

Acknowledgements:

Special thanks to NORDTECH and the Cornell Nanoscale Facility for funding and hosting this internship. Thanks to my CNF staff mentor Aaron Windsor, and CNF staff Shilling Du for their help and guidance. Thanks to Fatemi Lab, and its members Lingda Kong and Tathagata Banerjee for all of their helpful insights and guidance.

References:

[1] A.P.M. Place, L.V.H. Rodgers, P. Mundada et al. “New material platform for superconducting transmon qubits with coherence times exceeding 0.3 milliseconds,” Nat Commun 12(1), (2021).https://doi.org/10.1038/s41467-021-22030-5

[2] G. Marcaud, D. Perello, C. Chen, et al. “Low-Loss Superconducting Resonators Fabricated from Tantalum Films Grown at Room Temperature,” (2025). https://doi.org/10.48550/arXiv.2501.09885

[3] D.P. Lozano, M. Mongillo, X. Piao, et al. “Low-loss α-tantalum coplanar waveguide resonators on silicon wafers: fabrication, characterization and surface modification,” Mater. Quantum. Technol. 4(2), 025801 (2024).https://doi.org/10.1088/2633-4356/ad4b8c

[4] 1 M.P. Bland, F. Bahrami, J.G.C. Martinez, et al. “2D transmons with lifetimes and coherence times exceeding 1 millisecond,” (2025).

Characterization of Silicon Oxide Etching with Low Global Warming Potential Hydroolefin

CNF Summer Student: Elyas Talda
Student Affiliation: Rochester Institute of Technology

Summer Program(s): 2025 Cornell NanoScale Facility Research Experience for Undergraduates (CNF REU) Program

Mentor(s): Jeremy Clark , Cornell NanoScale Science and Technology Facility, Cornell University

Primary Source(s) of Research Funding: National Science Foundation under Grant No. NNCI-2025233,

Contact: clark@cnf.comell.edu, ehtalda@gmail.com

Summer Program Website(s): https://cnf.cornell.edu/education/reu

Primary CNF Tools Used: Gamma Automatic Coat-Develop Tool, ASML PAS 5500/300C DUV Wafer Stepper, P7 Profilometer, Zeiss Ultra SEM, Zeiss Supra SEM, Oxford 82 Etcher, Oxford 100 ICP-RIE Dielectric Etcher, YES EcoClean Asher, and Thermal Oxidation Furnace

Abstract:

The semiconductor industry utilizes hydrofluorocarbons (HFCs) for many different etch processes. HFCs, however, have high global warming potential (GWP). The American Innovation and Manufacturing Act of 2020 enabled the U.S. EPA to scale down the use and production of HFCs. Hydroolefins (HFOs), originally created by the refrigerant industry to reduce reliance on HFCs, show promise as an etch gas in reactively ion etched (RIE) anisotropic etching. This work explores the optimal etch conditions of

HFO-1234ze(E), or $C_3H_2F_4$ on the Oxford PlasmaLab 100 Inductively Coupled Plasma Reactive Ion Etcher. Etch rates remained similar to other oxide etch chemistries, though RIE lag remains a concern, especially with higher concentrations of $C_3H_2F_4$ in the plasma. Deposition and delamination occurred occasionally in the process of characterization, when $C_3H_2F_4$ concentration was too high or the DC voltage bias became too low. $C_3H_2F_4$ holds promise for regular use as a silicon oxide etch gas with more characterization and process research.

Summary of Research:

Silicon oxide is a common etch material in the semiconductor industry and is often etched with hydrotluorocarbons (HFCs) for their versatility and availability1. Though HFCs are not ozone-depleting, they have high global warming potentials (GWP), contributing to global warming in the atmosphere. The AIM Act of 2020 allowed the EPA to begin the scale down in use and production of HFCs, creating a need in the semiconductor industry for new silicon oxide etch gases. HFO-1234ze(E), or $C_3H_2F_4$ has shown potential in silicon etching but it has not been characterized definitively1,[2]. A broad analysis was thus conducted to test the etch rate, selectivity, sidewall angle, and RIElag of various etch recipes of $C_3H_2F_4$. RIElag is the effect of smaller features etching at a slower rate to larger features. It can be reduced by altering the properties of an etch plasma. The Oxford PlasmaLab 100 was used to characterize $C_3H_2F_4$ since, as an ICP etcher, it allowed the individual control of multiple different parameters, controlling the plasma both chemically and physically. Patterned and blank silicon oxide wafers were tested on the Oxford 100 over the course of the experiments.

About 1 micron of silicon oxide grown on Silicon test wafers in a wet oxide furnace. Most wafers were patterned using the Gamma Automatic Coat-Develop Tool, though some wafers were hand-spun, replicating the Gamma processes. BARC was spun on wafers for 30 seconds at 2400 rpm, before a 60-second, 205° bake. Next, UV210-0.6 photoresist was spun at 2900 rpm for 30 seconds, with a 60-second, 135° bake. The wafers were patterned using the ASML PAS 5500/300C DUV Wafer Stepper. Two patterns were used, a standard edge-clear pattern and the ALE Test Mask for RIElag that has trenches of varying width, from 5 micron to 300 nm, with large additional corner features. Finally, the wafers were developed with a 135° bake for 90 seconds, before a 60-second 724MIF develop.

Every patterned wafer had an BARC removal with a I-minute, 45-second ARC etch on the Oxford 82. After, step height of the large corner features was measured with the P7 Profilometer using a shortened version of a pre-existing sequence, testing 10 different comers. Each wafer was etched in the Oxford 100. Prior to each etch, the Oxford 100 was cleaned and seasoned for 2 minutes with either a bare silicon wafer or a blank silicon oxide wafer, to test for deposition. After etching in the Oxford 100, the P7 sequence was run again before the wafer was cleaned with a 5-minute photoresist-strip recipe on the YES EcoClean Asher. A last step height measurement was taken with the P7 sequence. Each relevant wafer's depth and sidewall angle of the largest and smallest feature was measured using the Zeiss SEM Ultra. Wafers with deposition etches were measured for the height of the deposition. Wafers that delaminated or etched less than 40 nm of silicon oxide were not measured on the SEM.

Table 1: Initial Characterization Etches and Results.

Etch Recipe and Time	Oxide Etch Rate (nm/min)	Selectivity Oxide:Resist	Avg. Sidewall Angle	RIELAG
$C_3H_2F_4$ High He (2 min)	217	6.3	95	0.72
CH_2F_2/High He (116 sec)	156	2.8	98	0.80
CHF_3/O2 Oxide (2 min)	168	1.7	93	0.83
C_4F_6/High He Oxide (2 min)	261	1.4	135	0.98
5 sccm CH_2F_2, 40 sccm C_4F_6, 3 sccm C_4F_8, 20 sccm Ar (2 min)	231	1.9	127	0.98

Table 2: Final Experiment Parameters

Parameter	Min	Max
ICP (W)	1500	2500
RIE (W)	40	80
Pressure mTorr	4	8
Gas Ring	Off	On
$C_3H_2F_4$ (sccm)	10	30
He (sccm)	20	90
Ar (sccm)	0	50

Table 1 (Left): The five etches used and their resulting etch rates. Table 2 (Right): Final Experiment Parameters.

A round of characterization etches compared the capabilities of the given $C_3H_2F_4$ recipe to that of other common silicon oxide etch recipes. Table 1 shows the five etches used and their resulting etch rate, selectivity, and RIElag. RIElag was calculated by the ratio of the smallest feature's depth to the largest feature's depth; the closer the value to 1, the less lag in etch rate of smaller features. The results confirmed that $C_3H_2F_4$ held potential as a silicon oxide etch gas. It had similar results in etch rate and sidewall angle, which was measured as the inside angle from the etched depth to the sidewall. Selectivity was improved from the other etches, but RIElag was worse. Thus, RIElag was the focused goal of continuing experimentation with additional goals of staying on target with selectivity, etch rates, and sidewall angle.

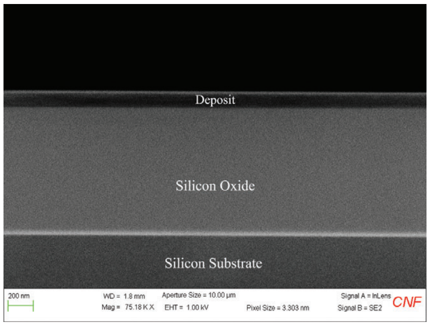

Figure 1: Deposition wafer.

Next, an experiment was designed using the JMP DOE software to find the optimal way to characterize multiple parameters within the etch recipe in a minimum number of wafers. The initial parameters used were the chamber pressure, the RF power, the ICP power, the usage of the gas ring to dispense $C_3H_2F_4$, and the concentration of $C_3H_2F_4$ to Helium. The experiment, however, immediately resulted in much deposition instead of etching. The experiment was ended to allow for more characterization attempts with blank silicon oxide wafers to determine better value ranges for each parameter. Many of these characterization attempts resulted in deposition, with some wafers having nearly 400 nm of C_2F_4 deposited in 2 minutes, and delamination, slowly approaching more appropriate value ranges. A deposition wafer is shown in Figure 1. From this characterization, it was determined that high concentrations of $C_3H_2F_4$ and low DC voltage bias were likely causes of deposition.

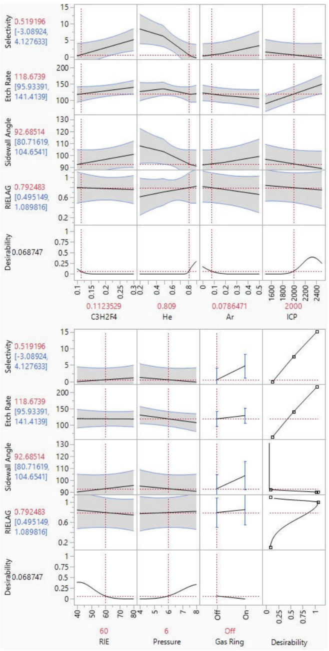

Figure 2: Results from Argon addition.

A secondary experiment design was created with JMP DOE. The modified parameters are shown in Table 2. Argon was added to the process to determine its influence. 20 wafers were run through this experiment. The results were formatted into a fit model and are shown in Figure 2. Etch rates ranged from 10 nm/min to 211 nm/min. Selectivity and sidewall angle remained on target with other silicon oxide etch recipes. RIElag varied with only a few recipes improving from the original's capability. From the results, it is evidenced that lower concentrations of $C_3H_2F_4$ with higher concentrations of Helium result in the best etch rate, RIElag, and sidewall angle. It should also be noted that there is a connection between increased RIE power and decreased RIElag, which would be a site for future research to build on. Though the results of this study were broad, they support further research and characterization on $C_3H_2F_4$ for future use across the semiconductor industry as a low GWP silicon oxide etch gas.

References:

[1] Windsor, Aaron J., Jeremy C. Clark, George McMurdy, Eric A. Joseph, Robert G. Syvret, Ronald J. Olson, and Judy J. Cha. 2025. "Viability ofHFO-1234ze(E) (Trans-1,3,3,3-tetrafluoropropene) as a Low Global Warming Potential Silicon Dioxide Etch Gas." Journal of Vacuum Science & Technology B Nanotechnology and Microelectronics Materials Processing Measurement and Phenomena 43 (2). https://doi.org/10.1116/6.0004194.

[2] H. Omori, A. Kikuchi, A. Yao and I. Mori, "Evaluation of etching property in C3HXF(6-X) plasma," 2016 IEEE 16th International Conference on Nanotechnology (IEEE-NANO), Sendai, Japan, 2016, pp. 127-130, doi: 10.1109/NANO.2016.7751309.

Characterization of the Heidelberg MLA 150

CNF Summer Student: Jason Xu
Student Affiliation:

Summer Program(s): 2025 Summer CNF NORDTECH Intern

Mentor(s): Giovanni Sartorello , Cornell NanoScale Science and Technology Facility, Cornell University

Primary Source(s) of Research Funding: National Science Foundation under Grant No. NNCI-2025233, The Northeast Regional Defense Technology Hub

Contact: tjp83@cornell.edu, jasonxu810@gmail.com

Research Group Website: https://www.nordtechub.org

Primary CNF Tools Used: AJA Q, AJA Q2, Filmetrics R50, FleXus Film Stress Measurement, Hamatech Hot Piranha, P-7 Profilometer, Veeco Icon AFM

Abstract:

This research on the Heidelberg MLA 150 focuses on three key areas to optimize its performance: Dose and Defocus Tests, Alignment Tests, and Resist Characterization. The Dose and Defocus Tests aim to identify the ideal energy (dose) and laser optics position (defocus) for machine operation, with particular emphasis on regularly monitoring and correcting defocus drift caused by software malfunctions or stage crashes. Alignment Tests verify the functionality of the machine's internal alignment system by assessing the precision with which the laser writes complimentary patterns based on camera-read substrate patterns. Any misalignments are quantified, and correction factors are calculated. Finally, Resist Characterization involves empirically determining optimal exposure doses for various resists, populating a database that future users can access for efficient and accurate material processing.

Summary of Research:

My research on the Heidelberg MLA 150 has been focused around three main tests/areas: Dose and Defocus Tests, Alignment Test, and Resist Characterization. The purpose of Dose and Defocus Tests is to determine the optimal Dose and Defocus for the machine to operate. Dose is a measure of the nominal energy used to expose the substrate, while defocus is a measure of the position of the machine's laser optics. We can determine the most optimal combination of dose and defocus by exposing test patterns at various dose and defocuses and reading the resolutions of the tests. Attention is focused on the Defocus, as it is much more likely to drift due to software malfunctions and stage crashes. As a result of these crashes, Dose and Defocus Tests must be carried out regularly to ensure that the optimal dose and defocus values are known. The purpose of Alignment Tests is to ensure that the alignment system within the machine is working properly, by loading a substrate that contains patterns spread around that may be read by a camera within the machine. The camera sends the information to the alignment system, which relays to the laser where it believes the substrate and staging is, which then writes a complimentary pattern to the original pattern on the substrate. We read how well the two patterns fit together, which tells us whether the alignment system is working properly [2]. Oftentimes, the alignment is not perfect, and we are able to calculate a correction factor to input into the machine by reading the offsets of the patterns. The rest of the time on the Heidelberg MLA 150 was spent on Resist Characterization. By testing a large range of doses on various resists, we were able to determine the optimal doses for many resists that we add to a database that future users may access and quickly determine the optimal dose to expose at.

Conclusions and Future Steps:

Dose and Defocus Tests and Alignment Tests must be regularly conducted due to stage crashes and other natural shifts. These ensure that users are always exposing at the most optimal dose and defocus and that the alignment system is working properly. Besides these tests, the database for Resist Characterization may always be added upon, and future time should be spent characterizing a larger selection of resists.

Acknowledgements:

Special thanks go out to Giovanni Sartorello for his support and mentorship throughout this internship. I would also like to acknowledge the Cornell NanoScale Facility for hosting this experience. This work was funded by a grant from NORDTECH.

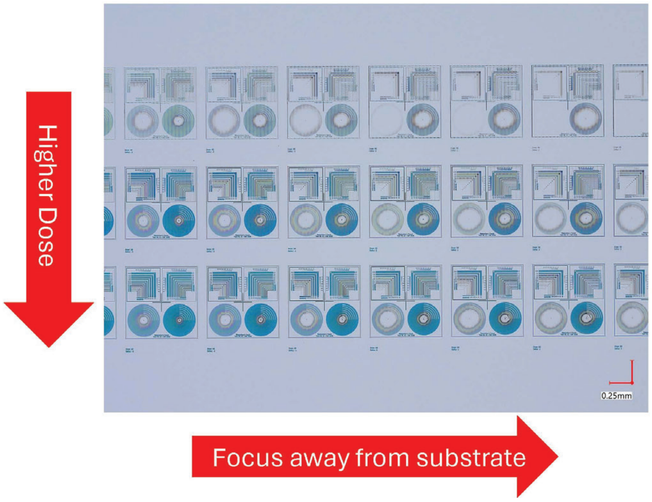

Figure 1: Dose and Defocus Test on a Wafer Coated in S1805.

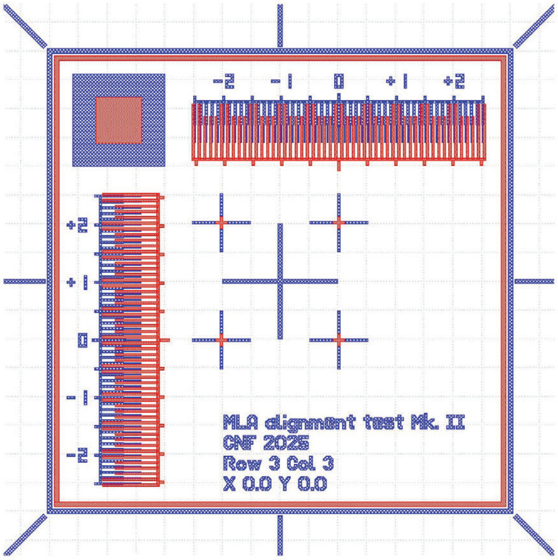

Figure 2: Alignment Test gds File.

Redistribution Layers on Glass Wafers

CNF Project Number: 3018-22
Principal Investigator(s): Shelby Nelson
User(s): Nick Stucchi

Affiliation(s): Mosaic Microsystems, LLC

Primary Source(s) of Research Funding: U.S. Department of Defense (DOD), Customer Contracts

Contact: Shelby.Nelson@mosaicmicro.com, Nick.Stucchi@mosaicmicro.com

Research Group Website: Website: https://www.mosaicmicro.com/

Primary CNF Tools Used: ABM Mask Aligner, AJA Sputter System(s), Bruker DektakXT Profilometer, CHA Mark 50 E-beam Evaporator, Class 1 Photolithography Spinners, Class 2 Photolithography Spinners, GCA AS200 Stepper, Hamatech Wafer Processor(s), Heidelberg MLA 150 Maskless Aligner, Oxford 82 RIE, Oxford PECVD, PT 720-740 RIE, YES Asher

Abstract:

Glass substrates have excellent electrical and mechanical properties which have led to an increasing interest for their use in advanced microelectronic and photonic packaging applications. Glass substrates offer a very low loss tangent at GHz frequencies, while being moisture insensitive and dimensionally stable. This work outlines a novel approach for fabrication of interposers using thin glass (200 micron and below), normally difficult to handle in standard processes. The process yields void-free, hermetic, copper-filled precision through glass vias (TGVs), along with redistribution layer (RDL) fabrication with up to three metal redistribution layers per side. Furthermore, Mosaic Microsystems is developing various methods to integrate photonic waveguides with thin glass interposers to match high-speed electronics packaging with high-speed photonic communication.

Summary of Research:

Due to Mosaic's patented Viaffirm® bonding technology it is possible to process 100 mm, 150 mm, and 200 mm thin glass wafers with the conventional silicon processing equipment at the CNF. RDL fabrication utilizes the photoresist spinners and the ABM Mask Aligner for contact alignment or the GCA AS200 Stepper for features that require near micron resolution. Electron-beam evaporation of various metal layers has been performed using the CHA Mark 50 E-beam Evaporator.

In addition, our team uses the Hamatech HMx900s auto wafer developers to develop double layer liftoff resist structures applied at CNF. Analysis tools at CNF such as the Filmetrics F50 and Keyence microscope aid in resist and final pattern analysis.

Conclusions and Future Steps:

We have successfully fabricated multi-layer RDL thin glass interposers. Our more recent work has focused on the fabrication of highly precise thin film resistors as well as microfluidic channels incorporated into the thin glass interposer. For the future, we will continue to improve upon our processes at CNF to deliver upon our customer's needs. We will also continue to develop methods of incorporating photonic waveguides with the thin glass interposers, of which key elements will occur at CNF.

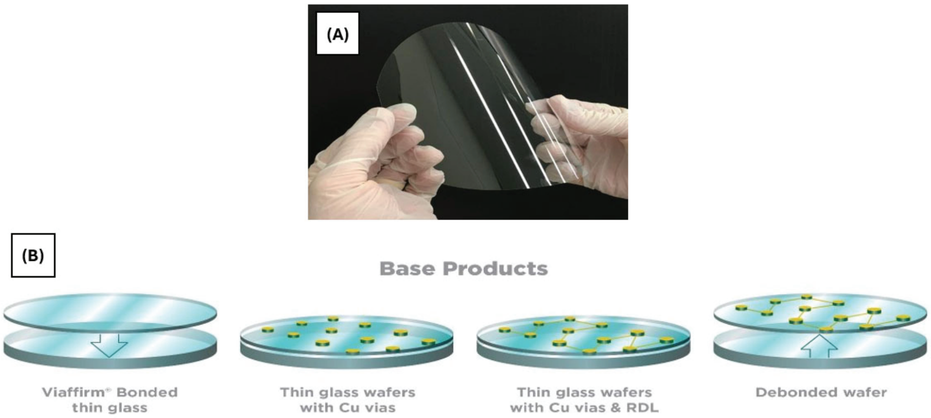

Figure 1: (A) Demonstration of the flexibility of thin glass. (B) Schematic outlining Mosaic's robust Viaffirm® bonding process.

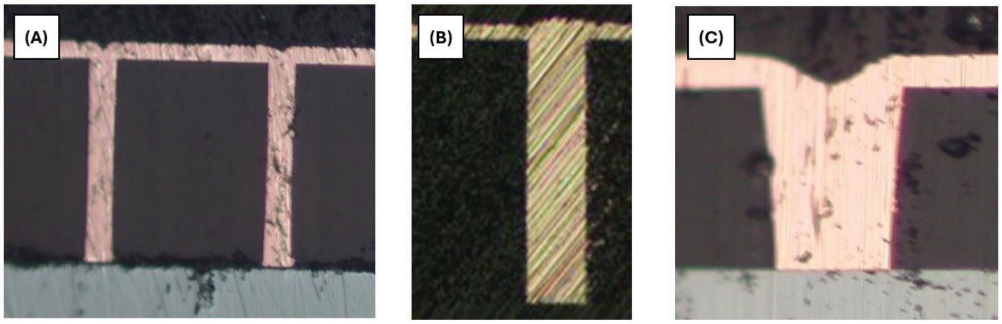

Figure 2: Cross-sections of fully filled copper vias with varying shapes and diameters. (A) 15 µm columnar via, (B) 25 µm columnar via, and (C) 35 µm tapered via.

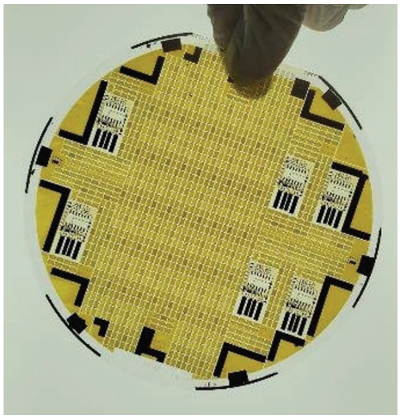

Figure 3: Example of a fully fabricated thin glass interposer with through glass vias and multiple redistribution layers.

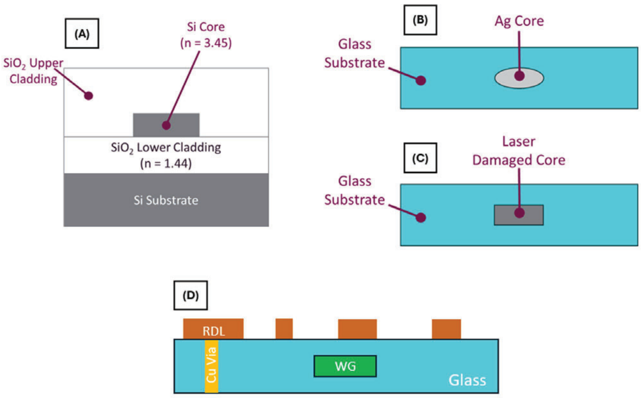

Figure 4: Schematic of various photonic waveguides. (A) Traditional silicon waveguide, (B) Ion-exchange waveguide, (C) Ultrafast laser inscription waveguide, and (D) Integration of electrical and optical communication.

electrical and optical communication.

Metal-Containing Resists for Extreme Ultra Violet

CNF Project Number: 3108-23

Principal Investigator(s): Robert L. Brainard

User(s): Munsaf Ali, Moira Niluxsshun, Harry Weinstein, Stephen Smith, Ryan Chae

Affiliation(s): Department of Nanoscale Science and Engineering, University at Albany, SUNY; Samsung-SDI

Primary Source(s) of Research Funding: Samsung-SDI

Primary Source(s) of Research Funding: U.S. Department of Defense (DOD), Customer Contracts

Contact: rbrainard@albany.edu, mali5@albany.edu, mniluxsshun@albany.edu, hgweinstein@albany.edu, ssmith30@albany.edu, ryan.chae@samsung.com

Primary CNF Tools Used: JEOL E-beam 6300, Woollam RC2 Spectroscopic Ellipsometer, Zeiss Supra SEM, Zeiss Ultra SEM

Abstract:

Since 2011, our group has developed Extreme Ultra Violet photoresists composed of amorphous thin-films of compounds containing tin, cobalt, platinum, palladium, bismuth and antimony in our project called Molecular Organometallic Resists for EUV (MORE).1-9 This project focuses on the development and characterization of metal-containing photoresist platforms for Extreme Ultra Violet lithography applications. Our goal is to develop materials suitable for both positive- and negative-tone EUV resists and E-beam resists. We leveraged Cornell Nanoscale Facility's nanofabrication and characterization capabilities to carry out E-beam lithography and SEM analysis of these platforms.

Summary of Research:

Platform Selection: Focus on Reproducibility

We prioritized work on organo-metallic resists, which showed promising initial results but suffered from reproducibility issues. Addressing this is foundational to ensuring consistent performance in both academic research and industrial integration.

CNF Usage and Progress

Between August 2024 and June 2025, we conducted multiple visits to CNF, steadily increasing the productivity of each session:

Imaging Trips Schedule

- CNF 3: Aug 12, 2024
- CNF 4: Oct 2, 2024
- CNF 5: Jan 13, 2025
- CNF 6: Apr 1, 2025
- CNF 7: Jun 25, 2025

Over time, our group; Increased participation (from 2 to 4 researchers per trip), conducted process planning meetings beforehand, reduced screening of new platforms in favor of optimizing high-performing candidates, improved familiarity with lithography and SEM tools

A significant improvement came from reducing beam current from 10 nA to 1 nA, dramatically increasing pattern fidelity and visibility via SEM and optical microscopy.

Technical Achievements

- Developed contrast curve data across several resist formulations (Figure 2).
- Achieved high-resolution imaging of both positive- and negative-tone resists
- Increased resolution from 50 nm to 20 nm using the JEOL 6300
- Demonstrated excellent line edge roughness (LER) in optimized formulations
- Used RC2 ellipsometry to monitor film thickness pre- and post-development

Figure 3 and Figure 4 present representative SEMs of successful patterns, showing clear resolution improvement.

Conclusions and Future Steps:

Our CNF trips became increasingly effective as the team-built process familiarity and focused on materials with the most promise. Key future work includes:

- Continued reproducibility studies of organo-molecular resists
- Further dose optimization and LER analysis
- Testing of various development protocols on positive and negative tone resist platforms
- Continued e-beam lithography and SEM imaging of optimized resists

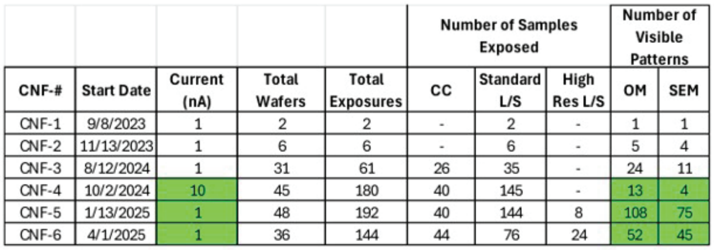

					Number of Samples Exposed			Number of Visible Patterns	
CNF-#	Start Date	Current (nA)	Total Wafers	Total Exposures	CC	Standard L/S	High Res L/S	OM	SEM
CNF-1	9/8/2023	1	2	2	-	2	-	1	1
CNF-2	11/13/2023	1	6	6	-	6	-	5	4
CNF-3	8/12/2024	1	31	61	26	35	-	24	11
CNF-4	10/2/2024	10	45	180	40	145	-	13	4
CNF-5	1/13/2025	1	48	192	40	144	8	108	75
CNF-6	4/1/2025	1	36	144	44	76	24	52	45

Figure 1: Shows lists experimental details from each visit.

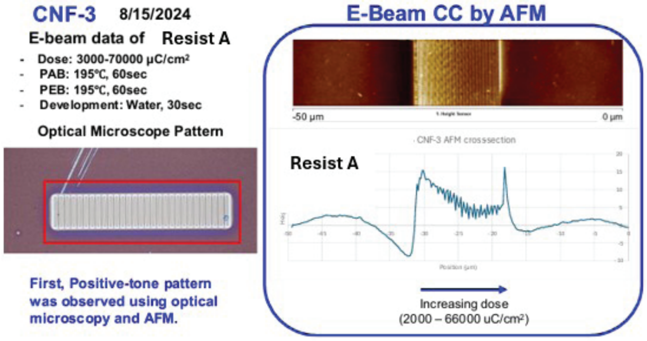

CNF-3 8/15/2024

E-beam data of Resist A

- Dose: 3000-70000 μC/cm²
- PAB: 195℃, 60sec
- PEB: 195℃, 60sec
- Development: Water, 30sec

Optical Microscope Pattern

First, Positive-tone pattern was observed using optical microscopy and AFM.

E-Beam CC by AFM

Figure 2: Positive-tone pattern Observed using optical microscope and AFM.

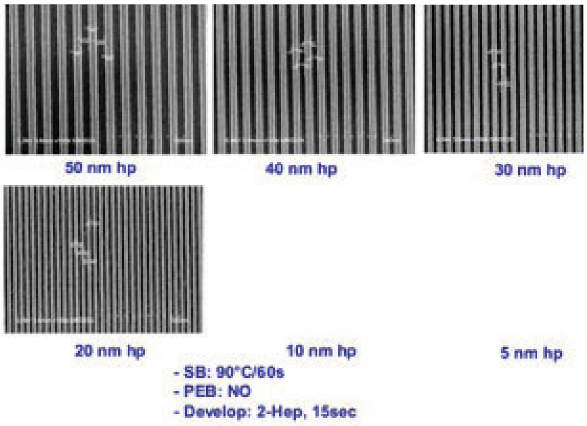

- SB: 90°C/60s
- PEB: NO
- Develop: 2-Hep, 15sec

Figure 3: SEM image of negative tone resist B at 20 nm resolution (non-confidential)

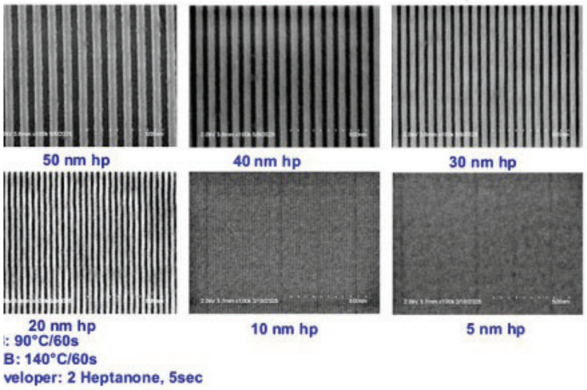

: 90°C/60s
B: 140°C/60s
veloper: 2 Heptanone, 5sec

Figure 4: SEM image of negative tone resist B at 20 nm resolution (non-confidential)

References:

[1] M. Sortland, J. Hotalen, R. Del Re, J. Passarelli, M. Murphy, T. S. Kulmala, Y. Ekinci, M. Neisser, D. A. Freedman, and R. L. Brainard, “Platinum and palladium oxalates: positive-tone extreme ultraviolet resists,” J. Micro. Nanolithogr. MEMS MOEMS, 14 (2015) 043511.

[2] M. Wilklow-Marnell, D. Moglia, B. Steimle, B. Cardineau, H. Al-Mashat, P. Nastasi, K. Heard, A. Aslam, R. Kaminski, M. Murphy, R. Del Re, M. Sortland, M. Vockenhuber, Y. Ekinci, R. L. Brainard, D. A. Freedman, “First-row transitional-metal oxalate resists for EUV,” J. Micro/Nanolith. MEMS MOEMS, 17 (4) (2018) 043507.

[3] B. Cardineau, R. Del Re, M. Marnell, H. Al-Mashat, M. Vockenhuber, Y. Ekinci, C. Sarma, D. Freedman, R. Brainard, “Photolithographic properties of tin-oxo clusters using extreme ultraviolet light (13.5 nm),” Microelectronic Engineering 127, 44-50 (2014).

[4] R. Del Re, J. Passarelli, M. Sortland, B. Cardineau, Y. Ekinci, E. Buitrago, M. Neisser, D. A. Freedman, and R. L. Brainard, ”Low-line edge roughness extreme ultraviolet photoresists of organotin carboxylates”, J. Micro/Nanolith. MEMS MOEMS 14(4), 043506 (2015).

[5] M. Wilklow-Marnell, D. Moglia, B. Steimle, B. Cardineau, H. Al-Mashat, P. Nastasi, K. Heard, A. Aslam, R. Kaminski, M. Murphy, R. Del Re, M. Sortland, M. Vockenhuber, Y. Ekinci, R. L. Brainard, D. A. Freedman, "First-row transitional-metal oxalate resists for EUV," J. Micro/Nanolith. MEMS MOEMS 17(4), 043507 (2018).

[6] J. Passarelli, M. Sortland, R. Del Re, B. Cardineau, C. Sarma, D. Freedman, R. Brainard; “Bismuth resists for EUV lithography,” J. Photopolym. Sci. Technol. 27(5), 655-661 (2014).

[7] J. Passarelli, M. Murphy, R. Del Re, M. Sortland, J. Hotalen, L. Dousharm, Y. Ekinci, M. Neisser, D. Freedman, R. Fallica, D. A. Freedman, R. L. Brainard, "Organometallic carboxylate resists for extreme ultraviolet with high sensitivity," J. Micro/Nanolith. MEMS MOEMS 14(4), 043503 (2015).

[8] M. Murphy, A. Narasimhan, S. Grzeskowiak, J. Sitterly, P. Schuler, J. Richards, G. Denbeaux, R. L. Brainard; "Antimony photoresists for EUV lithography: mechanistic studies"; Proc. SPIE, 10143, EUVL, 1014307 (2017).

Electrospray Propulsion Time-of-Flight Secondary Ion Mass Spectrometry Diagnostic

CNF Project Number: 3242-25

Principal Investigator(s): Elaine Petro

User(s): Giuliana Hofheins

Affiliation(s): Sibley School of Mechanical & Aerospace Engineering, Cornell University

Primary Source(s) of Research Funding: ASA Space Technologies Graduate Research Opportunities Fellowship (NSTGRO)

Primary Source(s) of Research Funding: U.S. Department of Defense (DOD), Customer Contracts

Contact: emp245@cornell.edu, gch72@cornell.edu

Research Group Website: https://www.astralab.mae.cornell.edu

Primary CNF Tools Used: C4500 Odd-Hour Evaporator, Zygo Optical Profilometer, AJA Sputter

Abstract:

Electrospray thrusters are electric propulsion systems offering exceptional thrust-to propellant weight efficiency in scalable form factors. However, system lifetimes are constrained by ion plume interception of downstream electrodes, where high-energy impacts (>1 keV) cause sputtering and secondary ion emission. These secondary ions indicate electrode degradation and electrochemical processes that limit system longevity. An electrospray propulsion secondary ion mass spectrometry diagnostic was developed to investigate ion plume-surface interactions across operational parameters. The system features a single, externally-wetted tungsten ion source with ionic liquid propellants, electron beam-evaporated metallic targets, and linear time-of-flight mass spectrometry. Silver target impacts demonstrate clear target sputtering through detection of silver and silver cluster ions, alongside propellant-related secondary ion markers, enabling comprehensive characterization of lifetime-limiting mechanisms.

Summary of Research:

Electric space propulsion systems generate thrust by accelerating propellant through electric and magnetic fields, offering superior fuel efficiency compared to chemical propulsion since exhaust velocity depends on applied power rather than chemical bond energy constraints [1].

Electrospray micropropulsion thrusters utilize electrostatic fields to extract and accelerate charged particles from liquid propellant at sharp emitter tips [2,3]. When kilovolt-level potentials are applied between the emitter and downstream extractor electrode, surface tension, electric, and hydrodynamic stresses form a Taylor cone. This induces ion emission through field emission evaporation, accelerating ions to velocities exceeding 10,000 m/s and generating thrust ranging from nanonewtons to micronewtons per emitter [4,5].

Many electrospray devices employ chemically complex room temperature ionic liquids (RTILs) as propellants, comprising organic cations and anions such as 1-ethyl-3- methylimidazolium tetrafluoroborate (EMI-BF4) and 1-ethyl-3-methylimidazolium bis(trifluoromethylsulfonyl)imide (EMI-Im) [6,7]. These propellants are attractive for their nonvolatile properties and bipolar operation capability, eliminating external neutralizer requirements. This combination makes RTIL electrospray thrusters ideal for missions requiring efficient, compact, low-mass, and low-power propulsion systems [8].

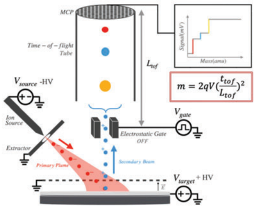

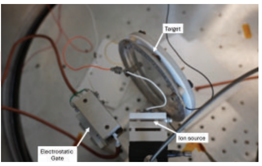

Figure 1 (left): Schematic of the electrospray propulsion TOF-SIMS diagnostic, where the ion source directs the ionic liquid primary beam at the target, where secondary ion emission is induced and directed toward the electrostatic gate and time-of-flight system with an MCP detector. The polarities of the two ion beams are reversed to collect negative secondary ions.

Figure 2 (right): The diagnostic as installed in the vacuum testing facility, including the ion source, the target created via e-beam evaporation, and the electrostatic gate portion of the linear time-of-flight spectrometer.

High-energy electrospray plume impacts (>1 keV) induce target surface sputtering, producing secondary ions that interact with electrostatic fields during thruster operation and testing [11]. Understanding their chemical composition is crucial for system performance characterization [12].

A novel electrospray time-of-flight secondary ion mass spectrometry (ESI TOF-SIMS) diagnostic was developed to characterize plume-surface interactions, as shown in Figure 1 and Figure 2. The experimental design features: (a) a tungsten single emitter primary electrospray ion source externally wetted with ionic liquid, (b) a high-voltage target assembly with secondary ion acceleration grid, (c) an electrostatic deflection gate, (d) a time-of-flight tube, and (e) a microchannel plate detector [13].

The primary molecular ion plume impacts a target surface at controlled incidence angles with energies dependent on source and target potentials. High-energy impacts remove secondary electrons, atoms, molecules, and ions from the target surface. Secondary ions of selected polarity are extracted via potential differences between the high-voltage target and grounded acceleration grid, creating a single-polarity, approximately monoenergetic beam that passes through the pulsed electrostatic deflection gate and down the linear time-of-flight tube to the detector.

The target consists of a 100 mm diameter silicon wafer with 100 nm silver deposition via e-beam evaporation using the CNF CVC4500 evaporator. Silver was selected for its two readily identifiable isotopes (^{107}Ag and ^{109}Ag) with nearly equal natural abundances, providing ideal detection and calibration capabilities. Atomically flat, uniform metallic surfaces ensure consistent SIMS signals, as surface topology variations can compromise analysis reliability.

Initial positive secondary ion analysis from a negative electrospray plume impacting a silver target is shown in Figure 3. This spectrum resolves numerous species below 100 amu, notably the hydrogen cation, boron isotopes, and numerous spectral 'families' depicting hydrocarbon-related peaks related to the organic primary impacting ions and/or oil contamination. In addition, peaks at 107, 109, 216 and 324 amu indicate sputtering of the target through detection of silver isotopes and silver cluster ions. Negative secondary ion spectra show the presence of fluorine ion in addition to cyanide and hydrocarbon ions. Initial results show multiple, distinct secondary species that not only prove the capability of the diagnostic but reveal secondary ions that limit the lifetime of electrospray systems [13,14].

Recent work has focused on analyzing secondary ions that form with propellant thin films as the target. The motivation for such work is due to the fact that over time, propellant accumulates on downstream electrodes in electrospray thruster systems. Therefore, at a certain point the secondary ions formed from propellant overspray is independent of the electrode material and entirely dependent on the accumulated propellant. This work has involved producing silver targets utilizing the CNF CVC4500 evaporator, spin coating these wafers with solvent/ionic liquid mixtures and bombarding the thin-film target in the ESI TOF-SIMS diagnostic and analyzing the secondary ions formed. Species from the baseline tests remain present (H+, B+, CnHm+), with additional features that mark the presence of the ionic liquid including the imidazole ring at 83 amu and the imidazole ring with the methyl chain at 96 amu, and most notably the full primary ion cation detection at 111 amu.

Post processing of the thin-film silver target by the Zygo optical profilometer at CNF, as shown in Figure 4, shows sputtering on the order of 100s of nm over the course of ~6 hour beam exposure to the target. The grid-like pattern is a product of the diagnostic mechanical setup, as the primary beam passes through a grounded transparent stainless-steel mesh that maintains the necessary electric fields before impacting the target. This information will be crucial in determining sputter rates moving forward.

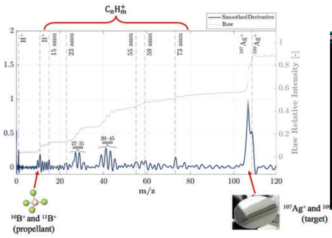

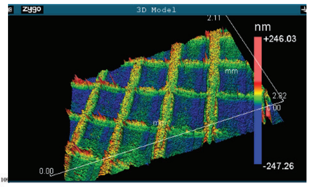

Figure 3 (left): Positive secondary ion mass spectrum from a 4 keV negative EMI-BF4 plume impact with an Ag target, out to 120 amu. The dominant peaks were the silver ion isotopes, with clear signs of the propellant through detection of boron isotopes.

Figure 4 (right): A 3D profile of the target after ion-plume bombardment over the course of 3 hours, showing the sputter depth due to beam exposure.

Conclusions and Future Steps:

A novel electrospray time-of-flight secondary ion mass spectrometry diagnostic successfully characterized plume-surface interactions in electrospray thrusters. Using a tungsten ion source with ionic liquid propellant under vacuum conditions, clear secondary ion emission in both polarities is confirmed, establishing the viability of electrospray TOF-SIMS for thruster analysis. Future work will determine secondary ion origins to distinguish target contamination from primary plume fragmentation, critical for separating intrinsic thruster effects from facility artifacts. Characterizing like-polarity secondary ions requires diagnostic modifications including acceleration stages and target biasing to overcome signal degradation below 2 keV. These enhancements will enable comprehensive analysis across varying operating conditions, propellants, and surfaces, providing insights into plume-surface interactions affecting spacecraft contamination and thruster performance.

References:

[1] D. M. Goebel, I. Katz, and I. G. Mikellides, Fundamentals of Electric Propulsion (John Wiley & Sons, 2023).

[2] P. C. Lozano, M. Martínez-Sánchez, and V. Hruby, "Electrospray propulsion," in Encyclopedia of Aerospace Engineering (John Wiley & Sons, Ltd, 2010).

[3] E. M. Petro, X. Gallud, S. K. Hampl, M. Schroeder, C. Geiger, and P. C. Lozano, J. Appl. Phys. 131, 193301 (2022).

[4] P. Lozano and M. Martínez-Sánchez, J. Colloid Interface Sci. 282, 415 (2005).

[5] X. Gallud and P. C. Lozano, J. Fluid Mech. 933, A43 (2022).

[6] J. K. Ziemer et al., in 2010 IEEE Aerospace Conference (IEEE, 2010), pp. 1–19.

[7] P. C. Lozano, B. L. Wardle, P. Moloney, and S. Rawal, MRS Bull. 40, 842 (2015).

[8] D. Krejci, F. Mier-Hicks, R. Thomas, T. Haag, and P. Lozano, J. Spacecr. Rockets 54, 447 (2017).

[9] N. M. Uchizono, A. L. Collins, C. Marrese-Reading, S. M. Arestie, J. K. Ziemer, and R. E. Wirz, J. Appl. Phys. 130, 143301 (2021).

[10] R. Bendimerad and E. Petro, J. Electr. Propul. 1, 27 (2022).

[11] P. Van der Heide, Secondary Ion Mass Spectrometry: An Introduction to Principles and Practices (John Wiley & Sons, Inc, 2014).

[12] N. M. Uchizono, C. Marrese-Reading, S. M. Arestie, A. L. Collins, J. K. Ziemer, and R. E. Wirz, Appl. Phys. Lett. 121, 074103 (2022).

[13] G.C. Hofheins, Ulibarri Z, Petro, E.M. Review of Scientific Instruments. 96, 063306 (2025)

[14] Hofheins, G. C., Sherman, H., Schaldenbrand, A., & Petro, E. M. (2025). Operating Conditions Parametric Study of Electrospray Propulsion Time-of-Flight Secondary Ion Mass Spectrometry Diagnostic. In AIAA SCITECH 2025 Forum (p. 2383).

Reports by CNF Principal Investigators & Users

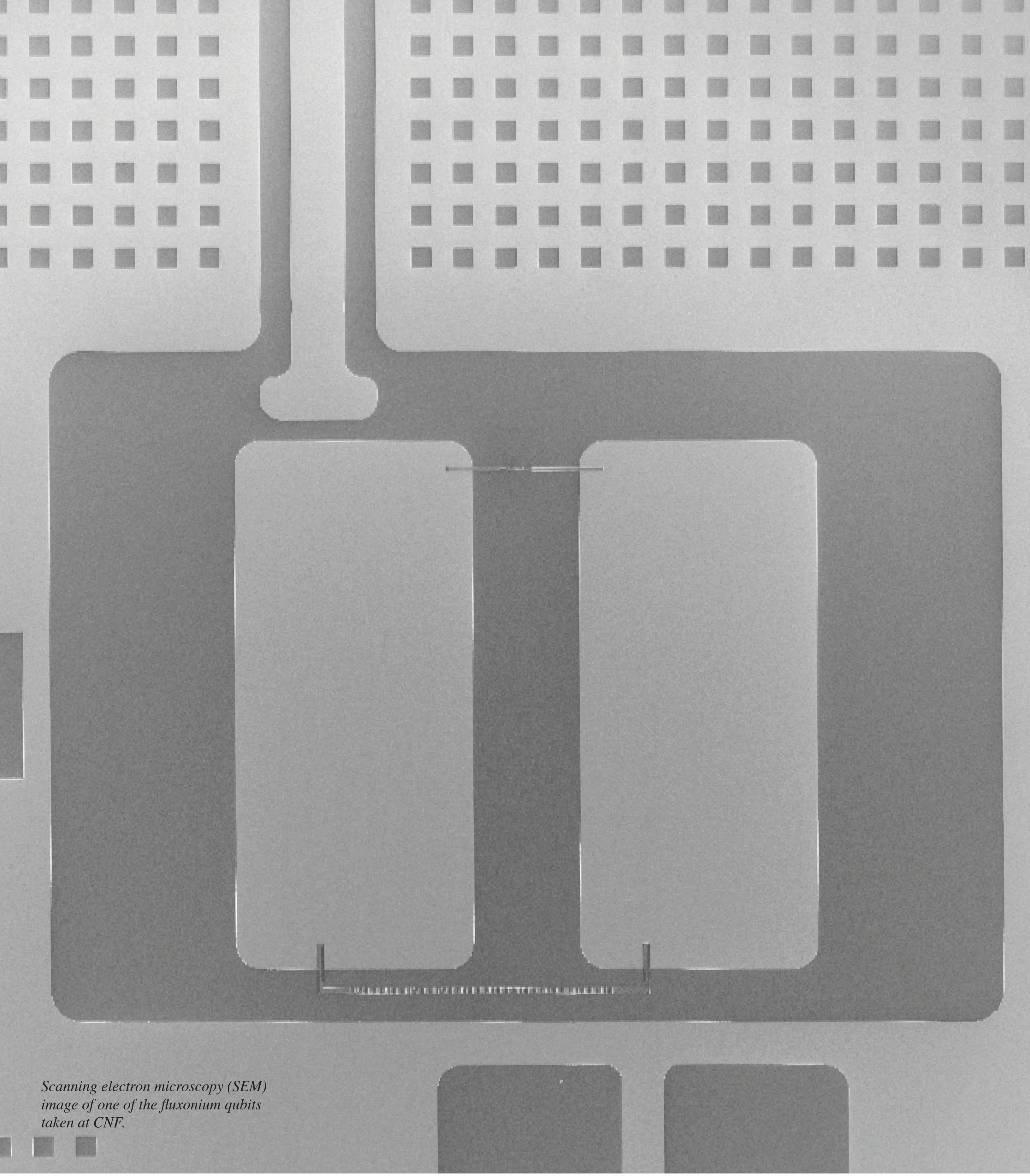

Scanning electron microscopy (SEM) image of one of the fluxonium qubits taken at CNF.

CNF is a member of the National Nanotechnology Coordinated Infrastructure (www.nnci.net) and is supported by the National Science Foundation under Grant No. NNCI-2025233, the New York State Empire State Development, Cornell University, Industry, and our Users.

The 2024-2025 CNF Research Accomplishments are also available on the web in http://cnf.cornell.edu/publications/research_accomplishments

CNF Cornell NanoScale Science and Technology Facility